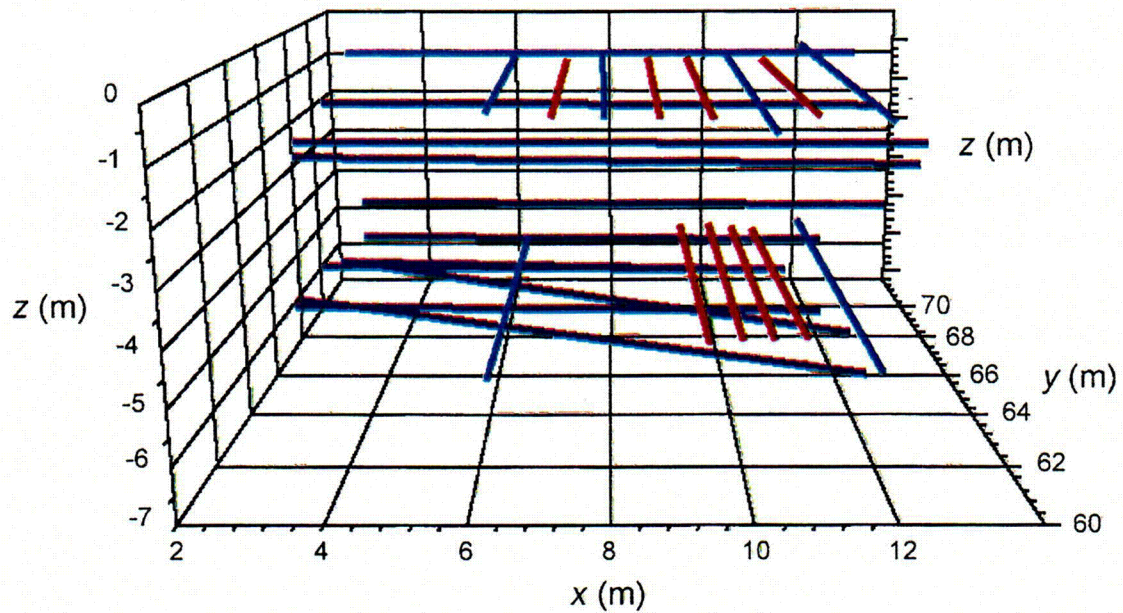


10.7-01.DOC.SITEDESC-R01

Source: CRWMS M&O (2000, Figure 34)

NOTE: This schematic of the Busted Butte unsaturated zone transport test shows the relative locations of the different experiment phases and borehole locations.

Figure 10.7-1. Busted Butte Unsaturated Zone Transport Test

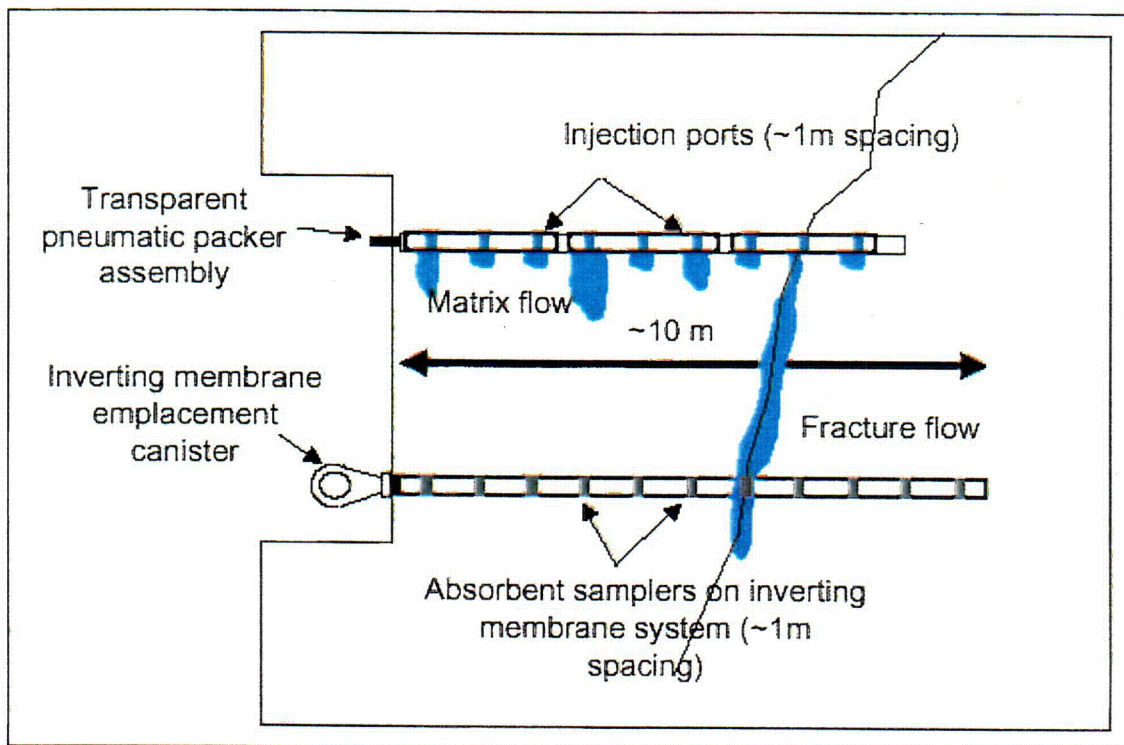


10.7-02.EPS.SITEDESC-R01

Source: CRWMS M&O (2000, Figure 87)

NOTE: The red lines represent injection boreholes, the dark blue lines collection boreholes, and the light blue lines are devoted to tomography. In this view, the Test Alcove is located in front of the figure, and the Main Adit is to the left of the figure (beyond the  $x = 2$  plane).

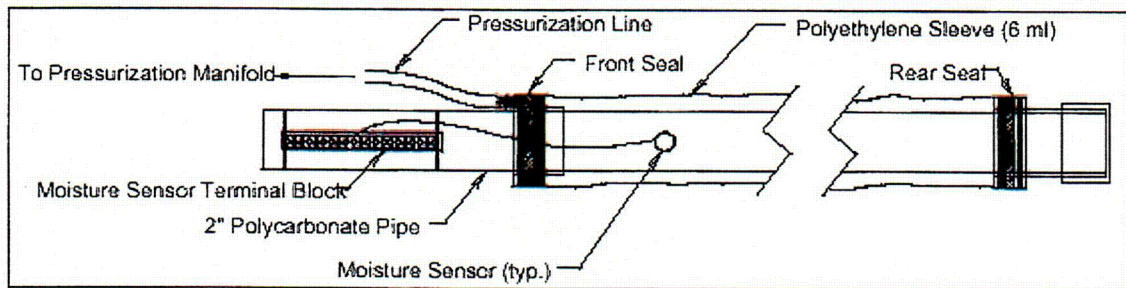
Figure 10.7-2. Three-Dimensional View of the Injection and Collection Boreholes



10.7.03.DOC.SIIEDESC R01

Source: CRWMS M&O (2000, Figure 35)

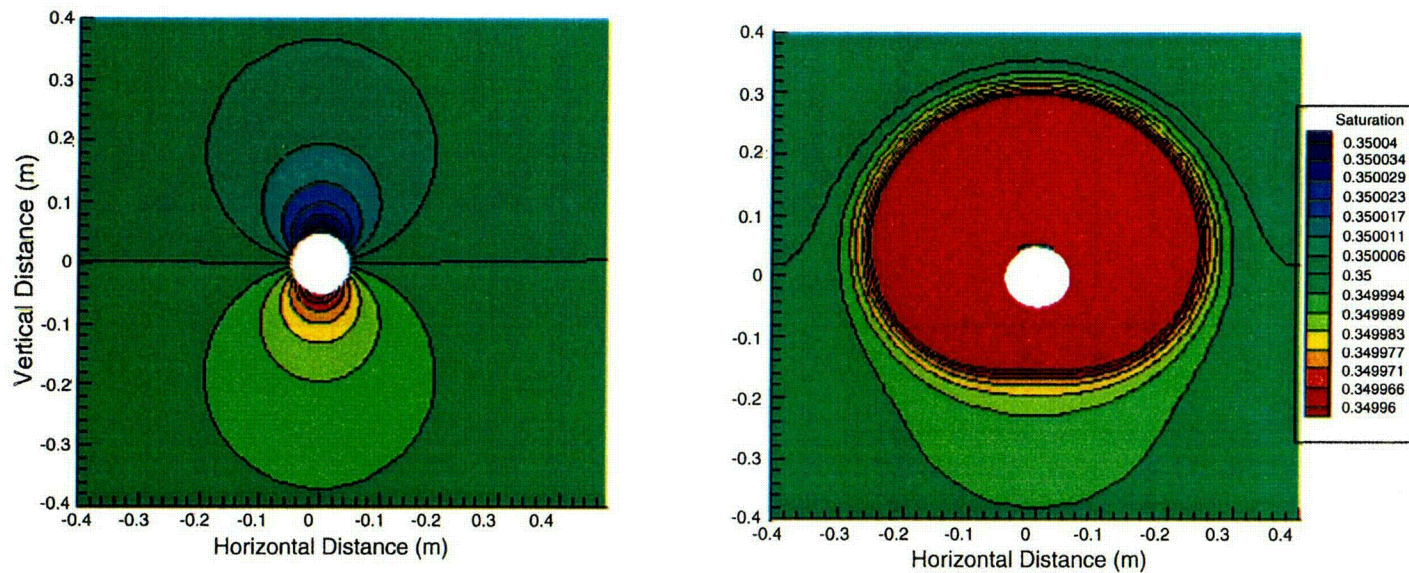
Figure 10.7-3. Injection and Collection System Configuration



F10.7-04.DOC.SITEDESC R01

Source: CRWMS M&O (2000, Figure 36)

Figure 10.7-4. Injection-System Transparent Packer

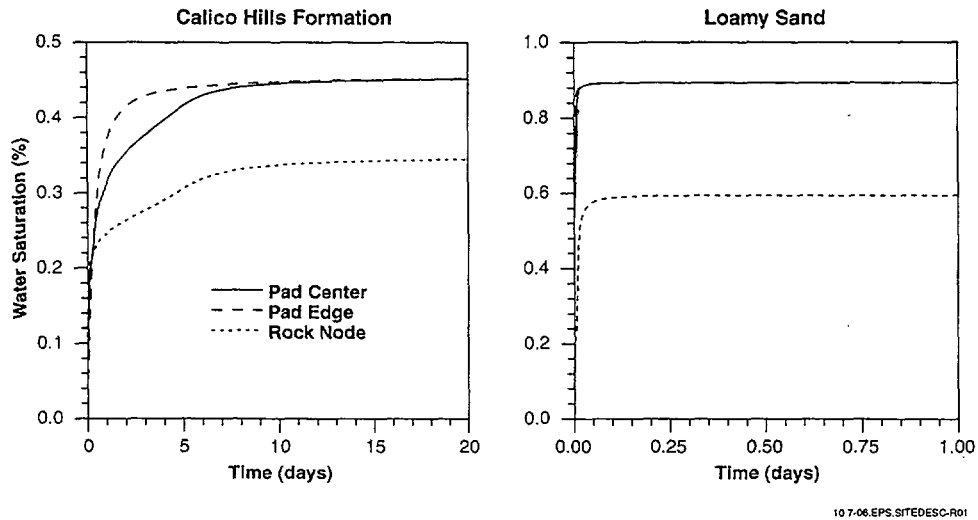


10.7-5.EPS.SITEDESC-R01

Source: CRWMS M&O (2000, Figure 39)

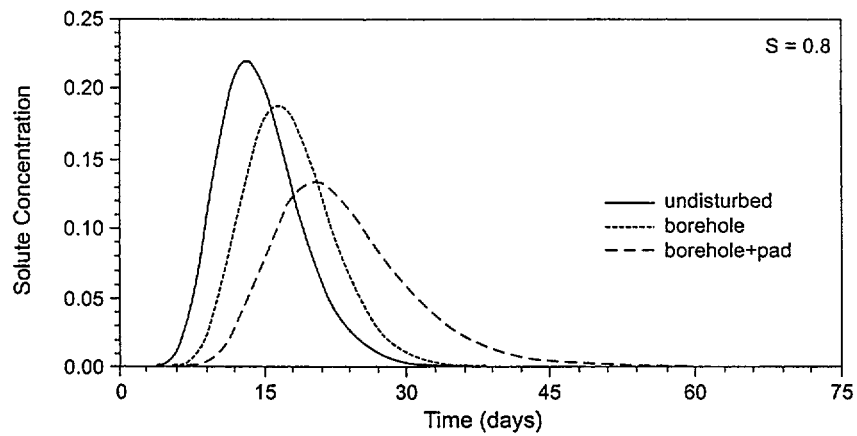
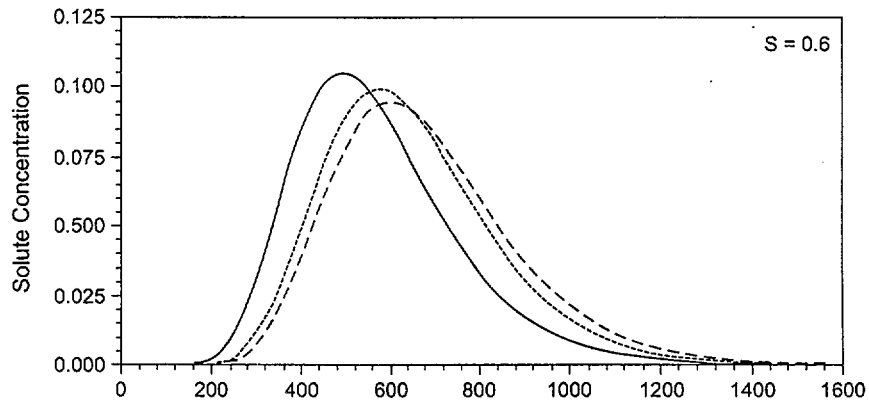
NOTE: The left frame shows the influence of a borehole, and the right frame shows the same condition with the addition of a pad.

Figure 10.7-5. Distributions of Saturation under Steady-State Water Flow Conditions within the Calico Hills Tuff



Source: CRWMS M&O (2000, Figure 40)

Figure 10.7-6. Water Saturation as a Function of Time for a New Pad Attached to the System

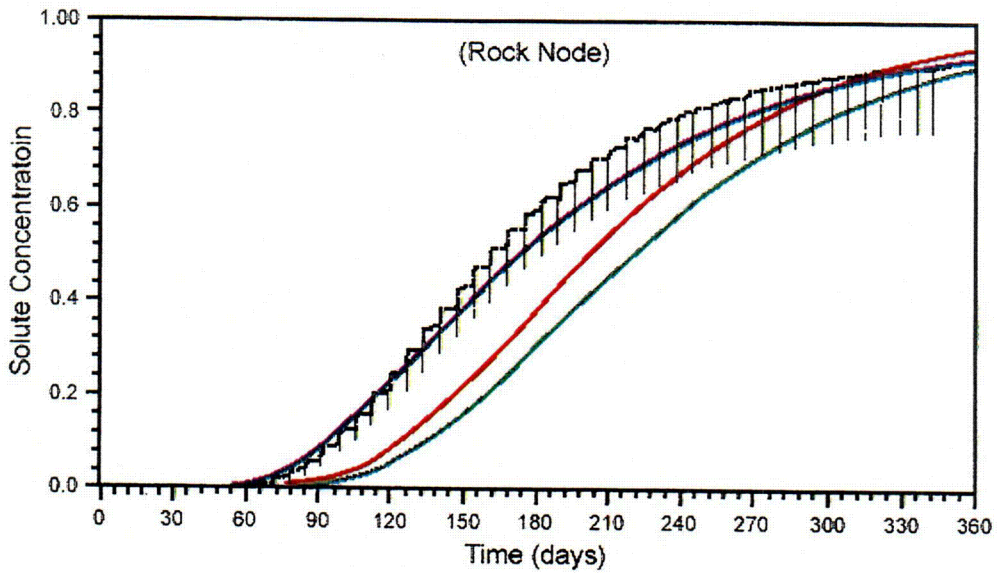
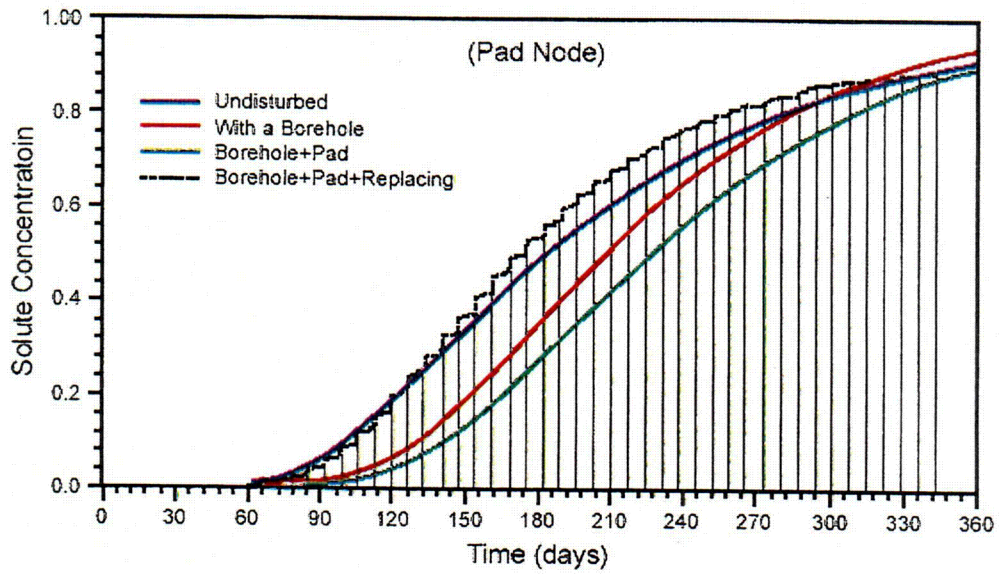


10.7-07.EPS.SITEDESC-R01

Source: CRWMS M&O (2000, Figure 41)

NOTE: The solute resident concentrations above were observed at a point corresponding to a position at the center of the pad during steady-state water flow conditions in Calico Hills Tuff.

Figure 10.7-7. Solute Resident Concentrations in Calico Hills Tuff

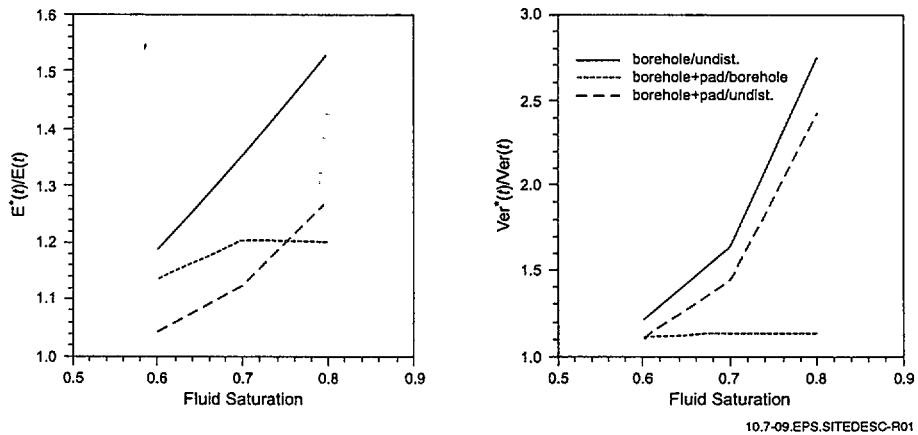


10.7-08.EPS.SITEDESC-R01

Source: CRWMS M&O (2000, Figure 42)

NOTE: A point injection of 10 mL/hr. was assumed, with a step input of solute located 30 cm above a collection pad.

Figure 10.7-8. Performance of a Collection Pad in Calico Hills Tuff

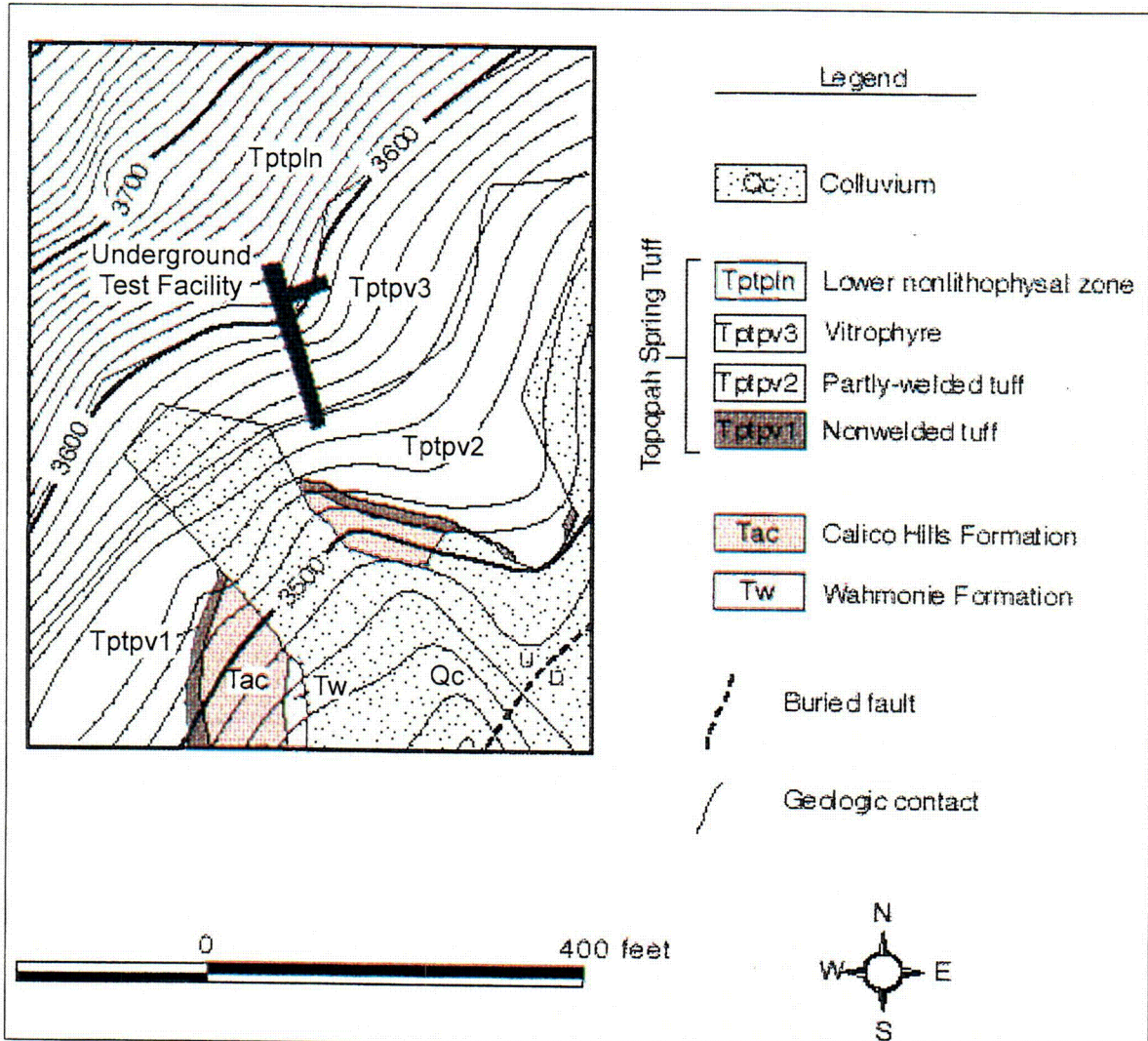


10.7-09.EPS.SITEDESC-R01

Source: CRWMS M&O (2000, Figure 43)

NOTE: The plots show influence of a borehole and a pad on (left) the dimensionless mean  $E^*(t)/E(t)$  and (right) the dimensionless variance  $Var^*(t)/Var(t)$  of solute travel times plotted as a function of fluid saturation for the Calico Hills Tuff.

Figure 10.7-9. Influence of Borehole and Pad on Solute Travel Times for Calico Hills Tuff

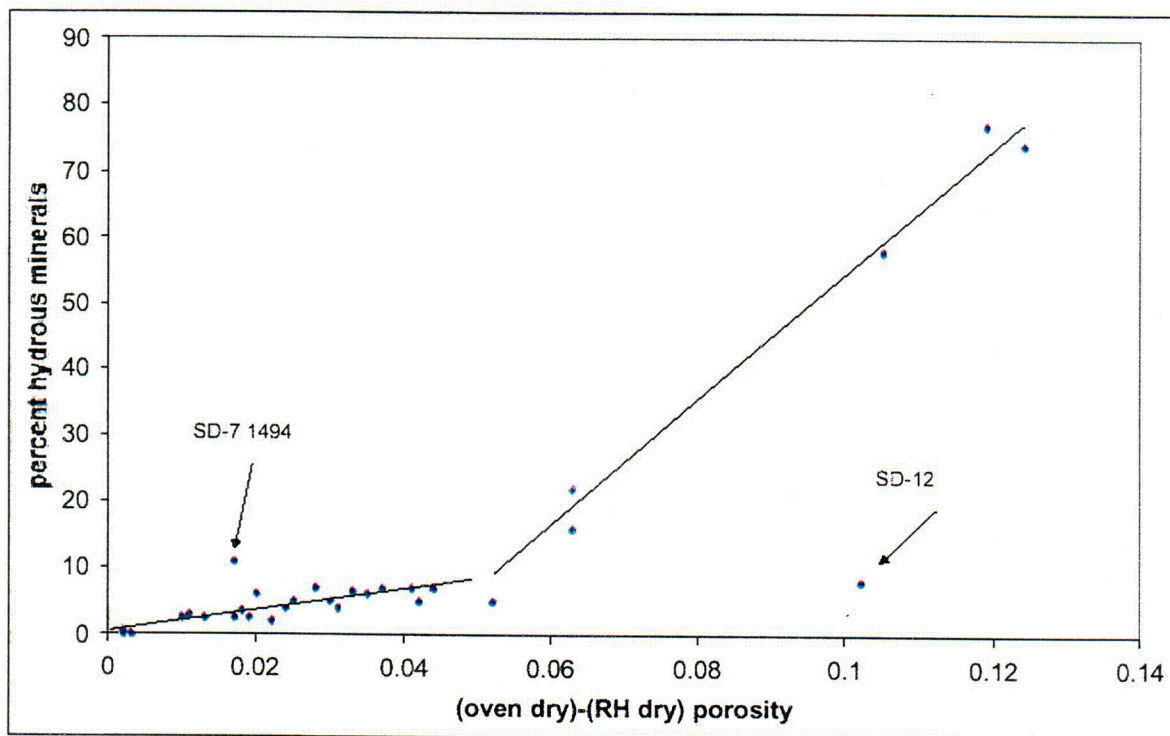


10.7-10.CDR.SITEDESC-R01

Source: CRWMS M&O (2000, Figure 44)

NOTE: The plot is a geologic map of the area around the underground test facility in the southeastern part of Busted Butte.

Figure 10.7-10. Busted Butte Geologic Map

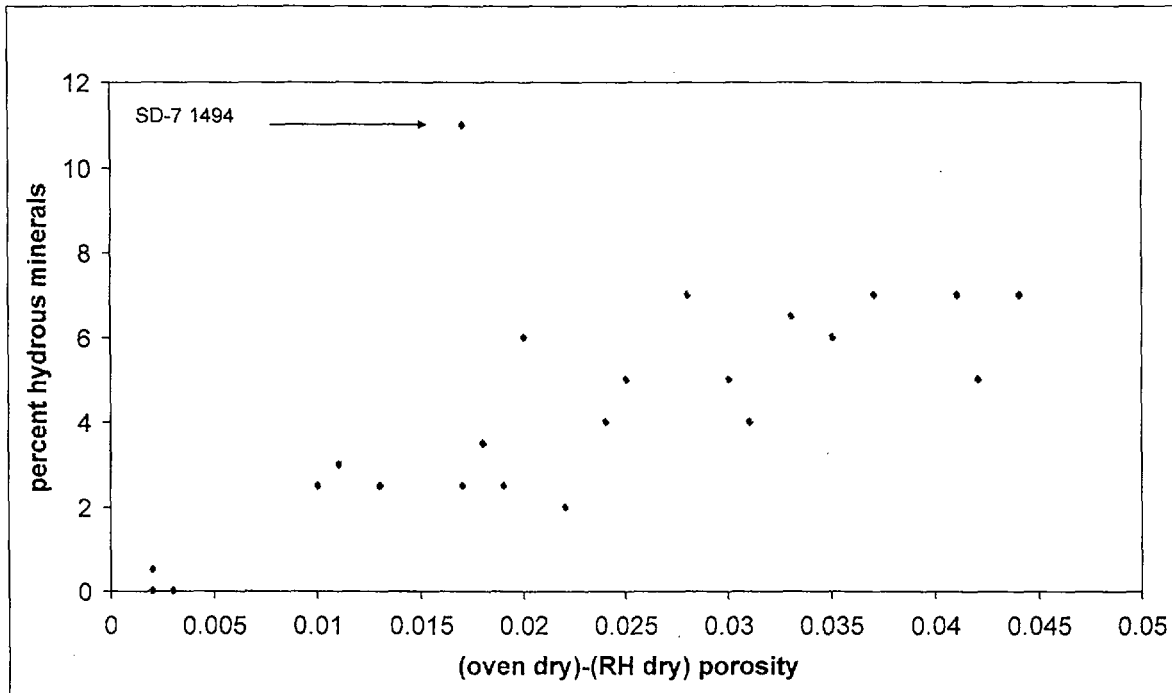


10.7-11.DOC.SITEDESC-R01

Source: Bussod (1998, Figure 15)

NOTE: RH = relative humidity (65%), oven-dried (60°C) porosity, oven-dry = 105°C oven-dried porosity.

Figure 10.7-11. Samples from the Vitric/Zeolitic Transition Zone (SD-7, 9, 12)



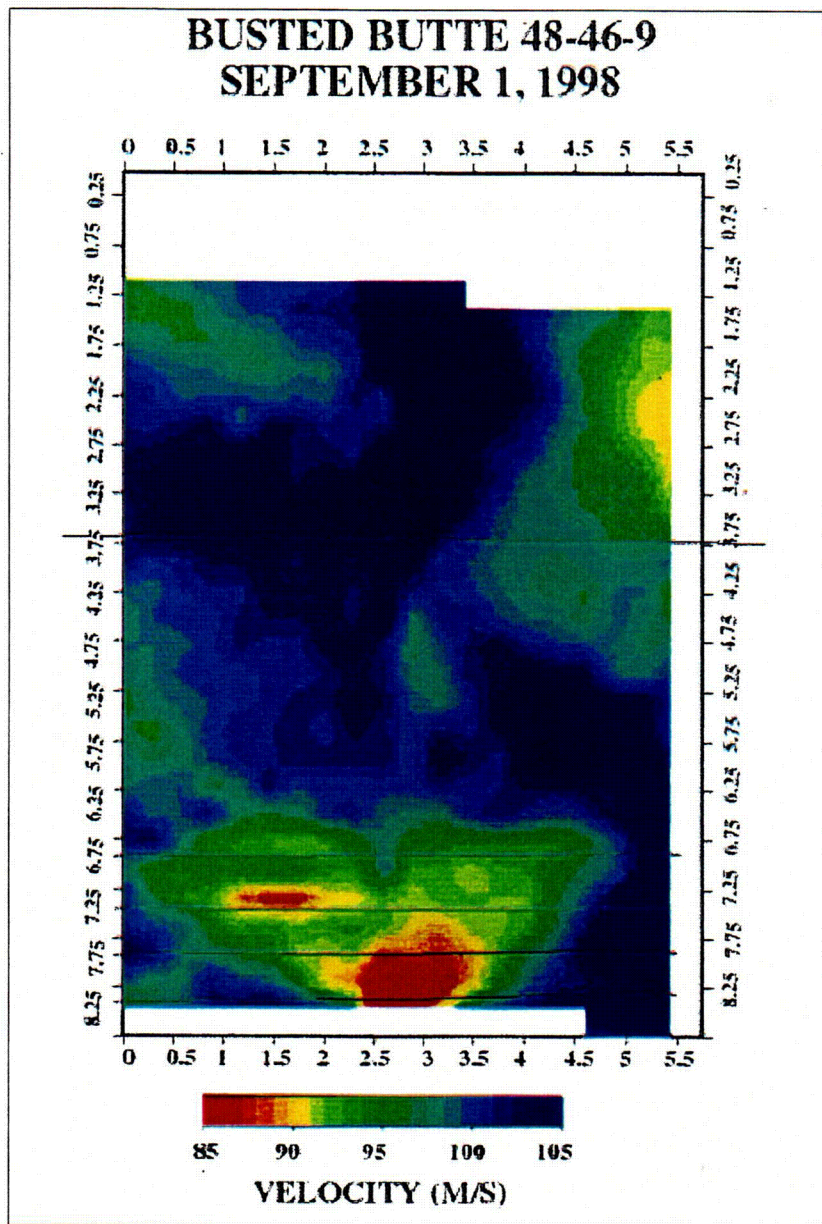
10.7-12.DOC.SITEDESC-R01

Source: Bussod (1998, Figure 16)

NOTE: RH = relative humidity (65%), oven-dried (60°C) porosity, oven-dry = 105°C oven-dried porosity.

Figure 10.7-12. Samples from the Vitric/Zeolitic Transition Zone (SD-7, 9, 12) with Delta Porosity Less than 0.05





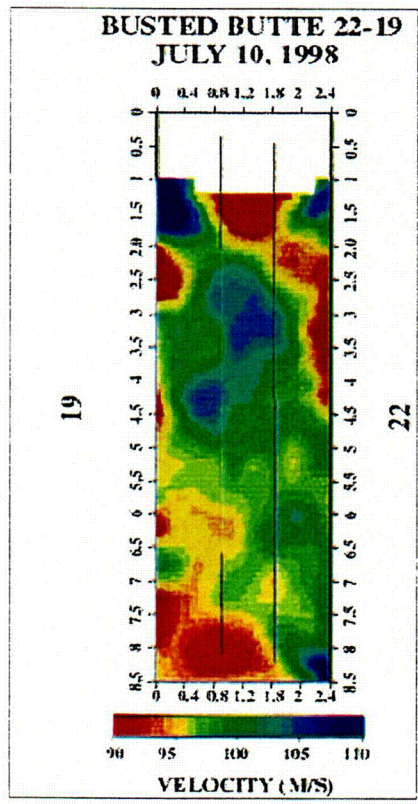
10.7-14.DOC.SITEDESC-R01

Source: Bussod (1998, Figure 20)

NOTE: The left axis represents the trace of borehole 48 and the right axis represents the trace of borehole 9. Borehole 46 is located between this pair at the 3-m position. The plot is a horizontal section with the top of the figure representing the right rib of the Main Adit. The four horizontal lines represent the trace of Phase-2B injection holes.

Figure 10.7-14. Ground-Penetrating Radar Pairs 48-46-9



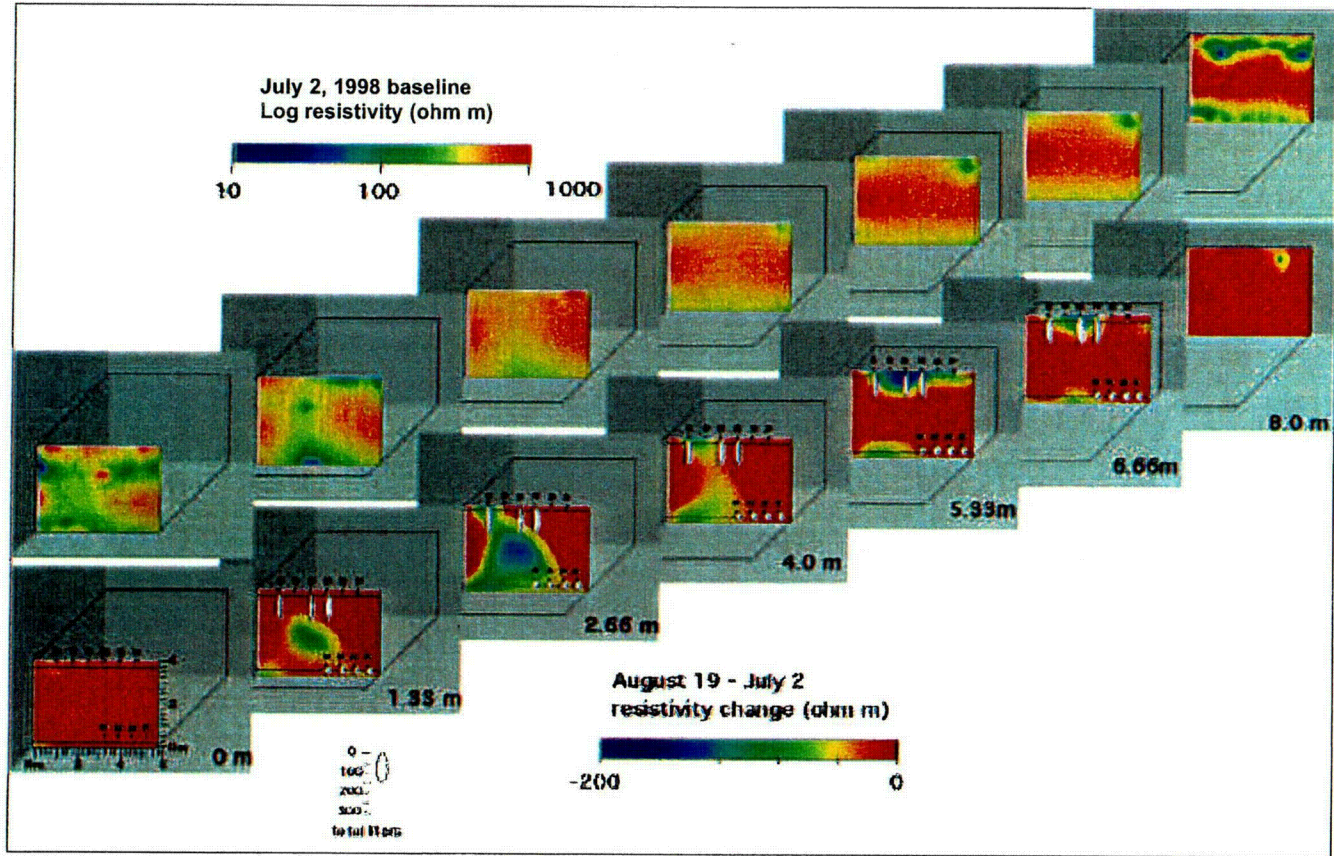


10.7-16.DOC.SITEDESC-R01

Source: Bussod (1998, Figure 22)

NOTE: The plot is a horizontal section with the top of the figure representing the left rib of the test adit. The vertical lines in the image represent, from left to right, the trace of injection holes 20 and 21 (Phase 2C).

Figure 10.7-16. Ground-Penetrating Radar Pair 22-19

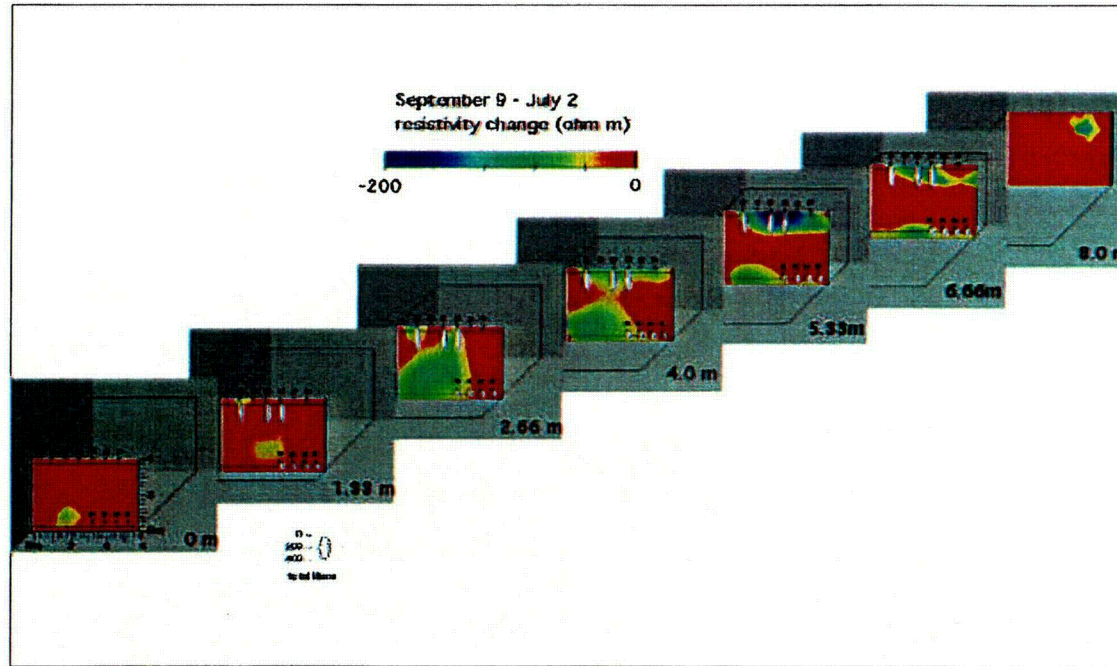


10.7-17.DOC.SITEDESC-R01

Source: CRWMS M&O (2000, Figure 55)

NOTE: The diagram shows vertical slices through block at 0, 1.33, 2.66, 4.0, 5.33, 6.66, and 8.0 m. The top series is an absolute image (baseline, July 2), and the bottom series is the August 19 to July 2 difference images. Illegibility of numerical scale of axes in bottom series does not affect illustrative purpose of figure.

Figure 10.7-17. Electrical Resistance Tomography Images of Test Block Viewed from Test Alcove: Baseline and August Differences



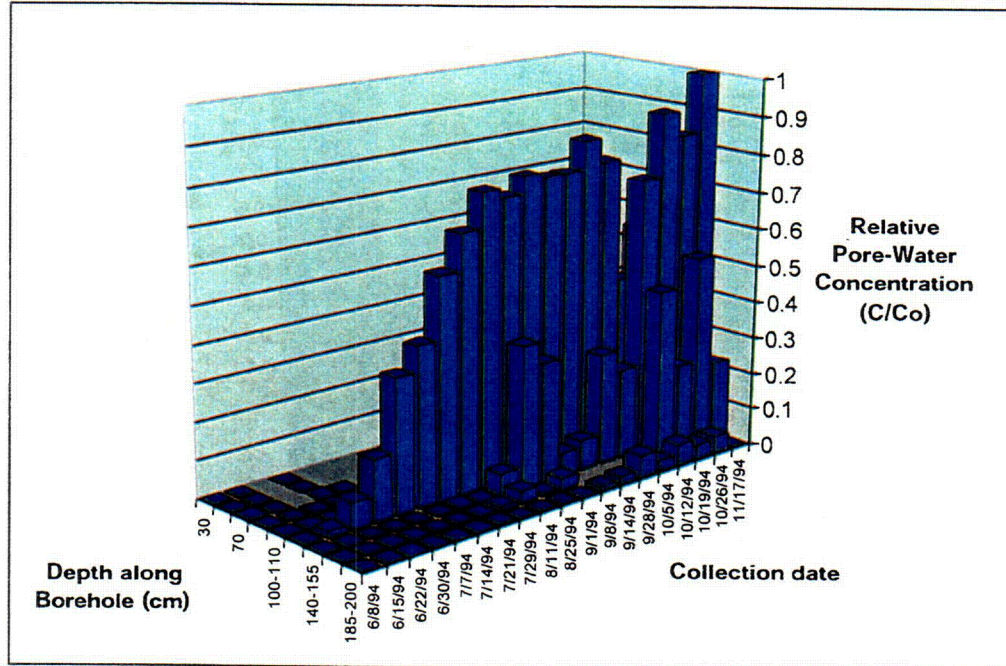
10.7-18.DOC.SITEDESC-R01

Source: CRWMS M&O (2000, Figure 56)

NOTE: The diagram shows vertical slices through the block at 0, 1.33, 2.66, 4.0, 5.33, 6.66, and 8.0 m that represent September 9 to July 2 difference images. Illegibility of numerical scale of axes does not affect illustrative purpose of figure.

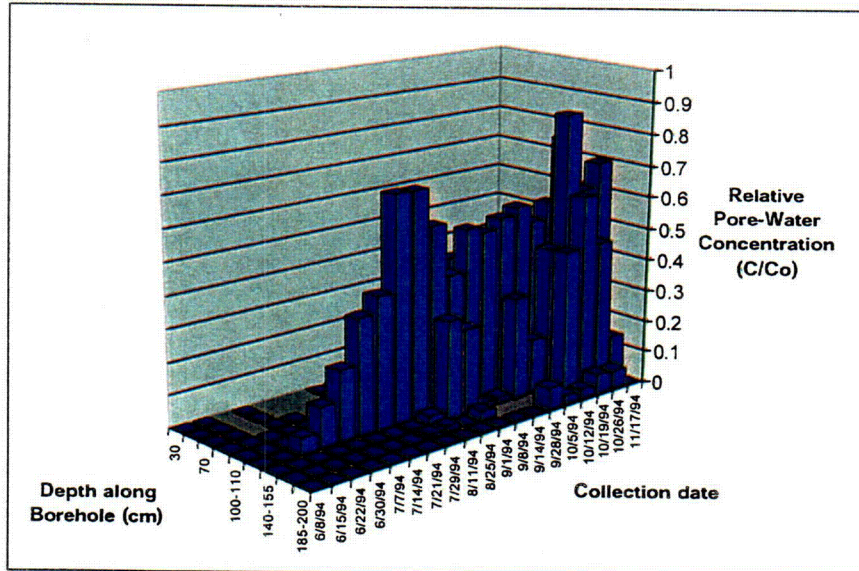
Figure 10.7-18. Electrical-Resistance Tomography Images of Test Block Viewed from Test Alcove: September Differences

(a) Bromide



10.7-19a.DOC.SITEDESC-R01

(b) 2,6-Difluorobenzoic Acid



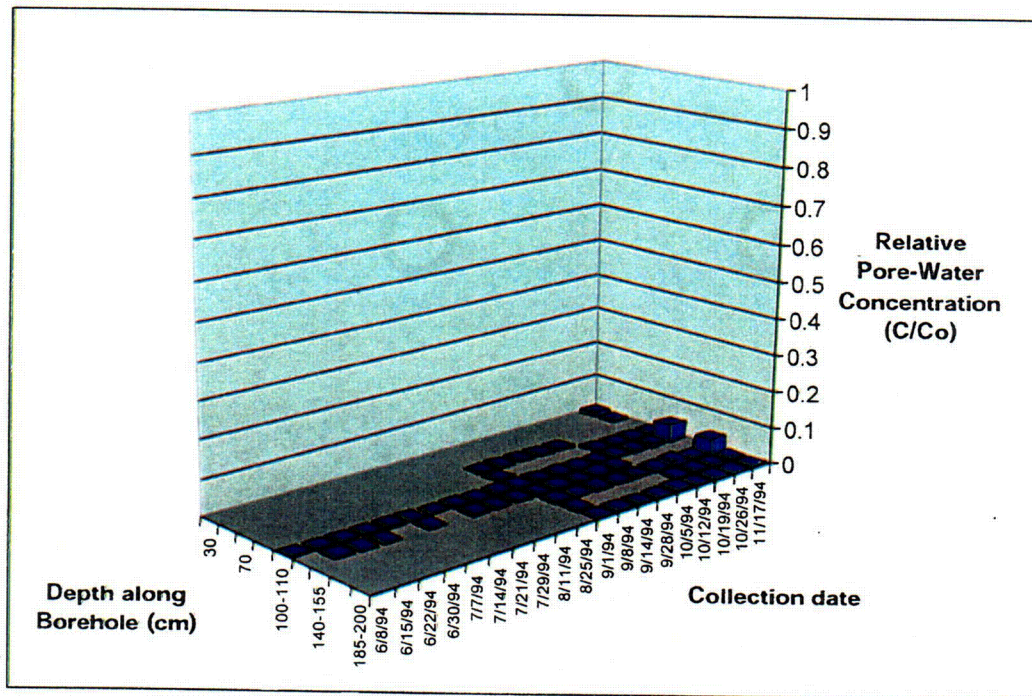
10.7-19b.DOC.SITEDESC-R01

Source: (a) CRWMS M&O (2000, Figure 58a); (b) CRWMS M&O (2000, Figure 58b)

Figure 10.7-19. Tracer Concentrations in Borehole 6



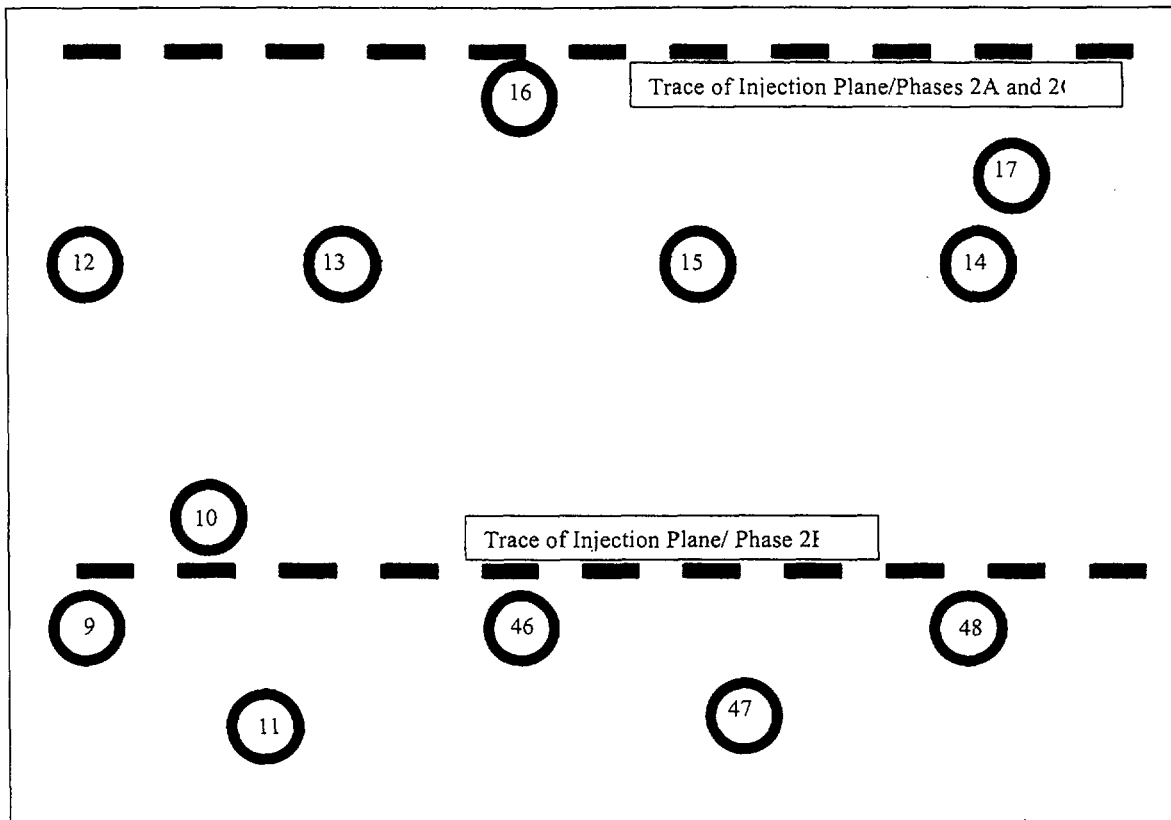
(e) Lithium



10.7-19e.DOC.SITEDESC-R01

Source: (e) CRWMS M&O (2000, Figure 58e)

Figure 10.7-19. Tracer Concentrations in Borehole 6 (Continued)

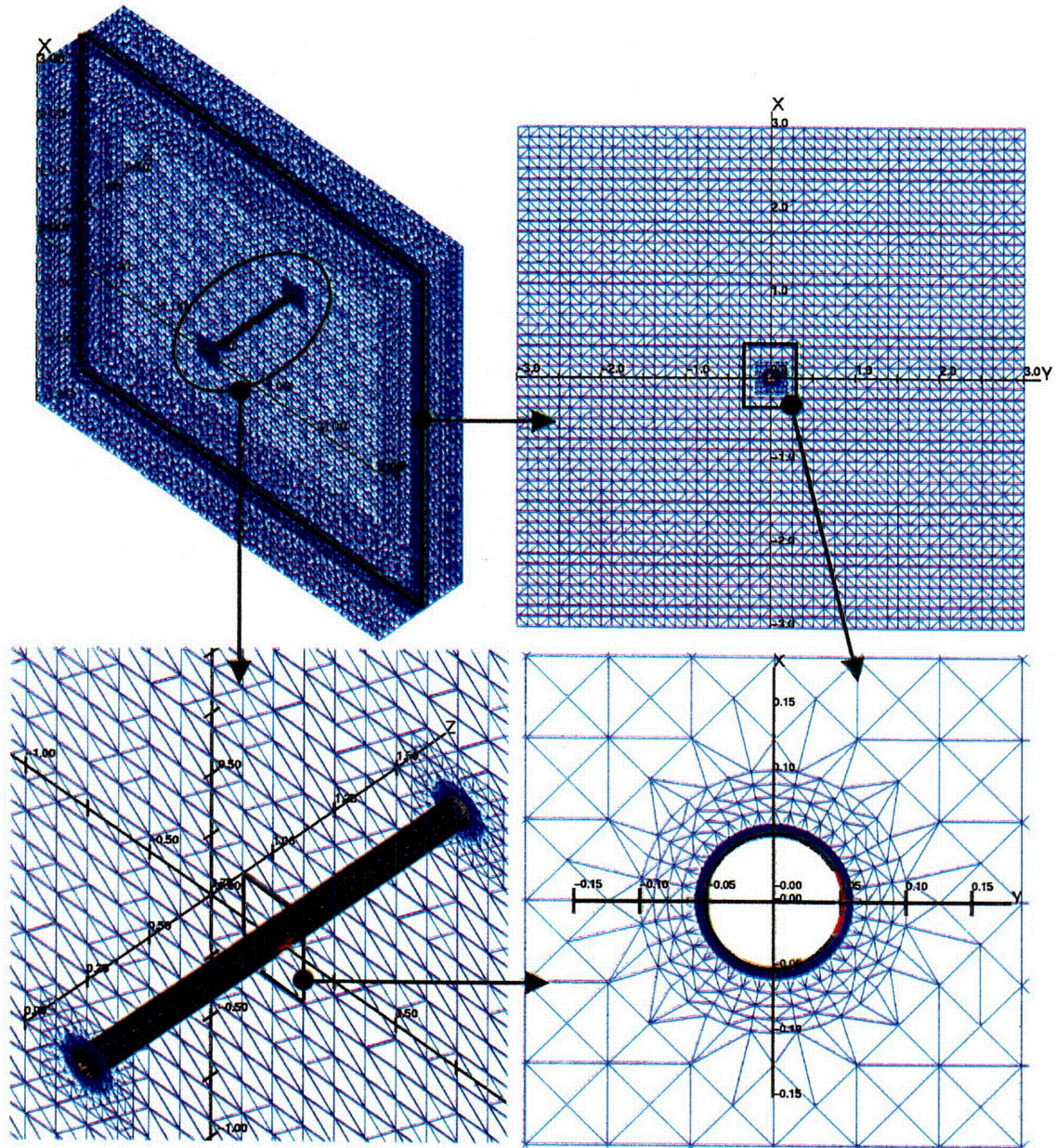


10.7-20.DOC.SITEDESC-R01

Source: CRWMS M&O (2000, Figure 59)

NOTE: Figure is not to scale.

Figure 10.7-20. Schematic Layout of Phase 2 Collection Boreholes

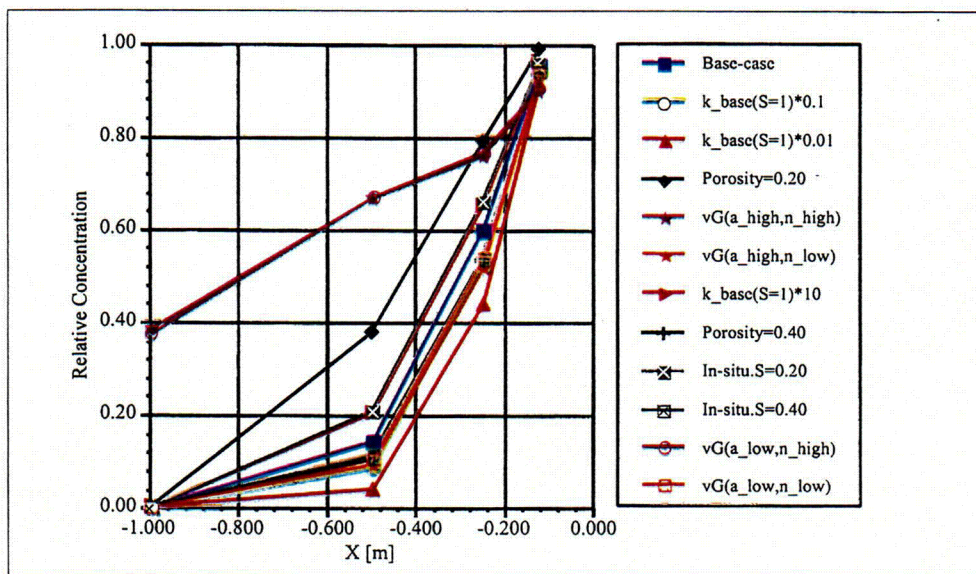


10.7-21.DOC.SITEDESC-R01

Source: CRWMS M&O (2000, Figure 61)

NOTE: LAGRIT-generated computational grid for single-borehole simulations. The grid has 82,000 nodes. The domain is 6 m x 6 m x 1.5 m and includes the porous rock matrix (blue) and the injection pad (red). Illegibility of grid axes does not impact the illustrative purpose of this figure.

Figure 10.7-21. Computational Grid

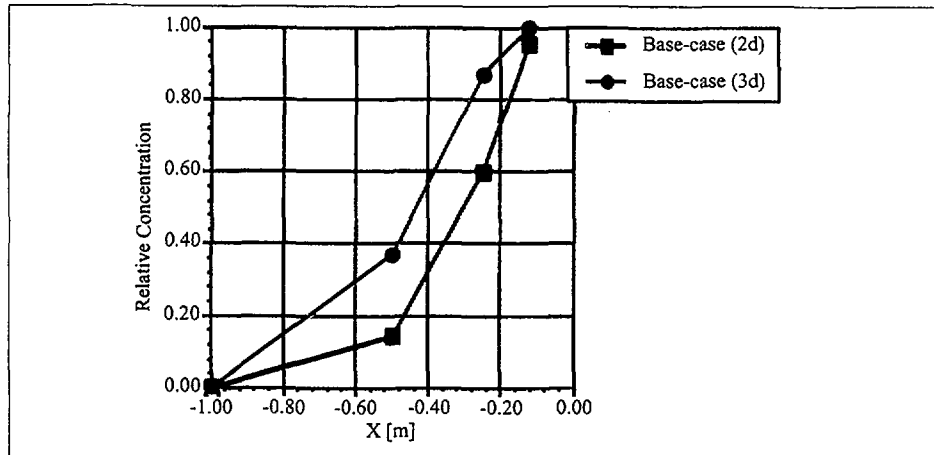


10.7-22.DOC.SITEDESC-R01

Source: CRWMS M&O (2000, Figure 62)

NOTE: Concentration is presented as a function of vertical distance from the injection point for different two-dimensional sensitivity runs.

Figure 10.7-22. Two-Dimensional Sensitivity Runs

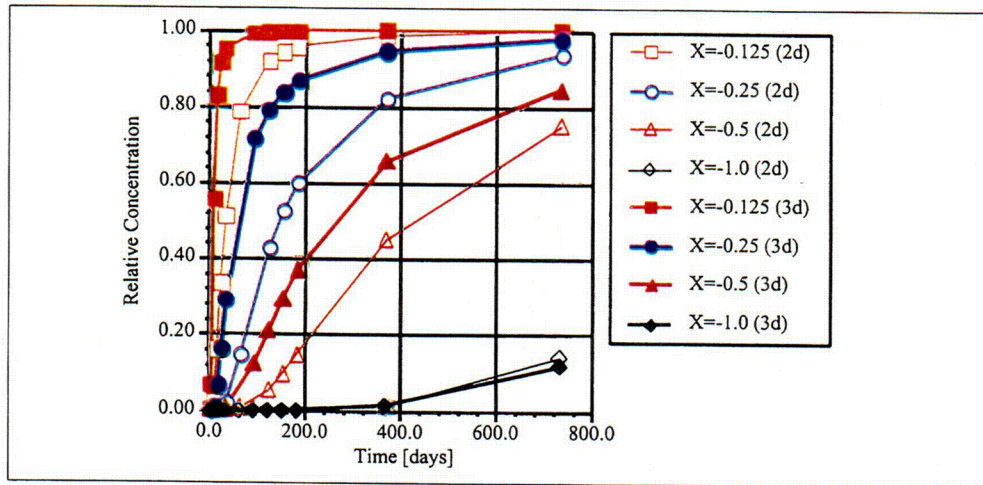


10.7-23.DOC.SITEDESC-R01

Source: CRWMS M&O (2000, Figure 63)

NOTE: The graph shows tracer concentration as a function of vertical distance from the injection point, and though the shapes of the curves are similar, the two-dimensional system lags the three-dimensional system by a concentration of approximately 0.20.

Figure 10.7-23. Tracer Concentration versus Distance for Two-Dimensional and Three-Dimensional Simulations

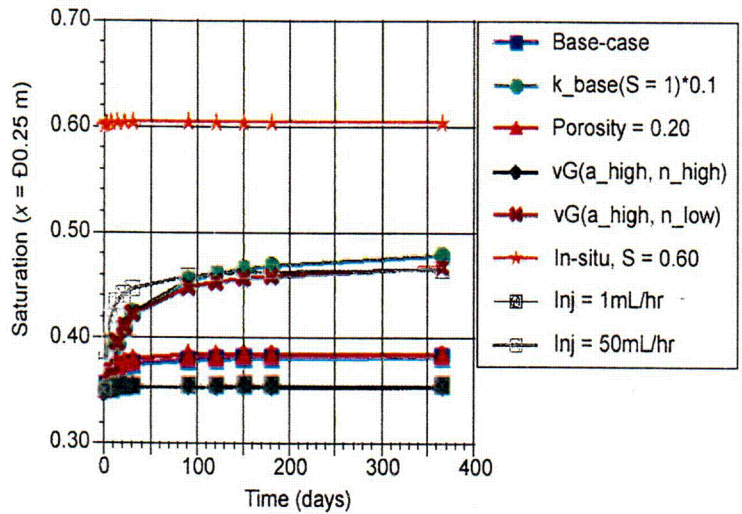


10.7-24.DOC.SITEDESC-R01

Source: CRWMS M&O (2000, Figure 64)

NOTE: The graph shows plots of tracer concentration as a function of time for different distances (meters) from the injection point. Curves for both two-dimensional and three-dimensional simulations are shown.

Figure 10.7-24. Time Profiles of Tracer Concentrations

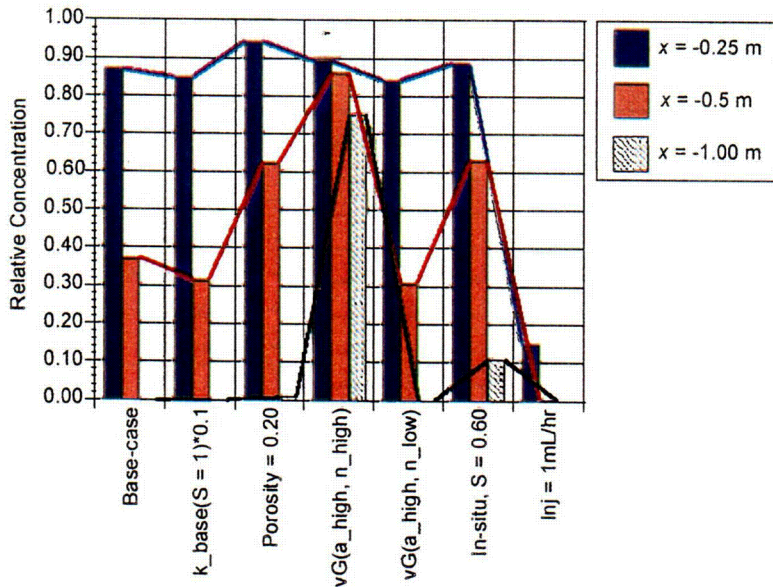


10.7-25.EPS.SITEDESC-R01

Source: CRWMS M&O (2000, Figure 65)

NOTE: The graph shows changes in saturation through time at a distance of 0.25 m from the injection point. Note that, in most cases, there is little change in saturation over a year.

Figure 10.7-25. Effect of Water Injection on Matrix Saturation

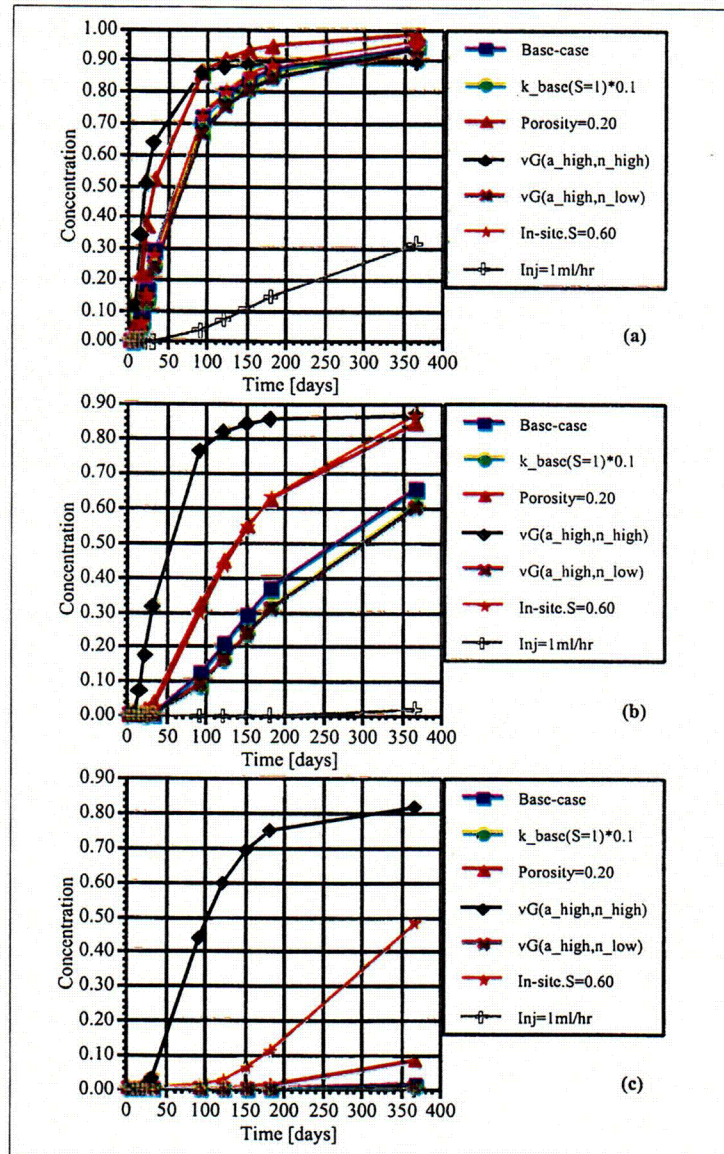


10.7-26.EPS.SITEDESC-R01

Source: CRWMS M&O (2000, Figure 66)

NOTE: The graph shows differences in concentration for different sensitivity runs at 180 days and three distances from injection. The sensitivity to the system parameters is not captured at the smallest distances but is apparent at a distance of 0.5 m.

Figure 10.7-26. Tracer Concentration for Different Sensitivity Runs

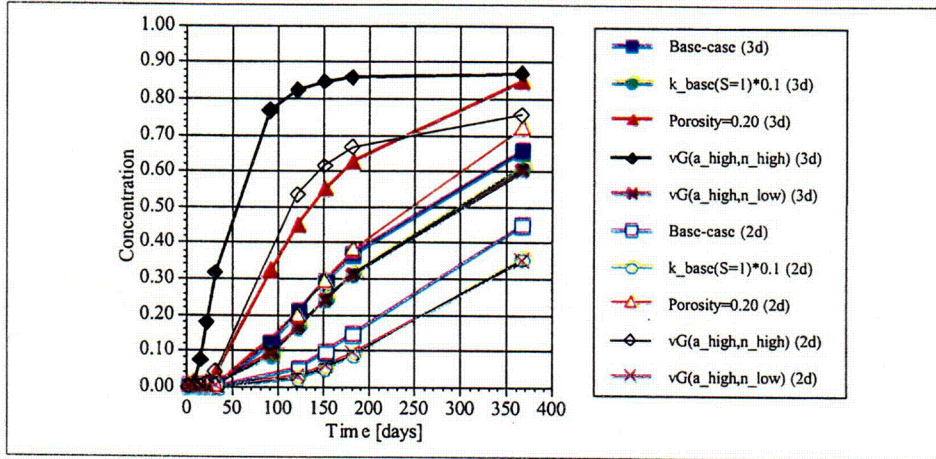


10.7-27.DOC.SITEDESC-R01

Source: CRWMS M&O (2000, Figure 67)

NOTE: These plots show concentration changes as a function of time for distances from the injection point of (a) 0.25 m, (b) 0.5 m, and (c) 1.0 m. Note that at a 1-m distance, there is, in most cases, little change in concentration after injecting tracer for 1 year.

Figure 10.7-27. Tracer Concentration versus Time at Various Distances from Injection

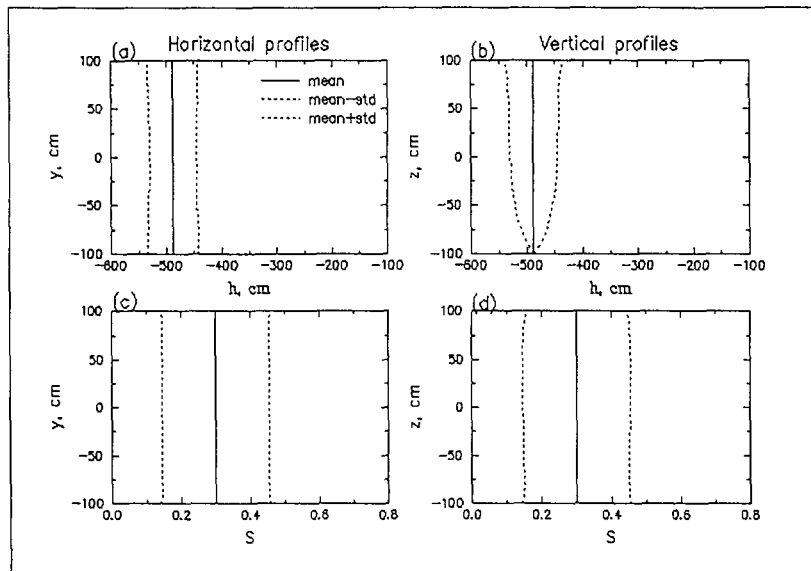


10.7-28.DOC.SITEDESC-R01

Source: CRWMS M&O (2000, Figure 68)

NOTE: These plots of concentration versus time show that differences between two-dimensional and three-dimensional values are fairly consistent between different runs. The concentration is measured at a distance of 0.5 m vertically below the borehole center.

Figure 10.7-28. Differences in Two-Dimensional and Three-Dimensional Predicted Concentrations

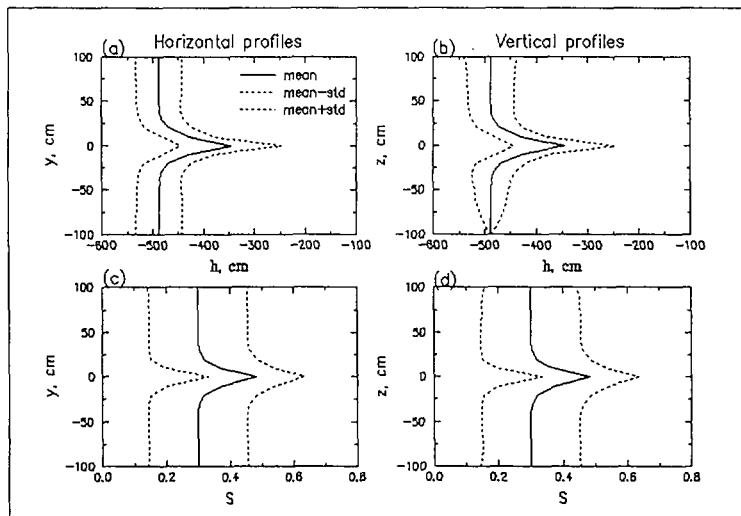


10.7-29.DOC.SITEDESC-R01

Source: CRWMS M&O (2000, Figure 69)

NOTE:  $h$  = pressure head;  $S$  = saturation

Figure 10.7-29. Steady-State Profiles of Pressure Head and Saturation

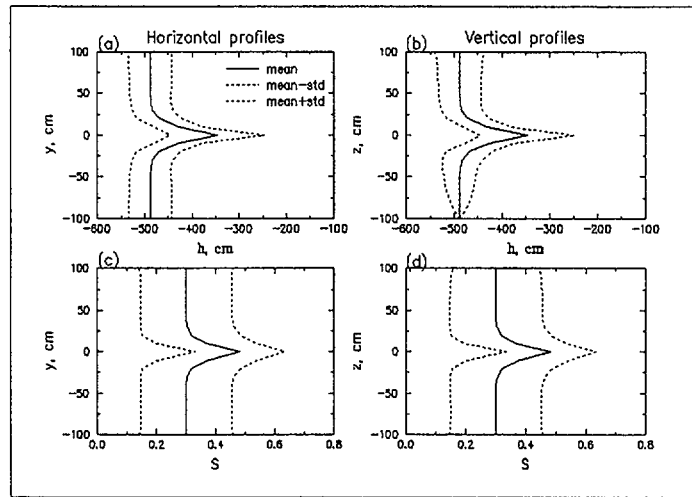


10.7-30.DOC.SITEDESC-R01

Source: CRWMS M&O (2000, Figure 70)

NOTE:  $h$  = pressure head;  $S$  = saturation

Figure 10.7-30. Case 1. Horizontal and Vertical Profiles of Pressure Head and Saturation at 150 Days after Injection Started

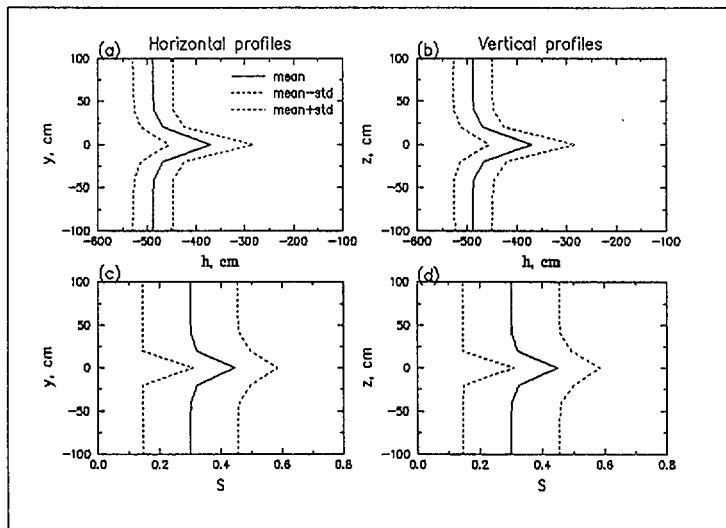


10.7-31.DOC SITEDESC-R01

Source: CRWMS M&O (2000, Figure 71)

NOTE:  $h$  = pressure head;  $S$  = saturation

Figure 10.7-31. Case 2. Horizontal and Vertical Profiles of Pressure Head and Saturation 150 Days after Injection Started, but with  $\lambda_f = \lambda_\alpha = 30$  Centimeters

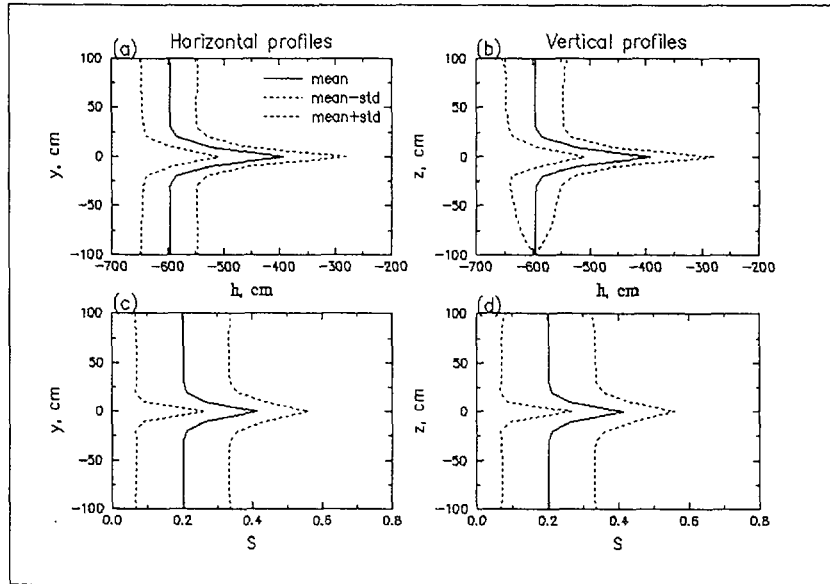


10.7-32.DOC SITEDESC-R01

Source: CRWMS M&O (2000, Figure 72)

NOTE:  $h$  = pressure head;  $S$  = saturation

Figure 10.7-32. Case 3. Horizontal and Vertical Profiles of Pressure Head and Saturation 150 Days after Injection Started, but with  $L_1 = L_2 = 400$  Centimeters

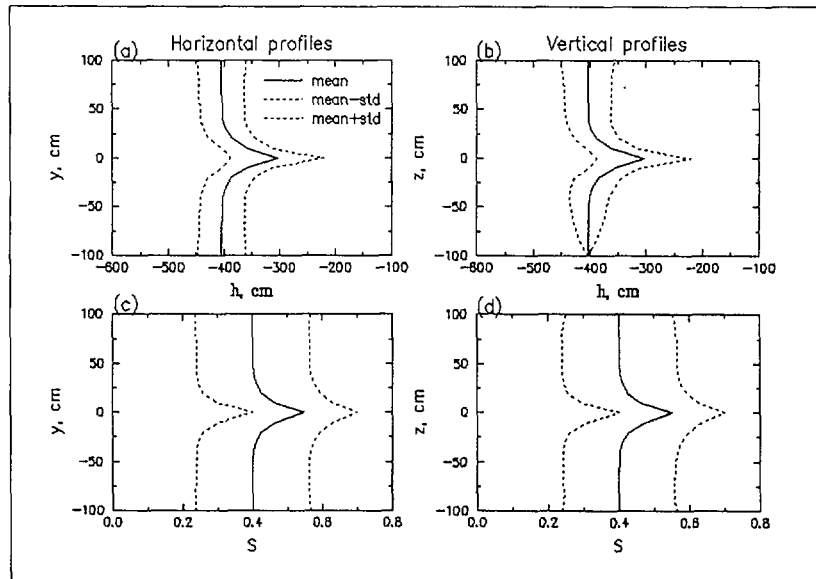


10.7-33.DOC.SITEDESC-R01

Source: CRWMS M&O (2000, Figure 73)

NOTE:  $h$  = pressure head;  $S$  = saturation

Figure 10.7-33. Case 4. Horizontal and Vertical Profiles of Pressure Head and Saturation 150 Days after Injection Started, but with  $S_0 = 20$  Percent

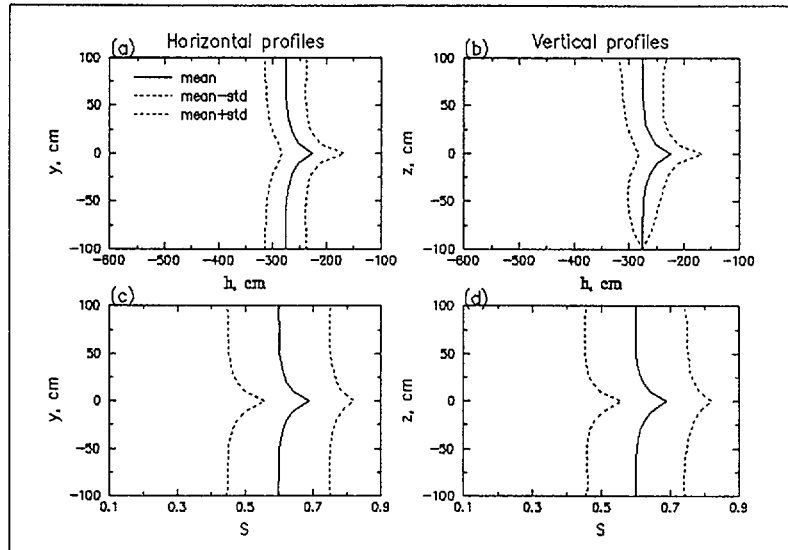


10.7-34.DOC.SITEDESC-R01

Source: CRWMS M&O (2000, Figure 74)

NOTE:  $h$  = pressure head;  $S$  = saturation

Figure 10.7-34. Case 5. Horizontal and Vertical Profiles of Pressure Head and Saturation 150 Days after Injection Started, but with  $S_0 = 40$  Percent

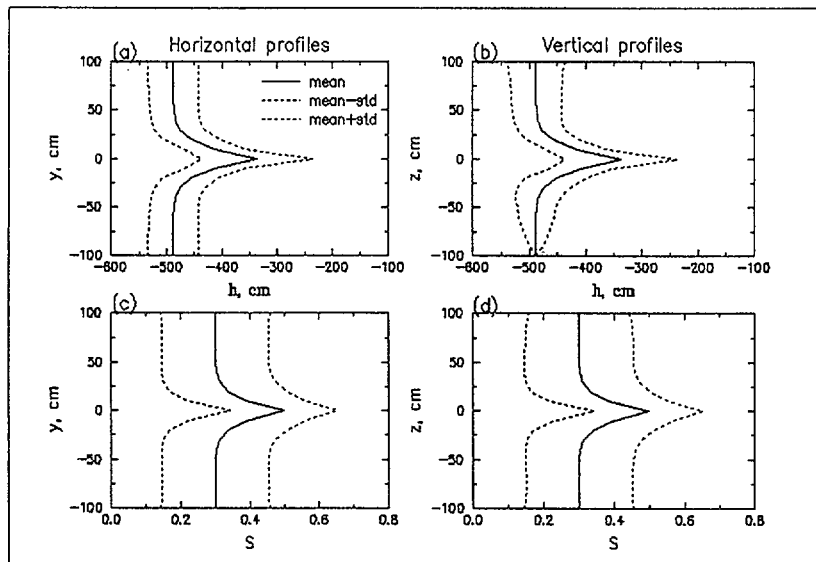


10.7-35.DOC.SITEDESC-R01

Source: CRWMS M&O (2000, Figure 75)

NOTE:  $h$  = pressure head;  $S$  = saturation

Figure 10.7-35. Case 6. Horizontal and Vertical Profiles of Pressure Head and Saturation 150 Days after Injection Started, but with  $S_o = 60$  Percent

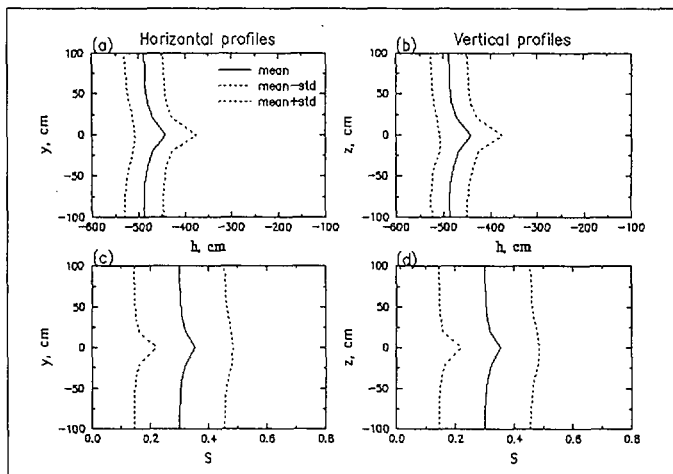


10.7-36.DOC.SITEDESC-R01

Source: CRWMS M&O (2000, Figure 76)

NOTE:  $h$  = pressure head;  $S$  = saturation

Figure 10.7-36. Case 7. Horizontal and Vertical Profiles of Pressure Head and Saturation 150 Days after Injection Started, but with  $\phi = 0.3$

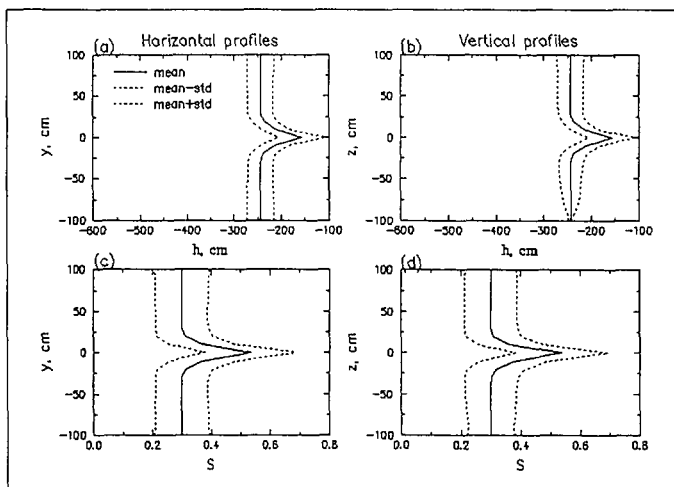


10.7-37.DOC.SITEDESC-R01

Source: CRWMS M&O (2000, Figure 77)

NOTE:  $h$  = pressure head;  $S$  = saturation

Figure 10.7-37. Case 8. Horizontal and Vertical Profiles of Pressure Head and Saturation 150 Days after Injection Started, but with  $\langle f \rangle = -4.258$  and  $L_1 = L_2 = 400$  Centimeters

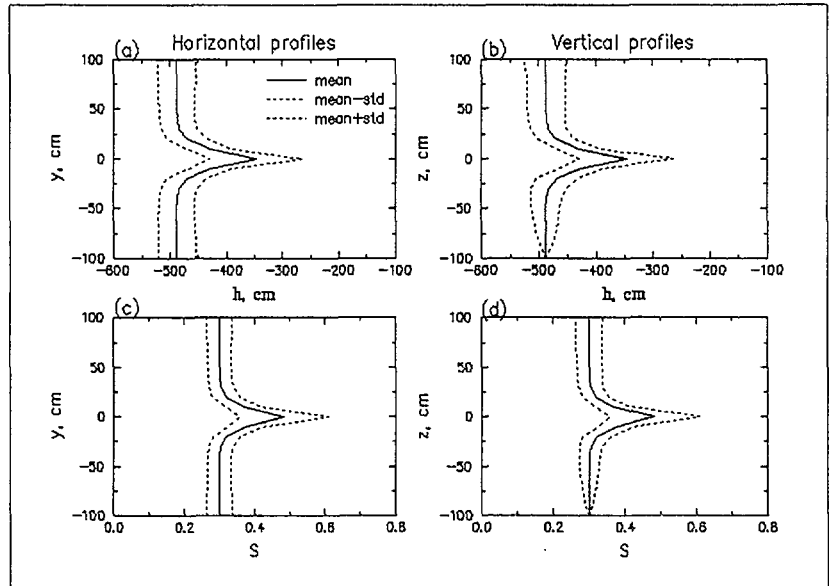


10.7-38.DOC.SITEDESC-R01

Source: CRWMS M&O (2000, Figure 78)

NOTE:  $h$  = pressure head;  $S$  = saturation

Figure 10.7-38. Case 9. Horizontal and Vertical Profiles of Pressure Head and Saturation 150 Days after Injection Started, but with  $\langle \alpha \rangle = 0.02$  per Centimeter

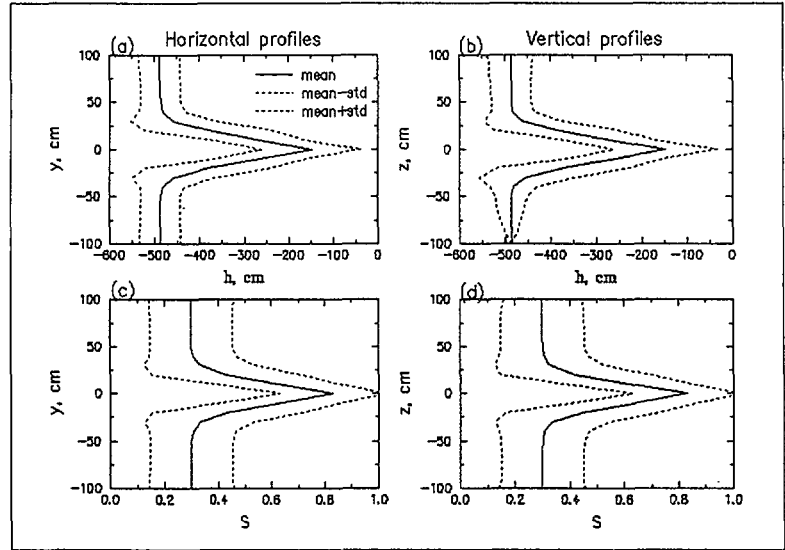


10.7-39.DOC.SITEDESC-R01

Source: CRWMS M&O (2000, Figure 79)

NOTE:  $h$  = pressure head;  $S$  = saturation

Figure 10.7-39. Case 10. Horizontal and Vertical Profiles of Pressure Head and Saturation 150 Days after Injection Started, but with  $\sigma_\alpha = 0$

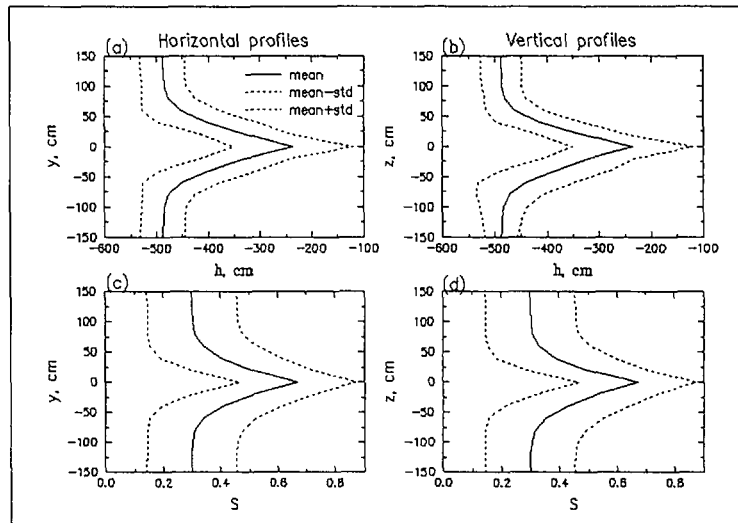


10.7-40.DOC.SITEDESC-R01

Source: CRWMS M&O (2000, Figure 80)

NOTE:  $h$  = pressure head;  $S$  = saturation

Figure 10.7-40. Case 11. Horizontal and Vertical Profiles of Pressure Head and Saturation 150 Days after Injection Started, but with  $Q = 10$  Milliliters per Hour

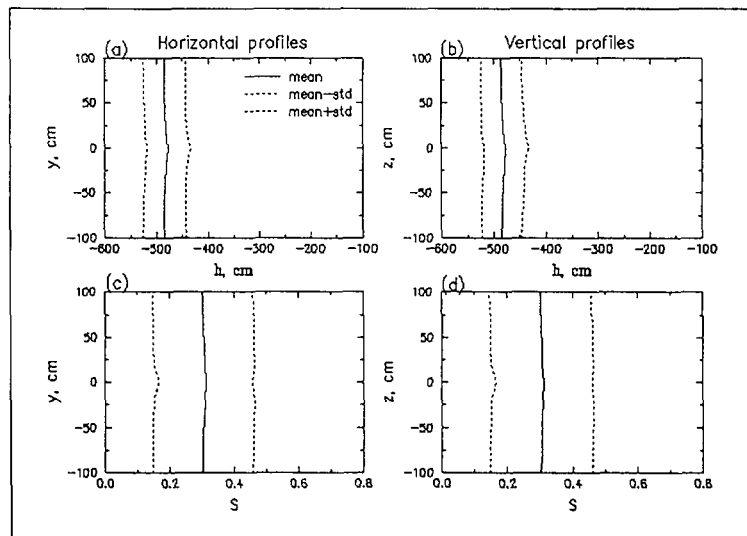


10.7-41.DOC.SITEDESC-R01

Source: CRWMS M&O (2000, Figure 81)

NOTE:  $h$  = pressure head;  $S$  = saturation

Figure 10.7-41. Case 12. Horizontal and Vertical Profiles of Pressure Head and Saturation 150 Days after Injection Started, but with  $Q = 50$  Milliliters per Hour and  $L_3 = 100$  Centimeters

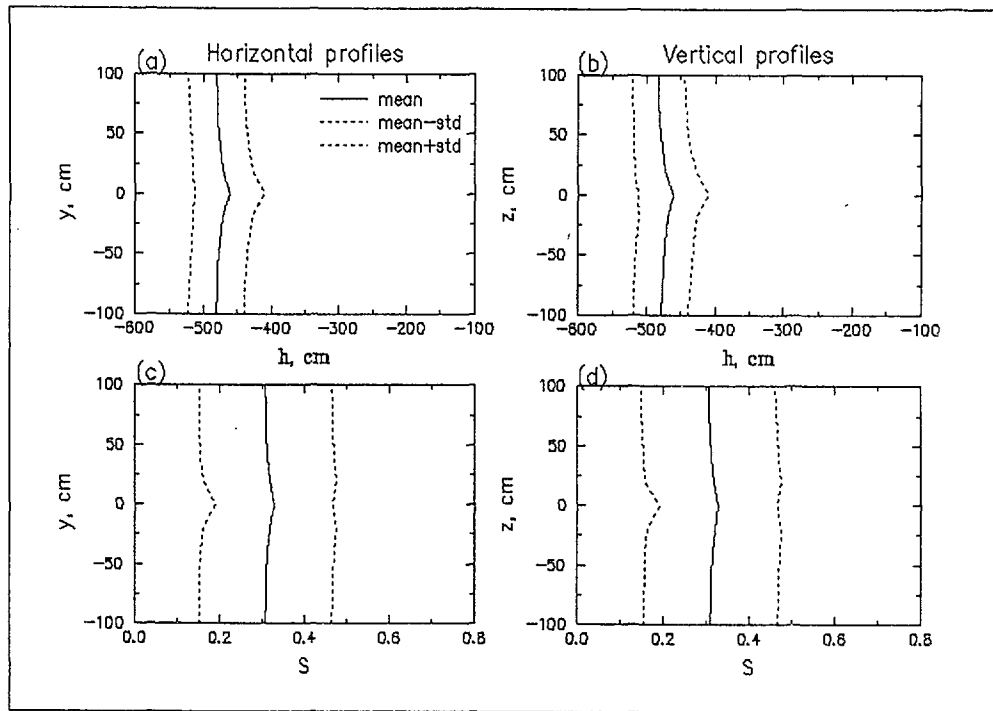


10.7-42.DOC.SITEDESC-R01

Source: CRWMS M&O (2000, Figure 82)

NOTE:  $h$  = pressure head;  $S$  = saturation

Figure 10.7-42. Case 13. Horizontal and Vertical Profiles of Pressure Head and Saturation 150 Days after Injection Started, but with  $\langle f \rangle = 0.314$ ,  $L_1 = L_2 = 400$  Centimeters,  $Q = 10$  Milliliters per Hour, and  $L_3 = 50$  Centimeters

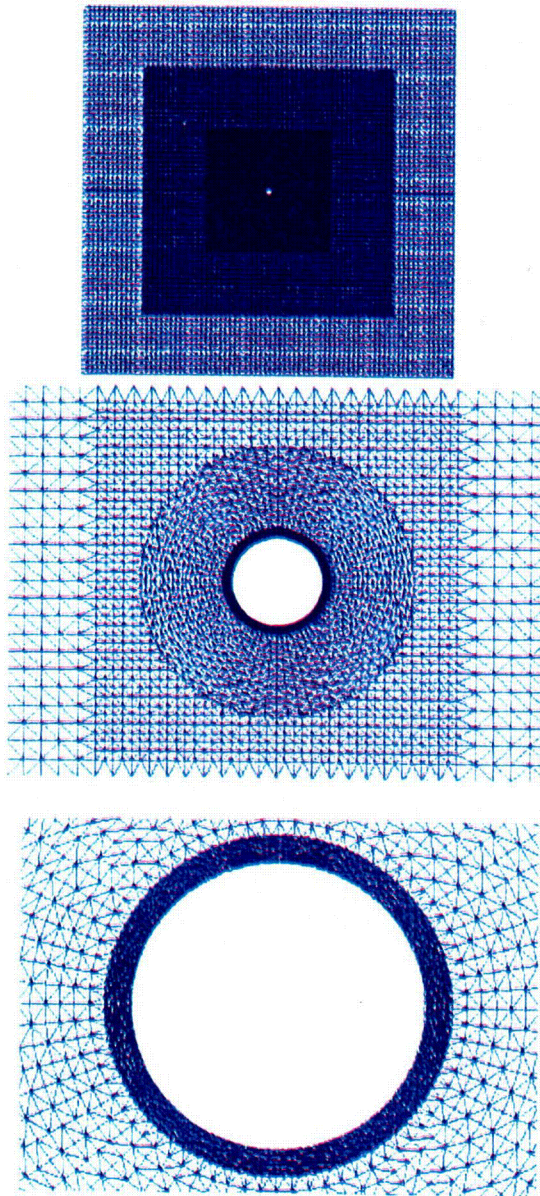


10.7-43.DOC.SITEDESC-R01

Source: CRWMS M&O (2000, Figure 83)

NOTE:  $h$  = pressure head;  $S$  = saturation

Figure 10.7-43. Case 14. Horizontal and Vertical Profiles of Pressure Head and Saturation 150 Days after Injection Started, but with  $Q = 50$  Milliliters per Hour and  $L_3 = 100$  Centimeters

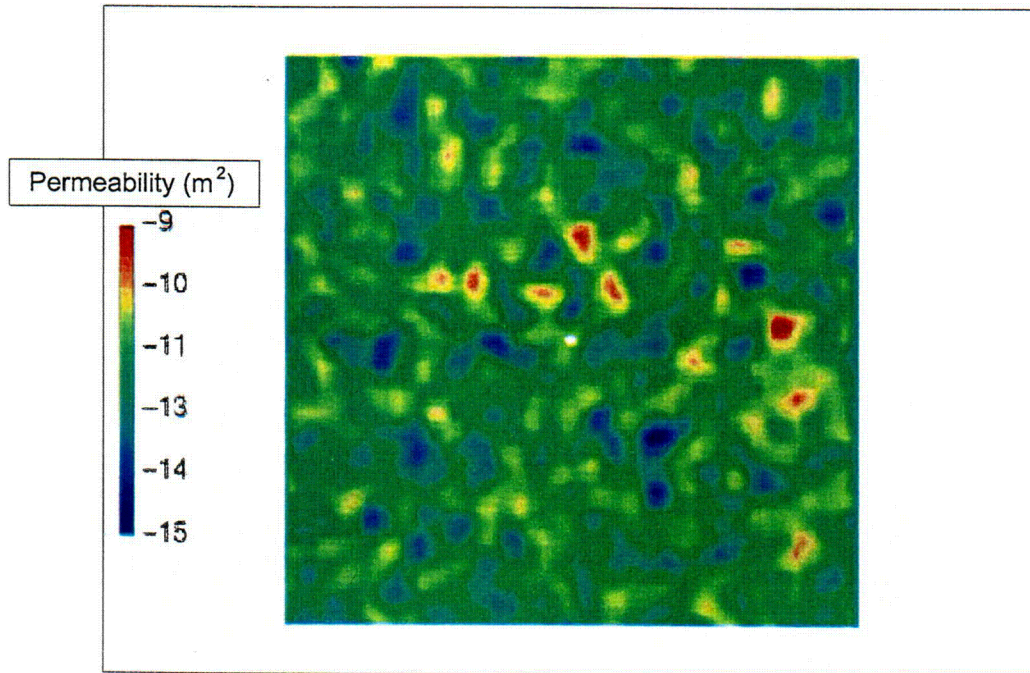


10.7-44.DOC.SITEDESC-R01

Source: CRWMS M&O (2000, Figure 84)

NOTE: Top: full view (6 m x 6 m); middle: intermediate close-up view (0.4 m x 0.5 m); bottom: close-up of borehole.

Figure 10.7-44. Finite-Element Grid Used in the Monte Carlo Simulation

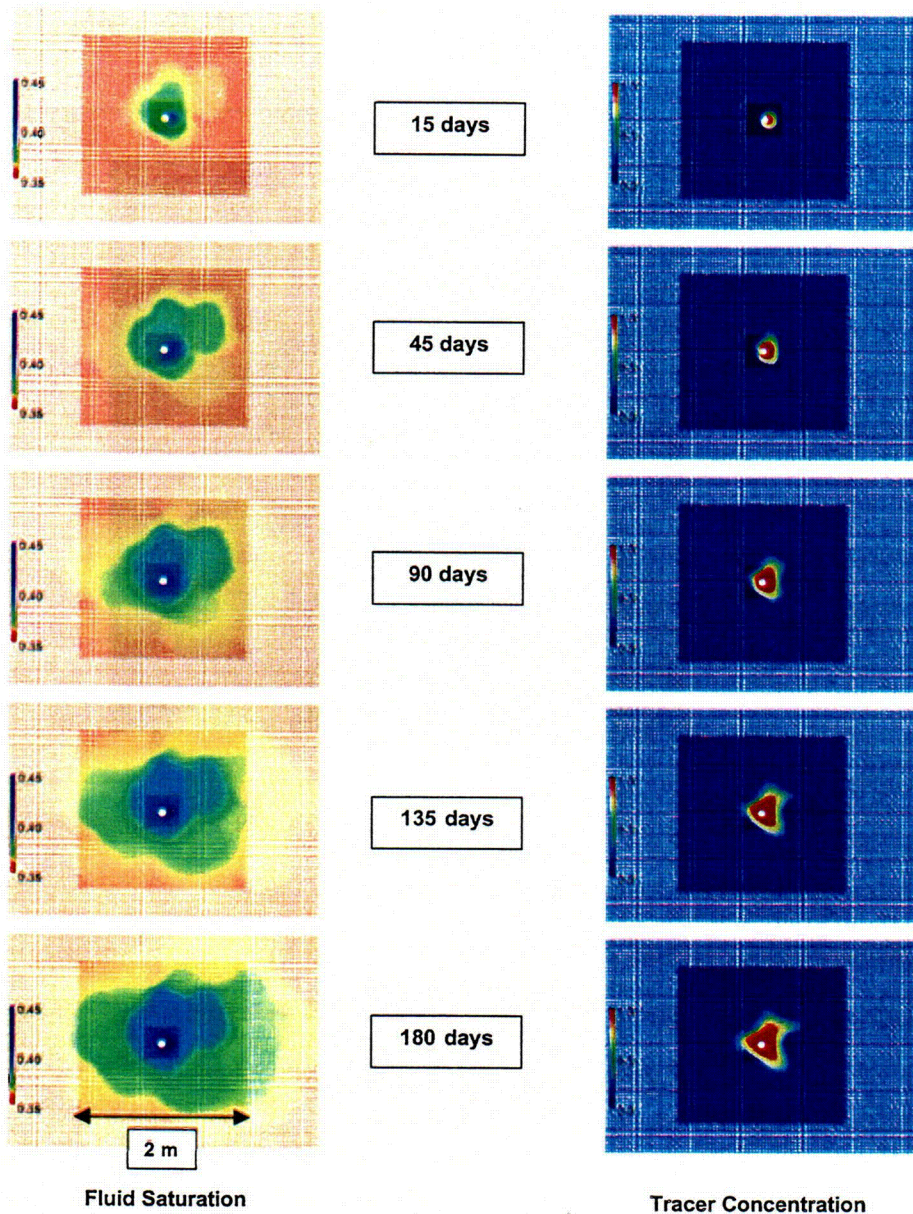


10.7-45.DOC.SITEDESC-R01

Source: CRWMS M&O (2000, Figure 85)

NOTE: This plot shows the permeability distribution for the Monte Carlo realization selected for discussion.

Figure 10.7-45. Permeability Distribution

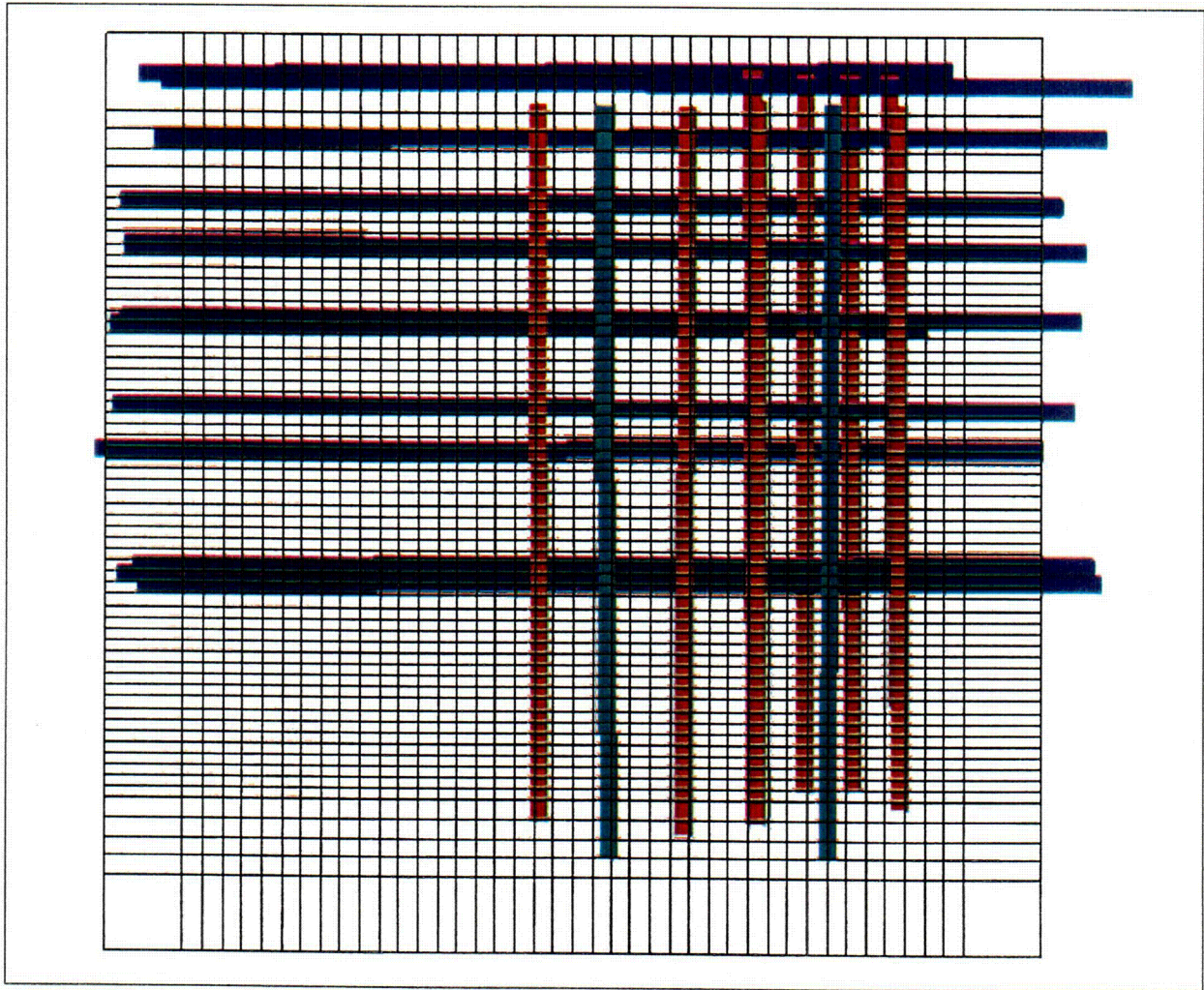


10.7-46.DOC.SITEDESC-R01

Source: CRWMS M&O (2000, Figure 86)

NOTE: These plots show fluid saturations (left panels) and tracer concentrations (right panels) at various times during a Monte Carlo simulation. Note the restricted range of saturation values used.

Figure 10.7-46. Fluid Saturations and Tracer Concentrations

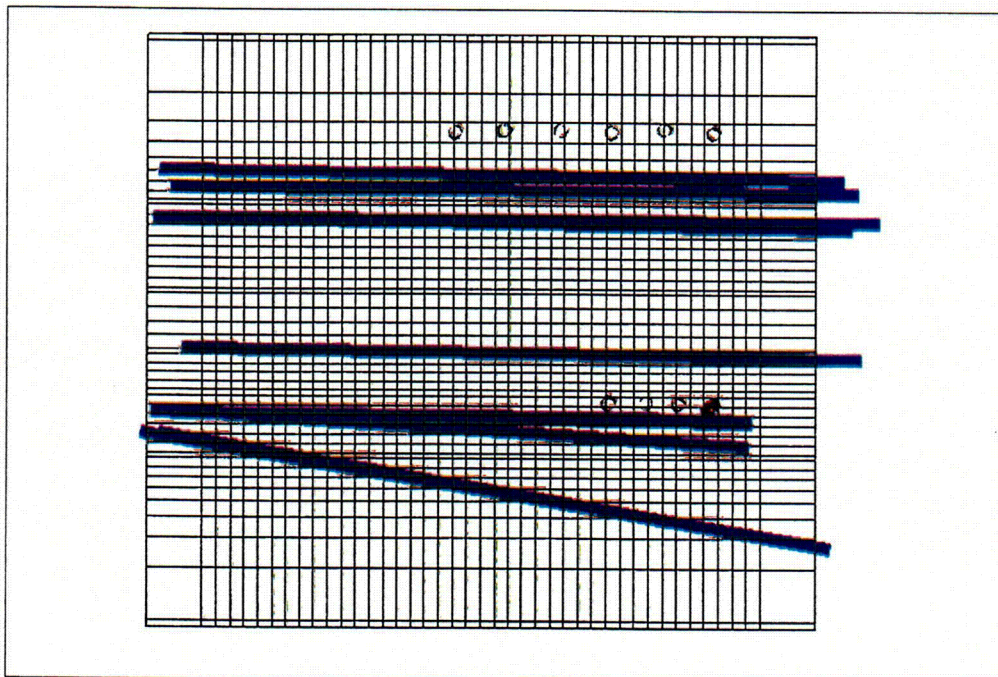


10.7-47.DOC.SITEDESC-R01

Source: CRWMS M&O (2000, Figure 88)

NOTE: Injection boreholes are depicted as red lines, collection boreholes as blue lines, and tomography boreholes as green lines.

Figure 10.7-47. Top View of Finite-Element Grid and the Injection and Collection Boreholes

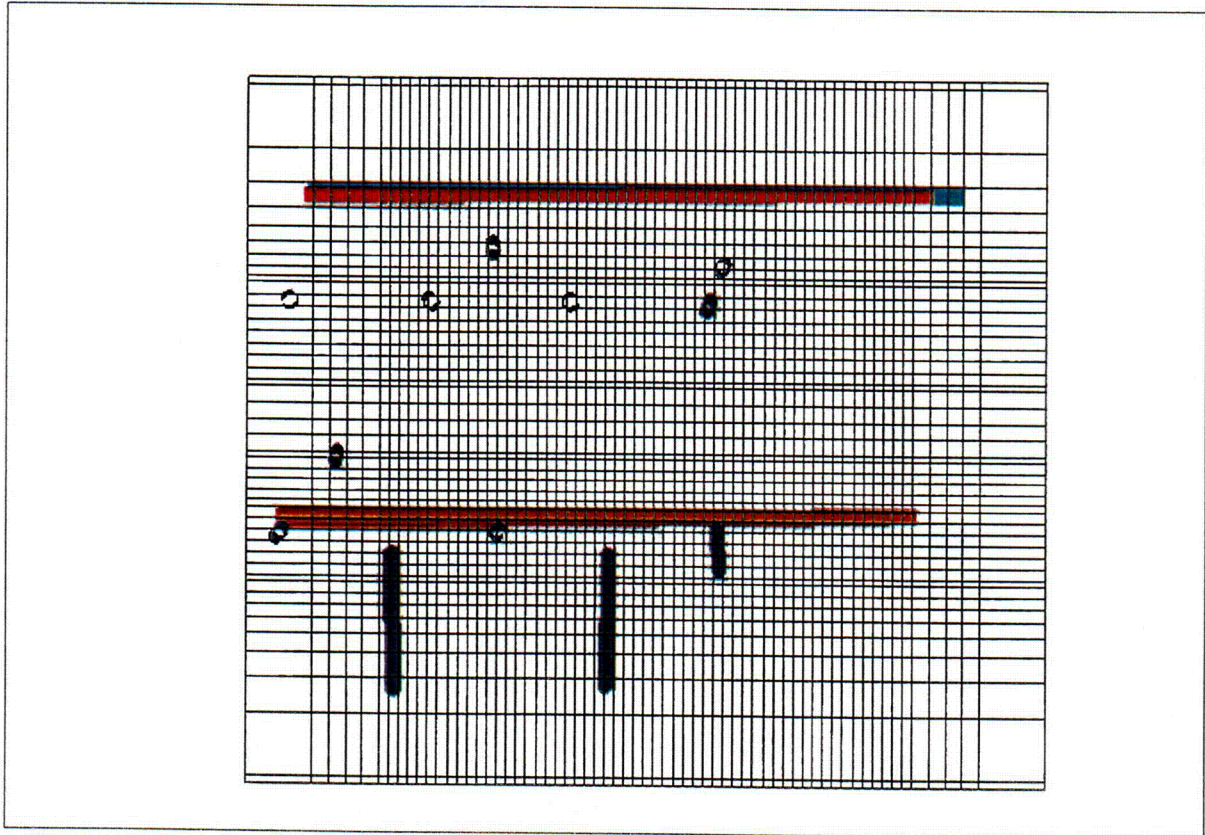


10.7-48.DOC.SITEDESC-R01

Source: CRWMS M&O (2000, Figure 89)

NOTE: The blue lines represent collection boreholes. Because the injection boreholes originate in the Test Alcove, they are perpendicular to the plane of the figure and are depicted as circles.

Figure 10.7-48. Finite-Element Grid as Seen from the Test Alcove

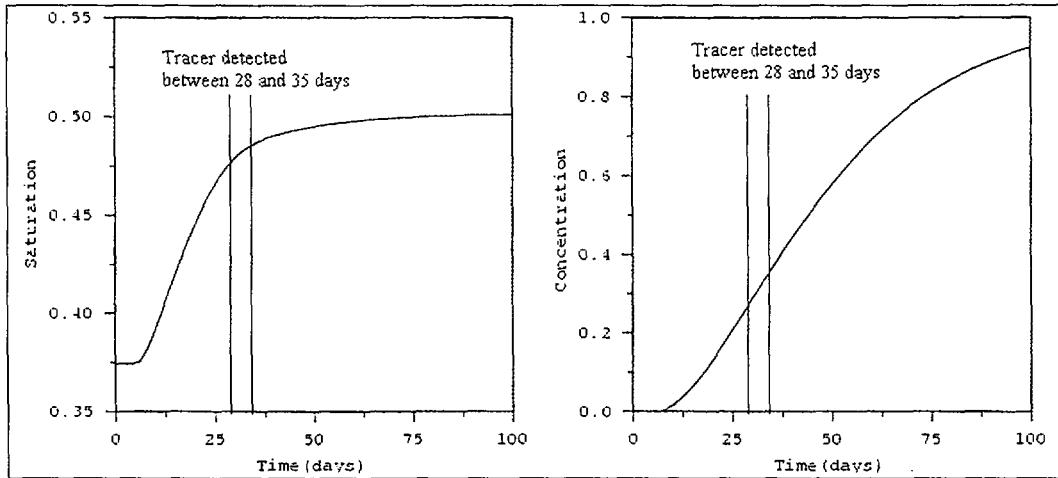


10.7-49.DOC.SITEDESC-R01

Source: CRWMS M&O (2000, Figure 90)

NOTE: The horizontal red lines represent the location of injection boreholes, which are perpendicular to the collection boreholes (blue). The collection boreholes originate in the Main Adit, but several are plunging down and, thus, show up as blue lines rather than circles. The green line represents one of the tomography boreholes.

Figure 10.7-49. Finite-Element Grid as Seen from the Main Adit

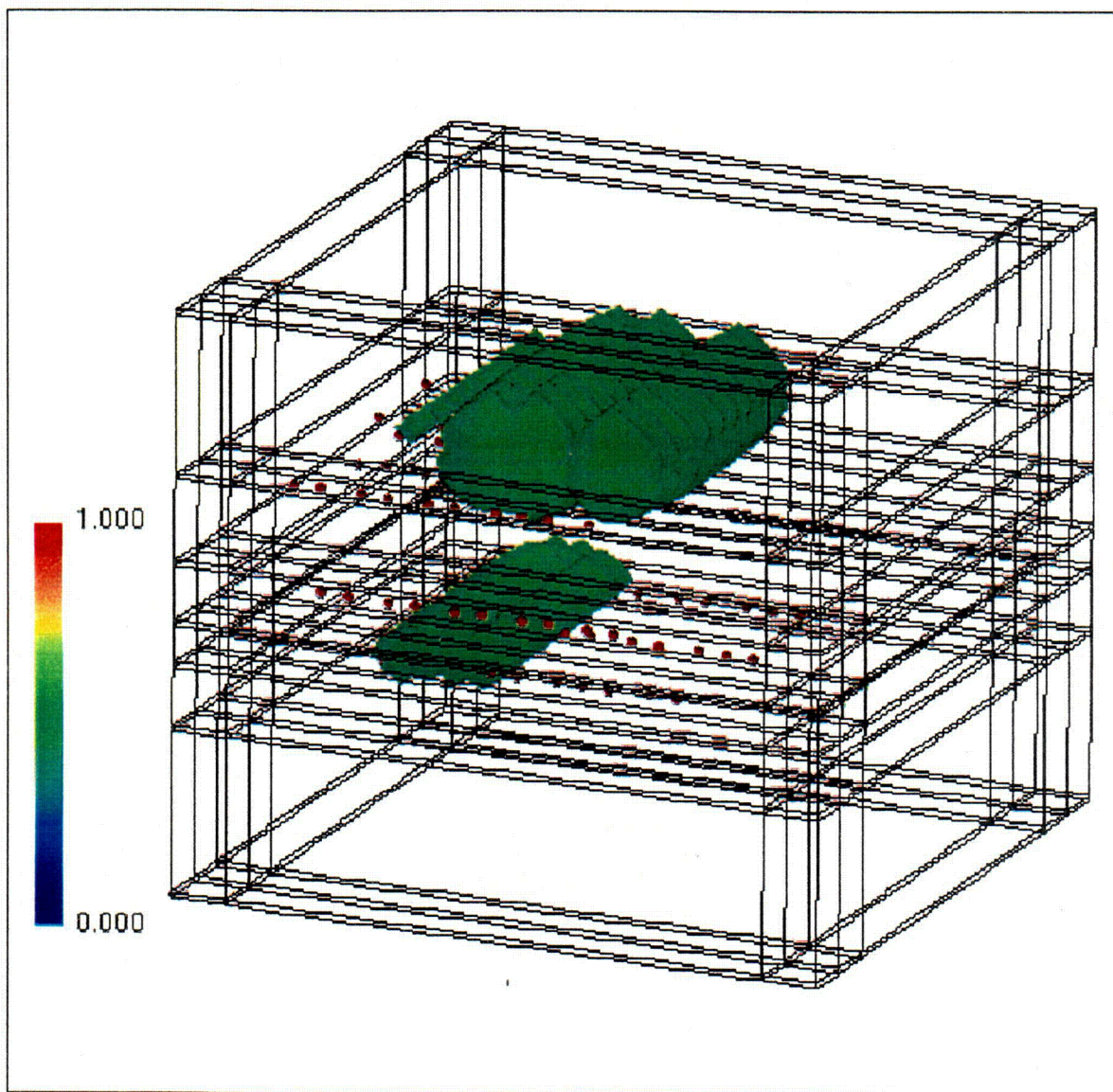


10.7-50.DOC.SITEDESC-R01

Source: CRWMS M&O (2000, Figure 91)

NOTES: The plots show the conservative breakthrough of tracer 28 cm from the injection pad: (a) saturation breakthrough, and (b) concentration breakthrough.

Figure 10.7-50. Using Equivalent-Continuum Model and Ttpv2 Properties to Predict Phase 1B

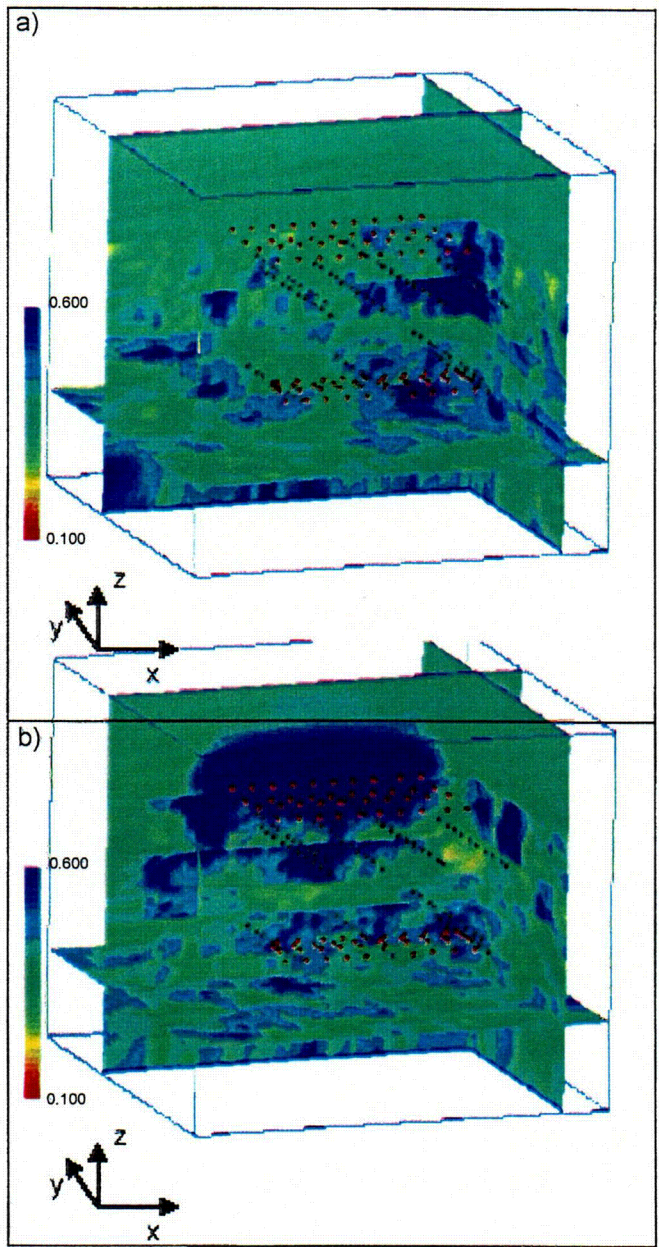


10.7-51.DOC.SITEDESC-R01

Source: CRWMS M&O (2000, Figure 92)

NOTES: The figure depicts the concentration plume after 1 year of conservative-tracer injection. The green isosurface represents a normalized concentration of 0.5; the red dots represent the sampling points along the collection boreholes.

Figure 10.7-51. Conservative Tracer Concentration Plume

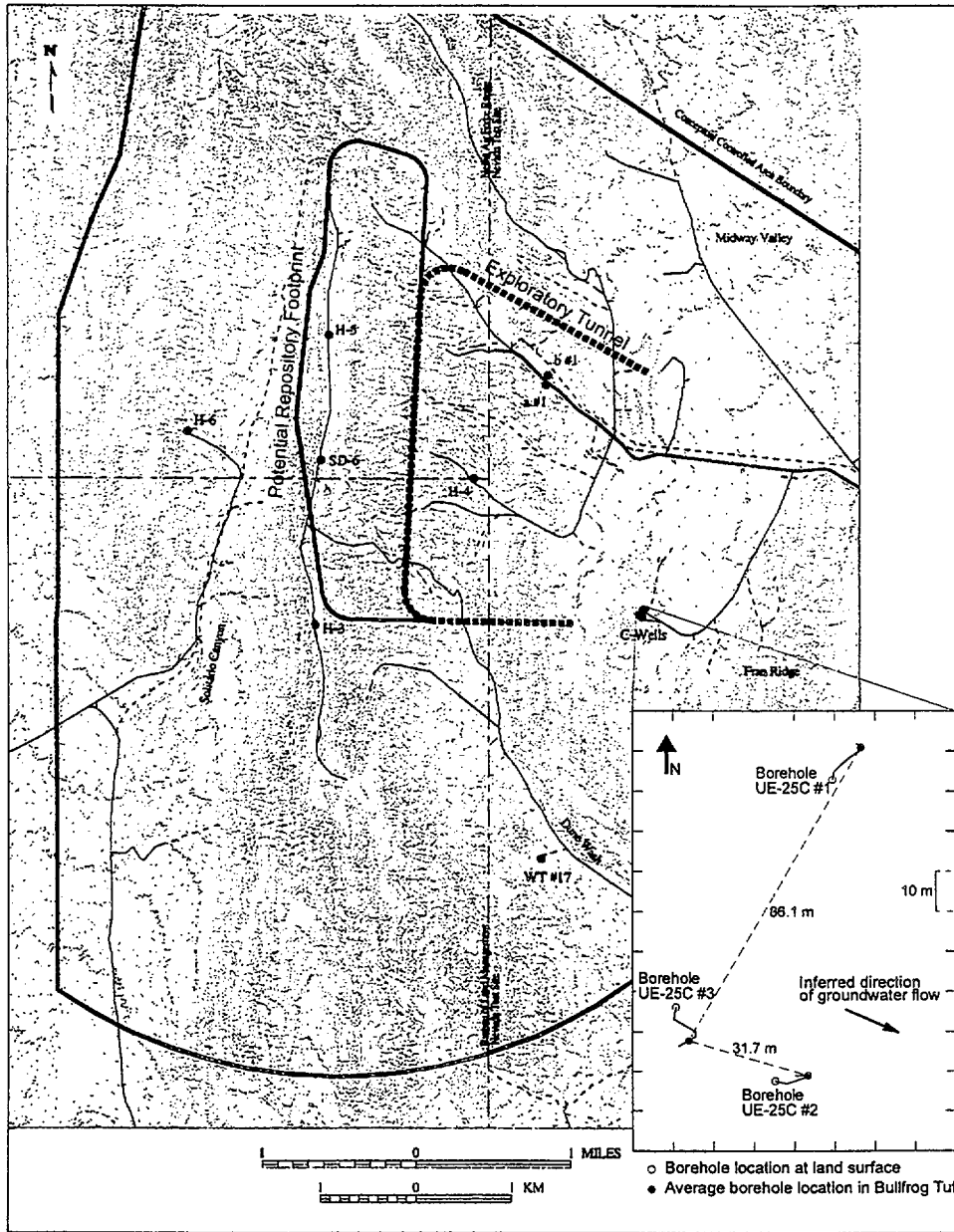


10.7-52.CDR.SITEDESC-R01

Source: CRWMS M&O (2000, Figure 93)

NOTES: These saturation profiles are from 10 to 60 percent of the heterogeneous Realization 1: (a) background saturation, and (b) saturation profile after 1 yr. of injection. Injection points are red dots and collection points are blue dots.

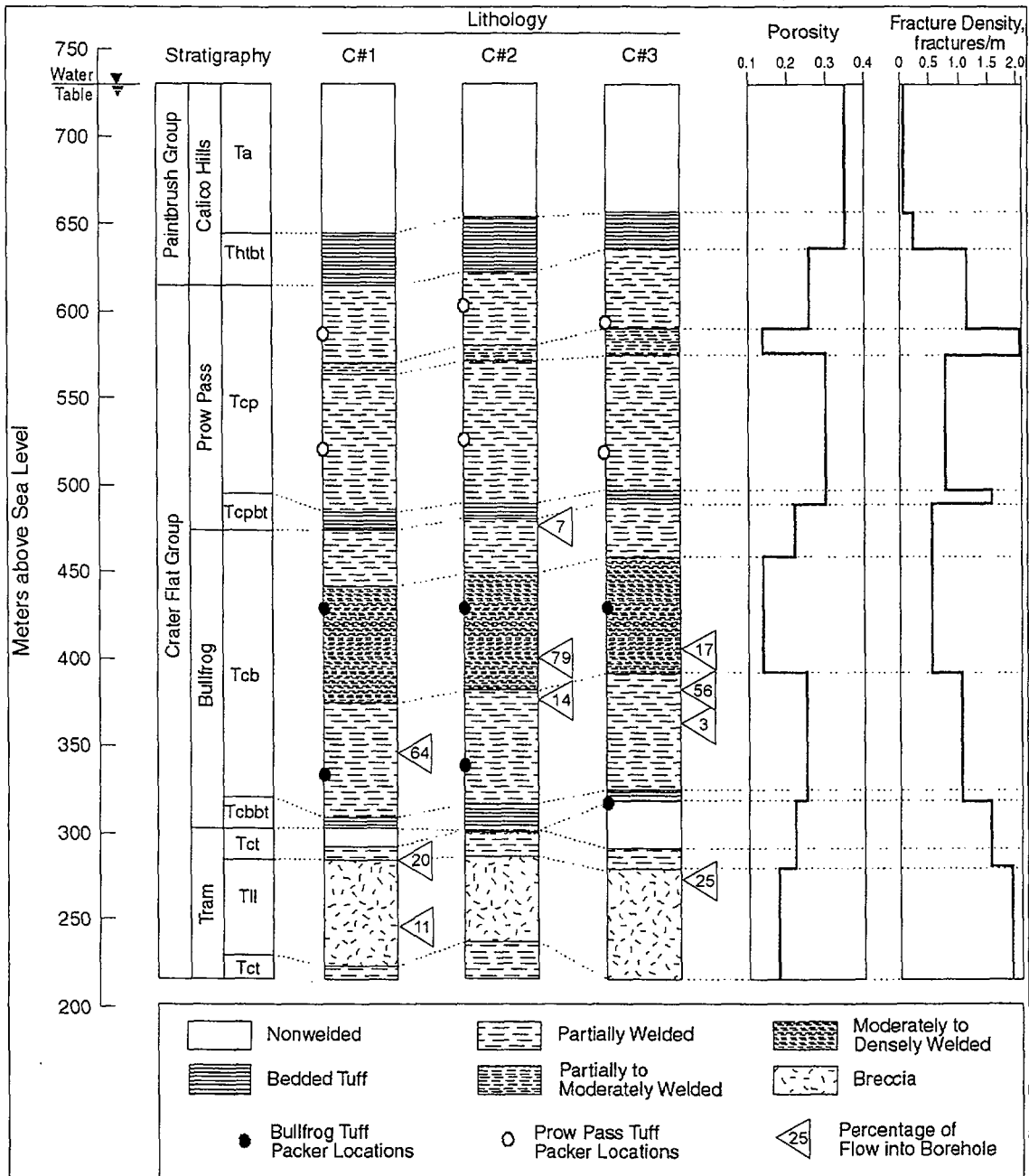
Figure 10.7-52. Saturation Profiles



10.7-53.DOC.SITEDESC-R01

Source: CRWMS M&O (2000, Figure 94)

Figure 10.7-53. Location and Layout of the C-Holes Complex

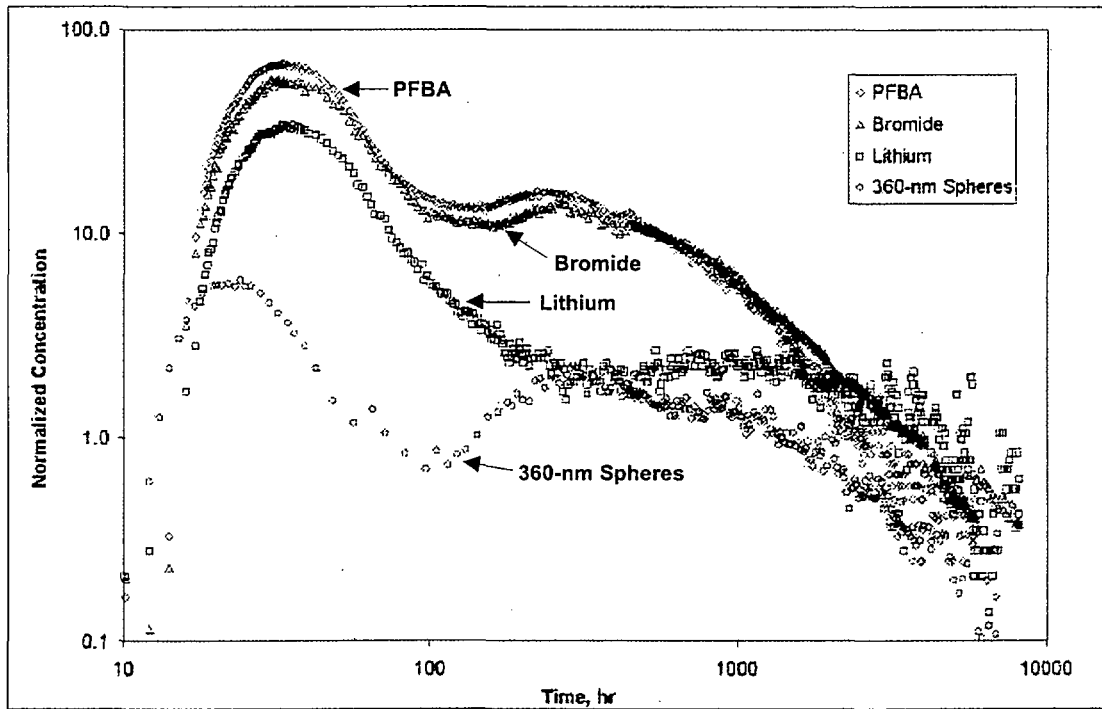


10.7-54.DOC.SITEDESC-R01

Source: CRWMS M&O (2000, Figure 95)

NOTE: Packer locations indicate intervals in which hydraulic and tracer tests were conducted by the U.S. Geological Survey and Los Alamos. (Note that the two Los Alamos tracer tests involving multiple tracers were conducted between c#2 and c#3.)

Figure 10.7-54. Stratigraphy, Lithology, Matrix Porosity, Fracture Density, and Inflow from Open-Hole Flow Surveys at the C-Holes

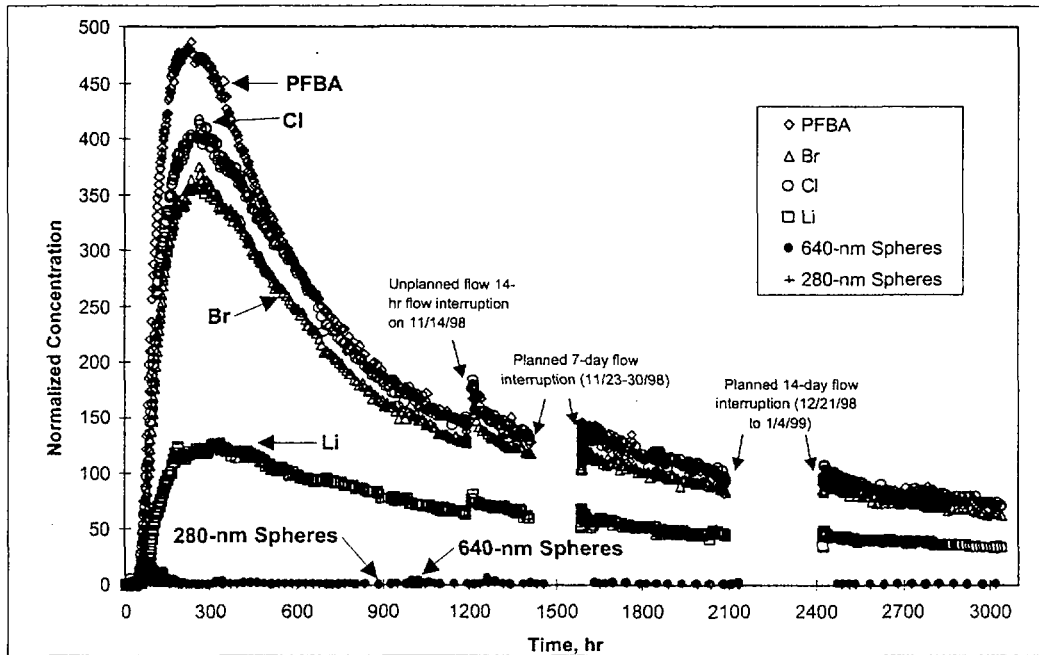


10.7-55.DOC.SITEDESC-R01

Source: CRWMS M&O (2000, Figure 96)

NOTE: Tracer recoveries were approximately 69 percent for pentafluorobenzoic acid (PFBA), approximately 69 percent for bromide, approximately 39 percent for lithium, and approximately 15 percent for microspheres. Concentrations are normalized to mass injected. Both axes are log scale.

Figure 10.7-55. Normalized Tracer Responses in the Bullfrog Tuff Multiple Tracer Test

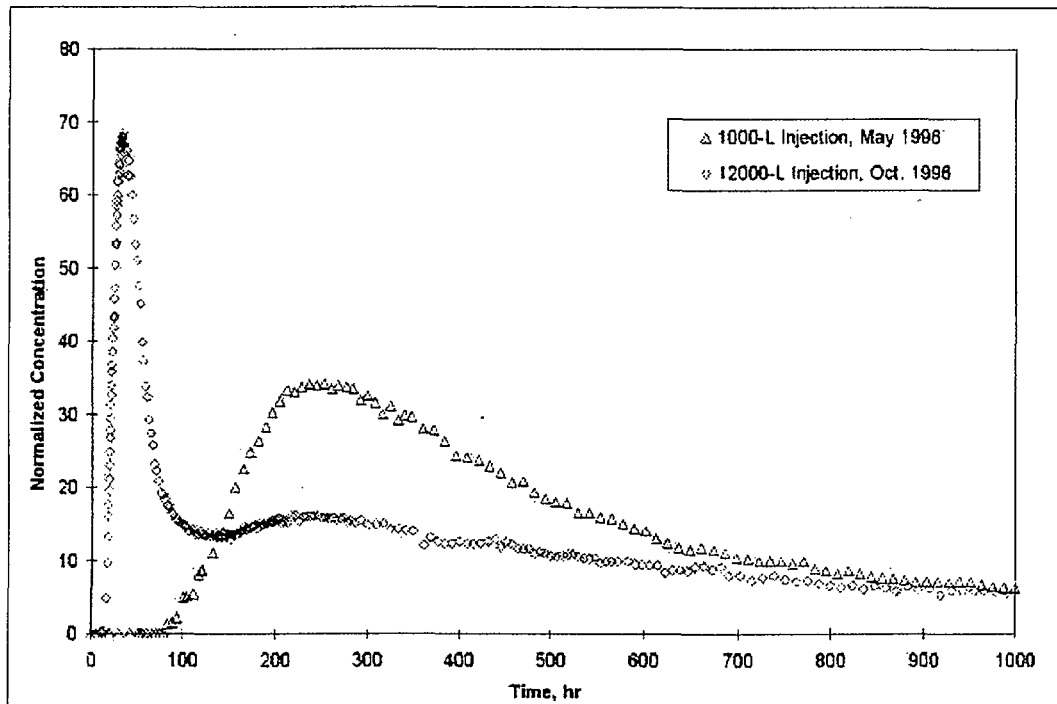


10.7-56.DOC.SITEDESC-R01

Source: CRWMS M&O (2000, Figure 97)

NOTE: Microsphere responses are shown more clearly in Figure 10.7-58. Tracer recoveries were 52 percent for pentafluorobenzoic acid (PFBA), 49 percent for chlorine, 43 percent for bromine, 19 percent for lithium, 0.3 percent for 640-nm spheres, and 0.1 percent for 280-nm spheres. Concentrations are normalized to mass injected.

Figure 10.7-56. Normalized Tracer Responses in the Prow Pass Tuff Multiple Tracer Test

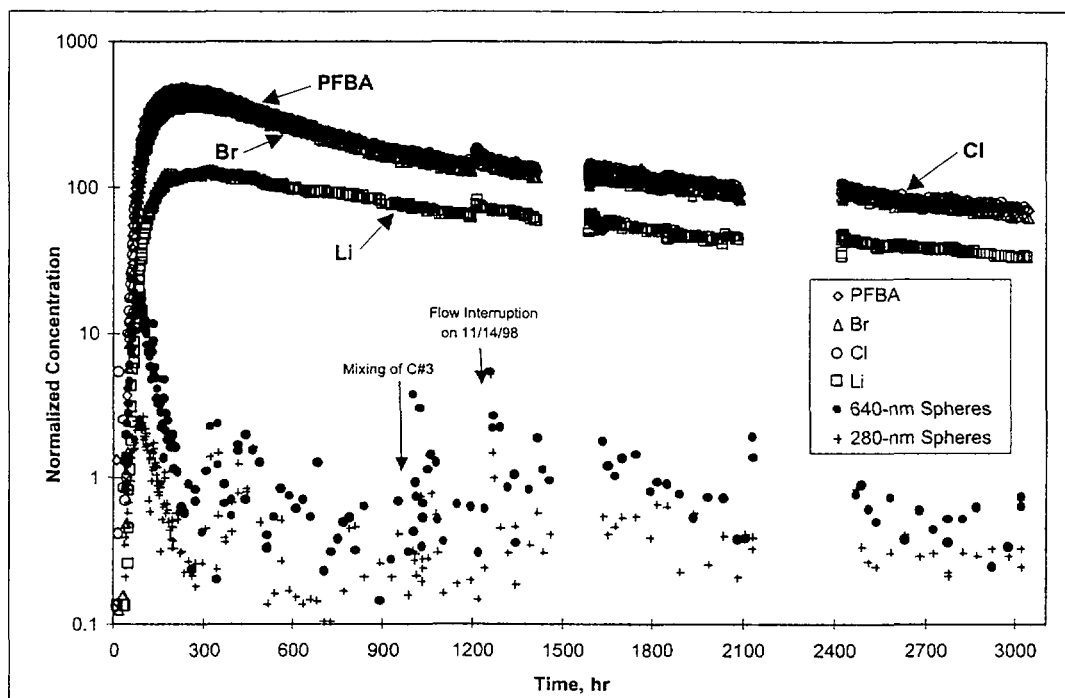


10.7-57.DOC.SITEDESC-R01

Source: CRWMS M&O (2000, Figure 98)

NOTE: The axes are both linear. These tests differed only in the amount of tracer solution injected. Concentrations are normalized to mass injected.

Figure 10.7-57. Normalized Pentafluorobenzoic Acid Responses in Two Different Tracer Tests in the Bullfrog Tuff

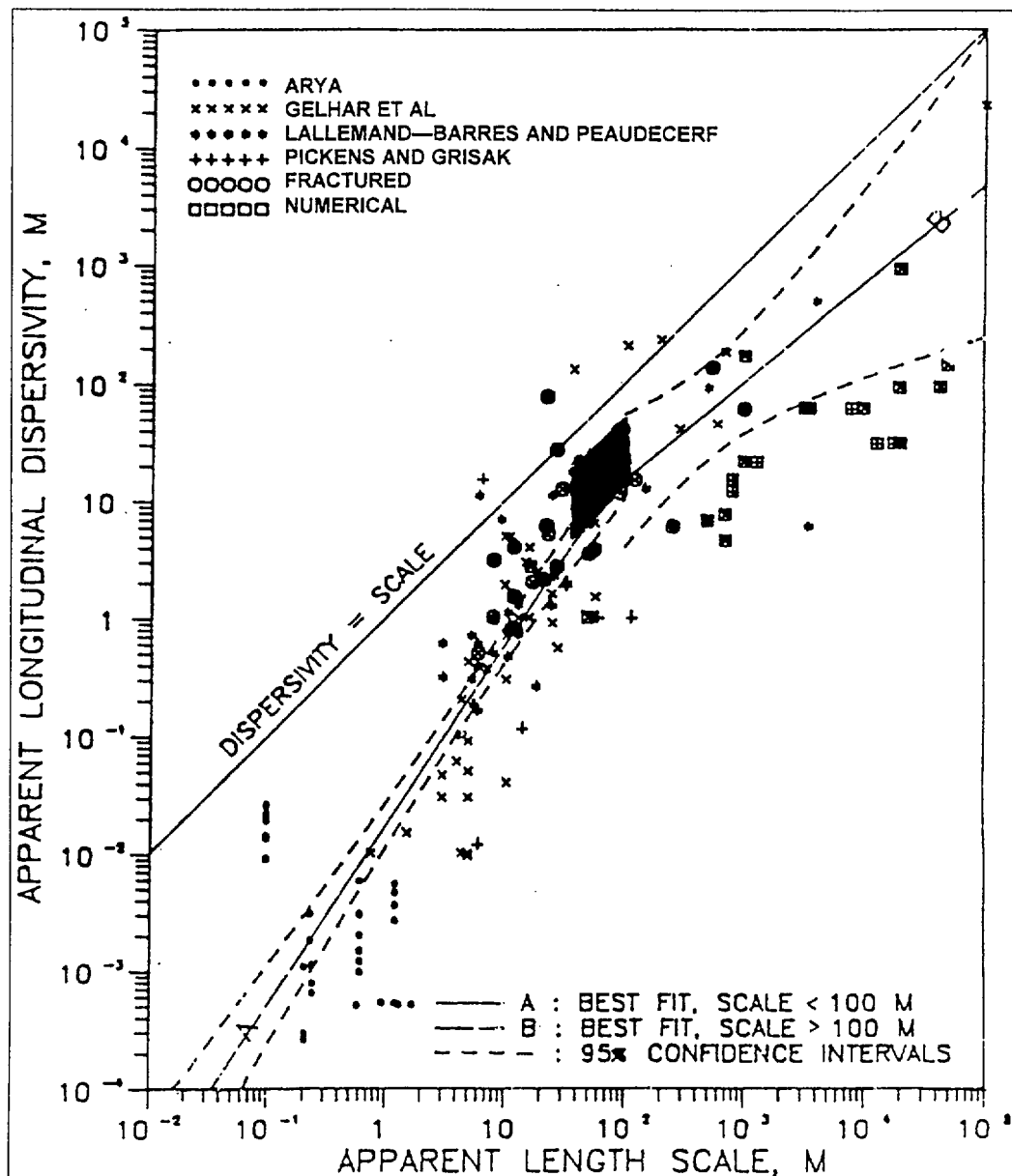


10.7-58.DOC.SITEDESC-R01

Source: CRWMS M&O (2000, Figure 99)

NOTE: The time scale (x axis) is linear. The microspheres appeared to respond after pressure transients associated with mixing the injection wellbore (C#3) and an unplanned flow interruption. Concentrations are normalized to mass injected.

Figure 10.7-58. Log Normalized Tracer Responses in the Prow Pass Tuff Multiple Tracer Test

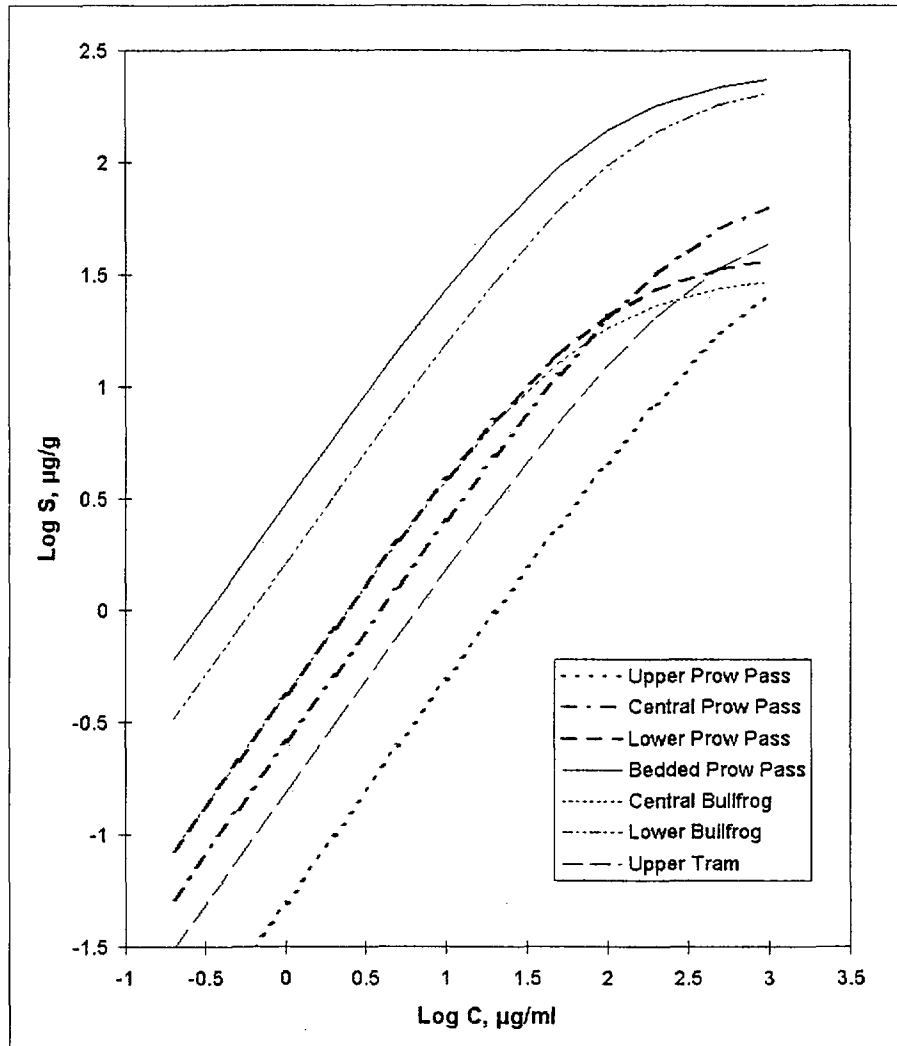


10.7-59.DOC.SITEDESC-R01

Sources: Neuman (1990); CRWMS M&O (2000, Figure 100)

NOTES: This figure shows the range of C-Holes values derived from interpretations of the Prow Pass and Bullfrog reactive tracer tests (darkened box). Note that the right edge of the box corresponds to the interwell separation distance, and the left edge of the box corresponds to the test interval thickness (taken to be the upper limit of transport distance).

Figure 10.7-59. Longitudinal Dispersivity versus Length Scale of C-Holes Values from Interpretations of the Prow Pass and Bullfrog Reactive Tracer Tests



10.7-60.DOC.SITEDESC-R01

Source: CRWMS M&O (2000, Figure 101)

NOTES: The units are ordered in the legend from shallowest to deepest. Lithium concentrations in the field tests ranged from less than 0.1 mg/L to 2,600 mg/L. These isotherms are based on log amount sorbed versus log solution concentration.

Figure 10.7-60. Fitted Langmuir Sorption Isotherms for Lithium Sorption onto C-Holes Tufts from Different Units/Lithologies

Table 10.2-1. Summary of Results for Solubility Experiments on Neptunium in J-13 Groundwater

Steady-State Concentration (M)			
pH	25°C	60°C	90°C
6.0	$(6.45 \pm 1.11) \times 10^{-4}$	$(9.40 \pm 1.22) \times 10^{-4}$	$(9.11 \pm 1.81) \times 10^{-4}$
7.0	$(3.06 \pm 0.20) \times 10^{-5}$	$(1.58 \pm 0.57) \times 10^{-5}$	$(8.61 \pm 2.26) \times 10^{-6}$
8.5	$(1.47 \pm 0.59) \times 10^{-5}$	$(1.66 \pm 0.92) \times 10^{-5}$	$(5.50 \pm 1.97) \times 10^{-6}$

Source: Efurd et al. (1996)

Table 10.2-2. Summary of Results for Solubility Experiments on Plutonium in J-13 Groundwater

Steady-State Concentration (M)			
pH	25°C	60°C	90°C
6.0	$(4.70 \pm 1.13) \times 10^{-8}$	$(9.01 \pm 2.01) \times 10^{-9}$	$(4.23 \pm 1.06) \times 10^{-9}$
7.0	$(2.36 \pm 1.23) \times 10^{-8}$	$(8.25 \pm 0.74) \times 10^{-9}$	$(4.29 \pm 2.05) \times 10^{-9}$
8.5	$(9.35 \pm 1.60) \times 10^{-9}$	$(6.22 \pm 1.75) \times 10^{-9}$	$(3.62 \pm 1.14) \times 10^{-9}$

Source: Efurd et al. (1996)

Table 10.2-3. Summary of Results for Solubility Experiments on Americium in J-13 Groundwater (Americium Tracer in Neodymium)

Steady-State Concentration (M)			
pH	25°C	60°C	90°C
6.0	$(1.8 \pm 0.06) \times 10^{-9}$	$(2.5 \pm 0.7) \times 10^{-6}$	$(1.7 \pm 1.9) \times 10^{-9}$
7.0	$(1.2 \pm 0.3) \times 10^{-9}$	$(9.9 \pm 0.74) \times 10^{-9}$	$(3.1 \pm 2.05) \times 10^{-10}$
8.5	$(2.4 \pm 1.9) \times 10^{-9}$	$(1.2 \pm 1.3) \times 10^{-8}$	$(3.4 \pm 2.1) \times 10^{-10}$

Source: Nitsche et al. (1993)

Table 10.2-4. Extractions of Solubility Values for Total System Performance Assessment

Element	Minimum Value (M)	Maximum Value (M)	Expected Value (M)	Coefficient of Variation	Distribution
Americium	$10^{-10}$	$10^{-6}$	$5 \times 10^{-7}$	–	uniform
Plutonium	$3 \times 10^{-9(a)}$	$10^{-6}$	$5.1 \times 10^{-7}$	–	uniform
Uranium	$10^{-8}$	$10^{-2}$	$3.2 \times 10^{-5}$	0.20	log beta
Thorium	$10^{-10}$	$10^{-7}$	–	–	log uniform
Radium	$10^{-9}$	$10^{-5}$	$10^{-7}$	0.10	log beta
Lead	$10^{-8}$	$10^{-5}$	$10^{-6.5}$	0.08	log beta
Neptunium	$5 \times 10^{-6}$	$10^{-3(a)}$	$1.4 \times 10^{-4}$	0.20	log beta
Protactinium	$10^{-10}$	$10^{-5}$	–	–	log uniform
Actinium	$10^{-10}$	$10^{-6}$	–	–	uniform
Tin	$10^{-11}$	$10^{-7}$	–	–	uniform
Nickel	$10^{-6}$	$10^{-1}$	$10^{-2.7}$	0.25	log beta
Strontium	$10^{-6}$	$10^{-3}$	$10^{-4}$	0.12	log beta
Samarium	$10^{-10}$	$10^{-6}$	–	–	uniform
Zirconium	$10^{-12}$	$10^{-7}$	–	–	log uniform
Niobium	$10^{-9}$	$10^{-7}$	–	–	log uniform

Source: Triay et al. (1997, Table 45)

NOTE: Values are from expert elicitations, except where updated by new experimental data from Efurd et al. (1996).

– = no data available

Table 10.3-1. Correlation of Stratigraphy and Sorption Samples

Unit Description	Lithologic Notation	Number of Sorption Samples
Upper Tiva Canyon, undifferentiated	Tpc	1
Lower, densely welded subunit of the Tiva Canyon Tuff	Tpcpv3	-
Partially to nonwelded lower subzones of the Tiva Canyon Tuff	Tpcpv1-2	-
Pre-Tiva Canyon Tuff bedded tuff	Tpbt4	-
Yucca Mountain Tuff	Tpy	-
Pre-Yucca Mountain Tuff bedded tuff	Tpbt3	-
Pah Canyon Tuff	Tpp	v = 1
Pre-Pah Canyon Tuff bedded tuff	Tpbt2	-
Topopah Spring Tuff upper partially to nonwelded zones <sup>a</sup>	Tptrv2-3	-
Topopah Spring Tuff upper, densely welded vitrophyre <sup>a</sup>	Tptrv1	2
Topopah Spring Tuff crystal-rich nonlithophysal zone <sup>a</sup>	Tptrn	7
Topopah Spring Tuff crystal-rich lithophysal zone	Tptrl	-
Topopah Spring Tuff lithic-rich zone	Tptf	-
Topopah Spring Tuff upper lithophysal zone <sup>b</sup>	Ttpul	-
Topopah Spring Tuff middle nonlithophysal zone <sup>b</sup>	Ttpmn	5
Topopah Spring Tuff lower lithophysal zone <sup>b</sup>	Ttpll	1
Topopah Spring Tuff lower nonlithophysal zone <sup>b</sup>	Ttpln	3
Topopah Spring Tuff lower, densely welded vitrophyre	Ttpv3	-
Topopah Spring Tuff lower, partially welded zone	Ttpv2	-
Topopah Spring Tuff lower nonwelded zone	Ttpv1	4 (z = 1, v = 3)
Pre-Topopah Spring Tuff bedded tuff	Tpbt1	4 (z = 2, v = 2)
Calico Hills Formation	Tac	19 (z = 18, v = 1)
Pre-Calico Hills Formation bedded tuff	Tacbt	-
Prow Pass Tuff upper nonwelded zone	Tcpunw	2 (z = 1, v = 1)
Prow Pass Tuff upper welded zone	Tcpuw	2
Prow Pass Tuff lower nonwelded zone	Tcplnw	z = 3
Bullfrog Tuff upper nonwelded zone	Tcbunw	-
Bullfrog Tuff upper welded zone	Tcbuw	2
Bullfrog Tuff lower nonwelded zone	Tcblnw	-
Tram Tuff upper nonwelded zone	Tctunw	-
Tram Tuff upper nonwelded zone	Tctuw	1

Source: CRWMS M&O (1997, Figure 1)

NOTES: <sup>a</sup> Quartz-latic units

<sup>b</sup> Units could include potential waste emplacement horizons

Stratigraphy based on CRWMS M&O (1997, Figure 1)

- = no samples; v = vitric; z = zeolitic

Table 10.3-2. Plutonium Sorption Distribution Coefficients (Under Atmospheric Conditions)

Solid Phase	$K_d$ Range in UE-25 J-13 Water (mL/g)	$K_d$ Range in Synthetic UE-25 p#1 Water (mL/g)
Vitric tuff	600–2,000	100–400
Zeolitic tuff	300–500	100–400
Devitrified tuff	40–100	20–70
Synthetic hematite	> 10,000	> 10,000
Montmorillonite	> 10,000	> 10,000
Clinoptilolite	600–3,000	2,000–5,000
Calcite	200–1,000	100–800
Gibbsite	0–10	10–90
Albite	3–10	< 10
Quartz	< 10	< 10

Source: CRWMS M&O (2000, Table 4)

Table 10.3-3. Sorption-Coefficient Distributions for Unsaturated Zone Units

Element	Rock Type	Min $K_d$ (mL/g)	Max $K_d$ (mL/g)	E[x]	COV <sup>a</sup>	Distribution Type
Americium	Devitrified	100	2,000	—	—	Uniform
	Vitric	100	1,000	400	0.20	Beta
	Zeolitic	100	1,000	—	—	Uniform
	Iron oxide	1,000	5,000	—	—	Uniform
Plutonium	Devitrified	5	70	—	—	Beta
	Vitric	20	200	100	0.25	Beta
	Zeolitic	30	200	100	0.25	Beta
	Iron oxide	1,000	5,000	—	—	Uniform
Uranium	Devitrified	0	2.0	0.5	0.3	Beta
	Vitric	0	1.0	0.5	0.3	Beta
	Zeolitic	0	10.0	4.0	1.0	Beta(exp)
	Iron oxide	100	1,000	—	—	Uniform
Neptunium	Devitrified	0	1.0	0.3	0.3	Beta
	Vitric	0	1.0	0.3	1.0	Beta(exp)
	Zeolitic	0	3.0	0.5	0.25	Beta
	Iron oxide	500	1,000	—	—	Uniform
Radium	Devitrified	70	300	—	—	Uniform
	Vitric	50	100	—	—	Uniform
	Zeolitic	800	2,000	—	—	Uniform
	Iron oxide	0	500	30	1.0	Beta(exp)
Cesium	Devitrified	10	700	—	—	Uniform
	Vitric	10	100	—	—	Uniform
	Zeolitic	300	3,000	—	—	Uniform
	Iron oxide	0	300	30	1.0	Beta(exp)
Strontium	Devitrified	5	30	—	—	Uniform
	Vitric	0	20	—	—	Uniform
	Zeolitic	200	2,000	—	—	Uniform
	Iron oxide	0	20	10	0.25	Beta
Nickel	Devitrified	0	200	50	0.33	Beta
	Vitric	0	50	30	0.33	Beta
	Zeolitic	0	200	50	0.33	Beta
	Iron oxide	0	500	—	—	Uniform
Lead	Devitrified	100	500	—	—	Uniform
	Vitric	100	500	—	—	Uniform
	Zeolitic	100	500	—	—	Uniform
	Iron oxide	100	1,000	—	—	Uniform
Tin	Devitrified	20	200	—	—	Uniform
	Vitric	20	200	—	—	Uniform
	Zeolitic	100	300	—	—	Uniform
	Iron oxide	0	5,000	—	—	Uniform
Protactinium	Devitrified	0	100	—	—	Uniform
	Vitric	0	100	—	—	Uniform
	Zeolitic	0	100	—	—	Uniform
	Iron oxide	500	1,000	—	—	Uniform
Selenium	Devitrified	0	1	0.1	1.0	Beta(exp)
	Vitric	0	1	0.1	1.0	Beta(exp)
	Zeolitic	0	1	0.2	1.0	Beta(exp)
	Iron oxide	0	200	30	1.0	Beta(exp)
Carbon	Iron oxide	10	100	—	—	Uniform
Actinium, Niobium, Samarium, Thorium, Zirconium: see Americium						
Chlorine, Technetium, Iodine		0	0	—	—	—

Source: CRWMS M&O (2000, Figure 2a)

NOTES: <sup>a</sup> Coefficient of variation:  $COV = \sigma[x]/E[x]$

Values determined by expert elicitation.

-- = no data available

Table 10.3-4. Sorption-Coefficient Distributions for Saturated Zone Units

Element	Rock Type	Min $K_d$ (mL/g)	Max $K_d$ (mL/g)	E[x]	COV <sup>a</sup>	Distribution Type
Americium	Devitrified	100	2,000	-	-	Uniform
	Vitric	100	1,000	400	0.20	Beta
	Zeolitic	100	1,000	-	-	Uniform
	Iron oxide	1,000	5,000	-	-	Uniform
Plutonium	Devitrified	5	100	50	0.15	Beta
	Vitric	50	300	100	0.15	Beta
	Zeolitic	50	400	100	0.15	Beta
	Iron oxide	1,000	5,000	-	-	Uniform
Uranium	Devitrified	0	5.0	2.0	0.3	Uniform
	Vitric	0	4.0	1.0	0.3	Uniform
	Zeolitic	5	20.0	7.0	0.3	Beta
	Iron oxide	100	1,000	-	-	Uniform
	Alluvium	0	8.0	N/A	N/A	Uniform
Neptunium	Devitrified	0	2.0	0.5	0.3	Beta
	Vitric	0	2.0	0.5	1.0	Beta(exp)
	Zeolitic	0	5.0	1.0	0.25	Beta
	Iron oxide	500	1,000	-	-	Uniform
	Alluvium	0	100	18	1.0	Beta
Radium	Devitrified	100	500	-	-	Uniform
	Vitric	100	500	-	-	Uniform
	Zeolitic	1,000	5,000	-	-	Uniform
	Iron oxide	0	1,500	30	1.0	Beta(exp)
Cesium	Devitrified	20	1,000	-	-	Uniform
	Vitric	10	100	-	-	Uniform
	Zeolitic	500	5,000	-	-	Uniform
	Iron oxide	0	500	30	1.0	Beta(exp)
Strontium	Devitrified	10	200	-	-	Uniform
	Vitric	20	50	-	-	Uniform
	Zeolitic	2,000	5,000	-	-	Log uniform
	Iron oxide	0	30	10	0.25	Beta
Nickel	Devitrified	0	200	-	-	Uniform
	Vitric	0	50	-	-	Uniform
	Zeolitic	0	200	-	-	Uniform
	Iron oxide	0	1,000	-	-	Uniform
Lead	Devitrified	100	500	-	-	Uniform
	Vitric	100	500	-	-	Uniform
	Zeolitic	100	500	-	-	Uniform
	Iron oxide	100	1,000	-	-	Uniform
Tin	Devitrified	20	200	-	-	Uniform
	Vitric	20	200	-	-	Uniform
	Zeolitic	100	300	-	-	Uniform
	Iron oxide	0	5,000	-	-	Uniform
Protactinium	Devitrified	0	100	-	-	Uniform
	Vitric	0	100	-	-	Uniform
	Zeolitic	0	100	-	-	Uniform
	Iron oxide	500	1,000	-	-	Uniform
Selenium	Devitrified	0	1.0	0.1	1.0	Beta(exp)
	Vitric	0	1.0	0.1	1.0	Beta(exp)
	Zeolitic	0	1.0	0.2	1.0	Beta(exp)
	Iron oxide	0	500	30	1.0	Beta(exp)
Carbon	Iron oxide	10	100	-	-	Uniform
Actinium, Niobium, Samarium, Thorium, Zirconium: see Americium						
Chlorine, Technetium, Iodine in tuff		0	0	-	-	-
Technetium in Alluvium		0.27	0.62	-	-	Uniform
Iodine in Alluvium		0.32	0.63	-	-	Uniform

Source: CRWMS M&O (2000, Figure 2b)

NOTE: <sup>a</sup>Coefficient of variation:  $COV = \sigma[x]/E[x]$   
 Values determined by expert elicitation.  
 - = no data available; N/A = not applicable

Table 10.3-5. Prediction of Neptunium Sorption on Clinoptilolite-Rich G4-1510 Tuff in J-13 Water

Initial Concentration (M)	pH	Measured $K_d$ (m)	Predicted $K_d$ (m) <sup>a</sup>
1 x 10 <sup>-7</sup> to 3 x 10 <sup>-5</sup>	7	1 x 10 <sup>-7</sup>	9 x 10 <sup>-8</sup>
	8.5	6 x 10 <sup>-8</sup>	5 x 10 <sup>-8</sup>

Source: CRWMS M&O (2000, Table 5)

NOTE: <sup>a</sup>Prediction assumes clinoptilolite is the only sorbing mineral in the tuff.

Table 10.3-6. Neptunium Sorption onto Clinoptilolite-Rich Tuffs in J-13 Water

Tuff Sample	Measured $K_d$ (m)	Predicted $K_d$ (m)	Clinoptilolite %
G1-1405	1 x 10 <sup>-7</sup>	1 x 10 <sup>-7</sup>	68 ± 7
G4-1505	9 x 10 <sup>-8</sup>	1 x 10 <sup>-7</sup>	74 ± 7
G4-1506	1 x 10 <sup>-7</sup>	1 x 10 <sup>-7</sup>	62 ± 7
G4-1510	8 x 10 <sup>-8</sup>	1 x 10 <sup>-7</sup>	59 ± 7
G4-1529	7 x 10 <sup>-8</sup>	1 x 10 <sup>-7</sup>	59 ± 8
G4-1625	9 x 10 <sup>-8</sup>	1 x 10 <sup>-7</sup>	61 ± 7
G4-1772	1 x 10 <sup>-7</sup>	1 x 10 <sup>-7</sup>	63 ± 5
G4-2077	5 x 10 <sup>-8</sup>	8 x 10 <sup>-8</sup>	51 ± 8

Source: CRWMS M&O (2000, Table 6)

NOTE: Atmospheric conditions; initial neptunium concentrations ranged from 6 to 8 x 10<sup>-7</sup> M; tuffs were wet-sieved to particle sizes ranging from 75 to 500 µm; the pretreatment period was 2 to 14 days; and the sorption period was 3 to 23 days.

Table 10.3-7. Uranium Sorption in J-13 Water under Oxidizing Conditions

Solid Phase	pH	$K_d$ (mL/g) <sup>a</sup>
G4-268, devitrified tuff	7	2 x 10 <sup>-1</sup>
	8.5	7 x 10 <sup>-1</sup>
GU3-1405, vitric tuff	7	-5 x 10 <sup>-1</sup>
	8.5	6 x 10 <sup>-1</sup>
Quartz	7	1 x 10 <sup>-1</sup>
	8.5	7 x 10 <sup>-2</sup>
Albite	7	-5 x 10 <sup>-2</sup>
	8.5	-1 x 10 <sup>-1</sup>

Source: CRWMS M&O (2000, Table 7)

NOTE: <sup>a</sup>The uncertainties in the data are ± 3 mL/g.

Table 10.3-8. Prediction of Uranium Sorption on Clinoptilolite-Rich G4-1510 Tuff in J-13 Water

Initial Concentration (M)	pH	Measured $K_a$ (m)	Predicted $K_a$ (m) <sup>a</sup>
2 x 10 <sup>-7</sup> to 4 x 10 <sup>-7</sup>	7	8 x 10 <sup>-7</sup>	8 x 10 <sup>-7</sup>
	8.5	8 x 10 <sup>-7</sup>	4 x 10 <sup>-7</sup>

Source: CRWMS M&O (2000, Table 8)

NOTE: <sup>a</sup> Prediction assumes clinoptilolite is the only sorbing mineral in the tuff.

Table 10.3-9. Plutonium (V) in J-13 Well Water with Fulvic Acid

Estimated Concentration (M)	1.0 x 10 <sup>-8</sup>	5.0 x 10 <sup>-8</sup>	1.0 x 10 <sup>-7</sup>	2.0 x 10 <sup>-7</sup>	5.0 x 10 <sup>-7</sup>
Control #1 (cpm)	265.5	1,436.1	2,939.1	5,825.8	15,880.5
Control #2 (cpm)	281.7	1,371.0	2,839.9	5,883.0	16,138.0
Standard #1 (cpm)	334.1	1,588.2	3,223.5	6,484.8	17,143.5
Standard #2 (cpm)	327.3	1,580.8	3,164.6	6,387.5	17,178.9
Control average (cpm)	273.6	1,403.5	2,889.5	5,854.4	16,009.2
Standard average (cpm)	330.7	1,584.5	3,194.1	6,436.1	17,161.2
Control concentration (M)	8.3 x 10 <sup>-9</sup>	4.3 x 10 <sup>-8</sup>	8.8 x 10 <sup>-8</sup>	1.8 x 10 <sup>-7</sup>	4.9 x 10 <sup>-7</sup>
Standard concentration (M)	1.0 x 10 <sup>-8</sup>	4.8 x 10 <sup>-8</sup>	9.7 x 10 <sup>-8</sup>	2.0 x 10 <sup>-7</sup>	5.2 x 10 <sup>-7</sup>
Difference in concentration (std – cont)	1.7 x 10 <sup>-9</sup>	5.5 x 10 <sup>-9</sup>	9.3 x 10 <sup>-9</sup>	1.8 x 10 <sup>-8</sup>	3.5 x 10 <sup>-8</sup>
Difference in ratio percent	17.3%	11.4%	9.5%	9.0%	6.7%

DTN: LAIT831341AQ98.001

NOTE: CPM = counts per minute

Table 10.3-10. Plutonium (V) in J-13 Well Water with Humic Acid

Estimated Concentration (M)	1.0 x 10 <sup>-8</sup>	5.0 x 10 <sup>-8</sup>	1.0 x 10 <sup>-7</sup>	2.0 x 10 <sup>-7</sup>	5.0 x 10 <sup>-7</sup>
Control #1 (cpm)	256.6	1,220.1	2,503.3	5,345.0	15,076.6
Control #2 (cpm)	259.4	1,240.6	2,419.9	5,227.5	15,530.8
Standard #1 (cpm)	333.4	1,578.7	3,213.7	6,225.6	17,197.9
Standard #2 (cpm)	336.2	1,636.8	3,184.0	6,456.9	17,224.4
Control average (cpm)	258.0	1,230.3	2,461.6	5,286.2	15,303.7
Standard average (cpm)	334.8	1,607.7	3,198.8	6,341.2	17,211.1
Control concentration (M)	7.8 x 10 <sup>-9</sup>	3.7 x 10 <sup>-8</sup>	7.5 x 10 <sup>-8</sup>	1.6 x 10 <sup>-7</sup>	4.6 x 10 <sup>-7</sup>
Standard concentration (M)	1.0 x 10 <sup>-8</sup>	4.9 x 10 <sup>-8</sup>	9.7 x 10 <sup>-8</sup>	1.9 x 10 <sup>-7</sup>	5.2 x 10 <sup>-7</sup>
Difference in concentration (std – cont)	2.3 x 10 <sup>-9</sup>	1.1 x 10 <sup>-8</sup>	2.2 x 10 <sup>-8</sup>	3.2 x 10 <sup>-8</sup>	5.8 x 10 <sup>-8</sup>
Difference in ratio percent	23.0%	23.5%	23.0%	16.6%	11.1%

DTN: LAIT831341AQ98.001

NOTE: CPM = counts per minute

Table 10.3-11. Plutonium (V) in Synthetic UE-25 p#1 Well Water with Fulvic Acid

Estimated Concentration (M)	$1.0 \times 10^{-8}$	$5.0 \times 10^{-8}$	$1.0 \times 10^{-7}$	$2.0 \times 10^{-7}$	$5.0 \times 10^{-7}$
Control #1 (cpm)	304.1	1,688.7	3,094.4	6,613.6	17,508.2
Control #2 (cpm)	301.0	1,698.7	3,488.6	6,924.6	17,115.6
Standard #1 (cpm)	333.8	1,705.2	3,538.5	7,052.1	17,487.7
Standard #2 (cpm)	340.9	1,717.4	3,476.2	7,025.7	17,934.1
Control average (cpm)	302.6	1,693.7	3,291.5	6,769.1	17,311.9
Standard average (cpm)	337.4	1,711.3	3,507.4	7,038.9	17,710.9
Control concentration (M)	$9.2 \times 10^{-9}$	$5.1 \times 10^{-8}$	$1.0 \times 10^{-7}$	$2.1 \times 10^{-7}$	$5.3 \times 10^{-7}$
Standard concentration (M)	$1.0 \times 10^{-8}$	$5.2 \times 10^{-8}$	$1.1 \times 10^{-7}$	$2.1 \times 10^{-7}$	$5.4 \times 10^{-7}$
Difference in concentration (std – cont)	$1.1 \times 10^{-9}$	$5.4 \times 10^{-10}$	$6.6 \times 10^{-9}$	$8.2 \times 10^{-9}$	$1.2 \times 10^{-8}$
Difference in ratio percent	10.3%	1.0%	6.2%	3.8%	2.3%

DTN: LAIT831341AQ98.001

NOTE: CPM = counts per minute

Table 10.3-12. Plutonium (V) in Synthetic UE-25 p#1 Well Water with Humic Acid

Estimated Concentration (M)	$1.0 \times 10^{-8}$	$5.0 \times 10^{-8}$	$1.0 \times 10^{-7}$	$2.0 \times 10^{-7}$	$5.0 \times 10^{-7}$
Control #1 (cpm)	290.0	1,633.3	3,274.2	6,739.4	17,191.5
Control #2 (cpm)	301.8	1,656.9	3,182.9	6,005.8	16,904.0
Standard #1 (cpm)	335.2	1,717.1	3,550.4	7,080.7	17,539.3
Standard #2 (cpm)	334.2	1,685.7	3,511.5	7,082.2	17,568.1
Control average (cpm)	295.9	1,645.1	3,228.5	6,372.6	17,047.8
Standard average (cpm)	334.7	1,701.4	3,530.9	7,081.4	17,553.7
Control concentration (M)	$9.0 \times 10^{-9}$	$5.0 \times 10^{-8}$	$9.8 \times 10^{-8}$	$1.9 \times 10^{-7}$	$5.2 \times 10^{-7}$
Standard concentration (M)	$1.0 \times 10^{-8}$	$5.2 \times 10^{-8}$	$1.1 \times 10^{-7}$	$2.2 \times 10^{-7}$	$5.3 \times 10^{-7}$
Difference in concentration (std – cont)	$1.2 \times 10^{-9}$	$1.7 \times 10^{-9}$	$9.2 \times 10^{-9}$	$2.2 \times 10^{-8}$	$1.5 \times 10^{-8}$
Difference in ratio percent	11.6%	3.3%	8.6%	10.0%	2.9%

DTN: LAIT831341AQ98.001

NOTE: CPM = counts per minute

Table 10.3-13. Minerals in Yucca Mountain Tuff with High Cation Exchange Capacities

Mineral	Maximum Abundance	Capacity (meq/g)
Clinoptilolite	90%	2.3
Mordenite	60%	2.3
Montmorillonite	40%	0.8–1.5
Illite	20%	0.13–0.42

Source: Triay et al. (1997, Table 53)

NOTE: CPM = counts per minute

Table 10.3-14. Intrinsic Constants for Metal Oxides

Metal Oxide	log $K_{s1}$	log $K_{s2}$	Point of Zero Charge
SiO <sub>2</sub>	-0.5	-8.2	4.3
Al <sub>2</sub> O <sub>3</sub>	-7.8	-11.3	9.3
FeOOH	-7.6	-11.4	8.5

Source: Triay et al. (1997, Table 54)

Table 10.3-15. Groundwater Compositions Used for Neptunium Sorption Modeling

Constituent	Concentration (mg/L)		
	UE-25 J-13 water	UZ water	UE-25 p#1 water
Sodium	45	26–70	171
Potassium	5.3	5–16	13.4
Magnesium	1.8	5–21	31.9
Calcium	11.5	27–127	87.8
Silicon	30	72–100	30
Fluoride	2.1	–	3.5
Chloride	6.4	34–106	37
Sulfate	18.1	39–174	129
Bicarbonate	143	–	698
pH <sup>a</sup>	6.9	6.5–7.5	6.7

Source: Triay et al. (1997, Table 56)

NOTE: <sup>a</sup> pH represents negative log of H<sup>+</sup> concentration and is not measured in mg/L.

– = no data available

UZ = unsaturated zone

Table 10.3-16. Additional Equations and Parameters Used To Model Uranium Sorption onto Devitrified Tuff

Type of Reaction	Equilibrium Reaction	log K
Aqueous reactions	$UO_2^{2+} + H_2O \leftrightarrow UO_2OH^+ + H^+$	-5.8
	$UO_2^{2+} + 2 H_2O \leftrightarrow UO_2(OH)_2 + 2 H^+$	-12.5
	$2 UO_2^{2+} + 2 H_2O \leftrightarrow (UO_2)_2(OH)_2^{2+} + 2 H^+$	-5.62
	$3 UO_2^{2+} + 5 H_2O \leftrightarrow (UO_2)_3(OH)_5^+ + 5 H^+$	-15.63
Uranyl adsorption reactions	$2 t\text{-Al}^+\text{Na}^+ + UO_2^{2+} \leftrightarrow (t\text{-Al})_2UO_2^{2+} + 2 Na^+$	1.8
	$t\text{-Al}^+\text{Na}^+ + UO_2^{2+} + H_2O \leftrightarrow t\text{-Al}^+UO_2OH^+ + Na^+ + H^+$	-1.5
	$MOH + UO_2^{2+} \leftrightarrow MOUO_2^+ + H^+$	0.60
	$MOH + UO_2^{2+} + Cl^- \leftrightarrow MOUO_2^+Cl^- + H^+$	2.8
	$2 MOH + UO_2^{2+} \leftrightarrow (MO)_2UO_2 + 2 H^+$	-2.8
Parameters	Type of site	Site density (eq/kg)
	Tetrahedral( <i>f</i> ) aluminum	$2 \times 10^{-2}$
	Octahedral aluminum (edge)	$2 \times 10^{-3}$

Source: Triay et al. (1997, Table 57)

Table 10.3-17. Depth Intervals and Bulk Densities of Alluviums

Borehole-02D		Borehole-09Sx		Borehole-03S	
Depth (ft)	Density (g/cm <sup>3</sup> )	Depth (ft)	Density (g/cm <sup>3</sup> )	Depth (ft)	Density (g/cm <sup>3</sup> )
395-400	1.3	145-150	1.3	60-65	1.3
400-405	1.2	150-155	1.3	65-70	1.2
405-410	1.3	155-160	1.3	70-75	1.3
410-415	1.3	160-165	1.2	75-80	1.2

Source: Triay et al. (1997, Table 9)

Table 10.3-18. Quantitative X-Ray Diffraction Results of Three Alluviums

Minerals	Samples		
	NC-EWDP-02D 410–415 ft, 75–500 $\mu\text{m}$	NC-EWDP-03S 75–80 ft, 75–500 $\mu\text{m}$	NC-EWDP-09Sx 160–165 ft, 75–500 $\mu\text{m}$
Smectite	2 $\pm$ 1	1 $\pm$ 1	6 $\pm$ 2
Kaolinite	1 $\pm$ 1	1 $\pm$ 1	–
Clinoptilolite	4 $\pm$ 1	13 $\pm$ 1	3 $\pm$ 1
Tridymite	3 $\pm$ 1	–	1 $\pm$ 1
Cristobalite	16 $\pm$ 1	10 $\pm$ 1	18 $\pm$ 1
Quartz	18 $\pm$ 1	17 $\pm$ 1	14 $\pm$ 1
Feldspar	54 $\pm$ 8	53 $\pm$ 8	58 $\pm$ 8
Calcite	–	4 $\pm$ 1	–
Mica	Trace	1 $\pm$ 1	Trace
Hematite	1 $\pm$ 1	–	Trace
Hornblende	Trace	Trace	–
Unidentified Phases	Trace	–	–
<b>Total</b>	<b>99 <math>\pm</math> 8</b>	<b>100 <math>\pm</math> 8</b>	<b>100 <math>\pm</math> 8</b>

Source: Triay et al. (1997, Table 10)

NOTE: – = no data available

Table 10.4-1. Comparison of Neptunium  $K_d$  Values from Batch and Column Measurements

Column Number	Tuff Sample	Water Type	Batch $K_d$ (mL/g)	Column $K_d$ (mL/g)
1	G4-1508, zeolitic	J-13	$1.7 \pm 0.4$ (G4-1510)	1.7
2	G4-1508, zeolitic	J-13	$1.7 \pm 0.4$ (G4-1510)	1.2
3	G4-1505, zeolitic	J-13	$2.1 \pm 0.4$	2.8
4	G4-1505, zeolitic	Syn. UE-25 p#1	$0.2 \pm 0.3$ (G4-1506)	0.4
5	G4-1505, zeolitic	Syn. UE-25 p#1	$0.2 \pm 0.3$ (G4-1506)	0.2
6	G4-1505, zeolitic	Syn. UE-25 p#1	$0.2 \pm 0.3$ (G4-1506)	0.2
7	G4-268, devitrified	J-13	$-0.04 \pm 0.2$	0.07
8	G4-268, devitrified	J-13	$-0.04 \pm 0.2$	0.01
9	G4-268, devitrified	J-13	$-0.04 \pm 0.2$	0.02
10	G4-268, devitrified	J-13	$-0.04 \pm 0.2$	0.01
11	G4-272, devitrified	Syn. UE-25 p#1	$0.2 \pm 0.3$ (G4-270)	0.06
12	G4-268, devitrified	Syn. UE-25 p#1	$0.2 \pm 0.3$ (G4-270)	0.03
13	G4-268, devitrified	Syn. UE-25 p#1	$0.2 \pm 0.3$ (G4-270)	0.03
14	GU3-1407, vitric	J-13	$0.1 \pm 0.5$	0.2
15	GU3-1407, vitric	J-13	$0.1 \pm 0.5$	0.1
16	GU3-1405, vitric	J-13	$0.03 \pm 0.2$	0.1
17	GU3-1405, vitric	Syn. UE-25 p#1	$0.2 \pm 0.4$ (GU3-1407)	0.1
18	GU3-1405, vitric	Syn. UE-25 p#1	$0.2 \pm 0.4$ (GU3-1407)	0.1
19	GU3-1405, vitric	Syn. UE-25 p#1	$0.2 \pm 0.4$ (GU3-1407)	0.1

Source: CRWMS M&O (2000, Table 11)

Table 10.4-2. Selenium Batch Adsorption on Nonwelded Zeolitic Tuff

Pretreatment Period (days)	Sorption Period (days)	$K_d$ (mL/g)
6.9	0.04	-0.2
6.9	0.04	0.3
6.8	13.9	0.0
6.8	13.9	0.2

Source: CRWMS M&O (2000, Table 12)

NOTE: Experimental conditions: J-13 water; 20°C; 75 to 500  $\mu\text{m}$  tuff particle sizes; 1.1 ppm initial selenium concentration; solution pH after sorption of 8.4; and samples from the same location in G-Tunnel, Bed-5, as the tuff used in the column experiments.

Table 10.4-3. Minerals Coating Fracture Walls in Yucca Mountain Tuffs

<b>Zeolites</b>		
Heulandite ↔ Clinoptilolite	$\text{Ca}_4\text{Al}_8\text{Si}_{28}\text{O}_{72} \cdot 24\text{H}_2\text{O} \leftrightarrow (\text{Na}, \text{K})_6\text{Al}_6\text{Si}_{30}\text{O}_{72} \cdot 24\text{H}_2\text{O}$	
(range of compositions with arbitrary division of Si/Al < 4.4 for heulandite and Si/Al > 4.4 for clinoptilolite)		
Mordenite	$(\text{Ca}, \text{Na}_2, \text{K}_2)_4\text{Al}_8\text{Si}_{40}\text{O}_{96} \cdot 28\text{H}_2\text{O}$	
Analcime	$\text{NaAlSi}_2\text{O}_6 \cdot \text{H}_2\text{O}$	
Chabazite	$\text{CaAl}_2\text{Si}_4\text{O}_{12} \cdot 6\text{H}_2\text{O}$	
Phillipsite	$(\text{K}_2, \text{Na}_2, \text{Ca})\text{Al}_2\text{Si}_4\text{O}_{12} \cdot 4-5\text{H}_2\text{O}$	
Erionite	$(\text{Ca}, \text{Na}_2, \text{K}_2)_4\text{Al}_8\text{Si}_{28}\text{O}_{72} \cdot 27\text{H}_2\text{O}$	
Stellerite	$\text{CaAl}_2\text{Si}_7\text{O}_{18} \cdot 7\text{H}_2\text{O}$	
<b>Silica</b>		
Quartz	$\text{SiO}_2$ —low-temperature polymorph of silica	
Tridymite	$\text{SiO}_2$ —high-temperature polymorph of silica	
Cristobalite	$\text{SiO}_2$ —highest-temperature polymorph of silica	
Opal	$\text{SiO}_2 \cdot n\text{H}_2\text{O}$	
Feldspars		
Plagioclase (albite)	Solid solutions of albite ( $\text{NaAlSi}_3\text{O}_8$ ) and anorthite ( $\text{CaAl}_2\text{Si}_2\text{O}_8$ )	
K-feldspar (sanidine)	Solid solutions of orthoclase ( $\text{KAlSi}_3\text{O}_8$ ) and albite ( $\text{NaAlSi}_3\text{O}_8$ )	
<b>Clays</b>		
Smectite family:		
Diocahedral (montmorillonite)	$(\text{Na}, \text{K}, \text{Mg}_{0.5}, \text{Ca}_{0.5}, \text{possibly others})_{0.33}\text{Al}_{1.67}\text{Mg}_{0.33}\text{Si}_4\text{O}_{10}(\text{OH})_2 \cdot n\text{H}_2\text{O}$	
Triocahedral (saponite)	$(\text{Ca}_{0.5}, \text{Na})_{0.33}(\text{Mg}, \text{Fe})_3(\text{Si}_{3.67}\text{Al}_{0.33})\text{O}_{10}(\text{OH})_2 \cdot 4\text{H}_2\text{O}$	
Sepiolite	$\text{Mg}_4(\text{Si}_2\text{O}_5)_3(\text{OH})_2 \cdot 6\text{H}_2\text{O}$	
Palygorskite	$(\text{Mg}, \text{Al})_2\text{Si}_4\text{O}_{10}(\text{OH}) \cdot 4\text{H}_2\text{O}$	
Illite	$(\text{H}_3\text{O}, \text{K})_y(\text{Al}_4\text{Fe}_4\text{Mg}_4\text{Mg}_6)(\text{Si}_{8-y}\text{Al}_y)\text{O}_{20}(\text{OH})_4$	
<b>Manganese Oxides/Hydroxides</b>		
Pyrolusite	$\text{MnO}_2$	(1x1 tunnel structure)
Cryptomelane family:	$A_{0-2}(\text{Mn}^{4+}, \text{Mn}^{3+})_8(\text{O}, \text{OH})_{16}$	(2x2 tunnel structure)
Cryptomelane	A = K	
Hollandite	A = Ba	
Coronadite	A = Pb	
Romanechite	$(\text{Ba}, \text{H}_2\text{O})_2\text{Mn}_5\text{O}_{10}$	(2x3 tunnel structure)
Todorokite	$(\text{Na}, \text{Ca}, \text{Ba}, \text{Sr})_{0.3-0.7}(\text{Mn}, \text{Mg}, \text{Al})_6\text{O}_{12} \cdot 3.2-4.5\text{H}_2\text{O}$	(3x3 tunnel structure)
Aurorite	$(\text{Mn}^{2+}, \text{Ag}, \text{Ca})\text{Mn}_3\text{O}_7 \cdot 3\text{H}_2\text{O}$	
Lithiophorite	$m\{\text{Al}_{0.5}\text{Li}_{0.5}\text{MnO}_2(\text{OH})_2\} \cdot n\{\text{Al}_{0.667}(\text{Mn}^{4+}, \text{Co}, \text{Ni}, \text{Mn}^{2+})\text{O}_2(\text{OH})_2\} \cdot p\text{H}_2\text{O}$	
Rancieite	$(\text{Ca}, \text{Mn}^{2+})(\text{Mn}^{4+})_4\text{O}_9 \cdot 3\text{H}_2\text{O}$	
<b>Iron Oxides/Hydroxides</b>		
Hematite	$\text{Fe}_2\text{O}_3$	
Magnetite	$(\text{Fe}, \text{Mg})\text{Fe}_2\text{O}_4$	
<b>Carbonates</b>		
Calcite	$\text{CaCO}_3$	
<b>Halides</b>		
Fluorite	$\text{CaF}_2$	

Source: CRWMS M&O (2000, Table 13)

Table 10.4-4. Characteristics of Fractured Devitrified-Tuff Columns

Characteristics	Column 1	Column 2	Column 3	Column 4
Sample Identifier	G1-1941	UE-25 UZ-16 919	G4-2981	G4-2954
SMF Barcode Number	N/A	0029365	0029366	0029368
Major Minerals in Tuff Matrix	Alkali Feldspar and Quartz	Alkali Feldspar and Quartz	Alkali Feldspar and Opal CT	Alkali Feldspar and Opal CT
Minerals Coating the Fracture	None (apparent Induced fracture)	Stellerite Magnetite	Hollandite Romanechite	Hollandite Romanechite
Water Type	Synthetic J-13	Synthetic p#1	Synthetic J-13	Synthetic J-13
pH	8.6	8.8	8.6	8.6
Concentration of <sup>237</sup> Np (M)	$1.4 \times 10^{-5}$	$4.8 \times 10^{-6}$	$1.4 \times 10^{-5}$	$1.4 \times 10^{-5}$
Length (cm)	12.6	6.1	6.0	Not determined
Diameter (cm)	6.1	5.2	5.2	Not determined
Volumetric Flow Rate (mL/hr.)	0.5	0.5	0.5	0.5

Source: CRWMS M&O (2000, Table 14)

NOTE: SMF = Sample Management Facility

Table 10.4-5. Batch-Sorption Results for Neptunium-237 in J-13 Well Water

Major Mineral in Solid Phase	$K_d$ (mL/g)	Solid-Phase Composition <sup>a</sup>
Stellerite	~ 0	N/A
Hollandite	700	100% Hollandite
Romanechite	600	N/A
Magnetite	7	85% Magnetite
		12% Hematite
		3% Goethite

Source: CRWMS M&O (2000, Table 15)

NOTE: <sup>a</sup>Determined by x-ray-diffraction analysis

INTENTIONALLY LEFT BLANK

Table 10.5-1. Rock-Beaker Diffusion Results for Nonsorbing Radioisotopes and Devitrified Tuffs

Tuff Sample	Major Minerals	Porosity	Diffusion Coefficient, $d$ (cm <sup>2</sup> /s)	
			HTO	TcO <sub>4</sub> <sup>-</sup>
G4-737	Alkali feldspar 68% Cristobalite 28%	0.07	$2.2 \times 10^{-6}$	$3.9 \times 10^{-7}$
GU3-304 #1	Alkali feldspar 75% Cristobalite 25%	0.06	$1.5 \times 10^{-6}$	$3.0 \times 10^{-7}$
GU3-304 #2			$1.6 \times 10^{-6}$	$3.0 \times 10^{-7}$
GU3-433	Alkali feldspar 76% Cristobalite 15%	0.10	$3.5 \times 10^{-6}$	
GU3-1119	Alkali feldspar 70% Quartz 19%	0.10	$2.0 \times 10^{-6}$	$4.9 \times 10^{-7}$
Topopah outcrop	Alkali feldspar 59% Cristobalite 23% Quartz 12%	0.07	$1.0 \times 10^{-6}$	$1.0 \times 10^{-7}$

Source: CRWMS M&O (2000, Table 16)

Table 10.5-2. Batch-Sorption Coefficients for Devitrified Tuffs

Tuff Sample	Major Minerals	Sorption Coefficient, $K_d$ (mL/g)				
		Np	Am	Cs	Sr	Ba
G4-737	Alkali feldspar 68% Cristobalite 28%	8	134	532	52	28
GU3-304	Alkali feldspar 75% Cristobalite 25%	8	No data	342	18	19
GU3-433	Alkali feldspar 76% Cristobalite 15%	9	154	1,264	20	61
GU3-1119	Alkali feldspar 70% Quartz 19%	8	136	494	42	27
Topopah outcrop	Alkali feldspar 59% Cristobalite 23% Quartz 12%	9	No data	465	20	25

Source: CRWMS M&O (2000, Table 17)

Table 10.5-3. Dimensions of Diffusion Cells

Diameter of tuff slab	6 cm
Length of tuff slab	1 cm
Volume of traced chamber	750 cm <sup>3</sup>
Volume of untraced chamber	80 cm <sup>3</sup>

Source: Triay et al. (1997, Table 68)

INTENTIONALLY LEFT BLANK

Table 10.6-1. Rock Compositions in Water-Conducting Features

Site	Rock	Quartz	Feldspar	Biotite	Clay	Calcite	Zeolite	Organic
Transitgas Tunnel	S.-Aare Granite	X	X	X	(X)	-	-	-
Grimsel Test Site	Mylonite Granite	X	X	X	(X)	-	-	-
Leuggren	Conderite Granite	X	X	X	(X)	-	-	-
Äspö	Granite	X	X	X	(X)	-	-	-
Yucca Mountain	Tuff	X	X	-	-	-	X	-
Morro de Ferro	Phonolite	X	X	-	(X)	-	-	-
Gorleben	Marl Sand	X	-	-	X	X	-	X
Wellenberg	Marl	X	-	-	X	X	-	(X)
Bangombé	Pelite Sandstone	X	-	-	X	X	-	(X)
Markham	Marl Sandstone	X	-	-	X	(X)	-	-

Source: CRWMS M&O (1997, Chapter VIIA, Table 1)

NOTES: X represents more than 10 percent of the weight; (X) represents more than 2 percent but less than 10 percent. Data in table are corroborating data only. "Organic" refers to the presence of organic compounds such as humic and fulvic acids.

Table 10.6-2. Hydrochemical Properties of Studied Groundwaters

Site	Transitgas-Tunnel			Menzenschwand
	Zone 3	Zone 1	Zone 2	
Water Type	Ca-HCO <sub>3</sub>	Na-Ca-SO <sub>4</sub> -HCO <sub>3</sub>	Na-SO <sub>4</sub>	Ca-Na-HCO <sub>3</sub>
pH	9.2	8.9	9.2	6.5
pe	+6	+6	0	+6
pNa	4.5	4.5 – 4.1	2.6 – 2.3	3.9
pCa	3.4	3.9 – 3.5	4.1 – 3.8	3.4
T & T <sub>geo</sub> (°C)	4 & 2	6 & 5	22 & 90	12 & 13

Site	Bad Säkingen	Grimsel Test Site	Zurzach	Leuggern
Water Type	Na-Cl	Na-Ca-HCO <sub>3</sub> -F	Na-SO <sub>4</sub> -HCO <sub>3</sub> -Cl	Na-SO <sub>4</sub> -HCO <sub>3</sub> -Cl
pH	6.5	9.6	8	7.8
pe	+6	-3	-3	-3
pNa	1.3	3.2	1.9	1.9
pCa	2.4	3.9	3.4	3.6
T & T <sub>geo</sub> (°C)	29 & 50	12 & 13	39 & 45	66 & 66

Site	Åspö S	Whiteshell CD	Morro BZ	Yucca USA
Water Type	Na-Ca-HCO <sub>3</sub>	Na-Ca-Cl	K-SO <sub>4</sub> -F	Na-HCO <sub>3</sub> -SiO <sub>2</sub>
pH	7.5	8.9	6.1	6.9
pe	-4	-	+1	+6
pAlk	1.5	0.4	3.5	2.7
pOC	3.7	-	4.4	-

Site	Wellenberg CH	Gorleben D	Cigar Lake CD	Bangombé GA	Markham UK
Water Type	Na-HCO <sub>3</sub>	Na-HCO <sub>3</sub> -OC	Na-HCO <sub>3</sub>	Na-Ca-Mg-HCO <sub>3</sub>	Mg-HCO <sub>3</sub>
pH	8.5	8.8 – 8.3	6.5	5.9 – 6.2	7.8
pe	-5.2	0 – -1	-	0 – +2	+7
pAlk	1.7	2.1 – 2.5	3.0	3.5 – 4.3	3.6
pOC	4.2	2.7 – 2.5	3.0	-	-

Source: Adapted from CRWMS M&O (1997, Chapter VIIA, Table 2)

NOTES: p signifies the negative log; H = hydrogen ion; e = redox potential; Alk = alkalinity; OC = organic carbon concentration; - = no data available; T = water temperature; T<sub>geo</sub> = temperature estimated by geothermometer

Data in table are corroborating data only.

Table 10.6-3. Percentage of Plutonium-239 Adsorbed onto Hematite Colloids in Natural Groundwater and Synthetic Groundwater

Time (min.)	Fe <sub>2</sub> O <sub>3</sub> J-13 Pu (V)%	Fe <sub>2</sub> O <sub>3</sub> J-13 Pu (IV)%	Fe <sub>2</sub> O <sub>3</sub> Syn. J-13 Pu (V)%	Fe <sub>2</sub> O <sub>3</sub> Syn. J-13 Pu (IV)%
10	43.5	56.9	81.8	65.9
30	45.2	58.8	84.2	66.0
60	45.1	59.7	83.3	65.6
240	54.7	59.7	87.2	65.5
360	59.0	59.7	86.9	65.8
1,440	70.4	59.7	86.7	65.5
2,880	73.5	59.8	87.1	65.8
5,760	76.4	60.3	86.9	65.8

Source: CRWMS M&O (1997, Chapter VIID, Table 2)

NOTE: Data in table are corroborating data only.

Table 10.6-4. Percentage of Plutonium-239 Adsorbed onto Goethite Colloids in Natural Groundwater and Synthetic Groundwater

Time (min.)	FeOOH J-13 Pu (V)%	FeOOH J-13 Pu (IV)%	FeOOH Syn. J-13 Pu (V)%	FeOOH Syn. J-13 Pu (IV)%
10	19.2	28.5	63.3	34.2
30	20.5	31.0	63.0	36.9
60	23.5	45.1	63.8	48.0
240	35.6	40.3	68.4	48.0
360	40.5	38.9	70.0	52.6
1,440	53.2	37.2	74.2	52.2
2,880	58.6	39.2	74.8	49.4
5,760	61.8	34.4	74.1	52.8

Source: CRWMS M&O (1997, Chapter VIID, Table 3)

NOTE: Data in table are corroborating data only.

Table 10.6-5. Initial Forward (Sorption) Rate ( $k_f$ ) of Plutonium-239 onto Colloids of Hematite, Goethite, Montmorillonite, and Silica

Minerals	$k_f$ for Pu (V) (pCi/mg colloid/min.)		$k_f$ for Pu (IV) (pCi/mg colloid/min.)	
	J-13	Syn. J-13	J-13	Syn. J-13
Hematite	7.28 ± 0.36	12.55 ± 1.59	12.69 ± 0.03	16.17 ± 0.09
Goethite	7.74 ± 1.64	13.43 ± 0.47	8.66 ± 1.19	11.88 ± 1.96
Montmorillonite	8.30 ± 0.03	10.11 ± 0.09	8.51 ± 0.04	18.06 ± 0.17
Silica-PST-1	0.55 ± 0.02	0.49 ± 0.04	1.74 ± 0.07	2.17 ± 0.05
Silica-ST-ZL	0.58 ± 0.005	0.59 ± 0.02	1.96 ± 0.00	2.19 ± 0.07

DTN: LA0004NL831352.001, LA0003NL831352.001, LA0004NL831352.003

NOTES:  $k_f$  values for hematite, goethite, and smectite were calculated from the data collected from the first 10 min. After 10 min., additional small amounts of plutonium were adsorbed during the remaining 95.83 hr. The  $k_f$  values for silica were calculated from the data collected from the first hr. (there was no 10-min. and 30-min. sorption for silica). After 1 hr., the amounts of plutonium sorbed by silica colloids increased with time. Therefore,  $k_f$  values reported here are the minimum values.

Table 10.6-6. Initial Backward (Desorption) Rate ( $k_b$ ) of Plutonium-239 from Colloids of Hematite, Goethite, Montmorillonite, and Silica

Minerals	$k_b$ for Pu (V) (pCi/mg colloid/min.)		$k_b$ for Pu (IV) (pCi/mg colloid/min.)	
	J-13	Syn. J-13	J-13	Syn. J-13
Hematite	$9.7 \times 10^{-7} \pm (5.8 \times 10^{-7})$	$6.9 \times 10^{-8} \pm (0.0)$	$-8.7 \times 10^{-8} \pm (1.3 \times 10^{-8})$	0.0000
Goethite	$3.8 \times 10^{-5} \pm (3.1 \times 10^{-7})$	$1.8 \times 10^{-5} \pm (1.5 \times 10^{-6})$	$1.9 \times 10^{-5} \pm (1.0 \times 10^{-6})$	$3.5 \times 10^{-5} \pm (1.2 \times 10^{-6})$
Smectite	$2.1 \times 10^{-5} \pm (2.9 \times 10^{-6})$	$1.9 \times 10^{-5} \pm (6.2 \times 10^{-6})$	$9.0 \times 10^{-4} \pm (8.3 \times 10^{-5})$	$8.7 \times 10^{-5} \pm (9.3 \times 10^{-6})$
Silica-PST-1	$9.6 \times 10^{-4} \pm (2.3 \times 10^{-4})$	$3.5 \times 10^{-4} \pm (6.3 \times 10^{-5})$	$2.0 \times 10^{-3} \pm (1.4 \times 10^{-4})$	$2.2 \times 10^{-3} \pm (1.3 \times 10^{-3})$
Silica-ST-ZL	$2.7 \times 10^{-4} \pm (1.2 \times 10^{-5})$	$5.1 \times 10^{-4} \pm (4.0 \times 10^{-5})$	$4.2 \times 10^{-3} \pm (7.2 \times 10^{-4})$	$3.6 \times 10^{-3} \pm (4.0 \times 10^{-4})$

DTN: LA0004NL831352.001, LA0003NL831352.001, LA0004NL831352.003

NOTES:  $k_b$  values were calculated using the data collected from the first 2 days' desorption process. After 2 days, additional small amounts of plutonium were desorbed from colloids during the remaining 266 days. Therefore,  $k_b$  values reported here are the highest values.

Table 10.7-1. Hydraulic Parameter Sets Used To Define the Material Properties for the Simulations

Material	Permeability (m <sup>2</sup> )	Residual Saturation	$\alpha$ (m <sup>-1</sup> )	n	Porosity
Calico Hill Tuff	$5 \times 10^{-12}$	0.0001	3.5	1.19	0.50
Loamy Sand	$4.65 \times 10^{-12}$	0.139	12.4	2.28	0.41
Filter Paper	$2.19 \times 10^{-11}$	0.05	17.0	1.12	0.85

Source: CRWMS M&O (2000, Table 19)

NOTE:  $\alpha$  and  $\eta$  are van Genuchten parameters discussed in Section 10.7.2.6.1.1.

Table 10.7-2. Descriptions of Samples Collected from Busted Butte for Erionite Survey

Sample	Lithology
SPC 517960	Altered interzone at the top of the lower vitrophyre (Tptpln/Tptpv3)
SPC 517962	Upper densely welded perlitic subzone (upper Tptpv3)
SPC 517963	Middle densely to moderately welded vitric subzone (mid Tptpv2)
SPC 517964	Middle moderately to nonwelded vitric subzone (mid Tptpv1)
LANL #2814	Lower densely welded perlitic subzone (lower Tptpv3)
LANL #2815	Upper densely to moderately welded vitric subzone (upper Tptpv2)
LANL #2816	Middle densely to moderately welded vitric subzone (mid Tptpv2)
LANL #2817	Lower densely to moderately welded vitric subzone (lower Tptpv2)
LANL #2818	Upper moderately to nonwelded vitric subzone (upper Tptpv1)
LANL #2819	Lower moderately to nonwelded vitric subzone (lower Tptpv1)
LANL #2820	Vitric pumice swarm at base of the Topopah Spring Tuff (basal Tptpv1)

Source: CRWMS M&O (2000, Table 20)

NOTE: SPC = sample management facility data control number; LANL = Los Alamos National Laboratory

Table 10.7-3. Quantitative X-Ray Diffraction Results for Erionite-Bearing Sample at Top of Lower Vitrophyre, Tpt

Sample	Smectite	Erionite	Chabazite	Clinoptilolite	Mordenite	Quartz	Feldspar	Mica/ Illite	Total
Tptpln/Tptpv3									
SPC 517960	tr	0.021	2 ± 1	32 ± 5	4 ± 1	28 ± 4	33 ± 8	tr	99 ± 11

Source: CRWMS M&O (2000, Table 21)

NOTES: Sample was run using the external standard method.  
tr = trace abundance

Table 10.7-4. Quantitative X-Ray Diffraction Results for Samples from Lower Tpt Section

Sample	Smectite	Opal-CT/ Cristob.	Quartz	Feldspar	Glass/ Amorph	Hematite	Mica/Illite	Calcite	Gypsum	Kaolinite	Total
<b>Tptpv3</b>											
SPC #517962	1 ± 1	2 ± 1	tr	4 ± 1	93 ± 2	-	tr	tr	-	-	100 ± 2
LANL #2814p1	1 ± 1	4 ± 1	tr	3 ± 1	92 ± 2	-	tr	-	-	-	100 ± 2
<b>Tptpv2</b>											
LANL #2815p1	-	4 ± 1	1 ± 1	5 ± 1	90 ± 2	-	-	tr	-	-	100 ± 2
SPC #517963	1 ± 1	-	tr	3 ± 1	95 ± 2	tr	tr	1 ± 1	tr	-	100 ± 2
LANL #2816p1	2 ± 1	4 ± 1	tr	4 ± 1	90 ± 2	-	tr	-	-	-	100 ± 2
LANL #2817p1	3 ± 1	3 ± 1	tr	3 ± 1	91 ± 2	-	tr	-	-	-	100 ± 2
<b>Tptpv1</b>											
SPC #517964	tr	-	tr	2 ± 1	95 ± 1	-	tr	3 ± 1	-	-	100 ± 1
LANL #2818p1	tr	2 ± 1	tr	2 ± 1	96 ± 1	-	tr	tr	-	-	100 ± 1
LANL #2819p1	3 ± 1	1 ± 1	tr	3 ± 1	91 ± 2	-	tr	tr	-	2 ± 1	100 ± 2
LANL #2820p1	2 ± 1	1 ± 1	4 ± 1	8 ± 1	84 ± 2	1 ± 1	tr	tr	-	-	100 ± 2

Source: CRWMS M&O (2000, Table 21)

NOTES: - = not detected; SPC = sample management facility data control number; LANL = Los Alamos National Laboratory; tr = trace abundance of less than 0.5 percent by weight  
 Errors are conservative, 2-sigma values.  
 Values are in weight percent.  
 Samples arranged by relative depth.

Table 10.7-5. Mineral Abundances (Weight Percent) in Calico Hills Formation Surface Samples from Busted Butte

Sample	Smectite	Clinoptilolite	Crist/ Opal-CT	Quartz	Feldspar	Glass	Hematite	Biotite	Total
<b>Vitric Tac</b>									
DEB 3/90-10	1 ± 1	-	-	2 ± 1	11 ± 1	86 ± 2	-	tr	100 ± 2
DEB 3/90-9	6 ± 2	-	-	4 ± 1	15 ± 2	74 ± 3	-	tr	100 ± 3
DTV-97-2	2 ± 1	-	1 ± 1	1 ± 1	2 ± 1	94 ± 2	-	tr	100 ± 2
DEB 3/90-8a	-	-	1 ± 1	1 ± 1	1 ± 1	97 ± 2	-	tr	100 ± 2
DEB 3/90-8b	1 ± 1	-	1 ± 1	4 ± 1	7 ± 1	86 ± 2	-	tr	100 ± 2
DEB 3/90-7	3 ± 1	1 ± 1	1 ± 1	7 ± 1	12 ± 1	76 ± 2	tr	tr	100 ± 2
<b>Zeolitic Tac</b>									
DTV-97-3	-	9 ± 1	1 ± 1	7 ± 1	16 ± 2	64 ± 3	1 ± 1	2 ± 1	100 ± 3
DEB 3/90-6	1 ± 1	12 ± 1	1 ± 1	7 ± 1	16 ± 2	62 ± 3	-	1 ± 1	100 ± 3
<b>Wahmonie</b>									
DEB 3/90-5	5 ± 2	-	-	1 ± 1	26 ± 3	54 ± 5	1 ± 1	9 ± 3	100 ± 5
DEB 3/90-4	4 ± 1	-	-	2 ± 1	24 ± 3	46 ± 6	2 ± 1	17 ± 5	100 ± 6

Source: CRWMS M&O (2000, Table 22)

NOTES: - = not detected; tr = trace abundance

Table 10.7-6. Mineral Abundances (Weight Percent) in Calico Hills Formation Samples from an Auger Hole into the Floor of the Busted Butte Test Alcove

Sample	Depth (cm)	Smectite	Clinoptilolite	Crist/Opal-CT	Quartz	Feldspar	Glass	Hematite	Biotite	Total
<i>Vitric Tac</i>										
AUG-1-P	375-383	3 ± 1	1 ± 1	1 ± 1	8 ± 1	12 ± 2	74 ± 3	tr	1 ± 1	100 ± 3
AUG-1-Q	383-389	6 ± 2	1 ± 1	1 ± 1	8 ± 1	18 ± 3	65 ± 4	tr	1 ± 1	100 ± 4
AUG-1-R	389-396	3 ± 1	1 ± 1	1 ± 1	7 ± 1	11 ± 2	76 ± 3	tr	1 ± 1	100 ± 3

Source: CRWMS M&O (2000, Table 23)

NOTE: tr = trace abundance

Table 10.7-7. Quantitative X-Ray Diffraction Results for USW H-5 Core and Drill Cuttings

Sample	Depth (m)	Smectite	Clinop-tilolite	Mordenite	Tridy-mite	Cristo-balite	Opal-CT	Quartz	Feldspar	Glass	Mica	Hematite	Calcite	Horn-blende	Total
<b>Tptpv3</b>		<b>482.2-505.7</b>													
1590/1600	486.2	35 ± 10	10 ± 5	-	-	17 ± 5	-	-	40 ± 10	-	-	-	-	-	102 ± 16
1610 (DC)	490.7	-	-	-	-	2 ± 3	-	1 ± 1	7 ± 3	90 ± 5	-	-	-	-	100 ± 7
1630/1640	498.3	tr	-	-	-	2 ± 1	-	1 ± 1	9 ± 1	88 ± 2	tr	-	-	-	100 ± 2
1650/1660	504.4	-	-	-	-	5 ± 1	-	2 ± 1	4 ± 1	89 ± 2	tr	-	-	-	100 ± 2
<b>Tptpv2</b>		<b>505.7-509.6</b>													
1666 (DC)	507.8	50 ± 10	10 ± 5	-	-	12 ± 3	-	1 ± 1	25 ± 5	-	-	-	-	-	98 ± 13
<b>Tptpv1</b>		<b>509.6-517.9</b>													
<b>Tpbt1</b>		<b>517.9-519.7</b>													
<b>Tac</b>		<b>519.7-573.0</b>													
1710/1720	522.7	3 ± 2	-	-	-	5 ± 3	-	5 ± 3	20 ± 10	70 ± 10	-	-	-	-	103 ± 15
1750 (DC)	533.4	-	tr?	-	-	5 ± 5	-	2 ± 3	5 ± 5	85 ± 5	-	-	-	-	97 ± 9
1762 (SW)	537.1	-	-	-	-	1 ± 1	-	1 ± 1	5 ± 5	95 ± 5	-	-	-	-	102 ± 7
1760/1770	538.0	-	6 ± 1	-	-	-	4 ± 1	3 ± 1	6 ± 1	81 ± 2	-	-	-	-	100 ± 2
1800 (SW)	548.6	-	-	-	-	2 ± 3	-	2 ± 3	10 ± 5	85 ± 5	1 ± 1	-	-	-	100 ± 8
1820/1830	556.3	tr	4 ± 1	-	-	-	2 ± 1	4 ± 1	10 ± 1	80 ± 2	-	-	-	-	100 ± 2
1852 (SW)	564.5	-	-	-	-	-	-	2 ± 3	7 ± 3	90 ± 5	1 ± 1	-	-	-	100 ± 7
1875 (SW)	571.5	-	tr?	-	-	-	tr?	2 ± 3	5 ± 5	92 ± 3	-	-	-	-	99 ± 7
<b>Tacbt</b>		<b>573.0-592.0</b>													
1890/1900	577.6	1 ± 1	11 ± 1	-	-	-	3 ± 1	4 ± 1	6 ± 1	75 ± 2	-	-	-	-	100 ± 2
1900/1910	580.6	tr	10 ± 1	-	-	-	1 ± 1	3 ± 1	8 ± 1	78 ± 2	tr	-	-	-	100 ± 2
1910/1920	583.7	tr	18 ± 1	-	-	-	5 ± 1	5 ± 1	7 ± 1	65 ± 2	tr	-	-	-	100 ± 2
1917 (SW)	584.3	-	25 ± 5	-	-	-	10 ± 5	30 ± 5	35 ± 10	-	tr	-	-	-	100 ± 13
1920/1930	586.7	3 ± 1	52 ± 3	-	-	-	7 ± 2	14 ± 1	16 ± 3	6 ± 5	2 ± 1	-	-	-	100 ± 5
1930 (DC)	588.3	2 ± 3	50 ± 10	-	-	-	-	15 ± 5	30 ± 5	-	1 ± 1	-	-	-	98 ± 13

Source: CRWMS M&amp;O (2000, Table 24)

NOTES: - = not detected; tr = trace abundance  
Values are in weight percent.

Table 10.7-8. Quantitative X-Ray Diffraction Results for Samples from Drillhole USW SD-6

Sample	Depth (m)	LANL Number	Smectite	Clino- ptilolite	Tridy- mite	Cristo- balite	Opal-CT	Quartz	Feld- spar	Glass	Hema- -tite	Mica	Horn- blende	Calcite	Total
<b>Tptpln</b>		<b>378.0-443.8</b>													
1450.3/1450.5	442.1	2975p1	-	-	-	12 ± 1	-	30 ± 2	56 ± 8	-	tr	tr	-	-	98 ± 8
<b>Tptpv3</b>		<b>443.8-455.7</b>													
1456.0/1456.2	443.8	2976p1	23 ± 7	3 ± 1	-	-	13 ± 4	2 ± 1	23 ± 3	36 ± 8	-	-	-	-	100 ± 9
1473.2/1473.3	449.1	2977p1	1 ± 1	-	-	-	5 ± 1	1 ± 1	4 ± 1	89 ± 2	-	tr	-	-	100 ± 2
1477.0/1477.2	450.3	2978p1	1 ± 1	-	-	-	6 ± 1	2 ± 1	7 ± 1	84 ± 2	-	tr	-	-	100 ± 2
1479.5/1479.7	451.0	2479p1	-	-	-	-	7 ± 2	1 ± 1	5 ± 1	85 ± 2	-	tr	-	2 ± 1	100 ± 3
1482.4/1482.5	451.9	2980p1	-	-	-	-	6 ± 1	1 ± 1	5 ± 1	88 ± 1	-	-	-	-	100 ± 2
1486.8/1486.9	453.2	2981p1	-	-	-	-	7 ± 2	1 ± 1	6 ± 1	86 ± 2	-	tr	-	-	100 ± 2
1489.8/1490.0	454.2	2982p1	-	-	-	-	12 ± 3	1 ± 1	10 ± 1	76 ± 3	-	1 ± 1	-	-	100 ± 3
1493.0/1493.2	455.1	2983p1	-	-	-	-	13 ± 3	1 ± 1	9 ± 1	77 ± 3	-	tr	-	-	100 ± 3
<b>Tptpv2</b>		<b>455.7-461.5</b>													
1496.5/1496.7	456.2	2984p1	-	-	-	-	17 ± 4	1 ± 1	11 ± 2	71 ± 4	-	tr	-	-	100 ± 5
1500.1/1500.2	457.3	2985p1	2 ± 1	-	-	-	17 ± 4	1 ± 1	12 ± 2	68 ± 4	-	tr	-	-	100 ± 5
1503.3/1503.4	458.2	2986p1	2 ± 1	-	-	-	20 ± 6	2 ± 1	16 ± 2	60 ± 6	tr	tr	-	-	100 ± 6
1506.2/1506.3	459.1	2987p1	3 ± 1	-	-	-	18 ± 5	1 ± 1	13 ± 2	65 ± 5	tr	tr	-	-	100 ± 6
1509.2/1509.3	460.0	2988p1	3 ± 1	-	-	-	15 ± 4	1 ± 1	11 ± 2	70 ± 4	tr	-	-	-	100 ± 5
1512.1/1512.2	460.9	2989p1	4 ± 1	-	-	-	14 ± 4	1 ± 1	12 ± 2	69 ± 4	-	tr	-	-	100 ± 5
<b>Tptpv1</b>		<b>461.5-471.7</b>													
1516.9/1517.0	462.4	2990p1	4 ± 1	-	-	-	9 ± 2	1 ± 1	10 ± 1	76 ± 2	tr	tr	-	-	100 ± 3
1521.5/1521.6	463.8	2991p1	5 ± 2	-	-	-	4 ± 1	1 ± 1	5 ± 1	85 ± 2	-	tr	-	-	100 ± 3
1524.9/1525.0	464.8	2992p1	5 ± 2	-	3 ± 1	2 ± 1	-	2 ± 1	11 ± 2	77 ± 3	tr	tr	-	-	100 ± 3
1527.8/1527.9	465.7	2993p1	3 ± 1	-	2 ± 1	4 ± 1	-	5 ± 1	21 ± 3	65 ± 3	tr	tr	-	-	100 ± 4
1546.5/1546.6	471.4	2994p1	1 ± 1	-	-	1 ± 1	-	5 ± 1	10 ± 1	83 ± 2	tr	tr	-	-	100 ± 2
<b>Tpbt1</b>		<b>471.7-473.8</b>													
<b>Tac</b>		<b>473.8-526.5</b>													
1560.8/1560.9	475.8	2995p1 <sup>a</sup>	tr	4 ± 1	6 ± 1	10 ± 1	-	27 ± 2	53 ± 8	-	tr	tr	-	-	100 ± 8
1563.3/1563.4	476.5	2996p2 <sup>a</sup>	-	6 ± 1	5 ± 1	13 ± 1	-	25 ± 2	53 ± 8	-	tr	tr	-	-	102 ± 8
1563.3/1563.4	476.5	2996p1	4 ± 1	4 ± 1	-	2 ± 1	-	2 ± 1	7 ± 1	81 ± 2	-	tr	-	-	100 ± 2
1566.7/1566.8	477.6	2997p1	-	2 ± 1	1 ± 1	2 ± 1	-	4 ± 1	10 ± 1	81 ± 2	tr	tr	-	-	100 ± 2
1570.3/1570.5	478.7	2998p1	-	1 ± 1	1 ± 1	3 ± 1	-	8 ± 1	16 ± 2	71 ± 2	tr	tr	-	-	100 ± 3

Source: CRWMS M&amp;O (2000, Table 25)

NOTES: <sup>a</sup>The analyses 2995p1 and 2996p2 are from large (greater than 5 cm) lithic clasts that occur at these depths. Stratigraphy from USW SD-6 Prognosis Update Log, SMF Contacts, dated 5/7/98  
 - = not detected; tr = trace abundance; LANL = Los Alamos National Laboratory  
 Values are in weight percent.

Table 10.7-9. Quantitative X-Ray Diffraction Results for Samples with Laboratory Porosity Measurements

Sample	Smectite	Clinop-tilolite	Mordenite	Tridymite	Cristobalite	Opal-CT	Quartz	Feldspar	Glass	Hematite	Mica	Hornblende	Chabazite	XRD Total	$\delta$ Porosity
SD-7 1494.0	1 ± 1	10 ± 1	-	-	-	5 ± 1	8 ± 1	19 ± 3	53 ± 3	-	tr	tr	4 ± 1	100 ± 4	0.017
SD-9 1430.9	5 ± 2	-	-	-	-	5 ± 1	tr	2 ± 1	88 ± 2	-	tr	-	-	100 ± 2	0.042
SD-9 1433.4	1 ± 1	57 ± 5	-	-	-	29 ± 8	4 ± 1	13 ± 3	-	-	-	-	-	104 ± 10	0.105
SD-9 1437.3	-	-	-	-	-	-	1 ± 1	1 ± 1	98 ± 1	-	tr	-	-	100 ± 1	0.003
SD-9 1440.2	3 ± 1	4 ± 1	-	-	-	6 ± 1	1 ± 1	4 ± 1	82 ± 2	-	-	-	-	100 ± 2	0.041
SD-9 1443.0	19 ± 6	3 ± 1	-	-	-	8 ± 2	1 ± 1	5 ± 1	64 ± 6	-	-	-	-	100 ± 7	0.063
SD-9 1445.2	4 ± 1	1 ± 1	-	-	-	9 ± 2	1 ± 1	4 ± 1	81 ± 2	-	tr	-	-	100 ± 3	0.052
SD-9 1448.5	4 ± 1	3 ± 1	-	-	-	9 ± 2	2 ± 1	6 ± 1	76 ± 2	-	tr	-	-	100 ± 3	0.044
SD-9 1450.9	1 ± 1	5 ± 1	-	-	-	5 ± 1	2 ± 1	6 ± 1	81 ± 2	-	tr	-	-	100 ± 2	0.035
SD-9 1454.2	1 ± 1	15 ± 1	-	-	-	7 ± 2	3 ± 1	7 ± 1	67 ± 2	-	tr	-	-	100 ± 3	0.063
SD-9 1458.2	2 ± 1	71 ± 6	1 ± 1	-	-	20 ± 4	2 ± 1	4 ± 1	-	-	-	-	-	100 ± 7	0.124
SD-9 1460.2	2 ± 1	72 ± 7	3 ± 1	-	-	18 ± 4	2 ± 1	1 ± 1	-	-	-	-	-	98 ± 8	0.119
SD-12 1371.8	-	-	-	-	-	1 ± 1	1 ± 1	2 ± 1	96 ± 1	-	tr	-	-	100 ± 2	0.002
SD-12 1374.8	tr	-	-	-	-	2 ± 1	2 ± 1	4 ± 1	92 ± 1	-	tr	-	-	100 ± 2	0.002
SD-12 1386.6	tr	2 ± 1	-	1 ± 1	-	7 ± 2	3 ± 1	8 ± 1	79 ± 2	tr	tr	-	-	100 ± 3	0.010
SD-12 1389.8	tr	2 ± 1	-	1 ± 1	-	7 ± 2	4 ± 1	12 ± 2	74 ± 3	tr	tr	-	-	100 ± 3	0.013
SD-12 1392.7	tr	2 ± 1	-	tr	-	11 ± 3	5 ± 1	13 ± 2	69 ± 3	-	tr	-	-	100 ± 4	0.017
SD-12 1395.7	tr	2 ± 1	-	1 ± 1	-	6 ± 2	3 ± 1	10 ± 1	78 ± 2	tr	tr	-	-	100 ± 3	0.019
SD-12 1402.2	tr	3 ± 1	-	1 ± 1	-	15 ± 5	8 ± 1	23 ± 3	50 ± 6	-	tr	-	-	100 ± 6	0.018
SD-12 1404.3	1 ± 1	3 ± 1	-	tr	-	7 ± 2	4 ± 1	13 ± 2	72 ± 3	-	tr	-	-	100 ± 3	0.024
SD-12 1407.7	3 ± 1	3 ± 1	-	-	-	3 ± 1	2 ± 1	6 ± 1	83 ± 2	-	tr	-	-	100 ± 2	0.020
SD-12 1410.6	1 ± 1	1 ± 1	-	-	-	3 ± 1	2 ± 1	8 ± 1	85 ± 2	-	tr	-	-	100 ± 2	0.022
SD-12 1440.0	1 ± 1	4 ± 1	-	-	-	7 ± 2	2 ± 1	8 ± 1	78 ± 2	-	tr	-	-	100 ± 3	0.030
SD-12 1440.8	1 ± 1	2 ± 1	-	-	-	1 ± 1	2 ± 1	6 ± 1	88 ± 2	-	tr	-	-	100 ± 2	0.011
SD-12 1447.0	tr	6 ± 1	-	-	-	2 ± 1	2 ± 1	5 ± 1	85 ± 2	-	tr	-	-	100 ± 2	0.033
SD-12-1450.2	1 ± 1	4 ± 1	-	-	-	3 ± 1	2 ± 1	8 ± 1	82 ± 2	-	tr	-	-	100 ± 2	0.025
SD-12 1452.7	1 ± 1	6 ± 1	-	-	-	3 ± 1	3 ± 1	6 ± 1	81 ± 2	-	tr	-	-	100 ± 2	0.037
SD-12 1456.6	1 ± 1	7 ± 1	-	-	-	3 ± 1	2 ± 1	5 ± 1	82 ± 2	-	tr	-	-	100 ± 2	0.102
SD-12 1458.9	1 ± 1	6 ± 1	-	-	-	3 ± 1	3 ± 1	8 ± 1	79 ± 2	-	tr	-	-	100 ± 2	0.028
SD-12 1462.1	1 ± 1	3 ± 1	-	tr	-	4 ± 1	2 ± 1	6 ± 1	84 ± 2	-	tr	-	-	100 ± 2	0.031

DTN: LAJC831321AQ98.005

NOTES: - = not detected; tr = trace abundance of less than 0.5 percent by weight; XRD = X-ray diffraction  
 Errors are conservative, 2-sigma values.  
 Values are in weight percent.

Table 10.7-10. Busted Butte Samples Used for Hydrologic Characterization

Sample ID	Specimen Type	Date Collected	Quantity/Los Alamos National Laboratory Number	Comments
SPC 7047	Ttpv2	11/7/97	1/2825,X1	Vertical core
SPC 7048	Tac	11/7/97	1/2826,X1	Vertical core
SPC 7048	Tac	11/7/97	1/2826,X2	Horizontal core
SPC 7048	Tac	11/7/97	1/2826,X3	Shavings
SPC 7049	Ttpv1	11/7/97	1/2827,X1	Vertical core
SPC 7049	Ttpv1	11/7/97	1/2827,X2	Shavings
SPC 7050	Ttpv2	11/7/97	1/2828,X1	Vertical core

DTN: LA9909WS831372.013

NOTE: The entire stratigraphic sequence of the test block was represented, which, from top to bottom, is: the base of the basal Topopah Spring welded basal vitrophyre, Ttpv2 and Ttpv2-lower, and the hydrologic Calico Hills, Ttpv1 and Tac.

Table 10.7-11. Preliminary Measured Sorption Coefficients

Rock Sample	Measured $K_d$ (mL/g)			
	Lithium	Manganese	Cobalt	Nickel
Tac (Ph. 1, BH #4)	1	16	38	34
Ttpv2 (Ph. 1, BH #7)	1	6	14	13

Source: CRWMS M&O (2000, Table 26)

Table 10.7-12. Sorption Mineralogy Samples

Sample Source	Sample Name	Sample Interval (ft)	Geologic Unit
Phase 1A, BH 3	UZTT-BB-PH1-3	0.0-1.2	Ttpv1
Phase 1A, BH 4	UZTT-BB-PH1-4	2.0-3.2	Tac
Phase 1B, BH 7	UZTT-BB-PH1-7	3.0-4.0	Ttpv2

Source: CRWMS M&O (2000, Table 27)

Table 10.7-13. Summary of Radionuclide Sorption Results

Sample	Approximate Average $K_d$ (g/g)		
	Neptunium	Americium	Plutonium
UZTT-BB-PH1-3	0.3	380	19
UZTT-BB-PH1-4	1.4	470	2,500
UZTT-BB-PH1-7	1.1	460	1,100

Source: CRWMS M&O (2000, Table 28)

Table 10.7-14. Chemical Composition of Busted Butte Pore Water, with J-13 Groundwater for Comparison

Constituent	Concentrations (mg/L)					
	Sample 3B	Sample 3N	Sample 3Q	Sample 3U	Average 3N-3U	J-13 Water
Br	0.06	0.07	0.06	0.06	0.06	-
Ca	17.73	24.35	21.16	19.81	21.77	12.5
Ce	< 0.5	< 0.5	< 0.5	< 0.5	< 0.6	-
Cl	16.13	19.06	17.71	16.74	17.84	6.5
Co	< 1.0	< 1.0	< 1.0	< 1.0	< 1.1	-
F	2.36	1.82	1.85	1.41	1.69	0.53
Fe	< 0.1	< 0.1	< 0.1	< 0.1	< 0.2	< 0.05
HCO <sub>3</sub> (est.)	33.0	52.7	45.6	40.6	46.3	137.2
K	4.14	3.35	3.37	3.44	3.39	4.5
Li	0.11	0.11	0.10	< 0.1	0.10	< 0.1
Mg	3.20	4.13	3.64	3.19	3.66	2.1
Mn	< 0.5	< 0.5	< 0.5	< 0.5	< 0.6	< 0.01
Mo	< 1.0	< 1.0	< 1.0	< 1.0	< 1.1	-
Na	17.67	21.36	19.63	17.89	19.63	44.6
Ni	< 1.0	< 1.0	< 1.0	1.34	1.34	-
NO <sub>3</sub>	22.76	26.48	22.62	20.99	23.36	1.3
PO <sub>4</sub>	< 0.1	< 0.1	< 0.1	< 0.1	< 0.2	-
Re	< 1.0	< 1.0	< 1.0	< 1.0	< 1.1	-
Si	29.69	31.85	34.10	31.00	32.32	29.6
Sm	< 0.5	< 0.5	< 0.5	< 0.5	< 0.6	-
SO <sub>4</sub>	31.29	33.63	31.36	30.08	31.69	18.6
Sr	0.37	0.49	0.42	0.38	0.43	-
TDS	178.5	219.4	201.6	186.9	203.6	257.4
pH	8.20	8.48	8.45	8.28	8.40	7.3-8.4
Gravimetric moisture content	0.123	0.134	0.15	0.109	0.133	N/A

Source: CRWMS M&O (2000, Table 29)

NOTE: N/A = not applicable; TDS = total dissolved solids

Table 10.7-15. Predicted Transport Distances for Given Concentrations

Concentration	Distance Traveled
0.01	0.85 m
0.1	0.67 m
0.25	0.56 m
0.50	0.45 m

Source: CRWMS M&O (2000, Table 33)

Table 10.7-16. Simulation Results at 180 Days

Distance from Injection Point	Saturation at 180 Days
0.125 m	0.402
0.25 m	0.381
0.50 m	0.366
1.00 m	0.357

Source: CRWMS M&O (2000, Table 34)

Table 10.7-17. Hydrologic Parameters Used for the Two-Dimensional Simulations

Simulation Variable <sup>a</sup>	Porosity	Permeability <sup>b</sup> (m <sup>2</sup> )	$\alpha^c$ (m <sup>-1</sup> )	$n^c$	Saturation (in situ)	Injection rate (mL/hr)
1. Base Case	0.30	$1.3 \times 10^{-12}$	0.82	1.31	0.30	10
2. $k_{\text{matrix}} = 0.1 * k_{\text{matrix}}$ (base)	0.30	$1.3 \times 10^{-12}$	0.82	1.31	0.30	10
3. $k_{\text{matrix}} = 10 * k_{\text{matrix}}$ (base)	0.30	$1.3 \times 10^{-12}$	0.82	1.31	0.30	10
4. Porosity = 0.20	0.20	$1.3 \times 10^{-12}$	0.82	1.31	0.30	10
5. Porosity = 0.40	0.40	$1.3 \times 10^{-12}$	0.82	1.31	0.30	10
6. $\alpha$ low, $n$ low	0.30	$1.3 \times 10^{-12}$	0.60	1.20	0.30	10
7. $\alpha$ high, $n$ low	0.30	$1.3 \times 10^{-12}$	1.20	1.20	0.30	10
8. $\alpha$ low, $n$ high	0.30	$1.3 \times 10^{-12}$	0.60	1.80	0.30	10
9. $\alpha$ high, $n$ high	0.30	$1.3 \times 10^{-12}$	1.20	1.80	0.30	10
10. In situ $S = 0.2$	0.30	$1.3 \times 10^{-12}$	0.82	1.31	0.20	10
11. In situ $S = 0.4$	0.30	$1.3 \times 10^{-12}$	0.82	1.31	0.40	10
12. In situ $S = 0.5$	0.30	$1.3 \times 10^{-12}$	0.82	1.31	0.50	10
13. In situ $S = 0.6$	0.30	$1.3 \times 10^{-12}$	0.82	1.31	0.60	10
14. In situ $S = 0.7$	0.30	$1.3 \times 10^{-12}$	0.82	1.31	0.70	10
15. In situ $S = 0.8$	0.30	$1.3 \times 10^{-12}$	0.82	1.31	0.80	10
16. In situ $S = 0.9$	0.30	$1.3 \times 10^{-12}$	0.82	1.31	0.90	10
17. In situ $S = 0.2$	0.30	$1.3 \times 10^{-12}$	0.82	1.31	0.20	1
18. In situ $S = 0.3$	0.30	$1.3 \times 10^{-12}$	0.82	1.31	0.30	1
19. In situ $S = 0.4$	0.30	$1.3 \times 10^{-12}$	0.82	1.31	0.40	1
20. In situ $S = 0.5$	0.30	$1.3 \times 10^{-12}$	0.82	1.31	0.50	1
21. In situ $S = 0.6$	0.30	$1.3 \times 10^{-12}$	0.82	1.31	0.60	1
22. In situ $S = 0.7$	0.30	$1.3 \times 10^{-12}$	0.82	1.31	0.70	1
23. In situ $S = 0.8$	0.30	$1.3 \times 10^{-12}$	0.82	1.31	0.80	1
24. In situ $S = 0.9$	0.30	$1.3 \times 10^{-12}$	0.82	1.31	0.90	1
25. In situ $S = 0.3$	0.30	$1.3 \times 10^{-12}$	0.82	1.31	0.30	50
26. In situ $S = 0.9$	0.30	$1.3 \times 10^{-12}$	0.82	1.31	0.90	50
Polypropylene pad	0.85	$2.2 \times 10^{-11}$	17.0	1.12	N/A	N/A

Source: CRWMS M&O (2000, Table 31)

NOTES: <sup>a</sup>The simulation variable column shows the parameter being varied (tested) in the simulation.

<sup>b</sup>Permeability is the intrinsic value (value under saturated conditions).

<sup>c</sup>The variables  $\alpha$  and  $n$  are the van Genuchten function parameters taken from laboratory measurements.

$S$  = saturation

Table 10.7-18. Hydrologic Parameters Used for the Three-Dimensional Simulations

Simulation Variable <sup>a</sup>	Porosity	Permeability <sup>b</sup> (m <sup>2</sup> )	$\alpha^c$ (m <sup>-1</sup> )	$n^c$	Saturation (in situ)	Injection rate (mL/hr)
1. Base Case	0.35	$1.3 \times 10^{-12}$	0.82	1.31	0.35	10
2. $k_{\text{matrix}} = 0.1 * k_{\text{matrix}} \text{ (base)}$	0.35	$1.3 \times 10^{-12}$	0.82	1.31	0.35	10
3. Porosity = 0.20	0.20	$1.3 \times 10^{-12}$	0.82	1.31	0.35	10
4. $\alpha$ high, $n$ low	0.35	$1.3 \times 10^{-12}$	1.20	1.20	0.35	10
5. $\alpha$ high, $n$ high	0.35	$1.3 \times 10^{-12}$	1.20	1.80	0.35	10
6. In situ $S = 0.2$	0.35	$1.3 \times 10^{-12}$	0.82	1.31	0.20	10
7. In situ $S = 0.6$	0.35	$1.3 \times 10^{-12}$	0.82	1.31	0.60	10
8. In situ $S = 0.9$	0.35	$1.3 \times 10^{-12}$	0.82	1.31	0.90	10
9. In situ $S = 0.2$	0.35	$1.3 \times 10^{-12}$	0.82	1.31	0.20	1
10. In situ $S = 0.35$	0.35	$1.3 \times 10^{-12}$	0.82	1.31	0.35	1
11. In situ $S = 0.6$	0.35	$1.3 \times 10^{-12}$	0.82	1.31	0.60	1
12. In situ $S = 0.9$	0.35	$1.3 \times 10^{-12}$	0.82	1.31	0.90	1
13. In situ $S = 0.2$	0.35	$1.3 \times 10^{-12}$	0.82	1.31	0.20	50
14. In situ $S = 0.35$	0.35	$1.3 \times 10^{-12}$	0.82	1.31	0.35	50

Source: CRWMS M&O (2000, Table 32)

NOTES: <sup>a</sup>The simulation variable column shows the parameter being varied (tested) in the simulation.

<sup>b</sup>Permeability is the intrinsic value (value under saturated conditions).

<sup>c</sup>The variables  $\alpha$  and  $n$  are the van Genuchten function parameters taken from laboratory measurements.

$S$  = saturation

Table 10.7-19. Case Description

Case	Description
1	$\langle f \rangle = -6.258$ , $\sigma_f^2 = 2.459$ , $\lambda_f = 20$ cm, $\langle \alpha \rangle = 0.01$ cm <sup>-1</sup> , $\sigma_\alpha^2 = 9 \times 10^{-6}$ (cm <sup>-1</sup> ) <sup>2</sup> , $\lambda_\alpha = 20$ cm, $\phi = 0.5$ , $L_1 = L_2 = 200$ cm, $L_3 = 50$ cm, $Q = 1$ mL/hr, $S_o = 30\%$
2	Same as in Case 1, except $\lambda_f = \lambda_\alpha = 30$ cm
3	Same as in Case 1, except $L_1 = L_2 = 400$ cm
4	Same as in Case 1, except $S_o = 20\%$
5	Same as in Case 1, except $S_o = 40\%$
6	Same as in Case 1, except $S_o = 60\%$
7	Same as in Case 1, except $\phi = 0.3$
8	Same as in Case 1, except $\langle f \rangle = -4.258$ and $L_1 = L_2 = 400$ cm
9	Same as in Case 1, except $\langle \alpha \rangle = 0.02$ cm <sup>-1</sup>
10	Same as in Case 1, except $\sigma_\alpha^2 = 0$
11	Same as in Case 1, except $Q = 10$ mL/hr
12	Same as in Case 8, except $Q = 50$ mL/hr, $L_3 = 100$ cm
13	Same as in Case 1, except $\langle f \rangle = -4.258$ and $L_1 = L_2 = 400$ cm, and $Q = 10$ mL/hr
14	Same as in Case 13, except $Q = 50$ mL/hr and $L_3 = 100$ cm

Source: CRWMS M&O (2000, Table 35)

NOTE:  $f = \ln K_s$  is the log-transformed saturated hydraulic conductivity (for Case 1, the mean  $\langle f \rangle$  and variance  $\sigma_f^2$  are obtained with  $\langle K_s \rangle = 6.552 \times 10^{-3}$  cm/hr. and  $\sigma_{K_s} = 2.143 \times 10^{-2}$  cm/hr.);  $\alpha$  is a parameter related to pore-size distribution;  $\lambda_f$  and  $\lambda_\alpha$  are the respective correlation lengths of  $f$  and  $\alpha$ ;  $\phi$  is porosity;  $L_1$  and  $L_2$  are the vertical and horizontal dimensions of the domain;  $L_3$  is the length of the third dimension used to calculate the injection rate for two-dimensional simulation;  $S_o$  is the background saturation; and  $Q$  is the actual injection rate.

Table 10.7-20. Summary of Monte Carlo Cases

Case Number	Correlation of $\alpha$ and Permeability	Correlation Length of Heterogeneities
1	None	0.2 m
2	Altman et al. 1996	0.2 m
3	Altman et al. 1996	0.1 m
4	Altman et al. 1996	0.5 m

Source: CRWMS M&O (2000, Table 36)

NOTE: All cases assume  $\ln(k_s) = 1.54$ , where  $k_s$  is in cm/hr.

Table 10.7-21. Statistical Results of Monte Carlo Simulations

	C = 0.01				C = 0.1				C = 0.5			
	x <sub>min</sub>	x <sub>max</sub>	y <sub>min</sub>	y <sub>max</sub>	x <sub>min</sub>	x <sub>max</sub>	y <sub>min</sub>	y <sub>max</sub>	x <sub>min</sub>	x <sub>max</sub>	y <sub>min</sub>	y <sub>max</sub>
<b>Case 1</b>												
Mean	-0.35	0.53	-0.45	0.42	-0.28	0.46	-0.37	0.35	-0.20	0.37	-0.29	0.27
Std. dev.	0.11	0.12	0.082	0.093	0.098	0.11	0.077	0.085	0.08	0.098	0.070	0.068
<b>Case 2</b>												
Mean	-0.30	0.47	-0.42	0.41	-0.23	0.41	-0.35	0.35	-0.16	0.33	-0.27	0.27
Std. dev.	0.019	0.014	0.015	0.012	0.016	0.013	0.013	0.013	0.010	0.012	0.011	0.013
<b>Case 3</b>												
Mean	-0.29	0.48	-0.41	0.41	-0.22	0.41	-0.35	0.35	-0.15	0.33	-0.27	0.27
Std. dev.	0.014	0.012	0.011	0.011	0.011	0.012	0.011	0.011	0.007	0.013	0.011	0.010
<b>Case 4</b>												
Mean	-0.28	0.49	-0.41	0.42	-0.22	0.42	-0.35	0.35	-0.15	0.34	-0.27	0.27
Std. dev.	0.027	0.024	0.022	0.024	0.022	0.020	0.019	0.018	0.015	0.017	0.018	0.017

Source: CRWMS M&O (2000, Table 37)

NOTE: Results are based on 50 realizations for each case.

Table 10.7-22. Property Sets for the Phase 2 Test

Busted Butte Layer	Matrix Material (Flint 1998)				Fracture Material (Bodvarsson et al. 1997)					Appendix C
	Layer	$\alpha_m$ (m <sup>-1</sup> )	$n_m$	$K_m$ (m <sup>2</sup> )	Layer	$\alpha_f$ (m <sup>-1</sup> )	$n_f$	$K_f$ (m <sup>2</sup> )	$\phi_f$	$\theta$
1. Tac1	CHV	3.5	1.19	$5 \times 10^{-12}$	CH1V	11.52	3.0	$2.43 \times 10^{-9}$	$7.14 \times 10^{-5}$	0.5
2. Tac2	CHV	3.5	1.19	$5 \times 10^{-12}$	CH1V	11.52	3.0	$2.43 \times 10^{-9}$	$7.14 \times 10^{-5}$	0.5
3. Tac3	CHV	3.5	1.19	$5 \times 10^{-12}$	CH1V	11.52	3.0	$2.43 \times 10^{-9}$	$7.14 \times 10^{-5}$	0.5
4. Tptpv1	BT1	0.56	1.31	$1 \times 10^{-13}$	CH1V	11.52	3.0	$2.43 \times 10^{-9}$	$7.14 \times 10^{-5}$	0.5
5. Tptpv1	BT1	0.56	1.31	$1 \times 10^{-13}$	CH1V	11.52	3.0	$2.43 \times 10^{-9}$	$7.14 \times 10^{-5}$	0.5
6. Tptpv2	PV2	2.2	1.25	$1 \times 10^{-16}$	TSW2	0.91	2.92	$6.6 \times 10^{-9}$	$1.29 \times 10^{-4}$	0.25

Source: CRWMS M&O (2000, Table 38)

NOTE:  $\alpha$  and  $n$  are the van Genuchten parameters,  $K$  is permeability,  $\phi$  is volume fraction, and  $\theta$  is porosity. The subscript m signifies matrix material and the subscript f signifies fracture material.

Table 10.7-23. Closest Sampling Point to the Injection Planes within Each Collection Borehole

Collection Borehole	Distance from Top Injection Plane (m)	Collection Borehole	Distance from Bottom Injection Plane (m)
16	0.61	46	0.175
17	0.80	48	0.175
14	1.17	9	0.175
15	1.17	10	0.59 (above plane)
13	1.17		
12	1.17		

Source: CRWMS M&O (2000, Table 39)

Table 10.7-24. Fluorescein Breakthrough Data from Upper Injection Boreholes

Borehole Number	5% Breakthrough Concentration	50% Breakthrough Concentration	Normalized Concentration at 1 Yr.
16	27 days	68 days	1.0
17	48 days	118 days	1.0
14	118 days	238 days	0.87
15	103 days	218 days	0.90
13	103 days	218 days	0.90
12	212 days	more than 1 yr.	0.46
Remaining collection boreholes	more than 1 yr.	more than 1 yr.	0.0

Source: CRWMS M&O (2000, Table 40)

Table 10.7-25. Fluorescein Breakthrough Data from Lower Injection Boreholes

Borehole Number	5% Breakthrough Concentration	50% Breakthrough Concentration	Normalized Concentration at 1 Yr.
46	4 days	30 days	1.0
48	20 days	91 days	0.98
9	53 days	166 days	0.91
10	171 days	more than 1 yr.	0.37

Source: CRWMS M&O (2000, Table 41)

Table 10.7-26. Retardation of Reactive Tracers

Tracer	Ttpv1, Tac $K_d$ (cc/g)	Ttpv2 $K_d$ (cc/g)
Lithium	1.0	0.0
Manganese	15.6	6.5
Nickel/Cobalt	34.0	13.0

Source: CRWMS M&O (2000, Table 42)

Table 10.7-27. Lithium Breakthrough Data from Upper Injection Boreholes

Borehole Number	5% Breakthrough Concentration	50% Breakthrough Concentration	Normalized Concentration at 1 Yr.
16	52 days	193 days	0.79
17	257 days	more than 1 yr.	0.12
14	more than 1 yr.	more than 1 yr.	0.0
15	more than 1 yr.	more than 1 yr.	0.02
13	more than 1 yr.	more than 1 yr.	0.0
12	more than 1 yr.	more than 1 yr.	0.0
Remaining collection boreholes	more than 1 yr.	more than 1 yr.	0.0

Source: CRWMS M&O (2000, Table 43)

Table 10.7-28. Lithium Breakthrough Data from Lower Injection Boreholes

Borehole Number	5% Breakthrough Concentration	50% Breakthrough Concentration	Normalized Concentration at 1 Yr.
46	28 days	267 days	0.62
48	63 days	327 days	0.55
9	242 days	more than 1 yr.	0.12
10	more than 1 yr.	more than 1 yr.	0.0

Source: CRWMS M&O (2000, Table 44)

Table 10.7-29. Manganese Breakthrough Data from Upper Injection Boreholes

Borehole Number	5% Breakthrough Concentration	50% Breakthrough Concentration	Normalized Concentration at 1Yr.
16	more than 1 yr.	more than 1 yr.	0.0
17	more than 1 yr.	more than 1 yr.	0.0
14	more than 1 yr.	more than 1 yr.	0.0
15	more than 1 yr.	more than 1 yr.	0.0
13	more than 1 yr.	more than 1 yr.	0.0
12	more than 1 yr.	more than 1 yr.	0.0
Remaining collection boreholes	more than 1 yr.	more than 1 yr.	0.0

Source: CRWMS M&O (2000, Table 45)

Table 10.7-30. Manganese Breakthrough Data from Lower Injection Boreholes

Borehole Number	5% Breakthrough Concentration	50% Breakthrough Concentration	Normalized Concentration at 1 Yr.
46	277 days	more than 1 yr.	0.06
48	328 days	more than 1 yr.	0.06
9	more than 1 yr.	more than 1 yr.	0.0
10	more than 1 yr.	more than 1 yr.	0.0

Source: CRWMS M&O (2000, Table 46)

Table 10.7-31. Nickel or Cobalt Breakthrough Data from Upper Injection Boreholes

Borehole Number	5% Breakthrough Concentration	50% Breakthrough Concentration	Normalized Concentration at 1 Yr.
16	more than 1 yr.	more than 1 yr.	0.0
17	more than 1 yr.	more than 1 yr.	0.0
14	more than 1 yr.	more than 1 yr.	0.0
15	more than 1 yr.	more than 1 yr.	0.0
13	more than 1 yr.	more than 1 yr.	0.0
12	more than 1 yr.	more than 1 yr.	0.0
Remaining collection boreholes	more than 1 yr.	more than 1 yr.	0.0

Source: CRWMS M&O (2000, Table 47)

Table 10.7-32. Nickel or Cobalt Breakthrough Data from Lower Injection Boreholes

Borehole Number	5% Breakthrough Concentration	50% Breakthrough Concentration	Normalized Concentration at 1 Yr.
46	more than 1 yr.	more than 1 yr.	0.0
48	more than 1 yr.	more than 1 yr.	0.0
9	more than 1 yr.	more than 1 yr.	0.0
10	more than 1 yr.	more than 1 yr.	0.0

Source: CRWMS M&O (2000, Table 48)

Table 10.7-33. Fluorescein Breakthrough Data from Upper Injection Boreholes with Physical Heterogeneities

Borehole Number	5% Breakthrough Concentration		50% Breakthrough Concentration		Normalized Concentration at 1 Yr.	
	Real. 1	Real. 2	Real. 1	Real. 2	Real. 1	Real. 2
16	28 days	36 days	70 days	106 days	1.0	0.96
17	70 days	60 days	238 days	161 days	0.7	0.91
14	173 days	170 days	more than 1 yr.	more than 1 yr.	0.35	0.38
15	126 days	126 days	278 days	267 days	0.72	0.76
13	118 days	142 days	247 days	347 days	0.80	0.54
12	222 days	247 days	more than 1 yr.	more than 1 yr.	0.42	0.29
Remaining collection boreholes	more than 1 yr.		more than 1 yr.	more than 1 yr.	0.0	0.0

Source: CRWMS M&O (2000, Table 49)

Table 10.7-34. Fluorescein Breakthrough Data from Lower Injection Boreholes with Physical Heterogeneities

Borehole Number	5% Breakthrough Concentration		50% Breakthrough Concentration		Normalized Concentration at 1 Yr.r	
	Real. 1	Real. 2	Real. 1	Real. 2	Real. 1	Real. 2
46	4 days	4 days	37 days	32 days	1.0	1.0
48	24 days	22 days	106 days	96 days	0.97	0.98
9	52 days	47 days	156 days	more than 1 yr.	0.94	0.94
10	197 days	202 days	more than 1 yr.	more than 1 yr.	0.28	0.26

Source: CRWMS M&O (2000, Table 50).

Table 10.7-35. Transport Parameters Deduced from Fits of the Bullfrog Tuff Tracer Responses

Parameter	Pathway 1 <sup>a</sup>	Pathway 2 <sup>a</sup>
Mass fraction in pathway	0.12	0.59
Residence time, linear flow (hr.)	37	995
Longitudinal dispersivity, linear flow (m)	5.3	18.8
Residence time, radial flow (hr.)	31	640
Longitudinal dispersivity, radial flow (m)	3.6	10.7
Effective flow porosity, linear (radial) <sup>b</sup>	0.0029 (0.0025)	0.026 (0.017)
$\frac{\phi}{b}\sqrt{D_m}$ for bromide (sec <sup>-1/2</sup> ) <sup>c</sup>	0.00158	0.000458
Microsphere filtration rate constant (hr. <sup>-1</sup> ) <sup>d</sup>	0.2	0.04

Source: CRWMS M&O (2000, Table 51)

NOTES: <sup>a</sup>Note that Pathway 1 refers to pathways that resulted in the first tracer peak, and Pathway 2 refers to pathways that resulted in the second peak.

<sup>b</sup>Based on flow log information, it was assumed that 75 percent of the production flow contributed to the Pathway 1 responses and 25 percent of the flow contributed to the Pathway 2 responses.

<sup>c</sup>This parameter is an effective matrix diffusion mass transfer coefficient. The value of the parameter for pentafluorobenzoic acid was assumed to be 0.577 times that for bromide.

<sup>d</sup>Multiple resuspension/detachment rate constants were assumed in each pathway to obtain a fit to the microsphere responses (see Reimus et al. 1999, Appendix C). Filtration coefficients (m<sup>-1</sup>) can be calculated from the filtration rate constants ( $k_{fil}$ ) using  $k_{fil}/V$ , where  $V$  = average linear velocity determined from mean fluid residence times.

Table 10.7-36. Transport Parameters Deduced from Fits of the Prow Pass Tuff Tracer Responses

Parameter	Value
Mass fraction participating in test	0.75
Residence time, linear flow (hr.)	1230
Longitudinal dispersivity, linear flow (m) <sup>b</sup>	23.1
Residence time, radial flow (hr.)	620
Longitudinal dispersivity, radial flow (m) <sup>b</sup>	6.3
Effective flow porosity, linear (radial)	0.0068 (0.0034)
$\frac{\phi}{b}\sqrt{D_m}$ for bromide (sec <sup>-1/2</sup> ) <sup>a</sup>	0.000968
640-nm sphere filtration rate constant (hr. <sup>-1</sup> ) <sup>a</sup>	0.043
280-nm sphere filtration rate constant (hr. <sup>-1</sup> ) <sup>a</sup>	0.07

Source: CRWMS M&O (2000, Table 52)

NOTES: <sup>a</sup>This parameter is an effective matrix diffusion mass transfer coefficient. The value of the parameter for pentafluorobenzoic acid was assumed to be 0.577 times that for bromide.

<sup>b</sup>Longitudinal dispersivities calculated after subtracting out apparent dispersion due to the recirculating flow field (see Reimus et al. 1999, Chapter 5)

Table 10.7-37. Comparison of Field-Derived and Laboratory-Derived Sorption Parameters for Lithium Ion

Parameter	Field $K_d$	Laboratory $K_d^a$
Prow Pass matrix $K_d$ assuming Central Prow Pass Tuff	0.66	0.13 (0.26 at infinite dilution)
Prow Pass matrix $K_d$ assuming Lower Prow Pass Tuff	1.68	0.084 (0.44 at infinite dilution)
Bullfrog matrix $K_d$ in Pathway 1 assuming Central Bullfrog Tuff <sup>b</sup>	0.24	0.19 (0.44 at infinite dilution)
Bullfrog matrix $K_d$ in Pathway 1 assuming Lower Bullfrog Tuff <sup>b</sup>	0.97	0.32 (1.64 at infinite dilution)
Bullfrog matrix $K_d$ in Pathway 2 assuming Central Bullfrog Tuff <sup>b</sup>	0.67	0.19 (0.44 at infinite dilution)
Bullfrog matrix $K_d$ in Pathway 2 assuming Lower Bullfrog Tuff <sup>b</sup>	2.75	0.32 (1.64 at infinite dilution)

Source: CRWMS M&O (2000, Table 53)

NOTES: <sup>a</sup>Values at infinite dilution were obtained from slopes of Langmuir isotherm fits to the data (asymptotic slope at very low concentrations). Other values were obtained from a simple linear fit to the entire range of data.

<sup>b</sup>Pathway 1 refers to pathways that resulted in the first tracer peak in the Bullfrog reactive tracer test, and Pathway 2 refers to pathways that resulted in the second peak in this test.  $K_d$  values were calculated from the smallest matrix retardation factors obtained from alternative interpretations of the test (see Reimus et al. 1999, Appendix C).

This comparison assumes linear sorption isotherms.

Table 10.7-38. Laboratory-Measured Matrix Diffusion Coefficients of Bromide and Pentafluorobenzoic Acid in Various C-Hole Tuffs

Tuff	Porosity	Permeability (mDarcy)	L (cm)	Matrix Diff. Coeff. ( $\text{cm}^2/\text{s} \times 10^6$ )		
				Br	PFBA	Br/PFBA
Central Bullfrog	0.094	0.00107	1.16	0.45	0.13	3.46
Lower Bullfrog	0.298	0.0949	0.84	1.0	0.35	2.86
Upper Prow Pass	0.272	4.72	0.91	6.0	1.9	3.16
Central Prow Pass	0.138	0.000786	1.23	0.4	0.13	3.08
Lower Prow Pass-1 <sup>a</sup>	0.288	0.455	2.27	3.0	1.1	2.73
Lower Prow Pass-2 <sup>a</sup>	0.288	0.455	1.82	3.0	1.0	3.0

Source: CRWMS M&O (2000, Table 55)

NOTES: <sup>a</sup>Duplicate experiments were conducted in the lower Prow Pass Tuff.

The porosities and permeabilities of the tuffs are also listed.

L = thickness of tuff wafer used in diffusion cell experiment; PFBA = pentafluorobenzoic acid

INTENTIONALLY LEFT BLANK

## 11. INTEGRATED NATURAL SYSTEM RESPONSE TO THERMAL LOADING

Of all of the characteristics of a high-level radioactive waste repository, the heat output of the emplaced waste is among the more readily predictable. The heat output of the waste rapidly declines, with about 75 percent of the total integrated heat generated during the first 300 yr. Depending on the design chosen, temperatures on the drift wall (the wall of the waste emplacement drift) might reach 225°C in this initial period, and temperatures in excess of 100°C might persist in the surrounding rock for thousands of years. The natural system can be divided into the near-field environment zone and the far-field environment zone. The part of the natural system considered in this section is the near field, which will be permanently altered by the thermal excursion. Although the far field may have slightly elevated temperatures, it will remain essentially unaltered.

This section presents the results of site characterization activities aimed at understanding the integrated natural system response to thermal loading. Among the responses are thermomechanical and thermochemical effects on fractures, thermochemical alteration of heated rock, and thermohydrological effects, such as rock drying or wetting, changes in relative humidity, and water flux and composition.

This section describes the thermohydrologic behavior (Section 11.2), geomechanics (Section 11.3), geochemistry (Section 11.4), and field testing (Section 11.5) at the site. A summary is given in Section 11.6.

### 11.1 OVERVIEW

This overview addresses how understanding the integrated natural system response of the near-field environment supports regulatory compliance, and how this understanding will be used to provide the technical basis needed for potential repository design decisions and performance analysis. The near-field environment is defined as the environment that develops within the rock extending from the drift walls outward to a distance where significant heat or excavation changes no longer occur in the properties or processes within the rock. "Significant" refers to the effect the change has on attributes considered in performance assessment, such as water flow paths and water chemistry (CRWMS M&O 2000b, p. 1-3). This section also discusses the need to examine hydrological, geochemical, and geomechanical processes and the importance of coupling these processes.

This discussion was based originally on the *Near-Field and Altered Zone Environment Report* (Wilder 1996). More recent work appears in the *Near Field Environment Process Model Report* (CRWMS M&O 2000b), the *Unsaturated Zone Flow and Transport Model Process Model Report* (CRWMS M&O 2000i), and the *Engineered Barrier System Degradation, Flow, and Transport Process Model Report* (CRWMS M&O 2000c). Detailed analyses supporting these process model reports appear in the *Multiscale Thermohydrologic Model* (CRWMS M&O 2000a), the *Thermal Tests Thermal-Hydrological Analyses/Model Report* (CRWMS M&O 2000e), and the *Drift-Scale Coupled Processes (DST and THC Seepage) Models* (CRWMS M&O 2000d).

Evaluations of the expected natural system response to thermal loading are based on the currently available understanding of natural system properties, parameters, and analyses, as well as reference designs, and some ongoing tests and analyses. In some cases, information from similar rock types or formations, as well as from specific mineral or chemical conditions, was used. The Drift Scale Test is the most complex of the three field tests needed to characterize the responses of Yucca Mountain to thermal loading and to test the model conceptualizations, but it has not been completed at this time. Analyses to date indicate that the models reasonably match test results. Future confirmation of the predicted Yucca Mountain environmental conditions will be required.

### 11.1.1 Definitions of Thermally Affected Zones in the Natural System

From early site characterization work, it was soon recognized that interactions between the natural system and waste could cause both permanent and transient property changes within a region that extends for a considerable distance into the rock mass. Beyond this first region, the near field, lies a second region, the far field, where only minor (not significant) and transient (such as slightly elevated temperatures) changes may occur. The distinction between the near field and far field is based on processes and resultant changes, rather than on a single geometric scale.

Although the same suite of processes exists throughout the near field, those that dominate near the waste are not necessarily the same as those that dominate farther out. The near field may extend considerably farther for some processes than for others, ranging from tens to hundreds of meters outward from the emplacement drift. It also evolves over time. The current Yucca Mountain Site Characterization Project definition of the near field zone is given in the *Near Field Environment Process Model Report* (CRWMS M&O 2000b).

The near field encompasses an inner region of rock and waste emplacement drift that is proximal to the waste packages and interacts with them. The near field also has an outer region where the environmental conditions do not interact directly with the waste packages, but can interact indirectly through property changes within the rock mass due to coupled processes. The inner near field can extend up to 20 m (66 ft) from the waste packages and the emplacement drifts. Temperatures within the inner near field may be above boiling. Thus, in this region, the early contact time for rock-water interactions may be shorter than at locations farther from the waste. In some reports, what is called the near field environment has included only this inner near field zone. This inner near field environment is also sometimes called the waste package environment.

In the outer near field, the rock mass may undergo fundamental property changes due to coupled processes related to emplaced waste. Some of the changes that occur may be reversible over long periods of time, but they are usually long-lived or permanent. For example, the outer near field would include nontransient changes in physical or chemical properties and chemical or mineralogical composition, but would not include transient effects such as reduction in liquid saturation of the rock pores or volumetric changes resulting from the thermal expansion. The outer near field is a region where temperatures are sufficiently low to allow liquid water to exist in pores and fractures, although it may include vapor-dominated regions as well. Components of the outer near field do not interact directly with the waste packages but, rather, interact with the

inner near field. Changes in the outer near field are more significant than those in the far field, where near-ambient conditions dominate and only transient effects occur.

## **11.1.2 Performance, Design, and Regulatory Considerations**

### **11.1.2.1 Evolution of the Safety Case**

The safety case is the set of arguments that will be made to show that the potential repository system will contain and isolate waste sufficiently to protect public health and safety. The emphasis of the safety case has changed over the years. When the Site Characterization Plan (DOE 1988, Section 8.3.5.8) was prepared in 1988, it addressed the existing U.S. Nuclear Regulatory Commission (NRC) generic regulations (10 CFR 60.113). It was planned that the containers would satisfy requirements of the regulations by providing substantially complete containment of the waste for 300 to 1,000 yr. The engineered barrier system requirement to release no more than 1 in  $10^5$  of the 1-k.y., radionuclide-specific inventory for up to 10 k.y. was allocated to the waste form. Because the container was assumed to perform for 1 k.y. as opposed to the waste form for 10 k.y. the emphasis for the near-field environment was to provide an environment that was compatible with 10 k.y. waste form performance by keeping the pH close to neutral. This was the reason for the requirement in the Site Characterization Plan (DOE 1988, Section 8.3.5.10) to limit the use of concrete or cementitious materials in the potential repository which could raise pH.

There were also Site Characterization Plan (DOE 1988, Sections 8.3.5.9 and 8.3.5.10) requirements to prevent water contact with waste by maintaining a capillary barrier (gap between waste package and borehole rock) and to limit rock from sloughing into waste-emplacement boreholes. The natural system was relied on to provide a groundwater travel time to the accessible environment that exceeded 1 k.y. and also to retard the transport of radionuclides by sorption and similar processes. The natural system was assumed to provide this function for up to 1 m.y. under some interpretations. Because of the emphasis on long times and on retardation of radionuclides, preventing destruction of the sorptive minerals (zeolites) was deemed important. To protect the sorptive minerals and other components of both the natural and engineered systems, a series of constraints was placed on temperatures. In the case of sorptive minerals, these temperature limits were placed because dehydration of zeolites would impact their sorptive capacities.

Early in the 1990's, the emphasis for isolation shifted toward the unperturbed natural system, although container lifetimes beyond 1 k.y. were considered. Concepts to maintain a very dry near-field environment (extended dryout) were also considered. Because of the possibly conflicting goals of maintaining high temperatures to keep packages dry and lower temperatures to prevent dehydration or alteration of sorptive minerals (as well as thermal performance issues of other components of the potential repository-waste disposal system), a series of thermal goals was formalized. During this time, the requirements for pH control or limits on use of concrete were relaxed.

By 1998, the safety case strategy evolved to rely increasingly on the engineered barrier system. Engineered barriers such as drip shields, backfill that provides a Richards (capillary) barrier, and ceramic coatings were being considered to complement the natural site characteristics that tend

to keep the waste packages dry (YMP 1998). Limited water contacting the waste packages helps to ensure a long waste package lifetime and a subsequent slow rate of release of radionuclides from the waste form. The potential of engineered barriers to complement the natural barriers in affecting concentration reduction of radionuclides during transport was also recognized. This strategy supported the Viability Assessment (CRWMS M&O 1998e, Section 4.2).

During fiscal year 2000, the safety case strategy, addressing revised draft NRC regulations, has evolved further based on a design alternatives study, continual refinement of site and engineered barrier data, field test results, and updated performance assessments (YMP 1999). The strategy continues to rely highly on engineered barriers, with the most important site barrier being the limiting of water seeping into the drifts. Current information indicates that geochemical processes that result from the coupling of heat and fluids generated from waste emplacement may form sorptive minerals (zeolites) within the near-field environment (CRWMS M&O 2000d, Figure 41). Furthermore, these changes may alter the hydrologic system. However, there are large uncertainties in the understanding of the natural system, and recent evidence suggests an average infiltration rate of 4.9 mm (0.02 in.) per year (DOE 1998b), which is much higher than originally anticipated. As a result, there has been increased emphasis on robust waste packages that can last for more than 10 k.y. and on a drip shield system that will protect these packages. However, the safety strategy continues to rely on the advantages that the Yucca Mountain site offers in terms of natural waste isolation barriers and site features, such as limited water flux and competent rock that favor the performance of engineered barriers (CRWMS M&O 2000g, Appendix A).

The strategy has also changed in response to changes in the regulations that apply to the repository system. The numeric subsystem performance objectives of the generic rule, 10 CFR 60, have been replaced by a site-specific, risk-informed, performance-based approach that relies on an integrated total system performance assessment, underlain with a sound foundation and technical basis (proposed 10 CFR 63 [64 FR 8640]). Although details may change in the final rule, this approach is expected to be maintained. Therefore, the current strategy defines process model reports that address the NRC's key technical issues. Each of the seven principal factors identified in the Repository Safety Strategy maps to U.S. Department of Energy (DOE) process model reports and NRC key technical issues.

#### **11.1.2.2 Importance of the Near Field to Waste Isolation**

The near field is important to waste isolation because it is the environment in which the waste packages and the waste form are impacted. Even if thermal conditions have returned to close to preemplacement values, the near field may have been altered during the thermal pulse that follows waste emplacement. The preemplacement natural site environment will last for only a short period of time after emplacement.

The impact of the near field environment on waste isolation depends largely on three factors; two are inherent properties of the system, and one can be varied by design. These three factors that define the near-field environment are:

- The preemplacement natural system—that is, the rock mass (inherent property)

- Radioactive decay heat from the waste (inherent property), and the processes associated with that heat
- Design aspects of the potential repository that control the postemplacement environment, including thermal loading, introduced materials, and engineering options, such as ventilation, backfill, or drip shields (design dependent).

The most important characteristic of the preemplacement rock mass around the potential repository is that it is unsaturated, which can minimize seepage of water into the emplacement drifts. This unsaturated preemplacement natural system provides the starting conditions for the near field. However, the characteristics will change almost immediately after waste emplacement because of the heat. Within the near field, the natural system will undergo significant changes and may perform quite differently than would be predicted without thermal loading.

The natural system, whether altered or not, can contribute to the isolation of waste from the accessible environment in three ways. First, it can limit the amount of water that can contact the waste and waste packages. Second, the natural system can inhibit radionuclide migration through chemical exchange or sorptive processes with the rock minerals and pore water. Third, the natural system can contribute to isolation by delaying transport.

Thermally driven processes within the near field can affect water distribution, specifically the redistribution of water due to waste heat. Processes that occur in the near-field environment can also contribute to significant changes in rock porosity and permeability, which can affect water contact with the waste. These processes can also significantly modify the mineralogy, resulting in changed sorptive capacities of the near field (which could be either helpful or detrimental). In addition, if dryout occurs within the near field, there is increased capacity for imbibition so that radionuclides in water imbibed from the fractures into the pores would tend to be physically held by capillary forces for a long time. Thus, the near field could positively affect isolation of waste.

The thermal characteristics of the waste are described in CRWMS M&O (2000a). Here, it is important only to recognize that an exponentially declining release of heat is a fundamental characteristic of the waste; that heat output is more accurately predictable than virtually any other parameter of the potential repository; that although heat output persists for hundreds of thousands of years, the exponential decline renders additional effects on the repository negligible within a few tens of thousands of years; and that along with the unsaturated nature of the site, heat from the waste is one of the major determinants of site response to emplacement of the waste and thus the ability of the site to isolate waste.

Although the site rock mass and heat from the waste are inherent properties of the system, intelligent design can maximize the positive interactions between rock mass and heat so that desirable effects are enhanced and undesirable effects are moderated. Among the important variables are the waste emplacement density (thermal loading), age of the emplaced waste, configuration of the waste within the emplacement drifts and spacing of the drifts in the repository, use of ventilation to remove heat and moisture, and use of components such as drip shields and backfill to control the environment around the waste packages.

### 11.1.2.3 Importance of the Near Field to Performance Assessment

Performance assessment must consider the interaction between the near field environmental conditions prevailing and the waste form and waste packages. The waste form contributes to isolation of radionuclides mainly by limiting the rate at which the waste can be released (CRWMS M&O 1998e, Section 4.2). The near-field environment factors that influence the rate of release are the amount, temperature, and chemical content of water that contacts the waste. The properties of the waste that determine this rate are discussed in Stout and Leider (1997, Section 2). The near field will be a major factor in the release rates from the waste form because the quantity, temperature, and chemicals in the water contacting the waste will be dominated by the near-field environment (CRWMS M&O 2000b and 2000c).

Container performance depends on the container design and materials selected and on their interaction with the near-field environment, specifically the quantity, temperature, and chemical content of both liquid water and water vapor as well as gas composition in the drift (i.e., presence or absence of O<sub>2</sub>, H<sub>2</sub>, and CO<sub>2</sub>). The mode of water contact (dripping, continuous contact, condensation) also is an important factor in container performance or, more specifically, on corrosion kinetics. Once again, these factors are all components of the near-field environment, and together with the processes noted for the waste form will be important to container performance. The influence of corrosion products and colloids, however, may be less significant.

Performance assessment is ultimately concerned with releases to the accessible environment and the dose to members of the public. The dose rate depends on the time that release from the engineered barrier system begins, the magnitude and duration of the release, and attenuation of radionuclide concentration resulting from depletion and dilution during radionuclide transport through the natural system from the potential repository to the accessible environment.

Radionuclide release from the engineered barrier system requires two conditions:

- A breach, or failure, of the metal barriers of the waste package, including the outer corrosion-resistant layer of the container, the inner structural layer of the container, and the cladding around the spent nuclear fuel pellets or pour canisters around the defense high-level glass waste forms. Such a breach is driven by the amount and chemistry of water contacting the waste package.
- Contact of the waste form by liquid water, which can dissolve or suspend radionuclides and transport them through the failed waste package and other elements of the engineered barrier system to the rock below the drifts. (Gaseous radionuclides, such as <sup>14</sup>C, are not included in these near-field environment discussions.)

Breach of the outer barrier is determined by its corrosion rate, including mechanisms of crevice corrosion, stress corrosion cracking, phase transformation, pitting, and general corrosion. (The potential effect of mechanical stress on container breach is discussed in Section 11.3.) The corrosion rate is a function of near-field conditions (humid air or liquid water contacting packages). The corrosion rate is accelerated under conditions of high relative humidity. Some of the rate parameters also depend strongly on the chemical composition of solids on the waste

package surface because the composition of salts can control the humidity at which a liquid film can form, as addressed in the *Physical and Chemical Environment Abstraction Model* (CRWMS M&O 2000f). These solids could be manufacturing residues or salts left by the evaporation of water. Breach of the inner structural barrier and pour canisters will be controlled almost entirely by the internal waste package environment until the outer barrier is breached. At that time, the near-field environment could affect corrosion. A more complete discussion of corrosion mechanisms and rates is presented in CRWMS M&O (2000j).

Postemplacement cladding failure will be controlled primarily by the temperature within the waste package. An additional factor is the amount of O<sub>2</sub> that is able to contact the cladding. Both factors are affected by the near-field environment. If temperatures are high at the time O<sub>2</sub> contacts cladding, the cladding will oxidize rapidly. In addition, if O<sub>2</sub> can contact the waste while the temperatures are still high, the waste will oxidize with significant volume increase, thereby bursting the cladding. Furthermore, oxidized fuel is much more soluble than nonoxidized fuel. Waste package temperature depends on the rate of heat transfer between the waste package and its surroundings. Heat transfer rate, in turn, depends on whether backfill is used, the spacing between drifts and between waste packages, the thermal output of waste, and the thermal conductivity of the surrounding rock. The heat transfer rate from waste packages is not expected to be particularly sensitive to the presence of liquid water or its chemistry within the repository drifts. The mode of heat transfer may be impacted, as well as distribution along the drift, but overall temperature gradients will be fairly insensitive.

Even if a waste package fails, negligible amounts of radioactive material will be released unless liquid water is advected into the drift, into the breached waste package, onto the waste form, back out of the waste package, and into the rock surrounding the repository. Hence, the timing of advected water entry, the flux of liquid water, and the water's chemistry will be important near-field environment variables for performance assessment after failure of waste packages. All of these issues may be dominated by changes within the near field from processes involving:

- Introduced materials, such as corrosion products, backfill, and altered drift liner materials
- Mineralogical changes that can influence near-field hydrologic properties and water chemistry
- Coupled thermal-mechanical-hydrological processes within the near field, which may completely change the flow fields above and below the potential repository.

Such processes could alter the physical and geochemical processes in the near-field environment that control waste package performance as well as the transport of radionuclides in both the unsaturated zone and the saturated zone below the potential repository.

#### **11.1.2.4 Importance of Near-Field Environmental Conditions to Design**

The performance assessment implications of near-field environmental conditions suggest that design goals should include the development of an engineered barrier system that, in concert with the natural system, will provide a long delay between emplacement and the first contact of waste by water. The overall design goal is to prevent water from contacting the waste form as

long as possible and to limit the amount of waste contacted by water after contact begins. The near-field environment that develops above the potential repository may change the amount, chemistry, and mechanisms (location, timing, and duration) of water seeping into drifts and ultimately contacting the waste form. Calculated fluxes around the drifts during the first few hundred years, driven by decay heat, can range up to hundreds of millimeters per year (Wilder 1996, Chapter 1). Thus, depending on the thermal load, percolation flux at the repository horizon from condensed water may far exceed that of meteoric water.

Survival of the waste package can be greatly increased if the relative humidity at the waste package surface is kept low. Current calculations suggest that a thermal loading strategy can be used to reduce humid air corrosion during the thermal pulse to rates below those under preemplacement conditions. The duration and magnitude of this reduction depend on many factors, including percolation flux. Although model results are believed to be accurate, the validity of the models used in the calculations is uncertain. Thus, it is important to experimentally test the thermohydrological model calculations that predict the ability to maintain low relative humidity for thousands of years. Discussion of the validation process is contained in the respective analysis model reports. If the model results are correct, design decisions can be made to use heat constructively for increasing waste package life.

The importance of near-field environment conditions is recognized in current design modifications. Recent results of site investigations indicate that the mean present-day infiltration flux could vary spatially from 0.4 to 16 mm/yr. (0.016 to 0.6 in./yr.), with large temporal and spatial variations above and below those values (CRWMS M&O 2000a). If the higher range of these fluxes were allowed to contact a significant fraction of the waste inventory, releases larger than acceptable dose limits could result. Hence, current design modifications include measures such as drip shields to divert water from waste packages.

#### **11.1.2.5 Importance of the Near Field to Regulatory Criteria**

The Energy Policy Act of 1992 directed the U.S. Environmental Protection Agency to promulgate a site-specific dose-based or risk-based radiation protection standard for Yucca Mountain to replace the release-based standard in 40 CFR 191 (1998), and the NRC to conform its regulations to this new standard. The NRC has proposed placeholder standards for the final EPA standards (CRWMS M&O 2000g, Appendix B). Assuming that the NRC, in conforming its regulations to a new U.S. Environmental Protection Agency standard, uses only a dose-based system performance objective, the near-field environment will remain important to demonstrating compliance, because it will be important to both design and performance assessment. In 1996, the NRC announced a restructuring of its program in preparation for reviewing a license application for a potential Yucca Mountain repository (Sagar 1997). The scope of the NRC program was adjusted to focus on only those topics most critical to potential repository performance and licensing, which were called key technical issues. Six of the NRC's 10 key technical issues are related to the near field, some more closely than others. The following three key technical issues are discussed in this section:

- Evolution of the near-field environment
- Thermal effects on flow
- Repository design and thermal-mechanical effects.

The following three key technical issues are linked through the effect of the near-field environment on performance assessment:

- Container life and source term
- Total system performance assessment and integration
- Radionuclide transport.

### **11.1.3 Discussion of Background Material**

#### **11.1.3.1 Emplacement and Repository Concepts**

Emplacement is currently envisioned in large-capacity, multibarrier waste packages placed within emplacement drifts (horizontal tunnels), with postemplacement cooling by ventilation, followed during closure by placement of a drip shield over the packages, and the possible use of backfill. Although concrete and grout are discussed later in this section, efforts have been made to reduce or eliminate their use to avoid deleterious geochemical interactions.

Section 11 addresses a variety of repository design options, with focus on the Site Recommendation (Wilkins and Heath 1999) and design. Seven design options were evaluated for the license application design selection study, with areal mass loadings ranging from 45 to 170 (MTU/a.). The selected design (Wilkins and Heath 1999) is based on an areal mass loading of 60 MTU/a.

The base case design (Wilkins and Heath 1999) features drift spacing of 81 m (255 ft), line-load waste package spacing, blending of fuel assemblies to achieve a more uniform heat load, and 50 yr. of drift ventilation. Prior to closure, drip shields are placed over the waste packages and the drifts may be filled with high capillarity (small grain size) sand backfill. As discussed below, 50 yr. of aging the waste reduces the heat output by about half. The license application design selection study evaluated drift spacings ranging from 33 to 81 m (108 to 266 ft), both point loads and line loads, durations of ventilation ranging from 25 to 75 yr., and closure with or without backfill. Spacing between the drifts was balanced against package-to-package spacing along the drifts to achieve the selected areal mass loading. In the line-load design, the waste packages are spaced so that the waste acts as a nearly uniform linear heat source, whereas a point-load design attempts to isolate individual packages. Ventilation is a means of removing the heat generated by the waste as it ages within the repository, and it reduces the magnitude of heat-induced changes in rock adjacent to the waste. Backfill, if used, introduces various thermal, hydrological, and chemical effects as discussed in Section 11.1.4.2.3.

#### **11.1.3.2 Waste Age**

Heat output of the waste is one of the most predictable characteristics of the repository, given the accuracy of the radionuclide decay constants and their established relation to heat output. Any particular spent nuclear fuel assembly will vary in heat output as a function of the reactor design, the original fuel enrichment, and length of time that it was irradiated, known as burnup. These factors are known; thus, the heat output can be calculated.

For the spent nuclear fuel expected at Yucca Mountain, the heat output of fuel that is 10 yr. out of the reactor core declines exponentially, thus by about 50 percent by 45 yr., 75 percent by 100 yr., and 90 percent by 300 yr. Because the half-life of the remaining radionuclides is long, the decline in heat output is very slow after 300 yr. About 25 percent of the total integrated heat output occurs after 300 yr.

One of the prime determinants of the thermal loading is the waste age. Although design factors such as areal mass loading (metric tons of U/acre) and postemplacement ventilation are important, the age of the fuel is the simplest and most direct determinant of the total integrated heat load per unit mass emplaced in the repository. Waste age has the greatest impact on peak waste package and rock temperatures and on the time that the peak occurs. In general, older waste results in a lower peak, which occurs at later times and declines more slowly. From a practical repository viewpoint, differences in waste age after somewhere between 50 and 100 yr. are of little significance. Thus, the 50 yr. of drift ventilation in the design (Wilkins and Heath 1999), combined with the age of the waste at emplacement, achieves most of the desired reduction in thermal load.

All of the designs evaluated in the license application design selection study allowed for 50 yr. or more of cooling prior to closure of the repository, either on the surface or underground with ventilation. One of the evaluated designs prevented the rock and waste packages from ever attaining the boiling point of water. All of the designs exhibited varying degrees and times of drying driven by the introduced heat.

#### **11.1.3.3 Relative Importance of Factors**

The purpose of identifying the most relevant factors is to center attention on which of the myriad variables may be the most important for overall potential repository design considerations and performance of the engineered barrier system. A key consideration is the nature of the interactions between the engineered barrier system and the near-field environment. These interactions are not separable; that is, the engineered barrier system impacts the inner near-field environment, but the inner near-field environment also impacts performance of the engineered barrier system. For example, it is known that areal mass loading defines the repository environment to a larger extent than other factors, which include drilling and ventilation to the radiation field from waste packages, although they may also be relevant. Furthermore, it is now known that how waste packages are configured in the potential repository has a far greater role in determining whether near-field thermal-hydrological behavior is beneficial (versus deleterious) than the areal mass loading of the repository itself (Wilder 1996, Chapter 1).

An overriding characteristic of the interaction between the engineered barrier system and the near-field environment is that the interaction results from coupled processes. The significance and magnitude of the coupling vary both spatially and temporally. The dominant processes are discussed below.

**Dominant Processes in the Inner Near Field**—In the inner near field, the dominant processes can be grouped into two categories: those occurring during the heating phase and those occurring after the waste cools. During the heating phase, the processes will include:

- Relative humidity reductions due to strong thermal gradients
- Removal of water from the system, which slows or shuts off many of the processes and results in weaker geochemical coupling between system components
- Thermal expansion under spatially varying thermal gradients, which will change rock and rock support system stresses
- Potential microcracking of both rock and rock support and invert systems, which may lead to possible rock fall
- Potential precipitation of salts from evaporating water
- Dormancy or sporation of microbial colonies
- Potential carbonation, depending on CO<sub>2</sub> availability, of concrete portions of the engineered barrier system
- Displacement of O<sub>2</sub> by water vapor.

The rates and significance of coupling will depend on the balance between two factors that have opposite effects. Elevated temperatures will increase the coupling rates and significance with introduced materials and microbial communities. However, when temperatures approach or reach the boiling point, evaporation and boiling will remove water from the system. Without water, microbial processes become minimal or are eliminated, many geochemical processes are halted (except processes involving vapor, which can progress faster), and aqueous corrosion or interactions with man-made materials are stopped. If water removal is significant, many of the coupled thermal-hydrological-geomechanical-geochemical processes become mostly just thermal-mechanical.

After cooldown, water will return to the near field through the fractured, densely welded host rock mainly by relatively rapid fracture flow and by very slow movement of moisture and resaturation through the matrix. The amount of water that can return through fractures will depend on how much condensate from water driven from the near field during the thermal phase can be stored in fractures and the matrix, and on the percolation flux at the time.

Once water returns, the near-field environment will be dominated by strongly coupled aqueous processes. How strongly the coupling will be reestablished depends on how effectively the thermal field prevents water return during heating and on how far the water removal extends. However, the reestablished aqueous coupling processes will be limited by kinetics of slower reaction rates at lower temperatures. The inner near field will likely be strongly influenced by the effects of processes that took place during the thermal phase. Water chemistry will depend mainly on interactions with introduced materials, precipitated salts left by the water that was evaporated, and, to some extent, on changes in mineralogy of the near-field rock. Interactions

with introduced materials, particularly with concretes, will partially depend on modifications to the introduced materials that resulted during the thermal pulse. Some effects, such as those from precipitated salts, may decrease with time. Because the time frames considered can be long (hundreds to thousands of years), the significance of these processes must be based on the specific time of concern.

**Dominant Processes in the Outer Near-Field Environment**—In the outer near-field environment, hydrological processes will be dominated by increased water availability and saturation associated with vapor condensation at elevated temperatures. Condensation of vapor can induce significant fracture fluxes, possibly strong gravity drainage, matrix imbibition, possible reflux to the dryout zone, and possible heat pipes. It should be noted that the relative importance of these processes depends on the properties of the fractures and matrix, and that strong refluxes to the boiling zone can significantly reduce temperature. Geochemical processes will be dominated by rock-fluid interactions, vapor contact at elevated temperatures, and reactive transport. The outer near-field environment will be less transient or dynamic than the inner near-field environment because residence times for water will be much longer. Because of the durations, the processes will tend to go toward completion, and the changes will tend to be more dramatic.

Many of the geochemical processes in the inner and outer near fields will be the same (e.g., recrystallization, dissolution and precipitation, cation exchange, sorption). However, their impact on rock properties will be different because of contrasts in heating and cooling rates and in the abundance and temperatures of liquid water. The difference will be in the magnitude and nature of chemical and mineralogical changes, and in the duration of specific processes. As a result, performance of the overall repository system will be affected differently in the two regions because of mineral-water interactions. In addition to mineral-water interactions, there will be a significant difference due to introduced material interactions. This is true not only because the introduced materials are located mainly in the drifts, but also because of the higher temperatures, dynamic or transient water conditions, and the large proportion of introduced materials in the inner near-field as opposed to the outer near-field environment. Thus, introduced materials could be a significant, if not dominant, factor in determining the inner near-field environment, whereas mineral-water interactions will be one of the principal factors that determines the outer near-field environment.

#### 11.1.3.4 Summary of Relative Importance

Although the dominant processes vary for the inner and outer near fields, evaluations have shown the overriding importance of hydrology and geochemistry, and the strong influence of heat on those processes. Thus, it is possible to begin to prioritize the most essential issues related to engineered barrier system design and performance. The most important inner and outer near-field environment parameters (i.e., the environmental parameters shown to have the greatest effects on the engineered barrier system and waste packages) are listed in Section 11.1.4. The parameters shown to have the greatest effects on the engineered barrier system and the waste package include the amount of water contacting the waste packages, water chemistry, and relative humidity; native microbial species are expected to have moderate or variable effect. Parameters expected to have minimal (little or controllable) effects on the engineered barrier system and the waste package include rockfall that physically damages the metal waste

containers (different priority if ceramic) and geomechanics. (These factors have secondary effects through coupling with more significant parameters.) The factors shown to have the greatest influence on the near-field environment include waste package layout, waste package heat output, areal mass loading, backfill, introduced (man-made) materials, percolation flux, microbiological effects, and hydrological properties. Factors expected to have lesser or limited effects on the near-field environment include construction activities (e.g., drilling, excavation, ventilation), radiation field from intact waste packages, and earthquakes. These parameters and some of the complex processes and interactions among them are addressed below with detailed discussions presented in the *Near Field Environment Process Model Report* (CRWMS M&O 2000b) and the *Engineered Barrier System Degradation, Flow, and Transport Process Model Report* (CRWMS M&O 2000c).

#### **11.1.4 Processes**

##### **11.1.4.1 Emphasis on Processes**

The natural system response to thermal loading will depend on the initial conditions and the hydrological, geochemical, and geomechanical conditions that develop over time in the rock extending for considerable distances into the mountain. For that reason, emphasis is placed not only on conditions that will result and their associated parameter values, but also on processes that will change the environmental conditions.

An understanding of processes and events as they unfold over time is essential for several reasons. For example, the degree of rock saturation is one important aspect of the potential repository environment. However, the initial saturation under ambient conditions is insufficient information on which to base design decisions. It is the amount, timing, and temporal distribution (steady state or episodic) of water contacting the waste that are pertinent to design. To estimate the amount of water expected to contact waste during a given time period, saturation data must be integrated with other factors, including:

- Percolation flux
- Fracture-matrix flow models
- Fracture distribution
- Emplacement configuration
- Areal mass loading
- Projected waste package thermal characteristics
- Repository design.

Similarly, events as wide ranging as construction activities, microbial processes, climate change, and many others may modify repository conditions. For these reasons, Section 11.1.4 focuses not only on technical information but also on the interaction of processes and the integration of values.

##### **11.1.4.2 Processes in the Inner Near-Field Environment**

Waste packages will interact with an inner near-field environment that will be altered from the original Yucca Mountain conditions. The changes will result from several factors, including repository construction, waste emplacement, and possible drift backfilling. All these activities

can cause chemical changes, possible mineralogical or basic rock-mass property changes, as well as hydrologic and thermal changes. These alterations may significantly affect the engineered barrier system design and performance.

Because the near-field environment results from coupled thermal-hydrological-mechanical-chemical processes that are initiated by repository-related activities, these activities and resulting processes leading to alteration of the near-field environment are discussed in Section 11.1.4. The specific near-field environment conditions that may result are summarized in later sections. The intention is not to give all possible scenarios but, rather, to indicate the types of activities and resulting processes that can alter the environment so that the impacts on design can be considered. An in-depth discussion of these processes is presented in Hardin and Chesnut (1997).

#### **11.1.4.2.1 Construction**

This discussion includes all activities involved in construction of the facilities that would take place before emplacement of waste. Specifically addressed are: excavation of rock, fluids introduced during drilling and excavation, ventilation, and materials introduced during construction. It does not include activities that would take place after construction (i.e., emplacement of waste, backfilling, and closure), which are discussed in Sections 11.1.4.2.2, 11.1.4.2.3, and 11.1.4.2.4, respectively.

##### **11.1.4.2.1.1 Rock Excavation**

Although blast effects would be important in some types of underground excavation, the excavation methods planned for drift excavation (tunnel boring machine) would avoid such effects. Thus, the most significant impacts assessed for excavation are the alteration of rock stress, discussed in Section 11.3. Changes in stress will result in an overall increase in hoop stresses, which will tend to close fractures, particularly during the period of increased temperature. Virtually all underground excavation requires some form of introduced ground support, which may affect not only mechanical stability of the openings, but also chemistry of the inner near field.

##### **11.1.4.2.1.2 Fluids Introduced during Drilling and Excavation**

The introduction of excavation and drilling fluids may increase the matrix saturation surrounding the drifts. However, no evidence was found of significant saturation increases during construction of the 5-mi.-long ESF access drift. In fact, the opening wall at the tunnel entrance was subjected to dryout from ventilation, as discussed below. Furthermore, construction of this ESF access drift involved drilling and excavation operations that are expected to be similar to those for planned construction and emplacement drifts. Wilder (1993a, Section 3.1; 1993b, Section 3.2) discusses the possible impacts of drilling and excavation, should they occur.

##### **11.1.4.2.1.3 Ventilation**

Ventilation during construction may lead to drying of the rock matrix surrounding the emplacement drifts, shafts, ramps, and access drifts by removing moisture from the rock via evaporation. This appears to have been the case within the ESF access drift. No dripping water

has been observed, except when the ventilation is shut off or when rock is isolated from ventilation. Ventilation after emplacement can also have significant effects including removal of water and heat (CRWMS M&O 2000h). These effects are discussed in Section 11.2.

#### **11.1.4.2.1.4 Introduction of Materials during Construction**

Materials will be introduced, both intentionally and unintentionally, during construction of the facilities. These may include crushed rock, granular minerals, engine exhaust, rubber products and other polymers, metals, and concretes. The major potential for perturbations of the environment due to introduced materials will occur after emplacement because of activation by temperature increases. The design has addressed this issue by choice of materials. In the Site Recommendation design (Wilkins and Heath 1999), for example, concrete has been significantly limited.

#### **11.1.4.2.2 Emplacement of Waste**

When waste is emplaced, heat from radioactive decay will cause changes in the environment, which will likely dominate the geochemical-hydrological-mechanical conditions. Heat has the potential to drive water away from the waste packages, to control the relative humidity, and to change the relative hydraulic conductivity, gas permeability, imbibition characteristics, and other rock mass properties.

##### **11.1.4.2.2.1 Dryout**

After waste emplacement, heat will lower the relative humidity of the gas phase and evaporate liquid water in waste emplacement openings and adjacent rock. Because of the increase in water vapor pressure, nearly all of the initial air may be driven away from the boiling zone (leaving the gas phase with 100 percent water vapor). Tests and analyses of rock-matrix drying show that vapor preferentially flows into openings and along fracture faces. Upon reaching the fractures, most vapor migrates to a cooler zone where it condenses and drains down fractures until it is entirely imbibed by the rock matrix, enters the saturated zone below the repository, or (if above the repository) drains back into the boiling zone where it boils again, forming a heat pipe by refluxing. Low wetting sorptivity of the repository host rock TSw2 (i.e., slow to imbibe water) appears to facilitate drainage to great depths below the repository. The extent to which condensate drains away from the emplacement zone depends largely on the competition between gravity drainage and imbibition by the rock matrix.

Results of the field tests (Section 11.5) at G-Tunnel (Nitao and Buscheck 1996) and at the Exploratory Studies Facility Single Heater Test (Finley et al. 1997) indicate that condensate drainage can be significant. Design options specifying widely spaced drifts appear to facilitate condensate drainage between the drifts, and the Site Recommendation design (Wilkins and Heath 1999) adopts this feature (Section 11.2).

##### **11.1.4.2.2.2 Rewetting**

As the rock cools below boiling conditions, vapor and liquid will flow back into the dried region toward the drifts. The flow will occur predominantly along fractures in the densely welded units of the repository horizon (CRWMS M&O 2000i, Section 3.7.4.3). Saturation gradients will also

cause water redistribution in the matrix; however, the very low permeabilities will cause matrix flow to be slow. Thus, flow along fractures will dominate rewetting of the dried-out zone.

Studies show that rewetting occurs at a much slower rate than drying. If most condensate drained away from the repository, rewetting would depend mostly on percolation flux from surface precipitation and might take thousands of years (Buscheck et al. 1996; Buscheck and Nitao 1993a). If most condensate remained above the repository, rewetting could be much faster. The details of emplacement configurations, fuel age, areal mass loadings, and percolation flux will have profound effects on the time of dryout and return of moisture to the waste package areas. Design must take these phenomena into account. Some information is available from thermal testing (Section 11.5), but it does not address the repository scale processes, only the local phenomena.

#### **11.1.4.2.2.3 Dissolution and Precipitation of Minerals**

Geochemical processes will be strongly coupled with thermohydrologic processes (CRWMS M&O 2000b, Section 2.1). Within the inner and outer near-field environments, and in the time and space intervals in which dryout occurs, the dominant processes will be vapor flow and chemical exchanges associated with it. Where the temperatures increase to very near boiling, the rock will undergo drying. This will result in the deposition of nonvolatile dissolved salts in rock pores and fractures. Before complete dryout occurs, the last remaining aqueous solutions may be highly concentrated salt solutions. The boiling temperatures of these residual fluids may be significantly elevated by their salt content relative to the boiling temperature of pure water. Some residual solutions may also continue to exist as thin films, stabilized further by forces acting at mineral surfaces. In any case, some salt minerals will be deposited. The zone of solute deposition will move outward with time. As water is removed, the nonvolatile dissolved material will be deposited as minerals in the throats of pores, particularly the smaller ones. This may result in fundamental changes of the matrix hydrologic properties. Studies have shown that, in addition to salt deposition, mineralogical changes can result from rock-water interactions at elevated temperatures.

The outer near field, where temperatures are elevated but below the boiling point, will be very active with both hydrologic and geochemical processes (Wilder 1996, Section 10.3). This zone has a very high potential for extensive dissolution and precipitation of minerals. Although the potential for rock-water interactions is present throughout this zone, the process of dissolution-precipitation would approach a state of equilibrium for water that remains in one place. Thus, the geochemical processes that are described here are more fully developed along fractures, which are the dominant pathways for vapor-moisture flow and where the kinetics are fast. Moisture movement within the matrix is too slow to move chemical constituents much beyond the pores that were their source. Thus, the geochemical processes discussed are largely restricted to the immediate region surrounding fractures. On a long-term basis, diffusive processes may allow interactions with interior block regions, but the magnitude would be relatively small in comparison. The water in the outer near field will consist of original pore water, condensate, and mixtures of both. Reactions will be driven by the presence of condensate, by the elevation of temperature, and by the presence of a temperature gradient (i.e., inner regions will be warmer than outer regions). Thermohydrological modeling (Buscheck and Nitao 1992, 1993b) suggests that the outer near field could achieve thicknesses of hundreds of meters above and below the

potential repository horizon. The near field below the repository horizon could extend downward into the saturated zone. The design chosen for the Site Recommendation (Wilkins and Heath 1999) has reduced areal mass loading, drift ventilation, and line loading along the drifts to reduce the extent of this zone (Section 11.2).

Numerous experiments have demonstrated that the chemical composition of water in the outer near field is likely to be controlled by the solubility of mineral phases present in the rock (Knauss 1987; Knauss and Peifer 1986; Knauss et al. 1986). However, some of these minerals are only metastable. For example, the concentration of dissolved silica will quickly become controlled by the solubility of cristobalite (a metastable polymorph of the stable silica mineral, quartz). Over the long term (hundreds to thousands of years), quartz will slowly precipitate at a rate governed by reaction kinetics (Rimstidt and Barnes 1980), and cristobalite will slowly dissolve. If all the cristobalite were to be dissolved, the concentration of dissolved silica would then fall to a level corresponding to the solubility of quartz. However, this conversion of cristobalite to quartz by dissolution-precipitation is sufficiently slow that only a fraction of the cristobalite that was present before emplacement will be destroyed in the thermal pulse period (Delany 1985). Thus, the solubility of cristobalite will remain a controlling factor long after the system has begun to cool.

In the outer near field, the presence of temperature gradients will lead to geochemical consequences, which may, in turn, modify the thermohydrological regime. The solubility of cristobalite, like that of most minerals (stable or metastable), is greater at higher temperatures. Along flow paths leading from the cooler outer regions to the warmer inner ones (e.g., above the repository), portions of the cristobalite and other minerals present will thus dissolve. Conversely, along flow paths leading from the inner to the outer regions (e.g., below the potential repository), cristobalite (and other minerals) will precipitate. Small fractures in which flow moves up the temperature gradient may become wider and smoother due to dissolution, enhancing further flow. Conversely, even large fractures leading down the temperature gradient may become filled with secondary minerals, further altering flow paths. Current analyses, however, suggest that the porosity change is small (less than 0.05 percent) and negative (CRWMS M&O 2000d, Page 110, Figure 41).

In the inner near field (which also exists both above and below the potential repository), a two-phase boiling zone will exist. Here, the temperature will be nearly isothermal, centered about the boiling point. Thermohydrological modeling for previous designs (Buscheck and Nitao 1992, 1993b) suggests that this zone could be up to 100 m thick. The Site Recommendation design (Wilkins and Heath 1999) has reduced the thickness of this zone by approximately an order of magnitude (CRWMS M&O 2000b, Section 3.2.3.2, Figure 3.8). The inner near field that lies above the repository horizon will also be a zone of significant geochemical activity (Wilder 1996), including intense reflux of corrosive condensate. Reflux is less likely to occur below the repository horizon, as the effects of gravity and the temperature gradient oppose one another there.

#### **11.1.4.2.2.4 Increased Stress**

The largest effect on the geomechanical behavior of the near-field environment is expected to be from thermal expansion and contraction during the thermal cycle as the rock heats and then

slowly cools. During the period of temperature increase, stress in the near-field rock will generally increase as the rock expands. Due to the geometry of the excavated drifts, the stress fields in the near-field environment will be complex. However, as the temperature decreases, the overall stress levels will again decrease.

Deformations within the rock mass can affect the hydrologic flow system. Many laboratory studies (Bandis et al. 1983; Barton et al. 1985) have documented that greater impact often results from shear rather than normal deformations. This is especially true once stresses are removed, as would be the case for the repository once the thermal pulse has decayed. Permanent changes in hydrologic properties or flow paths can result from stresses normal to fractures, but they tend to be smaller than those caused by shear displacements. This has also been observed in field studies (Wilder 1987).

#### **11.1.4.2.2.5 Materials Introduced during Emplacement**

In addition to construction materials, material will be brought in at the time of emplacement, including the container materials and engineered barrier system packing materials. The significance of such materials (except for dust, coatings, lubricants, and so forth) is long term once they interact (corrode) with the near-field environment. As noted, the major potential for perturbations of the environment due to man-made materials will exist after emplacement, when heat and microbial activity will increase the chances for impact on the geochemistry of the water. It is anticipated that introduced material will dominate the waste package or near-field environment chemistry, particularly if microbial activity becomes significant.

#### **11.1.4.2.3 Backfilling**

Environmental conditions that are most likely to be affected by backfilling include the hydrologic characteristics and an early, transient thermal effect of different heat conduction in the backfill compared with that of the rock mass. Backfilling would also influence the stability of the underground opening, but that is a design-related issue, not an environmental characteristic, except for spatially limited, potential effects on hydrologic characteristics. Backfill can have a significant effect on waste package temperatures, on relative humidity next to the packages, and on the potential for liquid water to contact the waste packages. Backfill in direct contact with waste package or drip shield surfaces can potentially affect the corrosion mechanisms of the metal surface. The current Site Recommendation design excludes the use of backfill (Wilkins and Heath 1999).

#### **11.1.4.2.4 Closure**

Major activities associated with closure that might affect the environmental conditions include ceasing of ventilation, emplacement of seals in openings, and the introduction of additional construction materials. Backfilling, if done, is planned to be deferred until closure; effects of backfilling are discussed above. Because closure details are yet to be determined, and further field studies of hydrothermal-chemical-mechanical coupling will be conducted before those details are developed, closure effects are not further discussed in Section 11.

#### **11.1.4.2.5 Climate or Site Environment Changes with Geologic Time**

Thermohydrologic discussions for the near-field environment included in Section 11.2 are based on the assumption that conditions remain unsaturated. They do not address climatic changes that might take place. However, they do address how sensitive the thermohydrologic response might be to differing percolation fluxes under present climate conditions. Conditions within and adjacent to the potential repository can be affected by potential variations in infiltration flux. Percolation flux at near-field environment depths depends on the overlying units' response to changes in net infiltration, which is related to climate. Thermohydrologic response to different climatic assumptions are addressed in detailed reports referenced in Section 11.2.

Current estimates suggest that the percolation flux at the near-field environment level is considerably greater than values used at the time of Wilder (1993a, 1993b), and that locally the percolation flux may be higher than values addressed in Wilder (1996). The percolation flux values evaluated in Section 11.2 are based on mean present-day infiltration flux values at 31 locations within the potential repository footprint. These values are taken from the unsaturated zone flow and transport model, and are summarized in CRWMS M&O (2000a). The values range from 0.41 to 16 mm/yr. (0.02 to 0.6 in./yr.). Analyses addressing more extreme future climates used local values ranging from zero to 125 mm/yr. (5 in./yr.).

#### **11.1.4.3 Processes in the Outer Near Field**

At Yucca Mountain, repository-associated processes or interactions can potentially cause significant property changes extending for considerable distances into the rock mass. As discussed in Section 11.1.1, the outer near-field environment is defined as the region of the natural system wherein fundamental changes to hydrologic, mineralogical, or chemical conditions take place. The changes are generally a result of increased temperature in the presence of water or water vapor. Alteration can also take place with increased temperature in the dryout zone where water exists as vapor rather than liquid. However, the alterations are greatest where both liquid water and elevated temperatures exist. Components of the outer near field do not interact directly with the waste packages; rather, they interact with the inner near field. The outer near field, with its associated conditions, differs from the far field, where near-ambient conditions tend to prevail. Many of the same processes occur in the inner near field, the outer near field, and, to some extent, the far field. However, the processes that dominate the system in the outer near field are not necessarily the same as the ones that dominate either the inner near field or the far field. Except for the coupling with introduced materials that occurs in the inner near field, the outer near-field processes are the most fully coupled.

Coupled processes dominate the outer near field, and the processes are coupled in complex ways, making it difficult to understand their effects on the environment. To facilitate explanations, the multiply coupled processes are discussed as being singly coupled or, where necessary, multiply coupled, but without evaluating all the interactions at the same time. Thus, the fully coupled processes are broken down into component parts, as they were for the preceding discussion of the inner near field.

For example, when Topopah Spring Tuff is exposed to water at elevated temperatures, the rock-water interaction will form new mineral assemblages, including carbonates and silica

depositions. These, in turn, could heal fractures and plug the original pore spaces, resulting in an overall reduction in permeability. Moreover, once the mineralogy changes the permeability, the coefficient of thermal conduction is modified, moisture conditions (involved in reactions) change, and the convection within the system is hindered. This type of back-coupling can be quite complex. However, such forward and backward coupling is important to potential repository performance. In this example, the changes in heat flow due to changed conduction and convection conditions could lead to vastly different temperatures within the near field and drifts. Although the coupling that is most dominant has been identified, the multiple coupling pathways are not fully identified at this time.

#### **11.1.4.4 Comparison of Processes in the Inner and Outer Near Field**

The environmental conditions that affect waste packages and radionuclides will be strongly perturbed by the heat of waste decay for many hundreds or thousands of years. As the thermal pulse moves farther into the rock mass, the thermal gradient decreases and the temperature eventually approaches equilibrium with the surrounding rock mass. Thus, a distinction between the inner and outer near-field environments is the transition from dominance of kinetics to equilibrium, although both processes will occur to some degree in each zone. For any given emplacement scenario, the rate at which temperature changes occur depends, in general, on the distance from the heat source: the greater the distance, the slower the temperature change. This temperature behavior provides one basis for defining or distinguishing the inner and outer near field.

In the inner near field, strong thermal gradients will exist for the first 1 k.y. This region will be dominated by kinetic effects, and hydrological processes will be dominated by water vaporization, water movement by means of gas-phase transport, and condensation in those outer regions of the near field where temperatures are below the boiling point. Geochemical processes will be dominated by evaporation and boiling, mineral dehydration, and solid-vapor interactions. The system will be highly dynamic. During heating, the dryout regions will continue to increase in size and therefore incorporate what had been condensation zones. Because of the dynamics, coupling between hydrology and geochemistry may not be well developed (water is removed before geochemical reactions change the system in significant or fundamental ways).

In the outer near field, hydrologic processes will be dominated by an increase in water availability and increased saturation associated with vapor condensation. There will be a general elevation of temperatures by tens of degrees C. The geochemical processes will be dominated by fluid-rock interactions and reactive transport. The outer near field will tend to be less dynamic than the inner near field in that the residence times for water will be much longer, and the dryout zone will not incorporate the condensation zones until long after geochemical-mineralogic changes have occurred, if at all. Within the outer near field, these interactions will result in significant coupling between hydrological and geochemical processes, such that fluid pathways and geochemical conditions will evolve in a synergistic way.

Although the geochemical processes (e.g., recrystallization, hydration-dehydration of mineral phases, dissolution-precipitation, rock-water interaction involving water in pores and fractures, cation exchange, and sorption) in both regions are the same, their impact on rock properties will be different. The differences are due to contrasts in heating and cooling rates, the abundance and

temperature of liquid water, whether kinetics or equilibrium dominate, and the duration of reactions. These differences will be expressed as differences in the magnitude and nature of chemical and mineralogical changes. As a result, potential repository performance will be affected differently in the two regions because of water-mineral interactions. The inner near field is considered to be those regions that achieve temperatures above the boiling point, and the outer near field is considered to be those regions that maintain temperatures low enough to allow liquid water to exist in pores and fractures. This distinction has the advantage of focusing attention on the dominant processes that may affect performance in different regions of the potential repository.

Because hydrothermal conditions are strongly coupled with geochemical processes, the hydrothermal conditions will be determined first (Section 11.2), then coupling with geochemical processes will be discussed (Section 11.4). In general, decay heat will result in regions of dryout and condensate buildup in the unsaturated zone. Modeling studies (Buscheck and Nitao 1993a, 1993b; Buscheck et al. 1994) have indicated that decay heat-driven changes in the saturation distribution could persist for more than 100 k.y. These effects, along with temperature changes, can alter the hydrological, geochemical, and geomechanical properties that influence fluid flow and radionuclide transport.

INTENTIONALLY LEFT BLANK

## 11.2 THERMOHYDROLOGIC BEHAVIOR AT THE POTENTIAL REPOSITORY

### 11.2.1 Introduction

Radioactive decay of high-level radioactive waste emplaced in a potential Yucca Mountain repository will produce an initial heat flux of  $16.7 \text{ W/m}^2$  for an areal mass loading of 60 MTU/a. (see Section 11.2.3.2 for the definition of areal mass loading). Even though the heat production rate decreases rapidly with time after emplacement, this heat flux will change the thermal and hydrologic environment, affecting both the host rock and conditions within the drifts in ways significant to key potential repository performance variables.

### 11.2.2 Thermohydrologic Processes at Yucca Mountain

Under ambient conditions, liquid-phase flow in the potential repository host rock arises as a result of the infiltration of rainfall and snowmelt. Although most total fluid-storage capacity is contained in the rock matrix pores, the matrix permeability is very low. For the drift-scale and mountain-scale base-case hydrologic property sets (CRWMS M&O 2000a, Section 4.1.1.18) the matrix permeability is as much as five and six orders of magnitude less than that of the repository host rock fractures; consequently, fractures dominate liquid-phase flow. After the radioactive waste emplacement, the thermally driven transport of water vapor away from the heat source causes a redistribution of the pore fluids within a potentially large volume of rock. Depending on the potential repository's thermal design, this volume can extend from the ground surface to some distance below the water table and over an area larger than the repository footprint. Water in the matrix pores evaporates, creating dryout zones around the emplacement drifts and condensation zones outside the dryout zones. The generation of steam replaces air within the boiling zone, reducing the gas-phase mass fraction of air to almost zero for a period of time.

The initial movement of water vapor is within the matrix pores. Once the decay-heat-driven water vapor has entered a fracture network, the flow direction is generally away from the heat source; however, if the fracture permeability is high enough, buoyant gas-phase convection can cause water vapor movement to be predominantly upward in the vicinity of the emplacement drifts. Depending on the potential repository's thermal design and the fracture permeability, vapor flow within fractures occurs over length scales of several to hundreds of meters.

Decay heat is transported away from the emplacement drifts (in the rock mass) by conductive and convective heat-transfer mechanisms. Thermal conduction is the dominant heat-transfer mechanism in the rock mass. Thermal radiation is the dominant heat-transfer mechanism within the open spaces inside the emplacement drifts; this applies particularly during the first several thousand years when temperatures in the drifts are relatively high. Water vapor transport results in much greater heat transport than does liquid-phase flow. Two important heat-transfer mechanisms involving the water vapor transport and phase change (i.e., evaporation and condensation) are heat pipes and buoyant gas-phase convection. Heat pipes result from vapor transport away from the heat source, and gravity-driven and/or capillary-driven condensate flow back toward the heat source (i.e., refluxing). Buoyant gas-phase convection results from mass-density gradients driven by temperature gradients in the rock mass. Depending on the potential repository's thermal design, this mechanism, which may occur at the drift and at mountain scales,

can increase the buildup of condensate above the repository. Buoyant gas-phase convection also contributes to heat transfer in the open spaces in the drifts.

The thermohydrologic behavior of the potential repository can be divided into three sequential periods: drying, steady state, and rewetting. The concept of these three periods is applicable over dynamically changing spatial regimes in addition to temporal regimes. At a given time, certain locations in a repository may have already progressed to the rewetting regime, while other locations remain in the drying regime. During the drying and steady-state periods, liquid-phase flux in the refluxing zone dominates over local percolation flux.

In the host rock, local thermohydrologic behavior is dominated by location (inside or outside the zone of boiling temperatures). Therefore, the spatial and temporal extent of the boiling zone is very important. Although thermohydrologic processes such as evaporation occur at below-boiling temperatures, the most important processes (i.e., refluxing and dryout) require that temperatures are at the boiling point of water. Note that the boiling temperature can be higher than the nominal boiling temperature (96°C) at the potential repository horizon. The key aspects of the system are boiling-period duration and boiling-period temperatures (i.e., temperatures high enough to indicate superheated conditions or refluxing/heat-pipe conditions).

Two important quantities influence thermohydrologic conditions within the emplacement drift: temperatures at the drift wall and the temperature gradient between the waste package and the drift wall. The likelihood of water seeping into the drift is strongly affected by whether temperatures at the drift wall are above the boiling point. If the local heat flux at the drift wall is greater than the product of the local liquid-phase flux and the heat of evaporation, water cannot seep into the drift. If the converse is true, then seepage into the drift is possible. The temperature gradient between the waste package and drift wall strongly affects how much lower the relative humidity (*RH*) on the waste package is than at the drift wall.

### **11.2.3 Thermohydrologic Issues Affecting Potential Repository Design Selection**

#### **11.2.3.1 Thermal Design Issues and Key System Performance Variables**

The potential repository design selection process involves trade-offs between competing goals, including performance, economic costs, uncertainty, and constructability. Thermal design goals include:

- Keeping temperatures below critical temperatures for engineered materials
- Keeping waste packages dry (i.e., low *RH*) until cool
- Limiting water seeping onto waste packages
- Limiting the spatial extent of boiling

The first design goal of keeping temperatures below critical temperatures for engineered materials concerns limiting the temperature-dependent degradation of key engineered barrier system components, such as the Zircaloy cladding of the spent nuclear fuel rods in the waste packages. Critical temperatures for engineered materials are material-dependent, but are generally above 300°C. For example, CRWMS M&O (2000j, Section 3.1.4.5) recommends that

the waste-package surface temperature be limited to levels below 300°C. In general, the greater the local heat generation rate, the hotter the waste package will become. Since backfill acts as insulation, a design with backfill will result in waste package temperatures greater than an otherwise equivalent design without backfill.

The second design goal of keeping waste packages dry until cool concerns limiting waste package degradational mechanisms that are enhanced with the presence of liquid films at elevated temperatures. Ambient conditions at the potential repository horizon are very humid (*RH* greater than 99 percent). Depending on the repository design, *RH* on waste packages can be significantly less than ambient for an extended period of time. Keeping waste packages dry until they are cool translates to maintaining conditions of reduced *RH* (less than 80 to 90 percent) for as long as possible. Because temperatures continuously decline with time, the longer reduced-*RH* conditions can be maintained on a waste package, the cooler that waste package will be once it has become humid.

Even though the environment in the potential repository drifts is expected to be dry, there is concern that thin films of brine could exist on the component surfaces. Hygroscopic salts enable aqueous solutions to exist at *RH* values less than 100 percent (CRWMS M&O 2000j, Section 3.1.3.1). Brines could form on these surfaces through evaporation of water that seeps into the drift or by water adsorption by hygroscopic salts directly deposited on these components from previous evaporation events or from particulates that enter the drifts. The latter is of concern because the deliquescence point of some salts is above the boiling point for water, which could result in brine formation at above-boiling temperatures, and the higher the temperature, the greater the corrosion potential.

Three primary factors contribute to reducing *RH* on waste packages. The first primary factor is inclusion of engineered barrier system components, such as backfill and drip shields (which overlie waste packages), in the design. These components insulate the waste package from the drift wall, thereby enhancing the temperature and *RH* difference between the drift wall and the waste package. The increased temperature difference raises the temperature of the waste package, but leaves the temperature of the drift wall unchanged. In an open drift (i.e., with nothing separating the waste package from the drift wall), the temperature difference between the waste package and the drift wall is controlled by thermal radiation. Because thermal radiation is an extremely efficient heat-transfer mechanism, this results in a small temperature difference. Because the temperature difference between the waste package and the drift wall reduces *RH* on the waste package with respect to the drift wall, it can be beneficial to insulate the waste package from the drift wall by using a low-thermal-conductivity backfill. A drip shield overlying the waste package will act as a thermal radiation shield, thereby enhancing the temperature difference between the waste package and the drift wall.

The second primary factor contributing to *RH* reduction on waste packages is the presence of above-boiling conditions in the host rock (resulting in rock dryout) at the drift-wall boundary. Dryout of the host rock results in *RH* reduction in the host rock and in the drift (and on waste packages). Generally, the humidity at the waste package cannot exceed that of the rock at the drift wall. Rock dryout also limits the tendency for water to seep into the drift. By minimizing

the seepage flux into the drift, the benefit of the temperature difference between the waste package and drift wall on *RH* reduction on waste packages is maximized.

The third primary factor contributing to *RH* reduction is limiting the tendency for water to seep into the drift. This can be accomplished in two ways. Keeping the drift wall above the boiling point will limit the tendency for seepage. After boiling has ceased at the drift wall, seepage can be limited by engineered barrier system designs that minimize wicking of water into the drift and promote drainage of any water that does seep into the drift. Wicking of water into the drift can be limited if a low-capillarity backfill is used. Such backfill material will also promote rapid drainage of water that seeps into the drift.

The third design goal of limiting water seepage into waste packages concerns limiting the potential for radionuclide release and transport if waste packages are breached. Several methods will limit water contacting the waste packages, including reducing potential seepage into the drift by maintaining above-boiling conditions at the drift-wall boundary. Another method is using an engineered barrier system design that minimizes wicking of water into the drift and promotes drainage of water that seeps into the drift.

The fourth goal (of preventing coalescence of the boiling zones) addresses the concern that coalesced boiling would result in an overlying zone of condensate (and percolation) buildup that might lead to an unstable and heterogeneous distribution of liquid-phase flux immediately above the repository horizon. Highly localized and/or episodic liquid-phase flux would be more likely to seep into emplacement drifts. The fourth goal also limits the spatial extent of coupled thermal-hydrologic-chemical behavior in the host rock and thereby limits the uncertainty that arises from the resulting potentially hard-to-assess effects in the host rock. Limiting the extent of boiling will also limit the magnitude and spatial extent of temperature rise, which will limit the magnitude of thermal-hydrologic-mechanical behavior in the host rock. Some changes, such as fracture closure due to thermal-mechanical stresses, may be temporary; others, such as the mineral alteration in fractures from thermochemical processes, may be permanent.

These four thermal-design goals are interdependent. For example, backfill may be used to keep *RH* low, but may make waste packages too hot at the time that peak temperatures occur. Similarly, reducing the uncertainty that arises from limiting boiling conditions comes at the cost of higher *RH* in the drifts due to decreased rock dryout.

### **11.2.3.2 Engineering Design Variables that Affect Heating Conditions**

The primary thermal-design variables that affect heating conditions and the resulting thermohydrologic behavior in the potential repository are areal mass loading, lineal mass loading, waste package spacing and sequencing, spent nuclear fuel age, fuel blending, duration and heat-removal efficiency of drift ventilation, and engineered barrier system design (e.g., backfill or drip shield emplacement). With respect to thermal power output, there are two primary classes of waste packages: commercial spent nuclear fuel, and all other waste package types, including defense and non-defense high-level radioactive waste. The commercial spent nuclear fuel waste packages generate much more heat than noncommercial waste packages (e.g., defense high-level

waste); thermal output from commercial spent nuclear fuel waste packages also declines much more slowly with time.

Areal mass loading, expressed in metric tons of uranium per acre, is a measure of the overall heat-generation density of waste inventory. The areal mass loading is the key factor in determining the magnitude of long-term thermohydrologic effects, including the radial and vertical extent of boiling in the host rock and the duration of boiling conditions in the emplacement drifts. The areal mass loading is calculated on the basis of the metric tons of U per acre of emplaced commercial spent nuclear fuel. The Site Recommendation design (Wilkins and Heath 1999, Enclosure 2, p. 1) emplaces 63,000 MTU of commercial spent nuclear fuel over an area of about 1,050 a., resulting in an areal mass loading of 60 MTU/a. The initial heat output for the entire waste inventory is  $7.08 \times 10^7$  W, resulting in an initial heat flux of  $16.7 \text{ W/m}^2$ .

Lineal mass loading, expressed in metric tons of uranium per meter of emplacement drift, is a measure of the average heat-generation density along the drifts. The lineal mass loading, along with spent nuclear fuel age, is a key factor in determining short-term thermohydrologic effects, such as the peak temperatures on waste packages and on the drift wall, and the temperature difference between the waste package and the drift wall.

Waste-package spacing and heat-source heterogeneity determine the variability of thermohydrologic conditions along drifts. Waste-package spacing pertains to the end-to-end distance between waste packages. If waste packages are spaced far apart along the drift (point-load waste-package spacing), heating conditions along the drift will be highly heterogeneous. If the waste packages are spaced nearly end to end (line-load waste-package spacing), the line of waste packages will act as a homogeneous line-source of heat.

Spent-nuclear-fuel age, expressed in years, quantifies the length of time the spent nuclear fuel assembly has been removed from the nuclear reactor core. Because the heat generation rate decays with time, younger spent nuclear fuel has a higher thermal power output than does older spent nuclear fuel. Spent-nuclear-fuel age, along with lineal mass loading, is a key factor in determining short-term thermohydrologic effects, such as peak temperatures, on waste packages and on the drift wall. Aboveground storage of spent nuclear fuel before emplacement in the potential repository will lower the peak temperatures.

Fuel blending (the mixing and matching of waste packages of different thermal power) can be used to reduce the heat-source heterogeneity along the drift. However, because of the difference in thermal output between commercial spent nuclear fuel and noncommercial waste packages (e.g., defense high-level waste), there is a limit to the effectiveness of fuel blending in reducing heat-source heterogeneity. An effective approach to minimizing the impact of any remaining heat-source heterogeneity (after fuel blending has been applied) is to utilize line-load waste-package spacing, which places waste packages nearly end to end (Buscheck et al. 1999, pp. 615 to 622).

Duration and heat-removal efficiency of drift ventilation strongly affect thermohydrologic conditions during the preclosure period. They can also continue to affect thermohydrologic conditions for hundreds of years after ventilation has ceased. Drifts can be ventilated up to the

end of the preclosure period. The percentage of heat removed from the potential repository system (heat-removal efficiency) increases with ventilation flow rate. The long-term effects of drift ventilation on thermohydrologic conditions increase with ventilation duration and heat-removal efficiency. As a thermal-management measure, drift ventilation is used to limit peak temperatures on waste packages and drift-wall surfaces, and to limit (or prevent) boiling conditions in the host rock.

Engineered barrier system design can have a dominant effect on thermohydrologic conditions in the drifts for tens of thousands of years. A summary of the engineered barrier system design and related performance issues is given in the *Engineered Barrier System Degradation, Flow, and Transport Process Model Report* (CRWMS M&O 2000c, Section 1.5). For thermohydrologic behavior, the primary engineered barrier system design components are the invert, backfill (if used), and drip shield. The engineered barrier system design does not influence overall heating conditions in the near-field host rock; however, it can influence the vertical symmetry of heating conditions around the drift perimeter.

The most important consideration is backfill emplacement. In an open drift, thermal radiation results in a symmetric heat-flux distribution around the drift-wall perimeter, resulting in a uniform temperature distribution around the drift. Because thermal radiation is a very efficient heat-transfer mechanism, it also results in a very small temperature gradient between the waste packages and the drift wall. The presence of backfill causes thermal conduction to replace thermal radiation as the dominant heat-transfer mechanism in the drift, resulting in a much greater temperature gradient between the waste package and the drift wall, which translates to a hotter waste package with lower *RH*. The thermal conductivity and thickness of the backfill, along with the local heat-generation rate, determine the magnitude of the temperature gradient. The hydrologic parameters of the backfill determine how much water from the host rock might be wicked into the drift due to capillary forces. (Backfill also serves the very important non-thermal function of protecting the waste packages from rockfall.) Different backfill designs are possible, including single-layer backfill and multiple layers of backfill that function as a capillary barrier.

Another important component in the engineered barrier system design is a drip shield that drapes over the top and around the sides of a waste package. The drip shield is a crucial barrier that prevents (or minimizes the tendency for) seepage flux reaching the waste package. The drip shield also acts as a thermal radiation shield, thereby enhancing the temperature difference between the waste package and the drift wall, which enhances *RH* reduction on the waste package.

The most significant aspects of the thermal design on thermohydrologic response of the potential Yucca Mountain repository to thermal loading from radioactive waste can be described by considering the following design attributes:

- **Boiling or Sub-Boiling Conditions in the Host Rock**—A sub-boiling thermal design will not result in rock dryout, which shortens the duration of significant *RH* reduction on waste packages for designs without engineered backfill; for designs with backfill, the duration of significant *RH* reduction can still be long. The potential benefit of a sub-

boiling design is that uncertainty may be reduced due to the decreased need to understand and model the potential effects of coupled thermal-hydrologic-chemical and thermal-hydrologic-mechanical behavior in the host rock.

- **Coalescence of Boiling Zones around Individual Drifts**—Rock dryout generally increases with increased areal mass loading. If the thermal design mass loading results in coalescence of the boiling zones (between adjoining drifts), a significant condensate zone can develop above the potential repository. When the repository begins to cool and rewetting begins, this condensate will increase the percolation flux above the repository horizon. If the thermal design mass loading does not result in coalescence of boiling zones, condensate will be able to drain continuously between the drifts, obviating the possibility of significant condensate buildup above the repository.
- **Heterogeneity of Heating along Drifts**—Line-load waste-package-spacing design results in more intense, localized, and persistent near-field rock dryout around the drifts and more efficient condensate shedding between the drifts. Point-load waste-package-spacing design results in less intense near-field rock dryout and more heterogeneous thermohydrologic conditions along the drifts. This heterogeneity makes it more likely for seepage and condensate within the drift to be focused onto cooler waste packages.
- **Use of Backfill and Its Material Properties**—The two most important thermal-design characteristics for backfill are its thermal conductivity and capillarity. The emplacement of backfill will increase the change in temperature ( $\Delta T$ ) between the waste package and the drift wall compared to the case without backfill. The magnitude will depend on the thermal conductivity. The larger  $\Delta T$  results in greater  $RH$  reduction on the waste package relative to the drift wall. A low-capillarity backfill reduces the tendency for capillary wicking of water into the drift and facilitates rapid drainage of water that does seep into the drift. Minimizing the presence of water in the drift allows for the maximum benefit of  $\Delta T$  on  $RH$  reduction on waste packages. A high-capillarity backfill facilitates capillary wicking into the drift, obviating the  $RH$ -reducing benefits of  $\Delta T$ . Once wicking has caused the backfill to reach a steady-state liquid-phase saturation state,  $RH$  reduction is no longer significant; therefore, a high-capillarity backfill will always result in temperature increase (relative to the no backfill case), but eventually will not provide  $RH$  reduction on waste packages.
- **Use of Drip Shield**—The use of a properly engineered drip shield will prevent (or minimize the tendency for) seepage flux reaching the waste package. The drip shield also acts as a thermal radiation shield, thereby enhancing the temperature difference between the waste package and the drift wall, which enhances  $RH$  reduction on the waste package. A concern is whether buoyant vapor flow could be trapped and condense under the drip shield; this concern is addressed by minimizing the gap between the drip shield and waste package and by not insulating the waste package from the drip shield (as would occur if backfill occupied the space between the waste package and drip shield).

### 11.2.3.3 Uncertainties of the Ambient and Thermally Perturbed System

In addition to the engineering design variables, there are uncertainties in the natural system, primarily in rock properties values in the potential repository horizon rock and infiltration flux. The distribution of infiltration flux (and percolation flux) plays a key role in determining the spatial extent and duration of rock dryout and the likelihood (and distribution) of water seeping into the emplacement drifts. Key rock properties of concern are those hydrologic properties governing capillarity (i.e., matrix imbibition and capillary wicking in fractures) and thermal conductivity. If the fractures have a higher capillarity than that of backfill (if it is used), water will not be wicked into the backfill. If the converse is true, then water can be wicked from the fractures into the backfill. Because of the pivotal role that fracture capillarity plays in determining whether water is wicked into the backfill, it is crucial to test the validity of the conceptual models (e.g., the active fracture model) and numerical models (including the property sets used in those models) of how water percolates through fractures under ambient and thermally perturbed conditions. The issue of model validation is addressed in the *Engineered Barrier System Degradation, Flow, and Transport Process Model Report* (CRWMS M&O 2000c, Section 3.6).

In addition to parameter uncertainty, there are modeling uncertainties that involve the ability to understand and predict unsaturated flow processes in fractured rock under ambient conditions and under thermally driven conditions that result in coupled thermal-hydrologic-chemical and thermal-hydrologic-mechanical behavior.

### 11.2.3.4 Variability of Thermohydrologic Response across the Repository

The thermohydrologic environment of the near-field host rock and the engineered barrier system that will arise from emplacing heat-producing radioactive waste is influenced by key factors relating to the natural system and potential repository design. These factors include:

- **Infiltration Flux**—Infiltration flux varies significantly over the potential repository footprint. The fluxes are greatest at the crest of Yucca Mountain and lowest along the flanks and in the alluvial-filled washes.
- **Hydrologic Properties in the Potential Repository Horizon Host-Rock Unit**—The most important properties are those governing capillarity, especially in the host rock unit. The capillary properties of the matrix govern how quickly matrix imbibition rewets the dryout zone. The capillary properties of the fractures affect the tendency for water to seep or wick (if backfill is used) into the drift.
- **Edge-Cooling Effect**—Cooling increases with proximity to the edge of the potential repository, significantly reducing the duration of rock dryout. (It should be noted that it is possible to take advantage of this phenomenon by placing the hotter waste packages at the edges.)
- **Overburden Thickness**—The depth of the potential repository horizon below the ground surface translates to thickness of insulating rock between the repository and the ground

surface, a constant-temperature boundary, which acts like a heat sink. If the repository is close to horizontal, the repository depth contours correspond to the surface topography, resulting in uneven insulation.

- **Thermal Properties in the Potential Repository Horizon Host-Rock Unit**—The repository intersects several different subunits of the Topopah Spring Tuff; these subunits have different enough thermal conductivity values to be significant.

## 11.2.4 Thermohydrologic System Response to Thermal Loading

### 11.2.4.1 Modeling Approach

A multiscale modeling approach is used to assess potential repository performance for various repository designs. The need for a multiscale modeling approach stems from the fact that the performance measures depend on thermohydrologic behavior within a few meters of the emplacement drifts and also on thermal and thermohydrologic behavior on a repository (or mountain) scale. A single numerical model (e.g., embedding a three-dimensional drift-scale model with a relatively fine mesh into a three-dimensional mountain-scale model with a coarse mesh) would require an unfeasible number (millions) of grid blocks. The multiscale thermohydrologic model has been developed for estimating the results that would be obtained if such a single model were possible (Buscheck et al. 1999, p. 615). In addition to coupling the drift scale and mountain scale, the multiscale thermohydrologic model also allows for consideration of the effects of different waste package types (e.g., different commercial spent nuclear fuel waste packages, codisposal of defense high-level waste) on the various performance measures. A summary of the assumptions in the multi-scale modeling approach is given in the *Engineered Barrier System Degradation, Flow, and Transport Process Model Report* (CRWMS M&O 2000c, Section 3.1.4).

The multiscale thermohydrologic model consists of four major submodels (Figure 11.2-1) and includes multiple scales (mountain and drift), multiple dimensions (one-dimensional, two-dimensional, and three-dimensional), and varying assumptions regarding the coupling of heat transfer to fluid flow (conduction only and fully coupled thermohydrologic). The results of the four families of submodels are integrated using the multiscale thermohydrologic abstraction code. The four families of submodels are:

- Line-averaged-heat-source, drift-scale, thermohydrologic submodel
- Smearred-heat-source, mountain-scale, thermal-conduction submodel
- Smearred-heat-source, drift-scale, thermal-conduction submodel
- Discrete-heat-source, drift-scale, thermal-conduction submodel

It is useful to think of the line-averaged-heat source, drift-scale, thermohydrologic submodel, which is two-dimensional, as the core submodel. The line-averaged-heat source, drift-scale, thermohydrologic submodels are run for many locations spaced evenly throughout the potential repository area for several areal mass loading values (nominal value and lower) to represent the influence of edge-cooling effects. For the *Multiscale Thermohydrologic Model* analysis model report (CRWMS M&O 2000a, Section 6.1), the line-averaged-heat source, drift-scale,

thermohydrologic submodels are run at 31 repository locations and for 5 areal mass loadings (Figure 11.2-2). The line-averaged-heat source, drift-scale, thermohydrologic submodel includes the hydrologic processes and parameters (e.g., surface infiltration rates, hydrologic properties) used to describe a location, given specific coordinates within the potential repository.

The remaining three submodels, which are thermal-conduction only, are required to account for the influence of three-dimensional mountain-scale heat flow and three-dimensional drift-scale heat flow on drift-scale thermohydrologic behavior. The coupling of three-dimensional mountain-scale heat flow to two-dimensional drift-scale thermohydrologic behavior is accomplished with the smeared-heat-source, mountain-scale, thermal-conduction and the smeared-heat-source, drift-scale, thermal-conduction submodels. The smeared-heat-source, mountain-scale, thermal-conduction submodel is three-dimensional and includes the influence of thermal property variation in the mountain, lateral heat loss at the potential repository edges, and overburden-thickness variation with location, assuming a uniform, planar (i.e., smeared) heat source throughout the potential repository area.

The smeared-heat-source, mountain-scale, thermal-conduction submodel accounts for the actual shape and location of the potential repository in Yucca Mountain (Figure 11.2-1). The smeared-heat-source, drift-scale, thermal-conduction submodel is a one-dimensional (vertical) submodel, run at the same 31 locations and for the same areal mass loadings as the line-averaged-heat source, drift-scale, thermohydrologic submodels. To obtain the line-averaged drift-wall temperatures throughout the repository (which is equivalent to temperatures produced by waste packages with average heat output), the relationship between the drift-wall temperature in the line-averaged-heat source, drift-scale, thermohydrologic submodel and the smeared repository-plane temperature in the smeared-heat-source, drift-scale, thermal-conduction submodel is used to modify the temperatures in the smeared-heat-source, mountain-scale, thermal-conduction submodel; the resulting drift-wall temperatures include the effects of the most important thermohydrologic processes at the drift scale and the geometry effects of the mountain scale. At this stage of the multiscale thermohydrologic abstraction code methodology, the influence of three-dimensional drift-scale heat flow has not yet been added. The result of this stage of the methodology is an intermediate model, called the line-averaged-heat-source, mountain-scale, thermohydrologic multiscale thermohydrologic abstraction code model (Figure 11.2-1). In the line-averaged-heat-source, mountain-scale, thermohydrologic multiscale thermohydrologic abstraction code model, the smeared-heat-source, mountain-scale, thermal-conduction submodel temperatures have been corrected for both the influence of thermohydrologic processes on temperature and the influence of two-dimensional drift-scale dimensionality (orthogonal to the axis of the drift).

The discrete-heat-source, drift-scale, thermal-conduction submodel is a three-dimensional drift-scale submodel, which includes individual waste packages (with distinctive heat-generation histories) and accounts for thermal radiation in addition to thermal conduction between the waste packages and drift surfaces. The drift-wall temperatures for an average waste package, calculated with the combined use of the line-averaged-heat source, drift-scale, thermohydrologic, smeared-heat-source, mountain-scale, thermal-conduction, and smeared-heat-source, drift-scale, thermal-conduction submodels, are further modified to account for waste-package-specific deviations using the discrete-heat-source, drift-scale, thermal-conduction submodel. This is

accomplished by relationships between local temperatures at various point locations along the drift (e.g., on the drift wall, drip shield surface, and waste package surface) and the corresponding line-averaged temperature in the discrete-heat-source, drift-scale, thermal-conduction submodel.

The results of the multiscale thermohydrologic model submodels are integrated with the use of the multiscale thermohydrologic abstraction code. This (final) stage of the methodology results in the discrete-heat-source, mountain-scale, thermohydrologic multiscale thermohydrologic abstraction code model (Figure 11.2-1). For the multiscale thermohydrologic model calculations supporting the total system performance assessment Site Recommendation, the integration is done for 623 repository subdomains (Figure 11.2-2b). Details are described in CRWMS M&O (2000a, Sections 6.1 to 6.6).

#### 11.2.4.2 Thermal Design, Thermohydrologic Behavior, and System Performance

Seven repository designs, which are called enhanced design alternatives, were evaluated as part of the License Application Design Selection study (CRWMS M&O 1999c). A comparison of key performance variables for these designs illustrates many of the concepts described in previous sections. The seven Enhanced Design Alternatives fall into three groups with respect to the spatial extent of boiling conditions.

- **Sub-Boiling Repository**—Enhanced Design Alternative I maintains sub-boiling temperatures throughout the repository for all time; boiling conditions are prevented to preclude the occurrence of coupled thermohydrologic-chemical processes (and resulting rock alteration) that arise from boiling conditions.
- **Coalesced Boiling Zones**—Enhanced Design Alternatives III, IV, and V have high enough areal mass loadings to result in coalesced boiling zones. The long duration of boiling conditions keeps water away from the emplacement drifts for an extended period of time.
- **Uncoalesced Boiling Zones**—Enhanced Design Alternatives IIa, IIb, and IIc have a high enough areal mass loading to cause boiling in the potential repository host rock, but not enough areal mass loading to cause the boiling zones to coalesce; the boiling zones are intentionally not allowed to coalesce to promote condensate (and percolation-flux) drainage between drifts and to limit the spatial extent of coupled thermohydrologic-chemical processes (and resulting rock alteration) that arise from boiling conditions.

Because the presence or absence of coalesced boiling zones is so important to evaluating potential repository performance to thermal loading, it is useful to note that without ventilation or surface aging of spent nuclear fuel, areal mass loadings greater than 70 MTU/a. generally result in coalesced boiling zones. The areal mass loading used in the Viability Assessment design, 85 MTU/a., resulted in as much as 5 k.y. of boiling conditions at the repository center (Hardin 1998a, Section 3.7.7.6). The areal mass loading used in the Site Recommendation design (Wilkins and Heath 1999, Enclosure 2, p. 1), 60 MTU/a., results in uncoalesced cylindrical boiling zones (CRWMS M&O 2000a, Section 6.11.1.4). This thermohydrologic response of the

system to the Site Recommendation design (Wilkins and Heath 1999, Enclosure 2) is described in more detail in the next section.

#### 11.2.4.3 Site Recommendation Design

The Site Recommendation design (Wilkins and Heath 1999, Enclosure 2) is for a 60-MTU/a repository with 5.5-m-diameter drifts spaced 81 m apart. The design assumes no aboveground aging of the waste and the continuous ventilation of the emplacement drifts during the entire 50-yr. preclosure period. The requirement for drift ventilation is to remove 70 percent of the waste heat from the entire emplaced waste inventory. It should be noted that this requirement is greater than the 50 percent heat-removal requirement of Enhanced Design Alternative II; this was done to further reduce peak temperatures in the near field and engineered barrier system. At the end of the preclosure period, drip shields are placed over the waste packages, followed by the emplacement of fine-grained (high-capillarity) sand backfill over the top and around the sides of the drip shield.

The thermal management strategy for the Site Recommendation design (as well as for the Enhanced Design Alternative IIA design) is to prevent coalescence of the boiling zones and promote the continuous drainage of condensate and percolation flux between drifts. The Site Recommendation design (Wilkins and Heath 1999, Enclosure 2) is similar to the Enhanced Design Alternative IIA design. The major difference from a thermal system performance point of view is the material properties of the backfill. The Site Recommendation design (Wilkins and Heath 1999, Enclosure 2) utilized a fine-grained sand backfill with relatively high capillarity, whereas the Enhanced Design Alternative IIA design utilized coarse-grained well-sorted sand with relatively low capillarity. Although most of the design parameters assumed for the Enhanced Design Alternative IIA analysis also hold for the Site Recommendation design analysis, it is important to note that some parameters did change. For example, the initial line-averaged heat-generation rate along the drifts increased substantially from the Enhanced Design Alternative IIA analysis to the Site Recommendation design analysis. This increase resulted from different assumptions about the waste-package inventory that would be emplaced.

Modeling results from simulations of the Site Recommendation design are shown on Figures 11.2-3 to 11.2-5. Several infiltration rates were considered for the Site Recommendation design analysis, representing low, mean, and high infiltration flux cases. Also, 623 repository subdomains were considered for this analysis.

During the preclosure period, temperatures at the drift wall remain below the boiling point for the mean and high infiltration flux cases, while temperatures climb above boiling for the low-flux case. During the preclosure period, peak waste package temperatures of 96° to 100°C occur at 10 to 25 yr. Edge-cooling effects do not strongly affect preclosure temperatures. Figure 11.2-3 shows the peak temperatures on the waste packages and the drift wall (again, averaged around the drift wall perimeter) for the three infiltration rates considered. It should be noted that the peak temperatures all occur shortly after the start of the postclosure period. During the postclosure period, the highest peak waste package temperature is 315°C (for the low-flux case), and this temperature occurs at 60 yr. The difference in peak waste package temperature between the hottest and coldest waste package is about 40°C. Due to the asymmetric distribution of

insulating backfill around the waste package, which focuses much of the heat generation from the waste package to the floor of the drift, peak temperatures on the lower drift wall are nearly 70°C hotter than at the upper drift wall. By 100 yr., the influence of edge cooling is considerable, with waste package temperatures varying by 120°C from the repository edge to the center of the repository.

Figure 11.2-4 shows the time and temperature at which waste packages first see *RH* levels of 85 percent (following the temperature peak). As was discussed earlier, *RH* on the waste package depends on three factors: *RH* at the drift wall, the temperature difference between the drip shield and the drift wall (which reduces *RH* at the drip shield relative to the drift wall), and the temperature difference between the waste package and the drip shield (which reduces *RH* at the waste package relative to the drip shield). The *RH* reduction at the drift wall decreases strongly with proximity to the edge of the repository due to reduced rock dryout. Significant reduction in *RH* at the drift wall persists for about 100 to 1,000 yr. for the mean and high infiltration-flux cases and for about 200 to 2,000 yr. for the low infiltration-flux case. The *RH* reduction on the drip shields and waste packages depends on the duration of rock dryout (and *RH* reduction in the host rock) as well as the temperature difference between the drip shield and drift wall and the temperature difference between the waste package and drip shield. Differences in the duration of *RH* reduction between the low infiltration-flux case and the other two cases arise as a result of the substantially increased duration of rock dryout in the low flux case. Eventually, *RH* on the drip shield becomes nearly 100 percent. For the mean and high infiltration-flux cases, it takes about 1,000 to 2,000 yr. for 100 percent *RH* to occur, and for the low infiltration-flux case, it takes about 3,000 to 6,000 yr. to occur. The *RH* reduction on the waste package persists long after *RH* reduction on the drip shield has ceased.

Figure 11.2-5a shows the time required for the drift wall to return to the nominal boiling point after peak temperatures have occurred. Figure 11.2-5b shows the maximum lateral extent of the boiling zone in the host rock at the plane of the waste packages. It should be noted that the maximum lateral extent of boiling is considerably greater for the low infiltration-flux case than for the mean or high flux cases. For the median waste package location, the maximum lateral extent of boiling is between 8.4 and 10.5 m (28 and 34 ft), depending on infiltration flux; this translates to 21 to 26 percent of the rock pillar separating drifts that can be driven to the boiling point. For the hottest (and driest) waste package location, the maximum percentage of the rock pillar separating drifts that can be driven to the boiling point lies between 24 and 44.4 percent.

The hydrologic properties of the backfill material play a critical role in system performance. Figure 11.2-6 compares *RH* reduction between the Site Recommendation design with high-capillarity backfill and the Enhanced Design Alternative IIa design with low-capillarity backfill (Buscheck et al. 1999). In the Site Recommendation design, as the temperature at the drift wall declines below the boiling point, water is able to wick by capillary flow from the fractures in the host rock into the backfill. This wicking by the backfill results in the capturing of flow from host rock fractures over a region that is wider than the drift footprint. Capillary wicking in the backfill, in conjunction with the duration of boiling temperatures at the drift wall, influences the onset of seepage into the drift. As Figure 11.2-6 shows, the low-capillarity backfill in the Enhanced Design Alternative IIa design results in significantly greater *RH* reduction than the

high-capillarity backfill in the Site Recommendation design. Other possible backfill designs, such as a two-layer capillary barrier, may result in even greater relative humidity reduction.

## 11.3 GEOMECHANICS

### 11.3.1 Introduction and Background

Understanding deformation, heat transfer, and fluid flow in a fractured rock mass is necessary for assessing the performance of a potential high-level radioactive waste repository. The potential repository horizon at Yucca Mountain contains a large number of fractures. Fluid flow in any fractured rock mass depends strongly on the local stress field, particularly as these stresses affect fracture apertures. The stress field in the repository near-field environment, i.e., the rock surrounding the waste emplacement drifts, will be altered by excavation effects and thermal stresses from the heat generated by radioactive decay. Numerical modeling of thermal-mechanical-hydrological processes is required because of the very long time that the repository must isolate wastes from the environment.

During the past few years, two major field tests, the Large Block Test and the Single Heater Test, have been conducted nearby and within the Exploratory Studies Facility (ESF). A third, larger and longer test, the Drift Scale Test, is currently under way. Data from these field tests are currently being interpreted and have already provided much insight into coupled thermal-mechanical-hydrological processes in fractured tuff under conditions that approximate those of an actual repository. Additionally, a large number of laboratory tests have been conducted on samples ranging from a few millimeters to 0.5 m in scale. The laboratory tests have provided essential data on rock properties and insight into the coupled thermal-mechanical-hydrological behavior of the rock under well-controlled conditions.

This section discusses the efforts to understand and predict coupled thermal-mechanical-hydrological behavior in the near-field environment of a potential high-level radioactive waste repository at Yucca Mountain. It describes some of the thermomechanical properties and coupled thermal-mechanical-hydrological behavior of the Topopah Spring Tuff, which forms the potential repository horizon at Yucca Mountain. Both laboratory and field results are presented, along with analysis and interpretation.

### 11.3.2 Ambient Site Geomechanical Characteristics

The rock in the potential repository horizon at Yucca Mountain is a densely welded ash-flow tuff located in the Topopah Spring member of the Paintbrush Group. A detailed geologic description of the rock and associated geologic units is given in Section 4.5.4. The potential repository horizon is located at a depth of about 300 m (984 ft) in TSw2 unit of the Topopah Spring Tuff.

**In Situ Stress**—Magnitudes and orientations for the principal in situ stresses at the potential repository horizon have been determined from measurements in drill holes USW G-1, USW G-2, and USW G-3 (Stock et al. 1985, p. 8697). The maximum principal stress at the potential repository horizon is vertical and has been estimated at 7.0 MPa, on average, due to the overburden. Horizontal stresses are low. The ratios of minimum and maximum horizontal stresses to vertical stress and their bearings are given in Table 11.3-1. The maximum horizontal stress is oriented in a northeasterly direction. In situ stresses at Yucca Mountain are also discussed in Section 4.7.6.

A stress profile for the rock near the ESF has been estimated using a two-dimensional finite-element analysis similar to that presented in Bauer et al. (1985, p. 1113). The analysis assumes plane strain conditions and linear elastic material response, with gravitational loading as the only loading mechanism. The stress profile can be found in Wilder (1996, Section 4.0).

Recent hydraulic fracturing tests have been conducted in the TSw2 unit at a depth of approximately 250 m (820 ft) as part of the Drift Scale Test block characterization (Lee and Haimson 1999, p. 749). The tests yielded principal horizontal stresses of  $2.9 \pm 0.4$  MPa oriented  $N15^\circ E \pm 14^\circ$  (maximum horizontal stress) and  $1.7 \pm 0.1$  MPa oriented  $N75^\circ W \pm 14^\circ$  (minimum horizontal stress). The vertical stress at this level was calculated to be 4.7 MPa.

**Rock-Mass Strength**—Rock-mass strength has been estimated based on a method developed by Hardy and Bauer (1991). The method uses laboratory compressive strength data from intact rock specimens and two rock-mass indices that incorporate the effects of joints: the rock-mass quality index (Barton et al. 1974) and the rock-mass rating index (Bieniawski 1989). The rock-mass indices include measures of joint spacing, surface roughness, orientation, and the groundwater environment. The methodology is described in detail in Section 4.7.5 and in Brechtel et al. (1995, Section 8). Strength estimates were based on empirical criteria developed by Yudhbir et al. (1983) and Hoek and Brown (1988). The average of the two strength estimates was used to develop a power law relationship of rock-mass strength as a function of confining pressure. The power law parameters were estimated using a least squares approach, yielding, for unit TSw2:

$$(\sigma_1)_{\text{ultimate}} = 25.4 + 23.687 (\sigma_3)^{0.571} \quad (\text{Eq. 11.3-1})$$

where  $(\sigma_1)_{\text{ultimate}}$  is the rock-mass strength and  $0 < \sigma_3 < 25$  MPa is the confining stress (CRWMS M&O 1997a).

### 11.3.3 Thermal Properties

**Thermal Conductivity**—The thermal properties of tuff samples from Yucca Mountain have been the subject of several laboratory studies, which are reviewed in Section 4.7.4.2. Thermal conductivity was found to depend strongly on water saturation and weakly on temperature. This finding was expected because the presence of water in fine cracks and pores both improves the thermal contact between mineral grains and displaces air, which has a much lower thermal conductivity than water. For thermomechanical unit TSw2, which encompasses the potential repository horizon, measurements at low temperatures ( $25^\circ$  to  $70^\circ\text{C}$ ) gave average thermal conductivities of  $1.50 \pm 0.44$  W/mK for 48 oven-dried samples,  $1.66 \pm 0.10$  W/mK for 24 air-dried samples, and  $2.29 \pm 0.42$  W/mK for 51 saturated samples (Brodsky et al. 1997, p. 32). Measurements on 125 dry samples at temperatures between  $110^\circ$  and  $290^\circ\text{C}$  produced an average thermal conductivity of  $1.59 \pm 0.10$  W/mK, within experimental error of the low temperature value (Brodsky et al. 1997, p. 32).

A comparison of observed and predicted temperatures for the Single Heater Test suggests that the laboratory thermal conductivities form effective upper and lower bounds for in situ thermal conductivities. The laboratory thermal conductivity values,  $C_{\text{dry}} = 1.67$  W/mK and  $C_{\text{wet}} = 2.0$  W/mK, were used in numerical simulations of the Single Heater Test to provide

interpolated estimates of rock-mass thermal conductivity as a function of saturation. The resulting expression

$$C(S_i) = C_{\text{dry}} + (C_{\text{wet}} - C_{\text{dry}})(S_i)^{0.5} \quad (\text{Eq. 11.3-2})$$

where  $C$  is thermal conductivity and  $S_i$  is initial saturation, produced very good agreement between predicted and observed temperatures in the Single Heater Test (CRWMS M&O 1999a, p. 8-48).

**Thermal Expansion**—Laboratory measurements of linear thermal expansion have been made on many tuff samples from Yucca Mountain. These measurements are discussed at length in Section 4.7.4.2.2 and the data are archived in the Yucca Mountain Site Characterization Project Reference Information Base. Thermal expansion coefficients for TSw2 tuff show a moderate temperature dependence below 100°C and a strong temperature dependence above 100°C. Hysteresis exists between the heating and cooling portions of the thermal cycle, and permanent elongations can sometimes be observed (Brodsky et al. 1997, p. 73). The increase in thermal expansivity with temperature is partly attributed to microcracks, induced largely along grain boundaries by differences in constituent mineral thermal expansion properties, and near 200°C, to phase changes in tridymite and cristobalite. Phase changes in some minerals can cause step changes in rock volume. At temperatures of about 200°C, cristobalite exhibits a volume increase of a few percent when it makes the transition from the alpha to the beta phase. The phase change is reversible, so that a volume decrease should also occur upon cooling below 200°C. In contrast to temperature, confining pressure has little effect on the coefficient of thermal expansion (Martin et al. 1996). Table 11.3-2 gives the linear coefficient of thermal expansion for TSw2 tuff over a range of temperatures at atmospheric pressure.

Field measurements of thermal expansion indicate that the laboratory values discussed above may be too high to describe rock-mass expansion in situ. Results of the Single Heater Test indicate that the coefficient of thermal expansion for the rock mass heated in this test is as much as 50 percent lower than that measured for laboratory samples (CRWMS M&O 1999a, pp. 12-1, 9-11). The reduction in the coefficient of thermal expansion at the field scale is likely due to the closure of fractures, which would thereby accommodate a portion of the thermal expansion. Lower thermal expansion values will reduce stress estimates for the rock surrounding the emplacement drifts.

#### 11.3.4 Mechanical Properties

**Deformation Modulus and Rock Strength**—Many laboratory measurements have been made to determine the mechanical properties of intact samples from the potential repository horizon. These data indicate that the intact rock is strong, with a uniaxial compressive strength of  $168 \pm 65$  MPa and a Young's modulus of approximately 33 GPa (CRWMS M&O 1997a). Uncracked samples have stress-strain curves that show nearly linearly elastic behavior until failure. Samples with cracks exhibit nonlinear stress-strain behavior, as expected when stress is above 50 percent of the failure stress. Stress-strain curves for 50.8-mm (2 in.) diameter saturated samples tested under drained conditions are shown on Figure 11.3-1. Most of the tests for compressive strength have been conducted on samples that were saturated with water and tested under drained conditions. This represents a minimum value for the rock matrix material, as

rocks are generally weaker when saturated with water. Rock compressive strength typically decreases with increase of temperature. Price et al. (1987) report that, for samples from the potential repository horizon, Young's modulus and the mean ultimate strength both decrease by an average of 16 percent as temperature is raised from 22° to 150°C. This result is based on tests conducted at both 0 and 5 MPa confining pressures.

Larger rock specimens almost invariably contain more inhomogeneities than the small cylinders tested in most laboratory work; hence, compressive strengths tend to be lower when larger specimens are tested. This scale effect has been well documented for intact Topopah Spring Tuff specimens by Price (1986), who found both uniaxial compressive strength and axial strain at failure to be inversely related to specimen diameter (Figure 11.3-2). Specimen diameters exceeding 250 mm (10 in.) are apparently required to avoid such size effects, even for intact samples. Young's modulus and Poisson's ratio, on the other hand, were found by Price (1986) to be largely independent of specimen diameter. Uniaxial compressive tests performed on a 0.5-m (1.6-ft) scale block of Topopah Spring Tuff by Blair and Berge (1997) presented an opportunity to measure strains associated with individual heterogeneities and relatively intact matrix material simultaneously. Such intermediate-scale blocks still exclude the large fractures present in the field, but they can provide mechanical data on fractured rock obtained under well-controlled laboratory conditions. Blair and Berge (1997, p. 28) obtained an overall Young's modulus of about 3 GPa at axial stresses below 4 MPa, which increased to 6 GPa above 4 MPa. Young's moduli measured across individual fractures were generally below 1 GPa. In portions of the block lacking visible vugs or fractures, Young's modulus varied between 7 and 31 GPa.

Laboratory studies performed on 0.5-m (1.6-ft) scale blocks of Topopah Spring Tuff also show a significant level of mechanical anisotropy correlated with the rock's ash-flow fabric. Similar blocks were loaded perpendicular to the rock fabric by Blair and Berge (1997, p. 24) and parallel to the rock fabric by Costantino et al. (1998, p. 2-21). Costantino et al. (1998, p. 2-17) found a Young's modulus of 40 GPa for axial stresses of 4 to 8 MPa (Table 11.3-3), about twice that found by Blair and Berge (1997, p. 28) for the perpendicular loading for intact portions of their block. The anisotropy in Young's modulus is a minimum of 25 percent and can be much greater when vuggy zones occur. This amount of anisotropy is significant for simulations of thermal-mechanical behavior of a potential repository.

Field tests of rock deformation modulus have shown a wide range of values. A plate loading test conducted in association with the Drift Scale Test indicated a modulus of 30 GPa on one side of the alcove and 11 GPa on the other side. Goodman jack tests in the same vicinity produced much lower moduli, in the range of 3 to 6 GPa, whereas estimates of modulus based on rock-mass quality were in the range of 15 to 34 GPa (CRWMS M&O 1998d, pp. 6-18, 6-27).

### 11.3.5 Time-Dependent Properties

**Creep Behavior**—Martin et al. (1995) investigated creep in laboratory samples of Topopah Spring Tuff at ambient and elevated temperatures. The observed creep deformation was consistent with a time-dependent crack growth mechanism, particularly at stresses above 90 percent of the rock's uniaxial compressive strength. The stress necessary to produce failure appeared to decrease with increasing temperature, but the data were not sufficient to quantify that effect. Temperature did cause a reduction in strength (Martin et al. 1995, pp. 18 to 20).

Blair and Berge (1997, p. 26) found that imposing low levels of compressive stress for periods of a few days on 0.5-m (1.6-ft) scale blocks of Topopah Spring Tuff caused time-dependent, inelastic crack closure. Creep behavior is also discussed in Section 4.7.4.3.7.

**Crack Growth**—Subcritical crack growth is of concern because the slow formation, growth, and coalescence of microcracks over long time periods would contribute to excavation damage and thereby alter rock physical, hydrological, and geochemical properties in the near-field environment. If sufficient crack growth occurs, chips or slabs may passively load the waste containers. Little work has been done in this area on tuff. However, Kemeny and Cook (1990) used a probabilistic approach that included time-dependent crack growth to examine borehole emplacement. They estimated that, over the lifetime of the repository, spalling would be likely to occur in a significant portion of any vertical emplacement boreholes that were used.

### 11.3.6 Thermomechanical Effects on Fracture Flow

The behavior of fluid flow through fractures at elevated stress and temperature conditions is a subject of ongoing research. Fracture flow is proportional to the cube of the fracture aperture (Raven and Gale 1985, p. 257). As normal stresses increase, apertures close and fluid flow is reduced. Thus, as the general level of compressive stress in the potential repository rises with heating, the apertures of many fractures may be reduced, lowering permeability. Thermomechanical effects are more complicated, though, in that heating may also increase shear stresses on favorably oriented fractures and cause shear displacements. Olsson and Brown (1994, pp. 5 to 6) and others have shown that shear displacements along fractures tend to increase fracture apertures and thus increase permeability.

Field measurements from heater tests at G-Tunnel, located in the northeast portion of the Nevada Test Site, indicated that rock-mass permeability increased during heating and did not return to initial levels upon cooldown, indicating that a mechanism other than normal closure of fractures dominated fracture flow behavior (Lee and Ueng 1991, p. 6). More recently, Barton et al. (1997) have presented evidence, based on the Mohr–Coulomb frictional slip criterion, that hydraulically conductive fractures in the Dixie Valley geothermal field are critically stressed, potentially active normal faults. The implication of their work is that slip on critically stressed fractures can increase permeability, particularly if asperities override each other and widen fracture apertures. At the same time, slip along normal faults may eventually decrease permeability, particularly if fault gouge is generated, as is evidenced by many faults that serve as barriers to groundwater flow. The impact on permeability is partly a function of the magnitude of the slip, but may also depend on other factors. However, the work of Barton et al. (1997) provides a means to predict which fractures are likely to become more hydraulically conductive. This result is significant for Yucca Mountain if either excavation-induced stress redistribution or thermal loading effects induce shear slippage along favorably oriented fractures.

Tests at the 0.5-m (1.6-ft) scale are instructive for evaluating the behavior of fractures and joints, because specimens of this size can include a number of natural heterogeneities. Fracture flow and uniaxial compression tests were recently conducted on a heated 0.3 by 0.3 by 0.6 m (1 by 1 by 2 ft) block of Topopah Spring Tuff containing an artificial, horizontal fracture (Costantino et al. 1998, p. 2-21). Fracture surface profiles, performed before the flow tests, indicated a large number of channels aligned with the ash-flow fabric. The channels were typically a few

millimeters wide and a few tenths of a millimeter deep and were generally uncorrelated between surfaces. Flow tests, involving more than 50 L of water, showed low imbibition of water through the fracture surfaces and little storage of water in connected porosity. These results are consistent with a similar finding from the Single Heater Test, which indicates that fracture flow dominates fluid movement upon initial heating, with minimal communication between fractures and the matrix (CRWMS M&O 1999a). The tests also showed fluid movement in the fracture plane to be anisotropic, with more flow parallel to the rock fabric, and to be independent of normal stress to 8 MPa. These results suggest that flow was primarily through channels that remained open and connected over a fairly wide range of applied stress. Hence, fractures having uncorrelated surfaces can be very conductive and very stiff at the same time. These results are significant for numerical simulations of the thermal-mechanical-hydrological behavior of the potential repository, as they indicate that fracture permeability may not decrease significantly as compressive stresses rise in the host rock with heating.

### 11.3.7 Field Observations of Thermal-Mechanical Effects

Efforts to understand and characterize coupled processes in a fractured rock mass at Yucca Mountain include the Single Heater Test, the Large Block Test, and the Drift Scale Test.

**The Single Heater Test**—A primary objective of the Single Heater Test was to study the in situ thermomechanical behavior of densely welded, nonlithophysal Topopah Spring Tuff (Tptpmn). A single 5-m (16 ft) long, linear heat source supplied heat to a pillar at the ESF over approximately 9 months. Temperature, water saturation, mechanical deformation, and other rock responses were monitored during the heating phase and for an additional 9 months during cooldown. Rock displacements were measured with multiple point borehole extensometers in three boreholes parallel to and a single borehole perpendicular to the heater. The extensometers consisted of six or seven anchors linked with invar rods. High-temperature sensors measured relative displacements between the borehole collar and each anchor. Type K thermocouples provided temperature data needed for thermal compensation of the invar rod expansions. Further experimental details of the extensometer system are given in CRWMS M&O (1999a, Section 9.1). Plan and cross-sectional views of the Single Heater Test geometry are shown on Figures 11.3-3 and 11.3-4.

The thermomechanical data obtained during the Single Heater Test include estimates of rock mass thermal expansion, rock mass modulus, and rock bolt load. The rock mass thermal expansion coefficient was determined from selected multiple-point borehole extensometer displacements and temperature changes (relative to ambient). Results for the longest gauge lengths available near the end of the heating cycle for the three multiple-point borehole extensometers oriented parallel to the heater are given in Table 11.3-4. Average temperature changes were used because of thermal gradients. The thermal expansion coefficient of the Single Heater Test rock mass below 200°C is as much as 50 percent lower than that given by laboratory measurements on small core samples. The lower in situ value is attributed in part to open fractures that accommodate a large portion of the thermal expansion in the field.

The rock modulus was measured using a Goodman jack in a single horizontal borehole (ESF-TMA-BJ-1) emplaced perpendicular to the heater, 5.5 m from the west face of the Single Heater Test block (Figures 11.3-3 and 11.3-4). The borehole jack measures rock modulus perpendicular

to the borehole and parallel to the heater. It was inserted into the borehole at various distances from the borehole collar, ranging from 2 to 6.2 m (7 to 20 ft), and pressurized. The jack pressure and the loading platen displacements were monitored during the tests, and rock mass modulus was calculated from the slope of the resulting pressure/displacement curves. Tests were conducted on several occasions between August 1996 and January 1998. Additional details are given in CRWMS M&O (1999a, Section 9.2). The measured modulus values range from 3.7 to 23 GPa, with most values below 10 GPa (Table 11.3-5). The highest value was obtained at 6.2 m (20 ft) near the heater and may be a result of fracture closure during heating. The modulus values are considerably lower than intact moduli obtained from laboratory tests on small core samples of Topopah Spring Tuff, as expected, because small core samples typically exclude visible fractures. No information is available on rock modulus anisotropy because the tests were limited to a single borehole.

Eight rockbolt load cells were installed on Williams B7X Hollow Core rockbolts, four on the heated side, and four on the unheated side, of the Thermomechanical Alcove (Figures 11.3-3 and 11.3-4). The objective was to evaluate the effect of elevated temperature on the long-term performance of this type of rock anchorage. Loads were found to decrease over time in all load cells, with larger losses of load occurring for the rockbolts on the heated side of the alcove, particularly for the two rockbolts nearest the heater (Table 11.3-6). The loss of load may result from the greater thermal expansion of carbon steel than tuff or may be due to creep of the rockbolt anchorage. The rockbolt load tests are discussed in CRWMS M&O (1999a, Section 9.3).

**The Large Block Test**—The objective of the Large Block Test was to create a planar, horizontal boiling zone in a fractured rock mass to observe coupled thermal-hydrological-mechanical-chemical behavior (Lin et al. 1995, p. 20). Specific aims of the Large Block Test were to study the dominant heat-transfer mechanism, condensate refluxing, rewetting of the dryout zone following the cooldown of the block, displacement of fractures, and rock-water interactions. One particular goal was to assess how episodes of normal and shear fracture displacements relate to changes in the thermal-hydrologic behavior of the rock mass.

The Large Block was exposed from an outcrop of nonlithophysal Topopah Spring Tuff at Fran Ridge by excavating the surrounding rock, leaving a rectangular prism 3 m × 3 m in cross section and 4.5 m high (Figure 11.3-5). Two subvertical sets of fractures and one set of subhorizontal fractures intersect the block. The subvertical fracture sets are approximately orthogonal, with a spacing of 0.25 to 1 m (1 to 3 ft) and are oriented generally in the northeast-southwest and northwest-southeast directions. A major subhorizontal fracture is located approximately 0.5 m (2 ft) below the top surface (Figure 11.3-5). Heaters were placed in five horizontal boreholes 1.75 m (6 ft) above the base of the block. A steel plate fitted with heating/cooling coils was mounted on top of the block to provide temperature control for the top surface. The vertical sides of the block were insulated with 5.0-cm (2-in.)-thick ultratemp boards, fiberglass insulation, and reflexitic bubbled polyethylene insulation.

The three-dimensional geomechanical response of the rock to heating was monitored using multiple-point borehole extensometers and surface-mounted fracture gauges. The extensometers were deployed in one vertical and five horizontal boreholes: two oriented east-west and three

oriented north-south. The borehole and extensometer anchor locations are shown on Figure 11.3-6.

The fracture gauges measure relative movements across and along the fracture trace, both parallel and perpendicular to the face. They were installed at 17 locations on the surface block (Figure 11.3-7). A few fracture gauge locations are visible as T-shaped grooves on Figure 11.3-5. Temperature and fluid flow were also monitored, and the geomechanical data were interpreted in conjunction with these other data sets.

Heating started on February 27, 1997, and ended on March 10, 1998. Temperatures near the center of the heater plane (Figure 11.3-8) increased from ambient to 90°C in the first few hundred hours of heating. The temperature history includes a sudden drop at about 600 hours (25 days) due to a power outage. The overall temperature history is consistent with conduction-dominated heat flow in the block, except for the temperature excursions at 2,525 and 4,475 hrs. at which times opening and sliding of fractures were also observed. While the thermal anomalies appear to be associated with episodes of increased water infiltration, the exact mechanism of their behavior is unknown.

Thermal expansion of the block began a few hours after the heating started, and horizontal expansion was consistent with the opening of vertical fractures. The data shown on Figure 11.3-9 were taken from an east-west multiple-point borehole extensometer, with anchor 0 at the west face and anchor 4 in the interior of the block. The total deformation observed is about 2.5 mm (0.01 in.). The overall horizontal deformation of the block after 40 days and 58 days revealed similar amounts of expansion in both the east-west and north-south directions (Table 11.3-7). Surprisingly, the horizontal expansion was essentially a linear function of height above the base of the Large Block. Horizontal deformation data and a horizontal deformation profile predicted with a three-dimensional continuum model of the block by Blair et al. (1996a) are shown on Figure 11.3-10. The observed and predicted deformations are similar near the base, but diverge dramatically above the heater plane. The model predicted maximum horizontal expansion near the heater plane consistent with the expected temperature profile. However, the observed horizontal deformation continued to increase with height, independent of the thermal profile above the heater plane.

Multiple-point borehole extensometer data from the upper third of the block show that most deformation occurred in discrete, vertical zones, perhaps due to opening of vertical fractures in this region. In addition, less strain was observed in the vertical direction than in the horizontal direction. Vertical extensometer data also indicate that the region of the block above the heaters moved upward as a unit.

Both the fracture gauge and multiple-point borehole extensometer data indicate that fractures generally opened during the test. Aperture changes (Figures 11.3-11 and 11.3-12) reveal that several of the fractures opened more than 0.1 mm (0.004 in.), and partial closure of only a few fractures was observed (Figure 11.3-11). Shear displacements were generally larger than normal displacements, and at three locations fractures moved at least 0.5 mm (0.02 in.) (Figure 11.3-12).

The overall block displacements, as determined by fracture gauge data, are shown on Figure 11.3-13. One of the most prominent fractures is a subhorizontal fracture about 50 cm

(2 in.) from the top of the block. All rock above this fracture moved to the east as a unit. Another major fracture is a north-south trending subvertical fracture that divides the block vertically into eastern and western subblocks. The fracture gauge data indicate that the eastern subblock moved upward with respect to the western subblock.

Finally, the geomechanical data shed light on an important coupling between mechanical and hydrothermal processes. While flow in vertical fractures is expected to dominate the hydrothermal response of the block, these data indicate a possible cause and effect between motion on horizontal fractures and the hydrothermal response that occurred at 2,525 hours. A few hours before the thermal excursion at 2,525 hr. (104 days), significant movement was recorded on the large horizontal fracture near the top of the block, as indicated by the horizontal deformation data on Figures 11.3-14 and 11.3-15. Unlike the thermal response, the fracture motions were distributed in time and space. The onset of fracture deformation preceded the thermal event by between 10 and 15 hours. It is possible that the horizontal fracture served as a primary conduit for focusing water flow within the block, or in changing the fracture interconnection in the block.

**The Drift Scale Test**—The Drift Scale Test is a major thermal field test currently under way in Alcove 5 of the ESF. The test location is near that of the earlier Single Heater Test. The principal objective of the DST is to study coupled thermal-hydrologic-chemical-mechanical processes at the potential repository horizon in the middle nonlithophysal unit of the Topopah Spring Tuff. The test geometry includes a heated drift, an access/observation drift, and a short connecting drift (Figure 11.3-16). The heated drift is horizontal, oriented approximately east-west, and has a diameter of 5 m (16 ft). It consists of an 11-m-long (36-ft-long) entry, which includes a plate-loading niche, and a 47-m-long (154-ft-long) test drift. The pillar between the heated drift and the access/observation drift is approximately 30 m (100 ft) thick. The surrounding rock mass is heated by nine electrical resistance heater canisters in the heater drift and 50 wing heaters in horizontal boreholes, 25 on either side of the heated drift (Figure 11.3-17). Drift-wall temperatures are not expected to exceed 200°C during the test. The heating phase is planned to last 4 yr. and should create a dry zone extending approximately 10 m (33 ft) into the host rock.

The coupled thermal-hydrologic-chemical-mechanical behavior of the Drift Scale Test is being monitored with a wide variety of scientific instrumentation deployed over nearly 200 boreholes or mounted inside the various drifts. A representative cross section containing several instrument boreholes is given on Figure 11.3-18. Rock-mass temperatures are being measured at approximately 1-m (3-ft) intervals with resistance temperature device sensors in several boreholes. Multiple point borehole extensometers have been installed in 17 boreholes to monitor displacements. The extensometer boreholes include two long horizontal boreholes parallel to the heated drift, three sets of four-borehole arrays drilled from the heater drift, and three boreholes drilled from the access/observation drift. Two cross-drift extensometers were installed in the heated drift to measure horizontal and vertical cross-drift convergence. Details of the extensometer installation are provided in CRWMS M&O (1998d, Sections 6.1 & 6.2).

A series of plate loading tests are also being conducted as part of the Drift Scale Test to measure rock mass modulus at ambient and elevated temperature. These tests are being conducted in the southeastern corner of the Drift Scale Test, about 5 m (16 ft) from the heated drift bulkhead, in a

special niche excavated for this purpose. The western wall of this niche is closer to the heat source than is the eastern wall. The plate loading tests will horizontally load both niche walls. Heating is expected to close fractures and thereby stiffen the rock mass, leading to a higher modulus in the western wall compared to the eastern wall over time. The plate loading tests are expected to quantify this effect. The resulting rock mass modulus data may be used directly in numerical models of drift stability and ground support interactions and in conceptual models of coupled thermal-hydrologic-chemical-mechanical behavior for the potential repository.

### 11.3.8 Mechanical Loading Conditions on Waste Packages

Several underground mechanisms have been identified that could lead to mechanical loading on the waste packages. These mechanisms include:

- **Creep**—Drift walls will converge over the long repository lifetime, but considerable ground movement would be required to load the waste packages.
- **Block Failures**—Blocks could fall into open spaces left by a collapsed ground support system. Block failures are the most credible loading scenario.
- **Seismic Loading Fault Displacements**—Rock burst failures are unlikely, even if ground support fails, due to the low stress levels at the potential repository horizon.
- **Hydrostatic Loading**—Loading is unlikely because the rock is unsaturated.

The types of loading that would result from these failures will be different and are assessed separately in the following sections. Thermal loading is the most likely cause of ground support failures and associated loading of the waste packages.

Loading and performance of the rock support system need to be addressed through numerical modeling and/or physical testing. Both point loads and distributed loads are possible. The type of loading that is most likely is strongly influenced by engineering design. For instance, point loading of waste packages can be mitigated by engineered alternatives, such as backfilling the drifts at the time of closure. Drift backfill could remain effective against drift collapse indefinitely. Even if settlement of backfill occurred, the amount of rock motion would be limited. Therefore, loading conditions must be discussed relative to the type of design.

Under the conditions that have been assessed, rock loading on the waste packages by block failures or by sloughing can be bounded. The method of tunnel support (if any) is undetermined at this time, but it is unlikely that any support system other than backfilling will last 10 k.y. If the drift collapses over time, the waste packages will be loaded by contact with the failed support system that, in turn, would be loaded by either blocks of rock or bulked rock rubble. If backfill is used, the contact would not be directly with the support system, and the potential for point loading would be greatly diminished.

A probabilistic approach could be used to estimate the stability of drifts over time. Kemeny and Cook (1990) used this approach to evaluate the long-term stability of boreholes in conjunction with a repository design that employed borehole emplacement. They estimated that, over the lifetime of such a repository, spalling would likely occur in a significant portion of the

emplacement boreholes. This analysis, although performed for boreholes, could be applied to drifts. However, other processes may apply to drifts. Where vertical fractures dominate, the potential for slabbing, or for block failures, into a large horizontal opening may be significantly greater than into vertical boreholes, such as those considered by Kemeny and Cook (1990). Slabs could load the ground support system liners, etc., but would not be likely to directly impact waste packages except through failed support system components.

**Creep**—Without backfill, uniform loading of the waste packages could result from creep closure of openings being imposed on a failed support system. In the case of backfill, creep closure could be imposed through the backfill. If sufficient long-term creep takes place to close the openings around the waste packages entirely, then the full lithostatic load might be imposed. In the event of severe creep, rock displacements will not be uniform because of the rock structure and the anisotropy of the stress field. Data are not available to address creep over a 10-k.y. time frame, but there is no indication that full lithostatic loading is likely to be imposed. Natural openings in other rock types have remained open over long periods (e.g., limestone caves and lava tubes), but no study has been made as to whether these natural analogs apply to Yucca Mountain.

**Block Failures**—The size of blocks that could enter the space left by a collapsed liner depends on the fracture spacing and the opening dimensions that result from the ground support failure. The ultimate bound on this opening dimension would be the full drift diameter, but the actual dimension should be somewhat smaller because total failure of the ground support is unlikely. An estimate of tabular block size for the ESF has been made by constraining the horizontal block dimension to the drift diameter and incorporating fracture spacing data obtained from the ESF Main Drift (Table 11.3-8). The fracture data are divided into four domains based on station position along the ESF Main Drift (Albin et al. 1997, pp. 33 to 39). The ESF is located in the middle nonlithophysal unit, which is more densely fractured than the lower lithophysal unit, which encompasses the bulk of the potential repository horizon. As such, tabular block sizes estimated for the ESF are likely to be smaller than for the potential repository. However, the method of analysis should be similar.

Four fracture sets were identified for the ESF Main Drift by Albin et al. (1997, pp. 33 to 39) based on orientation. Two fracture sets are steeply dipping, a third set dips about 30°, and the fourth set has an intermediate dip. Given the orientation of one fracture set (about 18° to the drift orientation), tabular blocks up to 16-m-long (the length of the fracture trace in a 5-m (16-ft)-diameter drift) could theoretically fall within the drift. However, a more realistic value can be estimated from the average spacing for the three prominent fracture sets. These sets would intersect to form blocks with one side oriented approximately 120° to the drift with a length of about 2 to 4 m (7 to 13 ft) and a width ranging from 0.3 to 1.1 m (1 to 4 ft). The vertical extent of the blocks would be roughly the spacing of the third, gently dipping fracture set, which varies from about 10 m (33 ft) to about 45 m (150 ft). Therefore, if a block fell into the drift, it could range in mass from 20,000 to 360,000 kg. It is less likely that a single block 45 m (150 ft) high would fail; therefore, the 360,000 kg block represents a conservative upper limit.

A statistical description of the probable block sizes formed by fractures around the emplacement drifts has been developed for each of the lithologic units of the repository host horizon (CRWMS

M&O 2000k, pp. 20 to 63). This work included assessment of the change in drift profile resulting from progressive deterioration of the emplacement both with and without backfill. Drift profiles were determined for four different time increments: static (i.e., upon excavation), 200 yr., 2,000 yr., and 10,000 yr. The effect of seismic events on rockfall was also analyzed. Block size distributions and drift profiles were determined for three seismic levels, including a 1,000-yr. event, a 5,000-yr. event, and a 10,000-yr. event. This analysis involved the use of the distinct element code and probabilistic key block theory through numerical code. These methods are based on industry accepted approaches for analyzing geotechnical problems. In general, the static key block results presented are representative of the observed key block occurrence in the ESF.

The CRWMS M&O (2000k) state the following conclusions. The available fracture data are suitable for supporting a detailed key block analysis of the repository host horizon rock mass. The seismic effect on the rockfall size distribution for all events analyzed is relatively minor. Time-dependent and thermal effects also showed minor impact on rockfall. Most of the emplacement drift openings were not affected by rockfall. The highest percentage of drift affected by rockfall was 16 percent in the Tptpmn unit.

The CRWMS M&O (2000k) analysis also showed that the license application design selection emplacement drift orientation azimuth of 108° is relatively favorable in terms of reducing the potential maximum size rock block compared to most drift orientations. This study also indicated that a re-alignment of the emplacement drifts to an azimuth of approximately 75° could potentially reduce the maximum possible rock block.

The results of the CRWMS M&O (2000k) study have shown that key blocks are most predominant in the Tptpmn unit, which agrees with field observations. The size of key blocks observed in the field is generally less than 1 m<sup>3</sup> (11 ft<sup>3</sup>), which agrees with the simulated distribution of block sizes presented in this study.

**Seismic Loading/Fault Displacements**—The information on seismic loading contained in Wilder (1993b, Section 4.1.3) remains relevant. An earthquake with an epicenter at nearby Little Skull Mountain was studied and damage to underground structures evaluated (Anderson et al. 1993).

The current design with large waste packages emplaced within drifts and resting on pedestals results in a limited potential for fault displacement impacts. Compared to borehole emplacement, the much larger drift opening will allow for greater fault creep and fault offsets without exposing the waste packages to excessive shearing loads or large deformations. The drift diameter is approximately 5 m (16 ft) and the waste packages are about 3 m in diameter. Therefore, a single offset of less than 2 m (7 ft), for the worst case scenario of a fault perpendicular to drifts, will merely cause the waste packages to rotate or be offset from the supporting pedestals. Only the very large offsets associated with major earthquake events (usually less than 8 m [26 ft]) would have enough offset to shear the waste packages. Furthermore, the waste packages are sufficiently strong that the rock in a sheared fault zone may break around the fairly short waste package rather than shear the waste package itself. However, the waste package could be dislodged from its pedestal and pressed against the rib of the drift.

**Hydrostatic Loading**—Another mechanism for uniform loading is hydrostatic loading. No hydrostatic loading is anticipated because the repository horizon is unsaturated. Any water that might be introduced inadvertently into the system may drain away before any appreciable head can develop.

### 11.3.9 Predictive Modeling

The rock mass forming the near-field environment is expected to be a fractured, welded tuff. Several numerical codes developed for simulation of rock-mass behavior provide for discrete cracks and fractures. These codes employ finite element, distinct element, and boundary element numerical techniques and can incorporate a wide variety of constitutive models. Some have been generalized to three dimensions. To predict rock damage over long periods of time and at changing temperature and moisture conditions, numerical codes must accommodate the appropriate constitutive equations for elasto-plastic moduli, nonlinear joint properties, and fracture propagation. Included properties of the rock are compressive and tensile strength, coefficient of friction, fracture stiffness, and fracture toughness, among others. The codes use these parameters, along with boundary stresses and thermally induced stresses, to obtain a stress distribution throughout the region of interest in the near-field environment.

Coupling thermal-mechanical models to the sophisticated hydrothermal models used by the hydrologic community is necessary for simulation of geomechanical behavior in the near field. An international cooperative research project, DECOVALEX (DEvelopment of the COupled models and their VALidation against EXperiments), was established for theoretical and experimental studies of coupled thermal, hydrological, and mechanical processes in hard rocks (Stephansson 1995, p. 387). In this work, different mathematical models and computer codes have been used to study problems of interest to geologic disposal of radioactive waste. Eleven codes were evaluated, including both two-dimensional and three-dimensional finite element codes, in which the rock was modeled as a porous/fractured medium, and a two-dimensional discrete element code, in which the rock was modeled as discrete deformable block assemblages (Jing et al. 1995, p. 393).

Two intercode benchmark comparisons were carried out as part of the DECOVALEX program. The BMT1 benchmark test considered a large-scale (kilometer) mass of rock and is described by Millard et al. (1995, pp. 410 to 411). The BMT2 benchmark problem involved a system of nine blocks of intact hard rock separated by two pairs of soft fractures (Chan et al. 1995, pp. 436 to 438). Both finite element and distinct element methods were used for each exercise. Chan et al. (1995, p. 449) found that heat convection significantly affects the distribution of temperature, thermal stresses, and displacements for BMT2, and that the predominant coupled effect is fracture closure caused by thermal expansion of the rock blocks. Thus, near-field coupled models need to incorporate this effect. The DECOVALEX results also indicated that the different modeling techniques produced very similar results for the BMT1 and BMT2 tests. This indicates that the use of continuum codes is merited for near-field studies.

Other work conducted in conjunction with the DECOVALEX program includes development of analytical solutions for coupled thermal-mechanical-hydrological behavior by Rehbinder (1995), and study of thermal-mechanical-hydrological behavior of sparsely fractured rock by Nguyen and Selvadurai (1995). In addition, Jiao and Hudson (1995) have presented a fully coupled

model for rock engineering systems. Much of the DECOVALEX work is documented in a special issue of the *International Journal of Rock Mechanics and Mining Sciences & Geomechanics Abstracts* (Stephansson 1995, p. 387).

Limited predictive modeling of geomechanical behavior in the near-field environment has been performed as part of the repository design or in conjunction with thermal tests, such as the Large Block Test (Blair et al. 1996a) and the Single Heater Test (Blair et al. 1998). CRWMS M&O (1998a) predicted drift closure and strength/stress ratios at times up to 150 yr. after emplacement. These predictions (Figure 11.3-19) were made with a finite-difference code and indicate zones of plasticity around the drifts extending approximately 2 to 3 m (7 to 10 ft) into the wall. These calculations were intended for use in the design of tunnel support and are of limited use in assessing the geomechanical behavior of the near-field environment.

Simulations of thermal tests have been performed using the two-dimensional version of the geomechanical FLAC (Fast Lagrangian Analysis of Continua) code (Itasca Consulting Group 1996). FLAC is a time-dependent, finite difference numerical code capable of treating mechanically and thermally induced stresses and deformations through a variety of built-in constitutive models. FLAC is an uncoupled thermomechanical model—the stress field depends on the temperature field, but the temperature field is independent of the stress field. There is no feedback to the NUFT calculations from the FLAC code. Therefore, the thermal field can be solved independently of the mechanical equilibrium problem. The primary coupling between thermal-hydrological and thermal-mechanical simulations is via the temperature field, whereas coupling between thermal-mechanical effects and thermal-hydrologic behavior is via mechanically induced changes in permeability. Thermal-hydrologic models are used to compute the temperature distribution; this information is then passed to the thermal-mechanical model for computation of stress and deformation fields. The thermal-mechanical model is set up with the same grid as the thermal-hydrologic model. The particular models being used are NUFT for the thermal-hydrologic behavior, and FLAC for the thermal-mechanical behavior.

Coupling between mechanical and hydrologic effects may also occur if the fracture deformation alters the moisture retention properties of the rock. Closure of fractures under normal stress may increase the moisture retention, while normal opening of fractures, shearing of asperities, and/or microfracturing of the rock may cause reduced moisture retention. Little data has been collected in this area and the effects are poorly known.

#### **11.3.10 Thermal-Mechanical Effects on Hydrology**

The Drift Scale Test is one of the thermal tests being conducted in the ESF. One of the test's major objectives is to study the coupled thermal-hydrologic-chemical-mechanical processes at the potential repository's horizon. The test objectives, design, and layouts are included in a previous test design report (CRWMS M&O 1996). Blair et al. (1997) have estimated changes in fracture permeability due to thermal-mechanical effects for the rock surrounding the Drift Scale Test. Their study suggests that shear slip along fractures may increase permeability by a factor of two to four over significant portions of the heated rock mass.

Blair et al. (1997) used stresses calculated by a two-dimensional thermomechanical analysis with the Mohr-Coulomb criterion to predict whether preexisting fracture sets slip due to thermal

stresses generated in the Drift Scale Test. A fracture flow model developed by Brown (1995, pp. 5943 to 5946), which includes shear offset, is then used to estimate permeability changes. The analysis is preliminary because it assumes an elastic medium whose properties do not change even when frictional slip and stress redistribution are likely to have occurred. The analysis also neglects permeability reductions as a result of increased normal stresses during heating.

Results show that thermal-mechanical effects may cause significant permeability enhancement in a major portion of the heated rock mass, including regions experiencing thermal stress gradients. This indicates that an enhancement of permeability may accompany the thermal pulse as it travels outward from the heat source.

To estimate regions of increased permeability for the Drift Scale Test, it is assumed that permeability will double at any location where fracture slip is predicted to occur. It is also assumed that slip on one set of fractures does not interfere with slip on any other set, and that changes in permeability predicted for one set of fractures can be added linearly to changes in permeability predicted for the other set. Thus, if a zone of enhanced permeability predicted for slip along a vertical set of fractures overlaps such a zone for a set of horizontal fractures, a total permeability enhancement of four times for the overlapping region is predicted.

Predicted zones of enhanced permeability due to Drift Scale Test excavation are shown in Figure 11.3-20. The drift excavation is predicted to increase the rock permeability surrounding the drift in a region extending up to one-half drift diameter into the drift wall. This is not unexpected; many mining studies have shown that wall rock permeability is often increased in underground excavations.

Figure 11.3-21 shows zones of enhanced permeability predicted for the Drift Scale Test 4 years after the start of heating. Permeability may be enhanced in two large V-shaped regions, symmetrically distributed above and below the wing heater plane. The scale of these regions is on the order of the separation of the drifts, the width is on the order of half the drift separation, and the area of increased permeability is removed from the actively heated regions.

Horizontal fractures are favorably oriented for slip when the maximum principal stress lies approximately  $30^\circ$  to the horizontal, and the ratio of maximum-to-minimum principal stress becomes large. These conditions are met for horizontal fractures in regions between the wing heater and the access drift centered at a distance about 4 m above and below the plane of the wing heaters.

Two zones are shown on Figure 11.3-21 where permeability is predicted to be enhanced by a factor of four. These zones occur where both fracture sets are expected to slip and are also symmetric above and below the heater plane. They occur to the side of the heater because the horizontal fractures are favorably oriented for slip in this region only. Comparison with stress plots shows that the permeability is enhanced in areas of high thermal gradients, as is expected from the formulation.

**Discussion**—In this study, only two fracture sets were used for estimation of change in permeability. This method can easily be adapted to three dimensions; this will be necessary for

analysis of more complicated geometries of both fractures and drifts encountered in the potential repository. The preliminary result is that the permeability of the Drift Scale Test may be enhanced by a factor of two to four over major regions due to thermal-mechanical effects, and that this happens in the first few months of heating.

Critical to the methodology linking the thermomechanical analysis to permeability is the concept that permeability enhancement occurs as a result of shear offset due to Mohr-Coulomb slip on preexisting fracture sets. Comparing displacement measurements made during the test with those predicted by the model can test this concept. Experiments, such as the Large Block Test (Lin et al. 1995, p. 20) and the Single Heater Test (Lin et al. 1997, p. 481), also provide opportunities to test the methodology. For example, the observation in the Single Heater Test that saturation may have increased in two regions below the heater (Ramirez and Daily 1997) might be a result of permeability enhancement due to thermal stresses. A thermomechanical analysis similar to the one performed for the Drift Scale Test would test this hypothesis.

The agreement between the thermal-hydrological and the FLAC temperature results indicates that stress and displacement results (calculated using FLAC) can be related to the thermal-hydrologic modeling for the ESF tests. Coupled thermal-mechanical-hydrological processes also could be modeled by using the temperature fields computed by a thermal-hydrological code (Buscheck and Nitao 1995) as input for FLAC calculations of stress and displacement results.

It is important to note that the wing heater geometry used in the Drift Scale Test introduces thermal-mechanical effects that may be much different from those encountered in the potential repository. More work needs to be done to assess permeability changes in a more realistic geometry.

### **11.3.11 Radiation Effects of Waste Emplacement on Geomechanical Properties**

The effect of radiation on the geomechanical properties of the host rock, though uncertain, is likely to be limited. The radiation field is expected to affect only rock exposed on the surface of excavated drifts and to penetrate only a few centimeters into the rock. The waste package itself will form a radiation barrier and, if spalling occurs, the rubble will bulk up and form an additional radiation shield. Moreover, radiation is expected to have a negligible effect on rock mechanical properties based on the work of Durham et al. (1986, p. 168), who conducted a series of unconfined compression tests on intact cylindrical specimens of Climax quartz monzonite and Westerly granite. For each rock type, half of the specimens were irradiated with gamma radiation prior to the compression tests. The tests showed no statistically significant difference in unconfined compressive strength, Young's modulus, or Poisson's ratio between the two groups. Durham et al. (1986, p. 168) concluded that gamma irradiation has no measurable effect on the mechanical properties of either rock type.

A similar series of uniaxial compression tests was performed by Blair et al. (1996b) on 44 specimens of Topopah Spring Tuff collected from a surface outcrop at Fran Ridge, part of the welded lithophysae-poor layer, that overlies the potential repository horizon. The specimens were carefully inspected and divided into two matched groups based on the presence of small cracks and infilled vugs, then half of each group were exposed to a 9.5-MegaGray (MGy) dose of gamma radiation over a 47-day period. The radiation dose was found to have no discernible

effect on the unconfined compressive (peak) strength or Young's modulus of the homogeneous, uncracked specimens. However, specimens that contained partially healed, preexisting vertical or subvertical cracks may have suffered some degradation of mechanical strength and Young's modulus, suggesting that exposure to radiation may have weakened the cementing material in the cracks. The cementing material is thought to be largely composed of carbonates, and the authors discussed two possible mechanisms that could weaken the cementing material when it is exposed to radiation: (1) degradation of the carbonate cement by nitric acid formed by irradiation of moist air in the pore space of the rock and (2) alteration of hydrated minerals in the cement through radiolysis of the waters of crystallization (Blair et al. 1996b, p. 13).

INTENTIONALLY LEFT BLANK

## 11.4 GEOCHEMISTRY

### 11.4.1 Ambient Yucca Mountain Environment

#### 11.4.1.1 Host Rock

Approximately 1,000 m (3,300 ft) of bedded, Tertiary volcanic tuffs underlie Yucca Mountain. These units comprise vitric and devitrified tuffs, with variable fracturing and degrees of welding ranging from nonwelded to densely welded. The potential repository would be located approximately 300 m (1,000 ft) below the ground surface and 350 m (1,150 ft) above the water table in a moderate to densely welded, devitrified rhyolitic tuff. Due to the high degree of welding, this rock unit has a matrix porosity of only about 10 percent of volume with a water saturation of about 90 percent; the 10 percent remaining matrix pore space comprise air and water vapor (about 1.5 percent by mass). Although the host-rock matrix has very low permeabilities, the target repository horizon contains some of the most extensively fractured rock under Yucca Mountain, thereby resulting in high bulk permeability. This fracture network is also significant to the repository environment as the expected primary conduit for the water, air, and water vapor transport in the unsaturated zone.

The potential repository location is targeted for the lower portion of the Topopah Spring Tuff, which is also referred to by its formal stratigraphic designation, Tpt. Differences in degrees of welding and distinctions of crystal-rich or crystal-poor zones within the Tpt provide a useful basis for subdividing it into more specific thermal-mechanical units (Ortiz et al. 1985). The subdivisions are particularly useful in hydrologic analyses. (Wilder [1993b, p. 20] provides details of the stratigraphic column and graphic representation of the thermal-mechanical units). The unit designations, in descending order, include the Paintbrush Tuff nonwelded (PTn) and the Topopah Spring welded (TSw1, TSw2, and TSw3) tuffs. The potential repository horizon is predominantly located in the thermal-mechanical subdivision TSw2. Unit TSw2 is crystal-poor, devitrified, and a moderately to densely welded tuff. Part of the repository would also reside in the lowermost part of the overlying TSw1 thermal-mechanical unit. The lower TSw1 is also a moderate to densely welded, crystal-poor tuff. Above and below the potential repository horizon, vitrophyric zones occur: the thermal-mechanical unit PTn lies above the TSw1, and the TSw3 lies below the repository host-rock level. Portions of these zones may also be referred to as the upper and basal vitrophyre of the Topopah Spring unit.

The petrology of the majority of host rock is a fine-grained matrix with gray-colored areas of vapor-phase-altered material that vary in size and are common in occurrence (Price et al. 1987). Both open and closed lithophysae occur, and open and healed fractures are observed throughout the host rock. The primary mineralogy of this tuff consists of phases that formed at temperatures in excess of 600°C in a magma chamber and prior to eruption. In addition, secondary mineralogy is consistent with formation during cooling and also later alteration of the tuff (temperatures less than 500°C). Finally, mineral formation on fracture surfaces is distinguishable from both the primary and secondary minerals (Wilder 1993b, p. 19).

The Tpt unit is chemically quite homogeneous, but with distinct differences in mineralogy reflecting the process of formation. The silica minerals, present as major constituents,

demonstrate a nearly constant total abundance; in contrast to this, the individual silica polymorph abundances (quartz, cristobalite, and tridymite) vary markedly (Bish et al. 1996). Within the potential repository block, alkali feldspar (varying between 55 and 65 percent by weight) and the silica polymorphs constitute more than 98 percent by weight of the mineralogy; the remaining minor phases are typically hematite and smectite, and manganese-oxides as common fracture coatings (usually higher in the repository horizon).

The fracture-surface mineralogy is different from the overall bulk rock mineralogy throughout the Topopah Spring Tuff, and it varies from one location to another. A fracture surface might include the minerals calcite, smectite, quartz (or other silica polymorph), alkali feldspar, any of several zeolites (stellerites, mordenite, chabazite, clinoptilolite, and heulandite), and clay minerals. Fractures are considered the main pathway for fluid transport in the potential repository horizon and, accordingly, the geochemistry of water and gases flowing through the repository block will, in part, be defined by the mineralogy of the surfaces contacted.

The upper Topopah Spring vitrophyre consists of the uppermost zone of the TSw1 and part of the overlying PTn unit. The upper vitrophyre is composed primarily of unaltered volcanic glass with a few mass percent smectite identified in the glassy portions, and occasionally some clinoptilolite-group zeolites are also encountered. The permeability of the PTn unit is relatively high and the fracture density relatively low compared with the densely welded tuffs (CRWMS M&O 2000l, Section 6.1.2). Consequently, even though this vitric zone is thin by comparison (about 3 to 7 m [10 to 23 ft]), it may have particular significance to the chemistry of water in the potential repository. Whereas water in the fractured Topopah Spring welded (TSw) tuffs is assumed to be dominantly fracture flow, in the generally unfractured PTn, matrix flow is expected to dominate the fluid transport in nonwelded units (CRWMS M&O 2000l, Section 6.1.2). Thus, the composition of the water flowing from the base of the PTn (and consequently into the top of the TSw) is anticipated to be strongly identified with the PTn pore water chemistry. The relevance of this case is presented in Section 11.4.1.2.1 and CRWMS M&O (1999b, p. 32).

Below the potential repository horizon, TSw3 is a basal vitrophyre 10 to 30 m (10 to 23 ft) thick that has significant alteration along the upper margin and gradational alteration in the upper and lower margins. This lower vitrophyre consists primarily of densely welded glass (40 to 90 mass percent) with some feldspar, quartz, and opal-CT. Significant alteration in the upper 2 to 5 m (7 to 16 ft) of this vitrophyre is indicated; 30 mass percent zeolites (clinoptilolite-heulandite) and 45 percent smectites are typical. The occurrence of this particular zone may reflect alteration due to syn-depositional devitrification of the Topopah Spring unit. Elsewhere in the vitrophyre, alteration minerals (smectites or zeolites) are observed sealing fractures, an indication of significant glass-groundwater interaction. In a repository environment, the presence of such alteration minerals with high sorptive capacity and high sensitivities to temperature and/or water vapor pressure changes could have significant impact.

## 11.4.1.2 Fluid Chemistry

### 11.4.1.2.1 Aqueous Compositions

Water samples from the vicinity of Yucca Mountain have been collected and analyzed over several years. Water sources relevant to the Yucca Mountain Site Characterization Project (YMP) include:

- Saturated zone waters from the Topopah Spring member of the Paintbrush Group
- Unsaturated zone waters—both from perched-water bodies and from pore waters extracted from unsaturated zone cores of potential repository-relevant rock units (e.g., PTn and TSw)
- Surface waters and precipitation observed in the Yucca Mountain area and surrounding regions.

A current review of samples, measured compositions, and field collection methods is presented in Section 5.3. A summary comparison of the compositions of saturated zone and unsaturated zone waters of the Yucca Mountain tuffs follows.

Groundwater compositions from Yucca Mountain and surrounding areas have been monitored and documented over time. Notably, compositions of saturated zone water from the tuffaceous units are considered adequately represented by well J-13 groundwater analyses. Well J-13 is located 36.8 degrees north latitude, 116.4 degrees east longitude at an elevation of 1011 m (3,317 ft). A committee review was conducted to report on the well's compositional representativeness as a reference fluid for the saturated zone, and, ultimately, it was determined that the major portion of J-13 well water did, in fact, derive from the same lithologic unit as the potential repository, Tpt (Harrar et al. 1990, p. 11.1).

Documentation from the repeated analyses of J-13 water demonstrates that, over a period of more than 10 years, a relatively uniform picture of the major constituents of this water has emerged despite differences in sampling methods, holding times, and analytical techniques (Harrar et al. 1990, p. 4.9). The Harrar et al. (1990) report compiled and evaluated the J-13 compositional data from numerous sources and compared it to perched waters from the unsaturated zone, waters from Rainier Mesa fracture flows, and experimentally derived fluids from various tuff-water interaction studies. The committee consensus was that the composition of J-13 water indeed falls within the expected bounds of the saturated zone water compositions at Yucca Mountain and was suitable for use as a reference case or baseline fluid for the YMP. Presently, an average J-13 water composition is used in the engineered barrier system as the starting chemistry employed in modeling chemical systems (CRWMS M&O 2000b, p. 51). J-13 suitability as a proxy for pore water in modeling studies of the unsaturated zone has been less obvious, but justified while pore water data were lacking. The more recent availability of extracted pore waters from the potential repository horizon has ameliorated these concerns.

Compositions of J-13 well water samples (and other saturated zone waters) are predominantly dilute sodium bicarbonate with high concentrations of aqueous silica (Harrar et al. 1990, p. 5-5).

Other cations that are typically present, in order of decreasing concentrations, include  $\text{Ca}^{2+}$ ,  $\text{K}^+$ , and  $\text{Mg}^{2+}$ , and additional anions present are  $\text{SO}_4^{2-}$ ,  $\text{Cl}^-$ ,  $\text{NO}_3^-$ , and  $\text{F}^-$ . The pH values are typically neutral to slightly basic (7 to 8), although occasionally samples are measured that fall outside this range. The analyses show that J-13 water is an oxygenated groundwater (e.g., no sulfide or nitrite detected); however, analyses of some water samples seem to indicate that reducing conditions may prevail at depth. It should be kept in mind that a variety of sampling and handling methods are represented by the compiled data in Harrar's report. Because some parameters are potentially affected by the methods used to draw them from the well, judgment must be reserved as to whether values for pH, redox-sensitive elements, and dissolved gases truly represent those of the in situ waters.

Water compositions representing the unsaturated zone of Yucca Mountain have been primarily determined from two types of samples: pore waters extracted from drill core, in most cases from nonwelded tuffs, and perched waters sampled from boreholes above and below the potential repository horizon. Another important source of unsaturated zone water is from flowing water intercepted along fracture surfaces, but these occurrences are rare; consequently, representative data are limited. The information that each sample type provides is potentially complementary.

Pore-water compositions are significant because they may be used to constrain models for water-rock-gas interactions in the unsaturated zone of the potential repository horizon. Extracting the pore water by centrifugation from rock core, however, is a difficult process, and from welded tuffs like the TSw, extraction of even very small quantities has not been routinely done. Water samples from the more porous PTn just above the potential repository unit, however, have been collected and analyzed. The PTn pore waters have been considered to be a reasonable representation of water that could enter the near-field environment. Since these tuffs are nonwelded and generally unfractured, percolation is predominantly by matrix flow in the PTn. Thus, the water that enters the TSw from above will have interacted strongly with the matrix pore water in the PTn and will reflect a similar chemical signature. More recently, a few limited volume samples from the Topopah Spring welded tuff have been extracted and analyzed for the major cation and anion chemistry. These analyses confirm important similarities in compositions with the PTn pore waters. Despite having only a few data points for the rock unit of interest, the analyses are consistent with water having interacted with the PTn matrix in that the chemistry reflects significant chloride and sulfate concentrations. Thus, for purposes of thermal-hydrologic-chemical and seepage modeling, the initial water chemistry employed is a pore water composition that results from an average of two TSw pore water samples (CRWMS M&O 1999a, p. 32).

Taking into account the existence of perched-water bodies at depth and in the vicinity of the potential repository site is important in understanding the response of Yucca Mountain to future changes in climate and precipitation. Their aqueous compositions reflect a history of infiltration rates and paths, water-rock and rock-gas interactions, microbial influences, and other potentially important processes. Unfortunately, perched waters have not been well characterized, and chemical analyses have been limited in number; nevertheless, for the available compositional data, they are generally similar to saturated zone water (CRWMS M&O 1998c, Section 5.0, p. 7).

Percolation waters claimed from fracture surfaces in the TSw block are considered to represent the mobilized fluids in the potential repository horizon. Unfortunately, outside of the laboratory, these waters are generally difficult to observe. Naturally occurring, percolating fracture waters have not yet been collected from the host rock horizon, and one possible explanation is that fracture flow is episodic in nature. The water percolating along the fracture network is expected to dissolve fracture-lining minerals, as well as precipitate secondary minerals upon the surfaces, so that an evolution in chemical composition will most likely develop along the flow path. The closest fracture flow water sampled from similar lithologic units is from nearby Rainier Mesa (about 48 km [30 mi.] northeast of Yucca Mountain); the analytical data for these waters are also cited in Harrar et al. (1990, p. 6.5, Table 6.1).

Although fracture waters have not been collected from the units underlying Yucca Mountain, a comparison of Rainier Mesa fracture waters to its corresponding host rock pore water may be a reasonable analog for comparisons in the potential repository block. Accordingly, the chemical parameters of fracture water may be several times less concentrated than those observed for pore waters of the matrix through which it passes. Compositions of perched-water bodies and pore waters in the unsaturated zone are also distinctly different, with pore waters generally being more concentrated and higher in pH. Generally, the perched waters are a dilute sodium bicarbonate, with very low Cl concentrations (about 4 to 8 mg/L), and Cl/Br ratios that are lower than other waters in the area (DOE 1998a, p. 7-14). General chemical trends toward higher concentrated pore waters from the PTn unit just above the potential repository horizon reflect higher concentrations of Cl (10 to 250 mg/L) than are found in other Yucca Mountain waters. Similarly, sulfate, Na, and Ca are elevated with respect to other waters sampled. One significant deviation in the chemical trends for more highly concentrated pore waters is the lower concentration, on average, of bicarbonate in pore water compared to saturated zone waters (Peters et al. 1992).

It is noteworthy that when comparing pore water chemistries to those of waters sampled in the field, the differences in sampling methods and volumes obtained potentially affect chemical measurements (Section 5.3.3 contains a summary of methods.) For example, rock core centrifugation used to collect pore water may lead to a volume of a few milliliters of pore water, whereas pumping from a well or borehole could tap an essentially unlimited water source. Clearly, fewer chemical parameters can be tested with limited-volume samples, and duplicate analyses may not be possible; this reduces certain self-consistency checks that are often implemented. Large sample volumes obtained from field-pumping techniques, in contrast, ensure that most chemical analyses can be performed, but potential disturbances (e.g., sample degassing) may compromise compositional data if proper measures are not taken during pumping.

Perched-water compositions are reportedly similar to waters from the saturated zone, although Cl/Br ratios, which fall into a lower range of values for perched water, generally distinguish the two (Section 5.3.6 and 5.3.9). This overall similarity between perched and saturated zone water compositions suggest they are subject to similar water-rock interactions. As reported in Section 5.3.9, these reactions predominantly involve mineral-rock dissolution and ion exchange. Waters percolating through the unsaturated zone into the saturated zone might be expected to reflect mixing with matrix-pore waters, but limitations on this mixing appear to be indicated by the wide compositional differences observed. For example, although not specifically addressed

in this section, the  $^{14}\text{C}$  signature for ambient Yucca Mountain conditions does not support isotopic interaction between rapid recharge in fractures and matrix pore water.

#### **11.4.1.2.2 Gas Chemistry**

Ambient gas compositions that are determined from borehole sampling in the unsaturated zone are reportedly very close to atmospheric values for  $\text{O}_2$ ,  $\text{N}_2$ , and Ar. On the other hand,  $\text{CO}_2$  concentrations from these boreholes are generally elevated with respect to the atmospheric value of about 350 ppmv. Measured values of unsaturated zone gas samples give an average value of approximately 1,000 ppmv for  $\text{CO}_2$  (CRWMS M&O 1998a, Section 5.3.4.2.4.6, p. 5.3-173). Compared with the dissolved aqueous phase  $\text{CO}_2$  measured for matrix pore waters, the gas-phase  $\text{CO}_2$  inventory in the host rock is less by about an order of magnitude. Oxygen gas (about 20 to 22 volume percent) is much more abundant than  $\text{CO}_2$ , but it is less soluble in water. In this case,  $\text{O}_2$  in the gas phase is the more important reservoir and transport pathway for  $\text{O}_2$ .  $\text{N}_2$  is potentially important as a nutrient for microbial activity.

### **11.4.2 The Thermally Perturbed System**

The geochemical evolution of the thermally perturbed Yucca Mountain may be described in terms of spatial and temporal distinctions. Two general regions are discussed here. The near-field environment is that region of rock and drift that is proximal to and interacts with the waste packages, and the altered zone is the environment between the near field and the unperturbed rock. Physical processes and parameters that dominate are used to define three time periods. Initially, a heating phase defines the "First Period," during which liquid water continues to be present in the near-field environment. The "Second Period" is characterized by a steam-dominated vapor phase in the pore and fracture spaces and a total or near total absence of liquid water. During this second interval, rising temperatures will exceed boiling, reach a maximum value, and then eventually fall. The "Third Period" begins at the point when temperatures in the near-field environment are sufficiently reduced to allow the reappearance of liquid water, either by inflow or condensation. The general geochemical evolution of Yucca Mountain is first discussed under the expected thermal loading conditions. Then, geochemical processes and parameters are described topically in Section 11.4.2.2.3, with reference to the periods in which they may be significant.

#### **11.4.2.1 General Overview**

Although Yucca Mountain's present-day mineralogy and mineral distribution indicate, to some extent, postemplacement alteration processes, the potential repository host rock has not been significantly altered by these processes. Nevertheless, where postemplacement alteration has occurred, inferences can be made concerning the impact that heating and resulting water movement have had on the host rock. The study of other natural analogs, outcome from field and laboratory tests, and computer simulations fed by existing data will be combined to understand the implications for the natural system from a potential repository. These processes and the relative locations in which they may be important are described below.

Distinctions in geochemical processes and their effects are generally recognized between the near-field environment and the altered zone. Although the same processes will occur throughout the natural system, different ones dominate and affect rock properties differently for these two areas. Generally, strong thermal gradients exist in the near field (closer to the source of heat) and create a dynamic environment that is dominated by kinetic effects. Here, the predominant geochemical processes are evaporation and boiling, mineral dehydration-hydration, and solid-vapor interactions, whereas the altered zone located farther from the heat and from the high rates of heating is closer to ambient conditions.

In the near-field potential repository environment proposed for Yucca Mountain, elevated temperatures from radioactive decay are expected to heat in situ pore water and fracture water, resulting in local geochemical interactions between ambient fluids and host rock. Warming of the rock immediately surrounding the drifts will cause CO<sub>2</sub> to degas from pore waters in the rock matrix (resulting from decreasing solubility with increasing temperature), and initially produce an increase in CO<sub>2</sub> partial pressures. At sufficiently high temperatures, evaporation or boiling will drive water vapor and exsolved CO<sub>2</sub> toward cooler regions of the surrounding rock. These processes generate a low relative humidity zone in the rock surrounding the drift. Small amounts of residual pore waters may remain in this dryout zone due to high, evaporative salt concentrations (therefore slightly higher boiling temperatures) and/or high capillary suction. Evaporation of the initial carbonate-containing waters will lead to CO<sub>2</sub> degassing and calcite precipitation, such that the residual fluids will be expected to develop higher pH values than those of pre-repository conditions.

In the host block dryout zone and the surrounding condensate zone, complex geochemical changes will evolve, driven by increasing temperature, varying CO<sub>2</sub> partial pressures, and redox change. Carbon dioxide, in particular, is involved in complex reactions and has the potential to control (or strongly affect) the pH of solutions, which, in turn, influences chemical reactions of interest. In ambient Yucca Mountain rock, CO<sub>2</sub> is present as CO<sub>2</sub> gas, dissolved carbonate species in water, and mineral solids. During heating, warming waters liberate CO<sub>2</sub> gas, and solution pH values increase. The resulting atmosphere will reflect some increased CO<sub>2</sub> partial pressures until temperatures reach boiling and the displacement of air by water vapor proportionately decreases the CO<sub>2</sub>. Coincidentally, as temperatures increase, mineral-water reaction rates increase, which may drive pH up and, in turn, decrease CO<sub>2</sub> gas concentrations through reactions involving aqueous carbonate (total carbonate rises with increasing pH). Thus, an initial rise in CO<sub>2</sub> concentrations in the gas phase may be followed by a decrease in CO<sub>2</sub> upon dryout. A condensate zone forms as the heated fluids are transported to cooler regions of the rock and condense. The condensate dilutes any initial liquid water present, and the elevated CO<sub>2</sub> gas concentrations equilibrate with the aqueous phase present. Thus, in the condensate zone, CO<sub>2</sub> dissolves back into the liquid and leads to a decrease in pH. With the expanding thermal region, a progression of the geochemical processes also continues outward.

In the process of heating the near-field environment, movement of water and water vapor may be generally understood to follow a predictable course. Water vapor from evaporated pore waters is driven outward and away from the source. The vapor moves along fractures to lower temperature regions and condenses on the fracture surfaces, where some may be imbibed into the matrix and/or some continues to flow. When vapor condenses in saturated rock of the

condensate zone, downward drainage along fractures will occur under the influence of gravity. Above the drifts, condensate (and ambient percolation if present) will follow the fracture network downward, and either drain into the heated drifts or cycle back again as vapor to repeat the process (known as refluxing). If the matrix saturation region is below the drift, then water drainage will simply be downward into cooler regions. Fluids that may enter the emplacement drifts may undergo additional reactions with introduced materials and may be boiled again, depositing salt precipitates in the drifts. The cycling flow of the gas and liquid throughout the system is discussed in detail in Section 11.2.

#### **11.4.2.2 Parameters and Key Processes**

Geochemical processes in the thermally perturbed rock, which will occur because of waste emplacement, will depend on the heat transferred into the rock surrounding the emplacement drifts and the hydrological regime associated with that heat. As shown in Figure 11.4-1, elevated temperatures couple (see yellow arrows) to mineralogy and solid material by means of several geochemical processes. These processes include dehydration, rock-water interactions, and changes in the mass and chemistry of water that is available for geochemical reaction. The consequences of geochemical effects will depend on the rate of temperature change, the maximum temperature reached, and the flux of water and vapor through the rock. Although generally the same processes apply in both the near-field and the altered-zone environments, conditions will differ and dominant processes will be determined by elapsed time and distance from waste emplacement.

##### **11.4.2.2.1 Temperature**

The heat produced by the potential repository waste will affect geochemical processes in several ways. For example, the equilibrium states of reactions are generally temperature dependent. Mineral solubilities, aqueous speciation, equilibrium-phase assemblages, mineral hydration states, and solid-state phase transformations all depend on temperature as well. The movement of water vapor, liquid water, and CO<sub>2</sub> gas at the elevated temperatures will interact with the existing tuff mineralogy (and introduced materials) to dissolve and precipitate phases and modify the water chemistry. Mineral stability and phase equilibria are temperature-dependent. At higher temperatures, the conversion of unstable cristobalite to more stable chalcedony or the stable quartz form is accelerated (though this may be significant only in the presence of liquid water). Changes in permeability and porosity, in turn, may accompany phase transformations and mineral dissolution-precipitation reactions, and flow paths may be altered for additional impact. Furthermore, the role of microbial activities may represent important interactions as temperatures increase.

##### **11.4.2.2.2 Liquid Water**

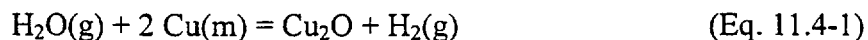
In the near-field environment, geochemical interactions will be strongest in the First and Third Periods, when the presence of liquid water is significant. Liquid water has a high dielectric constant, which facilitates the uptake of solutes, and it participates in acid-base and redox reactions. It accelerates many reactions (e.g., the conversion of less stable silica [SiO<sub>2</sub>] minerals, such as amorphous silica or cristobalite, to more stable silica minerals, such as chalcedony or

quartz). Given comparable controlling factors, such as mineral surface area to fluid volume ratios, the rates of dissolution and precipitation of minerals involving liquid water are generally much higher than those involving a vapor phase (Section 11.4.2.2.3). Liquid water also acts as a transport medium, allowing spatially separated substances to interact. This is particularly important in the near-field environment, which may contain, in addition to the original rock, various man-made materials including some quantity of cement, canister metal, other metals (e.g., in cables, wires, and rails), and radioactive waste. Although the original rock is a disequilibrium assemblage, and hence has thermodynamic driving forces present to change it, the introduction of man-made materials results in a greater number of chemical reactions progressing toward equilibrium. Liquid water is also necessary for the presence of microbial activity. Microbes may take advantage of the presence of thermodynamic driving forces, derive energy from them, and in the process establish new chemical pathways by which equilibrium is approached. They also may catalyze the overall process.

#### 11.4.2.2.3 Steam

Steam (which will be dominant in the Second Period) does have some potential as a medium for geochemical interactions. This is demonstrated at ambient Yucca Mountain by the presence of vapor-deposited minerals. These minerals, however, were formed at high temperatures (more than 600°C), in episodes associated with tuff emplacement (Williams et al. 1982, pp. 267 to 271; Vaniman et al. 1996). At the much lower temperatures that will prevail in the near-field environment, steam is likely to be involved in two main kinds of reactions: hydration-dehydration and redox. In the absence of liquid water, only H<sub>2</sub>O (steam-phase), O<sub>2</sub>, and H<sub>2</sub> are likely to be of significance to chemical reactions. Thus, H<sub>2</sub>O may be removed from or added to minerals, such as smectites and zeolites, and materials introduced during construction of the potential repository, such as concrete. Dehydration processes may begin in the First Period, but they are likely to extend (and be more prominent in) the Second Period, a result of higher temperatures and the ease of water removal from the system (liquid water being more restricted by path tortuosity than steam). Water may also be involved in redox reactions, tied to the consumption or production of O<sub>2</sub> or H<sub>2</sub>. In the near-field environment, this is likely to be significant, primarily regarding interactions with introduced metals used inside the drifts (Equation 11.4-1). Oxidation of introduced metals in the repository may potentially consume the supply of O<sub>2</sub>(g) before water starts acting as an oxidizing agent.

Steam, like liquid water, can act as an oxidant, resulting in the production of H<sub>2</sub> gas, which would then mix into the steam. This is illustrated by the following reaction involving Cu metal, which might be present in wires and cables:



The H<sub>2</sub> gas may then be carried off in the vapor phase. Such a reaction could occur early in the Second Period as steam displaces the O<sub>2</sub>-rich atmosphere originally present in the host rock pores and fractures. Oxygen may also be present in the steam-dominated vapor phase, having diffused in from the unperturbed zone margins, where a normal underground atmosphere continues to be present. CO<sub>2</sub> may also diffuse into the steam vapor phase, though it is unlikely to be reactive unless liquid water is present. The reentry of O<sub>2</sub> and CO<sub>2</sub> may be more important when the

overall zone is cooling and contracting; however, potentially it is significant in earlier periods. For example, minerals containing metals such as Fe may be affected in the Second Period by reaction with H<sub>2</sub> or O<sub>2</sub> present in the steam-dominated vapor phase. Thus, some Fe<sup>3+</sup> in smectite might be reduced to Fe<sup>2+</sup>, and vice versa, depending on the temperatures and vapor-phase compositions.

#### 11.4.2.2.4 Mineral Solubilities

Most minerals (e.g., quartz, chalcedony, cristobalite, albite [NaAlSi<sub>3</sub>O<sub>8</sub>], and potassium-feldspar [KAlSi<sub>3</sub>O<sub>8</sub>]) have normal solubility; that is, solubility increases with increasing temperature. Some minerals such as calcite, however, have retrograde solubility; their solubility decreases with increasing temperature. At the higher expected near-field environment temperatures, as long as cristobalite is still present, the concentration of dissolved silica will be closely controlled by equilibrium with this mineral. At lower temperatures (near ambient), the concentration of dissolved silica may be somewhat lower than cristobalite solubility and instead be a near steady-state value controlled by the dissolution rates of unstable silicate minerals and the growth rates of stable ones. That is, it may not correspond to a classical solubility control. Nevertheless, as the near-field environment goes through the initial heating stage, the concentration of dissolved silica will increase.

Calcite (CaCO<sub>3</sub>) is the major mineral in the fractures throughout the potential repository block (Section 8.9.2). It has retrograde solubility; consequently, additional calcite will be precipitated from aqueous solution in the near-field environment during the initial heating stage. Calcite is also a product of the carbonation (CO<sub>2</sub> addition) of concrete, which would begin in the First Period. Although concrete has previously been an important component in early potential repository designs, the most current potential repository proposal has significantly reduced the volume of this introduced material. The relevance of concrete in a repository is discussed in CRWMS M&O (1998c, Section 7.4.2.4).

#### 11.4.2.2.5 Mineral Dissolution and Precipitation

In a static, saturated nonisothermal system, the temperature dependence of reaction rates and equilibrium constants usually results in dissolution of material in a hotter location, followed by transport and deposition in a cooler location. (Retrograde solubilities, such as previously described for CaCO<sub>3</sub> are an exception.) By contrast, in a refluxing environment (boiling at the bottom, condensation at the top), the transport of components in liquid water is from top (slightly cooler) to bottom (slightly hotter). Liquid then moves in response to gravity, not temperature gradients.

In both the near-field environment and the altered zone, the dominant processes during dryout will be vapor flow and associated chemical exchanges. As boiling temperatures are reached, but before complete dryout occurs, residual fluids will be highly concentrated solutions of nonvolatile components, such as salts (a property contributing to elevated boiling temperatures compared with that of pure water). Thus, a zone may develop (expanding outward as the boiling zone proceeds) in which deposited salt minerals plug the rock pores and fractures. The concentration of these salts may be expected to produce fundamental changes in the matrix

hydrologic properties (such as porosity changes) and to result in mineralogical changes due to higher temperatures (cristobalite is partially converted to the more stable quartz).

Geochemical and hydrological processes are expected to be more significant in the First Period when temperatures are elevated but do not quite reach boiling. Dissolution and precipitation may occur in this process as a result of the continuing presence of liquid water. Indeed, where water is present and kinetics are rapid, as they are along fracture pathways, the geochemical processes are well developed for the rock region immediately surrounding the fractures. One key reaction mechanism expected is silica redistribution (e.g., cristobalite dissolution in one place, followed by chalcedony, opal, or quartz precipitation in another). This process is expected to be important in both the near-field and altered zone environments. Silica redistribution may alter, create, and close off (or reduce) fluid transport pathways. Hydrothermal plug-flow reactor experiments of Topopah Spring tuff reacted with de-ionized water have demonstrated significant dissolution and some precipitation of silica phases (e.g., Johnson et al. 1998); other studies do not show significant effects of silica redistribution on porosity changes (e.g., CRWMS M&O 2000d). Although other chemical constituents may similarly be redistributed (e.g., Al, Na, Ca, K, and Mg), it is the silica dissolution and precipitation that may dominate fluid flow changes. The impact of some additional phases, although much less significant in overall abundance, may nonetheless be important in other processes. For example, calcite ( $\text{CaCO}_3$ ) is a major mineral in the fractures of the potential repository zone and the dissolution and precipitation of calcite may impact fluid chemistry (pH, in particular). In the First Period, the retrograde solubility of calcite is expected to lead to its precipitation in the near-field environment during initial heating stages, which subsequently leads to an increase in pH. However, as boiling and evaporation drive the water vapor and  $\text{CO}_2$  into cooler regions, the vapor condensation and  $\text{CO}_2$  dissolution will decrease pH, favoring calcite dissolution in the condensation and drainage zones. Smectite formation along preferred flow paths is potentially significant for subsequent radionuclide retardation, owing to high sorption capacities (including ion exchange) and possibly high concentrations of these phases.

#### 11.4.2.2.6 Mineral Stability

Unaltered glass and metastable silica polymorphs in the Topopah Spring Tuff will be prominent in mineral evolution that develops in the thermally perturbed environment of a potential underground repository. Volcanic glass is inherently unstable and occurs predominantly above the Yucca Mountain groundwater table, indicating that the glass reacts relatively quickly in saturated conditions. This alteration of glass to an assemblage of secondary minerals will necessarily be accompanied by a volume change, which in turn affects porosity. The silica polymorphs are widespread among the repository-relevant units and vary in their distribution by depth and stratigraphic interval (e.g. CRWMS M&O 1998c, Section 6.1.3.1). Quartz and the metastable polymorphs (cristobalite, tridymite, and opal-CT) are all found in the unsaturated zone at Yucca Mountain, whereas in the saturated zone, tridymite does not occur at all, and the abundance of cristobalite and opal-CT are observed to decrease with depth. Cristobalite is the primary silica polymorph within the potential repository horizon, and it is known to undergo a displacive phase transformation at about 250°C that is accompanied by a volume increase of a few volume percent.

The silica activity in pore fluids is a particularly important geochemical parameter with regard to potential repository performance. Silica activity is approximately equal to the SiO<sub>2</sub> concentration for dilute solutions (expressed in moles/kg). The concentration changes, however, as a function of the silica polymorph dominating the solution chemistry. Repository performance is generally affected in two ways: (1) mineral stabilization is influenced by the silica activity in pore water, and (2) redistribution of silica depends on the silica activity. In the first case, mineral equilibria is affected through the stabilization and destabilization of mineral species. For example, clinoptilolite, mordenite, and smectite are stabilized by high silica activity, whereas analcime and illite are stabilized by low silica activity. In the second case, elevated silica activity in pore fluids reflects the potential for silica deposition, whereas with lower values the system is likely to dissolve metastable silica polymorphs.

A practical, conceptual model of Yucca Mountain mineral evolution under various thermal and hydrologic conditions may be developed with the integrated use of natural analogs and available thermodynamic and kinetic studies. This approach has been described more comprehensively in CRWMS M&O (1998c, Section 6.1.6). The ambient Yucca Mountain geochemical environment has been relatively stable for long periods of geologic history, but the heat anticipated from a potential repository will strongly perturb near-field and altered zone geochemical processes. The potential repository horizon is a disequilibrium assemblage, and a number of mineralogical reactions may be accelerated or induced by the thermal perturbation.

Based on natural analogs and theoretical studies, four potential mineralogical reactions are recognized which may be accelerated at Yucca Mountain by a thermal pulse from radioactive waste. The possible reactions include:

- Volcanic glass to clinoptilolite ± smectite ± opal-CT
- Tridymite, cristobalite, opal-CT to quartz
- Clinoptilolite, mordenite to analcime + quartz ± calcite
- Smectite to illite.

In predicting mineral evolution at Yucca Mountain, existing evidence of past alteration in the Tpt unit serves as a model for the geochemical and hydrological conditions of interest. Thus in considering natural analogs to compare with the evolving potential repository environment (CRWMS M&O 1998c, Section 6.1.6.3), Yucca Mountain itself may serve as one of the useful analogs. The reported diagenetic alteration observed there today includes the formation of zeolites, opal-CT, smectite, the smectite-to-illite transition, and the loss of volcanic glass and metastable silica polymorphs (CRWMS M&O 1998c, Sections 6.1.6.1, 6.1.6.2, 6.1.6.3). For example, vitric tuffs containing unaltered volcanic glass are found with minor smectite, opal-CT, heulandite, and Ca-rich clinoptilolite. Glass loss is associated with the formation of significant amounts of clinoptilolite and mordenite. Another alteration reaction is the disappearance of metastable silica polymorphs at depths generally corresponding to the appearance of secondary quartz (presumably through dissolution-precipitation) and the appearance of analcime. Furthermore, tridymite is not observed below the water table and is presumed lost to dissolution. Smectite reportedly develops through reactions that consume volcanic glass but is itself transformed progressively to illite with increasing temperature and/or decreasing aqueous silica activity.

To assess the impact to potential repository performance from the mineral reactions described, one approach is to consider the extremes in conditions possible from individual reactions. Thus, the reaction of volcanic glass results in two end-member conditions:

- No reaction of volcanic glass during thermal perturbation by the potential repository
- Complete reaction of volcanic glass in saturated regions at elevated temperatures to an assemblage of  $\pm$  clinoptilolite  $\pm$  smectite  $\pm$  opal-CT.

The first case reflects a conservative estimate, because unreacted volcanic glass offers no sorptive barrier. In the second case, alteration products help retard radionuclide migration and have a pronounced effect on hydrologic properties in the affected rocks.

Silica polymorphs and their transformations to stable forms are particularly significant in the Yucca Mountain mineral evolution. CRWMS M&O (1998c, Section 6.1.6, pp. 1 to 22) contains a comprehensive assessment of natural analog studies conducted at that time and related bibliographic information. The notable summary points are that hydrologic properties are altered through silica redistribution, mineral equilibria may be affected through the stabilization of mineral species, and the transformation of silica polymorphs are the rate-limiting step in the reaction of the sorptive zeolites clinoptilolite and mordenite to analcime-bearing assemblages.

Under all likely repository conditions, cristobalite and opal-CT are unstable with respect to quartz. The rate of reaction to quartz, however, is expected to be negligible in the unsaturated regions. Observations of mineral distribution under ambient Yucca Mountain conditions support slow reaction kinetics; that is, tridymite, glass, cristobalite, opal-CT, clinoptilolite, and mordenite have survived (some 10 m.y.). Reaction rates for saturated conditions may be bounded by applying dissolution-precipitation rate data from Renders et al. (1995) for an upper bound and the rate data of Ernst and Calvert (1969) for a lower bound. Alternatively, the Yucca Mountain self-analog studies may be used to infer a value of 100°C as the temperature by which all cristobalite and opal-CT are reacted to quartz under saturated conditions. Thus, under saturated conditions and the present-day geothermal gradient, the metastable phases may persist for times on the order of 10 m.y.; for temperatures greater than 100°C, times of 1 m.y. or less are expected (CRWMS M&O 1998c, Section 6.1.6.3.2).

Zeolites and smectites are important reaction products from volcanic glass at Yucca Mountain. The sorptive zeolites, clinoptilolite and mordenite, have been studied in natural analogs, including Yucca Mountain and the Yellowstone caldera. For unsaturated conditions, these zeolites are expected to have a negligible tendency to break down. For saturated conditions, and in the presence of cristobalite and opal-CT, these minerals may be stable to at least a temperature of 100°C (presumably by 100°C, the metastable silica phases are all reacted to quartz under saturated conditions). Thus, the conceptual model developed would have clinoptilolite and mordenite stable in the presence of cristobalite and opal-CT, but following the loss of the metastable silica polymorphs, these are expected to break down at temperatures exceeding 90°C. In addition, the stability and reaction of the sorptive zeolites may also depend on pH, so that under conditions of substantially lower pH than present-day Yucca Mountain, the reaction may proceed at even lower temperatures. Studies and previous findings may be found in CRWMS

M&O (1998c, Section 6.1.6, p. 2, Section 6.1.6.3, pp. 5 to 16). Summary data of hydration-dehydration studies may be found in Hardin and Chesnut (1997, pp. 2-29 to 2-31).

The transformation of smectite to illite occurs under saturated conditions and is favored by high temperatures and lower values of aqueous silica activity (Bish et al. 1996; Chipera et al. 1995). Here, two possible end-member models for the reaction process are formulated. The transformation to illite occurs only if cristobalite and opal-CT are lost and if the silica activity is controlled by quartz. The transformation to illite is temperature-dependent and requires 0.1 m.y. at 75°C for an activation energy of 19.6 kcal/mole, based on the kinetic model of Eberl and Hower (1976).

### **11.4.2.3 Evolution of In-Drift Water Chemistry**

#### **11.4.2.3.1 Water Sources and Relevant Geochemical Processes**

For the near field (and for the altered zone) the chemistry of the water moving toward the drifts will be modified by reaction with the rock through which it passes. This reaction will depend on the rock temperature, which will increase with proximity to the drifts (due to the thermal pulse). The mineralogy of zones in the natural system will be perturbed as well. Over time, the changes in the mineralogy, particularly in the fractures through which most inflow is channeled, may lead to evolution in the chemistry of water entering the drifts. Before water contacts the waste packages, its chemistry can be further modified due to the presence of introduced materials and microbial communities in the drifts.

The factors affecting the near-field environment water chemistry are depicted in the interaction matrix presented in Figure 11.4-2. The key parameters of the near-field environment are shown along the diagonal (blue shading); the coupled processes (the interactions that occur between parameters) are shown off the diagonal. Yellow arrows in clockwise and counterclockwise directions represent forward and backward coupling, respectively. The overall process is complex but understandable within the context of thermodynamic modeling (Wolery et al. 1990; Wolery 1992a, 1992b; Daveler and Wolery 1992; Wolery and Daveler 1992) and reactive transport modeling (Steeffel and Lasaga 1994; Steeffel and Yabusaki 1996).

To determine the composition of water that might contact the waste packages, the possible evolution of waters throughout the perturbed region must be considered. First, the chemistry of ambient water (present in the near-field environment) is probably of concern during only the earliest period after waste emplacement, when temperatures have not increased dramatically. Although rapid episodic recharge (ambient percolation) into the drift may be possible, an active ventilation system is proposed for the preclosure period of the potential repository and would be expected to dry fracture and pore spaces in the immediate vicinity of the drift (CRWMS M&O 2000b, p. 59).

As the near-field environment heats up, ambient waters will be subjected to evaporative processes and to mineral-water interactions. One of the more important trends expected during heating is the loss of CO<sub>2</sub> from the aqueous phase and the subsequent effects that process will have on the solution pH. As previously noted, the aqueous-phase inventory of CO<sub>2</sub> in the host

rock is about an order of magnitude more than exists in the gas phase under ambient conditions. Therefore, as evaporation liberates CO<sub>2</sub> gas, which moves away from the heat source into cooler regions, the solution's pH will drift upward. The solution also becomes increasingly concentrated by the loss of H<sub>2</sub>O. Dissolved salts may then raise the boiling temperature slightly, and higher temperature mineral-water interactions are possible. Eventually, salt minerals (e.g., NaCl, NaNO<sub>3</sub>, CaSO<sub>4</sub>) will precipitate, and the remaining liquid water will disappear.

Most waters in the near-field environment with the potential to reach the drift walls are expected to be ambient waters. However, some water may derive from refluxed condensate formed outside the dryout zone. Where humid air has reached cooler temperature rock, condensate will form. Compositionally, the condensing water is essentially distilled water, but it will rapidly react with minerals lining the fractures, as well as CO<sub>2</sub>, which was degassed from waters closer to the heat source. Thus, the condensate may have a dilute chemistry (depending on the extent of water-rock interactions) and somewhat lower pH values due to CO<sub>2</sub> dissolution than observed in ambient waters. The condensate zone that forms and surrounds the dryout zone may develop regions above the drifts in which drainage back to the drift is possible.

In the Third Period, when temperatures have cooled sufficiently to allow water to return to the near-field environment, water that may return into the drifts will be infiltrating waters from the surface and condensate. The percolating waters will be derived from meteoric water, which contains dissolved salts derived from sea spray and from other sources, such as playa dust swept into the atmosphere (Apps 1997). It is also saturated with O<sub>2</sub> and CO<sub>2</sub> (in equilibrium with the atmosphere). As the water transports through the soil, it may pick up additional CO<sub>2</sub> from decayed organic matter. The evolution to groundwater also occurs by chemical interaction with the minerals present in the soil and unsaturated zone. These reactions include ion exchange reactions with clays and feldspars, which are relatively rapid, as well as dissolution (and some precipitation) reactions. This groundwater is likely to be much like that present at Yucca Mountain today (Section 5.3), because it will be the result of the same processes. Slight differences might occur due to climatic change effects (e.g., causing a different loading of salts in the atmosphere, higher or lower rainfall), as well as somewhat warmer temperatures due to heat coming from the potential repository.

Condensate waters will be created by condensation of steam. These waters will not pick up atmospheric salts; however, O<sub>2</sub> and CO<sub>2</sub> from the underground atmosphere may dissolve. A condensate, though initially very dilute (essentially distilled water), would nevertheless interact rapidly with the rock by means of ion exchange and mineral dissolution processes due to the elevated temperatures. The extent of water-rock interaction will be a function of temperature, contact duration, and rock alteration state. This alteration state will, in turn, depend on the rock's history of interaction with condensate or other water.

Such groundwaters and condensate waters will form in the altered-zone environment long before sufficient contraction of the steam zone allows them to penetrate to the near-field environment. Ultimately, the water penetrating the near-field environment from the altered zone will be by means of fracture flow (as opposed to matrix flow). Numerous studies (Section 11.4.3.3) demonstrate that water chemistry in the altered zone is likely controlled by the solubility of mineral phases present in the rock. However, the composition of fracture waters will likely be

dominated by interaction of condensate and fracture-lining minerals, as recently observed in thermal field test samples (Section 11.4.3.3.3). A review of rock-water studies may also be found in Hardin (1998b, pp. 6-3 to 6-12). Wilder (1996) has additional information on waters in the altered zone. The remainder of this section focuses on geochemical processes and water chemistry evolution in the near-field environment. Nevertheless, the result of these processes will depend on the compositions of the entering waters (i.e., from the altered zone and from groundwater). Further work is required to clarify the characteristics of these compositions during the various Third-Period, near-field environment alteration stages.

#### 11.4.2.3.2 Development of Fluid Chemistries in the Near-Field Environment

The liquid waters entering the near-field environment will include groundwater, condensate, and mixtures thereof. As these materials move through the near-field environment and enter the drifts, they may continue to react with the rock and the steam phase as long as it is present. They may also continue to mix with each other. They may pick up salts (e.g., NaCl, NaNO<sub>3</sub>, CaSO<sub>4</sub>) left behind when preexisting ambient waters boiled. (These salts may be concentrated in and near the drifts, as they were the source of the heat and the initial loci of boiling.) Within the drifts, these waters may interact with the man-made materials that had been introduced during construction and waste emplacement. Such materials will include significant volumes of Fe and/or steel, and various construction-related materials. A comprehensive list of these materials and their chemical properties is contained in CRWMS M&O (2000b). Many of these materials will not be in their original emplaced form, but rather significant alteration may have occurred during heating. The waters of the near-field environment may also eventually be altered by exposure to the radioactive waste itself (e.g., spent nuclear fuel, waste glass).

Evaporation of hot, subboiling water is an important consideration in determining the water chemistry that will evolve, as well as in establishing the nature of secondary precipitates that may be deposited along fracture surfaces or in rock pores. These secondary precipitates would be dissolved much later in the Third Period by the reentry of liquid water. It is also important to determine the nature of mineral salts that may be deposited within the drifts as water is evaporated or boiled. The deposition of such salts inside the drift walls is important, not only for determining the effects on Third-Period water chemistries, but also for assessing potential corrosion effects long before that period. Salt deposits can facilitate corrosion (of introduced materials) at very low relative humidity. For example, concentrated salt solutions may remain present even under conditions at which pure water would completely evaporate or boil off. Even after all liquid water has been driven off, the presence of such salts will attract water. (Some of the original water may be incorporated into some crystal structures as waters of hydration.) Under the right conditions of temperature and relative humidity, the evaporation process may be reversed, whereupon these salts induce the formation of concentrated aqueous solutions, obtaining water from the vapor phase under conditions at which pure water would not condense. To assess such effects, one must determine the specific precipitates that would form. These, in turn, will reflect the initial water composition and the conditions of the evaporation process.

The chemical consequences of evaporation are distinct from those of boiling. These processes do not involve just the loss of the H<sub>2</sub>O component. An important distinction arises from the contrast in behavior of dissolved gases during the two processes. In evaporation, the dissolved gases are

generally in a state of near-equilibrium with an overlying atmosphere. The concentrations may adjust to maintain this state. CO<sub>2</sub> is one of the important dissolved gases because CO<sub>2</sub> is closely tied to pH, and pH is one of the most important variables in aqueous geochemical systems. Thus, this effect is more far-reaching than might be expected. Equilibrium with an overlying atmosphere may tend to keep the dissolved CO<sub>2</sub> nearly constant, and thus buffer the pH. Thus, the loss of the CO<sub>2</sub> from a bicarbonate-rich groundwater tends to drive up the pH, as discussed previously.

The addition of man-made materials to the near-field environment will modify the chemical environment and influence the geochemical reactions that may occur. The volumetrically significant presence of the corrosion allowance overpack of the waste canisters may give rise to chemically significant corrosion products. Metal oxidation can affect the redox potential of the environment and provide colloidal material for radionuclide transport.

Microbially mediated chemical processes can significantly alter the geochemical environment and have direct impacts on potential repository materials. Microbes are capable of using a wide range of organic compounds to serve as sources of carbon. Autotrophic organisms are capable of CO<sub>2</sub> fixation to satisfy carbon requirements for synthesis of cellular materials. Energy can be derived from either reduced organic or inorganic compounds. Hydrogen gas, nitrogen, ammonia, nitrite, ferrous iron, and reduced sulfur compounds, for example, can all be used as energy sources by various microbes. Similarly, oxygen or a wide array of inorganic compounds may be used as a terminal electron sink. Nutrient supply, rate of nutrient transport, and composition of the potential repository community will govern the specific types of metabolic activities that occur. Bacteria can also bind metals, secrete metal-complexing compounds, and transform metal ions to altered speciation states. These capabilities may enable the transport of radionuclides from the near-field environment. Additional discussions of the effects of introduced material and microbial activity are presented in Hardin (1998b, Chapter 7) and CRWMS M&O (2000c).

#### **11.4.2.4 Radionuclide Mobility**

No radionuclides are mobilized until after a waste package fails and the waste matrix has been exposed to the drift environment. Radionuclides then require aqueous mobilization (with the exception of a few limited species that have the potential for gaseous mobilization, e.g., <sup>14</sup>C) in order to escape from the waste form and then transport out of the engineered barrier system. Once released, aqueous mobilization may then be as a soluble species or as a suspended microparticulate or colloid. The radionuclides released from the engineered barrier system transport through the natural system, through the unsaturated zone and ultimately into the saturated zone. Aspects of radionuclide transport outside the engineered barrier system are addressed in Section 10. An overview of the modeling efforts regarding waste form degradation and related radionuclide mobilization may be found in CRWMS M&O (1998b, Section 6).

### 11.4.3 Methodology and Supporting Documentation

#### 11.4.3.1 Integrated Approach

Understanding the chemical processes that will occur in the near-field and altered-zone environments requires integrating concepts and data obtained from field and laboratory studies. Thus, the use of natural analogs is important for processing information over long periods of time, and field and laboratory experiments under accelerated conditions provide complementary information about processes under known or precisely controlled conditions. The overall approach incorporates the use of experimental and field data into the models' development process in order to maximize confidence in the evolving product.

In this integrated approach, analog and laboratory studies are needed to compensate for the deficiencies of each alone. For example, laboratory and field studies of ongoing processes (including field tests and some natural analogs) do not begin to approach equilibrium for the time scales appropriate to evaluating the performance of a potential geologic repository (i.e., conditions remain too close to initial conditions). Field studies of long-term processes (most natural analog studies) account for the effects of long periods. However, they carry uncertainties regarding initial conditions (e.g., what the initial conditions were, and what the effect would be of differences in initial conditions between a natural analog of this type and a potential repository). The strengths of each approach can be combined to provide an integrated approach that maintains consistency among all available observations.

Study of Yucca Mountain's alteration history may prove particularly useful in predicting mineral evolution under the influence of thermal changes from a potential repository. Among natural analogs considered, Yucca Mountain may serve as its own best analog in predicting mineral evolution (see also Section 13 of this document). Observations of rocks and theoretical studies indicate that four major mineralogical reactions may potentially be induced or accelerated by a thermal perturbation (waste emplacement). Some reaction components (Section 11.4.2.2.6) are thermodynamically unstable at Yucca Mountain (e.g., volcanic glass, cristobalite, tridymite, and opal-CT), yet they exist, reflecting the need to account for kinetics in the developing model. With respect to the engineered barrier system and introduced materials, long-term chemical processes involving metals may derive from historical analogs. (Many processes that will affect metal construction materials are identical to those that have affected metal archaeological artifacts.) Additionally, data from New Zealand and other geothermal fields may prove useful to chemical model assessment as these data represent materials that are more similar to present construction materials and methods. Section 13 of this document and CRWMS M&O (2000b) contain references and discussions on appropriate analogs for the engineered barrier system.

Experimental data from laboratory studies of tuff-water interactions contribute to understanding processes in both the near-field and altered-zone environments. For example, models for tuff-groundwater interactions at elevated temperatures (150° to 250°C) in well-mixed systems have been developed (Delany 1985; Knauss 1987) that correspond well with laboratory experiments. These models, generally developed using the EQ3/6 software of Wolery et al. (1990), and also described by Wolery (1992a, 1992b; Daveler and Wolery 1992; Wolery and Daveler 1992), successfully account for the evolution of fluid chemistry and the formation of product minerals.

This work is promising because it provides a link between observations of a complex process and fundamental thermodynamic and kinetic data. It is significant that the tuff-groundwater systems at 150° to 250°C described in the works cited do not closely approach overall thermodynamic equilibrium on the time scales of the experiments (typically 60 to 90 days). This emphasizes that some reactions in the potential repository system will not approach equilibrium on time scales that can be conveniently observed in laboratory experiments.

Another example of this approach is the use of reactive transport modeling in one-dimensional systems. Laboratory data collected during fluid flow through experiments in a tuff-filled column used reactive transport modeling. Thus, the column used in the laboratory may in the field correspond to reaction in some fracture systems, flow tubes, or along flow lines. Reactive transport modeling is based on integrating effects (e.g., mineral deposition and dissolution) that are controlled by chemical thermodynamics, chemical kinetics, and fluid transport (i.e., both transport of fluid and transport in fluid, including by diffusion), in a system that may be isothermal or nonisothermal. For example, the effects of mineral dissolution and precipitation along a flow path may increase or reduce permeability. This would alter the fluid flow rate, for a fixed-fluid driving force. In a two-dimensional or three-dimensional system, this could significantly alter the locations of the major flow paths. This would be more likely to occur in the near-field environment than the altered-zone environment, owing to the greater temperature gradients. One of the codes commonly used to simulate reactive transport is GIMRT (Steefel and Yabusaki 1996).

In CRWMS M&O (1998c), a more thorough case is made for the methods employed in the development and understanding of chemical processes at Yucca Mountain. The sections following summarize the relevant studies, the data acquired, and models and simulations employed in the integration process.

#### **11.4.3.2 Geochemical and Mineralogical Studies in the Near-Field Environment**

Studies that evaluate rock and water interactions and introduced materials with fluids have been conducted. Because the general interactions of water and rock are the same for the near field or the altered zone, the summary of these rock-fluid studies is presented once in Section 11.4.3.3. The studies of introduced materials are included here.

##### **11.4.3.2.1 Interactions with Introduced Materials**

Introduced materials, including metals, backfill materials, cementitious materials, and bonding agents, may serve as active parts of the designed engineered barrier. Other materials that are introduced, including surveillance instruments (thermocouples, gauges), construction and operation material (drilling rigs, roadbeds, exhaust fumes, chemical toilets, concrete, grout, rebar), and lubrication products (petroleum-based products, rope dressing) may not be removed because they have either become inaccessible or have not been identified as items to be removed. In normal mining operations, extended residence materials also include waste material and spills. The introduced materials will exist in gas, liquid, and solid phases, as inorganic and organic compounds, and in various reactive states. Some materials may be present in large quantities.

For example, backfill has been considered in some design proposals, and earlier designs employed large volumes of concrete.

Modifications of the natural environment from construction of a potential underground repository would, in themselves, alter the natural chemistry, some aspects of which may be critical to the robustness of the waste package or to the chemistry of the fluid leaving the repository. The product phases of materials disintegration, biodegradation, and corrosion may include oxides of metals, sulfides, chlorides, carbonates, and silicates, as well as organic compounds, alkali metals, and halogen elements. These materials have the potential to alter the pH, ionic strength, and composition of water that may be present at some time in the lifetime of the repository. The quality of water, whether present in an aqueous or vapor phase, will directly affect the dissolution of spent nuclear fuel, waste glass, and, ultimately, the concentration of dissolved or suspended radionuclides in water that exits breached containers. Therefore, the introduction of some man-made materials into the waste package environment may influence waste package performance. CRWMS M&O (2000b) contains a complete review of materials, properties, and issues.

#### **11.4.3.2.1.1 Metals**

Metals that may be introduced into the waste package environment for construction purposes will be primarily steel-iron and iron alloys, which can degrade through several mechanisms. Oxidation is one common degradation process. Such processes are strongly dependent on the Eh and pH of the environment within which oxidation occurs. Cast iron, if present in large volumes, can consume large quantities of O and influence the atmospheric chemistry around waste containers. Experimental studies of Cu corrosion in seawater and in the presence of sulfide ions (Mor and Beccaria 1975) indicate that a variety of copper sulfides can form that also depend on pH. The specific conductivity and resistance to corrosion of the metal depend on the corrosion product, which is pH dependent. In general, the rate at which metal ions are added to water depends on the corrosion products.

Much understanding of long-term chemical processes involving metals that may be used in a radioactive waste repository will be based on observations of historical analogs. Many processes that will affect metal construction materials are identical to those that have affected metal archaeological artifacts (see Section 13 of this document). Outside the YMP, interest in the degradation of metals is found in disparate sources, such as oil companies and the U.S. Naval Oceanographic and Atmospheric Research Laboratory. Because of this interest, and also because of the length of time that humans have been working with metal materials, much more information is available on the long-term degradation of metals than most other manufactured materials.

#### **11.4.3.2.1.2 Cementitious Materials**

The presence of cementitious material may greatly alter the geochemistry of a potential repository by providing a large reservoir of unstable calcium-silicate phases, which will dissolve and reprecipitate at the rock-water interface. The impact of such material is significant and has been discussed in detail in CRWMS M&O (1998b, Section 4.2.1.3.2; 1998c, Section 7.4.2.4.2).

However, the most current potential repository design proposal does not include substantial volumes of introduced concretes. Consequently, the issues are not readdressed here.

#### **11.4.3.2.2 Interactions of Radionuclides in Water Leaving the Near Field**

Based on measured sorption properties of Yucca Mountain rocks (Meijer 1992), performance assessment calculations suggest that the Yucca Mountain tuffs may not provide a sufficient retardation barrier for some radionuclides (e.g., Np, Tc, U, Ni, Se) to ensure the level of radionuclide isolation dictated by regulatory requirements. Therefore, it is necessary to evaluate whether the near-field environment can provide additional radionuclide retardation during the period following substantially complete radionuclide containment. It is also necessary to assess whether near-field materials or their degradation products may promote radionuclide transport due to adverse chemical or physical effects.

A variety of materials is necessary to construct the potential repository and engineered barrier system. Some of these materials and/or their alteration products will define the path that radionuclides must traverse to exit the near-field environment if the waste package were to be breached. The properties of some flow-path components, with regard to radionuclide transport, will differ significantly from the properties of ambient Yucca Mountain tuffs studied by the YMP to date.

##### **11.4.3.2.2.1 Flow-Path Components**

The path a radionuclide-bearing fluid might take from the waste form through the engineered barrier system and near-field environment to potential repository unaltered rock may intersect one or more of the following materials (i.e., flow-path components):

- Waste package filler, packing materials, and their degradation products
- Waste package metallic, corrosion-resistant barrier
- Waste package metallic, corrosion-allowance barrier and its corrosion products
- Waste package nonmetallic barrier and its alteration products (less significant under the new potential repository design proposal)
- Backfill and packing (e.g., silica sand or crushed tuff) and their alteration products
- Invert materials (e.g., silica sand and crushed tuff) and their degradation products
- Topopah Spring Tuff (host rock) that has been altered by hydrothermal interaction with ambient fluids and/or interaction with engineered barrier system and near-field environment components.

Materials expected to be present in the transport path in significant quantities include the corrosion products derived from the corrosion allowance overpack of the waste canisters. Such materials are of particular concern because they would be expected to play a major role in near-

field radionuclide transport because they interact strongly (i.e., retard, immobilize, generate radionuclide-bearing colloids) with radionuclides (Viani 1996a). Cementitious materials (concrete, grout, and their alteration products) used in potential repository construction posed concerns that have been mitigated by recent repository design changes. Significantly reduced volumes of cement and general elimination of these products below the drift have been specified in the most current design plans. A review of concerns related to cementitious materials in the transport path can be found in CRWMS M&O (2000b). In the following section, corrosion products and their effects on radionuclide transport are summarized.

#### 11.4.3.2.2 Corrosion Products in the Flow Path

The most abundant corrosion products resulting from degradation of the waste container are expected to be iron oxides derived from a relatively thick corrosion allowance overpack of low-carbon steel surrounding a corrosion-resistant inner barrier (Viani 1996b; Van Luik et al. 1992; Ahn and Soo 1995). This steel is expected to undergo generalized corrosion as a result of interaction with hot humid atmosphere and contact by liquid groundwater during the potential repository post-dryout period. The result of the corrosion process is expected to be the development of a porous accumulation of iron oxides surrounding the waste form and inner barrier. This porous medium has a high probability of being in the flow path of radionuclide-bearing fluids that leave the waste canister via breaches in the corrosion-resistant inner barrier. The corrosion products are expected to be finely divided and, accordingly, there may be potential for iron oxide colloids to be added to the groundwater. There will also be a potential for filtration of waste-form-derived colloids.

Depending on redox state and moisture conditions, low-carbon steel will corrode more or less uniformly by altering to iron oxides that can include FeO (wüstite), Fe(OH)<sub>2</sub>, Fe<sub>3</sub>O<sub>4</sub> (magnetite),  $\gamma$ -Fe<sub>2</sub>O<sub>3</sub> (maghemite),  $\alpha$ -Fe<sub>2</sub>O<sub>3</sub> (hematite), Fe(OH)<sub>3</sub> (amorphous iron hydroxide),  $\gamma$ -FeOOH (lepidocrocite), and  $\alpha$  FeOOH (goethite) (Evans 1960).

**Expected Oxide Phases**—Of the initial corrosion products that form under hot dry or humid warm conditions,  $\gamma$ -FeOOH (goethite) and  $\gamma$ -Fe<sub>2</sub>O<sub>3</sub> (hematite) are the phases that most likely will persist in the relatively low temperature, oxygenated, humid environment of the post-dryout repository. Based on the observed genesis and persistence of iron oxide phases in soils, other corrosion product phases, such as  $\gamma$ -Fe<sub>2</sub>O<sub>3</sub>, Fe<sub>3</sub>O<sub>4</sub>, and  $\gamma$ -FeOOH, are likely to be transitory (Schwertmann and Taylor 1989). Although hydrated oxides of Fe (III) appear to be the most likely initial constituents of the corrosion layers formed on low-carbon steel in the presence of water, these phases may transform to anhydrous  $\alpha$ -Fe<sub>2</sub>O<sub>3</sub> (hematite) in the long term.

The relative thermodynamic stability of goethite and hematite is not known with certainty, although tabulated data suggest that hematite plus water is slightly more stable than goethite (Johnson and Lundeen 1994; Schwertmann and Taylor 1989). Both goethite and hematite are widely distributed in soils, and each appears to persist as the most stable phase for specific ranges in ground surface conditions (Schwertmann and Taylor 1989). Repository regimes that maintain lowered water activity and elevated temperatures would favor the transformation of goethite to hematite, although the kinetics of this transformation may be slow enough to allow goethite to persist for thousands of years (Schwertmann and Taylor 1989).

#### 11.4.3.2.2.3 Interaction of Radionuclides with Corrosion Products

Interaction of radionuclide-bearing fluids with canister corrosion products is expected to be dominated by surface chemical effects. Iron oxides are very effective sorbents for a wide range of metal cations (e.g., transition metals, actinides) and many metal oxyanions (e.g., chromate, selenite, phosphate, carbonate, silicate) (Dzombak and Morel 1990; Benjamin et al. 1996). The sorption of U, Np, and Pu by iron oxides in the presence or absence of organic materials is discussed in Section 10.3.4. In systems with relatively low concentrations of complexing ligands (e.g., carbonate), partition coefficients ( $K_d$ ) for radionuclides such as U and Np can be as high as  $10^4$  to  $10^6$  mL/g (Turner 1995; Kohler et al. 1992; Tochiyama et al. 1995; Triay et al. 1995; Ho and Miller 1986). However, the presence of dissolved carbonate can significantly reduce the sorptive capacity of iron oxides for metals that form solution carbonate complexes, such as U and Np (Turner 1995; Hsi and Langmuir 1985; Van Geen et al. 1994).

It is clear that compared to the potential repository horizon and adjacent rock units at Yucca Mountain, sorption partition coefficients on iron oxides are several orders of magnitude larger for elements such as U and Np (Wilder 1996, Table 7-1). Hence, corrosion products could be an important barrier to radionuclide transport through the near field.

Because corrosion products are likely to be finely divided, a potential for the introduction of colloids to the waste stream also exists. The potential for iron-oxide colloid movement will depend on a number of factors, including fluid composition, oxide particle size, corrosion layer morphology and structure, temperature, and groundwater flow mode and flux through the layer. The absorption of Pu onto hematite and goethite colloids is described in Section 10.6.

#### 11.4.3.2.2.4 Simulating the Effect of a Hematite Corrosion Layer on Radionuclide Transport

**Bounding Transport Based on a Constant  $K_d$  Mode**—Can iron-oxides derived from the corrosion allowance material serve as a significant barrier to radionuclide transport? In order to bound the potential for radionuclide retardation, an upper limit to the radionuclide sorbed by a given mass of corrosion product can be estimated based on the maximum sorption site density and the surface area of the sorbent.

The maximum site densities estimated for iron oxides from measurements of adsorption maxima and estimates of proton donor-acceptor sites range between approximately 2 and 7 sites/nm<sup>2</sup> for cationic sorbates (Davis and Kent 1990; Dzombak and Morel 1990). Surface areas of natural and synthesized iron oxides vary widely but, in general, natural and/or poorly ordered synthetic oxides have relatively large specific surfaces (on the order of tens to hundreds of square meters per gram) (Davis and Kent 1990; Dzombak and Morel 1990). Assuming a maximum sorption site density of 2.31 sites/nm<sup>2</sup> (Dzombak and Morel 1990) and a specific surface of 20 m<sup>2</sup>/g (Davis and Kent 1990), and considering U as the sorbate, the site density-limited sorption would be approximately 0.02 g U per gram of oxide (approximately 550 kg U per container). Depending on actual site densities and surface areas, this value could vary by an order of magnitude in either direction.

Sorption may also be limited to a value less than the maximum site density when the solid-liquid partition coefficient ( $K_d$ ) is less than some critical value. When the  $K_d$  is below this value, a radionuclide-bearing groundwater will break through a sorbing layer (i.e., exit at its inflow concentration), even though the maximum sorption density has not been reached.

A simple calculation of the years for a radionuclide-bearing fluid to exceed the sorption capacity (either site density or  $K_d$ -limited) of a corrosion layer was made based on the following assumptions:

- The maximum sorption density is 2.31 sites/nm<sup>2</sup>.
- The specific surface of the oxides in the corrosion layer is 20 m<sup>2</sup>/g.
- Sorption is linear and is defined by a constant  $K_d$ .
- Six L/yr. of groundwater contact the waste from one canister.
- The concentration of radionuclide in the groundwater after contacting the waste is 1 mg/L.
- The radionuclide-bearing groundwater contacts a fraction of  $3 \times 10^4$  kg of iron oxide corrosion product that surrounds the waste.

Figure 11.4-3 shows the time it would take for a radionuclide to breach the corrosion product layer for sorption  $K_d$  values varying between  $10^2$  and  $10^5$  mL/g and fractional contact volumes between 0.01 and 0.20. For  $K_d$  values below approximately  $10^4$  mL/g, the time to break through is determined by the  $K_d$ ; above that value, breakthrough is determined by the maximum site density. The specific surface area of the corrosion product will control the specific  $K_d$  that determines whether the breakthrough is  $K_d$  or site-density limited.

Partition coefficients on the order of  $10^3$  to  $10^6$  mL/g for U on iron oxides have been experimentally measured at low sorbent to solution ratios (approximately 1 g/L) at pH levels between 5 and 9 (Turner 1995; Ticknor 1994). For  $K_d$  values greater than approximately  $10^3$  mL/g and volume fractions greater than 0.01, the calculation suggests that retardation would be on the order of thousands to hundreds of thousands of years. These retardation times imply that the corrosion layer can have a dramatic effect on the potential repository performance, especially for long-lived radionuclides, such as Np.

**One-Dimensional Flow and Transport Calculation of Uranium Retardation**—Results from batch sorption experiments (Figures 11.4-4, 11.4-5) and transport experiments (Figures 11.4-6, 11.4-7) have been used to retrieve surface complexation model parameters to describe sorption of U on hematite in 0.01 M NaCl solutions (Hardin 1998b). The diffuse layer surface complexation model was used together with a one-dimensional transport model to assess the effect of solution pH and CO<sub>2</sub> fugacity on U transport through a hematite corrosion layer.

**Transport Simulations**—The one-dimensional transport code, X1t (Bethke 1997), was used to simulate U transport through hematite for various fluid compositions. X1t simulations use the

method of operator splitting by which the calculation of mass transfer is performed separately from the chemical aspects of the computation. The physical and chemical parameters used in the simulations are shown in Table 11.4-1.

The simulations are an aid to understanding the sensitivity of transport to pH and CO<sub>2</sub> fugacity rather than to attempt a bound of all possible groundwater compositions. Nine different simulated fluids were used to assess the sensitivity of U transport to pH and total carbonate (Table 11.4-2). The range in pH and ionic strength considered largely spans the range displayed by Yucca Mountain groundwaters, but does not encompass low pH extremes that might arise due to microbiologically induced acidity. However, the pH values considered do span the range over which total carbonate varies from being less important (low pH) to where it is very significant (high pH) with respect to U transport. The fugacity of CO<sub>2</sub> was varied between 0 and approximately 10 times greater than atmospheric (10x atm; fugacity = 0.003). Ionic strength varied as necessary to maintain electrical balance at the given pH. The concentration of U in solution was set to approximately 1 mg/L ( $4 \times 10^{-6}$  M) to allow comparison with the results based on the simple mass-balance calculation presented above.

The ratio of sorbent to sorbate in a sediment or rock (for any given volume element) is much larger than the ratio of sorbent to sorbate in a batch experiment. The sorbent to sorbate ratio in a rock is controlled by the porosity and fluid saturation state of the medium. For these simulations, the ratio of sorbent to solution is about 7,875 g/L, almost four orders of magnitude larger than most laboratory experiments. Under conditions of unsaturated flow (for a given specific discharge and porosity), this ratio would be even larger.

**Simulation Results**—Figure 11.4-8 summarizes the results of the simulations. The concentration of U (C) relative to its influx concentration (C<sub>0</sub>) is shown at 10 cm (4 in.) into the corrosion layer for the nine different influent solutions. For two fluid compositions (pH 10 with CO<sub>2</sub>), U behaves conservatively, and breakthrough occurs in approximately 20 yr. Only one other fluid, pH 8, 10x atm CO<sub>2</sub>, is close to breaking through after  $3 \times 10^4$  yr. (C/C<sub>0</sub> of about 0.8). As expected, CO<sub>2</sub> concentrations have little effect on U transport at pH 6, but significantly affect transport at pH values of 8 and 10.

With the exception of the pH 10 fluids containing CO<sub>2</sub>, at all other nodes (not shown; see Viani et al. 1997) U concentrations are very low, and C/C<sub>0</sub> are less than  $10^{-5}$ , except for the pH 8, 10x atm CO<sub>2</sub> fluid at 30 cm (12 in.) (C/C<sub>0</sub> of about 0.01).

### 11.4.3.3 Geochemical and Mineralogical Studies in the Altered Zone

Several research studies were reviewed that contribute to the methodology employed in making and assessing the accuracy of expected long-term simulations of geochemical processes in the altered zone. Results of laboratory studies, thermal field testing, and simulations supporting the geochemical and mineralogical evolution are described briefly. By comparison with the near-field environment, the altered-zone environment presents the simpler and more traditional case of water-rock interactions. Related discussions of site geochemistry and mineral stability are also presented in Section 5 and CRWMS M&O (1998c, Section 6.1.6).

#### 11.4.3.3.1 Hydrothermal Alteration of Devitrified and Vitric Tuffs

A series of hydrothermal experiments were conducted in which samples of Topopah Spring tuffs (vitric and devitrified tuffs) were reacted with well J-13 water (e.g., Knauss et al. 1985; Knauss and Peifer 1986; Knauss et al. 1987; Knauss 1987). In these experiments, temperatures ranged between 90° and 350°C for times up to 303 days. Detailed analyses were made of the evolving fluid chemistry (fluid samples were taken during the runs) and of the mineralogy and chemistry of the reacted tuffs (analyzed after completion of the runs). Zeolites were identified as alteration products in most of the runs at 150° and 250°C (mordenite and dachiardite in runs with devitrified tuff, clinoptilolite in runs with vitric tuff). No zeolites were observed forming in runs at 90°C. Reaction of naturally zeolitized tuff at 90° and 150°C resulted in a change in the composition of the zeolite heulandite. This became more K-rich, but did not show evidence of dissolution. Around 90°C and below, zeolites appear to be slow to form on laboratory time scales. The most prominent change in the water chemistries was the increase in the concentration of aqueous silica. In systems with devitrified tuff, this concentration appears to be controlled by cristobalite solubility. In systems with vitric tuff, the aqueous silica concentrations are higher, approaching the solubility of amorphous silica. More detailed information on the experimental details and results can be found in the literature cited above.

Reasonably successful simulation models of many of these tuff-water interaction experiments were developed using EQ3/6 (e.g., Wolery et al. 1990; Wolery 1992a, 1992b; Daveler and Wolery 1992; Wolery and Daveler 1992). Delany (1985) reported the first successful model of this type for the 150°C run of Knauss et al. (1985) with devitrified tuff. A major feature of these models is the incorporation of kinetics and thermodynamic disequilibrium as opposed to complete equilibrium. Similar models were reported in subsequent reports by Knauss and coworkers describing tuff-water experiments.

#### 11.4.3.3.2 Evaporation of Synthetic J-13 Water

The J-13 well water was synthesized (Al and Fe were not included) and a series of open system evaporation experiments were conducted (Rosenberg et al. 1999). Subboiling temperatures were maintained and evaporation was permitted with and without crushed tuff present. Aqueous samples were collected and chemically analyzed to document the evaporative chemical evolution, and solids were characterized for mineral identification. In one experiment, 30 L of synthetic J-13 well water was evaporated to approximately 30 mL. The analyzed solids were identified by x-ray diffraction to be amorphous silica, aragonite, and calcite. The solution was then allowed to completely evaporate, and analysis of the solids additionally revealed halite, niter, and thermonatrite, and possibly gypsum, anhydrite, and hectorite. The solution analyses, after concentrating by about 1,000 times, indicated Ca and Mg precipitated, presumably as carbonates, while Na, K, and SiO<sub>2</sub> remained in solution, and Cl, F, NO<sub>3</sub>, and SO<sub>4</sub> remained in solution in nearly identical ratios. The solution pH stabilized at about 10. Experiments comparing the presence of tuff appeared to have little effect on the relative distribution of the anions in solution, except for possibly F, which had a relatively lower concentration ratio. The SiO<sub>2</sub> was lower in the solutions with tuff present suggesting that the tuff enhances SiO<sub>2</sub> precipitation. Calculations were performed on synthetic J-13 water to determine speciation-solubility and to simulate the evaporative evolution. Generally good agreement between the

modeling and experimental results has been demonstrated, even though there are limitations on the tools available for modeling highly concentrated salt solutions (e.g., thermodynamic databases).

#### 11.4.3.3.3 Field Observations

Several compilations of relevant Yucca Mountain water samples have been gathered and reported. They include chemical analyses for saturated zone waters, perched waters, tuff pore waters, and fracture waters (e.g. Harrar et al. 1990, Section 5.3 of this document). For modeling purposes, a single representative composition is required that best reflects ambient mobile waters potentially in contact with rock and introduced materials. Traditionally, the Yucca Mountain program has supported the use of an average J-13 well water composition (Harrar et al. 1990). Various water compositions from the targeted potential repository units would be preferred, but fracture waters and perched waters have not been collected and pore waters from the welded tuffs have not been available.

Recently, water samples have been obtained from new sources. Pore water samples have been extracted from the Tpt welded tuffs of the repository-equivalent rock. Also, from the thermal field test programs, condensate waters have been collected from boreholes intersecting heated rock mass. The condensate samples are not expected to replace the reference waters in chemical modeling, but they will be an important contribution to the simulations recorded for the thermally perturbed system (e.g., CRWMS M&O 2000d, pp. 58 to 60). The major cation and anion constituents have been measured for these samples.

Three pore water samples (from ambient welded Tpt tuff) were found to be concentrated in sulfate and chloride anions with high Ca and silica. The pH values measured for several samples were in the range of 7.6 to 8.39. Water samples were also collected from packer-instrumented boreholes on four occasions during the heating phase of the Single Heater Test, and several samples have been similarly collected during the heating phase of the Drift Scale Test. These thermal test waters have a wide range of characteristics, but in general are indicative of condensate waters reacted with rock and probably reacted with fracture minerals (CRWMS M&O 2000d, p. 58). Chemical analyses reveal aqueous SiO<sub>2</sub> concentrations are similar to or much higher than those in the pore water, but Cl and SO<sub>4</sub> are lower and pH is lower, suggesting that these waters are not simple mixtures of pore water and pure condensate. Waters from the thermal field tests are generally more dilute than perched waters or J-13 well waters. The field test waters also tend to have somewhat higher pH values (6.8-7.4).

Coupled thermohydrologic-chemical modeling of these condensate waters from the thermal field tests (CRWMS M&O 2000d) has demonstrated that a full suite of minerals (feldspars, clays, zeolites, silica phases, calcite, and gypsum) is usually required to reproduce the chemical character of the samples taken. However, it is primarily the CO<sub>2</sub> partial pressures, temperature, and interactions with calcite in the fractures that appear to control the pH.

Gases sampled from boreholes of the Drift Scale Test were also collected during the heating stage and analyzed for CO<sub>2</sub>. The gases are sampled through tubing that extends into different heated regions that have been isolated in the borehole by high temperature packers. The early

indications from the gas samples suggest that, as temperatures in the rock increase and approach boiling, CO<sub>2</sub> concentrations in the gas phase increase. This is consistent with pore water degassing and/or calcite dissolution. As the temperatures increase above boiling, the gas analyses demonstrate a decrease in CO<sub>2</sub> concentrations; this is consistent with replacement of air by water vapor (change in the air-mass fraction) and the loss of an aqueous reservoir from which to draw CO<sub>2</sub> (CRWMS M&O 2000d, pp. 45 to 56).

#### 11.4.3.3.4 Overview of Sorptive Properties in Ion Exchangers

The waste container is expected to prevent the movement of Cs and Sr out of the potential repository during the potential repository's early years, when their radioactivity is high. However, to consider the effects of early waste canister failure, it is necessary to be able to model ion exchange at the varying chemical, temperature, and water saturation regimes present in the repository during those times. Determining changes in the sorptive properties of zeolites, such as clinoptilolite, requires the means to simulate ion-exchange behavior at elevated temperatures if sorption is to be considered as a barrier in the altered zone warm regions.

Ion-exchange modeling will also be required to understand the transport behavior of long-lived radionuclides that are cationic, such as U and Np. Because the intracrystalline channels in clinoptilolite are approximately the same size as hydrated U and Np, sorption of U and Np is thought to be restricted to the external surfaces of the mineral, and not involve cation exchange. However, short-term (less than 1 mo.) batch sorption experiments that have been undertaken to date are not sufficient to rule out intracrystalline diffusion-limited ion exchange as a potential mechanism of sorption for uranyl and neptunyl cations. If and when a definitive test of this hypothesis is made, ion-exchange models may, in fact, prove necessary for modeling the potential of the zeolitic-bearing formations to retard U and/or Np. In contrast to clinoptilolite, sorption of uranyl and neptunyl cations on smectite and other minerals having accessible exchange sites has been shown to be controlled in part by ion exchange. Cation exchange models will be required to assess the effect of smectite precipitation during hydrothermal alteration of repository rocks and near-repository rocks on U and Np transport.

Finally, the ability to effectively model radionuclide adsorption using cation exchange models requires the ability to effectively model Ca, Mg, Na, and K exchange. Because the latter elements are closely connected to mineral alteration and mineral dehydration, cation exchange models will ultimately be necessary for both coupled thermal-hydrologic-chemical and thermal-mechanical calculations.

Clinoptilolite is the most abundant cation exchanger at Yucca Mountain. Its cation exchange properties will affect the partitioning of radionuclides between fluid and solid phases. Solid-solution models simulate the stability of clinoptilolite and its compositional changes during dissolution-precipitation, and are necessary to compute changes in clinoptilolite compositions during reaction path modeling simulations. The Vanselow and Gapon convention cation exchange models have been added to the geochemical modeling code EQ3/6, allowing exchange to be modeled for up to three independent sites. Solid-solution models that are numerically equivalent to the ion-exchange models were derived and also implemented in the codes.

Tests of the ion-exchange option model show that simulated adsorption isotherms closely match experimental data, and suggest that the adsorption of trace quantities of Cs and Sr at 25°C can be adequately modeled using a simple single-site model and available cation exchange data. There is good agreement between model prediction and measurement for Sr sorption over a wide range in  $K_d$  values. For Cs, the model underestimates  $K_d$  values for most of the smectite-rich samples and for samples with low cation-exchange capabilities. However, further work by Viani and Bruton (1996) has successfully simulated high-affinity exchange sites for Cs on smectite and illite.

Simulations show that sorption is very sensitive to clinoptilolite composition and that any attempt to obtain a statistical correlation between clinoptilolite abundance and measured  $K_d$  will be confounded by the compositional dependence. This finding also means that changes in clinoptilolite composition that might arise from interactions with potential repository components must be considered when predicting sorptive capacity. For example, if fluids interact with Ca-rich cement (a possibility in certain potential repository design proposals), migrate into surrounding host rock, and cause host rock clinoptilolites to become more Ca-rich, the sorptive capacity for radionuclides would decrease. The generally good agreement between model predictions and sorption measurements means that the mineralogical database (Bish and Chipera 1989; Broxton et al. 1986) can be used to predict Cs and Sr  $K_d$  values for tuffs for which sorption data is lacking. Application of the exchange model will also allow predictions to be made concerning the effects of temperature and solution composition on sorption, which are required to model the long-term sorptive behavior of clinoptilolite. The calculations suggest that the models are in accord with available high-temperature data. Calculations of the partition coefficients for Cs and Sr on clinoptilolite as a function of temperature suggest that increasing temperature decreases the tendency for Cs to sorb onto clinoptilolite, but favors sorption of Sr.

The studies mentioned here are reviewed in CRWMS M&O (1998c, Section 7.5.3.3). Because potential repository designs emphasize containment of potentially early-released radionuclides with high levels of radioactivity (e.g., Cs and Sr), the issues are not addressed in this section any further. Section 10 contains a discussion of factors affecting radionuclide transport.

#### **11.4.3.3.5 Natural Analogs To Gain Confidence in Geochemical Modeling**

Natural analogs help constrain model predictions that are based on chemical experiments, kinetics, and thermodynamics. In CRWMS M&O (1998c, Section 6.1.6.3), Yellowstone caldera and Yucca Mountain itself are discussed as analogs for future behavior of a potential repository. Bruton, Glassley et al. (1995) discuss the potential for using geothermal areas, such as those in the Taupo Volcanic Zone in New Zealand, as natural analogs to many of the processes that are anticipated to occur in the postemplacement environment at Yucca Mountain. The ability of the EQ3/6 software and the GEMBOCHS thermodynamic databases (Wolery 1992a, 1992b; Daveler and Wolery 1992; Wolery and Daveler 1992) to simulate groundwater-tuff interactions in the postemplacement environment at the potential Yucca Mountain repository was tested in high-temperature (greater than 200°C) systems using comparisons between observed equilibria and simulations of field relations in the Wairakei geothermal system. High-temperature systems were chosen in the initial studies because those systems are generally considered to be in equilibrium, but the magnitude and types of observed water-rock-gas interactions in these

systems do not represent conditions of the Yucca Mountain system. These analogs are generally high temperature and full liquid saturation, and a Yucca Mountain potential repository would be in the unsaturated zone with lower temperatures. Nevertheless, once confidence is gained in the ability to model systems in equilibrium, the codes can be tested in lower temperature systems in which kinetics is introduced as an additional variable.

The natural systems were used to test:

- Under what conditions and in what manner EQ3/6 can be used to forecast changes in rock and fluid chemistry during the flow of heated fluids through silicic rocks
- The thermodynamic data in GEMBOCHS and to select appropriate thermodynamic data when multiple sources exist, for use in predicting mineralogical and fluid chemistry changes in the near field and altered zone of the potential Yucca Mountain repository.

The work conducted addresses mineral equilibria and fluid chemistry in the Wairakei geothermal field at temperatures of about 250°C. Petrologic studies by Reyes et al. (1994) of mineral relations and fluid chemistry at 100° to 200°C at the Wairakei and Kawerau geothermal fields revealed a variety of zeolites (e.g., clinoptilolite, mordenite, stilbite, and dachiardite) that would enable further testing of the codes and thermodynamic databases at lower temperatures. Such simulations are especially required because of the need to address kinetic constraints on mineral precipitation and dissolution in lower temperature systems, and to resolve discrepancies in predicting zeolite stability in relation to other nonzeolite aluminosilicates (Viani and Bruton 1992). CRWMS M&O (1998c) provides details of the studies.

Testing of the codes and databases involved:

- Selection of representative water and gas compositions from Wairakei wells
- Reconstruction of downhole fluid compositions
- Calculation of the minerals predicted to be in equilibrium with each fluid
- Comparison of simulation results with observed vein and vug mineralogy.

Trends in water and gas chemistries and well discharge characteristics over time were analyzed. A set of representative water and gas analyses were identified from zones producing at about 250°C from three wells. The most common vein minerals at this temperature are wairakite, adularia, epidote, quartz, albite, chlorite, calcite, and prehnite (Reyes et al. 1993), which have been identified in the following assemblages:

- Wairakite
- Adularia (a variety of potassium-feldspar)
- Epidote solid solution
- Wairakite ± quartz
- Quartz + adularia
- Wairakite + epidote ± calcite
- Albite + quartz + epidote + chlorite + calcite
- Prehnite

- Wairakite + prehnite.

Calculations were carried out using EQ3, EQ6, and GEMBOCHS. Thermodynamic databases using different data for Al aqueous species and quartz solubility were used to identify the data set that produced the best matches between observed and calculated equilibria.

#### 11.4.3.3.5.1 Water-Rock Equilibrium Calculations

Geochemical calculations with EQ3/6 using measured Al concentrations and thermodynamic data for Al aqueous species from Pokrovskii and Helgeson (1995) combined with quartz solubility data from Fournier (1983) suggest that vein minerals are presently in equilibrium with subsurface fluids (Figure 11.4-9) in Wairakei producing zones. Good agreement is indicated when the affinity-temperature curves of observed minerals converge on zero at the measured downhole temperature. Matrix replacement minerals, although of much greater variety and number than vein minerals owing to initial rock mineralogy (Reyes et al. 1993), are consistent with calculated mineral stabilities at downhole temperatures.

One of the greatest areas of uncertainty in predicting the stability of aluminosilicate minerals involves the Al system and measurements of Al concentration in natural waters, as well as the thermodynamic data for Al aqueous complexes. The temperatures of the geothermal systems at Wairakei are sufficiently high to yield significant, measurable quantities of Al in solution. Combined with the observed stability of varied aluminosilicate minerals, these data can be used to test available thermodynamic data for Al aqueous complexes. Simulations were made using the SUPCRT92 (Johnson, J.W. et al. 1992) and Pokrovskii and Helgeson (1995) databases. Aluminum data from Pokrovskii and Helgeson (1995) reproduced observed mineral equilibria quite well; that of SUPCRT92 did not. Measured Al concentrations were used in these calculations; they were not automatically set using mineral equilibria as is often done (e.g., Bowers and Burns 1990; Chipera et al. 1995).

Given the above results, thermodynamic data for aqueous Al should be sourced from Pokrovskii and Helgeson (1995). That is, the Pokrovskii and Helgeson (1995) Al data best serve for use with the thermodynamic data of aluminosilicate minerals used in the study (from SUPCRT92 database). Further simulations in the range of 100° to 200°C should evaluate the Al databases at lower temperature. However, less discrepancy may be observed at lower temperatures because of convergence of the equilibrium constants for the  $Al^{3+}/AlO_2^-$  reaction at lower temperatures.

Wairakite, a high-temperature calcium-zeolite, is predicted to be about 1 to 1.5 kcal/mol undersaturated at about 250°C. In contrast, wairakite commonly occurs as a secondary mineral at 240° to 260°C at Wairakei. Therefore, the calculations suggest that the free energy of formation from the elements of wairakite at 25°C should be decreased by about 1 to 1.5 kcal/mol at about 250°C to increase its stability. Such a correction would equilibrate wairakite under downhole conditions. Thermodynamic data for wairakite may not seem to be relevant to the YMP. However, given the uncertainty in thermodynamic data for lower-temperature zeolites (e.g., clinoptilolite and mordenite) in comparison to other nonzeolitic aluminosilicates, it is useful to be able to ensure data reliability for one zeolite from which to reference other zeolites. Calculations of zeolite stability using calorimetric data for clinoptilolite, stilbite, and mesolite

(Johnson, G.K. et al. 1991; Howell et al. 1990) appear to overestimate the stability of these zeolites at temperatures greater than 200°C.

#### **11.4.3.3.5.2 EQ3/6 as a Predictive Tool**

A striking feature of the affinity-temperature diagrams constructed for the Wairakei wells (e.g., Figure 11.4-9) is that a number of minerals are close to equilibrium with downhole fluids (Glassley 1996, Figure 3.4-21). This might explain the wide variety of mineral assemblages observed at Wairakei. However, all assemblages are composed of different combinations of the same set of minerals. This common phenomenon is expressed by the metamorphic facies concept. It is rarely, if ever, feasible to use EQ3/6 to predict the exact assemblage of silicate minerals in equilibrium with a given fluid. Such a calculation can easily go awry if a mineral's thermodynamic data causes its stability to be overestimated, or if the code chooses a precipitate that is inappropriate because of kinetic constraints. It is, however, quite reasonable to use EQ3/6, when tempered with field and laboratory data and common sense, to establish facies of minerals that would be expected to precipitate under given conditions. Affinity-temperature diagrams are especially useful in this regard.

#### **11.4.3.3.5.3 Vein/Vug versus Matrix Mineralogy and Mineral Assemblages**

Solution composition and temperature control the stabilities of fracture-filling, vein-filling, and vug-filling minerals at Wairakei with apparently limited control by the matrix. Alteration minerals in veins and vugs are the same as those found as replacement minerals in the matrix, but they occur in assemblages composed of fewer phases. It is striking that vein and vug fills, which obviously have precipitated from solution, are characterized by one to three secondary minerals, fewer than the number of different replacement minerals in the matrix as a whole. The above findings suggest that the fractures, veins, and vugs represent fluid-dominated systems, whereas the matrix represents a rock-dominated system.

Petrographic observations suggest that the minerals replacing plagioclase in the matrix are common in fracture-vein-vug mineralogy; both seem to be Ca-dominated systems. At this time, the working hypothesis is that vein mineralogy is controlled mainly by fluid chemistry in the flowing system with negligible interaction with the host rock. The number of fracture-filling minerals may be controlled by the phase rule for mobile components.

In the postreplacement environment at Yucca Mountain, replacement mineralogy in the matrix would be expected to be controlled by temperature and primary mineralogy, provided sufficient water is present to effect such changes. On the other hand, the stability of minerals along flow paths (e.g., fractures) would be controlled by the evolution of water composition, as well as temperature. Factors that could affect water composition include boiling-condensation, interactions with cementitious and other manufactured materials, including metal waste package components, and so on.

The degree of mass transfer between matrix and fractures and the extent to which the bulk rock, or matrix, changes composition during alteration should be further examined in the New Zealand systems. If there is limited chemical exchange between the matrix and fractures, mineral

dissolution-precipitation during fluid flow in coupled hydrogeochemical models can be simulated much more simply because diffusion to and from the matrix does not have to be considered.

#### **11.4.3.3.6 Kinetics of Amorphous Silica Precipitation**

Dissolution of silica ( $\text{SiO}_2$ ) in response to water movement at elevated temperatures and subsequent precipitation of silica on cooling may significantly affect local porosity and permeability. Changes in porosity and permeability will, in turn, affect flow pathways, imbibition of water into the rock matrix, and heat transfer.

To ascertain how quickly alteration of the near-field environment and altered-zone environment will occur, it is necessary to rigorously determine the dissolution and precipitation rates of minerals that are present and to determine the formation rates of other minerals that may form in the future. Some laboratory measurements have been conducted using pure mineral phases and simple, controlled solutions. However, it has often been noted that inferences of rates from field measurements are not consistent with laboratory measurements.

Amorphous silica will play an important role in the evolution of the Yucca Mountain system (e.g., Wilder 1996). Carroll et al. (1998) measured the precipitation rate of this substance at the Wairakei geothermal borefield in New Zealand. The same report summarizes measured rates of amorphous silica precipitation in the laboratory at 60° to 120°C over a range of silica concentration. The measured field rates were compared to predictions based on the laboratory studies. It was the first stage of an effort to place bounds on kinetic effects.

This study confirmed the need for complementary laboratory and field studies of the factors that control mineral-water interactions in tuff. Amorphous silica precipitation rates appeared to be controlled by distinct mechanisms in laboratory versus field studies. Rates from the Wairakei field study were 10 to 300 times higher than those predicted from laboratory experiments. The deviation in rates increased with increasing degree of supersaturation and may have been influenced by the presence of dissolved solutes, such as Al. The field rates may be accelerated by surface defect-surface nucleation effects associated with the incorporation of trace amounts of Al into the precipitate. Further laboratory studies are required to evaluate this hypothesis.

These results indicate that laboratory measurements of precipitation rates may significantly underestimate the rates at which amorphous silica will form in the natural system when perturbed by potential repository heat. The laboratory precipitation rate constants obtained by Carroll et al. (1998) are consistent with those reported by Rimstidt and Barnes (1980). These constants may be used to obtain lower bounds on the rate of amorphous silica precipitation in silica redistribution at Yucca Mountain. However, until a more detailed rate model that explains both field and laboratory measurements becomes available, field-based rate constants should be used to obtain upper limits on the rate of such precipitation.

#### **11.4.3.3.7 Simulations of Fluid-Rock Interactions**

The experimental/modeling studies that are described were used to test models and their thermodynamic/kinetic data. As observed for the natural analog studies (Section 11.3.3.5), these

systems do not necessarily reflect the anticipated repository conditions of a thermally perturbed Yucca Mountain. These temperatures are often higher and the rock may be fully saturated in contrast to anticipated conditions. Thus, the full suite of mineralogic changes reported from these cited results may not all be representative of changes at Yucca Mountain. However, the ability to model such systems builds confidence in testing codes under conditions more like those anticipated for a Yucca Mountain repository.

#### 11.4.3.3.7.1 Thermal-Hydrologic-Chemical Modeling of Thermal Field Tests

Coupled thermal-hydrologic-chemical processes have been modeled for thermal field test studies (e.g., the Drift Scale Test) and thermal-hydrologic-chemical seepage studies (CRWMS M&O 2000d). Assessing the potential effects of the coupled thermal-hydrologic-chemical processes on the unsaturated zone flow and transport are the desired end. Simulations of the thermal-hydrologic-chemical processes encompassed in the reported Drift Scale Test coupled processes models include coupling between heat and fluid flow, aqueous and gaseous species transport, kinetic and equilibrium mineral-water reactions, and feedback of mineral precipitation/dissolution on porosity, permeability, and capillary pressure for a dual-permeability system (CRWMS M&O 2000d, p. 101). The thermal-hydrologic-chemical seepage model incorporated the most current repository design to represent heat transfer within a drift and the thermal-hydrologic-chemical processes in the near field environment.

The results from the Drift Scale Test thermal-hydrologic-chemical model simulations were reported for gas-phase concentrations of CO<sub>2</sub> and the chemistry of waters collected from boreholes during the first 2 yr. of heating (see Section 11.4.3.3.3). The initial rise measured in the CO<sub>2</sub> concentrations with temperature in borehole intervals was clearly captured by the model, even among boreholes with very different thermal histories. However, a discrepancy among the modeled and measured concentrations revealed the need to make a correction to the air mass fraction of the gas phase. During the initial stages of boiling, the collected gas sample was necessarily dried of water as the sample was being collected. This caused shift in the CO<sub>2</sub>/air ratio. As a consequence, the model gas concentration was very different than the measured gas concentrations based on a dry gas composition. An estimated correction made for the change in air mass fraction brought the model and field results more in line.

The water chemistry and the CO<sub>2</sub> concentrations in the gas phase were also compared and the general evolution of the Drift Scale Test waters has been able to be described by a relatively small set of aqueous species, minerals, and gas phase CO<sub>2</sub>. Minerals, including calcite, silica phases, and gypsum, were the most significant, whereas the addition of aluminosilicates (e.g., feldspars, clays, and zeolites) caused more rapid shifts in the water chemistry than were observed. Considering longer time intervals than the Drift Scale Test, the evolution could trend in the direction of the more complex system chemistry (e.g., Al, Fe, F).

The thermal-hydrologic-chemical seepage model evaluated a number of cases for different calibrated property sets, climatic changes, and geochemical systems (CRWMS M&O 2000d). Results during the early phase of heating and during dryout were similar to those observed in the Drift Scale Test, although the rewetting period (which has not yet begun) could not be compared. The thermal-hydrologic-chemical seepage model simulations indicate that there may be an

increase in the CO<sub>2</sub> gas and aqueous carbonate concentrations around the drift during rewetting (CRWMS M&O 2000d, p. 101). There were also some differences in the pH and CO<sub>2</sub> concentrations similar to the Drift Scale Test thermal-hydrologic-chemical modeling. Again, the system evaluated without the aluminosilicates is supported over the short period of heating of the thermal test (CRWMS M&O 2000d, p. 102).

#### 11.4.3.3.7.2 Reactive Transport Simulations of Tuff-Water Interactions

Thermal gradients and resultant advective mass transport within the altered-zone environment will invariably lead to porosity evolution as a consequence of reaction-controlled mineral dissolution and precipitation both along fractures and within bounding matrix blocks. Preliminary reactive transport modeling with the GIMRT code (Steeffel and Yabusaki 1996) has suggested that these processes result in modification of flow porosity both above and below the potential repository, which may be important (Glassley 1995; Hardin 1998b, Section 6.2.2).

Reactive transport simulations can be viewed as an iterative, five-stage process, in which the steps are:

- Precise specification of the initial chemical and hydrologic state of the fluid-rock system
- Translation (which often includes approximation) of the specifications into the analogous model parameters of the software
- Specification of certain system-independent numerical parameters (e.g., fundamental thermodynamic and kinetic data)
- Successful execution of the software
- Interpretation of calculated results.

Using this five-stage process, the approach taken in this study was to first establish the validity of the software-encoded numerical model by successfully predicting the outcome of two well-characterized, experimentally verifiable benchmark problems. Next, increasingly complex yet still experimentally verifiable problems having some relevance to porosity evolution in the backfill zone were addressed. Finally, a critical simulation of long-term porosity evolution in the altered-zone environment that cannot be addressed directly by physical experiment was conducted by modeling. These benchmark comparisons are reported in more detail in Wilder (1996, Section 10.4.4.1) and provide some confidence that the results are realistic, if not exact.

**Compositional Specifications and Parameterization of the Altered-Zone Environment**—The composition and relative abundance of mineral phases in the potential repository host rock (TSw2) were determined by Warren et al. (1984) and translated into model compositions-abundances by Delany (1985) for use in EQ3/6 calculations. (Section 4 contains additional data on tuff composition at Yucca Mountain.) The GIMRT code (Steeffel and Yabusaki 1996), unlike EQ3/6, is not yet configured to account for solid solutions. Therefore, to use this code, it is necessary to further approximate Delany's (1985) model TSw2 mineralogy by resolving its alkali feldspar and plagioclase compositions into the corresponding end-member potassium-feldspar,

albite, and anorthite components. Magnesium-beidellite and biotite compositions compose only 1.1 volume percent of the TSw2, and they represent the only Mg-bearing and Fe-bearing phases in the system. In these preliminary simulations, magnesium-beidellite and biotite were eliminated from the model tuff composition.

The fluid phase anticipated to form within and react with the TSw2 in the altered-zone environment is derived from condensation of a vapor phase moving radially outward from the potential repository. This condensate is likely to be a highly dilute, neutral-pH fluid. The fluid was modeled to initially contain very low concentrations of aqueous ions and complexes augmented by the additional component CO<sub>2</sub>, which is necessary due to the presence of atmospheric gases. The initial fluid composition, specified as the log molal concentration of basis species is much more dilute than J-13 water, reflecting its condensation from a vapor phase.

The thermodynamic database employed was contained in the file MASTERTEMP.DATA, which is a reformatted version of the composite database distributed with the EQ3/6 software package (Wolery 1992a; Daveler and Wolery 1992). The reactive transport modeling is therefore consistent with the EQ3/6 modeling, in the sense that the same supporting data are generally used.

Tuff-water reactions relevant to both the near-field and altered-zone environments were addressed in the work discussed in this section. The first set of simulations was initially aimed at the localized, interior backfill environment, which is part of the near-field environment. A primary goal of this initial round of simulations was to compare the results of GIMRT simulations with a laboratory experiment using a 31-cm (12-in.) column of crushed tuff and thus confirm the reactive transport modeling approach to tuff-water interactions as a whole. This work, therefore, has indirect relevance to the altered-zone environment. In this context, the simulations and the experiment can be viewed as a kind of accelerated testing (crushing can be viewed as an accelerant). This work is discussed in the present altered-zone environment section rather than in the near-field environment section to maintain continuity of the discussion of the reactive transport modeling methodology. The second set of calculations simulated the larger-scale outlying condensation zone (Buscheck et al. 1993b), where gravity-driven flow of vapor-exsolved fluid represents the most likely mechanism for driving significant, long-term porosity evolution in the altered-zone environment.

**Simulations with a 31-cm (12-in.) Column of Crushed Tuff**—The first set of simulations involved crushed welded tuff material having an initial porosity of 40 percent volume, where a constant outlet flux of 266.7 m/yr. was maintained over 6 mo. Because the porosity of actual backfill material and especially the in situ fluid flux are likely to be lower than the adopted values, the simulations provide an upper bound to the potential magnitude of porosity evolution.

In the first TSw2-backfill simulation, the model system consisted of groundwater flowing through a 31-cm (12-in.) column of crushed tuff at 90°C. Originally, this calculation was intended to model a proposed laboratory experiment. However, the rate of alteration at this temperature over a reasonable time period for an experiment was found to be too small to allow a meaningful comparison of simulation versus experiment. Six months of reactive flow resulted in a relatively uniform but minute increase in porosity (from 40 to about 40.25 volume percent), the

net result of minor dissolution of primary phases and trace precipitation of alteration minerals. This degree of change would be very difficult (perhaps impossible) to quantify in an experiment.

To overcome this problem, a second GIMRT simulation was performed in which a temperature of 250°C was assumed, although liquid water cannot be present at this temperature unless it is confined and under pressure. Therefore, although the simulated experiment is not directly relevant to the potential repository, it does provide a computational model that may be benchmarked against a physical model (i.e., a well-constrained experiment). Subsequently, the reaction rates can be simply extrapolated to temperatures at which liquid would be present (i.e., to potential-repository-relevant temperatures), and the simulation repeated with confidence in the validity of the computed results acquired through the benchmarking exercise. A temperature this high would more likely be attained very close to the canisters in the near-field environment. Values in the range of 100° to 150°C are more likely to represent the highest temperatures in the altered-zone environment. From an altered-zone environment perspective, higher temperature simply accelerates the alteration. Thermodynamic and kinetic considerations suggest that a temperature of 250°C will lead to readily observable porosity evolution and precipitation of alteration phases. Thus, a meaningful comparison of predictive capability and experiment becomes possible. Generally speaking, changes similar to those observed at 250°C would apply to lower temperatures at longer times, though presently there is no simple way to quantify this.

The enhanced solubilities and faster reaction rates of primary TSw2 minerals at the higher temperature and their effect on dissolution (and secondary phase precipitation) are readily apparent. At the inlet node (in the first 1 cm of the column), the fluid is initially undersaturated with all of the primary minerals. Despite concomitant precipitation of kaolinite, whose reaction rate and volume fraction ultimately attain 50 volume percent/yr. and 14 volume percent, respectively, the near-complete consumption of cristobalite, albite, and quartz causes porosity to increase from 40 to 70 percent at the inlet node (Figure 11.4-10). It also results in the late marked decline in saturation indices for these and all other silica-bearing phases. The 6-mo. outlet porosity has decreased from 40 to 38.8 percent.

The gradient in dissolution-precipitation behavior is expected to be sharpest across the first few nodes, where the fluid concentration gradient is steep. This is exactly the case. The region of enhanced porosity is restricted to the first few nodes and is characterized by very steep gradients, whereas the region of reduced porosity accounts for roughly 90 volume percent of the reaction domain and is characterized by much subtler variations.

To better illustrate the application of reactive transport modeling to the altered-zone environment, another GIMRT simulation was made for a 10-m (33 ft) column of tuff. The temperature is 95°C in the first 5 m (16 ft); thereafter, the temperature is decreased 1°C/m. The temporal evolution of mineral saturation indices at the inlet (0.25 m [0.82 ft]) and outlet (10 m [33 ft]) nodes is shown in Figures 11.4-11 and 11.4-12, respectively. Initial steady-state mineral saturation indices are attained after about 1 mo., during which time the fluid obtains supersaturation with quartz and the secondary phases kaolinite and pyrophyllite. However, it remains undersaturated with respect to cristobalite (and the primary feldspars) throughout the reaction domain. As a result, over the entire flow path, cristobalite (and the feldspars) will dissolve, whereas quartz, kaolinite, and pyrophyllite will precipitate. Given the relatively

sluggish dissolution rates of the feldspars at 95°C, dissolution of these primary sources of Al and consequent precipitation of kaolinite and pyrophyllite (Al sinks) will be very minor. Hence, the fundamental mechanism of porosity evolution in this environment is principally the replacement of cristobalite by quartz. At the inlet node, cristobalite becomes completely dissolved at about 650 yr. The dilute inlet fluid then begins to dissolve quartz, which disappears completely after 3.1 k.y. The fluid then begins to dissolve albite.

Figures 11.4-13 and 11.4-14 illustrate the output of GIMRT as time-integrated spatial variations in porosity and mineral volume fractions at 100 and 1,000 yr. (the calculation proceeded to 10 k.y.). The complete replacement of cristobalite (initial volume fraction = 39.6 percent) by quartz throughout the reaction domain leads directly to a background increase in porosity from 11 to about 16 percent after roughly 3.1 k.y. Superimposed is a secondary porosity enhancement, resulting from quartz dissolution (initiated following complete cristobalite consumption) at the first few inlet nodes, beginning with the inlet node at 650 yr. Because the 90° to 95°C dissolution rate of quartz is only about 40 percent that of cristobalite, it takes the dilute inlet fluid roughly 2.5 k.y. to completely dissolve the inlet-node quartz from its maximum concentration (29 volume percent), which coincided with cristobalite disappearance at 650 yr. This secondary quartz dissolution front advances quite slowly, and the advection of quartz-derived SiO<sub>2</sub> maintains nearly uniform levels of slight quartz supersaturation and resultant minor quartz precipitation over the entire downstream reaction domain. As a result, this secondary porosity enhancement is characterized by steep gradients that advance downstream very slowly.

Important implications for the postemplacement evolution of porosity in the altered-zone environment can be drawn from this simulation. First, thermodynamic, kinetic, and volumetric constraints strongly suggest that long-term (greater than 3 k.y.), gravity-driven flow of vapor-derived dilute condensate at 90° to 95°C could result in nearly 50 percent enhancement of the porosity (from 11 to 16 percent) as a consequence of mole-for-mole, quartz-for-cristobalite replacement. Should this local condensation zone persist for longer time periods, the in situ porosity may further increase dramatically, albeit slowly, to more than 65 percent by volume as quartz dissolution occurs. It is conceivable, if not likely, that the postemplacement altered-zone environment could evolve toward extreme porosity heterogeneity, characterized by relatively large porosities in the condensation-zone cap above the potential repository and relatively low porosities (which nevertheless exceed preemplacement porosity) in the outlying margins of this cap. These extremes may be joined by a narrow, steep-gradient interface. All dissolved silica may eventually precipitate farther downstream, presuming gravity-driven flow continues down thermal gradients. Hence, it is anticipated that a zone of very low (less-than-ambient) porosity may develop at depth, perhaps below and radially outward from the potential repository. Porosity may also decrease above the condensate cap.

**Conclusions**—Recognizing the abundance of compositional and hydrologic approximations, and the simplifications that are necessarily embodied in these still-preliminary models, they nevertheless serve to illustrate the time scales (thousands of years) and geochemical processes (e.g., cristobalite-for-quartz replacement) likely to govern active evolution of the altered-zone environment. They can also be used to suggest the potential for distant-future porosity distributions that are critically important. Initial modeling efforts suggest that postemplacement reactive transport will lead to porosity enhancement in the altered-zone environment, as in the

condensation cap overlying the potential repository. Some short-term field studies and related modeling do not necessarily show significant porosity changes due to redistribution of silica. Additional study would be needed to confirm or contradict this effect. Further modeling of fluid transport to regions below the emplacement drifts will evaluate the extent to which flow barriers may form due to porosity reduction.

#### 11.4.3.3.7.3 Range of Expected Groundwater Chemistry and Secondary Minerals

EQ3/6 simulations of tuff-water reaction were conducted at various temperatures to establish how the mineralogy and water chemistry would evolve as a function of time.

Heat-driven evaporation, boiling, and condensation processes will lead to movement of water vapor away from the potential repository. This will result in increased hydrologic saturation of some rocks in parts of the repository block (Nitao 1988; Buscheck and Nitao 1992; Buscheck et al. 1993a). The saturation may approach 100 percent by volume under some operation scenarios after waste is emplaced. During cooldown, or as a result of fracture flow or dehydration of hydrous minerals, it is possible that liquid water may return to regions in the near-field environment and altered-zone environment from which it had earlier been driven out.

Most minerals currently present in the rock making up the potential repository horizon are not in thermodynamic equilibrium with water (of more or less any likely composition) at elevated temperatures, nor is the glassy material preserved within the PTn or the TSw3 units. As a result, water will interact with existing minerals and glass, causing new minerals to form, existing minerals to change their compositions or dissolve, and water chemistry to be modified in the process.

The EQ3/6 simulations are described in greater detail in Hardin (1998b, Section 5.3). They were made using two tuffs: TSw2 tuff (devitrified, repository horizon) and TSw3 (glass, the underlying vitrophyre). Each tuff was reacted with average J-13 well water as reported by Harrar et al. (1990). The O<sub>2</sub> and CO<sub>2</sub> partial pressures were fixed at atmospheric values. Hardin (1998b, Section 5.3) contains details concerning the rate models. To account for uncertainty in the rates at which reactions may proceed, simulations were conducted to ensure that rate constants of dissolution and precipitation reactions would have an error of plus or minus an order of magnitude.

The extent to which reactions will progress in the near-field and altered-zone environments may be limited by water availability. If this is the case, the natural systems will progress only partway along the reaction paths suggested by the modeling described here.

**Results**—The water compositions and secondary mineral assemblages obtained at steady-state conditions at a given temperature for the tuffs are constrained by the fixed composition of the starting material and the solubilities of the starting phases. For vitric material, however, dissolution is treated as a congruent (uniform) process; hence, the amount of material dissolved (in other words, the extent of reaction progress) will determine the mineralogical products and water chemistry. In this case, a steady-state composition will not be achieved, except under extreme conditions in which very high absolute amounts of glass are dissolved.

The mineral assemblages described here must be considered as approximate to those that would form in real systems. They may not be correct in terms of the specific identities of the minerals formed. In particular, the occurrence of zeolites, such as mesolite, clinoptilolite, and stilbite, or the occurrence of muscovite in simulations must be taken to indicate that a zeolite(s) and a sheet silicate are expected to form. However, the specific kinds of phases may be difficult to predict because of several factors, including the limitations of existing thermodynamic databases and of models for the formation of solid solution phases.

Throughout reaction progress, saponite (a clay), carbonate, and fluorapatite are present at low abundances at all temperatures. These phases are joined by other clays (celadonite and smectite), a feldspar (microcline), and zeolites (clinoptilolite at low temperature, stilbite at 50° and 75°C, with mesolite present throughout the temperature range), relatively early in the reaction progress period, and they persist to steady-state conditions. The actual appearance time of specific phases depends on temperature. At 40°C, important secondary aluminosilicate phases do not appear until after approximately 100 days of reaction progress. At temperatures greater than 50°C, important aluminosilicates appear within a few days. However, in all cases, steady-state conditions with relatively high abundances of secondary minerals are not approached until thousands of days have elapsed. In all cases, one of the last phases to appear is a silica polymorph (in this case, chalcedony), but once formed, it quickly becomes the most abundant secondary phase. At high temperatures (90°C), garnet and tremolite appear in the secondary mineral assemblage. These phases probably would not be the stable phases that would form under these conditions, given evidence from metamorphic petrology in low-temperature systems. Also, it is not presently clear whether it is realistic to obtain zeolites as precipitates at temperatures much below 150°C.

The initial water composition reflects equilibration of J-13 water at the temperature of the simulation. This includes achieving both homogeneous (internal) equilibrium and heterogeneous equilibrium (involving precipitating minerals to remove supersaturations, save those allowed by the code user). At all temperatures, this initial composition is moderately alkaline (pH of approximately 8.5), oxidizing (theoretical Eh between 580 and 680 mV), and has a low ionic strength (approximately 0.0028 molal). Concentrations of the dissolved elements are low.

Water composition remains relatively constant at a given temperature, until reaction progress reaches approximately 100 days. At that point, the composition changes significantly due to formation of secondary mineral phases, and dissolution of significant quantities of the rock components. Calcium and Mg are both largely removed from solution due to precipitation of carbonates and, to a lesser extent, a variety of silicates.

Sodium, Si, and Al increase significantly, because the amount added to solution by dissolution of the solids is much greater than the amount removed by precipitation. Nevertheless, the final concentration reached for these elements is controlled by the solubilities of the major secondary phases. Silica, for example, is buffered at chalcedony saturation, at steady-state conditions. Therefore, in the altered-zone environment, where temperature and saturation remain relatively stable for long times, it is expected that dissolved silica would closely match the value corresponding to chalcedony saturation. The conservative elements Cl, F, Li, and phosphorus

showed no significant variation during reaction progress because they are not incorporated into any secondary phases that form in significant quantities.

The redox state (as represented by the oxygen fugacity) is effectively determined if the solution is in equilibrium with atmospheric gases. Although this may not be the case within the drifts at early times, it is most likely to be the case in the altered-zone environment. Hence, O<sub>2</sub> is judged to comprise approximately 20 percent by volume of the coexisting gas phase in the altered-zone environment.

Variation in pH is strongly controlled by the fact that CO<sub>2</sub> fugacity is fixed in these simulations. These results differ somewhat from those described from water evaporation modeling in Section 11.4.3.3.7.3. In the latter study, the effect of including rock interaction with water was not considered. The pH remains relatively alkaline when the CO<sub>2</sub> fugacity is controlled by equilibrium with atmospheric gases. Results of the Single Heater Test and early indications from the Drift Scale Test indicate that within the active boiling regime, excess CO<sub>2</sub> is generated by rock-water interactions. This would change the pH conclusions. However, it is unknown whether excess CO<sub>2</sub> will be generated within the altered-zone environment. The CO<sub>2</sub> generated in the boiling zone could be transported into the altered-zone environment, but after the initial thermal perturbation, the excess CO<sub>2</sub> should decrease, a finding consistent with postboiling in the Drift Scale Test.

For dissolution of relatively small volumes of glass, the secondary phases that form during reaction progress are similar to those formed in the tuffs (pyrolusite, clays, and zeolites), except for the respective amounts of secondary phases. These results are qualitatively consistent with the description of glass alteration (Levy 1984a, 1984b) in the vicinity of Yucca Mountain. The main exception is calcite, which persists to the end point of the calculations for all temperatures except 40°C. In contrast, dissolution of large volumes of glass rather quickly achieves a state in which the only secondary phases that are present are pyrolusite, chalcedony, and hematite. In no simulation with vitric material were muscovite or microcline present as reaction products at any temperature.

Water composition in simulations involving small degrees of glass dissolution reached end points that were nearly identical to those for the crystalline tuff-water system. The simulations involving exceptionally large volumes of glass ultimately achieved much higher total concentrations of all elements except Si, which dropped to very low values controlled by large volumes of precipitated chalcedony. In addition, at high degrees of glass dissolution, pH drops, reaching acidic values (approximately 3.8) in the low temperature simulations and slightly alkaline (approximately 7.8) in the 90°C simulation. This pH behavior primarily reflects the effects of temperature, the glass chemistry components, and the solubility of C-bearing aqueous species (e.g., HCO<sub>3</sub><sup>-</sup>) and solids (e.g., calcite) on pH. The low pH values may or may not be real, and appear to be associated with oxidation of minor glass components. If these values are real, they require significant volumes of glass to react with minimal volumes of water. In the altered-zone or near-field environments, it is unlikely this water would play a significant role. In these simulations, total dissolved elemental C decreased by three orders of magnitude.

To evaluate the effects of uncertainty in reaction rate constants on mineral development, simulations were conducted in which sanidine dissolution rate was varied by an order of magnitude (plus or minus). This was done to document the effect of this uncertainty on time predictions of when specific minerals will appear or vanish during the reaction progress. The results shown in Figure 11.4-15 for sanidine abundance demonstrate that the propagated error increases with time, until sanidine vanishes. The error bars represent uncertainty regarding the amount of the mineral present at any given time. The error in predicting when a phase appears or disappears from the model can be substantially greater than the amount predicted. For example, the maximum uncertainty in the amount of sanidine produced is about 50 percent, but the uncertainty of when it is consumed ranges from about -60 to +2,100 percent. The range of negative abundance shown on Figure 11.4-15 does not represent reality, but is an artifact of the plotted uncertainty being treated as a symmetric quantity. It should be noted that the uncertainty in rate constants might be matched or exceeded by the mineral surface area uncertainties that also appear in the rate equations for dissolution and precipitation.

**Conclusions**—These simulations were designed to provide preliminary bounds on the water compositions that could evolve within the altered-zone environment and migrate into the near-field environment, and for bounding the mineralogy that could evolve in the altered-zone environment. The key constraints on which the simulations were based are discussed in more detail in Hardin (1998b, Section 5.3). The results provide bounds on secondary mineralogy and water chemistry that create a baseline that can be refined in the future.

These results document that the timing of mineral development is most sensitive to dissolution kinetics. Precipitation kinetics are usually sufficiently fast that they do not significantly influence mineral development. Exceptions typically involve certain minerals that are generally slow to form (e.g., quartz, dolomite, and hematite). This knowledge allows uncertainty limits to be quantified for mineral development projections based mainly on dissolution kinetics.

These results also complement studies of the thermodynamic properties of mineral phases (Section 11.4.3.3.6) (Bruton 1995) documenting that specific mineral assemblages can be accurately predicted during repository evolution. However, the development of individual mineral compositions is less accurately predicted. The studies also provide quantitative descriptions of the uncertainty expected in simulations of the evolution of the altered-zone environment.

Retardation of radionuclides passing through the altered-zone environment is directly related to the identity and abundance of minerals along the flow path. Radionuclide transport must consider the effects of changing water chemistry as well as the impact of dissolution kinetics and thermodynamic properties on the solution chemistry.

#### **11.4.3.3.7.4 Mineral and Water Chemistry Changes during Evaporation**

Glassley (1994) made computer simulations of water chemistry evolution due to the evaporation of water (Hardin 1998b, Section 6.3.2). At the time water from well J-13 was assumed to be sufficiently similar to the pore-water chemistries to use its chemistry as a proxy for that of the water that would be evaporated from around the emplacement drifts. More recently, actual

pore-water chemistry analyses have become available (Sections 11.4.1.2.1 and 5.3.6.2). Simulations using these water compositions (which are somewhat different from each other) have yet to be performed. However, the calculations presented here generally illustrate the major results that would be obtained for virtually any likely ambient groundwater composition, at least to the 98 percent by volume water removal limit considered here.

Glassley (1994) noted that the results obtained in the simulations of J-13 water evaporation are sensitive to two important factors. The first is whether equilibrium with an overlying gas phase is assumed (which would normally be done for evaporation). If so, the results will depend on the composition of that gas phase (here taken to be atmospheric). The second factor is whether the precipitation of certain minerals to account for known metastabilities (e.g., kinetic inhibitions) is allowed. In the calculations discussed here, evaporation is simulated by the removal of the H<sub>2</sub>O from an initial mass of J-13 water. The temperature increases linearly from ambient (31°C) with H<sub>2</sub>O removal, so that at 96°C only about 2 percent of the H<sub>2</sub>O remains. Although this was an arbitrary path, similar results were obtained for constant temperatures of 31 and 96°C. The modeling was not continued beyond 2 percent water remaining. The solution at this point is still relatively dilute (with an ionic strength in the range 0.1 to 0.2 molal). Thus, the precipitation of salt minerals such as halite (NaCl), gypsum (CaSO<sub>4</sub>·2H<sub>2</sub>O), and NaNO<sub>3</sub> is not observed. Further modeling at higher evaporation is required to assess the formation of such precipitates.

As shown in Figure 11.4-16, the pH that evolves as temperature increases will tend toward slightly acidic (pH = 6.5) for a closed system (no gas atmosphere). In contrast, the pH evolves toward alkaline values (pH = 9.5) if the partial pressures of CO<sub>2</sub> and O<sub>2</sub> are held at atmospheric levels (gas phase control). In essence, the relatively low, fixed CO<sub>2</sub> partial pressure allows the loss of CO<sub>2</sub>. Another possibility not dealt with here would also allow the loss of CO<sub>2</sub>, but allow the CO<sub>2</sub> partial pressure to change depending on mass transfer and mass transport constraints. This would lead to a very similar pH increase. The closed system calculations are not realistic for an evaporation scenario; they were performed mainly to provide a point of comparison. In some runs, the precipitation of solid phases was not restricted; in others, quartz, tridymite (another SiO<sub>2</sub> phase), and talc (a Mg-rich clay phase loosely related to saponite, a smectite) were suppressed. Dolomite [CaMg(CO<sub>3</sub>)<sub>2</sub>] probably also should have been suppressed in these calculations, in which case more calcite and saponite would have formed. However, similar overall results would have been obtained.

Because of the overall gas exchange in the mountain (e.g., the mountain breathing), it might be anticipated that the CO<sub>2</sub> and O<sub>2</sub> would always approach atmospheric values. (It should be noted that the underground CO<sub>2</sub> partial pressure appears to be higher than the atmospheric,  $1 \times 10^{-3}$  bar versus  $0.32 \times 10^{-3}$  bar [Apps 1997].) However, several factors may affect gas exchange. Barometric pressure responses in the Topopah Spring unit were suppressed until the tunnel was opened into it. This indicates that rapid gas exchange is restricted to the overlying units, presumably due to higher permeability in those units. During the heating stage, and particularly when boiling is active, water vapor will displace the normal underground atmosphere. However, the evaporation process of concern here would be operative only until temperatures reach the boiling point. Normal atmospheric partial pressures of CO<sub>2</sub> and O<sub>2</sub> would be expected to prevail

during emplacement operations due to repository ventilation. If ventilation were maintained beyond the time of emplacement, then these conditions might prevail for longer times.

The  $\text{Na}^+$  and  $\text{Cl}^-$  concentrations are observed to increase in similar conservative fashion (e.g., the concentrations double when half of the water has been removed). The simulations were not run far enough to precipitate halite ( $\text{NaCl}$ ). Sulfate ( $\text{SO}_4^{2-}$ ) also behaves conservatively in these simulations, though gypsum ( $\text{CaSO}_4 \cdot 2\text{H}_2\text{O}$ ) would likely appear as a precipitate if the calculations had been run to higher extents of evaporation. In contrast,  $\text{Ca}^{2+}$  (Figure 11.4-17) does not behave conservatively, due to the precipitation of calcite ( $\text{CaCO}_3$ ) and, to a lesser extent, the formation of dolomite [ $\text{CaMg}(\text{CO}_3)_2$ ]. The somewhat complex results for  $\text{Ca}^{2+}$  are due to the dependence of calcite (and dolomite) solubility on temperature and pH, and the dependence of the pH on the presence (or absence) of a  $\text{CO}_2$ -buffering gas phase. The essential features of these factors have been discussed previously. The Si concentrations (Figure 11.4-18) are also rather complex. The initial J-13 water composition is supersaturated with respect to quartz, tridymite, and talc before any evaporation or heating begins. How these metastabilities are treated depends on the results obtained. For relatively short time frames, the most realistic approach is to not allow them to precipitate. After all, these metastabilities appear to hold in the underground system at Yucca Mountain today. (The supersaturation of talc may be questionable for a variety of reasons). Over geologically significant time periods, a stable phase, such as quartz, would be expected to precipitate at least to some degree. Thus, models that deal with these problems must consider reaction kinetics over the time periods of repository scenarios.

Although calcite is the most significant mineral to precipitate in these calculations, some minor precipitates also appear. These are saponite (Mg-rich smectite clay) and stilbite (a zeolite). Although the amounts formed are relatively small, these phases present ion-exchange capacity. This could be significant in retarding subsequent radionuclide migration. However, further work is required to determine if stilbite or any other zeolite can realistically form in this kind of scenario. Slow precipitation kinetics could be a limiting factor. Also, in the real system the evaporating water would react to some degree with the rock and this would lead to somewhat different results.

Using methods such as the one discussed above, the type of salt deposits and the amounts formed can be calculated from the amount of water estimated to enter the drift prior to boiling and from the estimated temperature history of the drift wall. Such estimates are highly dependent on the designs selected. Regardless of the design details, water will begin to evaporate in response to heat as the waste is emplaced. Initially, water in the near-field environment will be similar in composition to water in the pores and fractures, although it may also include water used in construction.

## 11.5 FIELD THERMAL TEST RESULTS AND DISCUSSION

The performance assessment of a potential high-level radioactive waste repository requires prediction of the performance of waste package materials, and the flow and transport characteristics of radioactive nuclides from the emplacement drifts to the accessible environment. Those predictions require information about the thermal-mechanical-hydrological-chemical conditions within the emplacement drift and the region between the drifts and the accessible environment, as functions of time and space. Model analyses are needed to predict the thermal-mechanical-hydrological-chemical conditions in a potential repository for its life span. Test data are needed to enhance the confidence in those model analyses.

Three field thermal tests have been or are being conducted to monitor the thermal-mechanical-hydrological-chemical processes and to provide data for enhancing the confidence in the model analyses. Those tests are the Large Block Test at Fran Ridge, the Single Heater Test, and the Drift Scale Test. Both the Single Heater Test and the Drift Scale Test are conducted at Alcove 5 of the Exploratory Studies Facility. A detailed description of the Large Block Test can be found in Wilder et al. (1997, Sections 2, 4). A detailed description of the Single Heater Test can be found in CRWMS M&O (1997c). A detailed description of the Drift Scale Test can be found in CRWMS M&O (1997b, Section 3). These tests are briefly described below to facilitate discussion of the test results. Additional discussions of the test results and analyses of the data can be found in analysis/model reports (CRWMS M&O 2000d, 2000e).

### 11.5.1 Description of the Large Block Test

The primary purpose of the Large Block Test was to investigate the coupled thermal-mechanical-hydrological-chemical processes in a controlled one-dimensional heating condition so that the test results could be readily compared with model calculations. A freestanding 3 by 3 by 4.5 m (10 by 10 by 15 ft) column of Topopah Spring Tuff was isolated at the outcrop at Fran Ridge, Nevada. The block's rock type was the same as the nonlithophysal unit of the Topopah Spring Tuff in the potential repository horizon in Yucca Mountain. Preconstruction characterization and pretest scoping model calculations indicated that the fracture characteristics, bulk permeability, initial moisture content, and block size were suitable for testing the coupled thermal-mechanical-hydrological-chemical processes. During construction, small rock blocks adjacent to the large block were collected for laboratory tests. The mineralogical composition of the small blocks, especially secondary minerals in the fractures, will serve as a geochemistry baseline. The mineralogical baseline will be used to investigate the chemical processes due to heating. Fractures in the block were mapped on the five exposed surfaces and in the boreholes, which were drilled to install instruments. Five heaters were installed in the block to form a horizontal heater plane at 2.743 m (9 ft) from the top. Instruments were installed in the boreholes to measure temperature, gas pressure, relative humidity, moisture content (using neutron logging), and deformation. In addition, instruments installed on the block surface included electrodes for electrical resistance tomography, fracture gauges, and resistance temperature devices to monitor the near-surface temperature gradients. Labeled native microbes were introduced into the heater boreholes and other boreholes in the block so that their survivability and migration could be studied. Four observation boreholes were constructed near the bottom of the block to conduct qualitative observations of fracture flows and microbial migrations. Coupons of candidate waste

package materials were placed at designated locations within the block. The four vertical sides of the block were coated with a layer of moisture barrier, then covered with three layers of insulation (from inside outward): Ultratemp boards, fiberglass, and reflexic. Water vapor was allowed to leave the block through the top. A heat exchange unit was installed on the top to control the top temperature.

The heaters were energized to their full power (450 W each) on February 28, 1997. The temperature on the top was allowed to rise to 60°C, then the heat exchange unit was turned on to control the temperature at that level. When the temperature near the heater horizon reached 140°C, the heater power was adjusted to keep the temperature between 135° and 140°C. The heating phase of the Large Block Test was terminated on March 10, 1998 (9,000 hours). The monitoring of the Large Block Test was terminated on September 16, 1998 (13,899 hr.). Cores were collected after the test; core analyses to assess the heating effects on the rock's mechanical, hydrological, and mineralogical characteristics are ongoing.

### **11.5.2 Temperature Distribution in the Block**

The temperature data for the Large Block Test and the data tracking number of the data can be found in CRWMS M&O (2000d, Section 3.6.3). Figures 11.5-1 and 11.5-2 show the highest temperatures measured along the two vertical boreholes, TT1 and TT2, respectively, as a function of time for the entire test history. TT1-14 and TT2-14 were the resistance temperature devices in the two boreholes located nearest the heater horizon. The downward spikes at 552 hr. (March 23 and 24, 1997), 1,036 hr. (April 12 to 15, 1997), and 3,802 hr. (August 5, 1997) in both figures were due to power outages. These short power outages did not significantly impact the block heating. The heaters were turned off on March 10, 1998 (8,999.5 hr.), at which time the temperature at TT1-14 was about 15°C greater than that at TT2-14. This temperature difference is probably due to two factors: TT2 was closer to the edge of the block than TT1, and therefore influenced more by the heat loss of the block; and the two vertical boreholes had different total depths (TT2-14 was 8.2 [3 in.] cm below the heater horizon, whereas TT1-14 was 2.1 cm below the heater horizon). The temperature drop at TT1-14 at 2,525 hr. (June 13, 1997) and the subsequent temperature fluctuations at both TT1-14 and TT2-14 were probably caused by thermal-hydrological events, which are discussed later.

As shown in CRWMS M&O (2000d, Section 3.6.3), the temperature variations along the horizontal resistance temperature device boreholes indicate that it is generally true that the temperature variations in the east-west horizontal boreholes were greater than those in the north-south boreholes. Nevertheless, the temperatures in the horizontal boreholes show that the block was heated fairly one-dimensionally.

#### **11.5.2.1 Boiling of Pore Water**

The relatively flat temperature region (about 97°C) at TT1-14 between 882 hr. (on April 6, 1997) and 1,125 hr. (on April 16, 1997) (Figure 11.5-1) was probably caused by the balance of energy from the heaters and the energy required to evaporate the pore water near the resistance temperature device TT1-14. In TT2-14 (Figure 11.5-2), the relatively flat temperature occurred between 1,880 hr. (on May 18, 1997) and 2,647 hr. (on June 18, 1997), at a temperature of about

98°C. If the flat temperature-time curve was indeed caused by evaporation, the longer duration of the flat temperature region at TT2-14 may have been caused by either a greater amount of pore water to be evaporated and/or a slower heating rate at TT2-14. As mentioned above, borehole TT2 is closer to the block side than TT1; therefore, greater heat loss in the block sides may have caused the slower heating rate at the resistance temperature devices in TT2. The temperature at which the flat temperature-time curve occurs relates to the boiling point of water. These results indicate that the boiling point of the pore water at TT1-14 was greater than at TT2-14 by about 1°C (98°C versus 97°C). The difference in the boiling point of water may be due to many factors, including the differences in the barometric pressure, the suction potential of the pores, or the difference in ionic concentration in the pore water. The boiling point of pure water at the elevation of the Large Block Test is 96.6°C. The boiling point of the water in the block, inferred by the measured temperature, was slightly greater than that of pure water. This is probably due to the suction potential of the pores and the ionic concentration in the water.

### 11.5.2.2 Thermal-Hydrological Processes

The sudden drops of temperature at TT1-14 at 2,525 hr. (June 13, 1997) (Figure 11.5-1) and at TT2-14 at 4,475 hr. (September 2, 1997) (Figure 11.5-2) and the subsequent temperature fluctuations were probably caused by thermal-hydrological processes. During the event, all temperatures converged to around the boiling temperature of the pore water, then the temperatures rose and fluctuation began. Close examination of those temperature data indicates that the temperature changes were related to hydrological processes, and condensate refluxing may have caused the temperature fluctuations. However, the causes of the onset of the June 13, 1997 (2,525 hr.), thermal-hydrological event are not clear. The thermal-hydrological event and the subsequent temperature fluctuations might have been caused by rain water that infiltrated into the block, or the release of overheated water within the block. It was reported that a weather station about 5 km (8 mi.) southeast of Fran Ridge registered rain on June 13, 1997 (2,525 hr.). However, there was no direct indication of precipitation at Fran Ridge during that time frame.

One cause of the September 2, 1997 (4,475 hr.), event was clearly related to rainfall. It rained hard at Fran Ridge on the night before this event. All measured temperatures along TT1 showed a decrease at the onset of this event; this indicates the influence of external rain water on this event and, again, the temperature fluctuations were probably caused by condensate refluxing. The temperatures stayed at the boiling point of water for almost 400 hr. for the June 13, 1997, (2,525 hr.), event, but only for about 40 hr. for the September 2, 1997 (4,475 hr.), event. This difference was probably due to the addition of insulation to the block surfaces at about 3,000 hr.; the additional heat in the block would have made the water evaporate more quickly. It is also possible that the matrix of the block during the September 2, 1997 (4,475 hr.), event had been dried out more than it had been during the June 13, 1997 (4,475 hr.), event. The implication of these thermal-hydrological events is that with proper conditions, condensate refluxing can be established in a heated rock mass.

### 11.5.3 Moisture Distribution in the Block

The moisture distribution in the block was measured by two methods: electrical resistance tomography and neutron logging. The electrical resistance tomograph measures the distribution of electrical resistivity of the rock mass in an imaging plane. Temperatures measured in the field, and the laboratory-determined relationship between the electrical resistivity and water saturation of Topopah Spring Tuff at elevated temperatures (Roberts and Lin 1997), are used to reduce the measured electrical resistivity distributions into the distribution of the rock mass water saturation. The electrical resistance tomograph images moisture distribution in two-dimensional planes in the block, whereas neutron logging determines the moisture content within about a 20-cm (8-in.) diameter column along a borehole. Electrical resistance tomographs have less resolution and are less accurate than neutron logging, but can image a bigger area. Temperature distribution data within the entire imaging plane of electrical resistance tomography are needed to reduce the measured electrical resistance data into moisture content. Normally, temperature is measured at a finite number of localities in a test region. These localized temperature data are interpreted to generate temperature information at every pixel in an electrical resistance tomography plane. The uncertainty in temperature distribution caused by this interpretation of measured temperature data will affect the accuracy of moisture distribution, which is deduced from the electrical resistance tomography data. The uncertainty in the moisture distribution has to be considered when the electrical resistance tomography results are used in integrated analyses of the field thermal test results.

Figure 11.5-3 shows electrical resistance tomography images from the east-west vertical plane of the Large Block Test for four dates and shows resistivity ratio, temperature, and saturation ratio, respectively. The east-west vertical plane passes through the middle of the block. The resistivity ratio and the saturation ratio are in respect to the baseline data obtained before the heating was started on February 28, 1997. The heaters were turned off March 10, 1998 (9,000 hr.). The ramp-down of the heater power was started October 6, 1997 (5,283 hr.), to keep a constant temperature in the block. The first three columns show the electrical resistance tomograph obtained during the final stage of the heating period when the block temperature was almost constant. The saturation ratio images on November 19, 1997 (6,338 hr.), and January 23, 1998 (7,898 hr.) (the third row), show a dryout region at the heater horizon (centered about 2.74 m [9 ft.] from the top), extending vertically near the west side of the block. The vertical dry zone may be related to one of the high-angle major fractures near the west side of the block (Wilder et al. 1997, Figure 2-10). There were no other major features in the saturation distribution, except one localized small region in each image, which shows increased moisture content. The saturation ratio images on February 24, 1998 (8,666 hr.), and March 19, 1998 (9,218 hr.), seem to indicate that dryness in the previous dryout zones was decreasing, but there was no significant change in moisture content in other locations. Field measurements indicate that due to dryness on the block surface, the signal quality in the later electrical resistance tomographs was not as good. Therefore, the apparent rewetting in the dryout zones may not be reliable.

Neutron logging was conducted in five vertical boreholes and 10 horizontal boreholes (six from the north side and four from the west side), as described in Wilder et al. (1997, Figures 4-1, 4-2, 4-5). Neutron counts were measured every 10 cm (4 in.) in each borehole. The measured neutron counts were converted to fraction volume water content using calibration results. To

illustrate the variation in the moisture content in the block due to heating, the preheat baseline fracture volume water content was subtracted from the in-heat measurements to generate the difference in fracture volume water. The data from one of the vertical neutron boreholes are presented as an example of the variation of the moisture distribution in the Large Block Test due to heating.

Figures 11.5-4 and 11.5-5 show the difference of fraction volume water content as measured along the neutron borehole TN3 on various days of heating. Borehole TN3 was the vertical neutron borehole located closest to the middle of the block (Wilder et al. 1997, Figure 4-1). The zero fraction volume water in these two figures means there was no difference from the preheat baseline data. These two figures clearly show the development of a dryout zone. The drying seemed to start at an area slightly below the heater horizon, about 2.74 m [9 ft] from the top. The maximum drying region then gradually extended below the heater horizon in most cases. Slight variations in the extent of the drying zone occurred in other boreholes. All neutron data along the vertical boreholes show that the width of the drying zone and the extent of the drying did not change significantly after day 334 (on January 28, 1998) and 361 (on February 24, 1998) of heating. The fraction volume moisture content in the driest region was about 0.85 to 1 percent.

In summary, both electrical resistance tomography and neutron logging show that the heating created a significant dryout zone in the block. The width of this dryout zone ranged from 1.5 to 1.7 m (4.9 to 5.6 ft). The electrical resistance tomography shows a localized vertical dryout region extending to the upper part of the block. This is not shown by the neutron data, probably because of the lack of a vertical neutron borehole in that part of the block. Within the dryout zone, the drying could reduce the moisture content to only about 1 percent fraction volume. No apparent re-wetting was observed by neutron logging or by electrical resistance tomography. This is consistent with the concept that re-wetting of a thermal dry-out region, except that which may be assisted by extrinsic factors such as infiltration, will be slower than the drying itself. And the amount of water available for the re-wetting will be less than that originally driven away by the heat.

#### **11.5.4 Model Analysis of the Thermal-Hydrological Results of the Large Block Test**

The NUFT model was used to analyze the temperature and neutron data of the Large Block Test (CRWMS M&O 2000e, Section 6.2.3). Both the drift-scale property set and the mountain-scale property set were used in the analyses. The model analysis was performed to identify a property set that would give a better prediction of the measured data. As mentioned before, the Large Block Test was designed to increase the understanding of processes, not for testing properties. The comparison concluded that both the drift-scale property set and the mountain-scale property set provided generally good predictions of the measured temperatures, but the drift-scale property set seemed to have the better statistical fitness. Both property sets were able to capture the major characteristics of the measured temperature variations with time and space. That is, the NUFT model was able to simulate the processes that affected the measured temperatures. Using the drift-scale property set, the NUFT model was able to capture the shape of the fraction volume of water versus depth curves measured by neutron logging quite well. But neither property set could predict the extent of the drying, nor the increase of water content outside the drying zone.

The NUFT model simulated the moisture distribution well in the Large Block Test. As expected, the NUFT model could not simulate the two thermal-hydrological events (Section 11.5.2.2).

### **11.5.5 Deformations in the Block**

Deformations within the block were measured by multiple-point borehole extensometers for the bulk displacements within the block, and by fracture gauges for the deformations across fractures on the block surfaces (Wilder et al. 1997, p. 19). Section 11.3 contains the results of the measured deformation in the block. In summary, the multiple-point borehole extensometer measurements showed that the block experienced expansion in the upper half during the heating phase of the test. The surface fracture gauge measurements showed that during the June 13, 1997 (2,525 hr.) thermal hydrological event (Section 11.5.2.2), the horizontal fracture near the top of the block (at about 30 to 60 cm [(12 to 24 in.) below the top) experienced opening of about 0.0094 to 0.011 cm [0.0037 to 0.004 in.] at the northern and eastern sides, and a 0.0058-cm [(0.0023-in.) shear displacement on the western side. Those deformations may affect changes of the block's hydrological properties.

### **11.5.6 The Large Block Test Summary**

The Large Block Test performed as designed. The block was heated in one-dimension. A uniform dryout zone was created at the heater horizon. The moisture distributions above and below the dryout zone varied, probably due to the heterogeneity of the block. Refluxing of condensates, due to the boiling at the heater horizon, was illustrated by the temperature fluctuations. The water, which was involved in at least one thermal-hydrological event, may have been supplied by rain. There was some indication of coupling between the block deformation and the thermal-hydrological processes. The NUFT model did reasonably well predicting processes that governed general temperature and moisture distributions. This model could not simulate the two thermal-hydrological events. The labeled microbes, which had been placed in the heater holes before the heating, were found in the observation holes about 1.7 m (5.6 ft) below the heater holes during the heating phase of the test. This indicates that the microbes survived the heating, and water was drained from the heater holes.

### **11.5.7 The Single Heater Test**

A primary purpose of the Single Heater Test was to investigate the thermal-mechanical responses of the rock mass to a single heater in a borehole. The objectives of the Single Heater Test were to provide data and information on the rock mass thermal and thermal-mechanical properties, preliminary information on the coupled thermal-chemical-hydrological-mechanical response, and preliminary information on ground support-rock interaction at elevated temperatures (CRWMS M&O 1996, p. 2-1). The test design and the borehole layout were focused on providing data for the thermal-mechanical responses. Boreholes for monitoring water saturation and other coupled thermal-mechanical-hydrological-chemical related responses were located to avoid interference with the thermal-mechanical measurements. The borehole layout of the Single Heater Test can be found in Figure 11.5-6. The Single Heater Test was also used to test the methodology of using chemical sensors in the Science and Engineering Associates membrane in situ sampling technology system for in situ chemical monitoring. The Single Heater Test results and data

tracking number of the test data can be found in CRWMS M&O (2000d). Only test results related to the near-field environment and altered zone are summarized in this section. A more detailed discussion of the test results can be found in CRWMS M&O (1999a).

### **11.5.8 Single Heater Test Results**

The multiple-point borehole extensometer measurements in the four multiple-point borehole extensometer boreholes provided more reliable results than other displacement measurements in the Single Heater Test. The multiple-point borehole extensometer boreholes MPBX-1 to MPBX-3 were parallel to the heater borehole; MPBX-4 was perpendicular to the heater borehole. During the test, MPBX-1 to MPBX-3 registered mostly expansion of the rock mass; MPBX-4 registered compression movement at the beginning of the heating, followed by expansion after about 40 to 50 days of heating (October 5, 1996, to October 15, 1996). Those results were modeled using FLAC. The results indicated good overall agreement between the calculated and measured deformations (CRWMS M&O 1999a, Figures 9-3 to 9-10, p. 9-27).

At the end of the heating phase of the Single Heater Test, the boiling point isotherm extended to about a 1-m radius from the heater borehole. Both electrical resistance tomography and neutron logging showed significant drying in a region that was at least four times bigger than the region where the temperature was higher than the boiling point of water. The electrical resistance tomography also showed slightly increased moisture content in regions below the heater borehole. The ground-penetrating radar results generally agree with those of the electrical resistance tomography and neutron logging. About 17 L of water were collected from zone 4 in borehole 16, one of the two packer boreholes. This zone was about 2 m (7 ft) from the heater borehole. The chemical composition of the water indicated that it was more diluted than J-13 water and the Topopah Spring Tuff pore water, except for the concentration of Ca. The Ca composition in borehole 16 water was about the same as in J-13 water. Also, the pH value in borehole 16 water ranged from 6.2 to 6.9, which was lower than the 7.4 value for J-13 water (Blair et al. 1998, Table 4-1). One of the interpretations of the chemical characteristics of the borehole 16 water is that the pore water in the rock mass near the heater borehole evaporated, condensed in the outer and cooler region, and then flowed along fractures into borehole 16. On its way to borehole 16, the condensed water interacted with minerals on the fracture surfaces to pick up Ca and generate greater CO<sub>2</sub> partial pressure, which lowered the pH in the water. Air permeability measured by cross-borehole injection between boreholes 16 and 18 indicated reduced permeability during heating, which then increased after cooling. Variations in water saturation and/or fracture aperture may have caused these changes in air permeability. The displacement measurements in the Single Heater Test, using multiple-point borehole extensometer, did not generate information suitable for inferring the coupling between the thermal-mechanical responses and thermal-hydrological responses.

### **11.5.9 Model Analysis of the Single Heater Test Results**

A portion of the Single Heater Test results was analyzed and is presented in CRWMS M&O (2000e). This report presented temperature data measured in three thermocouple boreholes (TMA-TC-1A, TMA-TC-4A, and TMA-TC-5A) and the temperature as a function of the radial distance from the heater (CRWMS M&O 2000e, p. 40). CRWMS M&O (2000e)

concluded that the simulated temperature in the Single Heater Test, using TOUGH2 with dual permeability active fracture modeling and the drift-scale property set, matches the trend of the measured temperature data well (CRWMS M&O 2000e, p. 73).

#### **11.5.10 The Single Heater Test Summary**

In summary, the Single Heater Test thermal-mechanical displacement measurements generated good information on the effect of heating on rock mass bulk deformation. The Single Heater Test generated information about the coupled thermal-hydrological-chemical processes in a heated rock mass, even though it was not designed for that purpose. The test confirmed that heat drives water away from the heated region in vapor form. The water vapor may be condensed when it reaches cooler regions. The condensed water may flow through fractures. Rock-water interaction between the condensed water and mineral coating on fracture surfaces can occur within a relatively short time (i.e., months).

Important coupled processes observed from the Single Heater Test include the following:

- Rock dryout occurred in regions below the boiling point temperature which was four times larger than the region where temperature exceeded the boiling point temperature.
- Moisture increased below the heater (presumably due to condensation).
- The chemical composition of sampled water was consistent with the concept of evaporation, condensation, and flow along fractures.
- The low pH in sampled water was probably caused by the excess CO<sub>2</sub> generated from the rock-water interaction during the flow along fractures.
- Air permeability measurements noted reduced permeability during heating and increased permeability after cooling, which was possibly from changes in fracture saturation and/or fracture aperture.
- The conceptual/mathematical model simulated temperatures consistent with measured temperatures.

#### **11.5.11 Drift Scale Test**

The Drift Scale Test was designed to collect data of in situ drift-scale coupled thermal-mechanical-hydrological-chemical processes. Figures 11.3-17, 11.3-18, and 11.5-7 show the drift configurations and borehole layout of the Drift Scale Test. The objectives and design of the Drift Scale Test are described in detail in CRWMS M&O (1997b, Sections 2, 3). The drift configuration of the Drift Scale Test consists of an access/observation drift, a connection drift, and a heater drift. The access/observation drift connects with the main Exploratory Studies Facility tunnel at about 2.88 km (1.79 mi.) from the North Portal of the main tunnel. The heater drift is about 47.5 m (156 ft) long, starting from a thermal bulkhead located near the intersection of the connection drift. The heat sources in the Drift Scale Test include nine canister heaters lined up on the heater drift floor and 25 wing heaters on each side. Each canister heater is about

4.7 m (15 ft) long and 1.7 m (5.6 ft) in diameter. Each wing heater is placed in a horizontal wing heater borehole that is 11.5 m (38 ft) long and drilled into the heater drift side wall about 0.25 m (0.82 ft) below the springline.

The total power of the canister heaters and wing heaters is about 68 kW and 143 kW, respectively. Each wing heater consists of two sections of heating elements. The outer (farther away from the heater drift) element has a rated power output of about 1.719 kW; the inner section has about 1.145 kW. Temperature is measured in resistance temperature device boreholes arranged radially from the heater drift. Temperature is also measured in two longitudinal neutron/resistance temperature device boreholes (CRWMS M&O 1997b, boreholes 79 and 80, Figure 3-1) parallel to the heater drift, about 3.5 m (11.5 ft) above the wing heater plane midpoint. Electrical resistance tomography is conducted in vertical planes parallel to the heater drift, and in two vertical planes perpendicular to the heater drift from the access/observation drift, at 4.57 and 24.69 m (15 and 81 ft) from the bulkhead. Neutron logging is conducted in two sets of boreholes from the access/observation drift. Each neutron borehole set (five boreholes) forms a fan-shaped vertical plane perpendicular to the heater drift, with three boreholes above and two below. The two neutron borehole sets are located 6.4 and 26.52 m (21 and 87 ft) from the bulkhead.

Gas sampling ports and water absorbing pads are installed in the membrane in situ sampling technology system in two sets of chemistry boreholes, which were drilled from the access/observation drift. Similar to the neutron boreholes, each chemistry borehole set forms a fan-shaped vertical plane perpendicular to the heater drift, with three boreholes above it and two under it. The two chemistry borehole sets are 8.23 and 28.35 m (27 and 93 ft) from the bulkhead. Four packers with gas injection-sampling facility were installed in two hydrology borehole sets drilled from the access/observation drift. The hydrology borehole arrangement is the same as for the membrane in situ sampling technology boreholes. The two hydrology borehole sets are located 10.06 and 30.18 m (33 and 99 ft) from the bulkhead. In addition, two more hydrology boreholes were drilled from the access/observation drift at 44.8 m from the bulkhead: one above the heater drift and one under it.

Rock mass displacement is measured by multiple-point borehole extensometers in the multiple-point borehole extensometer boreholes. These boreholes are identified and discussed in CRWMS M&O (1997b, Table 3-1, Figure 3-1). In situ measurements of the thermal conductivity and diffusivity are measured in three REKA (Rapid Evaluation of K and Alpha) boreholes 17.37 m (57 ft) from the bulkhead. All instrumentation boreholes, except the multiple-point borehole extensometer boreholes, were sealed by cement grout, packers, or a membrane.

The heaters in the Drift Scale Test were energized on December 3, 1997. The test is in the third year of its 4-yr. heating phase. After the heating phase, the heaters will be turned off to start a natural cooling phase, which will last for another 4 yr. or so.

#### **11.5.12 Drift Scale Test Results**

The thermal-mechanical-hydrological-chemical processes that can be inferred from the test results cannot be discussed until the test is complete. The temperature and the moisture

distribution data of the Drift Scale Test are analyzed in CRWMS M&O (2000e). The water chemistry and gas composition data of the Drift Scale Test are analyzed in CRWMS M&O (2000d). The Drift Scale Test results and data analyses, are found in CRWMS M&O (2000d).

Drift Scale Test data analyses conducted in CRWMS M&O (2000e) compared measured temperature and moisture distribution data with those simulated by TOUGH2 and NUFT model calculations to identify a property set that yielded the best prediction. In addition to the property set evaluations, CRWMS M&O (2000d) examined processes that can be inferred from Drift Scale Test results, including pore-water boiling, the moisture movement, the effect of the bulkhead on measured results, and rock mass drying.

### **11.5.13 Boiling of Pore Water in the Drift Scale Test**

The temperature data from the Drift Scale Test can be inspected to determine if one physical process can be distinguished from another. Two sensor arrays were considered: borehole fan arrays located 23 m and 12 m (75 and 39 ft) from the bulkhead. Boreholes 158 to 160, drilled from the heater drift, constitute the array 23 m (75 ft) from the bulkhead. Borehole 158 was drilled vertically upward, borehole 159 was drilled at 45° upward, borehole 160 was drilled horizontally toward the access/observation drift, borehole 161 was drilled 45° downward, and borehole 162 was drilled vertically downward, thus forming a fan of boreholes oriented at 45° from each other, with a common apex. The array 12 m (39 ft) from the bulkhead had a similar fan array consisting of boreholes 137 (vertically upward), 138 (45° upward), 139 (horizontal), 140 (45° downward), and 141 (vertically downward).

Figure 11.5-8 shows the temperature measured at a depth of about 2 m (7 ft) from the collar in boreholes 158 to 162 as a function of time (days) since heating. This figure shows the pore-water boiling, as measured from different orientations from the heater drift. Pore-water boiling and water reflux or influx at the temperature sensors are illustrated as a flat temperature-time curve at about the boiling point of water, which was about 96°C in the Drift Scale Test. Given the radial temperature gradient, if porosity and saturation are uniform, the time-temperature responses for similar positions within the boreholes should also be uniform. Differing profiles would indicate differing interactions with water, or nonuniform porosity-saturation or thermal conductivity. Monitored temperatures from the array at 23 m (75 ft) from the bulkhead (where end effects should be minimal) are shown as an example. All boreholes show either temperature flattening or inflection over time at the boiling point. The least flattening was exhibited in borehole 159 (oriented 45° upward). The most well-defined flattening (boiling) occurred in borehole 160 (horizontal) and lasted for about 35 days. If the data are accurate for borehole 158 (temperature plot is less uniform around 450 [on February 26, 1999] to 500 [on April 17, 1999] days), then this vertical borehole had the longest boiling or flattening. The array at 12 m (39 ft) from the bulkhead indicates similar responses, but the horizontal borehole (borehole 139) shows less well-defined flattening, and the 45° upward borehole shows no flattening or even inflection. Because flattening indicates the presence and boiling of water and not all boreholes exhibited the same response, there are either physical processes that are not uniform in all boreholes or rock that is

not uniform in properties and/or saturation. Because the pattern of differences is similar for the two fan arrays, it appears that more than property differences must be considered.

It should be noted that the fracture system is dominated by vertical fractures. For the vertically upward boreholes, water that was vaporized would likely move up the fracture as vapor and then condense and return along the same fracture to the area of the sensor. This would explain the nearly 120-day cycle of water boiling in vertical borehole 158. Water vapor tends to be driven radially away from heat, but as it condenses, it tends to drain vertically downward. Thus, there is not much water available at the 45°-upward borehole to maintain boiling. The boiling phenomenon at borehole 160 indicates that the horizontal boreholes are exhibiting effects of water influx, presumably from above. The difference in the boiling between boreholes 139 and 160 may be caused by localized heterogeneous hydrological properties and/or by the effect of the bulkhead.

A similar conclusion regarding boiling can be drawn for the 45°-downward-inclined boreholes (borehole 161), where a combination of water reflux and influx from above might explain the flattening. Because these sensors are located below the horizontal borehole sensors, it is possible that water from above migrated and caused boiling effects similar to those seen by the horizontal borehole sensors. The difference between the 45° downward and the horizontal regions may also be influenced by the Drift Scale Test's plane heat source created by the wing heaters.

The data from the vertical downward boreholes are more difficult to explain. These boreholes exhibit a similar response as the vertically upward boreholes, at least for boreholes 137, 141, 158, and 162. If the vertically upward responses were the result of reflux, then similar responses with flattening would not be expected with the vertically downward boreholes where the water vapor would be displaced below the sensor and condensate drainage would also be away from the sensor. One possibility is that water was continuously supplied to the sensor in boreholes 141 and 162 from below via a larger-scale convection cell. Model analysis can assess this possibility.

The boiling process seems to be in general agreement with the concept that water vapor is driven radially away from heat sources, and gravity affects the flow of the condensed water. Figure 11.5-9 shows the temperatures measured at about 0.4 m (1.3 ft) from the collar of 10 vertical boreholes drilled from the heater drift as a function of distance from the bulkhead. Five of them (boreholes 133, 137, 158, 168, and 170) were in the heater drift crown; the other five (134, 141, 162, 169, and 173) were in the heater drift invert. There was no temperature sensor at depth shallower than 1.5 m (5 ft) from the collar in borehole 141. The temperature value for borehole 141 was projected using the thermal gradient established by other measurements between the depths of 0.4 and 1.5 m (1.3 and 4.9 ft) from the collar. The temperature measured in the heater drift crown showed no effect of the bulkhead in that the temperature gradient from borehole 158 was approximately 1.3°C/m toward either end of the drift. However, the bulkhead effect seems to be significant for the invert temperatures. The gradient toward the end of the drift is similar to that within the crown. However, the gradient toward the bulkhead was nearly double that value (2.3°C/m).

The temperatures along borehole 80, which was parallel to the heater drift axis at about 3.5 m (11.5 ft) above the wing heater plane midpoint, show that in the rock above the heaters, the

bulkhead had no effect. The temperature in borehole 80 showed some episodic fluctuations at depth ranging 16 to 24 m (53 to 79 ft) and 32 to 36 m (105 to 118 ft). The borehole video showed an extended fracture zone between 33.9 and 34.8 m depth (111 and 114 ft). The temperature fluctuations may be related to vapor-gas movements in fractures.

#### **11.5.14 Moisture Distribution in the Drift Scale Test**

The rock mass drying in the Drift Scale Test, as monitored by ground-penetrating radar, electrical resistance tomography, and neutron logging, is illustrated by CRWMS M&O (2000e, Figures 6-35, 6-50 to 6-56). In general, drying started from the heater drift and near the wing heaters. There seemed to be more drying in regions below the heaters than above them. However, some localized dryings were observed. Drying started at borehole 67 several months before it started at borehole 50. This may be related to the thermal evolution of the Drift Scale Test, influenced by the bulkhead. The drying region in borehole 67 was still expanding at the end of 18 mo. of heating, but drying in this borehole seemed to have reached its maximum, a decrease of water content equal to about 0.16 volume of rock mass. In regions farther away from the heaters, drying had been more uniform along a borehole. The drying along borehole 80 was accompanied by a localized increase of moisture content. This might be related to heat pipe effects. The high water content region between 40 and 50 m (131 and 164 ft) from the collar was certainly associated with the temperature fluctuation.

#### **11.5.15 Thermal-Chemical Processes in the Drift Scale Test**

The measured CO<sub>2</sub> concentration in the Drift Scale Test after 12 and 15 mo. (on December 3, 1998, and March 3, 1999, respectively) of heating showed high values above and below the heaters. The CO<sub>2</sub> concentrations after 15 mo. of heating were greater than those after 12 mo. (CRWMS M&O 2000d, Figure 8). Four water samples were collected from hydrological boreholes 60 and 186 between December 11, 1998 (373 days), and January 26, 1999 (419 days). The chemical compositions of these water samples and the pore water of the Topopah Spring Tuff are shown in CRWMS M&O (2000d, Table 9). Water collected from the hydrological boreholes is generally more dilute (lower Cl and SO<sub>4</sub>) and lower pH than the initial pore water. The aqueous silica concentrations are similar to, or much higher than, those in the pore water, indicating that the collected waters were not simple mixes of the pore water and pure condensate water. The water from a hotter interval (60-3) had a greater pH and SiO<sub>2</sub> concentration than the water from a cooler interval (186-3). This trend is consistent with the evolution of pure condensate water. The concentration of HCO<sub>3</sub> is lower in 60-3 relative to 186-3. This is also expected because of the greater temperature in 60-3 (CRWMS M&O 2000d, p. 65).

#### **11.5.16 Model Analyses of the Drift Scale Test Results**

In CRWMS M&O (2000e), the measured temperature and moisture content data of the Drift Scale Test were compared with the simulated data using TOUGH2 and NUFT models, with property sets including the drift-scale property set, mountain-scale property set, and the DKM-TT99 (Dual-Permeability Model-Thermal Test 1999) property set (CRWMS M&O 2000e, Section 6.3.2.1).

CRWMS M&O (2000e) concluded that the temperatures predicted by the TOUGH2 and the NUFT simulations are in good agreement with the measured temperatures. The TOUGH2 simulations also showed that the temperature distribution was not very sensitive to the thermal conductivity values, and the thermal conductivity values in the drift-scale property set and the DKM-TT99 property set were within an acceptable range. Qualitatively, the moisture distribution calculated with the NUFT model agreed with the distribution measured by electrical resistance tomography, especially after 1 yr. of heating (CRWMS M&O 2000e, Figures 6-50 to 6-53). The TOUGH2 calculation of water saturation in the matrix was in general agreement with the Drift Scale Test neutron data in the region below the heaters. Above the wing heaters, the predicted saturation in the matrix was greater than the saturation measured by neutron logging (CRWMS M&O 2000e, Figures 6-36, 6-56).

In CRWMS M&O (2000d), model calculations using TOUGHREACT were conducted to analyze the evolution of the measured gas-phase CO<sub>2</sub> and the water chemistry. Model calculations predicted the locations of high CO<sub>2</sub> concentration and the range of the CO<sub>2</sub> concentration levels reasonably well. The model calculations also accurately predicted the evolution of the CO<sub>2</sub> concentration in the first 9 to 12 mo. of heating. But in the later months of heating, the model predictions were not as good (CRWMS M&O 2000d, Figure 10). The model prediction of the pH of condensate waters in fractures compared favorably with those data collected from the hydrological boreholes. The pH in the condensate water was related closely with the CO<sub>2</sub> concentration. The model analysis interpreted the dilution of Cl in fractures as being due to condensation and drainage below the heaters, and slow imbibition of the condensate water into the matrix (CRWMS M&O 2000d, pp. 66, 70). The model also predicted precipitation of calcite in the fractures above and to the margins of the heaters. Some calcite dissolution occurred below the wing heaters. In the matrix, there was a uniform region of calcite precipitation in the dryout zone. However, the change of either fracture or matrix porosity due to calcite precipitation and dissolution was no more than 0.1 percent, and the effect on permeability and capillarity changes was negligible (CRWMS M&O 2000d, p. 74).

However, there is not a good correlation between decreases in porosity and in permeability. A small change in porosity, if localized or if occurring at channels, can cause significant decreases in permeability. It should also be noted that the change in fracture permeability is not caused only by the change in porosity due to mineral precipitation and dissolution. Laboratory studies of fracture heating indicate that smoothing of the fracture asperities by dissolution and precipitation can effectively change the permeability (Daily et al. 1987, p. 7861). Most fractures in an underground rock mass are under compressive stresses. Decrease of fracture roughness will allow the fracture to be closed under compressive stresses, and fracture permeability will be significantly reduced. Therefore, mechanical effects should be considered in assessing the thermal-mechanical-hydrological-chemical processes.

#### **11.5.17 Drift Scale Test Summary**

After 18 mo. (June 3, 1999) of heating, the Drift Scale Test heated the rock mass to cause pore-water boiling, pore-water drying, CO<sub>2</sub> concentration changes, and water chemistry changes. Along with pore-water boiling, heat pipe effects may have occurred in regions above the heaters. Both TOUGH2 and NUFT models predicted the temperature and the drying-saturation

reasonably well. CRWMS M&O (2000e) concluded that thermal-hydrological model analyses showed that the temperature distribution in a repository is not sensitive to the thermal conductivity values used in the models. This indicates great confidence in using the thermal conductivity of the rock mass for predicting the average temperature distributions. Comparison of the measured temperature distributions and the simulated values in those model analyses was focused on the statistics of the mean temperatures. Detailed analysis of spatial and temporal temperature variations allowed the processes of moisture movements and variations, including possible convection with a scale greater than the size of the drift, to be investigated. The TOUGHREACT model provided reasonably good predictions of CO<sub>2</sub> variation due to heating and boiling-drying and the variation of the chemistry of the collected water. The thermal-hydrological models have not predicted some localized phenomena of boiling and drying. The bulkhead seemed to have some effect on the temperature distribution, the variation of heater drift CO<sub>2</sub> concentration, and maybe the spatial variations of the drying.

The Drift Scale Test is ongoing. Understanding of the thermal-mechanical-hydrological-chemical processes will improve as the test progresses.

## 11.6 SUMMARY

The integrated natural system response to thermal loading varies in space and time. The magnitude and nature of the response are dependent on the thermal characteristics of the waste and the design of the repository, as well as the properties of the host rock. It is a coupled response among thermal, hydrological, chemical, and mechanical processes. Although four-way coupling exists in nature, analyses are usually confined to thermohydrological, thermochemical, and thermomechanical processes, with some three-way analyses (thermohydrological-chemical and thermohydrological-mechanical). The following sections summarize the thermohydrologic, geomechanical, geochemical, and field thermal tests discussions presented in this chapter.

### 11.6.1 Summary: Thermohydrologic Behavior at the Potential Repository

Radioactive decay of high-level radioactive waste emplaced in a Yucca Mountain repository will change the thermal and hydrologic environment, affecting both the host rock and conditions within the drifts in ways significant to key repository performance variables. Thermal conduction is the dominant heat-transfer mechanism in the rock mass and in the backfill and invert materials. Thermal radiation is the dominant heat-transfer mechanism within the open spaces inside the emplacement drifts. Two key heat-transfer mechanisms involving the transport of water vapor and phase change are heat pipes and buoyant gas-phase convection. Thermally-driven transport of water vapor away from the heat source causes a redistribution of the pore fluids within a potentially large volume of rock. Water in the matrix pores evaporates, creating dryout zones around the drifts and condensation zones outside of the dryout zones. The generation of steam replaces air within the boiling zone, reducing the gas-phase mass fraction of air to almost zero for a period of time.

Two key quantities affect thermohydrologic conditions within emplacement drifts: temperatures at the drift wall and the temperature gradient between the waste package and the drift wall. The likelihood of water seeping into the drift is strongly affected by whether temperatures at the drift wall are above the boiling point. If the local heat flux at the drift wall is greater than the product of the local liquid-phase flux and the heat of evaporation, water cannot seep into the drift (and local rock dryout can occur). If the converse is true, then seepage into the drift is possible (and local rock dryout is suppressed). Three factors contribute to reducing relative humidity on waste packages. The first factor is inclusion of engineered barrier system components, such as backfill and drip shields in the design. These components insulate the waste package from the drift wall, enhancing the temperature (and relative humidity) difference between the drift wall and the waste package. The second factor is the presence of above-boiling conditions (and dryout) in the host rock. The third factor is limiting seepage into the drift. Keeping the drift wall above the boiling point will limit the tendency for seepage. Seepage is also limited by engineered barrier system designs that minimize wicking of water into the drift and promote drainage of any water that does seep into the drift.

Thermal-design variables affecting heating conditions and the resulting thermohydrologic behavior in the near field and engineered barrier system are areal mass loading, lineal mass loading, waste package spacing, spent-nuclear-fuel age, fuel blending, duration and heat-removal efficiency of drift ventilation, and engineered barrier system design (e.g., backfill or drip shield emplacement). Areal mass loading strongly affects long-term thermohydrologic conditions,

including the spatial extent of boiling in the host rock and the duration of boiling in the engineered barrier system. Lineal mass loading, along with spent-nuclear-fuel age, strongly affects short-term thermohydrologic conditions, such as the peak waste-package and drift-wall temperatures, and the temperature difference between the waste package and drift wall.

Waste-package spacing and heat-source heterogeneity affect the variability of thermohydrologic conditions along drifts. If waste packages are spaced far apart from each other along the drift (point-load spacing), heating conditions along the drift will be heterogeneous. If waste packages are spaced nearly end to end (line-load spacing), the line of waste packages will act as a homogeneous line-source of heat. Fuel blending also reduces the heat-source heterogeneity.

The duration and heat-removal efficiency of drift ventilation strongly affect thermohydrologic conditions during the preclosure period and continue to affect thermohydrologic conditions for hundreds of years after ventilation has ceased. As a thermal-management measure, drift ventilation is used to limit peak temperatures on waste packages and drift-wall surfaces, and to limit (or prevent) boiling conditions in the host rock.

Engineered barrier system design can have a dominant effect on thermohydrologic conditions in the drifts for tens of thousands of years. Emplacement of backfill causes thermal conduction to replace thermal radiation as the dominant heat-transfer mechanism in the drift, resulting in a greater temperature gradient between the waste package and the drift wall, which translates to a hotter waste package with lower relative humidity. The thermal conductivity and thickness of the backfill, along with the local heat-generation rate, determines the local temperature gradient. The hydrologic parameters of the backfill determine how much water from the host rock might be wicked into the drift due to capillary forces. In addition to a seepage barrier, the drip shield acts as a thermal radiation shield, thereby enhancing the temperature difference between the waste package and the drift wall, which enhances relative humidity reduction on the waste package.

Key ambient-system properties of concern for thermohydrologic behavior are those hydrologic properties governing capillarity (i.e., matrix imbibition and capillary wicking in fractures) and thermal conductivity. If the fractures have a higher capillarity than that of the backfill, water will not be wicked into the backfill. If the converse is true, then water can be wicked from the fractures into the backfill.

### **11.6.2 Summary: Geomechanical Behavior at the Potential Repository**

This section presented a brief overview of the mechanical and thermal properties of the Topopah Spring tuff, a description of three major field-scale thermal tests, a discussion of possible waste package loading scenarios, and a description of numerical modeling efforts to predict coupled thermal-mechanical-hydrological effects under conditions appropriate to the near-field environment of a potential waste repository.

Efforts to characterize the in situ geomechanical environment at Yucca Mountain have included hydraulic fracturing measurements of in situ stress and estimates of rock mass strength based on empirical criteria (Section 11.3.2). The maximum principal stress is vertical and about 7 MPa at the potential repository depth. Thermal properties have been measured on a large number of

laboratory specimens and also estimated from field data obtained in the Single Heater Test (Section 11.3.3). The thermal expansion coefficients obtained from the field data are generally lower than the laboratory values because open fractures accommodate a portion of the thermal expansion. Mechanical properties have been measured in the laboratory on test specimens ranging from 2.5 cm (1 in.) diameter cores up to 0.5-m (1.6-ft) scale blocks (Sections 11.3.4 and 11.3.5) and as part of the field-scale thermal tests (Section 11.3.7). The laboratory and field scale tests are complementary: the laboratory tests provide data on the intact rock matrix and the field tests, which incorporate fractures and other large non-homogeneities, provide rock-mass properties. The intact rock is stiff and strong, with a Young's modulus and unconfined compressive strength of approximately 30 GPa and 170 MPa, respectively. The field test strengths and moduli are generally lower, but the rock mass moduli can approach intact rock values in the more competent portions (Section 11.3.2). Thermal-mechanical effects on fluid flow through fractures have been inferred from field observations and a laboratory experiment on a 0.5-m (1.6-ft) scale tuff block (Section 11.3.6). The laboratory tests have also included an effort to assess the possible effect of radiation on elastic modulus and compressive strength (Section 11.3.11).

The three major thermal field tests, the 3-m scale Large Block Test, the Single Heater Test, and the much larger Drift Scale Test have the common objective of elucidating coupled thermal-mechanical-hydrological processes in much larger volumes of rock than can be studied in the laboratory. A variety of techniques, including borehole extensometers, tunnel convergence measurements, plate loading and borehole jacking tests, and fracture deformation gauges have provided geomechanical data from the field tests (Section 11.3.7). Four possible mechanisms for mechanical loading of waste packages, creep, block failures, seismic loading, and hydrostatic loading are discussed in Section 11.3.8. Point loading by block failures is considered the most probable loading scenario.

The discussion of numerical modeling efforts highlighted international efforts to develop sophisticated coupled thermal-mechanical models and to test them against common benchmarks and discussed efforts to model geomechanical behavior for the Large Block Test and the Single Heater Test (Section 11.3.9). Efforts to model thermal-mechanically induced hydrological effects in conjunction with the Drift Scale Test were discussed in Section 11.3.10. The modeling work suggests that shear displacements along preexisting fractures may result in zones of enhanced permeability.

### **11.6.3 Summary: Geochemical Behavior at the Potential Repository**

The heat produced by the repository waste will affect geochemical processes in several ways. For example, the equilibrium states of reactions are generally temperature dependent. Mineral solubilities, aqueous speciation, equilibrium-phase assemblages, mineral hydration states, and solid-state phase transformations all depend on temperature as well. The movement of water vapor, liquid water, and CO<sub>2</sub> gas at the elevated temperatures will interact with the existing tuff mineralogy (and introduced materials) to dissolve and precipitate phases and modify the water chemistry. Mineral stability and phase equilibria are temperature-dependent. At higher temperatures, the conversion of unstable cristobalite to more stable chalcedony or the stable quartz form is accelerated (though this may be significant only in the presence of liquid water). Changes in permeability and porosity, in turn, may accompany phase transformations and

mineral dissolution-precipitation reactions, and flow paths may be altered for additional impact. Furthermore, the role of microbial activities may represent important interactions as temperatures increase.

Geochemical and hydrological processes are expected to be significant in the initial stages of heating when temperatures are elevated but do not quite reach boiling. Dissolution and precipitation may occur in this process as a result of the continuing presence of liquid water. Indeed, where water is present and kinetics are rapid, as they are along fracture pathways, the geochemical processes are well developed for the region of rock immediately surrounding the fractures. Silica redistribution may be a key mechanism in both the near field and altered zone environment (e.g., the dissolution of cristobalite in one place followed by precipitation of chalcedony, opal, or quartz in another). Thus, pathways of fluid transport may be altered and, potentially, changes in porosity may develop. Other chemical constituents may similarly be redistributed (e.g., Al, Na, Ca, K, and Mg); however, their effects are likely to be less significant to fluid flow transport. On the other hand, calcite ( $\text{CaCO}_3$ ) is a major mineral in the fractures of the potential repository zone and the dissolution and precipitation of calcite may impact fluid chemistry (pH, in particular). Also, smectite formation along preferred flow paths is potentially significant for subsequent radionuclide retardation, owing to high sorption capacities (including ion exchange) and possibly high concentrations of these phases.

#### **11.6.4 Summary: Field Thermal Tests**

The field thermal tests have produced data that improve the understanding of the conceptual thermal-hydrologic, thermal-mechanical, and thermal-hydrologic-chemical processes. They have also enhanced the confidence of the models of those processes. The Large Block Test is completed in the field measurements, but not the analysis of the post-test cores. Therefore, the interpretation of the Large Block Test is not complete in terms of the rock-water interaction during the test. The Drift Scale Test is in its third year of heating. Therefore, the interpretation of the Drift Scale Test results should be considered as preliminary. Nevertheless, all field thermal tests confirm the concept that heat drives moisture away in vapor form. The vapor will flow mostly along fractures away from the heat source that will create a dryout region surrounding the heat source. The vapor will condense into water when it reaches the cooler region. Most of the condensate will flow in fractures. Some of the condensate will be imbibed into the matrix, but the amount may be much smaller than that which flows in the fractures. The orientation of the fractures and gravity will control the flow direction of the condensate. When the condensate flows back to the heat source, it will be evaporated and condensed, and condensate refluxing along fractures will occur. This condensate refluxing will provide a better chance for rock-water interaction. Without assistance from extrinsic factors, such as infiltration, re-wetting of the dryout region will be slower than the drying process. The field thermal tests so far have not observed re-wetting.

Models for thermal-hydrologic, thermal-hydrologic-chemical, and thermal-mechanical processes are able to predict the field test results reasonably well. Thermal-hydrologic and thermal-hydrologic-chemical models using dual-permeability can predict the temperature, moisture content, and the evolution of  $\text{CO}_2$  of the thermal tests quite well. The comparison of the calculated results with the measured data provides a high degree of confidence on the range of property values used. Thermal-mechanical models were able to interpret the general

characteristics of the trend of the measured displacements in the rock mass. Other codes may be needed to handle the effects of fractures on the displacement. Modeling of the process of condensate refluxing still needs to be developed.

INTENTIONALLY LEFT BLANK

## 11.7 REFERENCES

### 11.7.1 Documents Cited

Ahn, T.M. and Soo, P. 1995. "Corrosion of Low-Carbon Cast Steel in Concentrated Synthetic Groundwater at 80 to 150°C." *Waste Management*, 15, (7), 471-476. New York, New York: Elsevier. TIC: 236890.

Albin, A.L.; Singleton, W.L.; Moyer, T.C.; Lee, A.C.; Lung, R.C.; Eatman, G.L.W.; and Barr, D.L. 1997. *Geology of the Main Drift - Station 28+00 to 55+00, Exploratory Studies Facility, Yucca Mountain Project, Yucca Mountain, Nevada*. Milestone SPG42AM3. Denver, Colorado: Bureau of Reclamation and U.S. Geological Survey. ACC: MOL.19970625.0096.

Anderson, J.G.; Brune, J.N.; dePollo, D.; Gomberg, J.; Harmsen, S.C.; Savage, M.K.; Sheehan, A.K.; and Smith, K.D. 1993. "Preliminary Report: The Little Skull Mountain Earthquake, June 29, 1992." *Dynamic Analysis and Design Considerations for High-Level Nuclear Waste Repositories, San Francisco, California, August 19-20, 1992*. Pages 162-175. New York, New York: American Society of Civil Engineers. TIC: 233289.

Apps, J.A. 1997. "Hydrochemical Analysis." Chapter 14 of *The Site-Scale Unsaturated Zone Model of Yucca Mountain, Nevada, for the Viability Assessment*. Bodvarsson, G.S.; Bandurraga, T.M.; and Wu, Y.S., eds. LBNL-40376. Berkeley, California: Lawrence Berkeley National Laboratory. ACC: MOL.19971014.0232.

Bandis, S.C.; Lumsden, A.C.; and Barton, N.R. 1983. "Fundamentals of Rock Joint Deformation." *International Journal of Rock Mechanics and Mining Sciences & Geomechanics Abstracts*, 20, (6), 249-268. Oxford, United Kingdom: Pergamon Press. TIC: 224201.

Barton, C.A.; Hickman, S.; Morin, R.; Zoback, M.D.; Finkbeiner, T.; Sass, J.; and Benoit, D. 1997. "Fracture Permeability and Its Relationship to In Situ Stress in the Dixie Valley, Nevada, Geothermal Reservoir." *Proceedings from Twenty-Second Workshop on Geothermal Reservoir Engineering, January 27-29, 1997*. Pages 210-215. Stanford, California: Stanford University. TIC: 237673.

Barton, N.; Lien, R.; and Lunde, J. 1974. "Engineering Classification of Rock Masses for the Design of Tunnel Support." *Rock Mechanics*, 6, (4), 189-236. New York, New York: Springer-Verlag. TIC: 219995.

Barton, N.R.; Bandis, S.; and Bakhtar, K. 1985. "Strength, Deformation, and Conductivity Coupling of Rock Joints." *International Journal of Rock Mechanics and Mining Sciences & Geomechanics Abstracts*, 22, (3), 121-140. New York, New York: Pergamon Press. TIC: 217135.

Bauer, S.J.; Holland, J.F.; and Parrish, D.K. 1985. "Implications About In Situ Stress at Yucca Mountain." *Research & Engineering Applications in Rock Masses, Proceedings of the 26th U.S. Symposium on Rock Mechanics, South Dakota School of Mines & Technology, Rapid City, South Dakota, 26-28 June 1985*. Ashworth, E., ed. Pages 1113-1120. Boston, Massachusetts: A.A. Balkema. TIC: 218759.

Benjamin, M.M.; Sletten, R.S.; Bailey, R.P.; and Bennett, T. 1996. "Sorption and Filtration of Metals Using Iron-Oxide Coated Sand." *Water Research*, 30, (11), 2609-2620. New York, New York: Elsevier Science. TIC: 239734.

Bethke, C. 1997. *Xt Model of Transport in Reacting Geochemical Systems. Notes to Accompany the "Xt Modeling Workbook"*. Urbana, Illinois: University of Illinois. TIC: 247620.

Bieniawski, Z.T. 1989. *Engineering Rock Mass Classifications*. New York, New York: John Wiley & Sons. TIC: 226350.

Bish, D.L.; Carey, J.W.; Levy, S.S.; and Chipera, S.J. 1996. *Mineralogy-Petrology Contribution to the Near-Field Environment Report*. Milestone LA3668. Los Alamos, New Mexico: Los Alamos National Laboratory. ACC: MOL.19971111.0588.

Bish, D.L. and Chipera, S.J. 1989. *Revised Mineralogic Summary of Yucca Mountain, Nevada*. LA-11497-MS. Los Alamos, New Mexico: Los Alamos National Laboratory. ACC: NNA.19891019.0029.

Blair, S.C. and Berge, P.A. 1997. *Geomechanical Properties of Topopah Spring Tuff at the 0.5-m Scale: Preliminary Results of Compression Tests at Elevated Temperature*. UCRL-ID-125089. Livermore, California: Lawrence Livermore National Laboratory. TIC: 236600.

Blair, S.C.; Berge, P.A.; and Wang, H.F. 1996a. *Geomechanical Analysis of the Large Block Test*. UCRL-ID-122898. Livermore, California: Lawrence Livermore National Laboratory. ACC: MOL.19970506.0117.

Blair, S.C.; Berge, P.A.; and Wang, H.F. 1997. *Bounding Models for Estimating Changes in Fracture Permeability Due to Thermo-Mechanical Stresses in Host Rock Surrounding the Repository, 1: Permeability Changes Estimated for the Heated Drift Test*. Milestone SPLF2M4. Livermore, California: Lawrence Livermore National Laboratory. ACC: MOL.19980107.0411.

Blair, S.C.; Buscheck, T.A.; Deloach, L.D.; Lin, W.; and Ramirez, A. 1998. *Single-Heater Test Final Report*. UCRL-ID-131491. Livermore, California: Lawrence Livermore National Laboratory. TIC: 247559.

Blair, S.C.; Kelly, J.M.; Pine, O.; Pletcher, R.; and Berge, P.A. 1996b. *Effect of Radiation on the Mechanical Properties of Topopah Spring Tuff*. UCRL-ID-122899. Livermore, California: Lawrence Livermore National Laboratory. ACC: MOL.19961021.0132.

Blair, S.C. and Lin, W. 1997. *Thermal-Mechanical Behavior of a Heated 3m Block of Fractured Tuff*. UCRL-JC-128350. Livermore, California: Lawrence Livermore National Laboratory. TIC: 248080.

Blair, S.C. and Wood, S.A. 1998. "Geomechanical Observations During the Large Block Test." *High-Level Radioactive Waste Management, Proceedings of the Eighth International Conference, Las Vegas, Nevada, May 11-14, 1998*. Pages 769-771. La Grange Park, Illinois: American Nuclear Society. TIC: 237082.

Bowers, T.S. and Burns, R.G. 1990. "Activity Diagrams for Clinoptilolite: Susceptibility of this Zeolite to Further Diagenetic Reactions." *American Mineralogist*, 75, 601-619. Washington, D.C.: Mineralogical Society of America. TIC: 235378.

Brechtel, C.E.; Lin, M.; Martin, E.; and Kessel, D.S. 1995. *Geotechnical Characterization of the North Ramp of the Exploratory Studies Facility*. SAND95-0488/1 and 2. Two volumes. Albuquerque, New Mexico: Sandia National Laboratories. ACC: MOL.19950502.0004; MOL.19950502.0005.

Brodsky, N.S.; Riggins, M.; and Connolly, J. 1997. "Thermal Expansion, Thermal Conductivity, and Heat Capacity Measurements at Yucca Mountain, Nevada." *International Journal of Rock Mechanics and Mining Sciences, NYRocks '97, ISRM International Symposium, 36th U.S. Rock Mechanics Symposium, Columbia University, New York, USA, June 29-July 2, 1997*, 34, (3/4), 485. Oxford, United Kingdom: Elsevier Science. TIC: 235729.

Brown, S.R. 1995. "Simple Mathematical Model of a Rough Fracture." *Journal of Geophysical Research*, 100, (B4), 5941-5952. Washington, D.C.: American Geophysical Union. TIC: 237570.

Broxton, D.E.; Warren, R.G.; Hagan, R.C.; and Luedemann, G. 1986. *Chemistry of Diagenetically Altered Tuffs at a Potential Nuclear Waste Repository, Yucca Mountain, Nye County, Nevada*. LA-10802-MS. Los Alamos, New Mexico: Los Alamos National Laboratory. ACC: MOL.19980527.0202.

Bruton, C.J. 1995. *Testing EQ3/6 and GEMBOCHS Using Fluid-Mineral Equilibria in the Wairakei Geothermal System*. Letter Report MOL206. Livermore, California: Lawrence Livermore National Laboratory. ACC: MOL.19960409.0131.

Bruton, C.J.; Glassley, W.E.; and Meike, A. 1995. *Geothermal Areas as Analogues to Chemical Processes in the Near-Field and Altered Zone of the Potential Yucca Mountain, Nevada Repository*. UCRL-ID-119842. Livermore, California: Lawrence Livermore National Laboratory. ACC: MOL.19960408.0126.

Buscheck, T.A.; Gansemer, J.; Nitao, J.J.; and Delorenzo, T.H. 1999. "Multi-Scale Near-Field Thermohydrologic Analysis of Alternative Designs for the Potential Repository at Yucca Mountain." *Scientific Basis for Nuclear Waste Management XXII, Symposium held November 30-December 4, 1998, Boston, Massachusetts, U.S.A.* Wronkiewicz, D.J. and Lee, J.H., eds. 556, 615-622. Warrendale, Pennsylvania: Materials Research Society. TIC: 246426.

Buscheck, T.A. and Nitao, J.J. 1992. *The Impact of Thermal Loading on Repository Performance at Yucca Mountain*. UCRL-JC-109232. Livermore, California: Lawrence Livermore National Laboratory. ACC: NNA.19920408.0008.

Buscheck, T.A. and Nitao, J.J. 1993a. *The Impact of Repository Heat on Thermo-Hydrological Performance at Yucca Mountain*. UCRL-JC-114791. Livermore, California: Lawrence Livermore National Laboratory. ACC: NNA.19940121.0144.

Buscheck, T.A. and Nitao, J.J. 1993b. *The Analysis of Repository-Heat-Driven Hydrothermal Flow at Yucca Mountain*. UCRL-JC-112444. Livermore, California: Lawrence Livermore National Laboratory. TIC: 205778.

Buscheck, T.A. and Nitao, J.J. 1995. *Thermal-Hydrological Analysis of Large-Scale Thermal Tests in the Exploratory Studies Facility at Yucca Mountain*. UCRL-ID-121791. Livermore, California: Lawrence Livermore National Laboratory. ACC: MOL.19960501.0392.

Buscheck, T.A.; Nitao, J.J.; and Ramspott, L.D. 1996. *Near-Field Thermal-Hydrological Behavior for Alternative Repository Designs at Yucca Mountain*. UCRL-JC-124629. Livermore, California: Lawrence Livermore National Laboratory. ACC: MOL.19971217.0341.

Buscheck, T.A.; Nitao, J.J.; and Saterlie, S.F. 1994. "Evaluation of Thermo-Hydrological Performance in Support of Thermal Loading Systems Study." *High Level Radioactive Waste Management, Proceedings of the Fifth Annual International Conference, Las Vegas, Nevada, May 22-26, 1994*. 2, 592-610. La Grange Park, Illinois: American Nuclear Society. TIC: 210984.

Buscheck, T.A.; Nitao, J.J.; and Wilder, D.G. 1993a. "Repository-Heat-Driven Hydrothermal Flow at Yucca Mountain, Part II: Large-Scale In Situ Heater Tests." *Nuclear Technology*, 104, 449-471. La Grange Park, Illinois: American Nuclear Society. TIC: 235095.

Buscheck, T.A.; Wilder, D.G.; and Nitao, J.J. 1993b. *Large-Scale In Situ Heater Tests for Hydrothermal Characterization at Yucca Mountain*. UCRL-JC-112445. Livermore, California: Lawrence Livermore National Laboratory. ACC: NNA.19930331.0009.

Carroll, S.; Mroczek, E.; Alai, M.; and Ebert, M. 1998. "Amorphous Silica Precipitation (60 to 120°C): Comparison of Laboratory and Field Rates." *Geochimica et Cosmochimica Acta*, 62, (8), 1379-1396. New York, New York: Elsevier Science. TIC: 243029.

Chan, T.; Khair, K.; Jing, L.; Ahola, M.; Noorishad, J.; and Vuillod, E. 1995. "International Comparison of Coupled Thermo-Hydro-Mechanical Models of a Multiple-Fracture Bench Mark Problem: DECOVALEX Phase I, Bench Mark Test 2." *International Journal of Rock Mechanics and Mining Sciences & Geomechanics Abstracts*, 32, (5), 435-452. Oxford, United Kingdom: Elsevier Science. TIC: 235730.

Chipera, S.J.; Bish, D.L.; and Carlos, B.A. 1995. "Equilibrium Modeling of the Formation of Zeolites in Fractures at Yucca Mountain, Nevada." *Natural Zeolites '93: Occurrence, Properties, Use, Proceedings of the 4th International Conference on the Occurrence, Properties, and Utilization of Natural Zeolites, June 20-28, 1993, Boise, Idaho*. Ming, D.W. and Mumpton, F.A., eds. Pages 565-577. Brockport, New York: International Committee on Natural Zeolites. TIC: 243086.

Costantino, M.S.; Carlson, S.R.; and Blair, S.C. 1998. *References for Results of a Coupled Fracture-Flow Test at the 0.5-m Scale*. UCRL-ID-131493. Livermore, California: Lawrence Livermore National Laboratory. ACC: MOL.19981109.0131.

CRWMS M&O 1996. *Test Design, Plans and Layout Report for the ESF Thermal Test.* BAB000000-01717-4600-00025 REV 01. Las Vegas, Nevada: CRWMS M&O. ACC: MOL.19970114.0166.

CRWMS M&O 1997a. *Yucca Mountain Site Geotechnical Report.* B00000000-01717-5705-00043 REV 01. Two volumes. Las Vegas, Nevada: CRWMS M&O. ACC: MOL.19971017.0736; MOL.19971017.0737.

CRWMS M&O 1997b. *Drift Scale Test Design and Forecast Results.* BAB000000-01717-4600-00007 REV 01. Las Vegas, Nevada: CRWMS M&O. ACC: MOL.19980710.0155.

CRWMS M&O 1997c. *Single Heater Test Status Report.* BAB000000-01717-5700-00002 REV 01. Las Vegas, Nevada: CRWMS M&O. ACC: MOL.19980416.0696.

CRWMS M&O 1998a. *Near-Field/Altered Zone Coupled Effects Expert Elicitation Project.* Las Vegas, Nevada: CRWMS M&O. ACC: MOL.19980729.0638.

CRWMS M&O 1998b. "Waste Form Degradation, Radionuclide Mobilization, and Transport Through the Engineered Barrier System." Chapter 6 of *Total System Performance Assessment-Viability Assessment (TSPA-VA) Analyses Technical Basis Document.* B00000000-01717-4301-00006 REV 01. Las Vegas, Nevada: CRWMS M&O. ACC: MOL.19981008.0006.

CRWMS M&O 1998c. *Yucca Mountain Site Description.* B00000000-01717-5700-00019 REV 00. Las Vegas, Nevada: CRWMS M&O. ACC: MOL.19981202.0492.

CRWMS M&O 1998d. *Drift Scale Test Progress Report No. 1.* BAB000000-01717-5700-00004 REV 01. Las Vegas, Nevada: CRWMS M&O. ACC: MOL.19990209.0240.

CRWMS M&O 1998e. "Near-Field Geochemical Environment." Chapter 4 of *Total System Performance Assessment-Viability Assessment (TSPA-VA) Analyses Technical Basis Document.* B00000000-01717-4301-00004 REV 01. Las Vegas, Nevada: CRWMS M&O. ACC: MOL.19981008.0004.

CRWMS M&O 1999a. *Single Heater Test Final Report.* BAB000000-01717-5700-00005 REV 00 ICN 1. Las Vegas, Nevada: CRWMS M&O. ACC: MOL.20000103.0634.

CRWMS M&O 1999b. *Drift-Scale Coupled Processes (DST THC Seepage) Models.* TDP-NBS-HS-000007 REV 00. Las Vegas, Nevada: CRWMS M&O. ACC: MOL.19990830.0378.

CRWMS M&O 1999c. *License Application Design Selection Report.* B00000000-01717-4600-00123 REV 01. Las Vegas, Nevada: CRWMS M&O. ACC: MOL.19990528.0303.

CRWMS M&O 2000a. *Multiscale Thermohydrologic Model.* ANL-EBS-MD-000049 REV 00. Las Vegas, Nevada: CRWMS M&O. ACC: MOL.20000609.0267.

CRWMS M&O 2000b. *Near Field Environment Process Model Report.* TDR-NBS-MD-000001 REV 00. Las Vegas, Nevada: CRWMS M&O. ACC: MOL.20000421.0034.

CRWMS M&O 2000c. *Engineered Barrier System Degradation, Flow, and Transport Process Model Report*. TDR-EBS-MD-000006 REV 00. Las Vegas, Nevada: CRWMS M&O. ACC: MOL.20000324.0558.

CRWMS M&O 2000d. *Drift-Scale Coupled Processes (DST and THC Seepage) Models*. MDL-NBS-HS-000001 REV 00. Las Vegas, Nevada: CRWMS M&O. ACC: MOL.19990721.0523.

CRWMS M&O 2000e. *Thermal Tests Thermal-Hydrological Analyses/Model Report*. ANL-NBS-TH-000001 REV 00. Las Vegas, Nevada: CRWMS M&O. ACC: MOL.20000505.0231.

CRWMS M&O 2000f. *Physical and Chemical Environment Abstraction Model*. ANL-EBS-MD-000046 REV 00. Las Vegas, Nevada: CRWMS M&O. ACC: MOL.20000523.0155.

CRWMS M&O 2000g. *Repository Safety Strategy: Plan to Prepare the Postclosure Safety Case to Support Yucca Mountain Site Recommendation and Licensing Considerations*. TDR-WIS-RL-000001 REV 03. Las Vegas, Nevada: CRWMS M&O. ACC: MOL.20000119.0189.

CRWMS M&O 2000h. *Ventilation Model*. ANL-EBS-MD-000030 REV 00. Las Vegas, Nevada: CRWMS M&O. ACC: MOL.20000107.0330.

CRWMS M&O 2000i. *Unsaturated Zone Flow and Transport Model Process Model Report*. TDR-NBS-HS-000002 REV 00. Las Vegas, Nevada: CRWMS M&O. ACC: MOL.20000320.0400.

CRWMS M&O 2000j. *Waste Package Degradation Process Model Report*. TDR-WIS-MD-000002 REV 00. Las Vegas, Nevada: CRWMS M&O. ACC: MOL.20000328.0322.

CRWMS M&O 2000k. *Drift Degradation Analysis*. ANL-EBS-MD-000027 REV 00. Las Vegas, Nevada: CRWMS M&O. ACC: MOL.20000107.0328.

CRWMS M&O 2000l. *Conceptual and Numerical Models for UZ Flow and Transport*. MDL-NBS-HS-000005 REV 00. Las Vegas, Nevada: CRWMS M&O. ACC: MOL.19990721.0526.

Daily, W.; Lin, W.; and Buscheck, T. 1987. "Hydrological Properties of Topopah Spring Tuff: Laboratory Measurements." *Journal of Geophysical Research*, 92, (B8), 7854-7864. Washington, D.C.: American Geophysical Union. TIC: 226512.

Daveler, S.A. and Wolery, T.J. 1992. *EQPT, A Data File Preprocessor for the EQ3/6 Software Package. User's Guide, and Related Documentation (Version 7.0)*. UCRL-MA-110662 PT II. Livermore, California: Lawrence Livermore National Laboratory. TIC: 205240.

Davis, J.A. and Kent, D.B. 1990. "Surface Complexation Modeling in Aqueous Geochemistry." Chapter 5 of *Mineral-Water Interfacial Geochemistry*. Hochella, M.F., Jr. and White, A.F., eds. Reviews in Mineralogy Volume 23. Washington, D.C.: Mineral Society of America. TIC: 224085.

Delany, J.M. 1985. *Reaction of Topopah Spring Tuff with J-13 Water: A Geochemical Modeling Approach Using the EQ3/6 Reaction Path Code*. UCRL-53631. Livermore, California: Lawrence Livermore National Laboratory. ACC: HQS.19880517.2419.

DOE (U.S. Department of Energy) 1988. *Site Characterization Plan Yucca Mountain Site, Nevada Research and Development Area, Nevada*. DOE/RW-0199. Nine volumes. Washington, D.C.: U.S. Department of Energy, Office of Civilian Radioactive Waste Management. ACC: HQO.19881201.0002.

DOE (U.S. Department of Energy) 1998a. *Introduction and Site Characteristics*. Volume 1 of *Viability Assessment of a Repository at Yucca Mountain*. DOE/RW-0508. Washington, D.C.: U.S. Department of Energy, Office of Civilian Radioactive Waste Management. ACC: MOL.19981007.0028.

DOE (U.S. Department of Energy) 1998b. *Overview - Viability Assessment of a Repository at Yucca Mountain*. DOE/RW-0508. Washington, D.C.: U.S. Department of Energy, Office of Civilian Radioactive Waste Management. ACC: MOL.19981007.0027.

Durham, W.B.; Beiriger, J.M.; Axelrod, M.; and Trettenaro, S. 1986. "The Effect of Gamma Radiation on the Strength and Elasticity of Climax Stock and Westerly Granites." *Nuclear and Chemical Waste Management*, 6, 159-168. New York, New York: Pergamon Journals. TIC: 236715.

Dzombak, D.A. and Morel, F.M.M. 1990. *Surface Complexation Modeling, Hydrous Ferric Oxide*. New York, New York: John Wiley & Sons. TIC: 224089.

Eberl, D. and Hower, J. 1976. "Kinetics of Illite Formation." *Geological Society of America Bulletin*, 87, 1326-1330. [Boulder, Colorado]: Geological Society of America. TIC: 223629.

Ernst, W.G. and Calvert, S.E. 1969. "An Experimental Study of the Recrystallization of Porcelanite and Its Bearing on the Origin of Some Bedded Cherts." *American Journal of Science*, 267A, 114-133. New Haven, Connecticut: Yale University, Kline Geology Laboratory. TIC: 224645.

Evans, U.R. 1960. *The Corrosion and Oxidation of Metals: Scientific Principles and Practical Applications*. London, England: Edward Arnold Limited. TIC: 241095.

Finley, R.E.; Sobolik, S.R.; Francis, N.D.; Ballard, S.; George, J.T.; and Costin, L.S. 1997. "Preliminary Thermomechanical Results of a Heater Test in Welded Tuff." *International Journal of Rock Mechanics and Mining Sciences*, 34, (3-4), 483. New York, New York: Elsevier Science. TIC: 236884.

Fournier, R.O. 1983. "A Method of Calculating Quartz Solubilities in Aqueous Sodium Chloride Solutions." *Geochimica et Cosmochimica Acta*, 47, 579-586. New York, New York: Pergamon Press. TIC: 236664.

Glassley, W. 1995. *Preliminary, Scoping Estimates of Rates and Magnitudes of Changes of Coupled Hydrological-Geochemical Properties*. Milestone MOL79. Livermore, California: Lawrence Livermore National Laboratory. ACC: MOL.19950727.0020.

Glassley, W.E. 1994. *Report on Near-Field Geochemistry: Water Composition Changes Due to Evaporation*. Milestone MOL26. Draft. Livermore, California: Lawrence Livermore National Laboratory. ACC: MOL.19950406.0153.

Glassley, W.E. 1996. "Equilibrium Bounds on Water Chemistry and Mineralogical Changes Produced by Near-Field Relative Humidity Changes." Chapter 3 Section 3.4.1 of *Near-Field and Altered-Zone Environment Report*. Wilder, D.G., ed. UCRL-LR-124998. Volume II. Livermore, California: Lawrence Livermore National Laboratory. ACC: MOL.19961212.0122.

Hardin, E.L. 1998a. *Near-Field/Altered-Zone Models Report*. UCRL-ID-129179 DR. Livermore, California: Lawrence Livermore National Laboratory. ACC: MOL.19980504.0577.

Hardin, E.L. 1998b. *Near-Field/Altered-Zone Models Report*. UCRL-ID-129179. Livermore, California: Lawrence Livermore National Laboratory. ACC: MOL.19980630.0560.

Hardin, E.L. and Chesnut, D.A. 1997. *Synthesis Report on Thermally Driven Coupled Processes*. Milestone SPL8BM4. Livermore, California: Lawrence Livermore National Laboratory. ACC: MOL.19980113.0395.

Hardy, M.P. and Bauer, S.J. 1991. *Drift Design Methodology and Preliminary Application for the Yucca Mountain Site Characterization Project*. SAND89-0837. Albuquerque, New Mexico: Sandia National Laboratories. ACC: NNA.19910808.0105.

Harrar, J.E.; Carley, J.F.; Isherwood, W.F.; and Raber, E. 1990. *Report of the Committee to Review the Use of J-13 Well Water in Nevada Nuclear Waste Storage Investigations*. UCID-21867. Livermore, California: Lawrence Livermore National Laboratory. ACC: NNA.19910131.0274.

Ho, C.H. and Miller, N.H. 1986. "Adsorption of Uranyl Species from Bicarbonate Solution onto Hematite Particles." *Journal of Colloid and Interface Science*, 110, (1), 165-171. New York, New York: Academic Press. TIC: 226326.

Hoek, E. and Brown, E.T. 1988. "The Hoek-Brown Failure Criterion - A 1988 Update." *Proceedings of the 15th Canadian Rock Mechanics Symposium, Toronto, Canada, October 1988*. Pages 31-38. Toronto, Canada: University of Toronto Press. TIC: 240286.

Howell, D.A.; Johnson, G.K.; Tasker, I.R.; O'Hare, P.A.G.; and Wise, W.S. 1990. "Thermodynamic Properties of the Zeolite Stilbite." *Zeolites*, 10, 525-531. New York, New York: Elsevier Science. TIC: 238583.

Hsi, C-K.D. and Langmuir, D. 1985. "Adsorption of Uranyl onto Ferric Oxyhydroxides: Application of the Surface Complexation Site-Binding Model." *Geochimica et Cosmochimica Acta*, 49, 1931-1941. New York, New York: Pergamon Press. TIC: 224090.

Itasca Consulting Group 1996. *FLAC, Fast Lagrangian Analysis of Continua, Version 3.3*. Volume I. Minneapolis, Minnesota: Itasca Consulting Group. TIC: 236418.

Jiao, Y. and Hudson, J.A. 1995. "The Fully-Coupled Model for Rock Engineering Systems." *International Journal of Rock Mechanics and Mining Sciences & Geomechanics Abstracts*, 32, (5), 491-512. Oxford, United Kingdom: Elsevier Science. TIC: 235731.

Jing, L.; Tsang, C.F.; and Stephansson, O. 1995. "DECOVALEX - An International Co-Operative Research Project on Mathematical Models of Coupled THM Processes for Safety Analysis of Radioactive Waste Repositories." *International Journal of Rock Mechanics and Mining Sciences & Geomechanics Abstracts*, 32, (5), 389-398. Oxford, United Kingdom: Elsevier Science. TIC: 235918.

Johnson, G.K.; Tasker, I.R.; Jurgens, R.; and O'Hare, P.A.G. 1991. "Thermodynamic Studies of Zeolites: Clinoptilolite." *Journal of Chemical Thermodynamics*, 23, 475-484. London, England: Academic Press. TIC: 238081.

Johnson, J.W.; Knauss, K.G.; Glassley, W.E.; DeLoach, L.D.; and Tompson, A.F.B. 1998. "Reactive Transport Modeling of Plug-Flow Reactor Experiments: Quartz and Tuff Dissolution at 240°C." *Journal of Hydrology*, 209, 81-111. Amsterdam, The Netherlands: Elsevier Science. TIC: 240986.

Johnson, J.W. and Lundeen, S.R. 1994. *GEMBOCHS Thermodynamic Datafiles for Use with the EQ3/6 Software Package*. Livermore, California: Lawrence Livermore National Laboratory. ACC: MOL.19950727.0018.

Johnson, J.W.; Oelkers, E.H.; and Helgeson, H.C. 1992. "SUPCRT92: A Software Package for Calculating the Standard Molal Thermodynamic Properties of Minerals, Gases, Aqueous Species, and Reactions from 1 to 5000 Bar and 0 to 1000°C." *Computers & Geosciences*, 18, (7), 899-947. New York, New York: Pergamon Press. TIC: 234273.

Kemeny, J. and Cook, N. 1990. "Rock Mechanics and Crustal Stress." Section 5 of *Demonstration of a Risk-Based Approach to High-Level Waste Repository Evaluation*. McGuire, R.K., ed. EPRI NP-7057. Palo Alto, California: Electric Power Research Institute. TIC: 216677.

Knauss, K.G. 1987. "Zeolitization of Glassy Topopah Spring Tuff Under Hydrothermal Conditions." *Scientific Basis for Nuclear Waste Management X, Symposium held December 1-4, 1986, Boston, Massachusetts*. Bates, J.K. and Seefeldt, W.B., eds. 84, 737-745. Pittsburgh, Pennsylvania: Materials Research Society. TIC: 203663.

Knauss, K.G.; Beiriger, W.J.; and Peifer, D.W. 1987. *Hydrothermal Interaction of Solid Wafers of Topopah Spring Tuff with J-13 Water at 90 and 150°C Using Dickson-Type, Gold-Bag*

*Rocking Autoclaves: Long-Term Experiments.* UCRL-53722. Livermore, California: Lawrence Livermore National Laboratory. ACC: NNA.19870713.0081.

Knauss, K.G.; Beiriger, W.J.; Peifer, D.W.; and Piwinski, A.J. 1985. *Hydrothermal Interaction of Solid Wafers of Topopah Spring Tuff with J-13 Water and Distilled Water at 90, 150, and 250°C, Using Dickson-Type, Gold-Bag Rocking Autoclaves.* UCRL-53645. Livermore, California: Lawrence Livermore National Laboratory. ACC: NNA.19900207.0282.

Knauss, K.G.; Delany, J.M.; Beiriger, W.J.; and Peifer, D.W. 1986. "Hydrothermal Interaction of Topopah Spring Tuff with J-13 Water as a Function of Temperature." *Scientific Basis for Nuclear Waste Management VIII, Symposium held November 26-29, 1984, Boston, Massachusetts.* Jantzen, C.M.; Stone, J.A.; and Ewing, R.C., eds. 44, 539-546. Pittsburgh, Pennsylvania: Materials Research Society. TIC: 203665.

Knauss, K.G. and Peifer, D.W. 1986. *Reaction of Vitric Topopah Spring Tuff and J-13 Ground Water Under Hydrothermal Conditions Using Dickson-Type, Gold-Bag Rocking Autoclaves.* UCRL-53795. Livermore, California: Lawrence Livermore National Laboratory. ACC: NNA.19891102.0117.

Kohler, M.; Wieland, E.; and Leckie, J.O. 1992. "Metal-Ligand-Surface Interactions During Sorption of Uranyl and Neptunyl on Oxides and Silicates." *Proceedings of the 7th International Symposium on Water-Rock Interaction, Park City, Utah, July 13-18, 1992.* Kharaka, Y.K. and Maest, A.S., eds. 1, 51-54. Brookfield, Vermont: A.A. Balkema. TIC: 208527.

Lee, K.H. and Ueng, T-S. 1991. *Air-Injection Field Tests to Determine the Effect of a Heat Cycle on the Permeability of Welded Tuff.* UCRL-ID-105163. Livermore, California: Lawrence Livermore National Laboratory. ACC: NNA.19910912.0001.

Lee, M.Y. and Haimson, B.C. 1999. "Initial Stress Measurements in the Exploratory Studies Facility Yucca Mountain, Nevada." *Rock Mechanics for Industry, Proceedings of the 37th U.S. Rock Mechanics Symposium, Vail/Colorado/USA/6-9 June 1999.* Amadei, B.; Kranz, R.L.; Scott, G.A.; and Smeallie, P.H., eds. 2, 743-750. Brookfield, Vermont: A.A. Balkema. TIC: 247086.

Levy, S.S. 1984a. "Studies of Altered Vitrophyre for the Prediction of Nuclear Waste Repository-Induced Thermal Alteration at Yucca Mountain, Nevada." *Scientific Basis for Nuclear Waste Management VII, Symposium held November 1983, Boston, Massachusetts.* McVay, G.L., ed. 26, 959-966. New York, New York: Elsevier Science. TIC: 204393.

Levy, S.S. 1984b. *Petrology of Samples from Drill Holes USW H-3, H-4, and H-5, Yucca Mountain, Nevada.* LA-9706-MS. Los Alamos, New Mexico: Los Alamos National Laboratory. ACC: MOL.19970729.0322.

Lin, W.; Blair, S.; Buettner, M.; Buscheck, T.; Daily, W.; Gdowski, G.; Glassley, W.; Lee, K.; Ramirez, A.; Ruddle, D.; Roberts, J.; Trettenero, S.; Watwood, D.; and Carlson, R. 1997. "Thermal-Mechanical-Hydrological-Chemical Responses in the Single Heater Test at the ESF." *International Journal of Rock Mechanics and Mining Sciences*, 34, (3/4), 481. Oxford, United Kingdom: Elsevier Science. TIC: 246866.

Lin, W.; Wilder, D.G.; Blink, J.A.; Blair, S.C.; Buscheck, T.A.; Glassley, W.E.; Lee, K.; Owens, M.W.; and Roberts, J.J. 1995. "A Heated Large Block Test for High Level Nuclear Waste Management." *Mechanics of Jointed and Faulted Rock, Proceedings of the Second International Conference on the Mechanics of Jointed and Faulted Rock-MJFR-2, Vienna, Austria, 10-14 April 1995*. Rossmanith, H-P., ed. Supplementary volume. Pages 20-24. Rotterdam, The Netherlands: A.A. Balkema. TIC: 247051.

Martin, R.J.; Noel, J.S.; Boyd, P.J.; and Price, R.H. 1996. "Thermal Expansion as a Function of Confining Pressure for Welded Tuff from Yucca Mountain." *Rock Mechanics Tools and Techniques, Proceedings of the 2nd North American Rock Mechanics Symposium, NARMS '96, A Regional Conference of ISRM, Montreal, Quebec, Canada, 19-21 June, 1996*. Aubertin, A.; Hassani, F.; and Mitri, H., eds. 2, 1659-1666. Rotterdam, The Netherlands: A.A. Balkema. TIC: 237844.

Martin, R.J., III; Price, R.H.; Boyd, P.J.; and Noel, J.S. 1995. *Creep in Topopah Spring Member Welded Tuff*. SAND94-2585. Albuquerque, New Mexico: Sandia National Laboratories. ACC: MOL.19950502.0006.

Meijer, A. 1992. "A Strategy for the Derivation and Use of Sorption Coefficients in Performance Assessment Calculations for the Yucca Mountain Site." *Proceedings of the DOE/Yucca Mountain Site Characterization Project Radionuclide Adsorption Workshop at Los Alamos National Laboratory, September 11-12, 1990*. Canepa, J.A., ed. LA-12325-C. Los Alamos, New Mexico: Los Alamos National Laboratory. ACC: NNA.19920421.0117.

Millard, A.; Durin, N.; Stietel, A.; Thoraval, A.; Vuillod, E.; Baroudi, H.; Plas, F.; Bougnoux, A.; Vouille, G.; Kobayashi, A.; Hara, K.; Fujita, T.; and Ohnishi, Y. 1995. "Discrete and Continuum Approaches to Simulate the Thermo-Hydro-Mechanical Couplings in a Large, Fractured Rock Mass." *International Journal of Rock Mechanics and Mining Sciences & Geomechanics Abstracts*, 32, (5), 409-414. Oxford, United Kingdom: Elsevier Science. TIC: 235740.

Mor, E.D. and Beccaria, A.M. 1975. "Behaviour of Copper in Artificial Sea Water Containing Sulphides." *British Corrosion Journal*, 10, (1), 33-38. London, England: Institute of Materials. TIC: 244914.

Nguyen, T.S. and Selvadurai, A.P.S. 1995. "Coupled Thermal-Mechanical-Hydrological Behaviour of Sparsely Fractured Rock: Implications for Nuclear Fuel Waste Disposal." *International Journal of Rock Mechanics and Mining Sciences & Geomechanics Abstracts*, 32, (5), 465-479. Oxford, United Kingdom: Elsevier Science. TIC: 235741.

Nitao, J.J. 1988. *Numerical Modeling of the Thermal and Hydrological Environment Around a Nuclear Waste Package Using the Equivalent Continuum Approximation: Horizontal Emplacement*. UCID-21444. Livermore, California: Lawrence Livermore National Laboratory. ACC: NNA.19890317.0021.

Nitao, J.J. and Buscheck, T.A. 1996. "Discrete-Fracture Modeling of Thermal-Hydrological Processes at Yucca Mountain and the LLNL G-Tunnel Heater Test." *Scientific Basis for Nuclear Waste Management XIX, Symposium held November 27-December 1, 1995, Boston*.

Massachusetts. Murphy, W.M. and Knecht, D.A., eds. 412, 747-758. Pittsburgh, Pennsylvania: Materials Research Society. TIC: 233877.

Olsson, W.A. and Brown, S.R. 1994. *Mechanical Properties of Seven Fractures from Drillholes NRG-4 and NRG-6 at Yucca Mountain, Nevada*. SAND94-1995. Albuquerque, New Mexico: Sandia National Laboratories. ACC: MOL.19941007.0081.

Ortiz, T.S.; Williams, R.L.; Nimick, F.B.; Whittet, B.C.; and South, D.L. 1985. *A Three-Dimensional Model of Reference Thermal/Mechanical and Hydrological Stratigraphy at Yucca Mountain, Southern Nevada*. SAND84-1076. Albuquerque, New Mexico: Sandia National Laboratories. ACC: MOL.19980602.0331.

Peters, C.A.; Yang, I.C.; Higgins, J.D.; and Burger, P.A. 1992. "A Preliminary Study of the Chemistry of Pore Water Extracted from Tuff by One-Dimensional Compression." *Proceedings of the 7th International Symposium on Water-Rock Interaction, Park City, Utah, July 13-18, 1992*. Kharaka, Y.K. and Maest, A.S., eds. 1, 741-745. Brookfield, Vermont: A.A. Balkema. TIC: 208527.

Pokrovskii, V.A. and Helgeson, H.C. 1995. "Thermodynamic Properties of Aqueous Species and the Solubilities of Minerals at High Pressures and Temperatures: The System  $\text{Al}_2\text{O}_3\text{-H}_2\text{O-NaCl}$ ." *American Journal of Science*, 295, 1255-1342. New Haven, Connecticut: Kline Geology Laboratory, Yale University. TIC: 236803.

Price, R.H. 1986. *Effects of Sample Size on the Mechanical Behavior of Topopah Spring Tuff*. SAND85-0709. Albuquerque, New Mexico: Sandia National Laboratories. ACC: NNA.19891106.0125.

Price, R.H.; Connolly, J.R.; and Keil, K. 1987. *Petrologic and Mechanical Properties of Outcrop Samples of the Welded, Devitrified Topopah Spring Member of the Paintbrush Tuff*. SAND86-1131. Albuquerque, New Mexico: Sandia National Laboratories. ACC: NNA.19870601.0013.

Ramirez, A. and Daily, W. 1997. *Electrical Resistivity Monitoring of the Thermomechanical Heater Test in Yucca Mountain*. Milestone SP1090M4. One of four sections. Livermore, California: Lawrence Livermore National Laboratory. ACC: MOL.19980113.0391.

Raven, K.G. and Gale, J.E. 1985. "Water Flow in a Natural Rock Fracture as a Function of Stress and Sample Size." *International Journal of Rock Mechanics and Mining Sciences & Geomechanics Abstracts*, 22, (4), 251-261. Oxford, United Kingdom: Pergamon Press. TIC: 235724.

Rehbinder, G. 1995. "Analytical Solutions of Stationary Coupled Thermo-Hydro-Mechanical Problems." *International Journal of Rock Mechanics and Mining Sciences & Geomechanics Abstracts*, 32, (5), 453-463. Oxford, United Kingdom: Elsevier Science. TIC: 235725.

Renders, P.J.N.; Gammons, C.H.; and Barnes, H.L. 1995. "Precipitation and Dissolution Rate Constants for Cristobalite from 150 to 300°C." *Geochimica et Cosmochimica Acta*, 59, 77-85. New York, New York: Elsevier Science. TIC: 226987.

Revelli, M. 2000. "LLNL's YMSD/TH Input-Section 11.2." E-mail from M. Revelli (LLNL) to R. Quittmeyer (CRWMS M&O), February 22, 2000, with attachments. ACC: MOL.20000706.0205.

Reyes, A.G.; Giggenbach, W.F.; and Christenson, B.W. 1993. *First Report, EQ3-EQ6 Code Validation Contract*. Client Report 722305.15A. Taupo, New Zealand: Institute of Geological & Nuclear Sciences. TIC: 241764.

Reyes, A.G.; Giggenbach, W.F.; and Christenson, B.W. 1994. *Third Report, EQ3-EQ6 Code Validation Contract*. Client Report 724305.15C. Taupo, New Zealand: Institute of Geological & Nuclear Sciences. TIC: 241763.

Rimstidt, J.D. and Barnes, H.L. 1980. "The Kinetics of Silica-Water Reactions." *Geochimica et Cosmochimica Acta*, 44, 1683-1699. Oxford, England: Pergamon Press. TIC: 219975.

Roberts, J.J. and Lin, W. 1997. "Electrical Properties of Partially Saturated Topopah Spring Tuff: Water Distribution as a Function of Saturation." *Water Resources Research*, 33, (4), 577-587. Washington, D.C.: American Geophysical Union. TIC: 239736.

Rosenberg, N.D.; Knauss, K.G.; and Dibley, M.J. 1999. *Evaporation of J13 Water: Laboratory Experiments and Geochemical Modeling*. UCRL-ID-134852. Livermore, California: Lawrence Livermore National Laboratory. TIC: 246322.

Sagar, B., ed. 1997. *NRC High-Level Radioactive Waste Program Annual Progress Report Fiscal Year 1996*. NUREG/CR-6513, No. 1. Draft. Washington, D.C.: U.S. Nuclear Regulatory Commission. ACC: MOL.19970813.0082.

Schwertmann, U. and Taylor, R.M. 1989. "Iron Oxides." Chapter 8 of *Minerals in Soil Environments*. Dixon, J.B. and Weed, S.B., eds. SSSA Book Series: 1. 2nd Edition. Madison, Wisconsin: Soil Science Society of America. TIC: 237222.

Steefel, C.I. and Lasaga, A.C. 1994. "A Coupled Model for Transport of Multiple Chemical Species and Kinetic Precipitation/Dissolution Reactions with Application to Reactive Flow in Single Phase Hydrothermal Systems." *American Journal of Science*, 294, (5), 529-592. New Haven, Connecticut: Kline Geology Laboratory, Yale University. TIC: 235372.

Steefel, C.I. and Yabusaki, S.B. 1996. *OS3D/GIMRT Software for Modeling Multicomponent-Multidimensional Reactive Transport User Manual & Programmer's Guide*. PNL-11166. Richland, Washington: Pacific Northwest Laboratory. TIC: 240572.

Stephansson, O. 1995. "Introduction." *International Journal of Rock Mechanics and Mining Sciences & Geomechanics Abstracts*, 32, (5), 387. Oxford, United Kingdom: Elsevier Science. TIC: 236217.

Stock, J.M.; Healy, J.H.; Hickman, S.H.; and Zoback, M.D. 1985. "Hydraulic Fracturing Stress Measurements at Yucca Mountain, Nevada, and Relationship to the Regional Stress Field." *Journal of Geophysical Research*, 90, (B10), 8691-8706. Washington, D.C.: American Geophysical Union. TIC: 219009.

Stout, R.B. and Leider, H.R., eds. 1997. *Waste Form Characteristics Report Revision 1*. UCRL-ID-108314. Version 1.2. Livermore, California: Lawrence Livermore National Laboratory. ACC: MOL.19980512.0133.

Ticknor, K.V. 1994. "Uranium Sorption on Geological Materials." *Radiochimica Acta*, 64, 229-236. München, Germany: R. Oldenbourg Verlag. TIC: 237408.

Tochiyama, O.; Endo, S.; and Inoue, Y. 1995. "Sorption of Neptunium(V) on Various Iron Oxides and Hydrated Iron Oxides." *Radiochimica Acta*, [68, (2), 105-111. München, Germany]: R. Oldenbourg Verlag. TIC: 238248.

Triay, I.; Simmons, A.; Levy, S.; Nelson, S.; Nuttall, H.; Robinson, B.; Steinkampf, W.; and Viani, B. 1995. *Colloid-Facilitated Radionuclide Transport at Yucca Mountain*. LA-12779-MS. Los Alamos, New Mexico: Los Alamos National Laboratory. ACC: NNA.19930628.0067.

Turner, D.R. 1995. *A Uniform Approach to Surface Complexation Modeling of Radionuclide Sorption*. CNWRA 95-001. San Antonio, Texas: Center for Nuclear Waste Regulatory Analyses. TIC: 236937.

Van Geen, A.; Robertson, A.P.; and Leckie, J.O. 1994. "Complexation of Carbonate Species at the Goethite Surface: Implications for Adsorption of Metal Ions in Natural Waters." *Geochimica et Cosmochimica Acta*, 58, (9), 2073-2086. New York, New York: Elsevier Science. TIC: 212000.

Vaniman, D.T.; Bish, D.L.; Chipera, S.J.; Carlos, B.A.; and Guthrie, G.D., Jr. 1996. *Chemistry and Mineralogy of the Transport Environment at Yucca Mountain*. Volume I of *Summary and Synthesis Report on Mineralogy and Petrology Studies for the Yucca Mountain Site Characterization Project*. Milestone 3665. Los Alamos, New Mexico: Los Alamos National Laboratory. ACC: MOL.19961230.0037.

Van Luik, A.; Stahl, D.; and Harrison, D. 1992. "Progress in Waste Package and Engineered Barrier System Performance Assessment and Design." *Scientific Basis for Nuclear Waste Management XVI, Symposium held November 30-December 4, 1992, Boston, Massachusetts*. Interrante, C.G. and Pabalan, R.T., eds. 294, 663-673. Pittsburgh, Pennsylvania: Materials Research Society. TIC: 208880.

Viani, B.E. 1996a. "Integrated Testing." Chapter 7.0 of *Near-Field and Altered-Zone Environment Report*. Wilder, D.G., ed. UCRL-LR-124998. Volume II. Livermore, California: Lawrence Livermore National Laboratory. ACC: MOL.19961212.0122.

Viani, B.E. 1996b. *Materials to be Used for Radionuclide Transport Experiments*. Milestone SPL3A1M4. Livermore, California: Lawrence Livermore National Laboratory. ACC: MOL.19970114.0272.

Viani, B.E. and Bruton, C.J. 1992. *Modeling Fluid-Rock Interaction at Yucca Mountain, Nevada: A Progress Report*. UCRL-ID-109921. Livermore, California: Lawrence Livermore National Laboratory. ACC: NNA.19920805.0002.

Viani, B.E. and Bruton, C.J. 1996. *Assessing the Role of Cation Exchange in Controlling Groundwater Chemistry During Fluid Mixing in Fractured Granite at Äspö, Sweden*. UCRL-JC-121527. Livermore, California: Lawrence Livermore National Laboratory. TIC: 236539.

Viani, B.E.; Torretto, P.C.; and Matzen, S.L. 1997. *Radionuclide Transport Through Engineered Barrier System Alteration Products*. Milestone SPL3FM4. Livermore, California: Lawrence Livermore National Laboratory. ACC: MOL.19980115.0871.

Warren, R.G.; Byers, F.M., Jr.; and Caporuscio, F.A. 1984. *Petrography and Mineral Chemistry of Units of the Topopah Spring, Calico Hills and Crater Flat Tuffs, and Older Volcanic Units, with Emphasis on Samples from Drill Hole USW G-1, Yucca Mountain, Nevada Test Site*. LA-10003-MS. Los Alamos, New Mexico: Los Alamos National Laboratory. ACC: HQS.19880517.2569.

Wilder, D.G. 1987. *Influence of Stress-Induced Deformations on Observed Water Flow in Fractures at the Climax Granitic Stock*. UCRL-95539, Rev. 1. Livermore, California: Lawrence Livermore National Laboratory. ACC: NNA.19880425.0044.

Wilder, D.G. 1997. *Technical Bases for EBS Design*. Volume I of *Near-Field and Altered-Zone Environment Report*. UCRL-LR-107476, Rev. 1. Livermore, California: Lawrence Livermore National Laboratory. ACC: MOL.19980107.0365.

Wilder, D.G., ed. 1993a. *Scientific Overview of Near-Field Environment and Phenomena*. Volume II of *Preliminary Near-Field Environment Report*. UCRL-LR-107476. Livermore, California: Lawrence Livermore National Laboratory. ACC: NNA.19920501.0002.

Wilder, D.G., ed. 1993b. *Preliminary Near-Field Environment Report*. UCRL-LR-107476. Two volumes. Livermore, California: Lawrence Livermore National Laboratory. ACC: NNA.19920501.0002.

Wilder, D.G., ed. 1996. *Near-Field and Altered-Zone Environment Report*. UCRL-LR-124998. Volume II. Livermore, California: Lawrence Livermore National Laboratory. ACC: MOL.19961212.0121; MOL.19961212.0122.

Wilder, D.G.; Lin, W.; Blair, S.C.; Buscheck, T.; Carlson, R.C.; Lee, K.; Meike, A.; Ramirez, A.L.; Wagoner, J.L.; and Wang, J. 1997. *Large Block Test Status Report*. UCRL-ID-128776. Livermore, California: Lawrence Livermore National Laboratory. ACC: MOL.19980508.0727.

Wilkins, D.R. and Heath, C.A. 1999. "Direction to Transition to Enhanced Design Alternative II." Letter from D.R. Wilkins (CRWMS M&O) and C.A. Heath (CRWMS M&O) to Distribution, June 15, 1999, LV.NS.JLY.06/99-026, with enclosures, "Strategy for Baselineing EDA II Requirements" and "Guidelines for Implementation of EDA II." ACC: MOL.19990622.0126; MOL.19990622.0127; MOL.19990622.0128.

Williams, H.; Turner, F.J.; and Gilbert, C.M. 1982. *Petrography, An Introduction to the Study of Rocks in Thin Sections*. 2nd Edition. San Francisco, California: W.H. Freeman and Company. TIC: 247732.

Wolery, T.J. 1992a. *EQ3/6, A Software Package for Geochemical Modeling of Aqueous Systems. Package Overview and Installation Guide (Version 7.0)*. UCRL-MA-110662 PT I. Livermore, California: Lawrence Livermore National Laboratory. TIC: 205087.

Wolery, T.J. 1992b. *EQ3NR, A Computer Program for Geochemical Aqueous Speciation-Solubility Calculations. Theoretical Manual, User's Guide, and Related Documentation (Version 7.0)*. UCRL-MA-110662 PT III. Livermore, California: Lawrence Livermore National Laboratory. TIC: 205154.

Wolery, T.J. and Daveler, S.A. 1992. *EQ6, A Computer Program for Reaction Path Modeling of Aqueous Geochemical Systems: Theoretical Manual, User's Guide, and Related Documentation (Version 7.0)*. UCRL-MA-110662 PT IV. Livermore, California: Lawrence Livermore National Laboratory. TIC: 205002.

Wolery, T.J.; Jackson, K.J.; Bourcier, W.L.; Bruton, C.J.; Viani, B.E.; Knauss, K.G.; and Delany, J.M. 1990. "Current Status of the EQ3/6 Software Package for Geochemical Modeling." Chapter 8 of *Chemical Modeling in Aqueous Systems II*. ACS Symposium Series 416. Washington, D.C.: American Chemical Society. TIC: 225589.

YMP (Yucca Mountain Site Characterization Project) 1998. *Repository Safety Strategy: U.S. Department of Energy's Strategy to Protect Public Health and Safety After Closure of a Yucca Mountain Repository*. YMP/96-01, Rev. 2. Las Vegas, Nevada: Yucca Mountain Site Characterization Office. ACC: MOL.19980727.0001.

YMP (Yucca Mountain Site Characterization Project) 1999. *Repository Safety Strategy: U.S. Department of Energy's Strategy to Protect Public Health and Safety After Closure of a Yucca Mountain Repository*. YMP/96-01, Rev. 03. Las Vegas, Nevada: Yucca Mountain Site Characterization Office. ACC: MOL.19990406.0237.

Yudhbir; Lemanza, W.; and Prinzl, F. 1983. "An Empirical Failure Criterion for Rock Masses." *Proceedings of the Fifth International Congress on Rock Mechanics, Melbourne, Australia, 1983*. 1, B1-B8. Rotterdam, The Netherlands: A.A. Balkema. TIC: 226278.

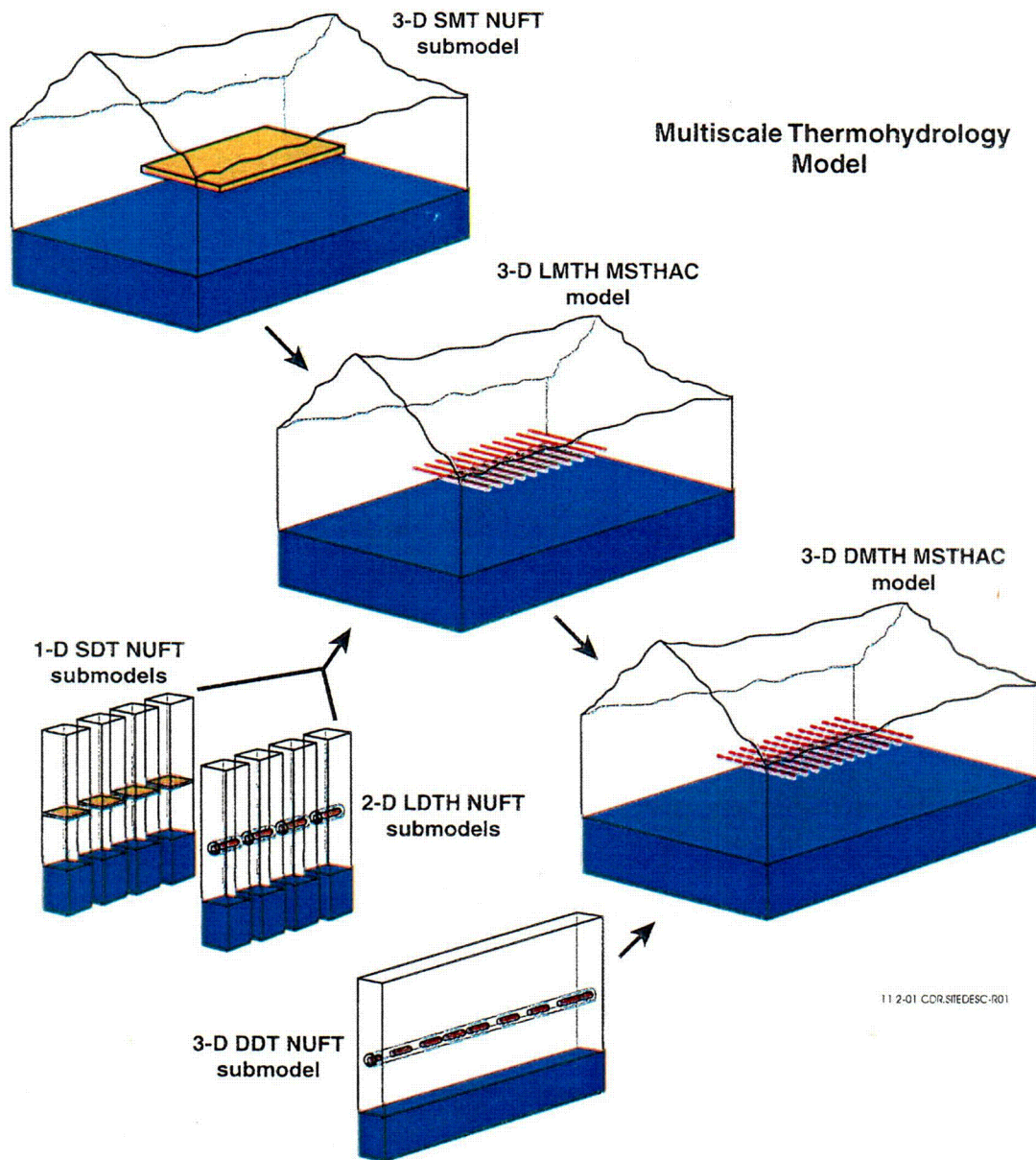
### 11.7.2 Codes, Standards, Regulations, and Procedures

10 CFR 60. Energy: Disposal of High Level Radioactive Wastes in Geologic Repositories. Readily available.

40 CFR 191. Protection of Environment: Environmental Radiation Protection Standards for Management and Disposal of Spent Nuclear Fuel, High-Level and Transuranic Radioactive Wastes. Readily available.

64 FR 8640. Disposal of High-Level Radioactive Wastes in a Proposed Geologic Repository at Yucca Mountain, Nevada. Proposed rule 10 CFR 63. Readily available.

Energy Policy Act of 1992. Public Law No. 102-486. 106 Stat. 2776. Readily available.

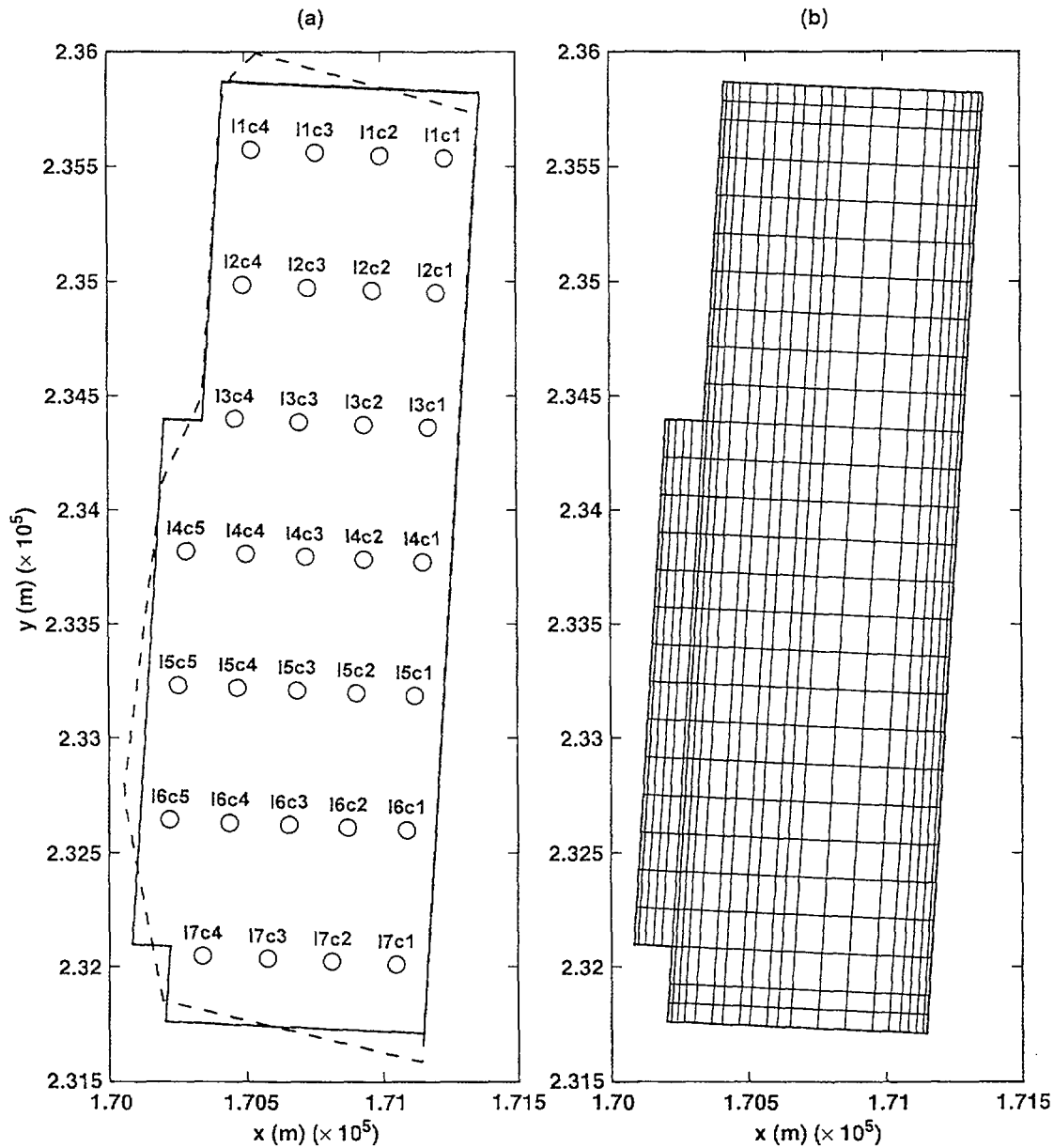


Source: Adapted from CRWMS M&O (2000a, Figure 1-1)

NOTES: The multiscale thermohydrologic model consists of four families of NUFT code-based submodels, including the SMT, SDT, LDTH, and DDT submodels, and the multiscale thermohydrologic abstraction code (MSTHAC), which integrates the results of the submodels. The intermediate result of the multiscale thermohydrologic model (MSTHM) is the line-averaged-heat-source, mountain-scale, thermohydrologic (LMTH) MSTHAC model. The final product of the MSTHM is the discrete-heat-source, mountain-scale thermohydrologic (DMTH) MSTHAC model.

LDTH = line-averaged-heat-source, drift-scale, thermohydrologic submodel; SMT = smeared-heat-source, mountain-scale, thermal-conduction submodel; SDT = smeared-heat-source, drift-scale, thermal-conduction submodel; DDT = discrete-heat-source, drift-scale, thermal-conduction submodel.

Figure 11.2-1. Multiscale Thermohydrologic Model

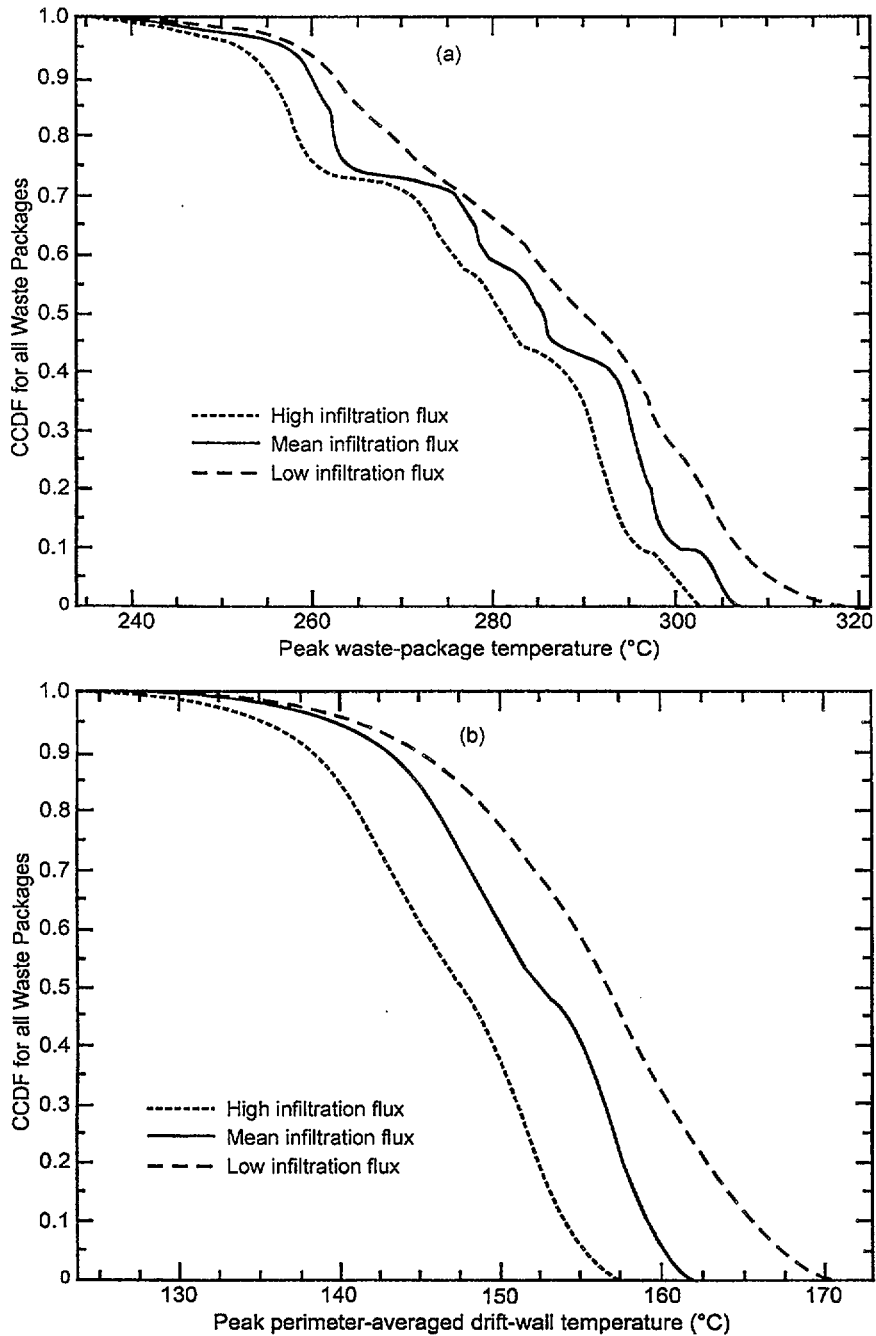


11.2-02 COR SITEDESC-001

Source: Adapted from CRWMS M&O (2000a, Figures 5-1, 5-2, and 6-2)

NOTE: Part (a) shows the 31 drift-scale (line-averaged-heat-source, drift-scale, thermohydrologic and smeared-heat-source, drift-scale, thermal conduction submodels) locations and the comparison of the potential repository area (dashed lines) and the approximation of the potential repository area (solid lines) assumed in the multiscale thermohydrologic model (MSTHM) calculations for the Total System Performance Assessment-Site Recommendation. Part (b) shows the 623 repository subdomains, where the thermohydrologic variables are calculated and the repository-scale numerical mesh of the repository area are used in the MSTHM calculations for the Total System Performance Assessment-Site Recommendation.

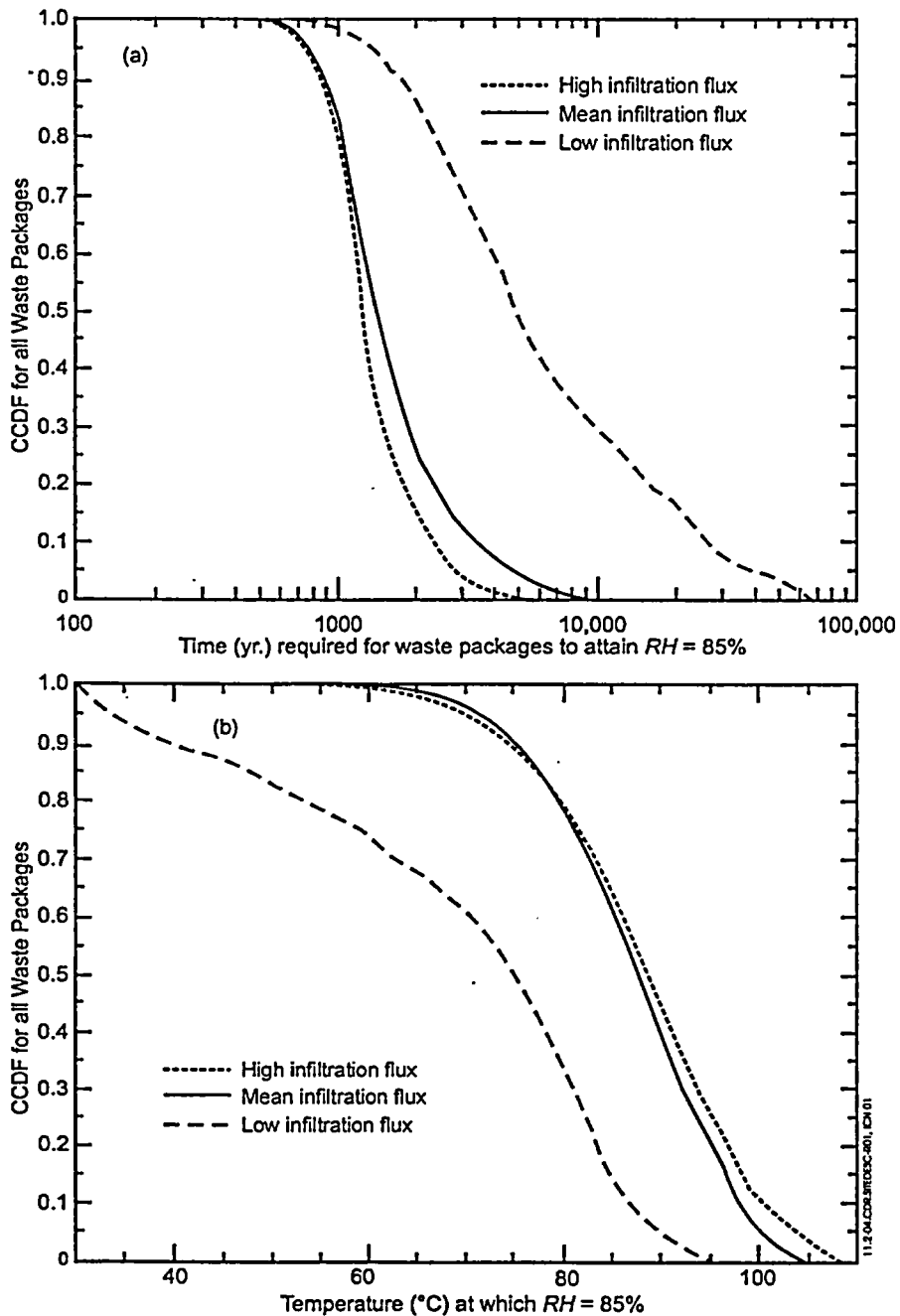
Figure 11.2-2. Potential Repository Area and Numerical Mesh Used in the Multiscale Thermohydrologic Model Calculations



Source: Revelli (2000, Figure 5)

NOTE: Part (a) shows the complementary cumulative distribution function (CCDF) of the peak waste package temperature for the nearly 5,000 combinations of waste package types and potential repository locations considered for Site Recommendation design at various infiltration fluxes. Part (b) shows the CCDF of the peak drift-wall temperature for the same cases.

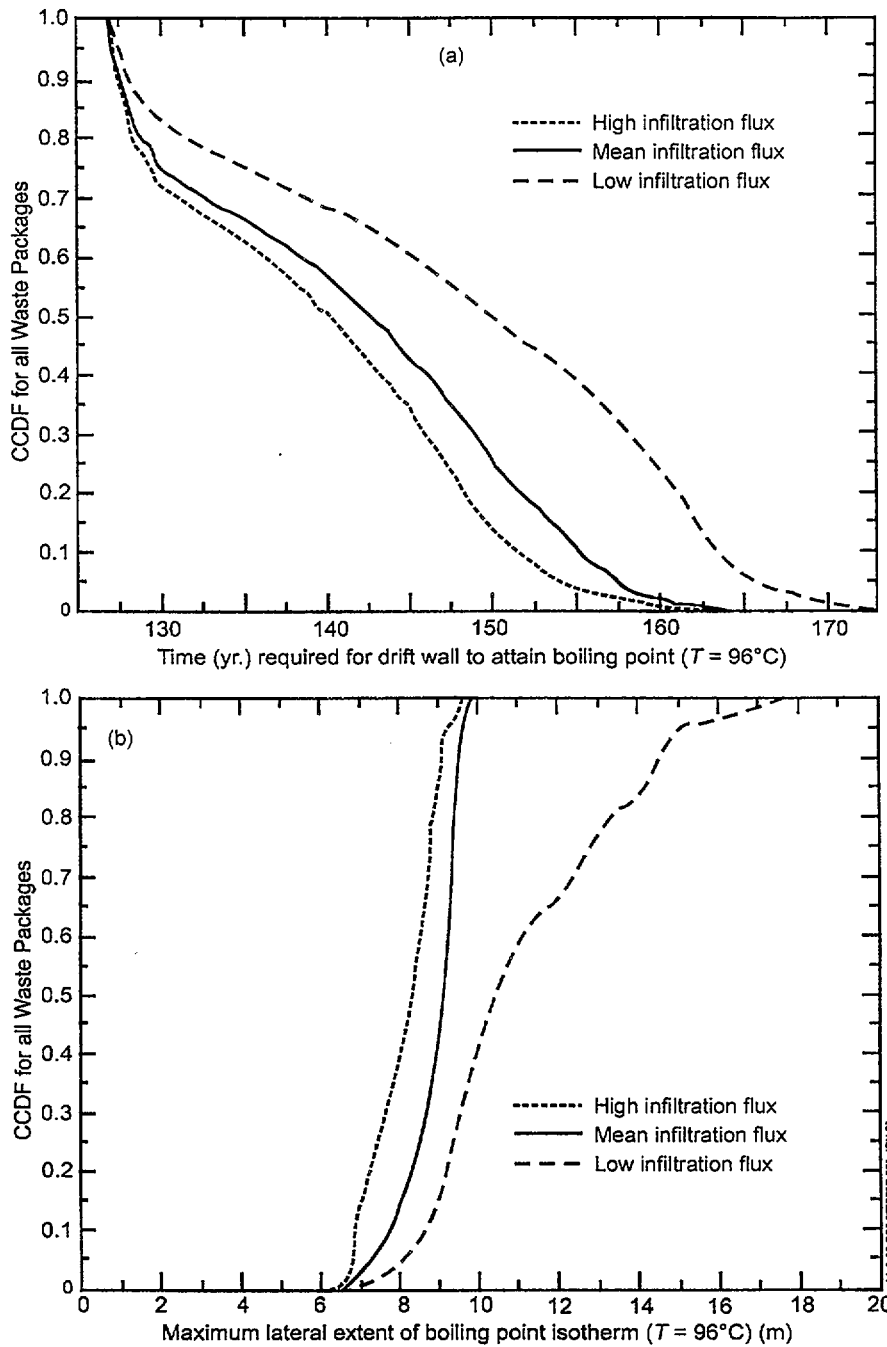
Figure 11.2-3. Complementary Cumulative Distribution Functions for Waste Package and Drift-Wall Peak Temperatures for Site Recommendation Design



Source: Revelli (2000, Figure 6)

NOTE: Part (a) shows the complementary cumulative distribution function (CCDF) for the time required for waste packages to attain a relative humidity (RH) of 85 percent for the nearly 5,000 combinations of waste package types and potential repository locations considered for Site Recommendation design at various infiltration fluxes. Part (b) shows the complementary cumulative distribution function of the waste package temperature at which waste packages reach a relative humidity of 85 percent for the same cases.

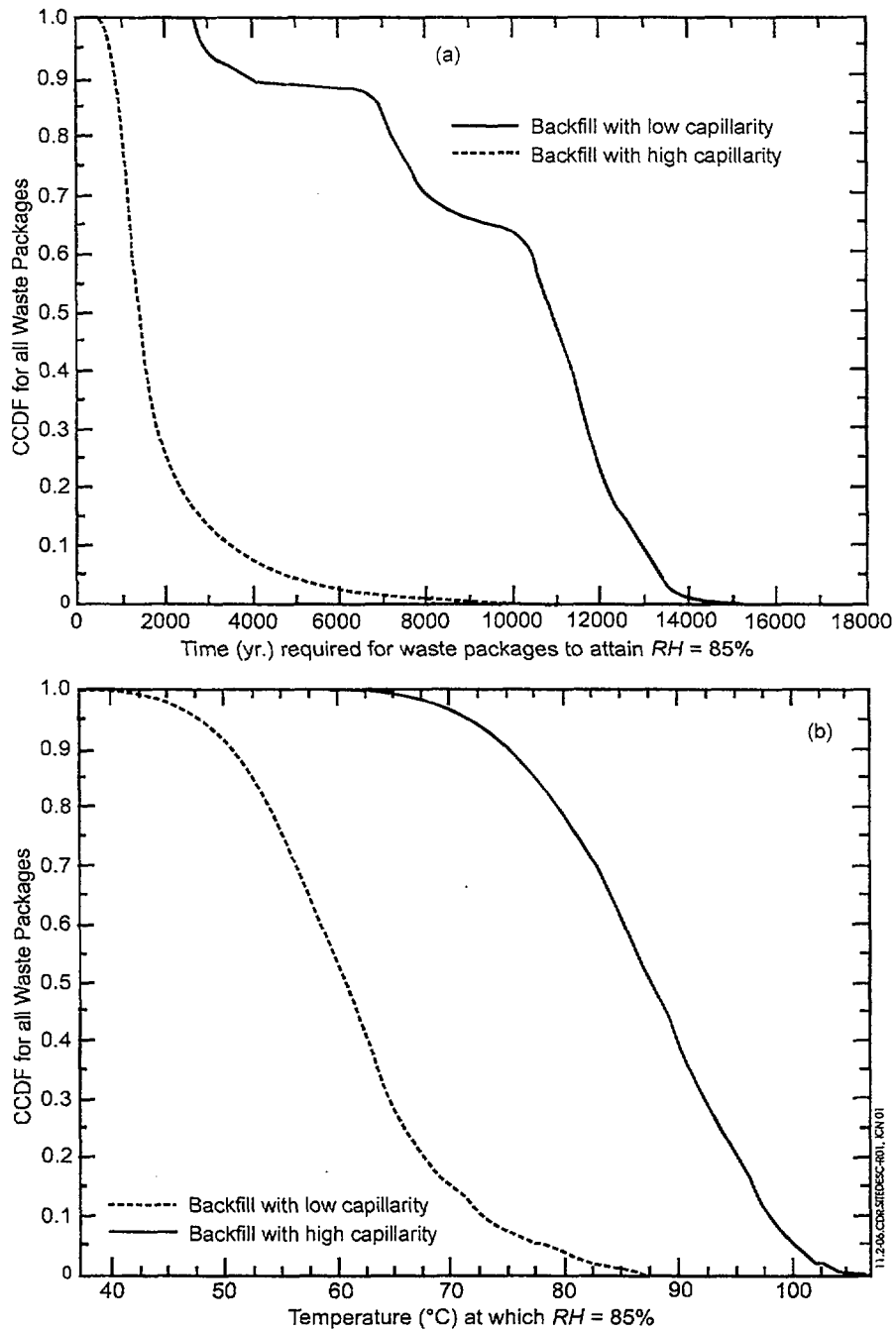
Figure 11.2-4. Complementary Cumulative Distribution Functions of Relative Humidity Reduction for Site Recommendation Design



Source: Revelli (2000, Figure 7)

NOTE: Part (a) shows the complementary cumulative distribution function for the time required for the drift wall to attain the boiling point temperature of  $96^{\circ}\text{C}$  during cooldown for Site Recommendation design at various infiltration fluxes. Part (b) shows the complementary cumulative distribution function of the maximum lateral extent of the boiling point isotherm.

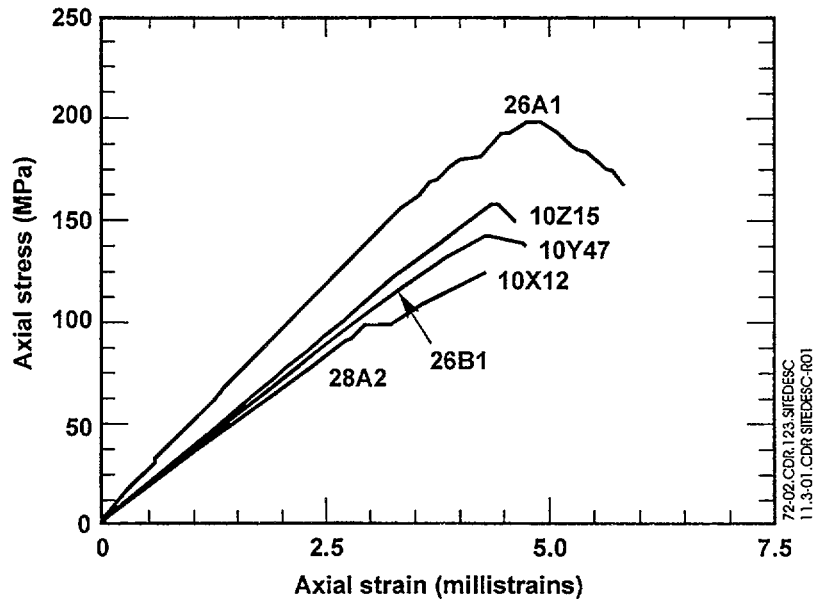
Figure 11.2-5. Complementary Cumulative Distribution Functions of Boiling Zone Extent and Duration for Site Recommendation Design



Source: Revelli (2000, Figure 8)

NOTE: Part (a) shows the complementary cumulative distribution function (CCDF) for the time required for waste packages to attain a relative humidity (RH) of 85 percent for the License Application design selection Enhanced Design Alternative IIa design (with low-capillarity backfill) and the Site Recommendation design (with high-capillarity backfill). Part (b) shows the CCDF of the waste package temperature at which waste packages reach a relative humidity of 85 percent for the same cases.

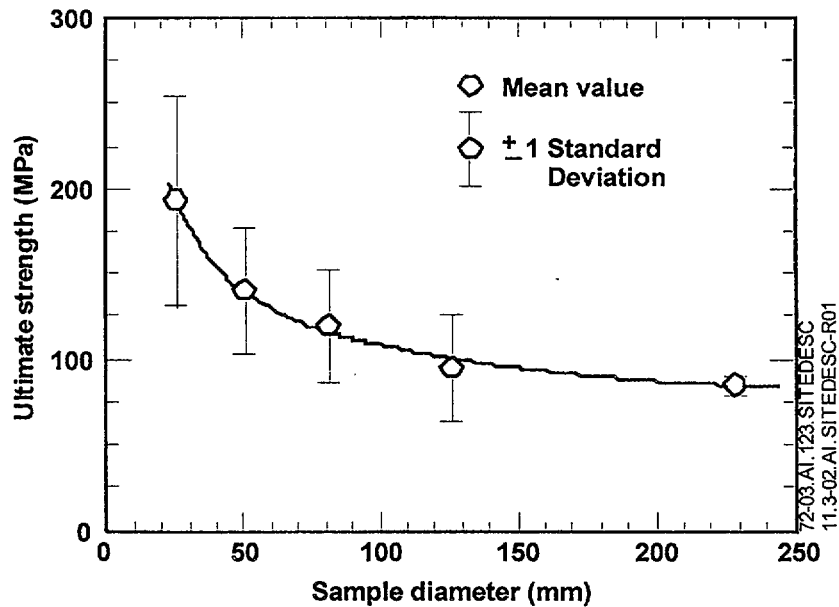
Figure 11.2-6. Complementary Cumulative Distribution Functions of Relative Humidity Reduction for Designs with Different Backfill



Source: Price (1986, Figure 5)

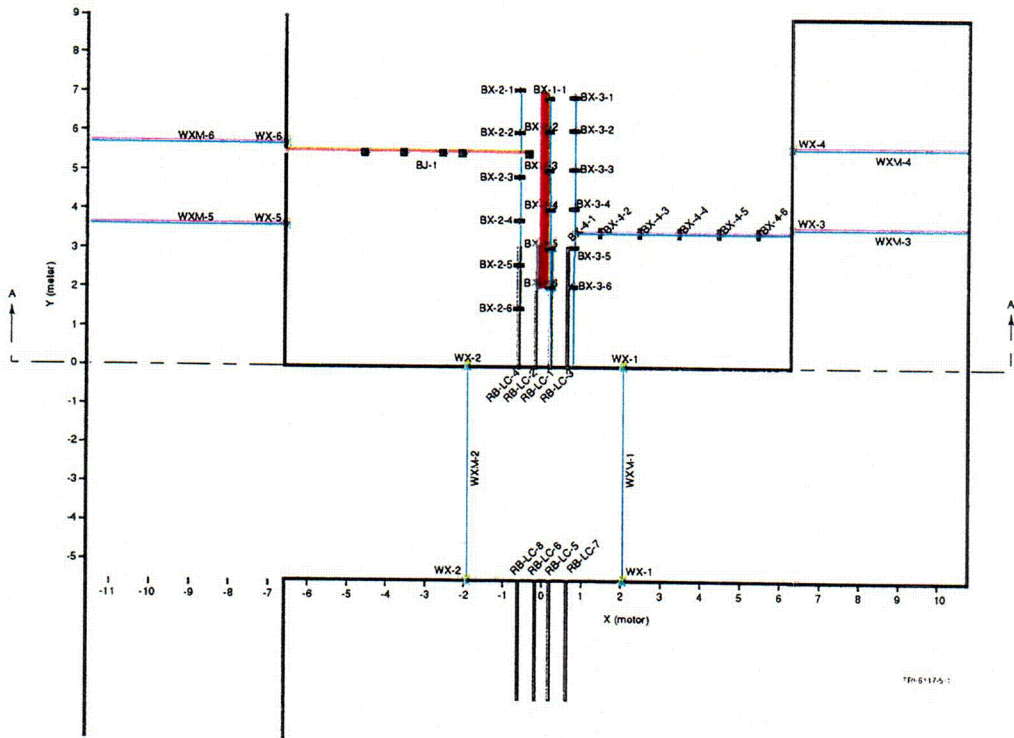
NOTE: Tested at a strain rate of  $10^{-5}$ /s at room temperature on 50.8-mm diameter samples. The labels for each curve represent the sample numbers.

Figure 11.3-1. Stress-Strain Curves from Uniaxial Compression Tests on Saturated Topopah Spring Tuff Samples



Source: Price (1986, Figure 11)

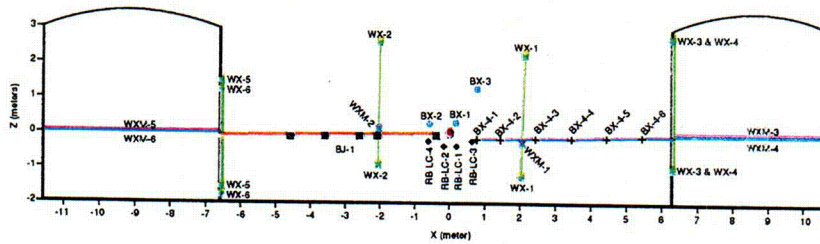
Figure 11.3-2. Ultimate Strength as a Function of Specimen Diameter from Uniaxial Compression Tests on Saturated Topopah Spring Tuff Samples



11.3-03.DOC.SITEDESC-R01

Source: CRWMS M&O (1999a, Figure 9-1)

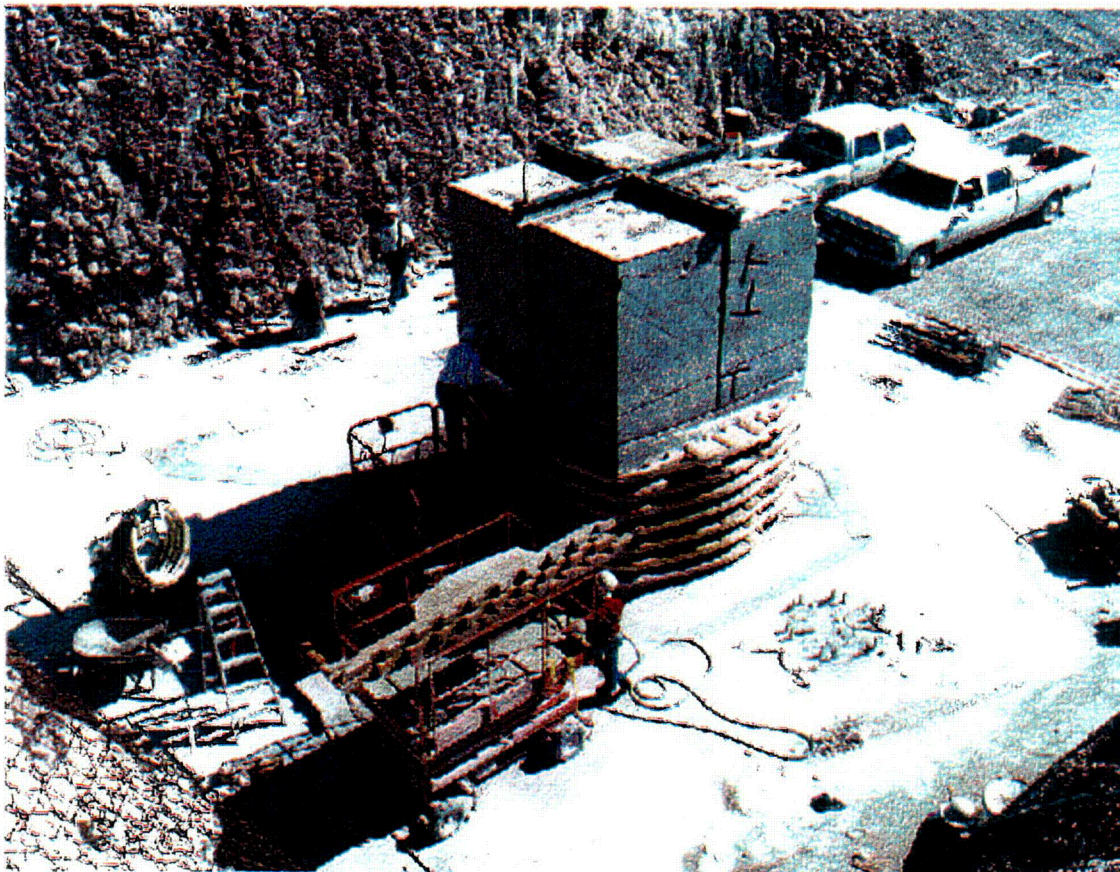
Figure 11.3-3. Plan View of the Single Heater Test Block Showing Monitoring Locations



11.3-04.DOC.SITEDESC-R01

Source: CRWMS M&O (1999a, Figure 9-2)

Figure 11.3-4. Cross Section of the Single Heater Test Block Showing Monitoring Locations

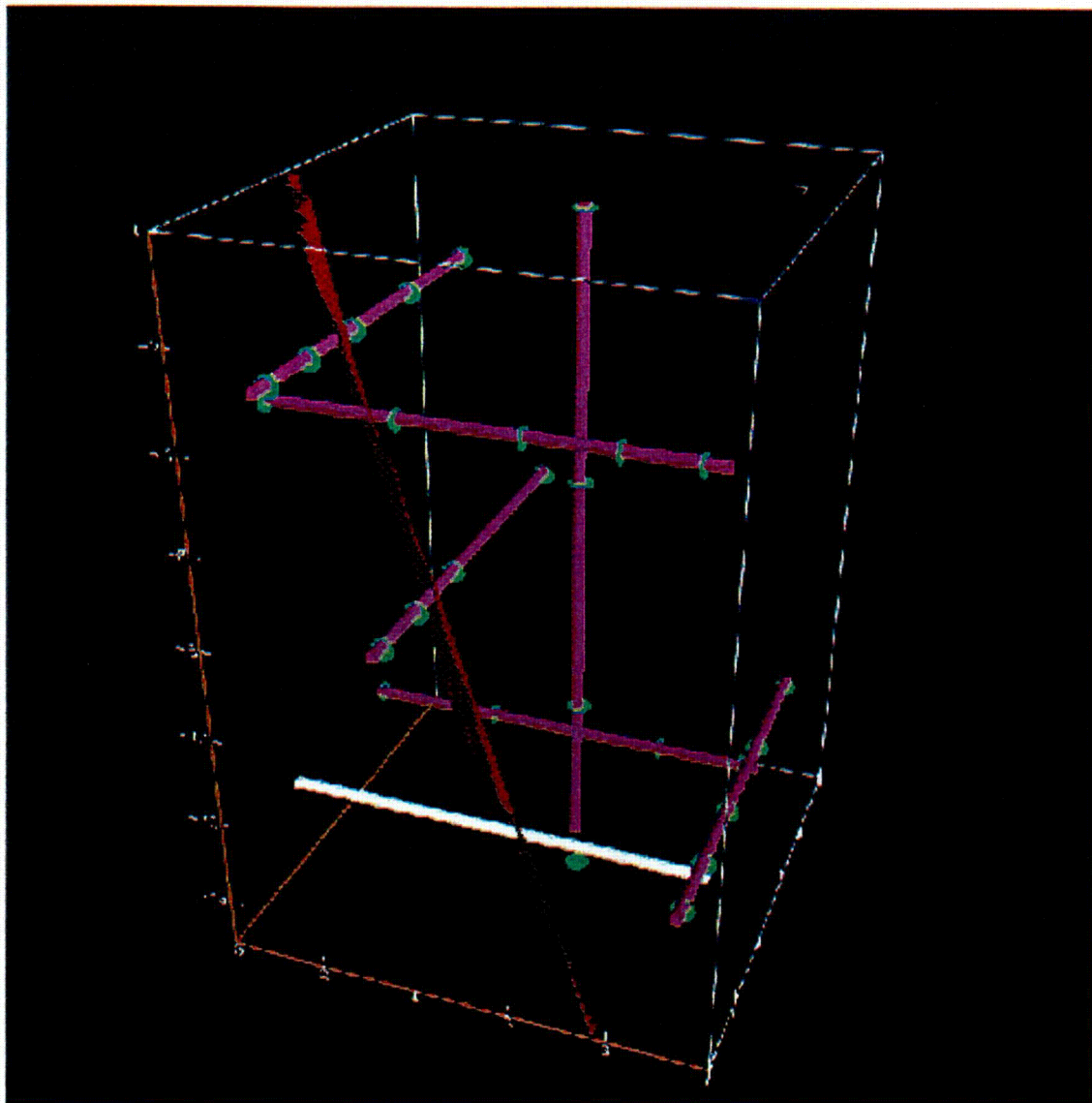


74-24.CDR.123.SIIEDESC  
11.3-05.CDR.SIIEDESC-R01

Source: Wilder et al. (1997, Figure 2-5)

NOTE: The upper portion of the block is exposed, while the lower portion of the block is supported with bracing. T-shaped grooves on the face of the block are the locations of fracture monitors.

Figure 11.3-5. Photograph of the Large Block

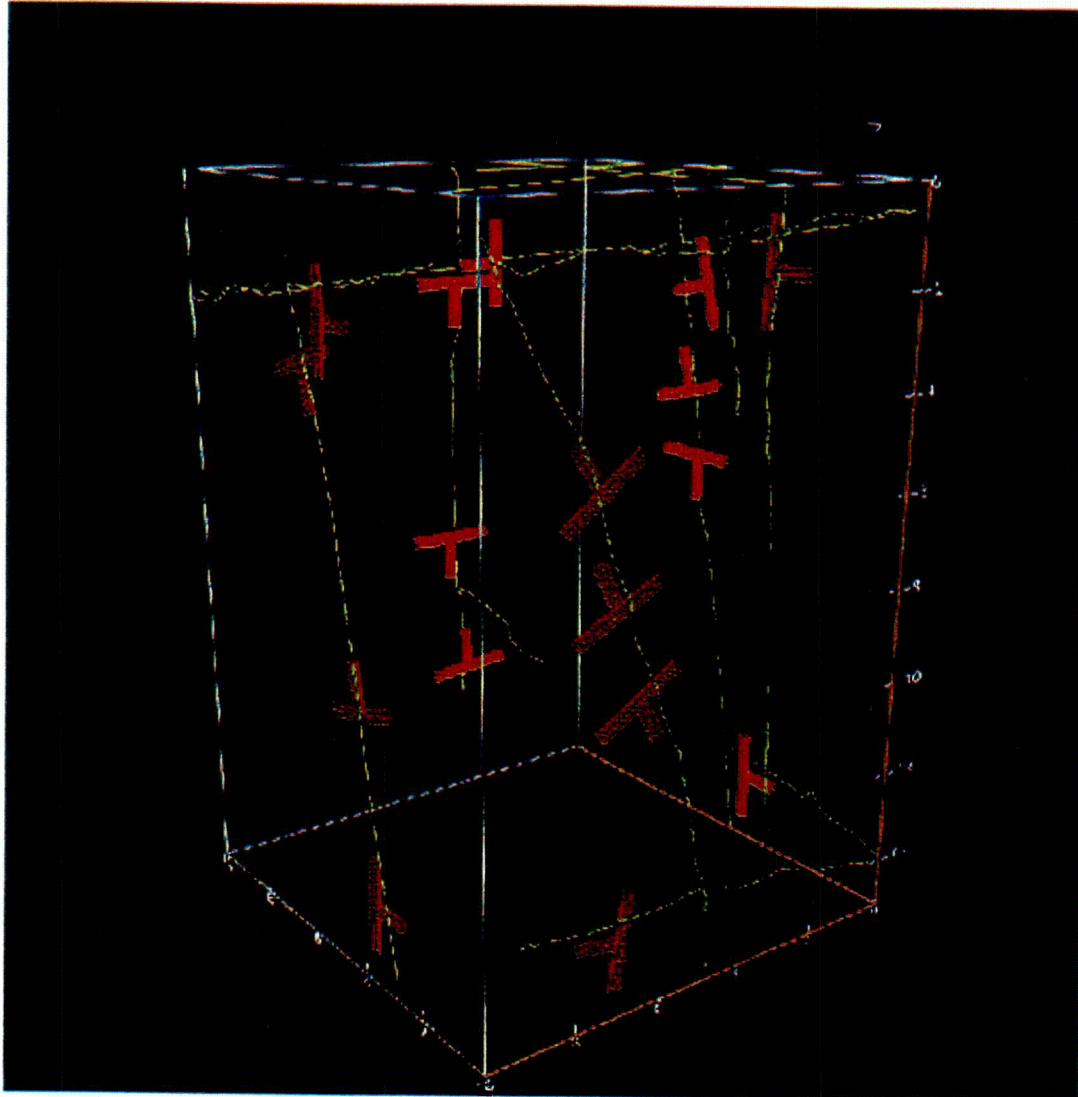


74-25.CDR.123.SITEDESC  
11.3-06.CDRSITEDESC-R01

Source: Wilder et al. (1997, Figure 4-7)

NOTE: The purple lines are MPBX holes, green rings are MPBX anchors, white line is an observation hole, stripe is a major fracture plane trending NW-SE.

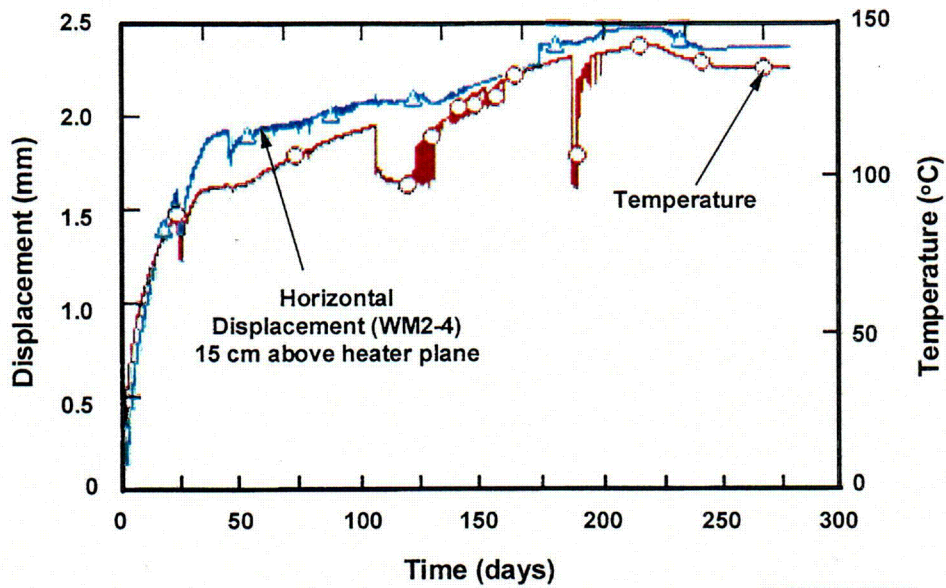
Figure 11.3-6. Location of Boreholes in the Large Block Used for Multiple-Point Borehole Extensometer Measurements



74-26.CDR.123.SITEDESC  
11.3-07.CDR.SITEDESC-001

Source: Blair and Lin (1997, Figure 3)

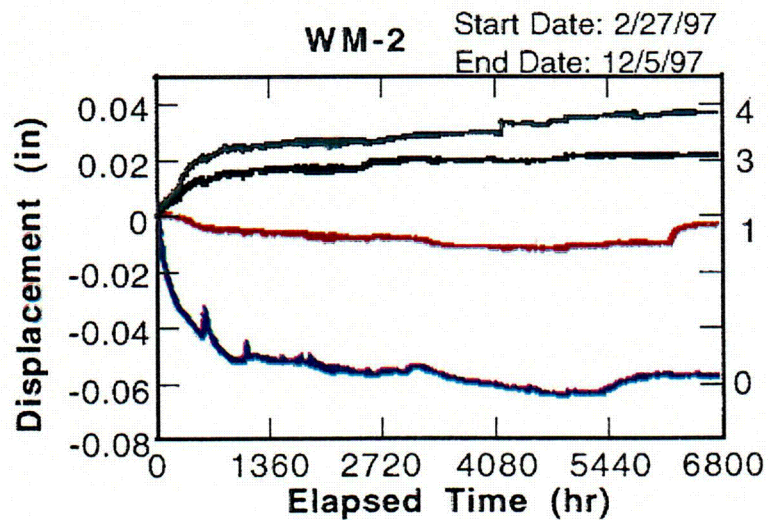
Figure 11.3-7. Locations of Surface-Mounted Fracture Monitors on the Large Block



11.3-08.DOC SITEDESC-R01

Source: Adapted from Blair and Lin (1997, Figure 4)

Figure 11.3-8. Temperature History near the Heater Plane for the Large Block Test

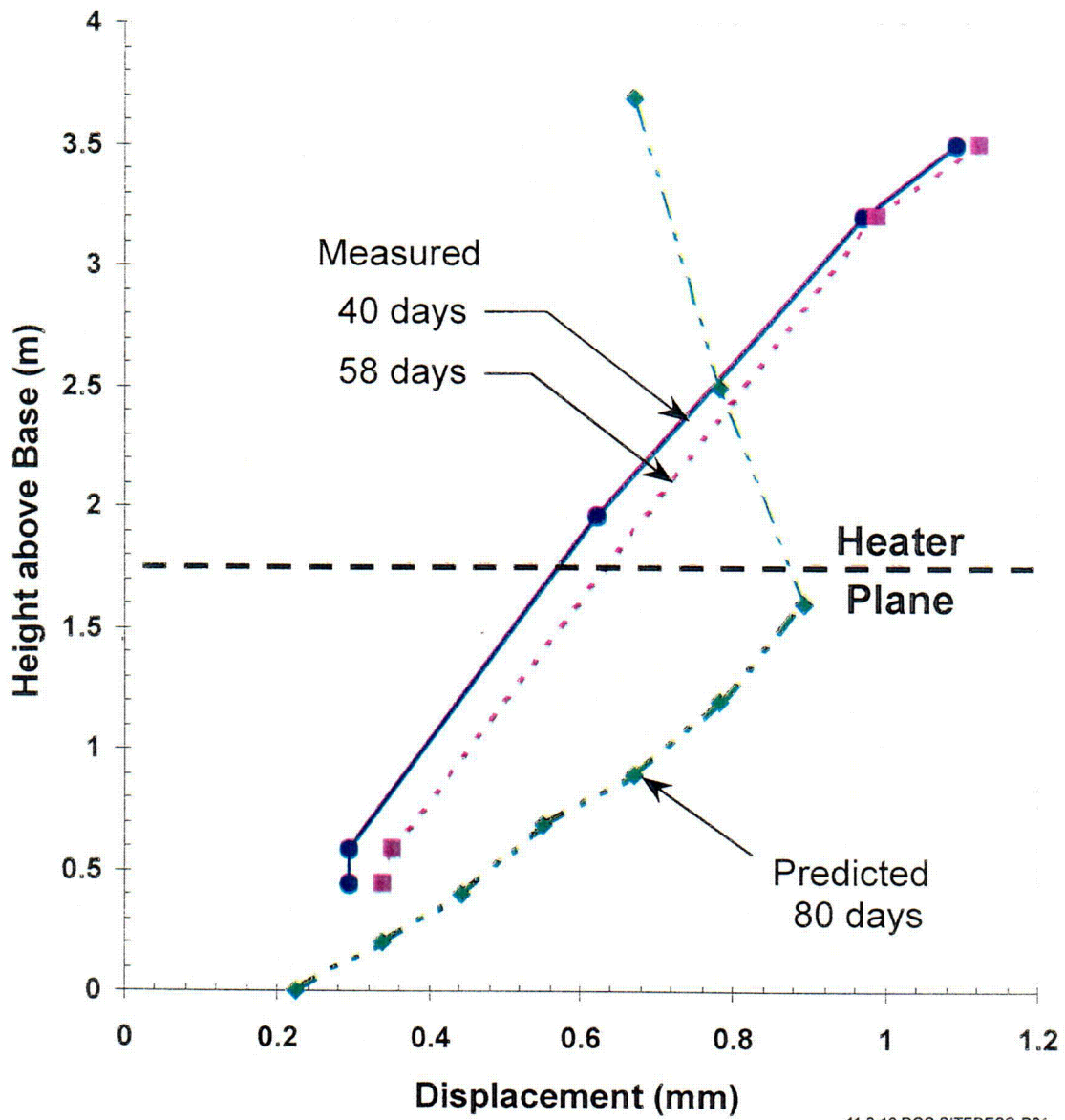


74-27b.CDR.123.SITEDESC  
11.3-09.CDR.SITEDESC-R01

Source: Blair and Lin (1997, Figure 5)

NOTE: Numbers (0 through 4) represent anchors.

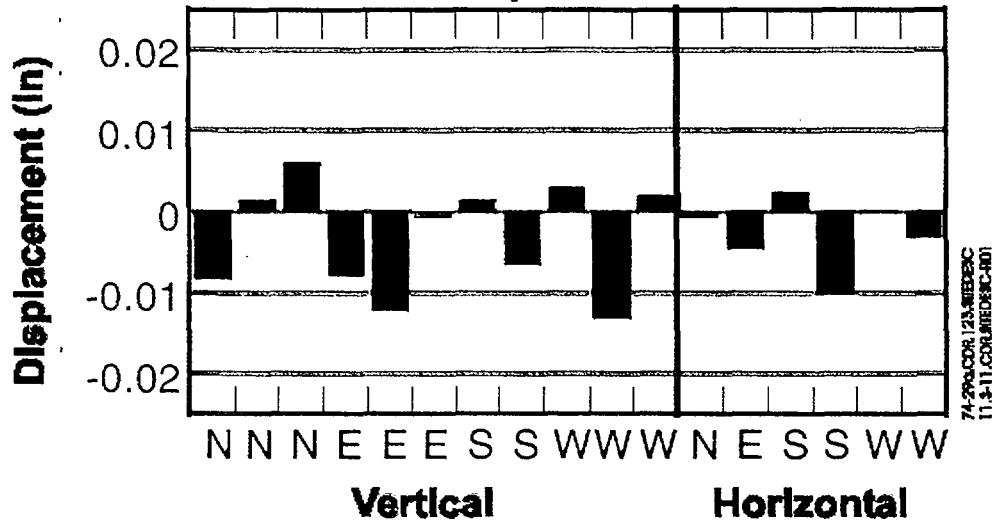
Figure 11.3-9. East-West Deformation Recorded with a Multiple-Point Borehole Extensometer Referenced to the Center of the Large Block



11.3-10.DOC.SITEDESC-R01

Source: Blair and Wood (1998, Figure 3)

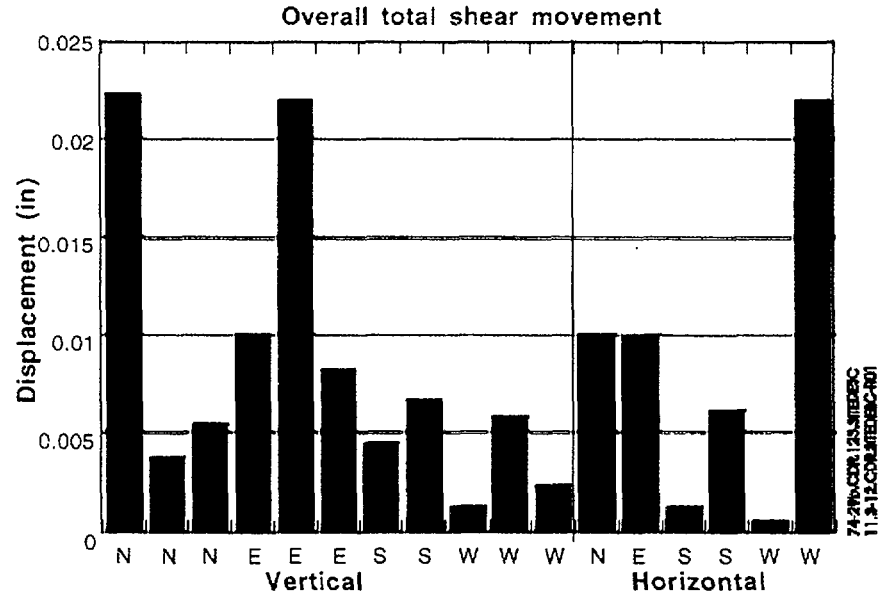
Figure 11.3-10. Predicted and Observed Horizontal Deformations for the Large Block



Source: Blair and Lin (1997, Figure 6)

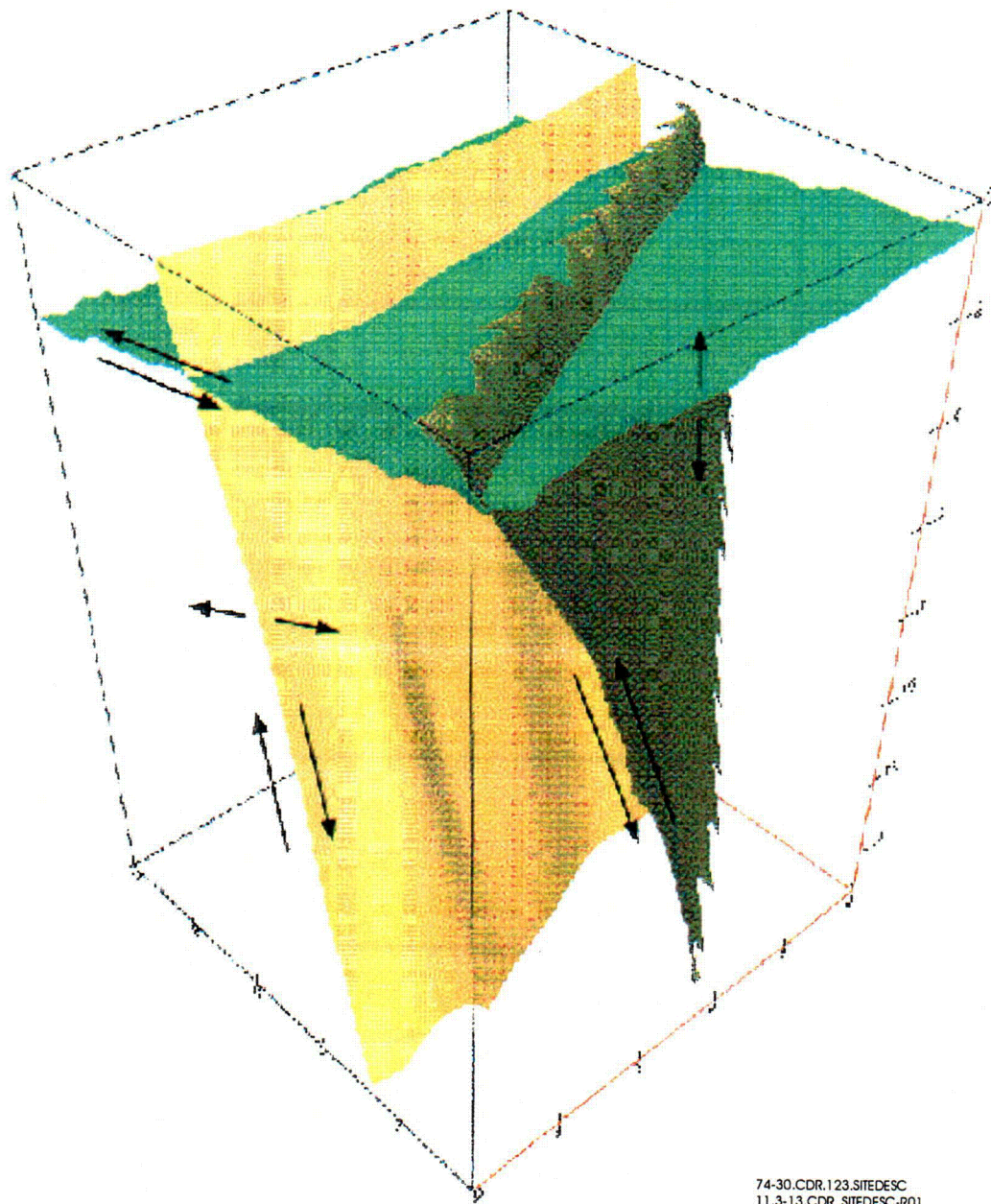
NOTE: Positive displacements indicate fracture closing.

Figure 11.3-11. Normal Displacements across Selected Large Block Fractures after 300 Days of Heating



Source: Blair and Wood (1998, Figure 5)

Figure 11.3-12. Shear Displacements along Selected Large Block Fractures after 300 Days of Heating

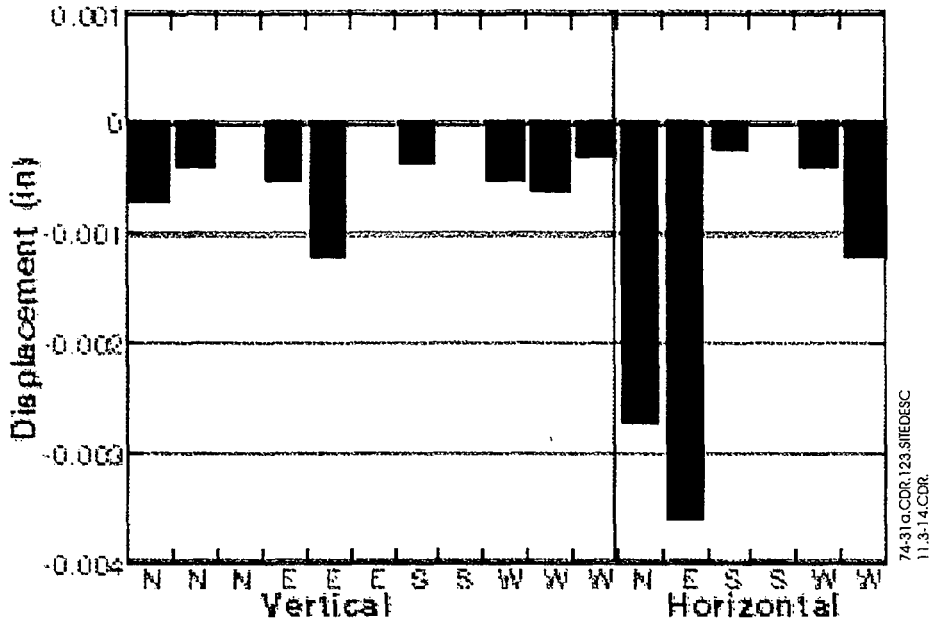


74-30.CDR.123.SITEDESC  
11.3-13.CDR.SITEDESC-R01

Source: Blair and Lin (1997, Figure 7)

NOTE: Arrows are not to scale and show only relative motion. North face is the front left plane; west face is the front right plane.

Figure 11.3-13. Relative Motions for Portions of the Large Block

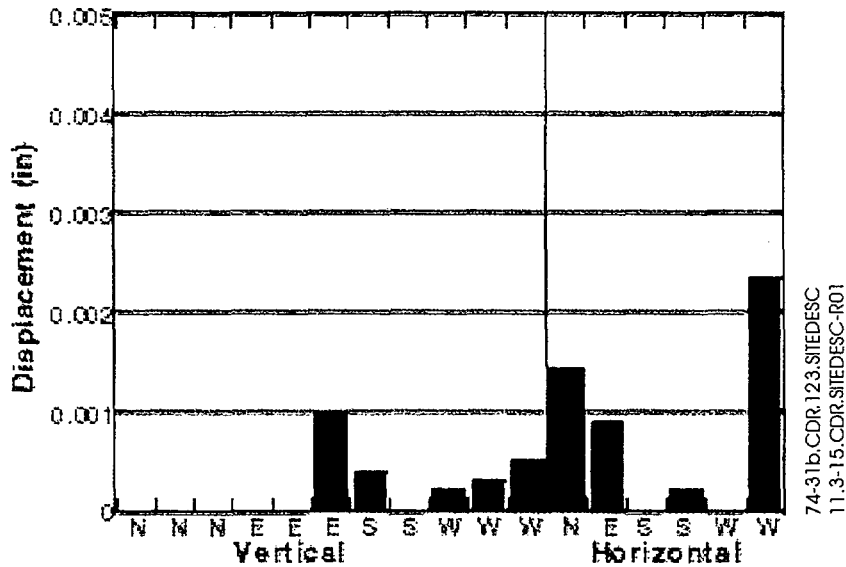


74-31b.CDR.123.SITEDESC  
11.3-14.CDR.

Source: Blair and Lin (1997, Figure 8)

NOTE: Negative displacements indicate fracture opening after 2,520 hours (104 days) of heating.

Figure 11.3-14. Normal Displacements across Selected Fractures Associated with the Thermal Excursion

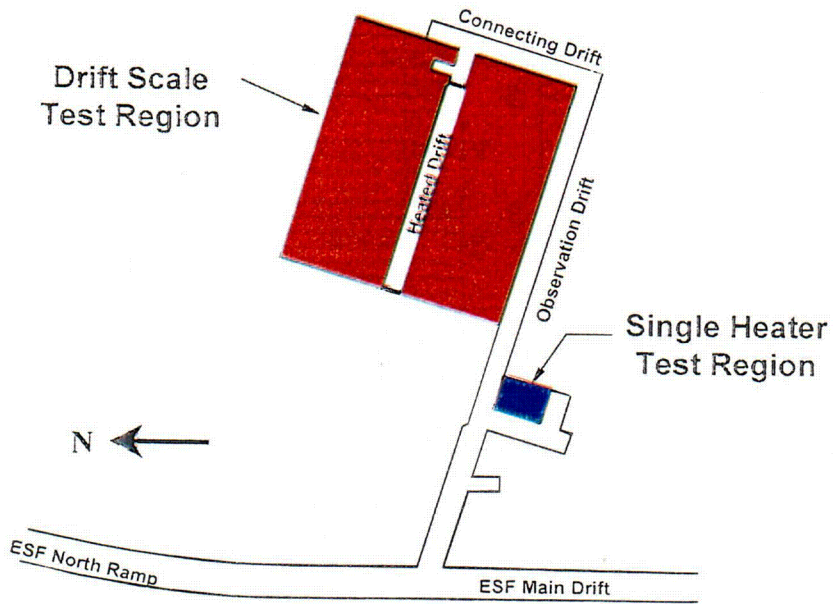


74-31b.CDR.123.SITEDESC  
11.3-15.CDR.SITEDESC-R01

Source: CRWMS M&O (1998c, Figure 7.4-31b)

NOTE: Displacements are after 2,520 hours (104 days) of heating.

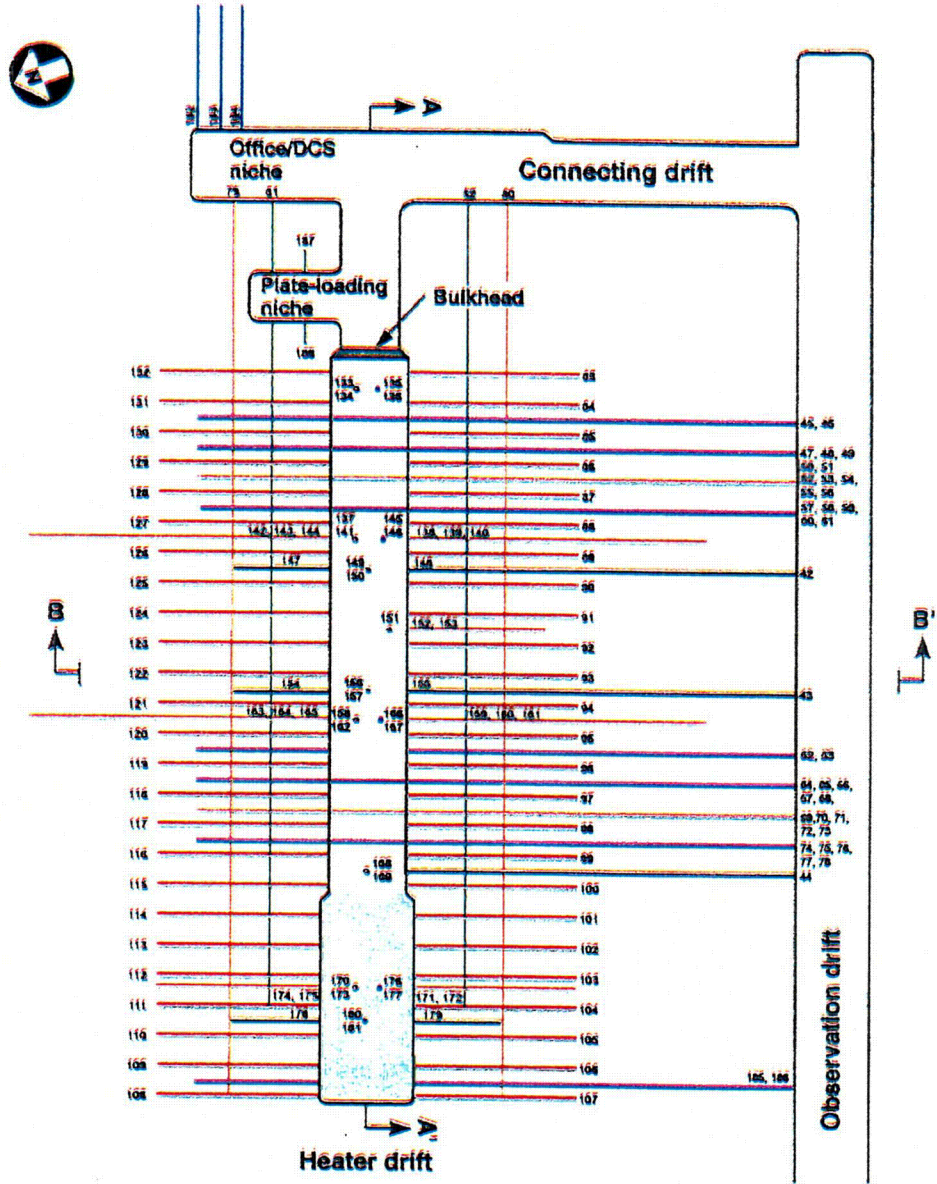
Figure 11.3-15. Shear Displacements along Selected Fractures Associated with the Thermal Excursion



11.3-16.DOC.SITEDESC-R01

Source: CRWMS M&O (1998d, Figure 1-1)

Figure 11.3-16. Plan View of Exploratory Studies Facility Thermal Test Facility

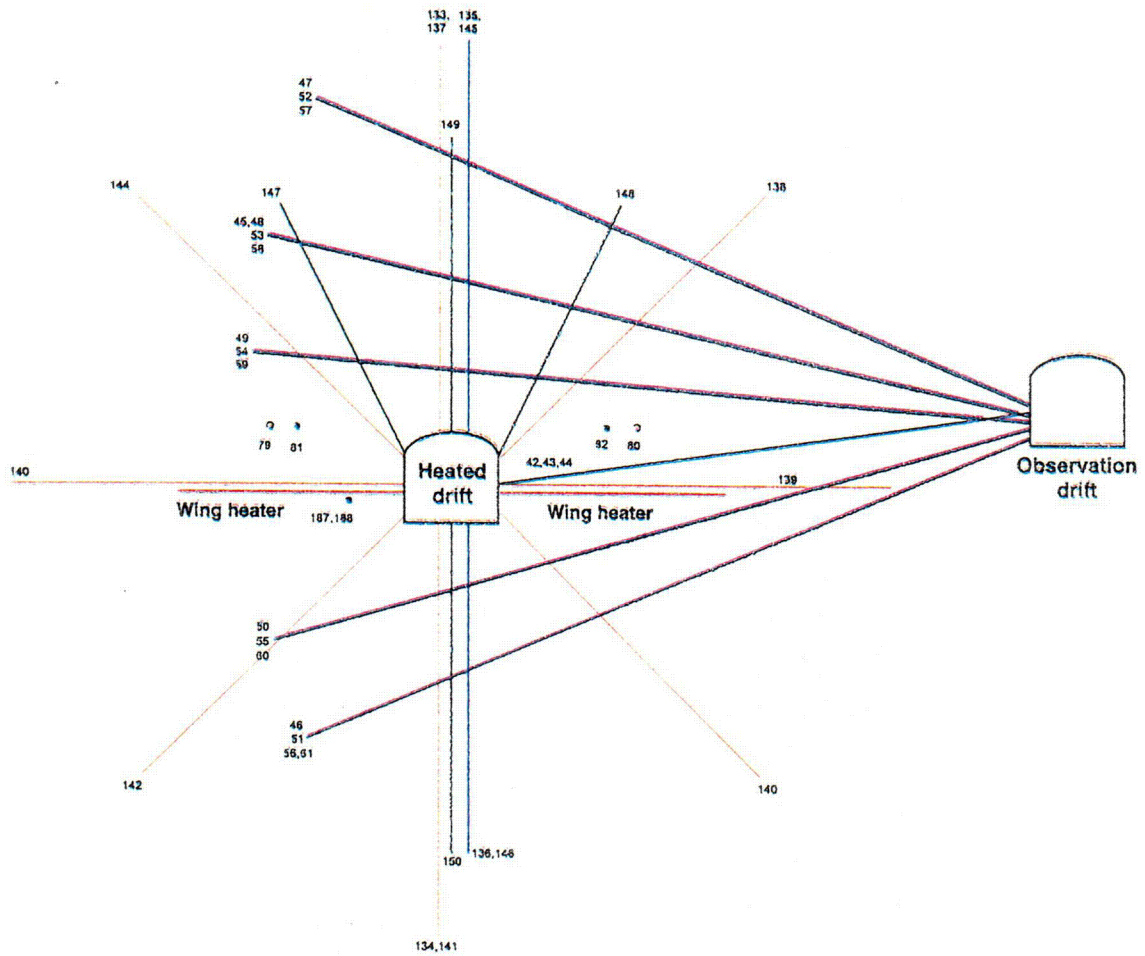


- | LEGEND: Boreholes                               |  | LEGEND: Ground support system  |  |
|---|--|--|--|
| <span style="color: red;">—</span> Wing heaters | <span style="color: blue;">—</span> Hydrological | <span style="border: 1px solid black; display: inline-block; width: 15px; height: 10px;"></span> Rockbolts and welded wire used throughout heated drift for safety and stability purposes only |  |
| <span style="color: orange;">—</span> Thermal   | <span style="color: black;">—</span> Chemical    | <span style="background-color: #cccccc; border: 1px solid black; display: inline-block; width: 15px; height: 10px;"></span> Cast-in-place concrete   |  |
| <span style="color: blue;">—</span> Mechanical  |  |  |  |

11.3-17.DOC.SITEDESC-R01

Source: CRWMS M&O (2000b, Figure 3-49)

Figure 11.3-17. Layout of the Drift Scale Test



**LEGEND: Boreholes**

- Wing Heaters
- Thermal
- Mechanical
- Hydrological
- Chemical

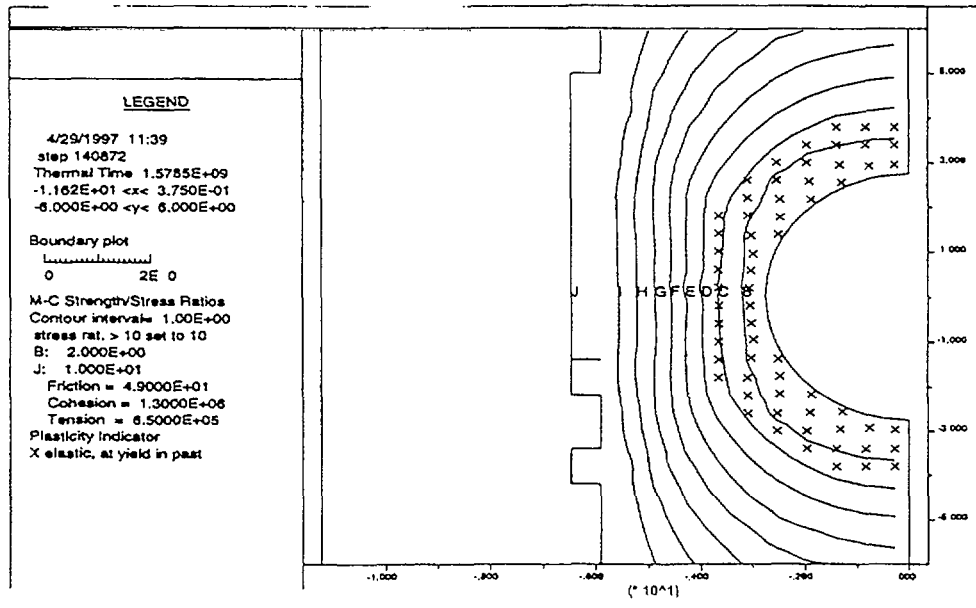
**REFERENCE ONLY**  
 (approximate scale: 1 cm ≈ 3 m)

11.3-18.DOC.SITEDESC-R01

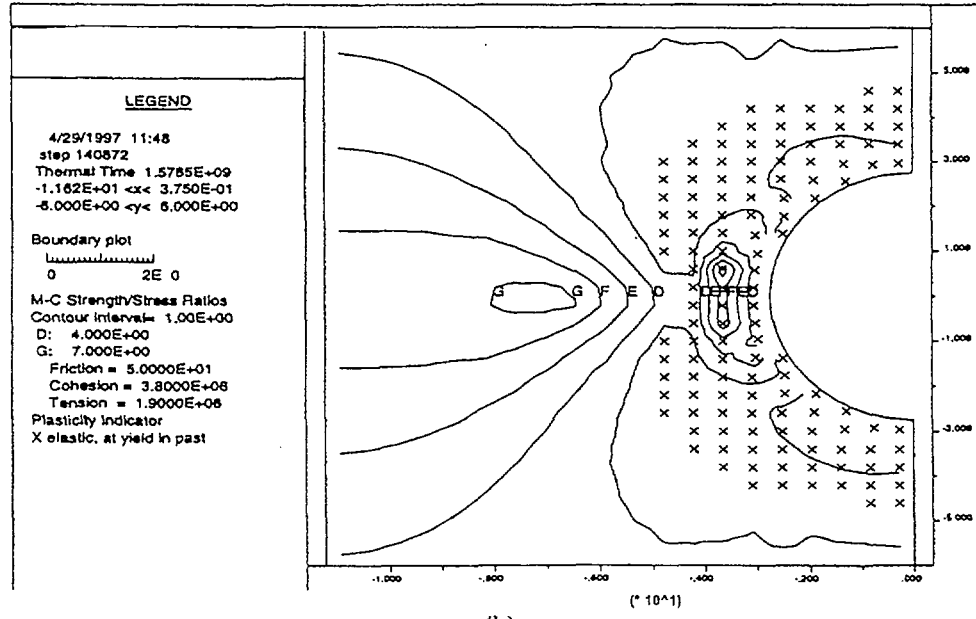
Source: CRWMS M&O (2000b, Figure 3-51)

NOTE: The track of cross section B-B' is shown on Figure 11.3-17.

Figure 11.3-18. Drift Scale Test Cross-Section B-B



(a)



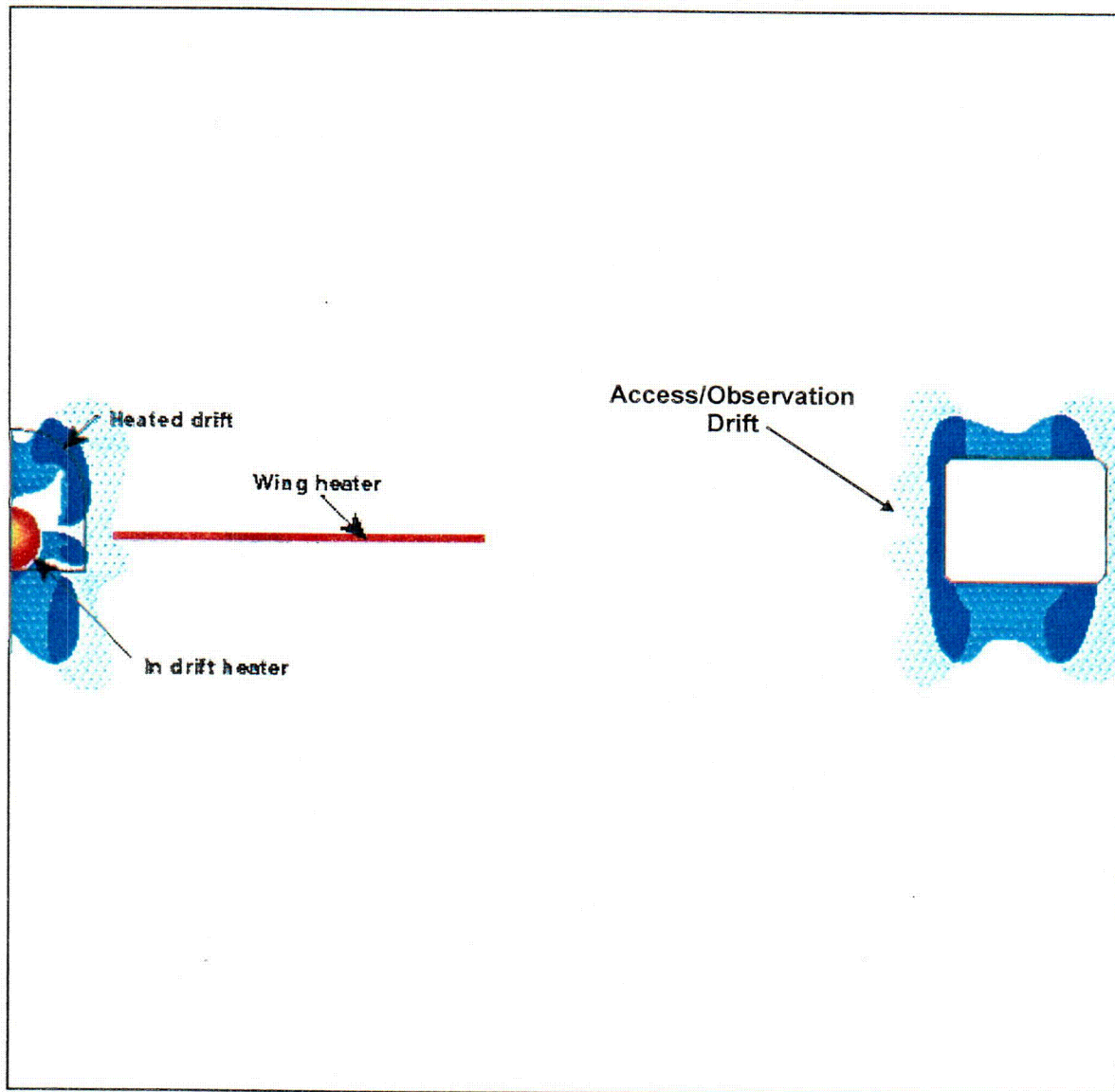
(b)

74-32.CDR.123.SI.EDESC  
11.3-19.CDR.SI.EDESC-R01

Source: Adapted from CRWMS M&O (1998a)

NOTE: Figure shows ventilation with air quantity of 60 m<sup>3</sup>/s and air temperature of 25°C at 50 years after emplacement for one month: (a) Rock Mass Quality (RMQ) = 1, (b) RMQ = 5.

Figure 11.3-19. Strength/Stress Ratio Contours and Plasticity Indicators for 100 Metric Tons of Uranium Per Acre

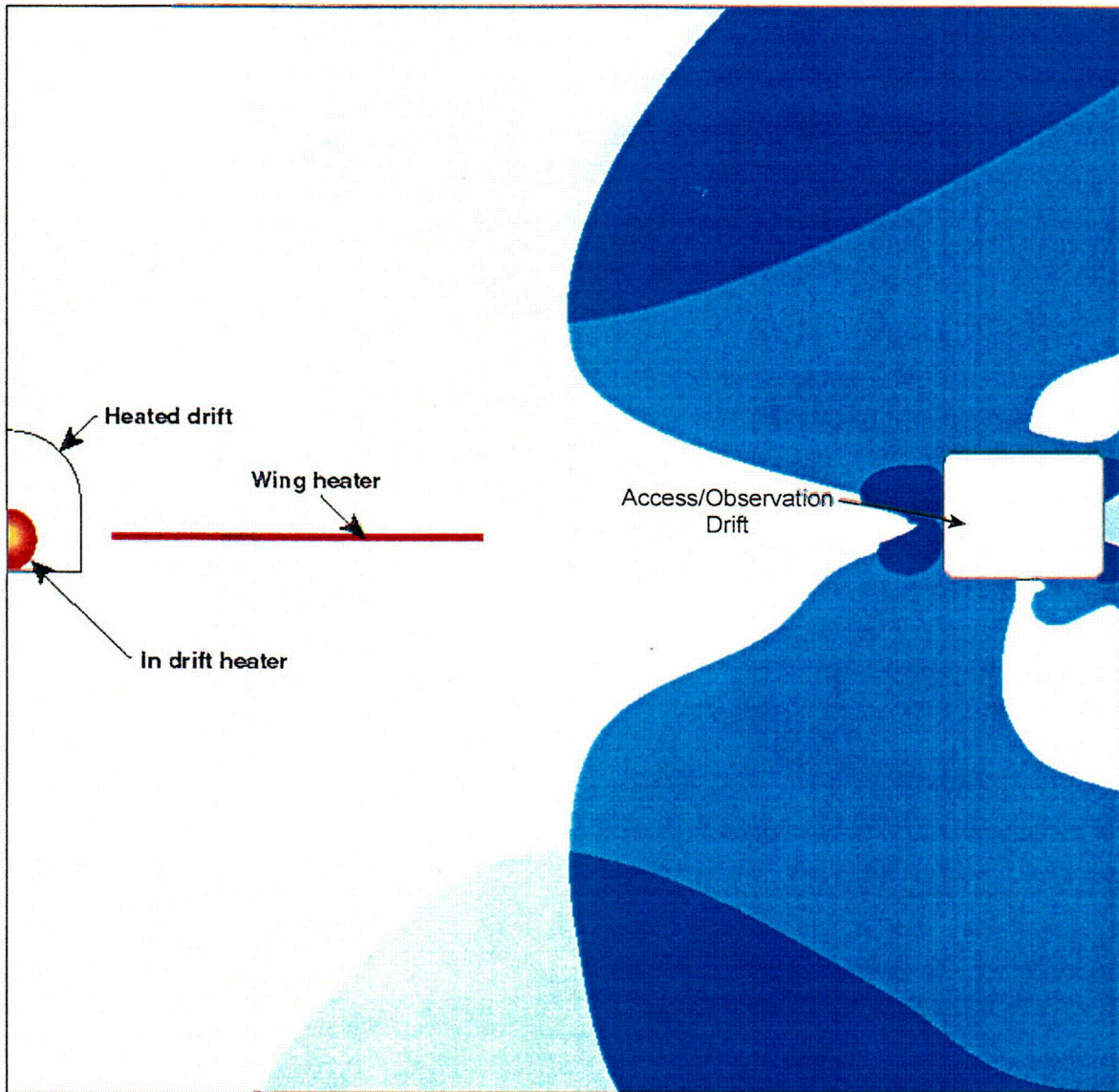


74-33a.CDR.123.SIIEDESC  
11.3-20.CDR.SIIEDESC-R01

Source: Hardin (1998a, Figure 4-62)

NOTE: Figure not to scale. Light shade indicates a zone where permeability is enhanced due to slip on vertical fractures. Medium shade indicates a zone where permeability is enhanced due to slip on horizontal fractures. Dark shade indicates a zone where permeability is enhanced due to slip on both vertical and horizontal fractures. View is looking east.

Figure 11.3-20. Predicted Zones of Enhanced Permeability due to Excavation prior to Heating for the Drift Scale Test



74-33b.CDR.123.SIIEDESC  
11.3-21.CDR.SIIEDESC-RO1

Source: Hardin (1998a, Figure 4-67)

NOTE: Figure not to scale. Light shade indicates a zone where permeability is enhanced due to slip on vertical fractures. Medium shade indicates a zone where permeability is enhanced due to slip on horizontal fractures. Dark shade indicates a zone where permeability is enhanced due to slip on both vertical and horizontal fractures.

Figure 11.3-21. Predicted Zones of Enhanced Permeability after Four Years of Heating for the Drift Scale Test

<b>Temperature</b>	<b>Vaporization Mobilization</b>	<ul style="list-style-type: none"> <li>Rock-water interactions</li> <li>Man-made material interactions (kinetics)</li> </ul>	<b>Thermodyn. of vapor</b>	<ul style="list-style-type: none"> <li>Dehydration</li> <li>Rock-water interactions (kinetics)</li> </ul>	<ul style="list-style-type: none"> <li>Dehydration</li> <li>Rock-water interactions</li> <li>Material (kinetics)</li> </ul>	<ul style="list-style-type: none"> <li>Stress changes</li> <li>Coefficient impacts</li> </ul>
<ul style="list-style-type: none"> <li>Latent heat</li> <li>Heat pipes</li> </ul>	<b>Moisture conditions</b>	<ul style="list-style-type: none"> <li>Volumetrics</li> <li>Water</li> <li>Rock</li> <li>Materials</li> </ul>			<ul style="list-style-type: none"> <li>Volumetrics</li> <li>water-rock</li> <li>Contact modes</li> </ul>	<ul style="list-style-type: none"> <li>Water contribution to crack growth</li> </ul>
		<b>Water chemistry</b>	<b>Vapor partial pressure</b>		<ul style="list-style-type: none"> <li>Reaction thermodyn.</li> <li>Solubility</li> <li>Precipitation</li> <li>Carbonation</li> </ul>	
			<b>Relative humidity conditions</b>	Vapor/rock interactions	Vapor/rock/solid interactions	
Altered flow paths	Altered flow paths		Changed flow conditions	<b>Hydrologic properties</b>	Water contact	<ul style="list-style-type: none"> <li>Healing of fractures</li> <li>Changes water avail. for cracking</li> </ul>
<ul style="list-style-type: none"> <li>Thermal conductivity changes</li> <li>Heat consumption release in chemical reactions</li> </ul>	Consumption release H <sub>2</sub> O (chemical reactions)	<ul style="list-style-type: none"> <li>Altered minerals</li> <li>Rock-water interactions</li> </ul>	Partial press. (salts)	<ul style="list-style-type: none"> <li>Fracture/pore plugging</li> <li>Fracture healing</li> <li>Colloid transport</li> </ul>	<b>Mineral and solid material (changes)</b>	<ul style="list-style-type: none"> <li>Volume changes (phase transform and mineral changes)</li> </ul>
				<ul style="list-style-type: none"> <li>Closing/opening fractures</li> <li>Microcracks</li> <li>Coalescence flow path</li> </ul>	<ul style="list-style-type: none"> <li>Stress impacts</li> <li>Mineral phase</li> <li>Microcracks (new surfaces)</li> </ul>	<b>Mechanical conditions (changes)</b>

74-11.AI.123.SITEDESC  
11.4-01.AI.SITEDESC-R01

Source: Wilder (1997, Figure 5-15)

NOTE: Yellow arrows indicate elevated temperature coupling.

Figure 11.4-1. Matrix of Coupled Geochemical and Mineralogical Processes

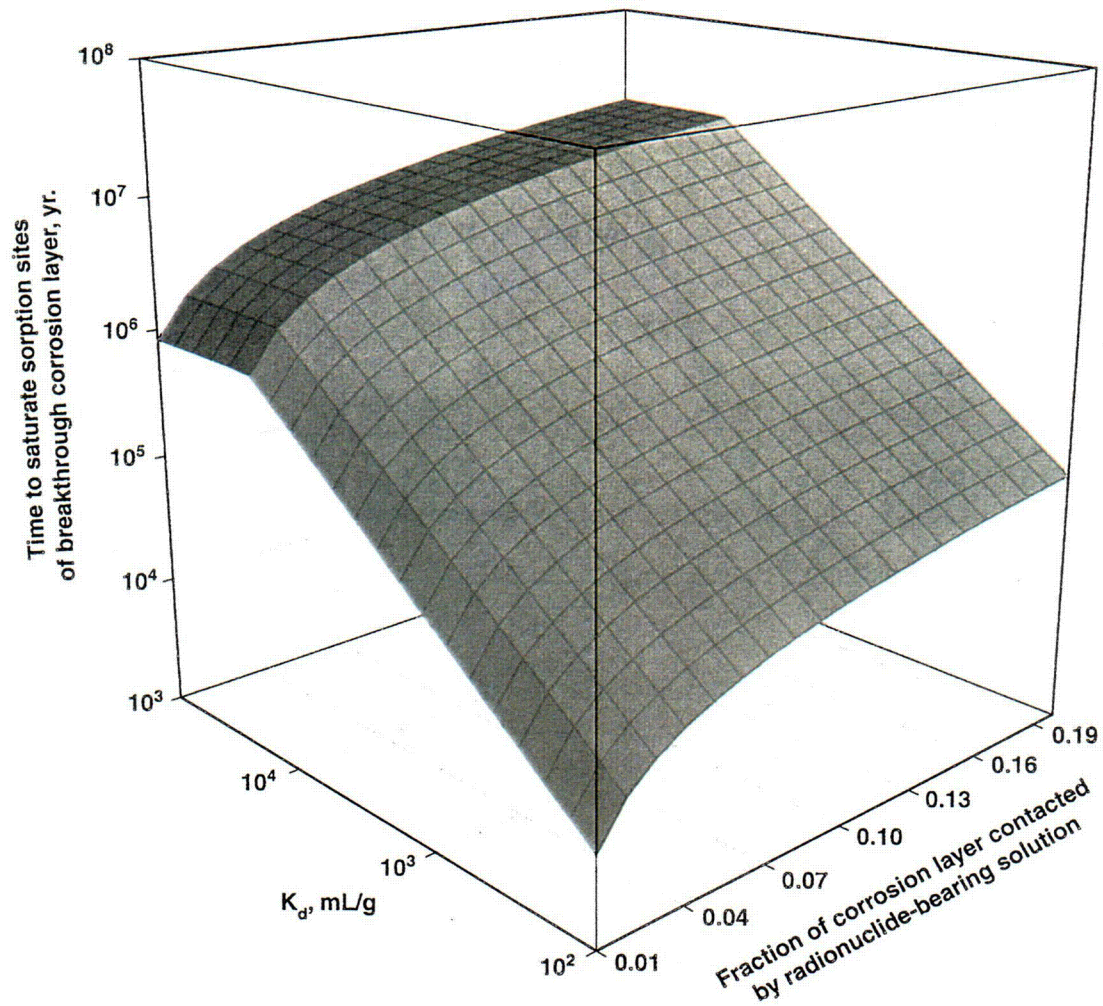
<b>Ambient percolation flux</b>	Latent heat convection						
	<b>Rock-mass temperature</b>	Dryout/evaporation	· Dryout/evaporation · Vapor/water mobilization	· Dryout/evaporation · Heat of vaporization · Buoyancy		· Rock-water interaction · Mineral dehydration	· Rock-water interaction · Mineral dehydration
		<b>Moisture in pores</b>	· Saturation gradients · Imbibition · Condensation · Capillary/gravity equil.	Vapor diffusion	· Moisture mobilization · Imbibition · Rock-water interaction	· Primary minerals water interaction · Buffering · Pore-water chemistry	
	· Convection · Latent heat · Heat pipe (refluxing)		<b>Moisture in fractures</b>	Vapor equilibrium	Condensate drainage	· Secondary minerals water interaction · Fracture water chemistry	
	· Heat pipe · Vapor heat redistribution · Heat release · Condensation	Vapor resaturation	Vapor resaturation	<b>Vapor in fractures</b>	Vapor escape from system	Vapor rock interaction	
		Imbibition	· Mixing · Dilution		<b>Net percolation flux</b>	· Mixing · Buffering	
		Changes in boiling point	Changes in boiling point	Changes in vapor pressure		<b>Water chemistry</b>	Rock-water interaction
				Changes in vapor pressure		· Chemical reactions · Rock-water interaction · Buffering	<b>Mineral changes</b>

74-10.AI.123.SITEDESC  
11.4-02.AI.SITEDESC-R01

Source: Wilder (1997, Figure 4-9)

NOTE: Yellow arrows in clockwise and counterclockwise directions represent forward and backward coupling, respectively. Key parameters are shown along the diagonal in blue. Coupled processes are shown off-diagonal.

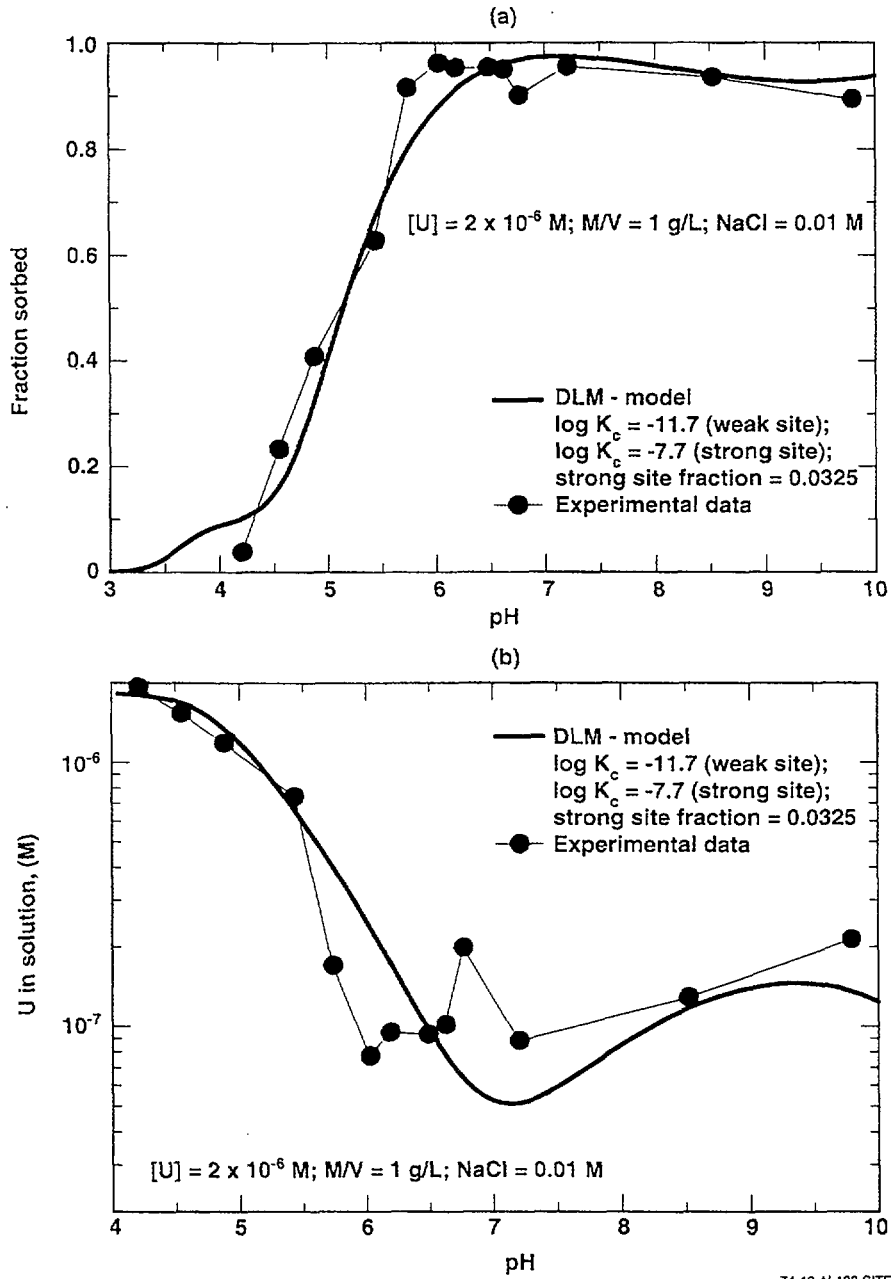
Figure 11.4-2. Matrix of Coupled Processes in the Near-Field Environment Related to Water Chemistry



74-12.CDR.123.SITEDESC  
11.4-03.EPS.SITEDESC-R01

Source: Hardin (1998a, Figure 6-33)

Figure 11.4-3. Calculated Years to Breakthrough of Radionuclide-Bearing Groundwater through Corrosion Layer as a Function of Partition Coefficient and Volume Fraction

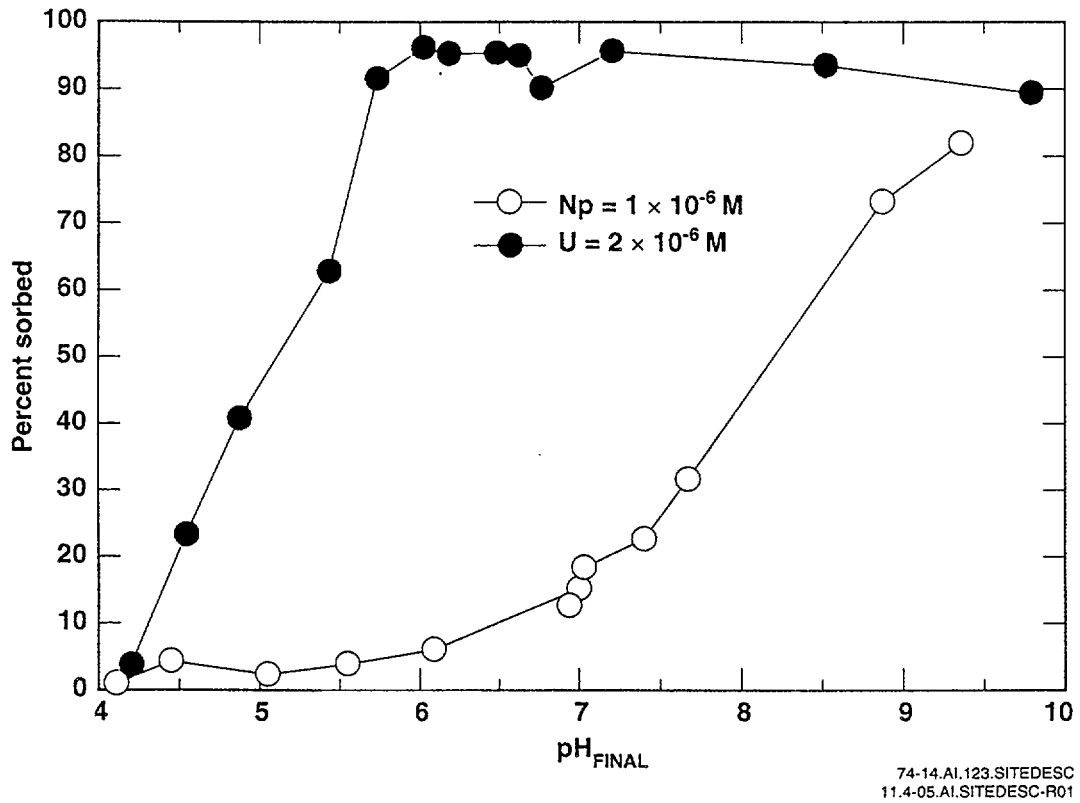


74-13.AI.123.SITEDESC  
11.4-04.AI.SITEDESC-R01

Source: Hardin (1998a, Figure 6-27)

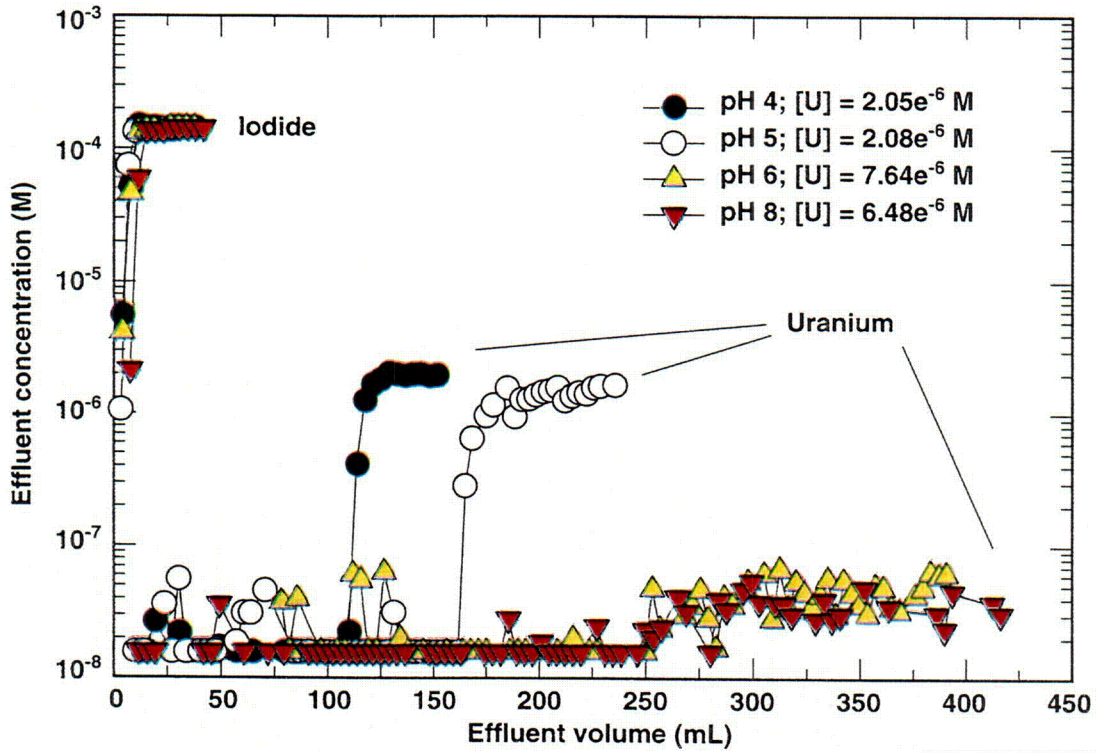
NOTE: Part (a) shows the fraction of uranium sorbed, and part (b) shows the concentration of uranium in a 0.01 NaCl solution at 26°C.

Figure 11.4-4. Comparison of Double-Layer Model Predictions with Experimental Data



Source: Hardin (1998a, Figure 6-28)

Figure 11.4-5. Percent Uranium and Neptunium Sorbed as a Function of Final pH in Four-Day Batch Experiments

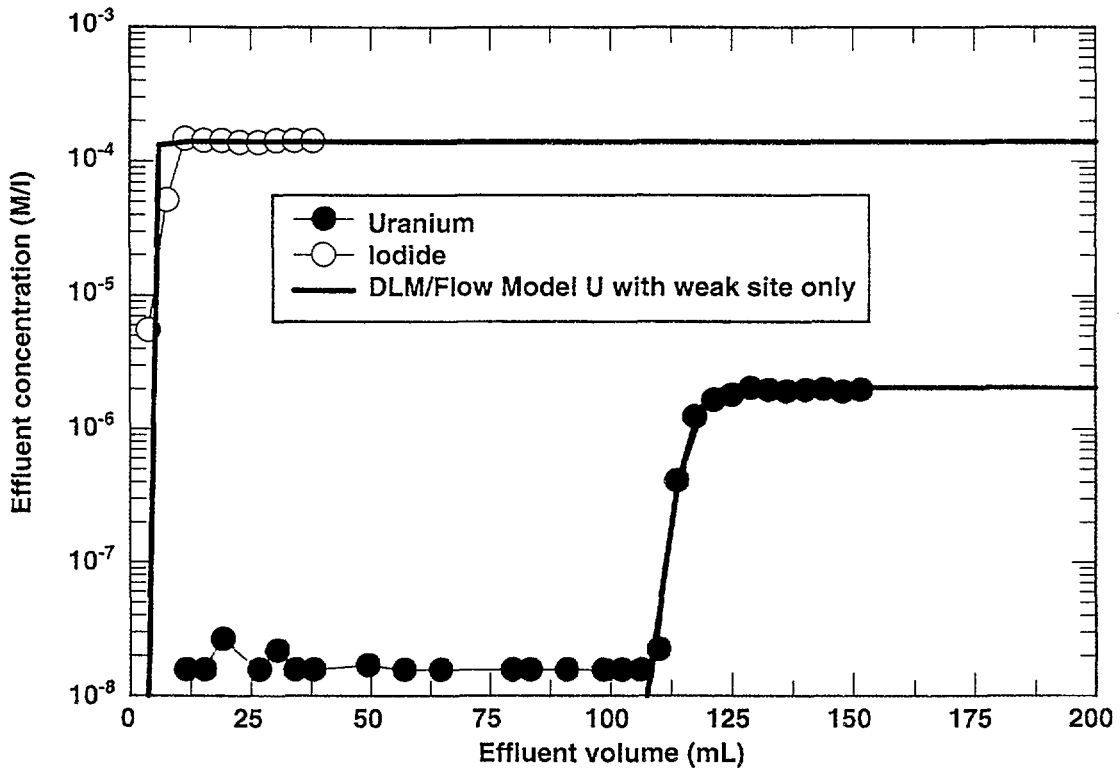


74-15.AI.123.SITEDESC  
11.4-06.AI.SITEDESC-R01

Source: Hardin (1998a, Figure 6-29)

NOTE: Effluent at 26°C for hematite:quartz columns at four pH values

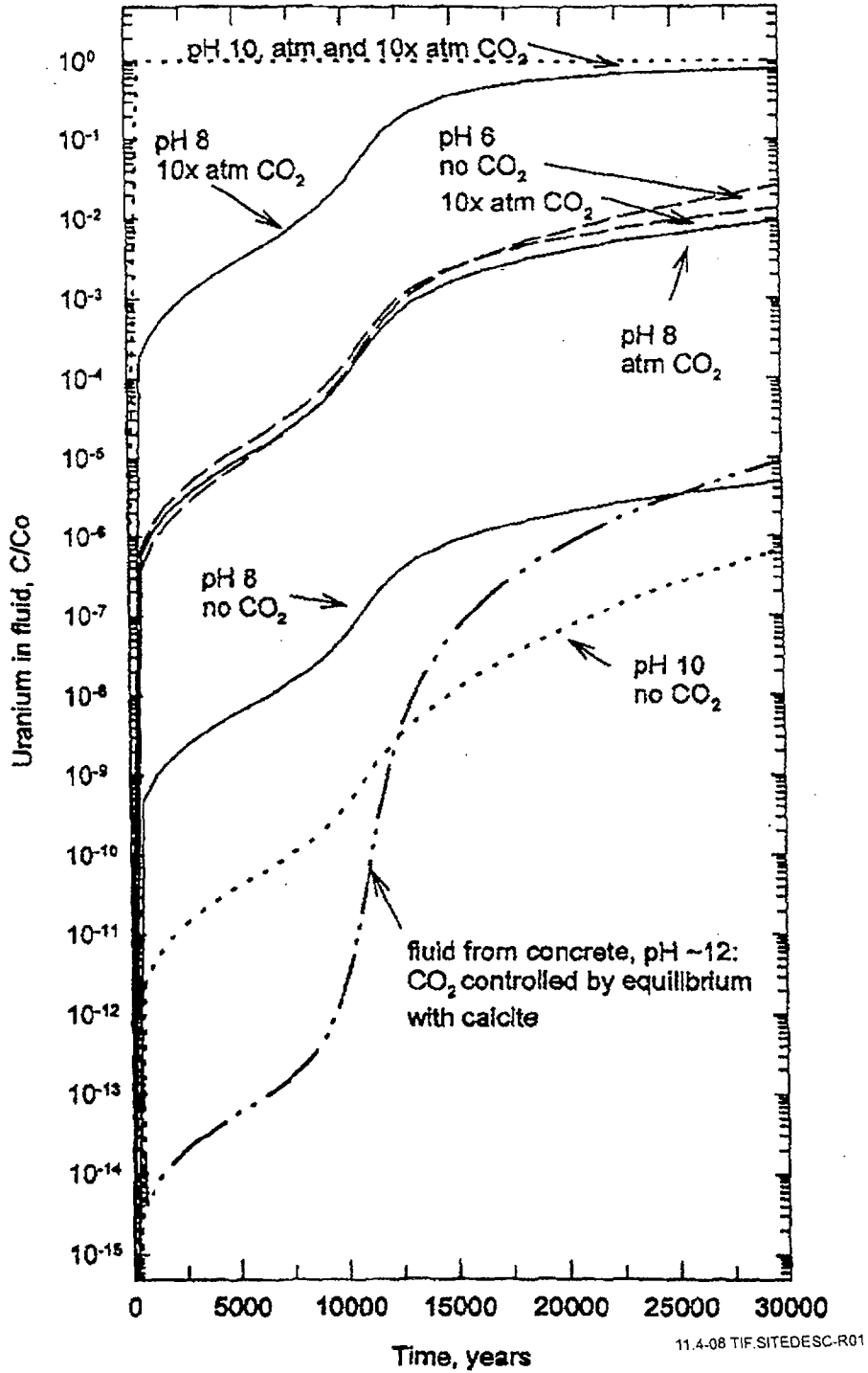
Figure 11.4-6. Variation in Iodide (a Conservative Tracer) and Uranium Concentrations as a Function of Effluent Volume



74-16.AI.123.SITEDESC  
11.4-07.AI.SITEDESC-R01

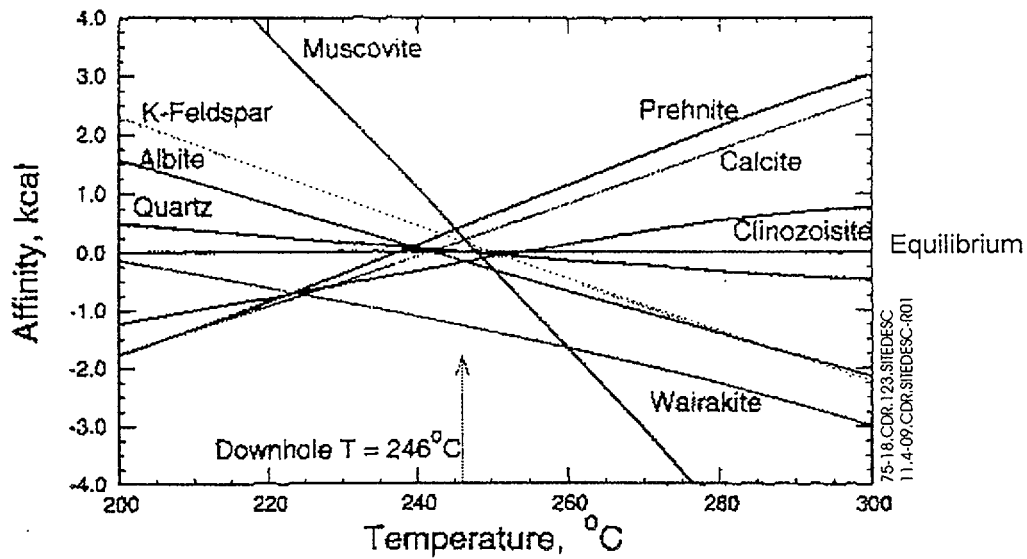
Source: Hardin (1998a, Figure 6-31)

Figure 11.4-7. Effluent Concentration as a Function of Effluent Volume for Simulated and Measured Concentrations



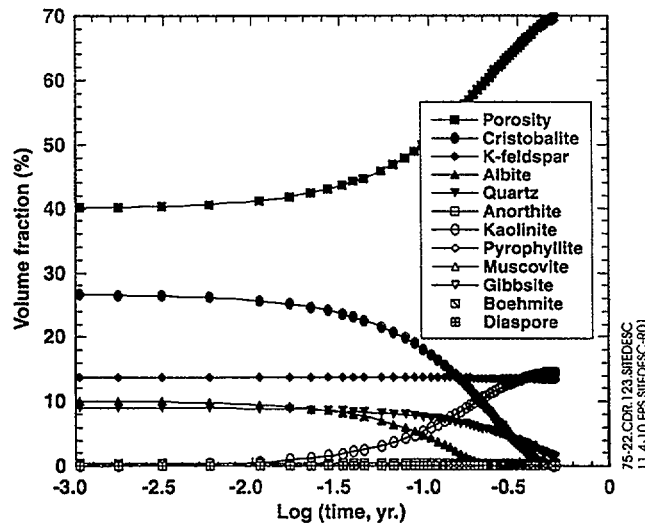
Source: Hardin (1998b, p. 6-32)

Figure 11.4-8. Variation in Relative Concentration of Uranium (C/Co) with Time at Node #1, 10 Centimeters into Hematite Corrosion Layer for Different Influent Fluid Compositions



Source: Glassley (1996, Figure 3.4-21)

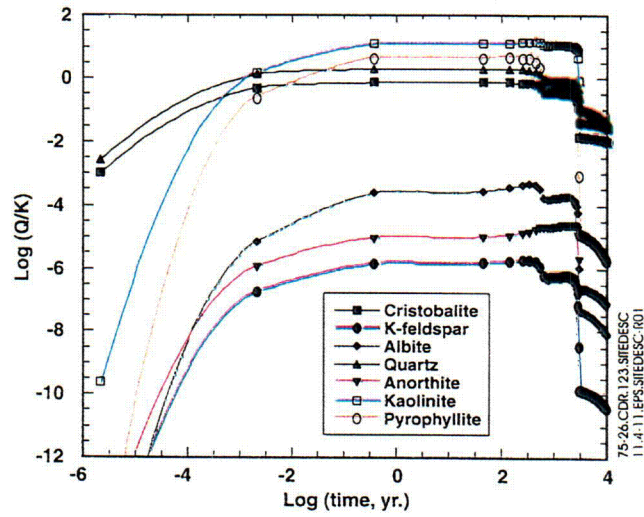
Figure 11.4-9. Affinity versus Temperature Diagram for Well Wk-28 Using SUPCRT 92 Thermodynamic Data for Aluminum Aqueous Species



Source: Wilder (1997, Figure 5-22)

NOTE: Represented at the inlet node (first 1 cm) of a 31-cm column of tuff at 250°C (GIMRT simulation) with a constant flux of 266.7 m/yr. at the outlet node

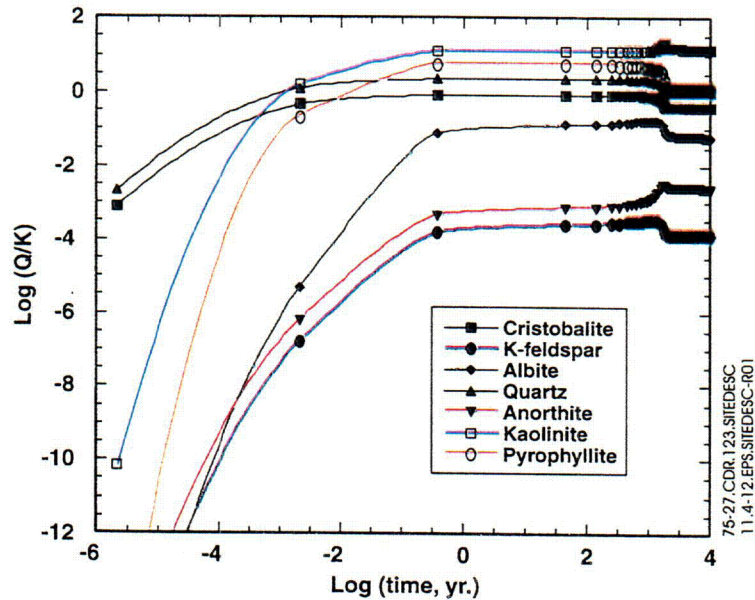
Figure 11.4-10. Porosity and Volume Fractions of Minerals over Time



Source: Wilder (1997, Figure 5-28)

NOTE: Conducted for the inlet node (0.25 m) of a 10-m column of tuff at 95°C for the first 5 m, decreasing 1 cm thereafter (GIMRT simulation)

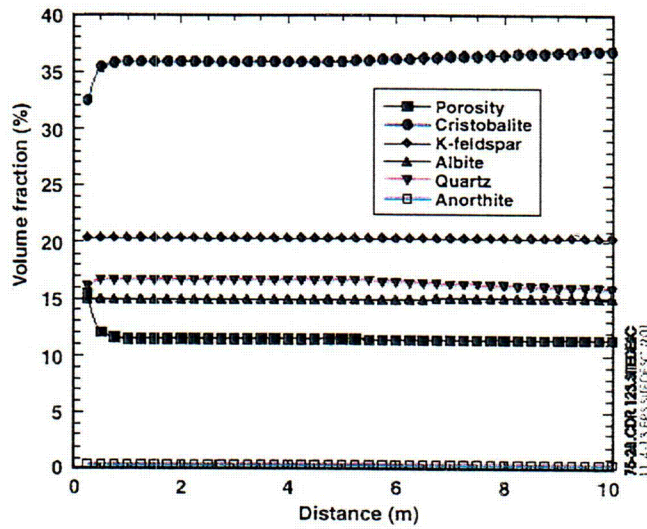
Figure 11.4-11. Mineral Saturation Indices (Log Q/K) versus Time at the Inlet Node of a Tuff Column



Source: Wilder (1997, Figure 5-30)

NOTE: Conducted for a 10-m column of tuff at 95°C for the first 5 m, decreasing 1 cm thereafter (GIMRT simulation)

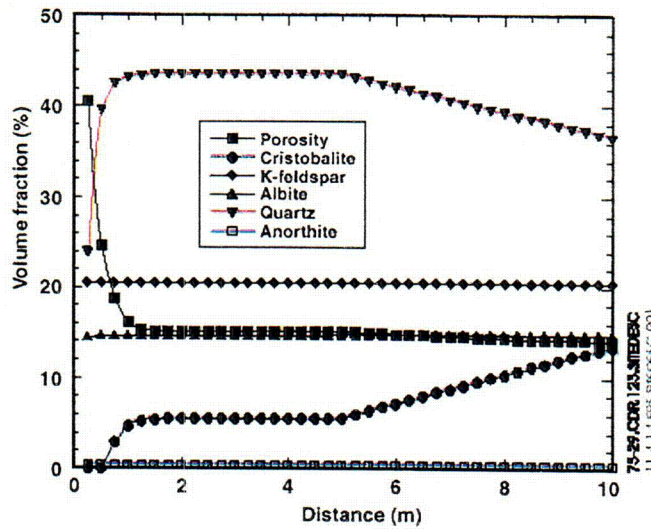
Figure 11.4-12. Mineral Saturation Indices (Log Q/K) versus Time at the Outlet Node of a Tuff Column



Source: Wilder (1997, Figure 5-13)

NOTE: Conducted for a 10-m column of tuff at 95°C for the first 5 m, decreasing 1 cm thereafter (GIMRT simulation)

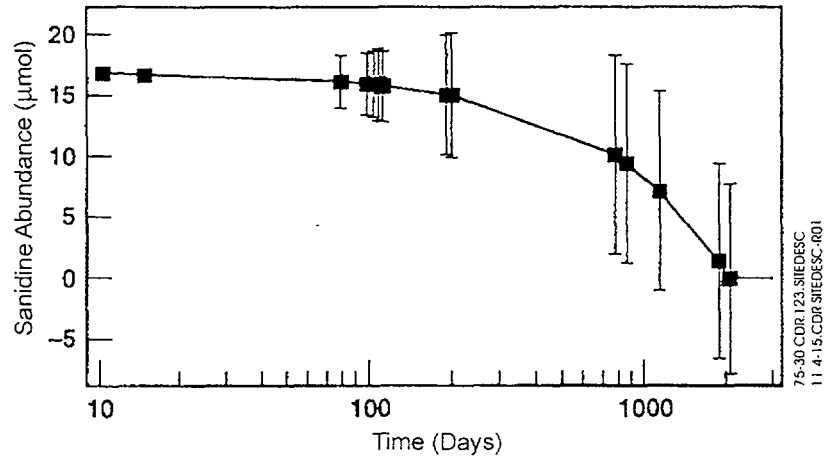
Figure 11.4-13. Porosity and Volume Fractions of Minerals versus Distance after 100 Years



Source: Wilder (1997, Figure 5-33)

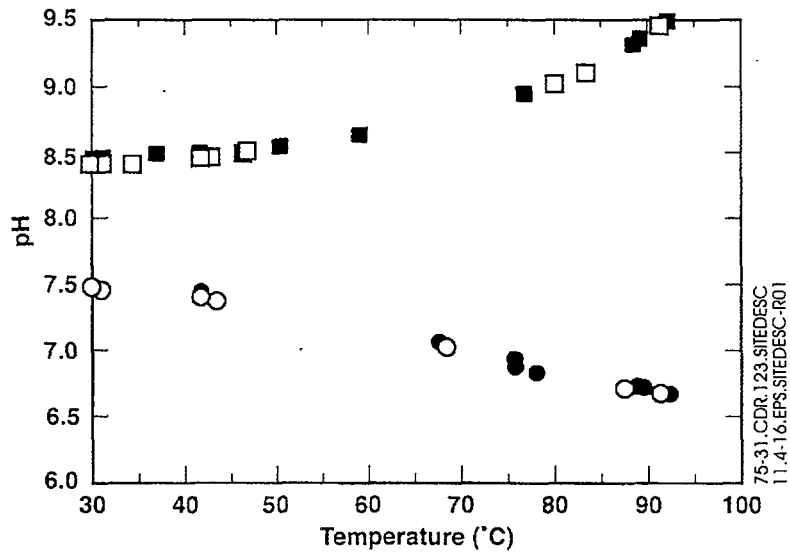
NOTE: Conducted for a 10-m column of tuff at 95°C for the first 5 m, decreasing 1 cm thereafter (GIMRT simulation)

Figure 11.4-14. Porosity and Volume Fractions of Minerals versus Distance after 1,000 Years



Source: Wilder (1997, Figure 5-16)

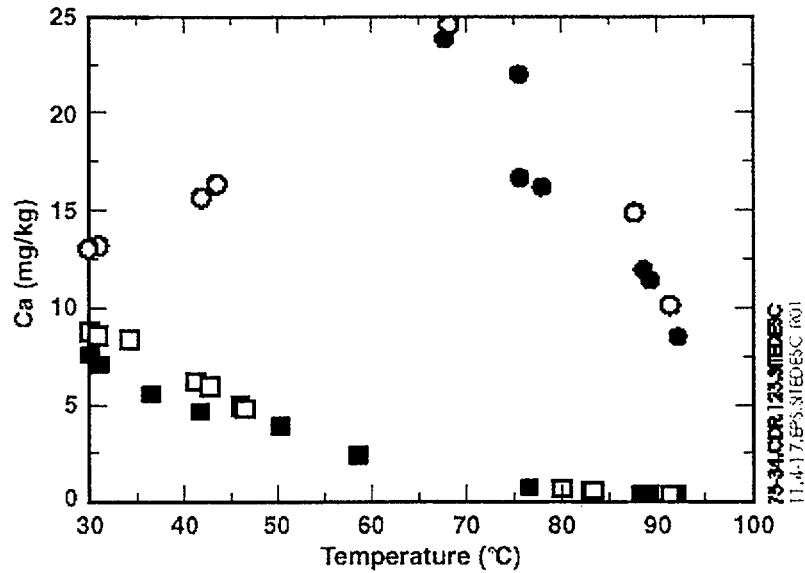
Figure 11.4-15. Estimates of Sanidine Abundance over Time



Source: Wilder (1997, Figure 4-10)

NOTE: Black circles and squares indicate that precipitation of solids was unrestricted. White circles and squares indicate that quartz, tridymite, and talc were suppressed.

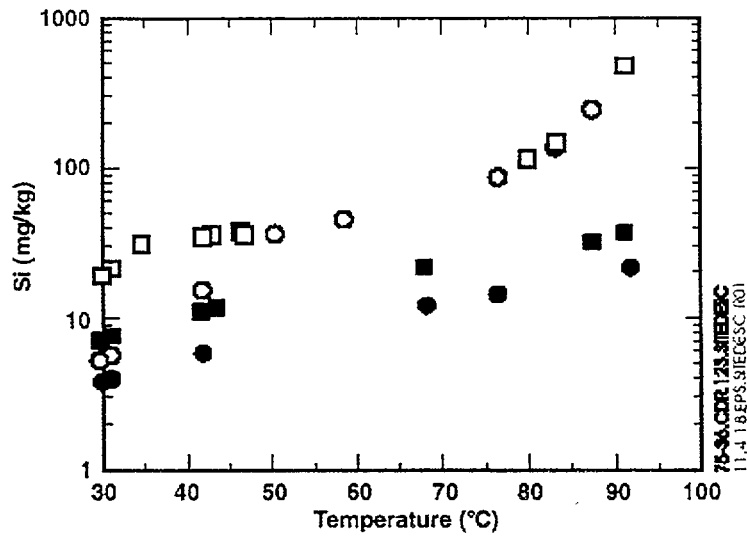
Figure 11.4-16. Calculated pH as a Function of Temperature during Evaporation



Source: Wilder (1997, Figure 4-16)

NOTE: Black circles and squares indicate that precipitation of solids was unrestricted. White circles and squares indicate that quartz, tridymite, and talc were suppressed.

Figure 11.4-17. Calculated Total Calcium Solution as a Function of Temperature during Evaporation

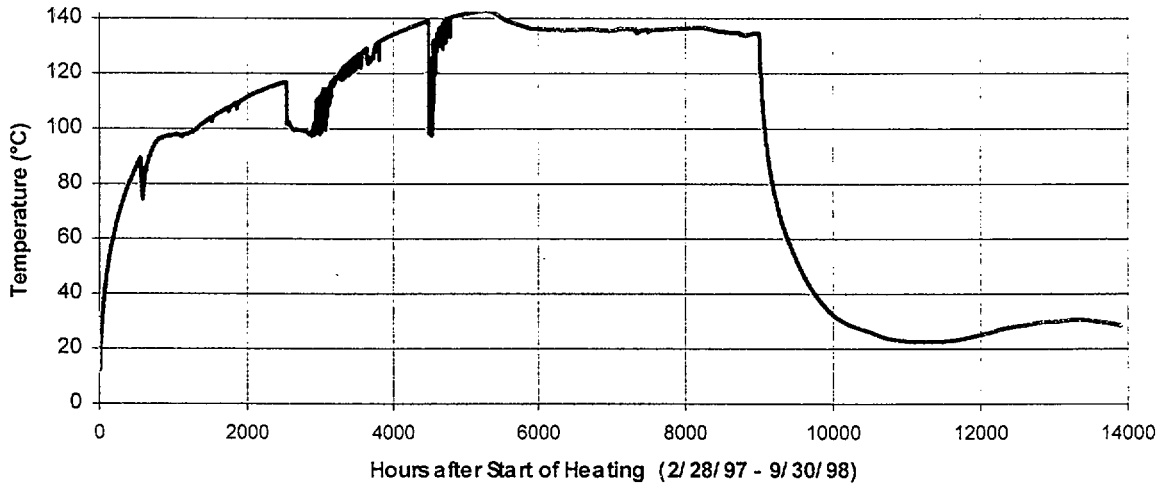


Source: Wilder (1997, Figure 4-18)

NOTE: Black circles and squares indicate that precipitation of solids was unrestricted. White circles and squares indicate that quartz, tridymite, and talc were suppressed.

Figure 11.4-18. Calculated Total Silicon Solution as a Function of Temperature during Evaporation

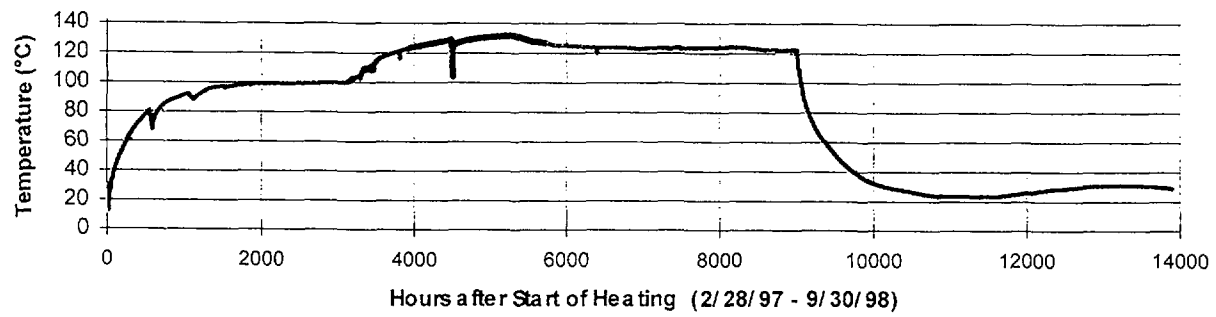
INTENTIONALLY LEFT BLANK



11.5-01.DOC.SITEDESC-R01

Source: CRWMS M&O (2000b, Figure 3-33)

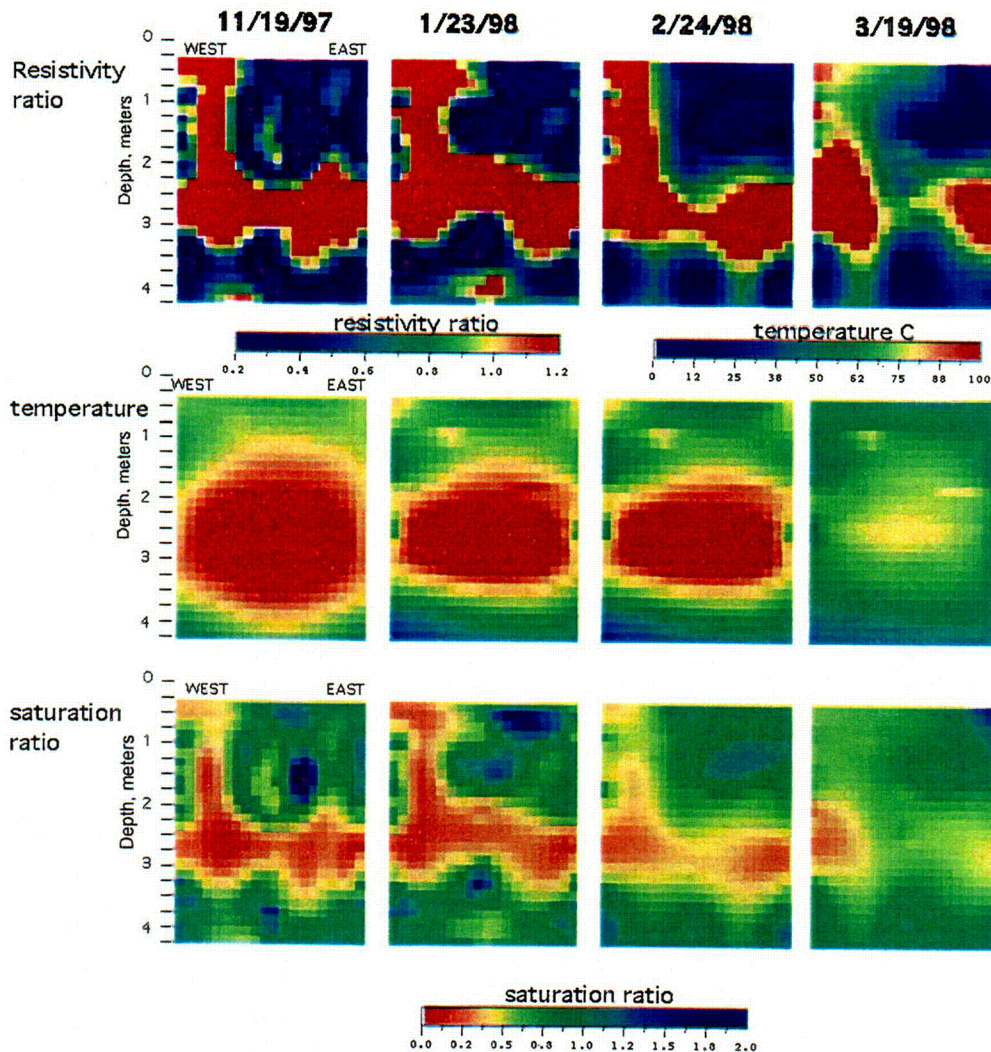
Figure 11.5-1. Temperature at Sensor 14 in Borehole TT1 of the Large Block Test as a Function of Time



11.5-02.DOC.SITEDESC-R01

Source: CRWMS M&O (2000b, Figure 3-34)

Figure 11.5-2. Temperature at Sensor 14 in Borehole TT2 of the Large Block Test as a Function of Time

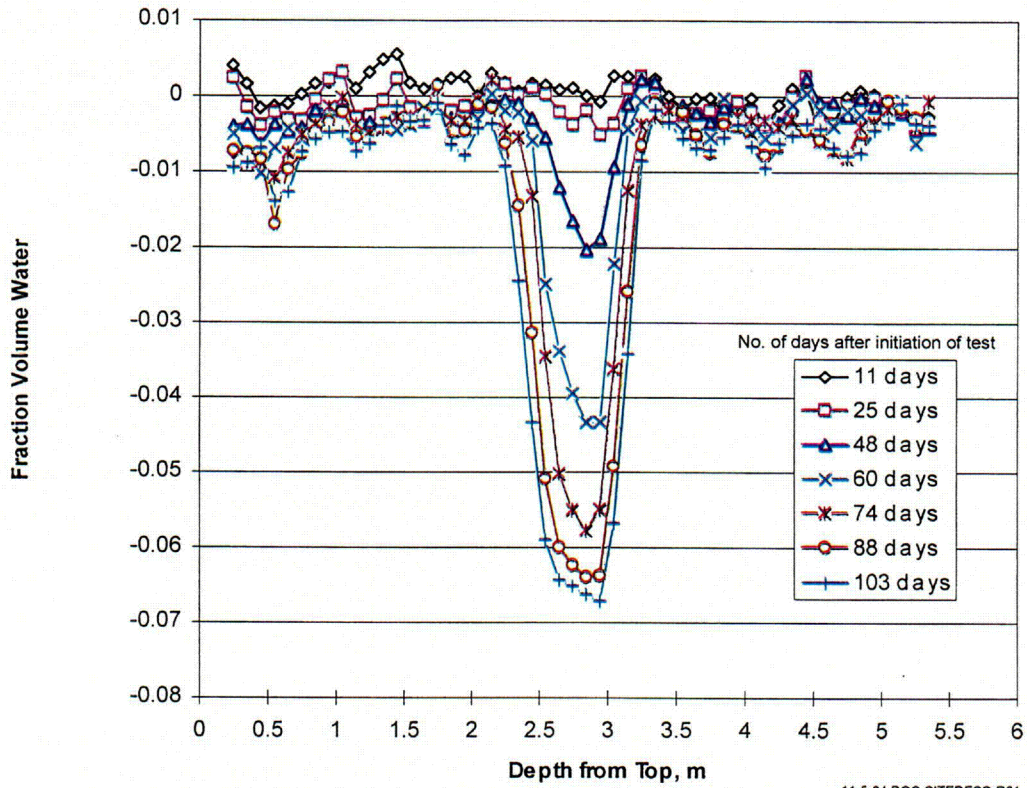


11.5-03,DOC.SITEDESC-R01

Source: CRWMS M&O (2000b, Figure 3-39)

NOTE: Heating started on 2/28/97.

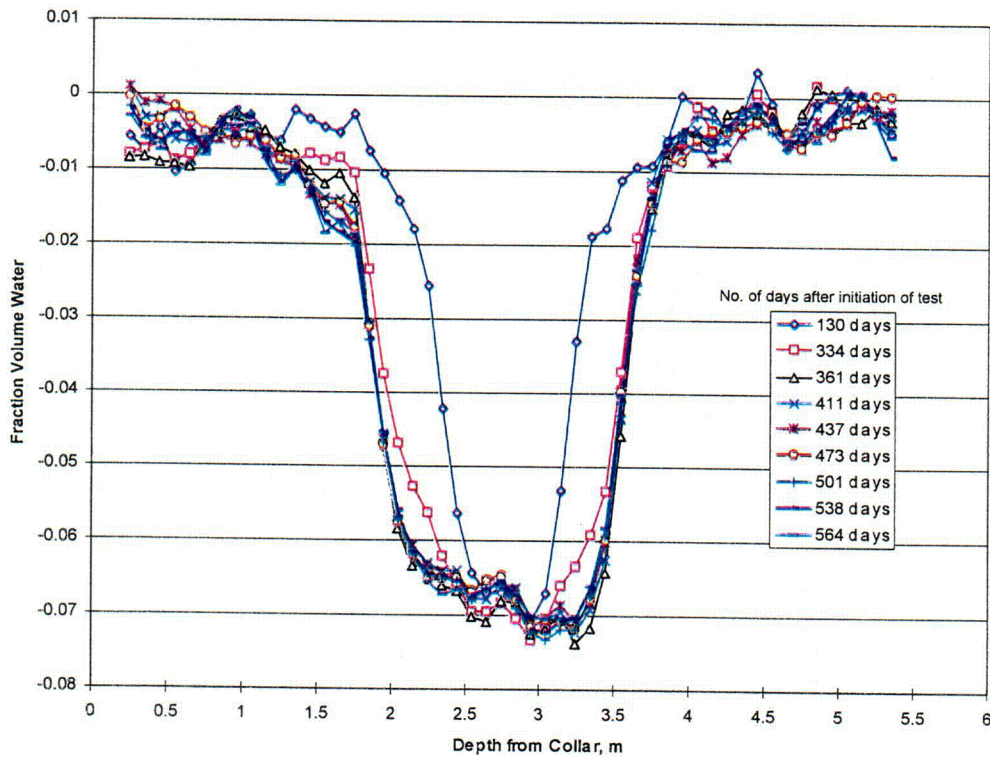
Figure 11.5-3. Electrical Resistance Tomographs of an East-West Vertical Cross Section of the Large Block Test Showing the Variation of Moisture Distribution within the Imaging Plane



11.5-04.DOC.SITEDESC-R01

Source: CRWMS M&O (2000b, Figure 3-40)

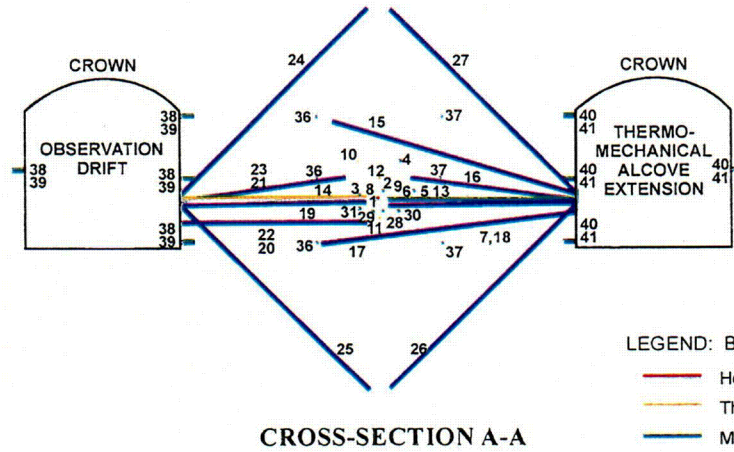
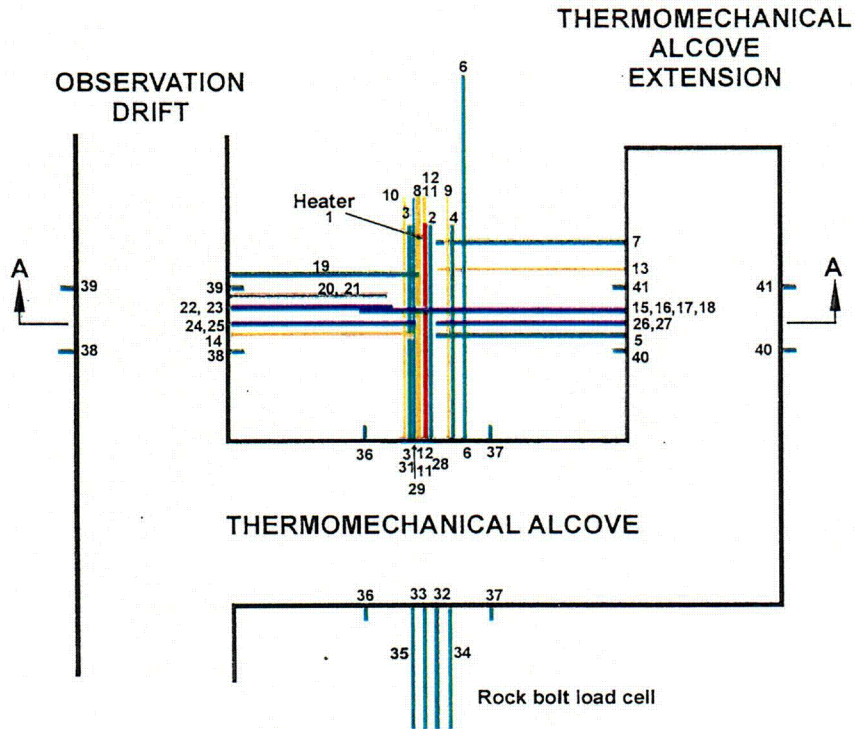
Figure 11.5-4. Differences in Fraction Volume Water in Borehole TN3 as a Function of Depth



11 5-05.DOC SITEDESC-R01

Source: CRWMS M&O (2000b, Figure 3-41)

Figure 11.5-5. Differences in Fraction Volume Water in Borehole TN3 as a Function of Depth



- LEGEND: Boreholes
- Heater
  - Thermal
  - Mechanical
  - Hydrological
  - Chemical

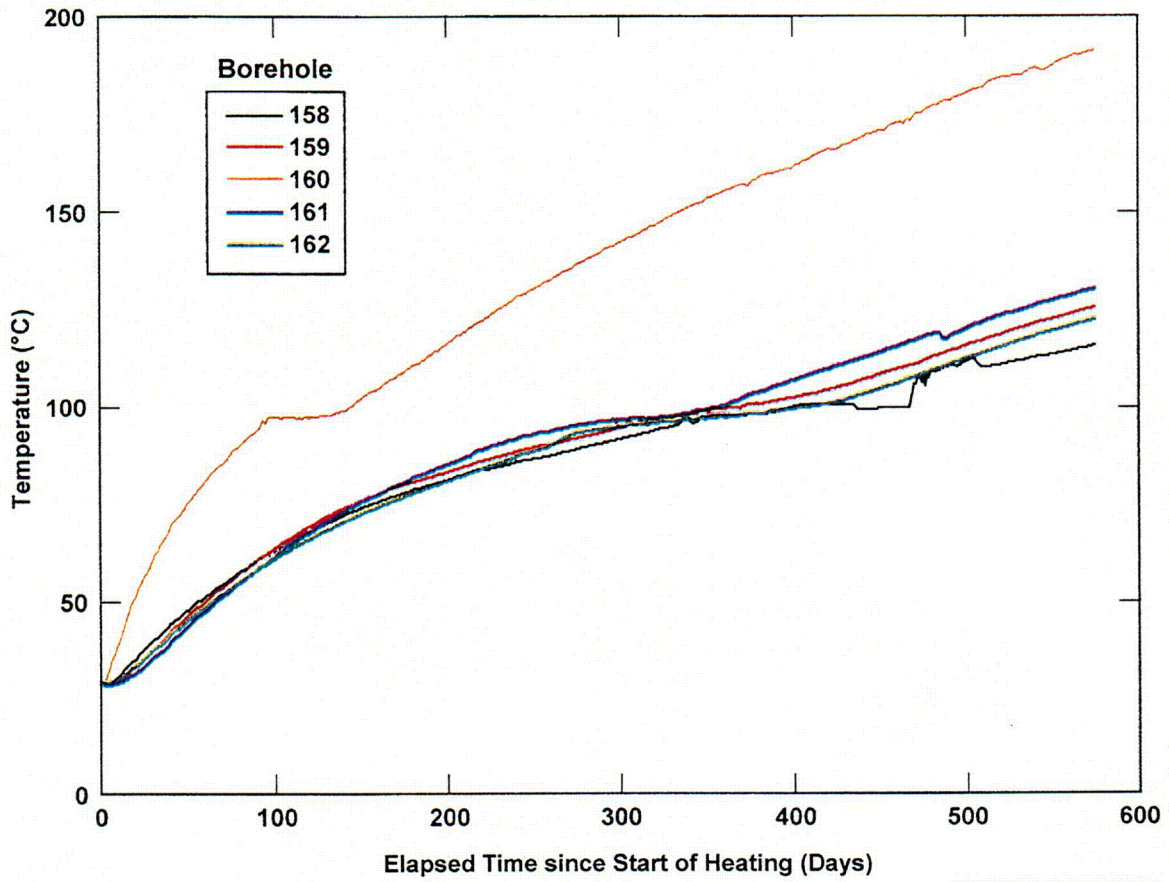
REFERENCE ONLY  
(NOT TO SCALE)

11.5-06,DOC.SITEDESC-R01

Source: CRWMS M&O (2000a, Figure 3-35)

Figure 11.5-6. Borehole Layout of the Single Heater Test



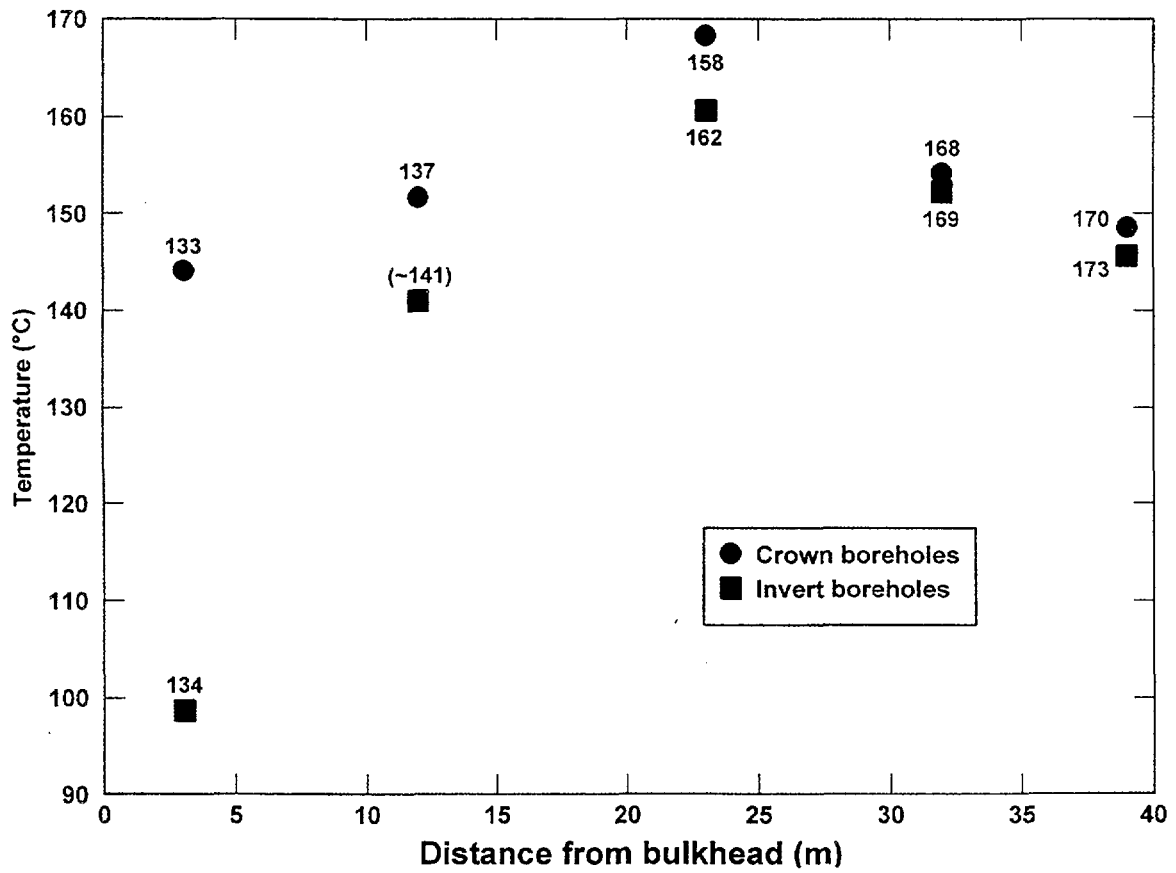


11.5-08.DOC.SITEDESC-R01

Source: CRWMS M&O (2000b, Figure 3-25)

NOTE: Depth of measurement is at 2 m from the collar of boreholes 158 through 162.

Figure 11.5-8. Temperature as a Function of Elapsed Time of the Drift Scale Test



11.5-09,DOC.SITEDESC-R01

Source: CRWMS M&O (2000b, Figure 3-26)

NOTE: The numbers in the figure represent borehole identifiers. Measurements were taken at about 0.4 m from the heated drift wall in all vertical boreholes.

Figure 11.5-9. Temperature as a Function of Distance from the Bulkhead at about 0.4 Meters from the Heater Drift Wall in All Vertical Temperature Holes of the Drift-Scale Test

INTENTIONALLY LEFT BLANK

Table 11.3-1. Principal Stresses at the Potential Repository Horizon at Yucca Mountain

Parameter	Average Value <sup>a</sup>	Range of Values
Maximum principal stress (vertical)	7.0 MPa (1,015 psi)	5.0 to 10 MPa
Ratio of minimum horizontal stress to vertical stress	0.5	0.3 to 0.8
Ratio of maximum horizontal stress to vertical stress	0.6	0.3 to 1.0
Bearing of minimum horizontal stress	N57°W	N50°W to N65°W
Bearing of maximum horizontal stress	N32°E	N25°E to N40°E

Source: Wilder (1996, Table 4-5)

NOTE: <sup>a</sup> Average value for a depth of about 0.3 km (1,000 ft).

Table 11.3-2. Coefficient of Thermal Expansion in Unit TSw2 by Temperature Range and Saturation State

Parameter	Saturation State	Statistic	Temperature Range ( °C)										
			25-50°	50-75°	75-100°	100-125°	125-175°	150-175°	175-200°	200-225°	225-250°	250-275°	275-300°
Mean Coefficient of Thermal Expansion (10 <sup>-6</sup> per °C) During Heatup	Saturated	Mean	7.14	7.47	7.46	9.07	9.98	11.74	13.09	15.47	19.03	25.28	37.13
		Standard deviation	0.65	1.51	1.21	2.41	0.77	1.28	1.40	1.75	3.09	6.87	14.27
		Count	19	19	19	19	19	19	19	16	16	16	16
	Dry	Mean	6.67	8.31	8.87	9.37	10.10	10.96	12.22	14.54	20.79	25.13	35.13
		Standard deviation	1.20	0.42	0.40	0.55	0.88	1.16	1.50	2.57	17.03	10.07	14.56
		Count	40	40	40	40	40	38	38	35	35	35	35
Mean Coefficient of Thermal Expansion (10 <sup>-6</sup> per °C) During Cooldown	Saturated	Mean	21.89	27.83	26.55	21.38	17.31	14.06	12.49	11.52	10.27	9.48	8.81
		Standard deviation	6.16	10.36	10.01	5.70	3.07	1.38	1.32	2.00	0.62	0.63	0.62
		Count	16	16	16	16	19	19	19	19	19	19	19
	Dry	Mean	20.57	24.31	24.20	21.16	18.45	14.34	11.74	10.51	9.54	8.87	7.48
		Standard deviation	4.88	7.55	8.08	6.24	9.36	4.23	3.03	2.26	1.79	1.56	1.99
		Count	35	35	35	35	38	38	40	40	40	40	40

Source: Brodsky et al. (1997, Tables 4 and 5)

Note: Count refers to the number of test measurements.

Table 11.3-3. Young's Modulus by Axial Stress Range for a 0.5-m Scale Block of Topopah Spring Tuff Loaded Parallel to the Ash-Flow Fabric

Axial Stress (MPa)	Young's Modulus (GPa)
0 to 1	2.8
1 to 4	17
4 to 8	40

Source: Constantino et al. (1998, p. 2-17)

Table 11.3-4. Thermal Expansion Coefficients for Longest Available Gauge Lengths near Heating Cycle Culmination

Extensometer Number	Anchor Numbers	Average $\alpha$ $10^{-5}/^{\circ}\text{C}$	Average Temperature ( $^{\circ}\text{C}$ )	Gauge Length (m)
TMA-MPBX-1	1 to 4	5.88	160.3	2.84
TMA-MPBX-3	2 to 6	4.14	70.07	4.0
TMA-MPBX-2	2 to 5	2.36	116.6	0.4

Source: CRWMS M&O (1999a, Table 9.3)

Note: To obtain length in feet, multiply meters by 3.28.

Table 11.3-5. Estimated Rock Mass Modulus in Borehole ESF-TMA-BJ-1 Using the Borehole Jack

Date	Distance from Collar				
	2.0 m	3.0 m	4.0 m	4.51 m	6.2 m
Rock Mass Modulus, GPa (Temp $^{\circ}\text{C}$ )					
8/26/98	6.9 (25)	3.71 (25)	No test	No test	No test
10/10/96	10.3 (27.5)	10.3 (27.7)	8.3 (30.2)	6.0 (34)	No test
11/26/96	<i>Results discarded (31.1)</i>	10.2 (35.9)	5.71 (46.4)	5.01 (55.4)	8.4 (141.8)
3/18/97	<i>Results discarded (35)</i>	6.3 (41)	10.3 (52)	5.7 (58.7)	22.8 (143.1)
10/23/97 1st run	No test	No test	6.28 (Ambient)	Discarded	8.28 (Ambient)
10/23/97 2nd run	No test	No test	8.97 (Ambient)	7.1 (Ambient)	10.0 (Ambient)
1/29/98 1st run	5.47 (Ambient)	9.67 (Ambient)	8.28 (Ambient)	7.60 (Ambient)	Not Calculated
1/29/98 2nd run	No test	No test	No test	No test	11.72 (Ambient)
1/29/98 3rd run	No test	No test	No test	No test	11.72 (Ambient)

Source: CRWMS M&O (1999a, Table 9-6)

NOTE: To obtain length in feet, multiply meters by 3.28.

Table 11.3-6. Change in Rockbolt Load Cell Readings during Heating

Location	Hot Side				Ambient Side			
Gate	RBLC-1	RBLC-2	RBLC-3	RBLC-4	RBLC-5	RBLC-6	RBLC-7	RBLC-8
% Change	7.05	3.00	1.11	1.88	1.56	0.81	1.60	2.27
Average % Change	Hot Side average change = 3.26%				Ambient Side average change = 1.56%			

Source: CRWMS M&O (1999a, Table 9-8)

Table 11.3-7. Horizontal Deformation by Direction through the Large Block at 40 and 58 Days

Direction	Borehole	Height (m)	Deformation at 40 Days (m)	Deformation at 58 Days (m)
E-W	WM-1	0.45	0.00029	0.00033
N-S	NM-1	0.58	0.00029	0.00035
N-S	NM-2	1.95	0.00062	-
E-W	WM-2	3.20	0.00097	0.00098
N-S	NM-3	3.50	0.00109	0.00112

Source: Blair and Wood (1998, Table 1)

NOTES: Measured with a multiple-point borehole extensometer

- = No value

To obtain length in feet, multiply meters by 3.28.

Table 11.3-8. Fracture Spacing by Domain in the Main Drift of the Exploratory Studies Facility

Set	Parameter	Domain 1	Domain 2	Domain 3	Domain 4
1	Fractures	798	540	2,851	428
	Drift length (m)	900	500	950	350
	Fractures per meter	0.89	1.08	3.11	1.22
	Spacing between fractures (m)	1.13	0.93	0.32	0.82
2	Fractures	230	134	215	168
	Drift length (m)	900	500	950	350
	Fractures per meter	0.26	0.27	0.23	0.48
	Spacing between fractures (m)	3.91	3.73	4.42	2.08
3	Fractures	86	51	21	26
	Drift length (m)	900	500	950	350
	Fractures per meter	0.10	0.10	0.02	0.07
	Spacing between fractures (m)	10.5	9.80	45.2	13.5
4	Fractures	62	0	0	0
	Drift length (m)	900	500	950	350
	Fractures per meter	0.07	0	0	0
	Spacing between fractures (m)	14.5	NA	NA	NA

Source: Wilder (1997, Table 4-8)

NOTE: NA = not applicable

To obtain length in feet, multiply meters by 3.28.

A domain is a group of fracture data based on station position along the main drift.

INTENTIONALLY LEFT BLANK

Table 11.4-1. Summary of Parameters Used to Simulate Transport of Uranium through the Hematite Corrosion Layer

Properties	Parameter of Flow System	Value Used
Flow System	Medium	Hematite
	Fractional porosity	0.40
	Specific discharge	2.1 cm/yr.
	Flow path length	1 m
	Dispersivity	0.01 m
	Diffusion coefficient	$1 \times 10^{-6} \text{ cm}^2/\text{s}$
	Simulation time	$3 \times 10^4 \text{ yr.}$
	Number of nodes	5
	Limiting Courant number	1
Hematite Sorbent	Specific surface	$20 \text{ m}^2/\text{g}$
Hematite Sorbent (Weak Sites)	Site density	$2.235 \text{ sites}/\text{nm}^2$
	Log $K_+$	7.35
	Log $K_-$	-9.17
Hematite Sorbent (Strong Sites)	Log $K_B$	-11.7
	Site density	$0.075 \text{ sites}/\text{nm}^2$
	Log $K_+$	7.35
	Log $K_-$	-9.17
	Log $K_B$	-7.7

Source: Hardin (1998a, Table 6-4)

Table 11.4-2. Composition of Fluids Used for Assessing the Effect of pH and CO<sub>2</sub> Fugacity on Transport of Uranium through a Hematite Corrosion Layer

Inlet Fluid Property	Simulated Condition								
	no CO <sub>2</sub>	atm CO <sub>2</sub>	no CO <sub>2</sub>	atm CO <sub>2</sub>	10x CO <sub>2</sub>	no CO <sub>2</sub>	atm CO <sub>2</sub>	10x CO <sub>2</sub>	Cement Water <sup>a</sup>
pH	6	6	8	8	8	10	10	10	12.17
CO <sub>2</sub> , fugacity	0.0	0.003	0.0	0.0003	0.003	0.0	0.0003	0.003	5.0x10 <sup>-13</sup>
O <sub>2</sub> , fugacity	0.20	0.20	0.20	0.20	0.20	0.20	0.20	0.20	0.20
Ionic strength, M	0.11	0.11	0.01	0.01	0.01	0.01	0.357	12.3	0.232
Na, M	0.01	0.01	0.01	0.01	0.01	0.01	0.298	22.4	0.200
Ca, M	NC	NC	NC	NC	NC	NC	NC	NC	0.0139
Al, M	NC	NC	NC	NC	NC	NC	NC	NC	1.78x10 <sup>-5</sup>
U, M	NC	NC	NC	NC	NC	4x10 <sup>-6</sup>	4x10 <sup>-6</sup>	4x10 <sup>-6</sup>	4x10 <sup>-6</sup>
SiO <sub>2</sub> , M	NC	NC	NC	NC	NC	NC	NC	NC	3.13x10 <sup>-6</sup>
Cl, M	0.1	0.1	0.01	0.01	0.01	0.01	0.01	0.01	.0200
SO <sub>4</sub> , M	NC	NC	NC	NC	NC	NC	NC	NC	1.85x10 <sup>-3</sup>

Source: Hardin (1998a, Tables 6-5 and 6-6)

NOTES: <sup>a</sup> The composition of this fluid is based on the calcium, aluminum, SiO<sub>2</sub>, and SO<sub>4</sub> predicted for a solution in equilibrium with typical cement phases: calcite, hillebrandite, katoite, ettringite, portlandite, and hematite. The NaCl concentration was set to 0.2 M (similar to an ordinary portland cement). The pH and fugacity of CO<sub>2</sub> were calculated using the REACT geochemical modeling code by adjusting OH<sup>-</sup> to maintain electrical neutrality, and by constraining the fugacity of CO<sub>2</sub> by equilibrium with calcite.

NC = component not considered in simulation

## 12. TECTONIC HAZARDS

### 12.1 INTRODUCTION

Tectonic processes operating in the vicinity of Yucca Mountain may potentially result in events that affect the performance of a repository at the site. Such events include igneous intrusions, volcanic eruptions, and earthquakes. For earthquakes, both vibratory ground motion and surface fault displacement are of potential concern. This section describes studies carried out to characterize the past occurrence of such events and the frequency of their future occurrence.

Characterization of tectonic events supports both design and performance assessment. Because igneous events occur with such low frequency near Yucca Mountain, they are not of concern during the preclosure period (up to 300 yr. [YMP 1999, Section 3.2.H]). Igneous events are, however, of concern during the postclosure period of performance (10,000 yr. (proposed 10 CFR 63.113(b) [64 FR 8640])). Intersection of a repository by a dike could lead to an enhanced source term or to dispersion of radioactive waste through a volcanic eruption. Earthquakes are of concern during both the preclosure and postclosure periods. Facilities important to safety or waste isolation during the preclosure period will need to be designed to accommodate an appropriate level of ground motion. For the postclosure period, assessments by waste package and engineered barrier system designers will address the potential for ground motion or fault displacement to degrade directly or indirectly the performance of these systems. Scientists will also evaluate the effects of fault displacement on the hydrologic system. In assessing the impacts of tectonic events, the frequency of their future occurrence is taken into account.

The analysis and characterization of tectonic hazards and their effects for use in total system performance assessment are summarized in the *Disruptive Events Process Model Report* (CRWMS M&O 2000d). Three of the Analysis/Modeling Reports supporting this process model report cover some of the results presented in this section of the *Yucca Mountain Site Description*. These Analysis/Modeling Reports are *Characterize Framework for Igneous Activity at Yucca Mountain, Nevada (T0015)* (CRWMS M&O 2000a); *Characterize Eruptive Processes at Yucca Mountain, Nevada* (CRWMS M&O 2000b); and *Characterize Framework for Seismicity and Structural Deformation at Yucca Mountain, Nevada* (CRWMS M&O 2000e). Characterization of seismic and volcanic effects for performance assessment is also addressed in the *Saturated Zone Flow and Transport Process Model Report* (CRWMS M&O 2000j), the *Engineered Barrier System Degradation, Flow, and Transport Process Model Report* (CRWMS M&O 2000k), and the *Waste Package Degradation Process Model Report* (CRWMS M&O 2000l).

Yucca Mountain is situated in an active tectonic environment. The geologic record provides clear evidence that both volcanoes and earthquakes have occurred in the vicinity during the Quaternary period (1.6 m.y.). The last nearby volcano erupted approximately 80 ka (see Section 12.2.4.1). The interval between successive earthquakes on active faults ranges from thousands to tens of thousands of years, with the smaller recurrence intervals applying to faults found more than 50 km west of Yucca Mountain. In part because of this low rate of activity, characterization of geologic parameters needed to assess the potential for future activity at Yucca Mountain is subject to significant uncertainties.

Analyses of volcanic and seismic hazards at Yucca Mountain have been carried out probabilistically. An extensive program of data collection was first carried out to characterize the past history of volcanic and earthquake occurrences. Realizing that, in spite of the large amount of data collected, significant uncertainties remained, panels of experts were convened to evaluate the data and provide inputs to the probabilistic hazard analyses. These analyses incorporated multiple hypotheses concerning future volcanic and seismic activity, captured a diversity of professional judgments on the range of interpretations consistent with the data, allowed sensitivities to various input distributions to be assessed, and were thoroughly documented. For igneous activity, the analysis provided the annual frequency with which an igneous dike intersects the emplacement block of the potential repository. For earthquake activity, the analysis provided the annual frequency of exceedance of different levels of ground motion and fault displacement at the potential repository. These results are for use in assessing the consequences of volcanic and seismic activity for the postclosure period and in developing seismic inputs for preclosure design.

### 12.1.1 Regulatory Framework

In addition to the statutes and regulations that generally require that the natural geologic systems at Yucca Mountain be characterized and evaluated (e.g., proposed 10 CFR 63.21(c) [64 FR 8640]), there are other documents that pertain more specifically to tectonic events. In particular, the U.S. Nuclear Regulatory Commission (NRC) has produced three guidance documents that are relevant:

- *Staff Technical Position on Investigations to Identify Fault Displacement Hazards and Seismic Hazards at a Geological Repository*, NUREG-1451 (McConnell et al. 1992)
- *Staff Technical Position on Consideration of Fault Displacement Hazards in Geologic Repository Design*, NUREG-1494 (McConnell and Lee 1994)
- *Branch Technical Position on the Use of Expert Elicitation in the High-Level Radioactive Waste Program*, NUREG-1563 (Kotra et al. 1996).

These documents have been taken into account in planning and carrying out data collection and analyses of tectonic events.

The NRC has also produced a series of issue resolution status reports addressing key technical issues for a geologic repository at Yucca Mountain. These reports discuss the basis for identifying the key technical issues and define acceptance criteria that will be used to evaluate whether the U.S. Department of Energy (DOE) has adequately characterized and assessed the issues. Two of the reports are of primary interest to tectonic disruptive events:

- "Issue Resolution Status Report (Key Technical Issue: Igneous Activity, Revision 2)" (Reamer 1999)
- *Issue Resolution Status Report Key Technical Issue: Structural Deformation and Seismicity* (NRC 1999).

In addition, the report *Issue Resolution Status Report Key Technical Issue: Repository Design and Thermal-Mechanical Effects* (NRC 1998) considers some aspects of seismic hazard analysis and design. Within this report, the NRC comments on the topical reports that the DOE has prepared to address seismic issues. Seismic topical reports that the DOE has completed and submitted to the NRC are the following:

- *Methodology to Assess Fault Displacement and Vibratory Ground Motion Hazards at Yucca Mountain* (YMP 1997a)
- *Preclosure Seismic Design Methodology for a Geologic Repository at Yucca Mountain* (YMP 1997b).

A third seismic topical report, *Preclosure Seismic Design Basis for a Geologic Repository at Yucca Mountain*, is planned.

Finally, the report *Issue Resolution Status Report Key Technical Issue: Total System Performance Assessment and Integration* (NRC 2000) is concerned with the potential for tectonic events to mechanically disrupt waste packages.

### 12.1.2 Key Observations

Assessments of tectonic events have resulted in the following key observations and conclusions:

- The eruption rate during the past 5-m.y.-cycle of basaltic volcanic activity near Yucca Mountain is among the lowest of volcanic fields in the western United States. Approximately 99.9 percent of the volume of the southwestern Nevada volcanic field, which encompasses the site, erupted by about 7.5 Ma. In terms of relative volumes, the southwestern Nevada volcanic field is considered to have virtually ceased activity since that time (Section 12.2.4.2).
- A probabilistic analysis of the annual frequency with which a potential geologic repository at Yucca Mountain (Enhanced Design Alternative II) would be intersected by an igneous dike indicates the mean annual frequency of intersection is  $1.6 \times 10^{-8}$  with a 90 percent confidence interval ranging from  $7.6 \times 10^{-10}$  to  $5.0 \times 10^{-8}$ . Using available data, 10 experts provided interpretations of volcanic sources and rates as input to this analysis. The experts also characterized the uncertainties associated with their inputs by providing weighted alternative interpretations (Section 12.2.6.2).
- The mean annual frequency of an eruption through the repository, conditional on a dike intersection, was also calculated based on the Enhanced Design Alternative II repository design and an extended analysis of the results of the expert elicitation. The eruption frequency is approximately half that of dike intersection. The results indicate that the frequencies of dike intersection and eruption through the repository are relatively insensitive to changes in the configuration of the repository footprint (Section 12.2.6.2).
- Faults with demonstrated Quaternary activity exist in the vicinity of Yucca Mountain. Slip rates for these faults are low, ranging from 0.001 to 0.07 mm/yr. Average recurrence intervals for earthquakes producing surface displacement on a given fault

range from about 5 k.y. to perhaps more than 100 k.y. Single-event displacements range from 10 mm to 4.5 m (Section 12.3.7.1).

- A probabilistic analysis of ground motion at Yucca Mountain indicates that the mean horizontal response spectrum with a  $10^{-3}$  annual frequency of exceedance is characterized by spectral accelerations of 0.162, 0.355, and 0.169 g for structural frequencies of 1, 10, and 100 (peak) Hz, respectively. The mean horizontal response spectrum with a  $10^{-4}$  annual frequency of exceedance is characterized by spectral accelerations of 0.471, 1.160, and 0.534 g for the same respective structural frequencies. These values are for a reference outcrop with rock properties found at a depth of 300 m at Yucca Mountain. They do not take into account the effect of the 300 m of tuff lying above the reference rock outcrop level (Section 12.3.10.3).
- A probabilistic analysis of fault displacement hazard at Yucca Mountain shows that, except for sites on block-bounding faults (e.g., Solitario Canyon, Bow Ridge), mean fault displacement levels are less than or equal to 1 mm for a  $10^{-4}$  to  $10^{-5}$  annual frequency of exceedance (Section 12.3.10.4).

### 12.1.3 Organization

The discussion of tectonic hazards is divided into two major parts: hazards due to igneous events (Section 12.2) and hazards due to seismic events (Section 12.3). Disruptive events of nongeologic origin, such as human intrusion and nuclear criticality, are not directly addressed in this document.

## 12.2 IGNEOUS ACTIVITY AND VOLCANIC HAZARDS

Assessment of the volcanic hazard at Yucca Mountain builds on the knowledge of the late Tertiary and Quaternary history of igneous activity. Investigations were performed to determine the ages and character of past volcanic episodes and to understand the tectonic setting with which the episodes and Yucca Mountain are associated (e.g., CRWMS M&O 1998h). Founded upon this extensive base of data, analyses, and interpretation, a probabilistic volcanic hazard analysis (PVHA) was carried out to determine the frequency with which igneous activity will intersect the volume of the potential repository (CRWMS M&O 1996). A panel of 10 experts representing a wide range of expertise in the fields of physical volcanology, volcanic hazards, geophysics, and geochemistry conducted the PVHA assessments. Their evaluations were combined to produce an integrated assessment of the volcanic hazard that reflects a range of alternative scientific interpretations. The PVHA assessment focused on the volcanic hazard at the site, which was defined as the annual probability of intersection of the potential repository by a basaltic dike. The hazard assessment provides input to an assessment of volcanic risk, which expresses the probability of radionuclide release due to igneous activity.

The PVHA included discussion of some aspects of the consequences of a volcanic event, but not all aspects required for the Total System Performance Assessment (TSPA)-Site Recommendation (SR). Additional analyses that were performed to complete the description of the volcanic hazard and effects are provided in analysis and modeling reports supporting the *Disruptive Events Process Model Report* (CRWMS M&O 2000d). The analysis and modeling report *Characterize Framework for Igneous Activity at Yucca Mountain, Nevada (T0015)* (CRWMS M&O 2000a) describes conceptual models for volcanism near Yucca Mountain and their impact on probability models; it presents the probability results for intersection of the potential repository by a basaltic dike and the probability of an eruption through the repository, conditional on a dike intersection based on the current repository footprint. These probability results provide the basis for all further consequence analysis. Studies of eruptive and subsurface features and processes associated with basaltic volcanoes used to develop additional background material and parameter distributions for the analysis of the consequences of volcanic eruptions through the repository are discussed in the analysis and modeling report *Characterize Eruptive Processes at Yucca Mountain, Nevada* (CRWMS M&O 2000b).

### 12.2.1 Data Sources

The principal sources of data, analyses, and interpretations for the assessment of igneous activity and volcanic hazard at Yucca Mountain are Yucca Mountain Site Characterization Project (YMP) site characterization studies (CRWMS M&O 1998h), the *Probabilistic Volcanic Hazard Analysis for Yucca Mountain, Nevada* (CRWMS M&O 1996), the *Disruptive Events Process Model Report* (CRWMS M&O 2000d), and supporting analysis and modeling reports (CRWMS M&O 2000a, 2000b).

### 12.2.2 Overview of Late Cenozoic Volcanism in the Great Basin and Relationship to Tectonic Setting

The Great Basin (Figure 12.2-1) was affected during the middle and late Cenozoic Era by extensional tectonism and magmatism caused by plate tectonic interactions at the western margin

of the North American continent. As a result, the Great Basin is a region of thinned lithosphere, high heat flow, active faulting, seismicity, abundant thermal springs, and the widespread distribution of late Cenozoic volcanic rocks (Figure 12.2-1) (e.g., Eaton 1982; Crowe et al. 1995, Chapter 3, Section III).

Volcanism in the Great Basin can generally be divided into two stages: a silicic episode involving eruption of large volume ignimbrites (Oligocene to middle Miocene) and a basaltic episode involving increasingly smaller volumes of basalt (middle Miocene to Quaternary). These two stages of volcanism also correlate in a general way with crustal extension rate: high rate of extension during the time of the silicic episode, low and declining rate of extension during the period of basaltic volcanism. Although the correlation between extension rate and voluminous silicic volcanism during the middle Tertiary is valid on a regional scale and on time scales of millions of years, local cessation of volcanism during periods of most rapid extension has been noted in several areas of the Basin and Range (e.g., Gans and Bohrsen 1998, p. 66).

Large-volume silicic volcanism (the "ignimbrite flare-up") is considered to be due to a large flux of basaltic magma into the crust (Johnson 1991, pp. 13,500 to 13,502; Best and Christiansen 1991, pp. 13,523 to 13,525) as a result of reactivation of the mantle wedge above a steepening subducted slab following the slowing of subduction rates after the Laramide orogeny (80 m.y. to about 45 m.y.) (Coney and Reynolds 1977, pp. 405 to 406; Cross and Pilger 1978, Figure 10; Lipman 1980, pp. 167 to 171). Basaltic intrusion, convection in the underlying mantle wedge, and thick crust inherited from the Laramide created an unusually hot crust by the end of the Oligocene epoch. Thermally weakened crust is considered a prerequisite for large-magnitude ductile extension in the Basin and Range Province in the late Oligocene to early Miocene (Morgan et al. 1986, p. 6263). The extensional collapse of over-thickened and thermally weakened crust followed the slowing of subduction and easing of compressional forces at the continental margin (Coney 1987, p. 183). Coupled with decreased basalt flux into the crust beginning in the late Oligocene (from breakdown of the mantle wedge), the thinned crust began to cool (Perry et al. 1993, p. 878).

Overall cooling of the Cordilleran crust in late Cenozoic time is consistent with slowing of extension rates, changes in style of deformation, and transition to the eruption of basalt. Two overlapping phases of extensional deformation are recognized during the Cenozoic—an early, middle Tertiary phase characterized by high strain rates, a shallow brittle-ductile transition, shallow fault penetration, and eruption of voluminous intermediate to silicic volcanic rocks; and a late, Miocene-Pleistocene phase (Basin and Range event) characterized by lower strain rates, deeply penetrating faults, the establishment of modern Basin and Range structural styles, and bimodal eruptions of basalt and high-silica rhyolite (Christiansen and Lipman 1972, pp. 270 to 276; Morgan et al. 1986, p. 6263; Armstrong and Ward 1991, pp. 13,216 to 13,217).

The high strain rates characteristic of Oligocene extension required a hot and thermally weakened crust, while lower strain rates and associated deep, high-angle faulting are consistent with a cooler, more brittle, and mechanically stronger crust (Morgan et al. 1986, p. 6263). Cooling of the crust is considered to favor the eruption of basalt because (1) cooling of the crust increases crustal density on a regional scale (enhancing buoyant ascent of basaltic magma), (2) contamination or mixing with more silicic crustal magmas is inhibited, and (3) basaltic

magmas intruded into brittle crust would have access to deeper crustal fractures that would favor rapid ascent without differentiation (Perry et al. 1993, p. 881).

### **12.2.3 Oligocene-Miocene Silicic Volcanism**

Intermediate to silicic calc-alkaline Cenozoic volcanism began in the northern Great Basin during the late Eocene and gradually swept south, ending in southern Nevada by the late Miocene (Stewart et al. 1977, Figure 2; Armstrong and Ward 1991, p. 13,209; Nelson et al. 1992, Figure 1). The Yucca Mountain region marked the southern limit of silicic time-transgressive volcanic activity in the Great Basin, with the formation of the southwestern Nevada volcanic field (Figure 12.2-1). This southward sweep is thought to be related to declining plate convergence rates and steepening of the dip of the subducted slab, resulting in activation of the asthenospheric mantle wedge and generation of basaltic magma to fuel crustal magmatic systems (Cross and Pilger 1978, Figure 10; Lipman 1980, pp. 167 to 171). Isotopic studies of zoned ignimbrite systems suggest that an equal or greater volume of basaltic magma derived from the mantle was required to generate these ash-flow tuffs, through fractional crystallization of basalt and mixing of basalt with melted crustal wall rock (Johnson 1991, pp. 13,485, 13,488 to 13,494; Perry et al. 1993, pp. 873 to 876). Eruption of calc-alkaline ash-flow tuffs reached a peak in the central Great Basin between 30 and 20 Ma (the "ignimbrite flare-up"), when more than 50,000 km<sup>3</sup> (12,000 mi.<sup>3</sup>) of tuff was erupted (Best and Christiansen 1991, Figure 3a). The period of most voluminous silicic volcanic activity in the Yucca Mountain region occurred between about 15 and 11 Ma (Sawyer et al. 1994, Table 1). Large-magnitude extension also migrated southward during the Cenozoic (Crowe et al. 1995, p. 4-2), although less systematically than silicic volcanism. The timing of extension and silicic volcanism may not be well correlated in any particular area or at all (Best and Christiansen 1991, Figure 10; Gans and Bohrson 1998, Figure 5); extension locally may predate, be contemporaneous with, or postdate silicic volcanism (Axen et al. 1993, p. 56; Sawyer et al. 1994, p. 1304) or have no association.

### **12.2.4 Miocene-Quaternary Basaltic Volcanism**

The initiation of true basaltic volcanism in the Great Basin and the Basin and Range tectonic province as a whole began in the early to middle Miocene (less than 17 Ma) (Figure 12.2-1) and generally postdates major silicic volcanism and periods of high extension rate in any particular region (e.g., Sawyer et al. 1994, pp. 1314 to 1316; Gans and Bohrson 1998, pp. 67 to 68, Figure 4; Christiansen and McKee 1978, p. 291). Basaltic volcanism in the Great Basin and adjoining regions has exhibited systematic trends in location, composition, and eruption volume through time. These trends can be related to both tectonic processes in the crust and melt generation processes in the underlying mantle.

Figure 12.2-1 shows the distribution of basaltic rocks in the western United States (excluding the Columbia Plateau) during two time periods: 16 to 5 Ma, from near the inception of basaltic volcanism to the end of the Miocene; and 5 to 0 Ma, from the end of the Miocene to the present. Basaltic volcanism was concentrated increasingly along major physiographic margins with time, in particular along the margins of the Great Basin and the Colorado Plateau. Post-Miocene eruption of basalt within the Great Basin interior has been sparse, with the notable exception of a band of post-Miocene basalt that extends from Death Valley to Lunar Crater in central Nevada, including the basalts in the vicinity of Yucca Mountain (Crowe, Vaniman et al. 1983, p. 4). The

migration of basaltic volcanism to the margins of the Great Basin correlates with increased extension and seismicity in these areas, indicating that the stress regime and local strain rate exert a broad control on the location of basaltic eruptions (Christiansen and McKee 1978, p. 305).

In the southwestern United States, in general, basaltic volcanic fields that erupted the largest volumes and had the highest eruption rates are associated with the Colorado Plateau margin (Taos, Cerros del Rio, San Francisco, Springerville, Zuni-Bandera, Mount Taylor, western Grand Canyon, St. George-Zion area) (CRWMS M&O 1998f, Chapter 4, Section III). Many of these basalt fields erupted tholeiitic basalt in addition to alkalic basalt, indicating higher degrees of partial melting at shallower mantle depths compared to the Great Basin/Basin and Range interior (Nelson and Tingey 1997, p. 1264). Basalt fields in the interior of the Basin and Range have volumes that seldom exceed a few tens of cubic kilometers, while fields along the Colorado Plateau boundary have volumes of 100 to 300 km<sup>3</sup> (24 to 72 mi.<sup>3</sup>) (San Francisco, Springerville, Zuni-Bandera, Taos). Long-term eruption rates for several volcanic fields on the Colorado Plateau margin exceed 50 km<sup>3</sup>/m.y. (12 mi.<sup>3</sup>/m.y.), while rates for fields within the Basin and Range are less than 20 km<sup>3</sup>/m.y. (4.8 mi.<sup>3</sup>/m.y.) (CRWMS M&O 1998f, Figure 4.2). The volume and eruption rates of basalt fields of the Colorado Plateau margin suggest higher production rates of basaltic magma in the mantle beneath these areas, compared with mantle beneath the Basin and Range interior. The eruption rate for the past 5-m.y. cycle of basaltic activity near Yucca Mountain is among the lowest of volcanic fields in the western United States (CRWMS M&O 1998f, p. 4-12), and basaltic volcanism is minor compared to other regions of the western United States (Figure 12.2-1).

#### 12.2.4.1 Data Acquisition and Methodology

**Geologic Mapping**—Maps showing the locations of Miocene and post-Miocene basalt centers are shown on Figures 12.2-2 and 12.2-3. The units of the post-Miocene basalts have been the focus of detailed field studies, including trenching and standard geologic mapping at scales of 1:24,000 to 1:4,000 (Faulds et al. 1994; CRWMS M&O 1998e, Appendix 2, M1-M5; Fleck et al. 1996, Figures 1, 2). In all cases, Quaternary volcanic centers have been mapped in greater detail than Pliocene centers.

**Geochronology**—Early determinations of the age of basalts in the Yucca Mountain region were obtained by the K-Ar method. This method is often accurate and reproducible for older basaltic rocks with sufficient radiogenic <sup>40</sup>Ar; younger basaltic rocks are generally more difficult to accurately date due to the low amount of radiogenic <sup>40</sup>Ar present in the rocks. In recent years, the K-Ar method has been increasingly replaced by the use of the <sup>40</sup>Ar/<sup>39</sup>Ar method. The <sup>40</sup>Ar/<sup>39</sup>Ar method has generally been used to date basalts older than 1 m.y. For younger basalts (e.g., Sleeping Butte and Lathrop Wells), the <sup>40</sup>Ar/<sup>39</sup>Ar method has been supplemented by the use of cosmogenic <sup>3</sup>He, U-Th disequilibria, and thermoluminescence (CRWMS M&O 1998e, Chapter 2, pp. 2-37, 2-39, 2-76 to 2-95) because of the difficulty of dating young basaltic rocks using the <sup>40</sup>Ar/<sup>39</sup>Ar method and the need to independently confirm the results of any one method.

The level of detail of the studies of geologic and geochronologic data as the age of basalt centers decreases has increased in an attempt to focus the work on assessment of the Pliocene and

Quaternary volcanic history of the Yucca Mountain region. It is this part of the geologic record that provides the most important basis for assessing volcanic hazard.

**Comparison of K-Ar and  $^{40}\text{Ar}/^{39}\text{Ar}$  Data for Post-Miocene Basalts**—The most extensive studies to establish ages for post-Miocene basalts of the Yucca Mountain region were carried out as part of Nevada Test Site studies using the K-Ar method (Fleck et al. 1996, Table 1) and as part of the YMP using the  $^{40}\text{Ar}/^{39}\text{Ar}$  method (CRWMS M&O 1998e, Table 2.B; Table 2.C; Heizler et al. 1999, p. 767). Comparison of the results of these studies serves as an independent check on the reproducibility of age determinations obtained for post-Miocene basalts of the Yucca Mountain region. Mean age comparisons are generally good for basalt episodes between 1 and 5 Ma, with a maximum difference in mean age determinations of about 8 percent for the basalt of Buckboard Mesa (Table 12.2-1). Even where mean age determinations are in agreement, however, there is uncertainty regarding the true age distribution of a given volcanic episode. For example, the Quaternary basalt centers of Crater Flat can be interpreted as all having the same age of about 1 m.y. or, alternatively, there may be a systematic decrease in eruption age from north to south in Crater Flat (Figure 12.2-4). For the two youngest volcanic episodes (Sleeping Butte and Lathrop Wells), agreement is poorer (about 20 to 30 percent difference), which is considered to reflect the difficulty of obtaining ages for young basalts using these methods. In the case of the Sleeping Butte centers, only a few age determinations have been attempted, and the data are insufficient to assess which age determination is more correct (CRWMS M&O 1998e, p. 2-39).

The age of the Lathrop Wells volcanic center has been debated for a number of years (Turrin et al. 1991, 1992; Wells et al. 1990; Wells, S.G. et al. 1992). Recent  $^{40}\text{Ar}/^{39}\text{Ar}$  ages (Heizler et al. 1999, p. 767) on both basalt whole-rock samples and tuff xenolith sanidine samples are reproducible and indicate an age of about 80 k.y. This age is consistent with  $^3\text{He}$  ages (CRWMS M&O 1998e, Table 2.4) and  $^{36}\text{Cl}$  ages (Zreda et al. 1993, Table 1) measured at Lathrop Wells, indicating that the true age of the Lathrop Wells center is between about 70 and 90 k.y.

**Geochemistry**—Major element, trace element, isotopic, and mineral chemistry data have been obtained for all post-Miocene basalt units (Bradshaw and Smith 1994, Table 1; Perry and Straub 1996; Fleck et al. 1996, Tables 3, 4; CRWMS M&O 1998f, Chapter 4, Sections V, VI, Appendix 4.1). Chemistry of major and trace elements was analyzed by X-ray fluorescence and instrumental neutron activation analysis (e.g., Perry and Straub 1996, pp. 2, 5). Isotopic compositions of Sr, Nd, and Pb were measured by solid-source mass spectrometry (Perry and Straub 1996, p. 6). Mineral chemistry was analyzed by electron microprobe (Perry and Straub 1996, p. 6).

#### 12.2.4.2 Basaltic Volcanism in the Yucca Mountain Region

The commencement of basaltic volcanism occurred during the latter part of the caldera-forming phase, as extension rates waned, and small-volume basaltic volcanism has continued into the Quaternary (CRWMS M&O 1998e, Chapter 2). In terms of eruption volume, the 15-m.y. history of volcanism in the Yucca Mountain region is viewed as a magmatic system that peaked between 13 and 11 Ma, with the eruption of more than 5,000 km<sup>3</sup> (1,200 mi.<sup>3</sup>) of ash-flow tuffs, and has been in decline since, with relatively minor volumes of basalt erupted since 11 Ma (Figure 12.2-5). Approximately 99.9 percent of the volume of the southwestern Nevada volcanic

field erupted by about 7.5 Ma with the eruption of tuffs from the Stonewall Mountain volcanic center, the last active caldera system of the southwestern Nevada volcanic field (Sawyer et al. 1994, Table 1, Table 3). The last 0.1 percent of eruptive volume of the volcanic field consists entirely of basalt erupted since 7.5 Ma (CRWMS M&O 1998c, Table 3.1) (Figure 12.2-6). In terms of relative volumes, therefore, silicic volcanism in the southwestern Nevada volcanic field is considered to have ceased eruptive activity about 7.5 Ma. Considered in terms of total eruption volume, frequency of eruptions, and duration of volcanism, basaltic volcanic activity in the Yucca Mountain region defines one of the least active basaltic volcanic fields in the western United States (CRWMS M&O 1998f, Figure 4.2, for post-Miocene basalts of Crater Flat).

Post-caldera basalts in the Yucca Mountain region can be divided into two episodes: Miocene (eruptions between about 9 and 7.3 Ma) and post-Miocene (eruptions between about 4.8 and 0.08 Ma). The time interval of about 2.5 m.y. between these episodes is the longest eruptive hiatus of basalt in the Yucca Mountain region during the last 9 m.y. (CRWMS M&O 1998c, Table 3.1). This eruptive hiatus also marks a distinct shift in the locus of post-caldera basaltic volcanism in the Yucca Mountain region to the southwest (Figure 12.2-2). The Miocene basalts and post-Miocene basalts are thus both temporally and spatially distinct. This observation emphasizes the importance of considering the age and location of the post-Miocene basalts (about the past 5 m.y. of the volcanic history of the Yucca Mountain region) when calculating the volcanic hazard at the potential Yucca Mountain repository. The PVHA experts almost exclusively considered the time period of interest to be post-5 Ma (with significant weight given to the post-1 Ma period) as the time period of interest in assessing volcanic hazard at Yucca Mountain (CRWMS M&O 1996, Figure 3-62).

The post-Miocene basalts formed during at least six episodes of volcanism (based on age groupings) that occurred within 50 km (31 mi.) of the potential repository (Figure 12.2-3). These six episodes, in order of decreasing age, consist of the (1) basalt of Thirsty Mesa, (2) Pliocene Crater Flat and Amargosa Valley, (3) Buckboard Mesa, (4) Quaternary Crater Flat, (5) Hidden Cone and Little Black Peak (the Sleeping Butte centers), and (6) Lathrop Wells. Three of these basalt episodes are in or near the Crater Flat topographic basin, within 20 km (12.4 mi.) of Yucca Mountain. Several aeromagnetic anomalies in the Amargosa Valley have characteristics that indicate buried basaltic volcanic centers (Langenheim et al. 1993, p. 1840). One of these anomalies (anomaly B of Langenheim et al. 1993) was drilled and basalt cuttings were dated at 3.85 Ma using the  $^{40}\text{Ar}/^{39}\text{Ar}$  method (CRWMS M&O 1998e, Table 2.B). The total eruption volume of the post-Miocene basalts is about  $6 \text{ km}^3$  ( $1.4 \text{ mi.}^3$ ). The volume of individual episodes has decreased progressively through time, with the three Pliocene episodes having volumes of approximately 1 to  $3 \text{ km}^3$  ( $0.24$  to  $0.72 \text{ mi.}^3$ ) each and the three Quaternary episodes having a total volume of only about  $0.5 \text{ km}^3$  ( $0.12 \text{ mi.}^3$ ) (Figure 12.2-5) (Table 12.2-2). All of the Quaternary volcanoes are similar in that they are of small volume, about  $0.15 \text{ km}^3$  ( $0.04 \text{ mi.}^3$ ) or less (Table 12.2-2) and typically consist of a single main scoria cone surrounded by a small field of basalt flows, which commonly extend about 1 km (0.62 mi.) from the scoria cone.

The seven (or eight if Little Cones is counted as two volcanoes) Quaternary volcanoes in the Yucca Mountain region occur to the south, west, and northwest of Yucca Mountain in a roughly linear zone defined as the Crater Flat Volcanic Zone (Crowe and Perry 1990, p. 328). Five of the seven Quaternary volcanoes are in or near Crater Flat and lie within 20 km (12.4 mi.) of the Yucca Mountain site (Figure 12.2-3). Models that attempt to relate volcanism and structural

features in the Yucca Mountain region have emphasized the Crater Flat basin because of the frequency of volcanic activity associated with Crater Flat and its proximity to the potential Yucca Mountain repository (e.g., Smith, E.I. et al. 1990, p. 84; Connor and Hill 1995, p. 10122).

#### 12.2.4.3 Geochemistry and Petrology of Yucca Mountain Region Basalts

The geochemistry of Yucca Mountain region basalts gives insight into mantle source characteristics, the fraction of melt generated in the mantle as a function of time, and ascent history. Magma chemistry data also are used to determine parameters for important variables used in consequence modeling, such as magmatic viscosity, magma temperature, and density (CRWMS M&O 2000b). A large geochemical database that includes major elements, trace elements, and radiogenic isotopes exists for basalts of the Yucca Mountain region (Vaniman et al. 1982, Table 2; Perry and Straub 1996; Bradshaw and Smith 1994, Table 1; Fleck et al. 1996, Tables 3, 4; CRWMS M&O 1998f, Chapter 4, Sections V, VI). Basalts of the Yucca Mountain region are classified as alkali olivine basalts, as are most post-Miocene basalts in the interior of the Great Basin.

Alkali olivine basalts have high (about 4 to 5 weight percent) total alkalis ( $\text{Na}_2\text{O} + \text{K}_2\text{O}$ ) and are generated at relatively great depth by small degrees of partial melting (less than 15 percent) (Jaques and Green 1980, p. 304, Figure 9). Experimental data (Takahashi 1980, p. 272; Takahashi and Kushiro 1983, Figure 15, Table 3) indicate that alkalic basalts compositionally similar to those of the Great Basin equilibrated at pressures of 14 to 20 kb, equivalent to a depth of 45 to 65 km (28 to 40 mi.). Mg/Fe ratios of basalts in the Yucca Mountain region are relatively low, indicating significant fractionation of olivine and pyroxene en route to the surface. On average, Pliocene basalts have slightly higher Mg/Fe ratios than Quaternary basalts (CRWMS M&O 1998f, Figure 4.5). If this difference is significant, it indicates that higher extension rates in the Pliocene favored more rapid transit to the surface with less opportunity for fractional crystallization.

Post-Miocene basalts of the Yucca Mountain region vary widely in concentrations of incompatible trace elements, which reflect differences in the composition of the mantle and the conditions of mantle melt generation beneath the Yucca Mountain region. Incompatible trace elements are those that are not easily incorporated into common mantle mineral structures. Thus, upon melting, they are the first released into the melt. Concentrations of La and Th and La/Th ratios, for instance, vary considerably, in some cases even within individual volcanic centers (CRWMS M&O 1998f, Figure 4.6). An important observation concerning the genesis of basalts in the Yucca Mountain region is that basalts younger than about 3 m.y. have higher concentrations of many incompatible trace elements (e.g., Sr, Th, U, La, Ce) than older basalts (Vaniman et al. 1982, pp. 351 to 353; Farmer et al. 1989, pp. 7887 to 7888; Fleck et al. 1996, p. 8223). For melting of mantle source rocks, elements such as La and Th are diagnostic of relative degrees of partial melting (e.g., high percentage of partial melt equals a relatively low concentration of La and Th). These criteria can only be used as a broad guideline, since source heterogeneity also has to be taken into account. However, the three Pliocene basalt centers (Thirsty Mesa, southeast Crater Flat, Buckboard Mesa) (Figure 12.2-3) have generally lower La and Th concentrations than Quaternary centers, implying larger degrees of partial melting of the mantle source, an interpretation that is consistent with their higher eruption volumes (CRWMS M&O 1998f, Figure 4-6). The combination of decreasing eruptive volume through time and the

geochemical data discussed above indicates that the intensity of mantle melting processes beneath the Yucca Mountain region is waning. Fleck et al. (1996, p. 8225) observed that the waning volcanism through time is also valid when the time frame is extended to include basalts of Miocene age (less than 11 Ma), and concluded that a general decrease through time in the amount of partial melting of the mantle source is the most reasonable explanation.

Nd, Sr, and Pb isotopic data have been obtained for most of the post-Miocene volcanic centers of the Yucca Mountain region (Farmer et al. 1989, Tables 3, 4; Perry and Straub 1996; Fleck et al. 1996, Table 4; CRWMS M&O 1998f, Table 4.1). The high  $^{87}\text{Sr}/^{86}\text{Sr}$  (about 0.707) and low  $\epsilon_{\text{Nd}}$  (about -10) of the basalts from the Yucca Mountain and adjacent region are unusual for alkali basalts of the western United States and are interpreted as reflecting the isotopic composition of a lithospheric mantle source (Farmer et al. 1989, p. 7893; Fleck et al. 1996, p. 8224). A lithospheric source is consistent with a relatively shallow generation depth of 45 to 65 km (28 to 40 mi.), as previously discussed.

**Crater Flat Volcanism**—Basaltic volcanism at Crater Flat occurred in three episodes at approximately 3.7, about 1, and 0.08 Ma (Figure 12.2-3). All of the basalt erupted at Crater Flat is alkalic (Vaniman et al. 1982, p. 343), indicating relatively small degrees of partial melting in the mantle throughout the lifetime of the field. The volume of alkali basalt erupted through time has decreased from about  $1.5 \text{ km}^3$  ( $0.36 \text{ mi.}^3$ ) in the oldest cycle (including the basalt of Amargosa Valley) to about  $0.1 \text{ km}^3$  ( $0.02 \text{ mi.}^3$ ) at the youngest center, Lathrop Wells (CRWMS M&O 1998c, Table 3.1). The relatively long lifetime of the Crater Flat field, combined with the small volume of erupted material, results in one of the lowest eruptive rates of any basaltic volcanic field in the southwestern United States (CRWMS M&O 1998f, Figure 4.2).

Although declining volumes through time indicate a waning magmatic system, the normative compositions of basalt from different episodes (Vaniman et al. 1982, Figure 3) do not clearly indicate a shift to more undersaturated compositions (and, hence, smaller degrees of partial melting) through time. Differences in normative composition of Crater Flat magmas may be related more to fractionation history (e.g., amphibole removal) than differences in degree of partial melting, which is evident in trends in La/Sm ratios and Ti content (Vaniman et al. 1982, pp. 346 to 347, Figure 4).

Another factor bearing on the evolution of the Crater Flat field is changes in the fractionation depth of magmas through time, which is probably related to changes in magma chamber depth (Perry and Crowe 1992, p. 2359). Lavas of the oldest episode contain plagioclase, olivine, and clinopyroxene phenocrysts, while lavas of the younger episodes contain only olivine. Experimental studies of alkali basalt (Knutson and Green 1975, Figure 1; Mahood and Baker 1986, pp. 256 to 257) indicate that clinopyroxene will crystallize early in the crystallization sequence relative to plagioclase at pressures exceeding 8 kb. The lack of plagioclase in lavas of the younger episodes indicates fractionation at high pressure, within the lower crust or upper mantle. The high Sr (which partitions into plagioclase) of the younger episodes also indicates that plagioclase was not an important fractionating phase in the younger episodes. Sc (which partitions into clinopyroxene) is lower in the youngest episodes relative to the oldest episode, indicating fractionation of clinopyroxene at high pressure. In contrast, lava of the oldest episode contains plagioclase phenocrysts, relatively low Sr, and relatively high Sc (Vaniman et al. 1982, Table 2), indicating fractionation at lower pressure where plagioclase and

olivine dominate fractionation. These relationships indicate that magma chambers were relatively shallow (middle to upper crust) at 3.7 Ma but were deep (lower crust or upper mantle) during the two younger episodes (Perry and Crowe 1992, p. 2359). This interpretation implies a decreased generation rate for basaltic magma in the Quaternary because a decreased magma flux into the crust could not sustain shallower magma chambers. Fleck et al. (1996, Figure 4, p. 8223) noted that the higher abundances of plagioclase phenocrysts in older basalts extend to basalts of late Miocene age and likewise concluded that younger basalts equilibrated at higher pressure or higher water pressure, consistent with a reduced magma flux into the crust.

#### **12.2.4.4 Eruptive History of Yucca Mountain Region Quaternary Basaltic Centers**

The decrease in eruption volumes between Pliocene and Quaternary volcanic centers in the Yucca Mountain region corresponds to a change in predominant eruption style. Pliocene eruptions were predominantly of Hawaiian type, which suggests small ratios of pyroclastic deposits to lava flows. In the Quaternary, volcanic centers formed by a mix of Hawaiian- and strombolian-type eruptions, suggesting larger ratios of pyroclastic deposits to lava flows compared to Pliocene centers (CRWMS M&O 1998d, p. 6-11). The change to higher pyroclastic deposits/lava flow ratios in the Quaternary is consistent with smaller fractions of basaltic melt generated in the mantle. Compared to large volume melts, small volume mantle melts are high in volatile constituents (H<sub>2</sub>O, CO<sub>2</sub>) that favor high pyroclastic deposit to lava flow ratios.

Evidence that some basaltic volcanic centers in the Yucca Mountain region were not monogenetic (forming in an eruptive episode spanning weeks to years, and involving a single magma batch) was first introduced by Wells, S.G. et al. (1990, p. 551), who observed soils between scoria deposits south of the Lathrop Wells cone that suggested significant time intervals between emplacement of the scoria deposits. The most recent studies at Lathrop Wells combining new geochronology and field studies weaken the evidence for polycyclic volcanism and suggest that the center formed in a single episode about 80 ka (CRWMS M&O 1998e, Chapter 2, p. 2-107; Heizler et al. 1999, p. 767). The origin of scoria deposits on the south side of the Lathrop Wells cone originally described by Wells, S.G. et al. (1990, p. 551) remains enigmatic, however, and may be inconsistent with an entirely monogenetic origin of the Lathrop Wells center (CRWMS M&O 1998e, pp. 2-2, 2-74; CRWMS M&O 1998h, p. 1-3).

Bradshaw and Smith (1994, p. 180) and Smith, E.I. et al. (1996, p. A-502) have concluded that both Red Cone and Black Cone of the Quaternary Crater Flat (Figure 12.2-4) volcanic episode are polycyclic, with eruptions that spanned 100 to 150 k.y.

#### **12.2.4.5 Geophysical Evaluations Related to Yucca Mountain Region Basaltic Volcanism**

Geophysical studies can potentially provide constraints on the location of basaltic volcanism by identifying the subsurface relationship between crustal structure and volcanism, or by directly identifying intrusive bodies in the crust. Magnetic and seismic data have been the most useful for understanding the location of basaltic volcanism in the Yucca Mountain region.

Aeromagnetic data have been gathered at a variety of scales in the Yucca Mountain region (summarized in CRWMS M&O [1998c, Chapter 3, Section VI]; see also Connor et al. [1997]). A number of aeromagnetic anomalies in the Yucca Mountain region have been interpreted as

buried or partially buried basaltic centers (Kane and Bracken 1983; Langenheim et al. 1993, p. 1840; Connor et al. 1997). Two anomalies, in western Crater Flat and the northern Amargosa, have been drilled and confirmed to be buried basalt with ages of about 11 and 3.8 m.y., respectively (Crowe et al. 1995, pp. 2-12, 2-19). A map presented by Earthfield Technology (1995, Appendix II) indicates the presence of as many as 40 to 60 aeromagnetic anomalies within about 35 to 40 km (22 to 25 mi.) of Yucca Mountain that are interpreted as intrusive bodies; six of these lie within about 5 km (3.1 mi.) of the potential repository site. The Earthfield Technology (1995, p. 3) results were based on the merging of three aeromagnetic data sets, the Timber Mountain, Lathrop Wells, and Yucca Mountain surveys. Subsequent to release of Earthfield Technology (1995), it was discovered that the report "was flawed by an incomplete and mislocated Timber Mt. Survey" (Feighner and Majer 1996, p. 1). Inspection of the flight survey map in Earthfield Technology (1995, Figure 2) and a corresponding map enclosed in Feighner and Majer (1996, Appendix I) indicates that the Timber Mountain survey, which encompasses about 50 percent of the coverage area and the majority of the aeromagnetic anomalies, was mislocated approximately 20 km (12 mi.) to the south-southwest of its correct location (CRWMS M&O 2000a, Section 6.3.1.6). For this reason, further analysis of the anomalies presented by Earthfield Technology (1995, Appendix II) that lie within the Timber Mountain survey is not warranted. The six anomalies located within 5 km (3.1 mi.) of the potential repository site (the Yucca Mountain survey) are associated with mapped faults and are probably due to faulting of magnetic Topopah Springs Tuff (Feighner and Majer 1996, p. 2; Reamer 1999, p. 32).

The most reliable and detailed data available for magnetic anomalies in the Yucca Mountain region are presented in Conner et al. (1997) and Magsino et al. (1998). These data were obtained using ground magnetic surveys of 14 selected aeromagnetic anomalies located to the north, east, west, and south of the potential repository site (Magsino et al. 1998, Figure 1-1). Collectively, these surveys represent a comprehensive assessment of aeromagnetic anomalies nearest the potential repository site and provide confidence that the geologic record of basaltic volcanism near Yucca Mountain is adequately understood. Of the 14 surveys, seven provide no evidence of buried basalt and three were conducted over areas with known surface exposures of basalt, partly to enhance understanding of the relationship between volcanism and geologic structure (Magsino et al. 1998, Section 4). Four of the 14 surveys provide evidence of buried volcanic centers (Connor et al. 2000, Plate 3).

The most recent seismic reflection studies across Crater Flat show that the Crater Flat basin is an asymmetric graben that is deepest to the west (Brocher et al. 1998, Figure 6). Most of the basalts of Crater Flat are above the deepest part of the basin, suggesting a correlation between the location of basalts in the Yucca Mountain region and areas of greatest extension (CRWMS M&O 2000a, Section 6.4.1.5).

Teleseismic data give some insight into the physical state of upper mantle basalt sources beneath the Yucca Mountain region. Low upper mantle seismic velocities beneath much of the Basin and Range Province suggest that the upper mantle contains a small percentage of partial melt. Ascent of this melt through the crust to produce basaltic volcanism may depend partly on where local extensional stresses are conducive to magma ascent (Smith, R.L. and Luedke 1984, p. 64).

Against the general background of small melt fractions in the Basin and Range mantle, three northeast-trending zones of enhanced partial melting have been proposed based on identification of low-velocity mantle anomalies (Spence and Gross 1990, p. 10,842; Dueker and Humphreys 1990, pp. 1329 to 1330). The northernmost and southernmost of these zones correspond to pronounced magmatism: the Snake River Plain-Yellowstone zone and the Jemez zone of the southeastern Colorado Plateau margin (Figure 12.2-1). The middle zone extends from central Utah to southern Nevada and corresponds with surface volcanism in the St. George area of Utah (Dueker and Humphreys 1990, Figure 3; Nelson and Tingey 1997, p. 1263) and the Crater Flat area of southern Nevada (Evans and Smith 1992, p. 2379). The volume of basaltic volcanism associated with the St. George zone is far less than the zones to the north and south. At Crater Flat, in particular, the past 4 m.y. of basaltic volcanism has produced only about 2 km<sup>3</sup> (0.48 mi.<sup>3</sup>) of basalt (CRWMS M&O 1998d, Table 6.12). If the low-velocity anomaly beneath Crater Flat does represent a higher volume of partial melting relative to the rest of the Basin and Range, the observed small volume that has erupted suggests that the local extensional stress regime does not strongly favor magma ascent and eruption. Biasi (1996, p. 2) reported new teleseismic data and teleseismic tomography interpretations that do not require magma to exist within the crust beneath Yucca Mountain or Crater Flat. Small amounts of partial melt within the mantle (greater than 45 km [28 mi.] depth) cannot be ruled out beneath southern Crater Flat and adjacent portions of Amargosa Valley.

#### 12.2.4.6 Structural Controls on Basaltic Volcanism

When considering different scales (regional and local) of spatial control on volcanism, it is important to distinguish between deep (mantle source) and shallow (upper crustal structure and stress field) processes. Volcanism is seen as occurring in the Yucca Mountain region on a regional scale because of melting processes in the upper lithospheric mantle that produce small volumes of alkali basalt, a basalt type generated by relatively small percentages of mantle melting compared to other basalt types (CRWMS M&O 1996, Appendix E; CRWMS M&O 1998f, p. 4-4). The exact mechanism of mantle melting in the Yucca Mountain region is poorly understood but may be controlled by a complex combination of processes, including the effect of residual heat in the lithospheric mantle from previous episodes of volcanism and the presence of a plate subduction system, local variations in volatile (water) content, variations in mantle mineralogy and chemistry, and the effect of regional lithospheric extension (CRWMS M&O 1996, Appendix E). Researchers who have analyzed magmatic processes in the Yucca Mountain region generally agree that the magnitude of mantle melting has drastically decreased since the middle Miocene and that all melts in the past few million years have been generated within relatively cool (compared to asthenospheric mantle) ancient lithospheric mantle (Farmer et al. 1989, p. 7893; Reamer 1999, p. 47), a factor that may contribute to the relatively small volume of basaltic melt erupted in the Yucca Mountain region since the Miocene (e.g., CRWMS M&O 1996, Appendix E, p. RC-2).

On a more local and shallow scale, most researchers conclude that (1) volcanism is correlated with zones of past or present crustal extension and (2) once dikes feeding volcanoes enter the shallow upper crust, their location and orientation is influenced by the orientation of the local stress field and the presence of faults that may locally control vent location and alignment. The evidence cited for these two conclusions includes several northeast-oriented vent alignments in the Yucca Mountain region and the association of eruptive centers with known or inferred faults

(Smith, E.I. et al. 1990, p. 83; Connor et al. 1997, p. 78; Reamer 1999, Section 4.1.3.3.3; Fridrich et al. 1999, p. 211).

Alternative conceptual models—how and where magmas form, and what processes control the timing and location of magma ascent through the crust to form volcanoes—have been used to develop spatial models for probability analyses (CRWMS M&O 2000a, Section 6.3.3). The majority of PVHA experts related the areas of greatest frequency of for future volcanic activity to the region where previous volcanism has occurred and in which extensional deformation has been and continues to be greatest (i.e., the southwestern portion of the Crater Flat basin) (CRWMS M&O 1996, Appendix E, pp. RC-5, BC-12, AM-5, MS-2, GT-2). This corresponds to the southwestern part of the Crater Flat structural domain (Figure 12.2-7), as defined by Fridrich (1999, pp. 174 to 176) (CRWMS M&O 2000a, Section 6.4). The alignment of basaltic vents in Crater Flat basin along the major transtension zones within the basin suggests that these zones controlled the ascent of basalt through the upper crust (Fridrich et al. 1999, p. 210). The youngest basalt in Crater Flat basin, the 80-ka Lathrop Wells cone, is spatially coincident with the site of strongest late Quaternary tectonism in the Crater Flat basin and is temporally coincident with a pulse of heightened faulting activity in this area (Fridrich et al. 1999, p. 211).

#### **12.2.4.7 Evidence for Simultaneous Faulting and Volcanic Eruption**

In an extensional tectonic environment, magma may ascend through the crust along fractures that serve as pathways for magma ascent. In the case of basaltic volcanism, the formation of fracture pathways releases seismic energy that typically results in earthquakes with a maximum magnitude of M 4.0 to 5.0 (Yokoyama and de la Cruz-Reyna 1990, pp. 274, 280). Volcanogenetic earthquakes may, however, trigger larger tectonic earthquakes on nearby faults that have sufficient strain accumulation.

In the Yucca Mountain region, basaltic ash has been found as a minor to dominant component in fissure fillings and stratabound alluvial horizons exposed by trenching of several faults near Yucca Mountain. (The basaltic ash consists of 0.1- to 0.5-mm glass shards containing phenocrysts of olivine and microcrystals of plagioclase; the glass shards have sharp edges, indicating minimal abrasion from surface transportation (CRWMS M&O 1998f, Figure 4.19). Correlation of these ashes (or ash) to the contemporary eruptive source has been used to constrain the age of the ash and therefore provide information about the slip history of a fault (CRWMS M&O 1998f, Chapter 4, Section VI-C). The most concentrated occurrence of ash in a trenched fault exposure was found in Trench 8 across the trace of the Solitario Canyon fault (Ramelli et al. 1996, p. 4.7-14). This ash occurs at the bottom in a 65-cm-wide fissure that represents the largest recorded Quaternary displacement event (more than 1 m) on the Solitario Canyon fault (Ramelli et al. 1996, p. 4.7-15).

Pure ash separates were analyzed for trace elements by Instrumental Neutron Activation Analysis and compared to the composition of all Quaternary eruptive centers in the Yucca Mountain region (CRWMS M&O 1998f, Section VI-C). These geochemical comparisons leave little doubt that the ash found in the Solitario Canyon fault (Trench 8), the Windy Wash fault (Trench CF3), the Fatigue Wash fault (Trench CF1), and the Stagecoach Road fault (Trench T1) originated from the eruption of the Lathrop Wells volcanic center, south of Yucca Mountain (CRWMS M&O 1998f, Section VI-C). Based on geochronology results from Lathrop Wells, the

age of this ash is about 80 k.y. (CRWMS M&O 1998f, Section VI-C). This conclusion is consistent with geochronology results from stratigraphic units exposed in Solitario Canyon fault Trench 8 (Ramelli et al. 1996, p. 4.7-15).

In contrast to the above interpretation, a direct age of the ash sample from Solitario Canyon fault Trench 8 using the  $^{40}\text{Ar}/^{39}\text{Ar}$  method yielded an apparent plateau age of  $0.86 \pm 0.16$  m.y. (CRWMS M&O 1998f, Section VI-C, Figure 4.18). This age is consistent with ages of the Quaternary basalt centers in Crater Flat, all of which have ages near 1 m.y., but not with that of the Lathrop Wells Center. Examination of the ash sample by scanning electron microscope, however, shows that about 0.5 percent of the dated sample consists of Miocene, high-K rhyolitic glass (CRWMS M&O 1998f, Section VI-C) that is optically cloudy and difficult to distinguish from the basaltic glass. It is likely that this high-K contaminant is the cause of the erroneously old  $^{40}\text{Ar}/^{39}\text{Ar}$  age.

### **12.2.5 Eruptive and Subsurface Effects of Basaltic Volcanism**

Studies of the eruptive and subsurface effects of basaltic volcanism have been conducted to provide information about natural volcanic systems and the parameters that can be used to model their behavior (CRWMS M&O 2000b). This information is used to develop parameter-value distributions appropriate for analysis of the consequences of volcanic eruptions through the potential repository at Yucca Mountain (CRWMS M&O 2000h). Knowledge of such effects supports the evaluation of disruptive event scenarios as part of the analysis to assess the repository's long-term performance. Of particular interest are estimates of the amount of debris that would be entrained by magma rising through the repository and the effects such magma would have on the geochemical and geohydrological processes operating in its vicinity. The analysis and modeling report *Characterize Eruptive Processes at Yucca Mountain, Nevada* (CRWMS M&O 2000b) discusses the following broad topics relevant to basaltic volcanism in the Yucca Mountain region that relate to effects:

- The geometry of volcanic feeder systems, which are of primary importance in predicting how much of the potential repository would be affected by an eruption
- The physical and chemical properties of the magmas, which influence both eruptive styles and mechanisms for interaction with radioactive waste packages
- Eruptive processes, including the ascent velocity of magma at depth, the onset of bubble nucleation and growth in the rising magmas, magma fragmentation, and velocity of the resulting gas-particle mixture
- The duration of eruptions, their power output, and mass discharge rates
- Geologic constraints regarding the interaction between magma and waste packages
- The bulk grain size produced by relevant explosive eruptions, and grain shapes.

Information on the rate of occurrence for rising magma intersecting a repository is discussed in Section 12.2.6.

### 12.2.5.1 Analog Studies of Material Entrainment

Field studies were conducted at the Lucero volcanic field in New Mexico and the San Francisco volcanic field in Arizona (Figure 12.2-1) to evaluate quantities of xenoliths erupted from volcanoes that shared some eruptive characteristics with Yucca Mountain region volcanoes (CRWMS M&O 1998g, Section C). Due to the geologic setting of these volcanic fields, the quantity of debris entrained by rising magma can be related to strata at depth below the volcanoes. The data provide information on the quantity of debris that can be entrained in rising magma per meter along the volcanic plumbing for a range of eruption mechanisms, including strombolian, hydrovolcanic, and effusive.

Upper-crustal xenoliths erupted from small-volume basaltic volcanoes of the Lucero volcanic field in west-central New Mexico (Valentine and Groves 1996) and of the San Francisco volcanic field in north-central Arizona (CRWMS M&O 1998g, Section D) were studied to assess the relative importance of various entrainment mechanisms. Total xenolith volume fractions were found to range from 0.3 to 0.9 in hydrovolcanic facies to less than  $10^{-4}$  to  $10^{-2}$  in most strombolian facies.

The volcanoes erupted through thick, well-characterized sequences of Paleozoic and lower Mesozoic sedimentary rocks, so that in some cases erupted xenoliths could be correlated with sedimentary units and, hence, depth ranges. The abundance of xenoliths from a given subvolcanic unit was divided by that unit's thickness to obtain an average entrainment rate (xenolith volume fraction derived per unit depth in the conduit). For small basaltic eruptions driven primarily by the expansion of magmatic volatiles (strombolian and Hawaiian eruption styles), entrainment rates were found to range from 0 to about  $10^{-4}$ /m and were typically within the range of  $10^{-8}$  to  $10^{-6}$ /m. Entrainment was found to be most sensitive to the mechanical properties of the wall rocks and is thought to depend mainly on brittle failure related to offshoot dikes, pore pressure buildup, and thermal stresses (Valentine and Groves 1996, p. 85). Entrainment rates in the uppermost few hundred meters of the Earth's crust can be much higher for hydrovolcanic explosion mechanisms, which are driven by interaction of hot magma with surface or groundwater (CRWMS M&O 1998g, pp. 5-14, 5-18). For this type of eruption, rates can range as high as  $10^{-4}$  to  $10^{-3}$ /m. These entrainment rates are averaged over thicknesses of individual stratigraphic units beneath the volcanoes; local entrainment rates could be higher (Valentine and Groves 1996, p. 81).

### 12.2.5.2 Effects of Basalt Intrusions on Silicic Tuffs

**Field Studies**—This section discusses studies of alteration of silicic pyroclastic rocks by shallow basaltic intrusions. Two sites were chosen for study because in combination they are good analogs for the various rocks in the vadose zone at Yucca Mountain and allow the type and spatial scale of alteration that would accompany a basaltic intrusion into the potential repository to be constrained. The two sites are the Slanted Buttes area of Paiute Ridge, eastern Nevada Test Site, where variably vitric and zeolitized silicic tuffs (some of which correlate to those at Yucca Mountain, some 40 km [25 mi.] away) were intruded by basaltic dikes and sills; and Grants Ridge, New Mexico.

At Grants Ridge, a thick sequence of unconsolidated rhyolite ignimbrite, fallout, and reworked volcanoclastic deposits were intruded by a basaltic plug that fed a scoria cone eruption. Erosion of the site has since produced a natural cross section through the scoria cone, its feeding system, and the pyroclastic host rocks. Data were gathered on geochemical and mineralogical alteration effects at both sites. The data indicate that alteration is limited typically to within 5 to 10 m of the intrusion (CRWMS M&O 1998g, p. 5-41).

**Slanted Buttes (Paiute Ridge) Site**—Vitric and zeolitized tuffs of middle-Miocene age intruded by shallow high-alumina alkali basalt magmas developed localized contact metamorphic zones at Slanted Buttes in the northeastern part of the Nevada Test Site (CRWMS M&O 1998g, p. 5-42). The sill and dikes were probably intruded into a shallow, unsaturated environment a few hundred meters from the paleosurface, as indicated by reconstruction of stratigraphy above the intrusions (CRWMS M&O 1998g, p. 5-42). The depth of intrusion is comparable to the potential repository environment at Yucca Mountain. At two dikes, each of similar width (about 9 m wide), the contact metamorphic zones were found to range from 0.5 to about 4 m wide on either side of the dikes (CRWMS M&O 1998g, pp. 5-43 to 5-44). The dike responsible for the localized thermal zone (0.5 m [1.6 ft]) is about 2 km (1.2 mi.) from a basaltic plug, whereas the other one is within 100 m. The contact aureole beneath a 45-m-thick (148 ft) sill is localized and extends to about 5 m (16 ft) below the sill. The sill is an offshoot from a dike and is about 1 km (0.62 mi.) away from a plug. Shallow emplacement into an unsaturated environment may be responsible for the localized nature of the contact metamorphic zones due to insufficient heat (CRWMS M&O 1998g, p. 5-56).

Silicic and zeolitized tuffs within the contact aureoles were found to be devitrified and/or fused and quenched to form vitrophyres. Within the contact zone, the vitric component of the Ammonia Tanks Tuff of the Timber Mountain Group was totally replaced by feldspar, quartz, and cristobalite. The Tiva Canyon Tuff of the Paintbrush Group beneath the sill was found to contain a vitrophyre and a devitrified zone side by side and a clinoptilolite-rich tuff occurs about 3 m (9.8 ft) away. Variations in major, trace, and rare earth elements are subtle except for water content (CRWMS M&O 1998g, p. 5-57).

Based on the natural analog studies, there is no indication of extensive hydrothermal circulation and alteration, brecciation, and deformation related to magmatic intrusion into the vitric and zeolitized tuffs. Field and analytical evidence from the localized contact metamorphic aureoles and devitrification of the silicic tuffs adjacent to the intrusion, minimal hydrothermal alteration, and presence of low-temperature minerals at close proximity to the intrusions also suggest insignificant effects of the shallow basaltic intrusions on the vitric and zeolitized tuffs (CRWMS M&O 1998g, p. 5-57).

**Grants Ridge Site**—A study was conducted at Grants Ridge, New Mexico (Figure 12.2-1), to assess the effects of contact metamorphism on poorly consolidated late Pliocene ash-flow tuffs and overlying volcanoclastic layers that were intruded by a basaltic plug and capped by thick scoria deposits (CRWMS M&O 1998g, p. 5-57). The area is characterized by a northeast-trending discontinuous mesa. The plug responsible for the widespread basaltic lavas capping the mesa is located in the northeastern part of this discontinuous mesa (termed East Grants Ridge) about 12 km (7.5 mi.) southwest of Mt. Taylor, New Mexico.

Physical features (e.g., color variation and degree of compaction), mineralogical data, and chemical data from the silicic tuffs around the basaltic plug indicate variable thermal effects. Despite the size of the basaltic intrusion (about 150 m [490 ft] wide), the contact metamorphic zone developed around the basaltic plug is only about 5 m (16 ft) wide. The poorly-cemented ash-flow tuff along the contact aureole is baked, fused, deformed, and injected with basalt lava. Variation in color and the degree of compaction of the silicic ash-flow tuff provide evidence for the localized nature of the thermal effect (CRWMS M&O 1998g, pp. 5-71 to 5-72).

Variations in mineralogical and geochemical compositions are consistent with the changes in color and compaction of the silicic rocks. The volcanic glass, water composition, F, Cl, and Fe contents increase away from the intrusion. Conversely, the amount of recrystallized minerals and the alkali contents are higher along the contact (CRWMS M&O 1998g, p. 5-72).

The field and laboratory data suggest that the effect of the intrusion on the unwelded pumice-rich ash-flow tuff was minimal. Because devitrification generally is enhanced by aqueous solution, the abundance of volcanic glass within a short distance (about 5 m [16 ft]) from the intrusion suggests a dry environment. Thus, in the absence of aqueous solutions, the width of the contact metamorphic aureole generally is confined to a narrow zone regardless of the size of the intrusion (CRWMS M&O 1998g, pp. 5-71 to 5-74).

**Modeling Studies**—A modeling study was conducted to estimate the spatial scale over which an intrusive event can significantly affect the potential repository (CRWMS M&O 1998g, pp. 5-74 to 5-91). The approach was based on simplified numerical simulations of thermally induced convective flow of air where the thermal driving force is the heat from magmatic intrusions (CRWMS M&O 1998g, p. 5-83). In an unsaturated zone, such as at the potential repository site, the pore fluid that is likely to have the largest spatial scale of thermally driven flow is air, and these calculations thus result in a conservative estimate of spatial scale of subsurface effects.

The modeling study indicates that magmatic intrusions in an unsaturated tuff would not cause significant convection at horizontal distances greater than about 2.5 km (1.5 mi.) (CRWMS M&O 1998g, p. 5-91). Intrusion gas was found to travel less than about 500 m (1,640 ft) laterally and the horizontal distance over which an intrusion affects convective airflow was found to be less than 2.5 km (1.5 mi.). These findings make sense, considering that while it is easy to move large volumes of air because of the very low density of air, those volumes carry very little energy. Further, the small amount of heat being physically transported by the air is dissipated by conduction through the matrix, which rapidly damps the convective motion.

### **12.2.5.3 Eruptive Processes Parameters for Consequence Models**

It is assumed that any future eruption (during the repository lifetime) will be of a character similar to the Quaternary basaltic eruptions in the Yucca Mountain region. In particular, the eruptive styles and composition recorded at the Lathrop Wells volcano, the most recent in the region, are emphasized. Information about natural volcanic systems and the parameters that can be used to model their behavior is presented in CRWMS M&O (2000b). This information is used to develop parameter value distributions appropriate for analysis of the consequences of volcanic eruptions through the potential repository at Yucca Mountain (CRWMS M&O 2000h).

**Characteristics of Eruptive Conduits, Dike Widths, and Dike Swarms**—Most observed basaltic eruptions begin as fissure eruptions, discharging magma where a dike intersects the ground surface, and they rapidly become focused into conduit eruptions. Because of the effect of (1) the conduit diameter and (2) depth (to which a conduit extends before merging into a simple feeder dike) on the number of waste packages disrupted by a potential eruption at Yucca Mountain, it is important to constrain both these variables. The best potential source of data for these parameters would be a study of basaltic volcanic necks exposed by erosion in the southwestern United States, where direct measurements of conduit radius and its variation with depth could be made. However, such data are lacking; while many such features have been mapped as part of regional studies, they were not measured in detail, at least for the range of compositions of interest to the YMP. Without access to direct measurements of conduit width, estimates of this parameter are evaluated based on analog studies (CRWMS M&O 2000b, Section 6.1). Doubik and Hill (1999, pp. 60 to 61) recently argued, based on an analogy between the Lathrop Wells volcano and Tobalchik (Kamchatka, Russia) volcano, that the Lathrop Wells conduit may have been as wide as 50 m (164 ft) at the depth of the potential repository. The 50-m (164-ft) estimate of conduit diameter is large, considering that Doubik and Hill (1999, p. 59) calculated a 48-m (157-ft) diameter for the Tobalchik conduit developed during a much larger eruption (CRWMS M&O 2000b, p. 25). For the TSPA-SR, the conduit (or vent) diameter cumulative distribution function is defined with a minimum value of 15 m (49 ft), a median value of 50 m (164 ft), and a maximum value of 150 m (492 ft) (CRWMS M&O 2000b, p. 47). The maximum value (150 m) for the conduit diameter in the distribution corresponds to the diameter of the Grants Ridge conduit/plug in New Mexico (CRWMS M&O 1998g, p. 5-60).

Dike width and the number of dikes associated with the formation of a new volcano would affect the number of waste packages hit by an intrusive event (CRWMS M&O 2000g). Dike widths are interpreted to have a log normal distribution with a minimum of 0.5 m (1.6 ft), a mean of 1.5 m (4.9 ft), and a 95th percentile width of 4.5 m (14.8 ft) (CRWMS M&O 2000b, Section 6.1). This distribution, which is based on data for dikes in the Yucca Mountain region reported by Crowe, Self et al. (1983, p. 266), is consistent with values reported by Delaney and Gartner (1997, p. 1182).

Each volcano in the Yucca Mountain region is fed by one main dike along which a central cone and other vents may form, but subsidiary dikes are also present. For example, the Lathrop Wells volcano likely is underlain by three dikes: the dike that fed the main cone, a dike that fed spatter and scoria mounds in a parallel chain just to the east of the main dike, and possibly a dike that fed scoria vents near the northern edge of the volcano (CRWMS M&O 1998e, Appendix 2-M). In addition, there may be small dikes that radiate outward from the main cone's feeder conduit. The Paiute Ridge intrusive complex, which appears to have fed at least one volcanic vent (evidenced by the presence of lava flow remnants and a plug-like body), may have as many as 10 dikes, in addition to sill-like bodies (CRWMS M&O 1998g, Figure 5.15). To account for the possibility of dike swarms, rather than single dikes, during formation of a new volcano, a log normal distribution for the number of dikes that has a minimum value of 1, a mean value of 3 (reflecting the assumption that the most likely new volcano will be similar to the Lathrop Wells volcano), and a 95th percentile value of 10 (assuming Paiute Ridge as an extreme event) is recommended in the TSPA-SR (CRWMS M&O 2000b, Section 6.1).

**Characteristics of Igneous Material**—The physical and chemical properties of the magmas play roles in determining eruptive styles and mechanisms for interaction with radioactive waste packages. Magma chemistry data is needed to determine parameters for important variables, such as magmatic viscosity, magma temperature, and density. The recent eruption at Lathrop Wells is used to represent the composition of future eruptions. The major element variation for Lathrop Wells is based upon 45 analyses of lava flows (Table 12.2-3) (CRWMS M&O 2000b, Table 2).

Eruptive styles in the Yucca Mountain region range from violent strombolian on one end of the spectrum to quiescent aa lava on the other (CRWMS M&O 2000b, Section 6.3). Eruption style is primarily controlled by volatile content (which is dominated by water) and the rate at which volatiles are exsolved from the magma. The observed eruptive styles indicate a large range in volatile content, and hence water, of Yucca Mountain region magmas. Based on experimental data for material similar in composition to Yucca Mountain region basalts, future basaltic activity in the Yucca Mountain region should be anticipated to range from 0 to 4 percent water, with values approaching 4 percent being uncommon (CRWMS M&O 2000b, Section 6.2.2).

Corrosive gases released from an igneous event will play a role in the performance of the waste packages. A survey of data compilations from the literature, including volcanoes from convergent, divergent, and hot-spot tectonic settings, was used to estimate the mole percent of constituents in volcanic gas (CRWMS M&O 2000b, Section 6.2.3) (Table 12.2-4). Species with the largest mole percent concentrations are, in decreasing order, H<sub>2</sub>O, CO<sub>2</sub>, and SO<sub>2</sub>. Concentrations for minor species, which are corrosive, have large uncertainties relative to mean values.

The ranges of magmatic temperatures are well known for magmas as a function of critical parameters (i.e., pressure and water content) upon which they depend. Direct measurements are available for the low end of the spectrum of water content. Experimental data are used to constrain magmatic temperatures for magmas with elevated water content. Calculated saturation pressures and corresponding temperatures, as a function of water content, for Lathrop Wells lavas (Table 12.2-5) are consistent with a long, well-established body of experimental data (CRWMS M&O 2000b, Section 6.2.4). For water content ranging from 0 to 4 percent by weight, calculated liquidus temperatures are between 1,169 and 1,046°C.

**Eruptive Processes**—Quaternary basalts of the Yucca Mountain region display facies that indicate a range of eruptive processes (CRWMS M&O 2000b, Section 6.3). The Lathrop Wells volcano is a good example of a range of eruptive processes recorded by a single volcano (CRWMS M&O 2000b, Section 6.3). The surface of the main cone is composed mainly of loose scoria with a relatively high vesicularity. The cone is surrounded, particularly to the south, west, and north, by a fallout blanket up to about 3 m (10 ft) thick (within 1 km [0.6 mi.] of the cone) composed of the same loose scoria. Remnants of this fallout deposit are exposed at the surface northward up to 2 km (1.2 mi.) from the crater. About 20 km (12 mi.) north of the crater, the reworked equivalent of the fallout deposit is observed in trenches cut into the Solitario Canyon fault. These features all suggest a relatively high-energy eruption with an ash column that rose kilometers into the air so that clasts were cool when they fell to the ground and finer ash that was dispersed widely by winds (termed a “violent strombolian eruption” by many volcanologists). Other parts of the Lathrop Wells volcano were emplaced by quite different mechanisms

(CRWMS M&O 2000b, Section 6.3). For example, mounds of coarse, partially welded spatter indicate local, relatively low-energy strombolian eruption. Recent quarry exposures show welded scoria and agglutinate, typical of strombolian eruption, in the main cone, suggesting that only the late stages of the cone-forming eruptions were violent strombolian. Thick, stubby aa flows suggest short-duration, high mass flux effusive eruption. Other volcanoes of the Yucca Mountain region are less well preserved, but they seem to exhibit a similar range in eruptive styles at individual centers.

The solubilities of volatiles such as H<sub>2</sub>O and CO<sub>2</sub> in basaltic magmas are proportional to pressure. At depth, magmas will have relatively high volatile contents, but as they ascend through progressively lower lithostatic pressure, they will become oversaturated and bubbles will nucleate. Continued rise results in increasing numbers and sizes of bubbles (caused by combined exsolution of volatiles and decompression and coalescence growth of the bubbles); these two processes increase the specific volume of the magma and, as a consequence, its velocity also increases gradually (according to conservation of mass). Explosive eruption occurs when, at shallow depths, the magma reaches a foamy state. With further decompression, it fragments, switching from a melt with dispersed bubbles to a gas with dispersed fragments or clots of melt. At and above this fragmentation depth, the gas-melt mixture accelerates rapidly until it leaves the volcanic vent at speeds of tens to a few hundreds of meters per second (miles per hour). A further complication in this sequence of events is the possibility of loss of volatiles through the walls of the conduit or dike as magma ascends. This can reduce the effective volatile content for the eruption.

Fragmentation depths modeled for the range of initial volatile content (0 to 4 percent) considered for the Yucca Mountain region range from about 200 to 900 m (656 to 2953 ft) (Figure 12.2-8) (CRWMS M&O 2000b, Section 6.3.2). Velocity as a function of depth above the fragmentation surface is inferred from plots shown on Figures 12.2-9 and 12.2-10 that relate eruption velocity to initial dissolved water content of the magma at depth and mass flux rate (CRWMS M&O 2000b, Section 6.3.3). CRWMS M&O (2000b, Section 6.3.4) provides a discussion of estimates of total eruption duration (formation of the entire volcano) and volume for expected basaltic eruptions in the Yucca Mountain region. Eruption duration is difficult to estimate because during formation of a volcanic center it is likely that eruptive discharge rates could have varied substantially. For total eruption duration (formation of the entire volcano), a log normal distribution with a minimum of 1 day, a mean of 30 days, and a maximum of 15 yr. is recommended (CRWMS M&O 2000b, Section 6.3.4). For the TSPA-SR, uncertainty in the frequency and duration of violent strombolian eruptions is captured in the volcanic ash dispersion and deposition (ASHPLUME) analysis through the distribution used to characterize the volume of contaminated ash available for transport in a violent eruption (CRWMS M&O 2000h).

**Entrainment of Repository Material in Ascending Magma**—In assessing the effects of a potential volcanic eruption through a repository at Yucca Mountain, it is necessary to determine the degree to which repository material, including radioactive waste, might be entrained in the ascending magma. Wall rock debris entrained in erupted volcanic material (Section 12.2.5.1) provides a possible analog for this effect. For a variety of reasons, use of this analog is subject to uncertainties. Some of these uncertainties are volcanological in nature and some are related to the engineered system.

Volcanological uncertainties include the following: (1) the interaction between a rising dike and the perturbed stress field around repository drifts; (2) the interaction between rising, vesiculating magma and the partially open drifts (e.g., would magma run like lava flows for long distances down the drifts, would it pile up quickly to block the drift and therefore allow magma to continue rising, or would it explode down the drift?); and (3) the depth to which conduits might extend (i.e., if a wide conduit is formed, but only extends 200 m below the surface, then it will not have as large a disruptive effect on the potential repository). Several topics related to the dike-drift interactions are discussed in CRWMS M&O (2000f), including waste container temperature due to flow of magma down a blind drift; steady-state gas flow down the drift to interact with containers; the ability of the pressure pulse from a dike to cause containers and drift contents to be piled up ("snow plowed"); and, qualitatively, the interaction of the self-generated crack leading the dike with the stress-altered region around the drift.

There are few data available on the interaction of magma with undisturbed country rock and subsequent eruption of the lithic debris for the range of eruptive styles that can be reasonably expected at Yucca Mountain. As noted above, Valentine and Groves (1996, pp. 79 to 84) report data on the quantity of wall rock debris erupted from various depths during strombolian, Hawaiian, effusive, and hydrovolcanic activity at two volcanoes. Hydrovolcanic eruptions, represented by lapilli and block-rich tuff, ranged from 0.32 to 0.91 volume fraction of wall rock debris, with most of that originating in the uppermost approximately 510 m (1,673 ft) of the dike/conduit feeder systems (Valentine and Groves 1996, Table 1, p. 83). Strombolian, Hawaiian, and effusive eruptions ejected much lower volumes of wall rock debris, commonly resulting in total volume fractions of  $10^{-3}$  to  $10^{-5}$ . Doubik and Hill (1999, p. 60) state that the Lathrop Wells volcano has a relatively high average lithic volume fraction of  $9 \times 10^{-3}$ , but they do not provide any data, location or stratigraphic information, or description of the method used to arrive at this value. Doubik and Hill (1999, p. 60) use similarity in lithic content as a justification for using the relatively large and violent Tobalchik eruptions as analogs for the Lathrop Wells volcano (and hence potential eruptions at Yucca Mountain itself).

**Ash Plumes and Their Deposits**—As noted above, explosive eruptive styles of Quaternary volcanoes in the Yucca Mountain region include both strombolian and violent strombolian. Strombolian eruptions are characterized by short duration bursts that throw relatively coarse fragments of melt out on ballistic trajectories. Most of the fragments (clasts) are deposited immediately around the vent, with only a very small fraction of finer particles rising higher and being dispersed by wind to form minor fallout sheets. Violent strombolian eruptions, on the other hand, are characterized by vertical eruption of a high-speed jet of a gas-clast mixture. As the eruptive mixture rises in the jet, it entrains and heats air, which in turn reduces the bulk mixture density until the jet becomes buoyant and continues to rise as a plume. The plume rises to an altitude of neutral buoyancy compared to the surrounding atmosphere, in which it then spreads laterally as an anvil or "umbrella" cloud that is transported downwind. Clasts fall out from both the vertical eruption column and from the umbrella cloud according to their settling velocities. Settling velocity in air depends on the bulk density (the melt density corrected for the porosity, or vesicularity, of the clasts), shape, and size.

Bulk particle size and distribution and clast shape are therefore important parameters that need to be considered in the performance assessment model. As discussed in CRWMS M&O (2000b, Sections 6.5, 7), the following characterization of these parameters is used in the TSPA-SR. For

mean particle size erupted during violent strombolian phases, a log triangular distribution with a minimum of 0.01 mm (0.0004 in.), a mode of 0.1 mm (0.004 in.), and a maximum of 1.0 mm (0.04 in.) is used. The standard deviation of particle size distribution for a given mean is assumed to be a uniform distribution between 1 and 3 ( $-\log_2$  units). A shape factor of 0.5 is used for the clast characteristics. A range of values is used for the density of erupted particles depending on particle diameter. For particle diameters less than or equal to 0.01 mm, (0.0004 in.) density is 0.8 of the magma density. For particles greater than 10 mm (0.4 in.), density is 0.4 of the magma density. For particles between 0.01 and 10 mm (0.0004 and 0.4 in.), density should decrease linearly with increasing diameter.

## **12.2.6 Probabilistic Volcanic Hazard Analysis**

From 1995 to 1996, the U.S. Department of Energy sponsored the PVHA project to assess the probability of a future volcanic event intersecting the potential repository at Yucca Mountain (CRWMS M&O 1996). To ensure that a wide range of approaches was considered for the hazard analysis, 10 experts of various backgrounds and affiliations were chosen to participate in the project and evaluate the data. Their evaluations (elicitations) were then combined to produce an integrated quantitative assessment of the volcanic hazard that reflects a range of alternative scientific interpretations. This assessment focused on the volcanic hazard at the site, which was defined as the annual probability of intersection of the potential repository by a basaltic dike. The hazard assessment provides input to an assessment of volcanic risk, which expresses the probability of radionuclide release due to igneous activity.

### **12.2.6.1 Probabilistic Volcanic Hazard Analysis Process**

The major procedural steps in the PVHA were selecting the expert panel members, identifying the technical issues, eliciting the experts' judgments and applying temporal and spatial aspects of probability models, and compiling and presenting the results.

**Selecting the Expert Panel Members**—From more than 70 nominees, 10 individuals were selected to participate in the PVHA project. Efforts were made to balance the panel with respect to technical expertise (physical volcanology, geochemistry, and geophysics) and institutional/organizational affiliation. The 10 experts and their affiliations are listed in Table 12.2-6.

**Identifying Technical Issues**—The PVHA panel of experts convened between February and December 1995. A technical facilitator/integrator led carefully structured, intensive interactions among the panel members. The experts participated in workshops, field trips, and other interactions, which were used to identify sources of agreement and disagreement among them. Each expert played the role of an informed technical evaluator of data, rather than a proponent of a particular model. On occasion, however, some experts were asked to present particular interpretations to facilitate discussion and consideration of alternative interpretations. In all of the interactions, it was made clear that the purpose of the PVHA was to identify and quantify uncertainty, not to eliminate it. It was also emphasized that the purpose was not necessarily to achieve consensus. Instead, disagreement was expected and accepted.

At the core of the PVHA project were four workshops. The primary objective of the workshops was to ensure the experts' understanding of the issues, alternative volcanic hazard models, and the data available on which to base a technical assessment. The first three workshops focused on the data, volcanic hazard models, and interpretations relevant to the PVHA. The workshops included presentations of data and interpretations from technical specialists from Los Alamos National Laboratory, the USGS, University of Nevada, Las Vegas, the Center for Nuclear Waste Regulatory Analyses, as well as from experts on the PVHA panel. During the fourth workshop, the experts reviewed the preliminary assessments developed by each panel member, after which the individual elicitations were revised, based on feedback received. Two field trips held during the course of the PVHA provided the opportunity for the panel members to observe geologic relationships pertaining to eruptive style, the definition of a volcanic event, and the distribution and timing of volcanic activity in the Yucca Mountain region.

**Temporal and Spatial Aspects of Probability Models**—Prior to the third PVHA workshop, an interactive meeting was held for the benefit of the expert panel members to focus on the calculation methods available to construct volcanic hazard models. The calculation methods are used to model the two main aspects of probability models: the temporal and spatial aspects.

Temporal models describe the frequency of occurrence of volcanic activity through time and include homogeneous and nonhomogeneous models. Many of the experts used homogeneous Poisson models to define the temporal occurrence of volcanic events, which assumes a uniform rate of volcanism based on the number of volcanic events that occurred during various periods in the past. Nonhomogeneous models were used by some experts to consider the possibility that volcanic events are clustered in time or to describe the possible waning or waxing of volcanic activity in the region during the recent geologic past.

Spatial models describe the spatial distribution (location) of future volcanic activity. Three types of models were used. Volcanic source zones represent regions in which the future occurrence of volcanoes is assumed to be spatially homogeneous. These source zones are defined based on several criteria: the spatial distribution of observed basaltic volcanic centers (especially post-5-Ma centers), structurally controlled provinces, regions defined based on geochemical affinities, tectonic provinces, and other criteria. Nonhomogeneous, parametric spatial distributions of future volcano occurrences were also modeled, for example, that the location of future volcanoes will follow a bivariate Gaussian distribution based on the location of volcanoes in Crater Flat. Finally, nonhomogeneous, nonparametric spatial density models were used by some experts to assess the spatial distribution of future volcanoes. These models make use of a kernel density function and smoothing parameter based on locations of existing centers to obtain the spatial distribution for location of future volcanoes.

**Eliciting the Experts' Judgments**—Formal elicitation followed the third workshop. The process consisted of a 2-day individual interview with each expert. To provide consistency, the same interview team was used for all elicitations. Following the elicitation interview, each expert was provided with a written summary of his elicitation, which was prepared by the interview team. The expert reviewed and clarified the summary and had the opportunity to revise any assessments. To promote a full understanding of each individual's judgment, the preliminary assessments made by each member of the expert panel were presented and discussed at the fourth workshop. Following this workshop, each expert had a final opportunity to revise his

assessments before the results of the PVHA were finalized (CRWMS M&O 1996, Appendix E). A summary of input parameters for the PVHA probability models is found in CRWMS M&O (1998b, Table 10-5).

**Definitions and Parameters of a Volcanic Event and Implications for Alternative Probability Calculations**—An important issue in the PVHA and alternative volcanic hazard assessments for the potential repository is the definition of a “volcanic event.” The definition can affect the outcome of probability calculations and must be clearly understood in order to meaningfully compare the results of alternative probability calculations. Volcanic event was defined individually and slightly differently by each PVHA expert, but the experts generally agreed that, fundamentally, a volcanic event is the formation of a volcano (with one or more vents) resulting from the ascent of basaltic magma through the crust as a dike or system of dikes (CRWMS M&O 1996, Appendix E). For the purposes of probability models discussed in CRWMS M&O (2000a, Section 6.3.2), a volcanic event is defined as a point (x, y) in space representing a volcano, and an associated dike having length, azimuth, and location relative to the point event (Figure 12.2-11). The duration of a volcanic event was generally estimated by each expert to be no more than a few years or tens of years (CRWMS M&O 1996, Appendix E [e.g., pp. BC-4, WD-2, RF-2, MK-4, AM-2, GW-2]).

Typical dike dimensions assigned by the experts were a dike width of 1 m and a dike length of 1 to 5 km (0.6 to 3 mi.) (CRWMS M&O 1996, Appendix E). The most likely values for maximum dike lengths were estimated at 17 to 22 km (11 to 14 mi.) (CRWMS M&O 1996, Figure 3-62). The values of maximum dike length represent tails of distributions that have a small impact on the probability of intersection. The aggregate dike-length distribution derived from the PVHA has 5th percentile, mean, and 95th percentile values of 0.6, 4.0, and 10.1 km (0.4, 2.5, and 6.3 mi.) (CRWMS M&O 2000a, Figure 4). The most commonly assigned dike orientation centers around N30°E (CRWMS M&O 1996, Figure 3-62).

The selection of parameter distributions that affect probability models and critiques of alternative conceptual frameworks and parameter selection within the framework of the volcanic history of the Yucca Mountain region are discussed in more detail in CRWMS M&O (2000a, Section 6.3.2).

**Consideration of Tectonic Setting and Models**—Each volcanic expert (Table 12.2-6) considered tectonic setting and models in developing their interpretations of volcanic sources in the Yucca Mountain region. Information on the tectonics of the site area was presented to the experts at two of the workshops associated with the PVHA process (CRWMS M&O 1996, pp. C-12, C-15). Each expert discussed the volcanic and tectonic setting in his elicitation summary (CRWMS M&O 1996, Appendix E). In addition, experts also described how tectonic structure was incorporated into their interpretation of volcanic sources. Tectonic models were employed to the degree that each expert found them useful in characterizing sources of future volcanism. Brief summaries of each expert’s use of tectonic setting and models follows.

Carlson did not see a connection between the tectonic history of post-Miocene extension in the Yucca Mountain region and post-8 Ma volcanism (CRWMS M&O 1996, Appendix E, p. RC-1). He concluded that evidence of clustering was weak and that the distribution of volcanoes appears to be random (CRWMS M&O 1996, Appendix E, p. RC-3). He found that the strongest

evidence of structural control related Crater Flat volcanism, including the Lathrop Wells center, to the area that exhibits the most evidence for extension in the Quaternary (CRWMS M&O 1996, Appendix E, p. RC-5).

Crowe stated that late Miocene and younger basaltic volcanism in the Yucca Mountain region can be attributed to partial melting of a hydrous upper mantle that may or may not be related to low rates of surface extension (CRWMS M&O 1996, Appendix E, p. BC-1). He also indicated that in less active regions of the southern Great Basin, such as at Yucca Mountain, it is difficult to relate centers of basaltic volcanism to individual faults or tectonic features (CRWMS M&O 1996, Appendix E, p. BC-3). Zones based on the observed distribution of past activity and zones based on structural control comprised his interpretation of sources for future volcanism. A pull-apart basin, the northwest-trending Walker Lane, and a northeast-trending structural model formed the basis for those zones based on structural control (CRWMS M&O 1996, Appendix E, pp. BC-10 to BC-12, Figure BC-1).

Duffield noted that, in the Yucca Mountain region, Quaternary volcanic deposits appear to be located along the northeastern boundary of the Walker Lane structural zone (CRWMS M&O 1996, Appendix E, p. WD-1). He also stated that for determining where volcanoes will occur within the near geologic future, knowledge of the magma-generating process was less important than a knowledge of where Quaternary volcanoes have occurred. His interpretation of volcanic sources relied primarily on the locations of Quaternary volcanoes. A secondary factor was the location of the Walker Lane (CRWMS M&O 1996, Appendix E, p. WD-3, Figure WD-1).

Fisher determined that basaltic volcanism in the Yucca Mountain region is the result of regional extension (CRWMS M&O 1996, Appendix E, p. RF-1). He identified a Crater Flat and a Sleeping Butte field which were used as the basis for field shape, spatial smoothing, and zonation approaches to defining volcanic sources. While the identified fields did not include Yucca Mountain, their boundaries were defined probabilistically for the first two approaches (CRWMS M&O 1996, Appendix E, p. RF-3). Fisher related the fields to magma ascent processes (CRWMS M&O 1996, Appendix E, p. RF-4 to RF-5). He interpreted the Walker Lane to have little significance with respect to local volcanism (CRWMS M&O 1996, Appendix E, p. RF-4).

Hackett found that locations of post-caldera basaltic volcanism were influenced by regional extension and north-trending, fault-bounded structural depressions (CRWMS M&O 1996, Appendix E, p. WH-1). He concluded that the most likely locations of future volcanism should be those areas where young volcanoes have erupted in the past (CRWMS M&O 1996, Appendix E, p. WH-2). Volcanic source zones were defined based on the distribution of past volcanism for different time periods, with the zone based on the past 1 m.y. being given the highest weight (CRWMS M&O 1996, Appendix E, p. WH-4, Figure WH-1).

Kuntz stated that magma delivery to the surface in the Yucca Mountain region might be controlled at depth by a north-south structure such as a deep fault. Alternatively, he noted that the north-south orientation might simply reflect the orientation of the melting anomaly and structural control might be lacking. At shallow depths, Kuntz concluded that near-surface structures affect the orientation of volcanic features (CRWMS M&O 1996, Appendix E, pp. MK-2 to MK-3). Kuntz noted a sharp boundary at the eastern edge of the Crater Flat

volcanic field based on observed volcanism, but a lack of evidence for structural control. He observed that integrated density contrasts might play a role in localizing eruptions (CRWMS M&O 1996, Appendix E, pp. MK-3 to MK-4). Kuntz employed four approaches for defining volcanic sources: a uniform zone, zonation based on the distribution of past basaltic volcanism, spatial smoothing, and field shape. Because of uncertainty in what controls the eastern boundary of the Crater Flat volcanic field, his interpretations allowed for uncertainty in that boundary (CRWMS M&O 1996, Appendix E, pp. MK-6 to MK-7) for the spatial smoothing model.

McBirney determined that deep-seated features control long-term, regional patterns, while shallow structures influence short-term, local behavior. He identified a number of structural settings that he qualitatively ranked in terms of frequency of future eruptions (CRWMS M&O 1996, Appendix E, pp. AM-1, AM-4, AM-5). He noted that evidence indicates the Crater Flat area is a pull-apart basin bounded on the west by the Bare Mountain fault, but with the eastern boundary more difficult to define (CRWMS M&O 1996, Appendix E, p. AM-3). McBirney employed two approaches to defining volcanic sources: a zonation approach and a spatial smoothing approach. For the zonation approach he identified zones based on tectonic and structural features including a pull-apart basin, intersections of strike-slip faults, caldera ring fractures or radial fractures, fault-bounded blocks of uplifted basement, and large, transcurrent fault systems (CRWMS M&O 1996, Appendix E, pp. AM-4 to AM-5).

Sheridan emphasized the concept of volcanic fields. He noted that near-surface faults do not play a major role in the location of volcanic fields, but that they may influence the locations of vents and cones (CRWMS M&O 1996, Appendix E, pp. MS-1 to MS-2). Sheridan used both the field-shape and zonation approaches to defining volcanic sources (CRWMS M&O 1996, Appendix E, p. MS-4).

Thompson observed that the Yucca Mountain region is located at the boundary between the Basin and Range province, characterized by extension, and the Walker Lane, characterized by oblique-normal and strike-slip movement. He noted that both dike emplacement and normal faulting are mechanisms to accommodate extension and areas where there is evidence that these mechanisms have been operating recently are the most favorable sites for future volcanism (CRWMS M&O 1996, Appendix E, pp. GT-1 to GT-2). Thompson used a zonation approach for defining volcanic sources and discriminated between a zone in which volcanism is predominant and one in which Quaternary normal faulting is predominant. Uncertainty in the eastern boundary of the volcanic zone was accommodated by assigning some weight to an interpretation that the boundary is transitional (CRWMS M&O 1996, Appendix E, pp. GT-4, GT-5).

Walker inferred that the Crater Flat volcanic zone is underlain by a melting anomaly in the mantle. He observed that structural control is indicated by the alignment of volcanic cones, but noted that it was difficult to assess whether the orientation was due to structural control or the shape of the melting anomaly. Walker concluded that the Death Valley-Pancake Range volcanic belt, which includes the Crater Flat volcanic zone, could reflect the shape of a melting anomaly or some sort of tectonic line, such as a deep-seated fault (CRWMS M&O 1996, Appendix E, p. GW-1). In defining volcanic sources, Walker emphasized spatial smoothing and field-shape approaches, but also included a zonation approach. For the spatial smoothing approach, he indicated that 90 percent of the probability density should lie within the Crater Flat volcanic

zone, reflecting the observed activity over the past 5 m.y., but allowing some probability that future volcanism will occur outside the zone (CRWMS M&O 1996, Appendix E, pp. GW-3, GS-4).

In summary, the experts generally found that a deep-seated melting anomaly determined the location of the volcanic field in the Yucca Mountain vicinity. Some experts concluded that crustal structures might control the location of volcanic vents and cones at the surface. The greatest weight was given to spatial models based on the locations of past volcanic activity, with spatial smoothing, field shape, and zonation approaches being used. Because of uncertainty in the eastern boundary of zones defined on the basis of Crater Flat volcanism, a number of experts developed interpretations that incorporated uncertainty in that boundary.

**PVHA Results**—Although the PVHA assumed volcanic events to have both an extrusive and intrusive component (volcano and dike), the output of the PVHA was the annual frequency of intersection of the potential repository footprint by an intrusive basaltic dike (CRWMS M&O 1996, Section 4.3). The PVHA did not calculate the conditional probability that a dike intersecting the repository footprint would result in an extrusive volcanic eruption through the repository. The latter probability, which was developed subsequent to the PVHA, is discussed in Section 12.2.6.2.

Each of the 10 experts independently arrived at a probability distribution that typically spanned about two orders of magnitude of the annual probability of intersection. From these individual probability distributions, an aggregate probability distribution was computed that reflects the uncertainty across the entire expert panel (CRWMS M&O 1996, Figure 4-32). The distributions were combined using equal weights to obtain a composite distribution. The mean value of the aggregate probability distribution is  $1.5 \times 10^{-8}$  intersections/year, with a 90 percent confidence interval of  $5.4 \times 10^{-10}$  to  $4.9 \times 10^{-8}$  (CRWMS M&O 1996, Section 4.3). The composite distribution spans about three orders of magnitude of intersection frequency. The computed mean frequency of intersection for the individual experts' models spans about one order of magnitude, indicating that most of the uncertainty in characterizing the hazard arises from uncertainty in defining the parameters of the hazard model rather than from differences in scientific interpretations. The probability distribution arrived at by the PVHA accounted for undetected events (buried volcanic events or intrusive events that never reached the surface). The undetected event frequency ranged from one to five times that of observed events, with most estimates in the range of 1.1 to 1.5 (CRWMS M&O 1996, Figure 3-62).

The PVHA results indicate that the statistical uncertainty in estimating the event rate is the largest component of intra-expert uncertainty (CRWMS M&O 1996, Figure 4-33). The next largest uncertainty is uncertainty in the appropriate spatial model. Other important spatial uncertainties include the spatial smoothing distance, the time period of interest, event counts at the northwest Crater Flat center, and the frequency of hidden events (CRWMS M&O 1996, Figure 4-33).

**Alternative Estimates of the Intersection Probability**—Several alternative estimates of the intersection probability have been presented between 1982 and 1998 (see Table 12.2-7). Most of the published intersection probabilities, including the mean intersection probability estimated in the PVHA, cluster at values slightly greater than  $10^{-8}$ , indicating that this probability estimate is

fairly robust, given the range of alternative temporal and spatial models considered in probability calculation.

#### **12.2.6.2 Recalculated Probabilities**

Results of the PVHA (CRWMS M&O 1996, Section 4.3) have been recalculated to account for the current footprint of the potential repository (Enhanced Design Alternative II Design B, CRWMS M&O 1999) and extended to include the probability of an eruption within the repository footprint, conditional on a dike intersection (CRWMS M&O 2000a, Section 6.5). Figures 12.2-12 and 12.2-13 show the updated individual probability distributions and aggregate probability distribution for the intersection of a basaltic dike with the repository, based on current configurations. Figure 12.2-14 shows the spatial distribution of the volcanic hazard defined by the PVHA expert interpretations. Part (a) shows a map of the frequency of occurrence of volcanic events as defined above. Plotted at each point on the map is the average frequency of volcanic events occurring at that location. The potential repository lies outside the region of highest event frequency (Crater Flats region to the west) but near enough to possibly be affected by dikes generated within this region. The estimated rate of volcanic events in the location of the potential repository is lower than that in Crater Flat but higher than that in regions to the east. Part (b) shows a map of the contributions to the frequency of intersecting the repository by a basaltic dike. Plotted at each point on the map is the frequency of volcanic events occurring at the location that produce dikes that intersect the repository. There is a large contribution to the frequency of dike intersection from potential volcanic events in Crater Flat. There is also a large contribution from potential volcanic events in the immediate vicinity of the potential repository.

In order to evaluate the effects of a volcanic event within the potential repository, information is needed on the length and orientation of the intersecting dike and the probability that an eruptive center (the vent above the conduit feeding an erupting volcano) forms within the repository footprint. CRWMS M&O (2000a, Section 6.5) develops these assessments. The calculation of conditional distributions for the number of eruptive centers within the repository footprint requires an assessment of the number of eruptive centers associated with a volcanic event and the spatial distribution for eruptive centers along the length of the dike. The PVHA experts were not asked to make this assessment as part of their characterization of the volcanic hazard. However, the number of eruptive centers associated with a volcanic event can be derived from the PVHA experts' evaluation of the number of volcanic events that have occurred in the Quaternary using the following assumptions:

- The mapped Quaternary volcanoes in the Yucca Mountain region are representative of the type being characterized for calculation of the consequences of an eruptive event through the potential repository. In particular, each volcano consists of at least one vent where a subsurface conduit intersects the ground surface.
- Each hypothetical volcanic event for which the associated dike intersects the potential repository has at least one eruptive center located somewhere along the length of the dike.

- The location of an eruptive center along the length of a dike or dike segment is defined by a uniform probability distribution.

CRWMS M&O (2000a, Section 5) notes that the latter two assumptions are conservative in that they produce the maximum frequency of occurrence of eruptive centers and allow for the occurrence of multiple eruptive centers within the potential repository.

The length of intersection within the footprint of the potential repository compared to the total length of the dike, the number of eruptive centers per volcanic event, and the spatial distribution of eruptive centers along the length of the dike provide the bases for assessing the frequency with which one or more eruptive centers will occur within the repository footprint (CRWMS M&O 2000a). There are alternative ways to apply the assumptions regarding the number or eruptive centers per volcanic event and the spatial distribution of eruptive centers along the length of the dike. In keeping with the concept of uncertainty characterization employed in the PVHA, these alternatives were used to develop alternative assessments of the conditional distribution for the number of eruptive centers within the repository footprint. These were then combined using relative weights assigned to each to produce a composite assessment. Weights assigned to each model were derived by separately examining the three issues addressed by the alternative approaches (CRWMS M&O 2000a, Section 6.5.2.2, pp. 88 to 89).

The resulting values for the recalculated annual frequency of intersection of the potential repository footprint by a dike associated with a volcanic event and the annual frequency of a volcanic event producing one or more eruptive centers within the repository are presented in Table 12.2-8. The values listed in Table 12.2-8 are the weighted combination of the alternative models for eruptive centers (CRWMS M&O 2000a, Section 7.0). The recalculated values for intersection are very similar to those for the original PVHA (Section 12.2.6.1), indicating that the analysis is insensitive to minor changes in the potential repository footprint.

Conditional distributions for the length and azimuth of the intersecting dike and the number of eruptive centers occurring within the potential repository footprint have been developed for the six values of frequency of intersection in Table 12.2-8 (CRWMS M&O 2000a, Section 6.5.3.2). These distributions are very similar for all six conditions. The alternative models for specifying the number and spatial distribution for eruptive centers associated with a volcanic event have relatively small effects on the conditional distribution for the number of eruptive centers occurring within the repository footprint.